

Multi-channel field theory and two-point correlations for the BEC-BCS crossover

- Dissertation -

Nikolai Kaschewski

October 2026

RPTU Rheinland-Pfälzische Technische Universität Kaiserslautern Landau

Multi-channel field theory and two-point correlations for the BEC-BCS crossover

Dissertation

Nikolai Kaschewski

Vom Fachbereich Physik der Rheinland-Pfälzischen Technischen Universität
Kaiserslautern-Landau zur Verleihung des akademischen Grades
"Doktor der Naturwissenschaften" genehmigte Dissertation

Betreuer: **Priv.-Doz. Dr. Axel Pelster**
Zweitgutachter: **Prof. Dr. James R. Anglin**

Datum der wissenschaftlichen Aussprache:
13. October 2026

DE-386

This page has been intentionally left blank

Abstract

The crossover from the Bose-Einstein condensation (BEC) regime to the Bardeen-Cooper-Schrieffer (BCS) regime is realised in many systems in nature. This ranges from the superfluidity of heavy nuclei, over superconducting electrons in metals and cold atomic gases slightly above absolute zero, to stellar remnants like neutron stars. All these systems share one common property, namely that they exhibit, at least partially, the BEC to BCS crossover. For this reason, ultracold Fermi gases represent an important experimental platform, serving as quantum simulators of systems far beyond laboratory setups. In order to guarantee a transfer of knowledge and results between different physical systems, a deeper theoretical understanding of ultracold Fermi gases is indispensable. Against this background, the goal of this thesis is to develop a theoretical framework for consistently describing ultracold Fermi gases. To this end, the present thesis works out two genuine improvements to the already well-established theory of the BEC to BCS crossover.

In the first part, we point out an ambiguity in the standard field-theoretical description of the BEC-BCS crossover, which is rooted in an arbitrary choice of interaction processes. Any two-particle interaction can be exactly expressed as three different virtual processes, known as Hartree (direct), Fock (exchange) and Bogoliubov (pairing) channels. The choice of channels decides the qualitative set of effects explained, and most theories rely either on selecting exactly one channel or an arbitrary mixture of multiple channels. To resolve this ambiguity, we partition the interaction and let the system decide, by minimising the energy, how likely each process is in every scattering event. The resulting *Weighted Hartree-Fock-Bogoliubov* theory turns out to include effects beyond the standard universal Fermi gas. Namely, it becomes necessary to introduce the effective range as a new system parameter in order to solve another long-standing issue related to divergent ground-state energies due to the Hartree channel. With this, we find in a mean-field description for a three-dimensional Fermi spin mixture that the superfluid phase splits into two phases, one supporting and the other not supporting the Hartree channel. This is an important advancement, since we are now able to glimpse beyond the simplified description with vanishing effective range, which has been known so far for ultracold gases. This is certainly relevant in extreme environments like nuclei or neutron stars, as there the mean-particle distance is of the order of the effective range.

In the second part of the thesis, we present another improvement where we include, for the sake of simplicity, only the Bogoliubov channel. There, we consider two-point correlation functions to explain recent experimental breakthroughs by developing a quantum gas microscope in the continuum. By imposing general symmetry requirements like the Pauli principle for Fermi systems, we obtain basic constraints on fermionic density-density correlation functions. Those constraints lead to an equation of state which differs from the thermodynamic equation of state. We apply the resulting theory to a two-dimensional Fermi spin mixture in the ground state, closely resembling experimental setups. With this, we verify that our beyond-mean-field description not only agrees with the Pauli principle, but also explains experimentally observed anti-correlation effects of opposite-spin fermions. This effect lacked a physical explanation so far, which we provide by tracing them back to the contributions of irreducible Feynman diagrams on the correlation functions, which emerge naturally within our theory.

In conclusion, this thesis presents formal improvements for the theoretical description of the BEC to BCS crossover in ultracold Fermi gases. In particular, we suggest two generalisations of the standard approach which are, in principle, straightforward to apply to any system exhibiting BEC to BCS crossover physics. Furthermore, we show that our

findings not only provide a consistent description but that they are also explain recent experimental findings.

Kurzzusammenfassung

Der Übergang von einem Bose-Einstein-Kondensations (BEK) Regime in ein Bardeen-Cooper-Schrieffer (BCS) Regime findet sich in vielen unterschiedlichen Systemen in der Natur. Diese erstrecken sich über die Supraflüssigkeit schwerer Atomkerne, über supraleitende Elektronen in einem Metall und kalte atomare Quantengase nahe am absoluten Temperaturnullpunkt bis zu den Überbleibseln schwerer Sterne wie beispielsweise Neutronensternen. All diese Systeme haben die gemeinsame Eigenschaft, dass sie, zumindest teilweise, einen Übergang von dem BEK- zu dem BCS-Regime erlauben. Aus diesem Grund stellen ultrakalte Fermi-Gase eine wichtige experimentelle Plattform dar, da sie als Quantensimulatoren im Labor dienen, um die zuvor genannten Systeme zu simulieren. Es ist daher von enormer Wichtigkeit, ein tiefes Verständnis dieser Systeme zu besitzen, um einen reibungslosen Transfer von Erkenntnissen zwischen den einzelnen Systemen zu ermöglichen. Vor diesem Hintergrund ist das Ziel der vorliegenden Arbeit, einen theoretischen Rahmen zu entwickeln, um ultrakalte Fermi-Gase konsistent zu beschreiben. Um dies zu erreichen, präsentiert die vorliegende Arbeit zwei originelle Erweiterungen der bereits seit langem etablierten Theorie des BEK-BCS-Übergangs.

Im ersten Teil wird daher zunächst auf eine willkürliche ad-hoc-Annahme verwiesen, die in der Literatur üblich ist und eine Wahl von Streuprozessen beinhaltet. Jede Wechselwirkung zweier Teilchen kann exakt durch drei virtuelle Prozesse beschrieben werden, welche als Hartree (Direkt), Fock (Austausch) und Bogoliubov (Paarbildung) Kanäle bekannt sind. Die Wahl eines Kanals schränkt die Menge an qualitativ beschriebenen Phänomenen einer Theorie drastisch ein. Allerdings beruhen die meisten Ansätze darauf, mit physikalischer Intuition einen Kanal auszuwählen, oder Kanäle willkürlich aufzuteilen. Um diese Willkürlichkeit zu eliminieren, wird in dieser Arbeit die Wechselwirkung zwischen den Kanälen aufgeteilt, wonach das System durch Minimierung der Energie selbst entscheidet, wie relevant jeder Kanal im Einzelnen ist. Die so resultierende *gewichtete Hartree-Fock-Bogoliubov* Theorie beinhaltet physikalische Effekte, die über das bekannte, universelle Fermi-Gas hinausgehen. Es erweist sich als notwendig, die sogenannte effektive Reichweite als neuen Systemparameter in Betracht zu ziehen und damit ein lange bekanntes Problem der divergenten Grundzustandsenergie durch den Hartree-Kanal zu lösen. In Molekularfeldnäherung stellt sich heraus, dass sich die supraflüssige Phase in zwei neue Phasen aufteilt, wobei eine Phase den Hartree-Kanal erlaubt, die andere jedoch nicht. Diese Erkenntnis ist von Bedeutung, da so der Einfluss von Effekten untersucht werden kann, die über die naive Beschreibung mit verschwindender effektiver Reichweite hinausgehen. Dies ist sicherlich für die Beschreibung von Neutronensternen und Atomkernen relevant, da dort die mittlere Distanz zwischen den Teilchen von derselben GrößSenordnung wie die effektive Reichweite ist.

Im zweiten Teil der Arbeit wird eine weitere Verbesserung vorgestellt, die sich der Einfachheit wegen auf nur den Bogoliubov-Kanal beschränkt. Es werden Korrelationsfunktionen untersucht, um so kürzlich gewonnene, experimentelle Erkenntnisse zu erklären, die durch die Entwicklung der Quantengasmikroskopie im Kontinuum gewonnen wurden. Durch die Forcierung von allgemeinen Symmetrieregeln wie des Pauli-Prinzips für Fermionen werden bestimmte Einschränkungen für fermionische Dichte-Dichte Korrelationsfunktionen etabliert. Dies führt zu einer Zustandsgleichung, welche sich von der thermodynamischen Zustandsgleichung unterscheidet. Die so entwickelte Theorie wird auf eine zweidimensionale Fermi-Spin-Mischung im Grundzustand angewandt, was der experimentellen Realisierung nahe kommt. Damit wird die Beschreibung jenseits der Molekularfeldnäherung verifiziert, was zeigt, dass die hier präsentierte Theorie in der

Lage ist, die beobachteten Antikorrelationen von Fermionen unterschiedlichen Spins zu erklären. Bisher wurde keine theoretische Erklärung dieser Antikorrelationen vorgestellt, was in dieser Arbeit durch eine Analyse der zugrunde liegenden irreduziblen Feynman-Diagramme jedoch erstmalig gelingt.

Zusammenfassend stellt die vorliegende Dissertation formale Erweiterungen der Theorie des BEK-BCS-Übergangs in ultrakalten Fermi-Gasen dar. Insbesondere werden zwei Verallgemeinerungen der bereits etablierten Theorie vorgestellt, welche prinzipiell einfach auf andere Systeme anzuwenden sind, die ebenfalls den BEK-BCS-Übergang erlauben. Ferner zeigt diese Arbeit, dass die zugrunde liegenden Verallgemeinerungen nicht nur in sich konsistent sind, sondern auch in der Lage sind, jüngste experimentelle Erkenntnisse korrekt zu beschreiben.

Contents

Abstract iii

Kurzzusammenfassung v

Contents vii

List of Publications ix

List of Figures xi

List of Tables xiii

List of Abbreviations xv

1 Introduction 1
- 1.1 Superconductivity . . . 2
- 1.2 Superfluidity . . . 5
- 1.3 Fano-Feshbach resonances . . . 8
- 1.4 BEC-BCS crossover . . . 11
- 1.5 Fermi superfluids in extreme environments . . . 14
- 1.6 Summary of superfluid systems . . . 17
- 1.7 Outline of thesis . . . 18

2 Theory of superfluids 23
- 2.1 Phenomenological theories for superfluids . . . 23
- 2.2 BCS and Leggett BEC-BCS crossover theories . . . 27
- 2.3 Functional integral approach to BEC-BCS crossover . . . 30
- 2.4 Diagrammatic approach to BEC-BCS crossover . . . 36
- 2.5 Arbitrariness of approaches . . . 39

3 Weighted Hartree-Fock-Bogoliubov theory 41
- 3.1 Introduction . . . 42
- 3.2 Decomposing interactions . . . 42
- 3.3 Saddle-point analysis of WHFB action . . . 53
- 3.A More general Hubbard-Stratonovich transformations . . . 58

4 Three-dimensional Fermi spin-mixtures 65
- 4.1 Introduction . . . 66
- 4.2 Scattering Renormalization in three dimensions . . . 66
- 4.3 Ground state properties . . . 71

4.4 Thermodynamics of WHFB ground state . . . 86
4.5 Impact of Thermal fluctuations . . . 95
4.A Calculating the Cooper pair size . . . 102
4.B Asymptotic expansions for weak and strong interactions . . . 105

5 Two-point correlation functions 109
5.1 Introduction . . . 110
5.2 Field theory of correlation functions . . . 112
5.3 Linear response theory with gauge fixing . . . 118
5.4 Real-space correlation functions . . . 132
5.5 Anti-bunching of fermions in the continuum . . . 138
5.A Explicit expressions for D-dimensional loop functions . . . 144
5.B Gauge invariance and ladder summation . . . 146

6 Summary 153

7 Outlook 157
7.1 WHFB approach in 2D . . . 157
7.2 Collective modes of WHFB approach . . . 160
7.3 Correlation functions from WHFB theory . . . 164
7.4 Systems with non-singular interactions . . . 165
7.5 Further directions . . . 166

A Field theoretical considerations 171
A.1 Second quantization . . . 171
A.2 Quantum (statistical) field theory . . . 178

B Matsubara summations 191
B.1 Matsubara frequencies . . . 191
B.2 Complex integration contours . . . 192
B.3 Extension: Discrete Matsubara sums . . . 195
B.4 Numerical strategy at $T = 0$ . . . 204

Acknowledgement 207

Selected Schools, Conferences and Stays 209

Curriculum Vitae 211

Bibliography 236

List of Publications

[P1] N. Kaschewski, A. Pelster, and C. A. R. Sá de Melo, "Weighted Hartree-Fock-Bogoliubov method for interacting fermions: An application to ultracold Fermi superfluids", Phys. Rev. Res. **7**, 033186 (2025).

[P2] N. Kaschewski, A. Pelster, and C. A. R. Sá de Melo, "Equal-spin and opposite-spin density-density correlations in the BCS-BEC crossover: Gauge symmetry, Pauli exclusion principle, Wick's theorem, and experiments", Phys. Rev. A **114**, 023323 (2026).

List of Figures

1.1 List of superconductors 4
1.2 Helium-II: Lambda point and phase diagram 5
1.3 Helium phase diagrams 7
1.4 Illustration of Fano-Feshbach resonances 9
1.5 Illustration of BEC-BCS Crossover 11
1.6 Phase diagram of the BEC-BCS crossover 12
1.7 QCD Phase diagram and Neutron star 15
1.8 Different fermionic superfluids 18

2.1 Illustration spontaneous $\mathrm{U}(1)$-symmetry breaking 25
2.2 Mean-Field BEC-BCS Crossover 29
2.3 Feynman Diagrams of pair fluctuations 36
2.4 Feynman Diagrams of particle-hole induced interactions 38

3.1 Hartree-Fok-Bogoliubov Feynman Diagrams 48

4.1 Scattering lengths of ^{6}Li and ^{40}K 69
4.2 Partitioning of the interaction 72
4.3 Ground state phase diagram 73
4.4 Hartree self-energy in the WHFB ground-state 75
4.5 Superfluid order parameter in the WHFB ground-state 76
4.6 Chemical potential in WHFB ground-state 77
4.7 Chemical potential and order parameter at unitarity 82
4.8 Chemical potential in the strong coupling regime of the WHFB ground-state 85
4.9 Free energy of WHFB ground-state 87
4.10 Isothermal Compressibility of WHFB approach 91
4.11 Contact of the WHFB ground-state 92
4.12 Cooper pair size of the WHFB ground-state 94
4.13 Effective range for finite temperatures 96
4.14 Fixed-temperature self-consistent solutions of WHFB theory 97
4.15 Fixed temperature slice phase diagram 98
4.16 Fixed effective range self-consistent solutions of WHFB theory 99
4.17 Fixed range slice phase diagram and critical temperature 100
4.A.1 Contour of pair size integration 103
4.B.2 Illustration of cutting out the Fermi surface 106

5.1 Experimental measurement of density-density correlation functions 111
5.2 Saddle-Point response Feynman diagrams 126
5.3 Building blocks of irreducible diagrams 127

5.4 Diagrammatic representation of pair vertex 128
5.5 Irreducible diagrams in Gaussian fluctuation response tensor 129
5.6 2D BEC-BCS crossover in various approaches 131
5.7 Equal-spin density-density correlation functions of Fermi spin mixture . . 133
5.8 Opposite-spin density-density correlation functions of Fermi spin mixture 134
5.9 Charge density-density correlation functions of Fermi spin mixture 136
5.10 Reducible and irreducible terms in real-space correlation functions 137
5.11 Equal-/opposite spin and charge density-density correlation functions . . 140
5.12 Location and width of correlation holes 142
5.B.1 Diagrammatic representation of GPF grand-canonical potential 147
5.B.2 Derivative rules of Feynman diagrams 148
5.B.3 Feynman Diagrams of GPF number equation 149
5.B.4 Feynman Diagrams of D, K and response functions 150
5.B.5 Feynman Diagrams of mean-square particle number 151

7.1 Self-consistent solutions of WHFB equations in 2D 158
7.2 2D Phase diagram and Tan's contact 159
7.3 Speed of sound in 3D WHFB theory 163

A.1 Fermi and Bose harmonic oscillators 172
A.2 Illustration of discrete and continuous path integration 181
A.3 Wick rotation 186

B.1 Illustration of Matsubara summation contour in complex plane 193
B.2 Illustration of Matsubara transformation for finite time steps 197
B.3 Convergence of Matsubara sums at $T = 0$ 205

List of Tables

1.1 Literature values for some known magnetic s-wave Fano-Feshbach resonances, including the scattering states as well as position B_0, width Δ and background scattering length a_{BG}, and broadness parameter a_{bg}/R^* of the Fano-Feshbach resonances. We underline the resonances relevant for this thesis in the first column. 10

2.1 Typical values for Debye temperature Θ_{D}, critical temperature T_{c} and relative temperature $T_{\mathrm{c}}/\Theta_{\mathrm{D}}$ of some pure metal superconductors. 28

4.1 Typical values for ^{6}Li and ^{40}K in ultracold setups. We mentioned the experimental peak densities $\overline{n_0}$ in $3D$ harmonic traps in the first line. In the last line we calculated the effective range parameter $k_{\mathrm{F}} r_{\mathrm{e}}$. 68

5.1 Table for different cases covering distinct levels of approximation, depending on the preservation (✓) or violation (×) of gauge invariance (Gauge) and the Pauli exclusion principle (Pauli). The corresponding line styles for figures 5.7, 5.8, 5.9, 5.11 and 5.12 are indicated as well. 132

5.2 Comparison of parameters used in numerical evaluation of correlation functions in Fig. 5.11 and experimental parameters found when evaluating the data and used for the auxiliary field Quantum Monte-Carlo (QMC) calculation [187]. We present the values sorted by the columns of Fig. 5.11 and give theoretical and experimental values of scattering parameter $\ln k_{\mathrm{F}} a$, binding energy ε_{B} in units of ε_{F} and temperature. The temperature used in our theoretical evaluation is always $T^{\mathrm{theo}} = 0$. 139

List of Abbreviations

BEC Bose-Einstein Condensate

BCH Baker-Campbell-Hausdorff

BCS Bardeen-Cooper-Schrieffer

BKT Berezinskii-Kosterlitz-Thouless

CFL Colour-Flavour locking

CSC Colour superconductor

CQGMs continuous quantum gas microscopes

DMD Digital Mirror Device

DoF Degree of Freedom

EoS Equation of State

FFLO Fulde-Ferrell-Larkin-Ovchinnikov

GL Ginzburg-Landau

GMB Gor'Kov Melik-Barkhudarov

GPF Gaussian Pair Fluctuations

HFB Hartree-Fock-Bogoliubov

HS Hubbard-Stratonovich

HSF Hartree Superfluid

LSE Lippmann-Schwinger Equation

NSR Nozières and Schmitt-Rink

PR Pauli-respecting

RPA Random-Phase-Approximation

SP Saddle-Point

SSF Standard Superfluid

QCD Quantum Chromodynamic

QMC Quantum Monte-Carlo

UV Ultra-violet

WHFB Weighted Hartree-Fock-Bogoliubov

Chapter 1

Introduction

> It is important to do everything with passion, it embellishes life enormously.
>
> Lev Landau in a letter to his niece

1.1 Superconductivity . . . 2
1.1.1 Discovery of superconductivity . . . 2
1.1.2 Bardeen-Cooper-Schrieffer theory . . . 3
1.2 Superfluidity . . . 5
1.2.1 Discovery of superfluidity in liquid Helium . . . 5
1.2.2 Properties of conventional superfluids . . . 6
1.2.3 Superfluid ^{3}He: A fermionic superfluid? . . . 7
1.3 Fano-Feshbach resonances . . . 8
1.3.1 Atomic scattering . . . 8
1.3.2 Broad and narrow resonances . . . 10
1.4 BEC-BCS crossover . . . 11
1.5 Fermi superfluids in extreme environments . . . 14
1.5.1 Superfluids of subatomic particles . . . 14
1.5.2 Astrophysical superfluids . . . 16
1.6 Summary of superfluid systems . . . 17
1.7 Outline of thesis . . . 18

In this chapter, we present a detailed introduction into the topic of this thesis. First, we briefly summarise two key topics of macroscopic quantum phenomena, namely superconductivity and superfluidity. Following this, we present a concise outline for Fano-Feshbach resonances, which enables us to directly tune interactions in quantum many-body systems. This mechanism allows the two effects of superconductivity and superfluidity to culminate in the emergence of the crossover between Bose-Einstein Condensate (BEC) and Bardeen-Cooper-Schrieffer (BCS) regimes, which is the main topic of this thesis. Following this, we discuss Fermi superfluids in extreme environments. Although this thesis deals with the BEC-BCS crossover in the context of cold quantum gases, the end of this chapter provides a broad overview of fermionic superfluids over all scales. Lastly, we will outline the further content of this thesis.

1.1 Superconductivity

Even though this thesis deals with superfluids, a historical overview of the topic should nevertheless start with the theory of superconductivity. This is because many concepts developed for superconductors were later transferred to Fermi superfluids.

1.1.1 Discovery of superconductivity

At the turn of the 19^{th} century, J. Dewar and J. Fleming speculated that *'the electrical specific resistance of all pure metals will probably vanish at the absolute zero of temperature'* [1]. Even though later measurements made them revoke this statement, the idea of a vanishing electric resistance was in the world. About two decades later, in 1911, H. K. Onnes managed to cool a mercury sample below the boiling point of liquid ^{4}He, observing that the resistance of the probe abruptly dropped below the accuracy of his measurement device. He baptised this phenomenon *'supraconductivity'*, which later was adapted to become the familiar terminus of *superconductivity*. As such, Onnes disproved the rule of Matthiessen that the resistance of a metal at low temperatures should be of the form

$$\rho(T) = \rho_0 + \Delta\rho(T). \tag{1.1}$$

He not only showed that, for mercury, we have $\rho_0 = 0$, but also that $\Delta\rho(T)$ has to abruptly jump at a critical temperature $T_\text{c} \approx 4.2\ \text{K}$. In a subsequent experiment, Onnes showed that currents, once started in a superconductor, do not vanish when the voltage is switched off, a phenomenon which is known as persistent current. Onnes was awarded the Nobel Prize in physics in the year 1913 *'for his investigations on the properties of matter at low temperatures which led, inter alia, to the production of liquid helium'* [2]. From a viewpoint over 100 years in the future, it seems odd that the discovery of liquid helium was awarded rather than that of superconductors. At the time, the Nobel Committee thought differently.

The discovery of superconductivity led to a surge of interest in the theory of electric conduction, where people began to doubt the established explanations. Even A. Einstein speculated, shortly after developing the general theory of relativity, that superconductors are caused by closed chains of molecules [3]. This idea seems at least unconventional now, but at the time, without any knowledge of quantum many-body theory, it seemed like a reasonable explanation. Many ideas were proposed, even before it was discovered that a superconductor is not just an ideal conductor.

In 1913, lead was shown to be superconducting with a critical temperature of $7\ \text{K}$. Based on this discovery, W. MeiSSner and R. Ochsenfeld investigated the magnetic properties of a lead sample in 1933. They realised that below the critical temperature, the lead sample completely expelled the magnetic field [4], rendering it a perfect diamagnet. In analogy, this is sometimes called superdiamagnetism. It turned out that this so-called MeiSSner-Ochsenfeld effect only occurs for sufficiently low magnetic fields $\boldsymbol{H}$. In fact, there is a critical magnetic field above which a given metal is in a normal conducting state, which depends on the temperature in a generic form [5]

$$H_\text{c}(T) = H_0\left[1 - \left(\frac{T}{T_\text{c}}\right)^2\right], \tag{1.2}$$

with T_c being the critical temperature when no magnetic field is applied. Already the fact that all of those conventional low-temperature superconductors obey this basic rule tells

us that there must be a universal cause for superconductivity, which is independent of the material. A fundamental understanding of superconductivity emerged in the 1950s, but some previously developed phenomenological theories proved surprisingly accurate.

In 1935, the brothers F. and H. London developed a phenomenological theory based on extending Maxwell's equations of electrodynamics, including a superconducting current [6–8], which was in 1953 expanded towards a non-local theory by A. Pippard and W. Bragg [9]. The most important consequence of the London-Pippard theory is the development of the penetration depth λ_{L}, describing how deep a magnetic field leaks into a superconductor before the total magnetic induction diminishes to zero due to the movement of superconducting electrons. The London-Pippard theory is applicable to homogeneous type-I superconductors, but fails to describe inhomogeneous type-II superconductors.

To tackle type-II superconductors, we have to discuss the Landau theory. It was developed by L. Landau and phenomenologically describes phase transitions by an *order parameter* and a minimisation prescription for the free energy in a system. The Landau theory was able to describe basic properties of the phase transition, even though it was a static approach, i.e. only applicable to type-I superconductors. It was later extended by V. Ginzburg in order to include also spatial variations, i.e. the kinetic energy of the order parameter [10]. Thereafter, A. Abrikosov used this Ginzburg-Landau (GL) theory to describe also inhomogeneous type-II superconductors [11], resulting in the Nobel Prize in 2003 *'for pioneering contributions to the theory of superconductors and superfluids'* [12] for Ginzburg and Abrikosov.

The resulting theory predicts a second characteristic length-scale in the system, the GL coherence length ξ_{GL}. As the name suggests, this length describes the typical distance at which electronic correlations are exhibited. It is thus the scale of possible thermal fluctuations in the superconducting state. With this approach, Abrikosov was able to derive a condition on the ratio of λ_{L} and ξ_{GL} in order to distinguish between type I and type II superconductors. The latter type of superconductors exhibit a variety of 4 different phases, some of which are spatially inhomogeneous. A few years later, L. Gor'Kov also contributed to this approach by deriving the resulting equations from a more microscopic approach to superconductivity [13], namely the Bardeen-Cooper-Schrieffer theory discussed below. For this reason, the GL theory is sometimes referred to as Ginzburg-Landau-Abrikosov-Gor'Kov (GLAG) formulation. In the following, we will outline this more fundamental theory of superconductivity used by Gor'Kov.

1.1.2 Bardeen-Cooper-Schrieffer theory

In the mid-1950s, there were several groups trying to develop a microscopic theory of superconductivity. One approach, which would become important decades later, was the idea that a superconductor is a Bose-Einstein condensate of charged bosons. First suggested by R. Ogg [15], it was then extended by M. Schafroth [16]. This approach of charged bosons was afterwards refined by Schafroth, S. Butler and J. Blatt in 1957 in the sense that two electrons in a superconductor form a tightly bound, molecular-like state [17]. They did show that, as soon as the spatial extent of the di-electrons becomes less than the average distance between electrons, a Bose-Einstein condensate of composite bosons is formed. The pairing is necessary because electrons are fermionic particles and cannot occupy the same quantum state. Schafroth, Butler and Blatt showed that this mechanism explains the MeiSSner-Ochsenfeld effect and the vanishing of the electric resistance [17]. In the end, the attractive interactions mediated by phonons in most solids are too weak to form such

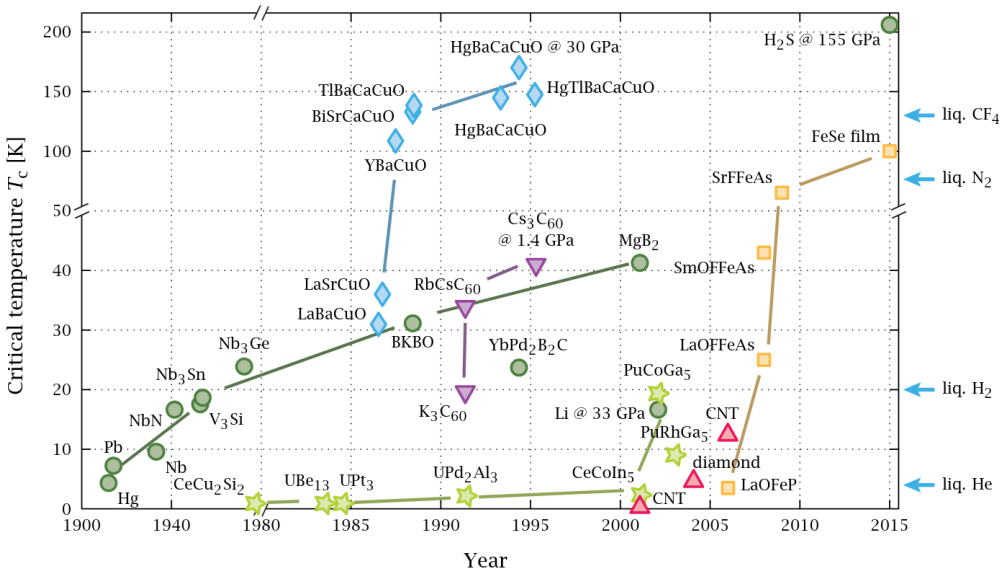


Figure 1.1: Illustration of various superconductors. The x-axis shows the year of their discovery, the y-axis depicts the critical temperature T_c in K. The BCS superconductors are represented by the green circles.
Reprinted from [14] with permission from World Scientific Publishing Co., Inc., permission conveyed through Copyright Clearance Center, Inc. Copyright © 2016, World Scientific Publishing Co., Inc.

tightly bound pairs. Thus, at least in conventional superconductors, this mechanism is not the source of superconductivity. In the end, J. Bardeen, L. Cooper and J. Schrieffer found the solution. Also in 1957, but after the publication of Schafroth *et al.*, they published the famous paper, titled *Theory of superconductivity* [18] following an earlier publication on the same topic [19], in which they explained superconductivity as an effect of large, delocalized pairs of electrons in momentum space, the so-called *Cooper pairs*. This theory could explain all experimentally observed effects, ranging from the Meissner-Ochsenfeld effect to persistent currents due to zero electrical resistance. This milestone was awarded the Nobel Prize in physics in 1972 *'for their jointly developed theory of superconductivity, usually called the BCS-theory'* [20] and is one of the most important developments in many-body quantum theory.

Since the development of the BCS theory, a lot has happened in the field of superconductors. First, every few years, then, since the 1980s, basically every year, new superconductors are discovered, see Fig. 1.1 for an incomplete list. Soon after, so-called high-T_c superconductors were discovered, the first one in 1986 by J. Bednorz and K. Müller [21]. This discovery earned them the Nobel Prize in the subsequent year, *'for their important breakthrough in the discovery of superconductivity in ceramic materials'* [22]. In the same year, their discovery was refined by another group, further increasing the critical temperature to almost 100 K [23]. It turned out quite fast that those high-T_c superconductors are not BCS superconductors. Until today, a theoretical explanation is still missing. Most of those high-T_c systems are complicated oxide systems, so-called cuprates, see the blue diamonds in Fig. 1.1, in contrast to the green circles illustrating BCS systems. The hunt for superconductors with critical temperatures at room temperature subsequently started, driving much of condensed matter physics for decades. It was found that, in general, high pressures allow higher critical temperatures, which reduces the technical applicabil-

ity. Since the 1990s, the highest T_c at atmospheric pressure superconductors are mercury superconductors based on $\mathrm{HgTiBaCaCuO}$ with critical temperatures above $130\ \mathrm{K}$ [24]. The current record-holder at atmospheric pressure is $\mathrm{Hg_{12}Ti_3Ba_{30}Ca_{30}Cu_{45}O_{127}}$, with a critical temperature of $137\mathrm{K}$ [25, 26]. At extremely high pressures of $170\ \mathrm{GPa}$ critical temperatures of up to $250\ \mathrm{K}$ were reached [27]. Irrespective of the pressure, no room temperature superconductor with $T_c > 273\ \mathrm{K}$ has been found, and until today it remains unclear whether such materials can even exist.

In the view of conciseness, we will proceed now with a similar concept, which was discovered 26 years after superconductivity: superfluidity.

1.2 Superfluidity

A phenomenon directly linked with superconductivity is superfluidity. In fact, a superconductor is a special version of a superfluid, namely a charged superfluid of electrons. The topic of this thesis is neutral superfluids. Thus, we now outline the history of superfluidity as well as the discovery of fermionic superfluids.

1.2.1 Discovery of superfluidity in liquid Helium

When ^{4}He is cooled below its boiling point of $T = 4.22\ \mathrm{K}$, it becomes liquid, exhibiting the so-called λ-point when looking at the specific heat [29]. An illustration of this is seen in Fig. 1.2. At atmospheric pressure, this happens at approximately $T_\lambda = 2.1768\ \mathrm{K}$. Below this temperature, one commonly speaks of Helium-II, above this temperature of Helium-I. In the year 1938, first P. Kapitza [30], then later in the same year A. D. Misener and J. F. Allen [31] were able to make a peculiar observation. When Helium enters the state of Helium-II, the viscosity of the liquid suddenly drops below the precision of the measurement device. Even though hints of this sudden reduction of the viscosity were already known since at least 1935 [32], only with Kapitza, Misener and Allen did the consensus arise that the viscosity of liquid ^{4}He vanishes for $T < T_\lambda$. In his paper, Kapitza called Helium a *superfluid*, thereby imprinting the modern name for this phenomenon in 1938. Furthermore, he proposed a connection to superconductors 20 years before the development of the BCS theory of superconductivity [18]. Kapitza ultimately received a half-share of the Nobel Prize in physics in 1978 *'for his basic inventions and discoveries in the area of low-temperature physics'* [33], which is undoubtedly connected to his discovery of superfluidity. Later on, several follow-up experiments were performed [34–36], studying the quite intriguing

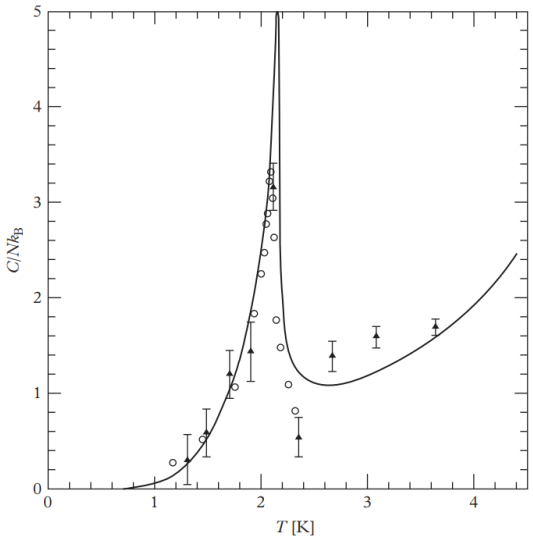


Figure 1.2: Heat capacity of ^{4}He against the temperature in K, the so-called λ-point.
Reprinted from [28] with permission from Oxford Publishing Limited through PLSclear. Copyright © 2016, Oxford Publishing Limited.

properties of ^{4}He, which at the time was the only known superfluid. Still today, almost 90 years after its discovery, superfluid ^{4}He is a material of research interest [37–41]. Simultaneously with those experimental discoveries, theoretical investigations tackled the mystery of Helium-II. First proposals included a diamond-like structure of ^{4}He atoms below the λ-point [42, 43]. However, this was quickly dismissed by F. London [44] and L. Tisza [45] in 1938. They proposed that superfluid ^{4}He shows a macroscopic occupation of the quantum mechanical ground state, a phenomenon described by S. Bose and A. Einstein earlier in 1924/25, now entitled Bose-Einstein condensation [46–48]. As ^{4}He is a bosonic particle, meaning a particle with integer spin, it follows the Bose-Einstein statistics. This means that the average number of particles with energy E is described by

$$\langle n_{\mathrm{B}}(E)\rangle = \frac{1}{e^{\beta(E-\mu)}-1}, \tag{1.3}$$

with $\beta = 1/(k_{\mathrm{B}}T)$ being the inverse temperature and μ the chemical potential.

This consideration of the superfluidity appearing in ^{4}He being rooted in a BEC of the bosonic atoms originates from the observation that the critical temperature of a BEC of ^{4}He turns out to be $T_{\mathrm{BEC}} \approx 2.7$ K, which is of the order of $T_\lambda \approx 2.17$ K. It did not take long until L. Landau developed the phenomenological *two-fluid model* to explain the properties of superfluid ^{4}He. In 1941, Landau published a set of works in which he introduced the phenomenological two-fluid model to describe the superfluidity of Helium-II [49]. The essential idea is that Helium-II consists of two types of atoms, those that are normal fluid and those that are superfluid. He described the superfluid as an ideal liquid without viscosity, and the normal fluid governed by the NavierStokes equations.

Having discussed the early history of superfluid physics, we continue to characterise superfluids in general.

1.2.2 Properties of conventional superfluids

As already mentioned in Sec. 1.2.1, the basic and most known property of superfluids is the loss of internal viscosity. However, the more defining properties, separating it from ideal liquids, are the persistent flow, analogously to the persistent current in a superconductor, and the absence of dissipation, irrespective of the size of the capillary. As outlined in the previous part, Landau described a superfluid phenomenologically using the two-fluid model. He also discovered the Landau criterion, which states that as long as a superfluid flows with a velocity smaller than the Landau critical velocity v_{L}, it cannot absorb energy through excitations. Hence, it retains its velocity, preventing the fluid from slowing down. Furthermore, this is the phenomenological reason a superfluid flows without any viscosity, internal or external. This has been verified on numerous occasions and leads to peculiar phenomena such as the famous fountain effect, in which superfluids flow up a barrier wall [43]. A second important property of superfluids is the quantisation of circulation in the form of quantised vortices. In a classical fluid, the circulation of a vortex can be chosen continuously. So any amount of circulation inserted into the system can lead to a vortex. In a classical fluid, friction dissipates energy, leading to turbulent flow and dissolving the vortex. In a superfluid, this is different. These can only absorb quantised packets of circulation, which leads to the formation of quantised vortices. Those vortices are stable under ideal conditions, as there is no friction in the fluid. Quantised vortices are an important tool to verify superfluidity, as they form a benchmark property of superfluids.

Those properties were all observed in bosonic ^{4}He, which was the only known superfluid at the time. It took another 35 years from the discovery of superfluid ^{4}He until, in

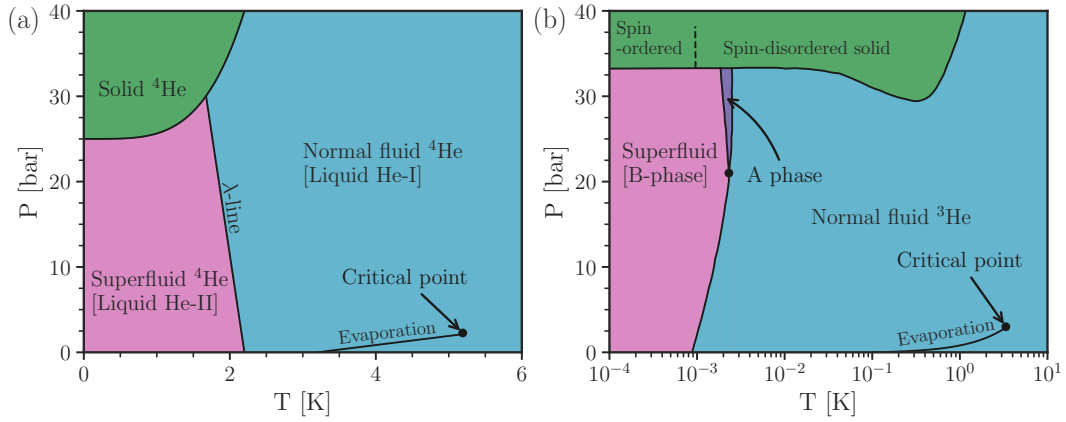


Figure 1.3: Phase diagrams of ^{4}He in panel (a) and ^{3}He in panel (b) in the temperature-pressure plane. Note that the temperature axis is scaled logarithmically in panel (b). Figure produced with data from Refs. [28, 52, 53].

1972, D. Osheroff, R. Richardson and D. Lee showed that also the fermionic counterpart, ^{3}He, possesses a superfluid state [50, 51]. We provide a concise introduction to superfluid ^{3}He in the next part.

1.2.3 Superfluid ^{3}He: A fermionic superfluid?

^{4}He is a bosonic atom, meaning it follows the Bose-Einstein statistics (1.3) due to its integer spin. A phase diagram of ^{4}He is presented in Fig. 1.3 (a), showing the two types, I and II, as well as the high-pressure solid phase of ^{4}He. In contrast, ^{3}He is a fermion. It follows a different statistics, namely the Fermi-Dirac statistics, due to its half-integer spin. Pauli argued [54] that indistinguishable fermions can not occupy the same quantum state. A decade later, M. Fierz derived this property of fermions and bosons mathematically, known as the spin-statistic theorem [55]. In contrast, bosons can occupy identical states which, in the most extreme case, forms a BEC, where a macroscopic number of atoms are in the same quantum state. Therefore, fermions can not form a BEC, and hence the explanation of ^{4}He's superfluidity can not be applied to ^{3}He.

Although electron superconductivity in a solid had already been known and, since 1957, explained by the BCS mechanism [18], a direct connection to superfluid helium was not drawn. However, some theoreticians speculated that similar physics occurs in fermionic ^{3}He, making it superfluid [56, 57], analogously to a BCS superconductor. The experimental issue was cooling the sample to the required temperature to test this hypothesis. Compared to the critical temperature of bosonic Helium, which is at $T_\lambda \approx 2.18$ K, the critical temperature of fermionic Helium turned out to be just $T_c \approx 2.419$ mK, which is four orders of magnitude lower. As mentioned at the start of this section, this was finally possible in 1972 [50, 51], when for the first time knowingly a Fermi superfluid was observed. Lee, Osheroff and Richardson were awarded the Nobel Prize in 1996 *'for their discovery of superfluidity in helium-3'* [58]. In the same year, A. Leggett explained the superfluidity of ^{3}He based on the BCS theory of superconductors [59]. Due to strong interactions, ^{3}He forms triplet pairs rather than standard BCS singlet pairs. This facilitates two superfluid phases, called A and B phases, shown in Fig. 1.3 (b), one of which also shows magnetic order. Thus, unlike conventional superconductors/Fermi superfluids, ^{3}He is an unconventional superfluid. Together with Abrikosov and Ginzburg, Leggett won the

Nobel Prize in 2003 *'for pioneering contributions to the theory of superconductors and superfluids'* [12].

The discovery of Fermi superfluids sparked new interest. Only a few years later, Leggett made one of the most striking developments, based on the works of BCS and Schafroth/Butler/Blatt, which is the BEC-BCS crossover. Before we discuss this phenomenon, we have to address how to tune the interaction strength in the next section.

1.3 Fano-Feshbach resonances

In both ^{4}He and ^{3}He, the interaction properties are fixed and can not be tuned externally. Therefore, it was a remarkable discovery that atomic Fano-Feshbach resonances allow controlling the interaction strengths of cold quantum gases experimentally. Thus, in the following, we describe the mechanism by which this is possible.

1.3.1 Atomic scattering

In order to understand the mechanism behind the BEC-BCS crossover, we first need to understand how to modify the interaction strength of two-particle scattering in a quantum gas. The tool for this is the so-called Fano-Feshbach resonance, developed by H. Feshbach [60] and U. Fano [61], originally used to describe nucleon scattering in atomic nuclei. In cold atomic gases, Fano-Feshbach resonances are described considering two scattering channels, commonly denoted as open and closed channels, corresponding to different internal states of the two-particle wavefunction. Those could be, for instance, different spin configurations, such as singlet/triplet states. The open channel has only scattering states of positive energy compared to two free particles. The closed channel can host at least one bound state with a given energy ε_B. Since we define the zero of the energy with respect to the open channel, this bound-state energy can be positive or negative. For the two channels, an interaction potential is assumed, often a Lennard-Jones potential, but also simplified box potentials are possible [62]. The splitting δE between the two channels in modern quantum gas setups is changed by applying a magnetic induction B, which causes a Zeeman splitting of the two channels. This is why alkali atoms are especially susceptible to tunable interactions via Fano-Feshbach resonances, as they have one electron in the outer shell. Therefore, approaching particles in the open channel couple to the closed channel and, in particular, the bound state, depending on the energy offset δE and on the sign of ε_B. This ultimately changes the scattering length a depending on the applied magnetic induction B which reads [63–67]

$$a(B) = a_\mathrm{bg}\left(1 - \frac{\Delta}{B - B_0}\right). \tag{1.4}$$

Here a_bg is the background scattering length for far detuned B, Δ stands for the width of the resonance, and B_0 represents the resonant magnetic induction when the bound state crosses the closed channel's asymptotic energy. At $B = B_0$, the incoming particles couple resonantly to the bound state, leading to a divergent scattering length. We illustrate the channels in the left column of Fig. 1.4, where the open (solid blue line) and the closed (solid red line) channels are shown versus the distance of the two atoms. The horizontal red line represents the closed-channel bound state. The upper row shows the case when the magnetic induction is so far detuned that the bound state lies above the free state of the scattering particles. During a scattering event, the dressed bound state of this system is

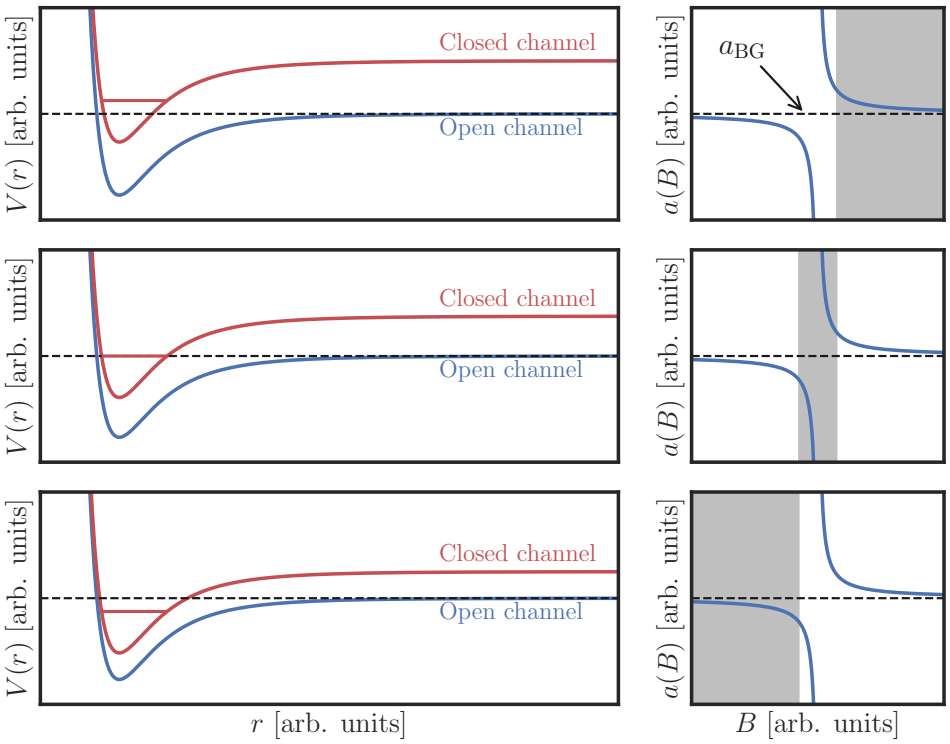


Figure 1.4: Illustration of the concept of Fano-Feshbach resonances. The left column shows the interatomic scattering potentials of open (solid blue line) and closed (solid red line) channels together with the closed-channel bound state for different values of the applied magnetic induction B. The right column depicts the respective regions (grey shaded region) of the scattering length versus the magnetic induction, in which the scattering potentials look schematically as shown to the left. Illustration inspired by Ref. [67]

close to the incoming particle energy and can be populated, thereby forming a bound state. The scattering length, hence, is positive, as shown in the grey region of the right panel. This seems counterintuitive, as a positive scattering length typically indicates a repulsive interaction. This is only partially true, as a positive scattering length also indicates the presence of a true two-body bound state [68]. The middle row shows the situation close to resonance, where $B \approx B_0$. Here, the incoming particles couple strongly to the bound state in the closed channel, leading to a divergence of the scattering length as shown in the middle-right panel. This is due to the resonance being right at the offset of the emergence of a bound state. The divergence can be positive or negative, depending on the bound state energy relative to the asymptotic energy of the open channel. The lower row shows the case where the bound state energy is smaller than the asymptotic energy of a particle in the open channel. In this situation, the particles are off-resonant to the bound state, as the dressed bound state energy is far detuned from the scattering energy. Thus, the bound state is accessed only virtually, leading to weak attractive interactions. Hence, the scattering length is negative as shown in the right panel. The above two-channel model provides a good description of ultracold scattering events, but is challenging to apply. In most practical applications, however, the closed channel is disregarded, and an effective one-channel model is introduced. There, the magnetic induction effectively tunes the depth of the interatomic potential. If no bound state is supported, we have $a < 0$, and conversely, if a bound state appears, there is a sign switch and we find $a > 0$.

Atom	States $\|F, m_F\rangle$	B_0 in G	Δ in G	a_{bg} in a_0	a_{bg}/R^*
^{6}Li [69, 70]	$\|1/2, 1/2\rangle - \|1/2, -1/2\rangle$	832	−262	−1593	27
^{6}Li [65, 71]	$\|1/2, -1/2\rangle - \|3/2, -3/2\rangle$	690	−122	−1727	29
^{6}Li [65, 71]	$\|1/2, 1/2\rangle - \|3/2, -3/2\rangle$	811	−222	−1490	46
^{6}Li [65, 70]	$\|1/2, 1/2\rangle - \|1/2, -1/2\rangle$	543	0.1	59 – 60	8×10^{-4}
^{40}K [65, 72, 73]	$\|9/2, -9/2\rangle - \|1/2, -7/2\rangle$	202	8	174	2.2
^{7}Li [65]	$\|1, 1\rangle - \|1, 1\rangle$	736	−52	−25	0.8
^{39}K [65, 74]	$\|1, 1\rangle - \|1, 1\rangle$	402	−192	−29	2.1

Table 1.1: Literature values for some known magnetic s-wave Fano-Feshbach resonances, including the scattering states as well as position B_0, width Δ and background scattering length a_{BG}, and broadness parameter a_{bg}/R^* of the Fano-Feshbach resonances. We underline the resonances relevant for this thesis in the first column.

Before continuing with the many-body physics, we will briefly discuss the different cases of broad and narrow resonances.

1.3.2 Broad and narrow resonances

We characterise the width of a Feshbach resonance with a parameter R^*, which describes the strength of the coupling between open and closed channels. For $a_{\mathrm{bg}}/R^* \gg 1$ we speak of a broad Feshbach resonance, which means that $a(B)$ changes slowly when changing B, essentially decoupling the closed channel. In those cases, the aforementioned single-channel model is applicable. Such resonances are favourable experimentally because they are easy to control and stable over time scales usually seen in experiments. The opposite case occurs for $a_{\mathrm{bg}}/R^* \ll 1$. Here, the closed channel has to be taken into account explicitly as it strongly couples to the closed channel [67]. Such resonances in general pose a large imaginary value of the scattering length $a(B)$, leading to huge atom losses in an atomic trap, which appear on time scales much shorter than typical timescales found in an experiment. This makes narrow resonances extremely difficult to tackle experimentally and theoretically. Thus, for the remainder of this thesis, we assume a broad resonance and as such $a(B) \in \mathbb{R}$. We mention some prominent resonances in Table 1.1, where we show the element and the respective hyperfine states scattering in the form of $|F, m_F\rangle$, with F denoting the total spin quantum number and m_F the magnetic quantum number, whose energy is addressed by the Zeeman field. Two resonances are in particular interesting for us, i.e. the 832 G resonance of ^{6}Li and the 202 G resonance of ^{40}K, as they have a relatively large resonance width a_{bg}/R^*, making them a broad resonance. Both of those resonances are underlined in Table 1.1. The other two broad resonances of ^{6}Li at 690 G and 811 G might also seem experimentally favourable, however, due to the quantum states used, especially the high total spin quantum number $F = 3/2$ of the first state, makes them impractical. Scattering events here can dissipate energy and lead to spin flips. This changes the state of the excited atom, giving both particles kinetic energy and ejecting them from the trap. Therefore, we will omit them from now on in the discussion. We also show the data for the narrow resonance of ^{6}Li at 543 G as well as for some resonances of bosonic Li and K isotopes.

Having mentioned the basics of Fano-Feshbach resonances, we continue the discussion with the BEC-BCS crossover in the next section.

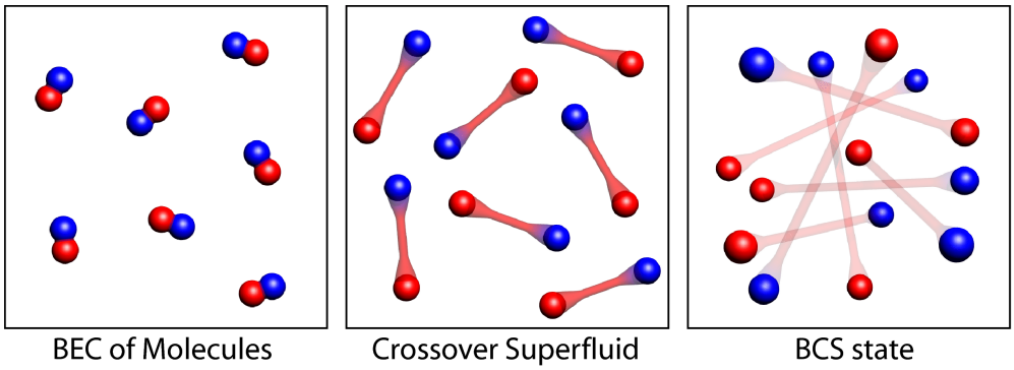


Figure 1.5: Illustration of the BEC-BCS crossover. Left panel depicts the BEC side of closely bound molecules, middle panel represents the crossover, where the size of the Cooper pairs is approximately the mean particle distance. Ultimately, the right panel shows the BCS state, in which large Cooper pairs form.
Figure reprinted from [64] with permission from Springer Nature. Copyright © 2008, Nature Publishing Group.

1.4 BEC-BCS crossover

Building on the two works of BCS [18] and Schafroth, Butler, and Blatt [17], D. Eagles, in 1969, developed a theoretical approach predicting Cooper pairing without the effect of superfluidity [75]. Around a decade later, A. Leggett developed a similar idea concerning liquid ^{3}He [76]. This so-called BEC-BCS crossover should become a vital part of condensed matter physics within the next few decades. The key idea is that, using Fano-Feshbach resonances known from the previous section, atomic interactions can be tuned from weakly to strongly attractive. Weak attractive interactions do not support a two-body bound state but can facilitate a BCS state of many-body bound states, known as Cooper pairs. Tuning the interactions to strong attraction, a two-body bound state emerges. Those bound states, either singlet or triplet states, are energetically favourable and, as such, the fermionic atoms form bosonic molecules. These follow a Bose-Einstein statistic and can form a molecular BEC [77–79]. Since the interaction strength can be tuned continuously, the transition from the BCS to the BEC regime is not an abrupt phase transition, but rather a crossover. Those two asymptotic regimes are separated by the unitary regime, where the scattering length diverges. It exists close to the threshold magnetic induction B_0, where the Feshbach resonance is located. This region is of great theoretical and experimental interest due to the scale invariance occurring when the scattering length diverges. We illustrate the concept in Fig. 1.5, where in the left panel we see the BEC side, where opposite spin fermions, visualised by different colours, pair together to form molecules. There, the average distance between the particles is much larger than the extent of the molecules. In the right panel, we see an illustration of the weakly interacting BCS state, where opposite-spin fermions form pairs with a large spatial extent that exceeds the average distance between the particles. The crossover superfluid is shown in the middle panel, where the size of the fermionic pairs is of the order of the average particle distance. This regime is also denoted as the unitary regime, which we will discuss more at a later point. Over the crossover, the superfluid phase transition happens below a critical temperature, which, from weak to strong interactions, first increases monotonically, after which it stagnates at the critical temperature of a molecular Bose gas.

After Leggett's findings, numerous theoretical investigations were undertaken to un-

derstand the properties of the BEC-BCS crossover. Intensive research efforts were focused on the critical temperature T_c of the superfluid-normal fluid phase transition. Leggett's initial approach, as a mean-field theory, predicts a qualitatively wrong behaviour of T_c away from the BCS regime. This problem was solved in a diagrammatic T-matrix approach by P. Nozières and S. Schmitt-Rink in 1985 [80], by including beyond-mean-field effects in the form of a resummation of certain types of Feynman diagrams, the details of which are beyond the scope of this introduction. They predicted the correct qualitative trend of the critical temperature throughout the whole crossover by preventing the divergent behaviour of T_c on the strongly interacting Bose-Einstein side. Diagrammatic approaches like this have been further developed to date [81–85]. The critical temperature resulting from such an approach is shown in Fig. 1.6 as the solid blue line, in contrast to the Leggett prediction, which is depicted as the solid pink line. The region between those two curves is known as the pseudogap, where incoherent pairs are already formed, but do not lead to a coherent superfluid.

A more formal approach, and the main formalism used in this thesis, was developed at the beginning of the 1990s by C. Sá de Melo, J. Engelbrecht and M. Randeria [87, 88]. In the first publication, they introduced a formal field theoretical approach based on functional integration in order to reproduce the results of Nozières and Schmitt-Rink (NSR) and, following the work of Gor'Kov, derived a time-dependent Ginzburg-Landau theory of the phase transition itself. In the second publication, they tackled another important problem, the $T = 0$ crossover and collective excitations. They found two distinct modes that decouple at small energies and momenta into pure amplitude and phase modes of the order parameter. This gives rise to a gapless phase mode in agreement with the Goldstone theorem [89–91]. Hence, the mode is sometimes referred to as the Goldstone mode. The second mode is a gapped amplitude mode lying inside the pair-breaking continuum. This means that the energy of this mode is so large that it already exceeds the energy needed to break up a pair. Due to the similarity to a Mexican hat potential, this is sometimes called a Higgs mode. However, this is a misnomer, as there are fundamental differences to a Higgs-like mode, like the damping caused by the breaking of Cooper pairs [92] and the absence of a gauge field in a neutral

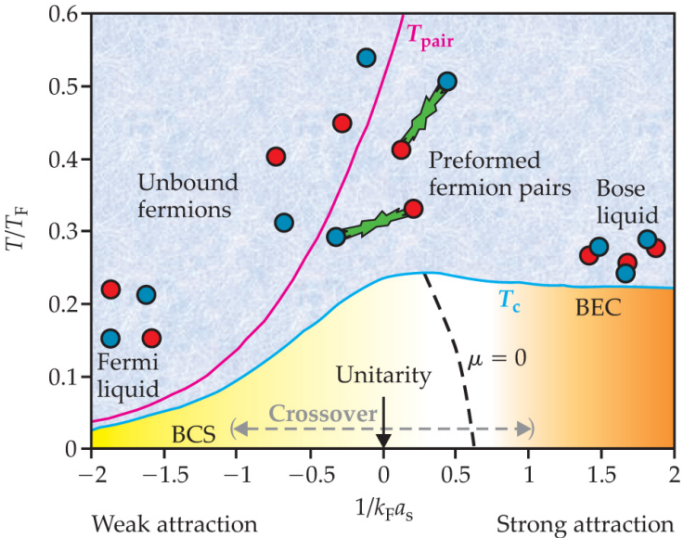


Figure 1.6: Phase diagram of the BEC-BCS crossover. The x-axis denotes the interaction parameter $1/k_F a_s$, with k_F as Fermi momentum, from weak (left side) to strong (right side) interactions. The y-axis shows the dimensionless temperature T/T_F, where T_F stands for the Fermi temperature. The purple line shows the pairing temperature obtained by a BCS mean-field theory, while the blue line shows the actual superfluid phase transition temperature, obtained by including Gaussian pair fluctuations.
Reproduced from [86], with the permission of the American Institute of Physics. Copyright © 2008, American Institute of Physics.

superfluid. Further, for finite momenta, those modes mix, and no pure phase or amplitude mode exists. The formalism in the second publication did not include a depletion of the order parameter due to changes in the density/chemical potential, which was added a few years later in the context of the BEC-BCS crossover in polariton systems [93].

Another important aspect of the theoretical description, especially in the weakly interacting regime, is the change in the interaction strength acting on the order parameter due to the interactions not associated with pairing. This idea was originally intended for superconductors long before the development of the theory of the BEC-BCS crossover by Gor'Kov and T. Melik-Barkhudarov in 1961 [94], following a work on the excitation spectrum [95]. This is called the Gor'Kov Melik-Barkhudarov (GMB) theory. Including those so-called particle-hole fluctuations reduce the critical temperature of a superconductor by a factor of 2.2, which also applies to the weakly interacting regime of the crossover. Even though some efforts were made to unify GMB and NSR approaches for the whole crossover by diagrammatic means [96–100], no formally consistent field-theoretical solution is yet available. In any case, several aspects of the BEC-BCS crossover were subject to extensive theoretical studies over the last decades, including the two-dimensional crossover to study Berezinskii-Kosterlitz-Thouless (BKT) physics [101–108], population-imbalanced Fermi gases [109–119] leading to Fulde-Ferrell-Larkin-Ovchinnikov (FFLO) physics, the excitation spectrum already pointed out earlier [92, 107, 120–130], hydrodynamic properties [131, 132], and vortices [133, 134]. Even superfluids with more than two distinguishable particles, so-called colour superfluids, were investigated [135–138].

Experimental realisations accelerated in the 2000s since reaching the extreme low-temperature regime required to observe the BCS state was not possible earlier. At the beginning of the 2000s, this was finally experimentally achieved due to advances in the control of magnetic fields, tuning the Fano-Feshbach resonances and more efficient cooling methods [73, 139–146]. Those advances led to first publications, claiming to see a superfluid on the BEC side of the crossover in cold atomic gases [147, 148]. Experimental setups were at first limited to inhomogeneous trapping potentials [149–152]. Thus, in those setups the critical temperature including beyond mean-field effects were therefore calculated [153, 154]. In recent years, the use of a Digital Mirror Device (DMD) became more common and easier to implement, therefore also homogeneous traps for Fermi and Bose systems could be realised experimentally [155–159]. This led to a more profound understanding of the BEC-BCS crossover, independent of the trapping potential. In 2010, the first realisation of a two-dimensional (2D) BEC-BCS crossover was achieved, also opening the path to experimentally investigate low-dimensional quantum effects and BKT physics. In this context, in both 2D and 3D, the study of the excitation spectrum provides a vital tool to compare experiment and theory, further strengthening the understanding.

The experimental study of the critical temperature is of particular interest in order to test the predictions of the functional integral/diagrammatic NSR theories as well as the GMB corrections [94]. However, a reliable direct thermometry is not yet generally accepted by the community, although some ideas were put forward, most of which are model-dependent thermometry methods [160–163]. Recently, model-independent machine learning algorithms to determine the T_c were developed in Bonn [164, 165]. However, their training still relies on adiabatic sweep methods [166, 167] and hence might be biased by the sweep itself. A concept worth mentioning is the idea of a quantum engine that utilises quantum statistics to generate work, exploiting the BEC-BCS crossover. This is deeply connected to a quantum theory of thermodynamics, which was experimentally realised as a Pauli engine [168] at the University of Kaiserslautern-Landau. All those

experimental setups deal with locally homogeneous systems, where the spatial potential changes slowly compared to the de-Broglie wavelength.

Furthermore, the internal structure of the BEC-BCS crossover is routinely investigated. Just to mention two prominent examples, the experimental studies of quantum vortices proved to be a quite fruitful playground for investigating degenerate Fermi systems [169, 170], the first undeniable proof of superfluidity in Fermi gases was the observation of lattices of quantised vortices [148]. Moreover, theoretically modelling those quanta of angular momentum has been the subject of intense study [124, 133, 134, 171, 172]. The second selected field of the local structure of the BEC-BCS crossover are N-point correlation functions, with a particular focus on 2-point correlations. Correlation functions yield information about the likelihood of measuring N particles of given internal structure (like spin) at different relative positions. In the case of two-point correlation functions in a homogeneous system, they yield a measure of how likely it is, given a certain particle, to find another particle at a given distance. The theoretical study of correlation functions in the BEC-BCS crossover has been sparse, although some analytical [106, 173–175], purely numerical [176] or QMC calculations [177–179] exist. At the same time, most experimental setups have been limited to the indirect measurement of spatial correlations [150, 180–182] due to a lack of a continuous measurement device which was able to resolve the spatial structure precisely enough. Recent developments of continuous quantum gas microscopes are altering this [183–188], as real-space correlation functions on arbitrary distances are becoming quantitatively accessible.

Having discussed the literature regarding the BEC-BCS crossover in ultracold systems, we continue by exploring the possibility of finding the BEC-BCS mechanism in extreme environments.

1.5 Fermi superfluids in extreme environments

The topic of degenerate fermions is not only related to ultracold quantum gases but also occurs widely in other setups. As such, they pose as excellent quantum simulators [189–192]. The concept of a quantum simulator was first proposed by R. Feynman at a conference in 1981 [193]. The idea is that a quantum system, such as quantum gases, represents a highly controllable setup, which can be used in order to emulate systems that are not easy, or even impossible, to investigate in the laboratory. A system in question are superheavy nuclei, which are, in most cases, unstable and decay too fast to investigate them. A second example are astrophysical objects, including neutron stars, where the crust is believed to form a neutron superfluid. The core is thought to form a so-called colour superfluid, where three different internal species, here the colour charges of the quarks, form pairs in a mechanism similar to a BCS superconductor. The same might happen in the cores of white dwarfs. Slightly more exotic, there exist theories which even hypothesise that dark matter or cosmic inflation might be rooted in Fermi superfluids. All those concepts will be discussed briefly because broad information about them might be gathered in a cold quantum gas setup. An important development, indispensable for investigating the upcoming systems, was the theoretical description of relativistic superfluids and superconductors [194].

1.5.1 Superfluids of subatomic particles

Shortly after the publication of the BCS theory, people realised that this mechanism might not be restricted to electrons. Even before Leggett's discussion regarding the possibility

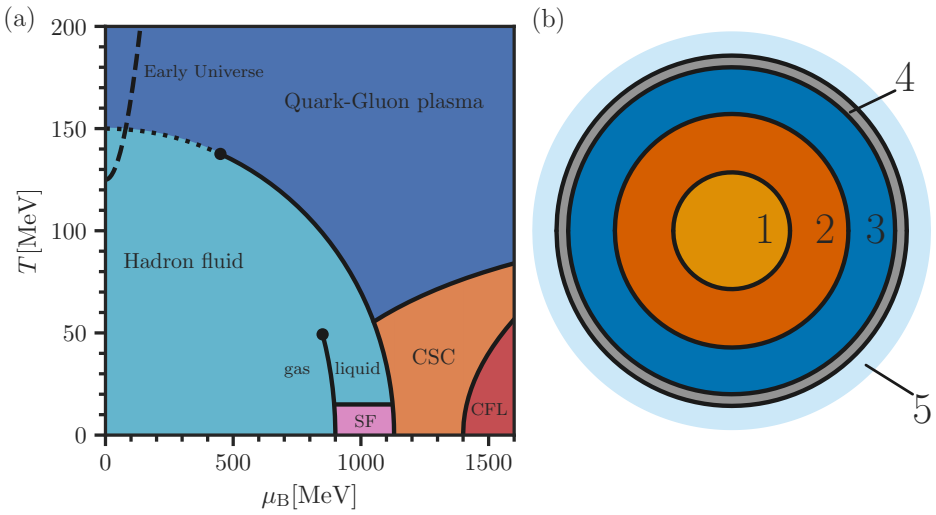


Figure 1.7: Panel (a): Schematic phase diagram of QCD matter, using data from Refs. [199–203]. The phase diagram shows the plane spanned by temperature T and baryonic chemical potential μ_B, both in MeV. The light blue region depicts the hadron fluid, dark blue characterises the quark-gluon plasma. The solid line in between represents a discontinuous phase transition separated from the dotted line as a smooth crossover by a critical point. The pink region is the hadron superfluid, where nucleons become superfluid. The orange and red regions for large baryonic chemical potential and low temperatures represent the Colour superconductor (CSC), with the Colour-Flavour locking (CFL) sub-phase shown in red. Panel (b): Illustration of generic neutron star structure, using data from Refs. [204–206]. Region 1 is the neutron star core, reaching from 15 to $12\ \mathrm{km}$ depth, possibly hosting a CSC phase. Region 2 extends from 10 to $0.5\ \mathrm{km}$, known as the outer core, filled with superconducting protons. Region 3 represents the inner crust, stretching from 0.5 to $0.1\ \mathrm{km}$, where there exists a lattice of iron ions, surrounded by superfluid electrons, followed by the outer crust, region 4, up to the surface, where the electron gas surrounding the iron lattice is normal fluid. Region 5 is a thin atmosphere of mainly hydrogen and helium, with a width of only a few centimetres.

of superfluid Fermi gases, the first approaches to superfluidity in nuclear systems were developed, going back to the end of the 1950s [195]. The key aspect here is that the hadrons, i.e. particles made from three valence quarks, are composite fermions. At the time, the scientific community mainly thought about protons and neutrons. Unlike the later idea of the BEC-BCS crossover, tuning the interaction in nuclear systems is not as straightforward as for cold gases and in general, the only way to address the interaction strength is to modulate the density. Therefore, the dimensionless scattering parameter can not switch sign, and hence no true crossover is possible. Instead, by varying the density, the unitary regime is approached asymptotically, never truly reached or crossed. Since neutron-neutron scattering does not permit a bound state, clean neutron setups are only ever in the BCS regime and have a negative scattering length of $a_n = -18.5\ \mathrm{fm}$ [196–198]. The same is true for proton-proton scattering, although they can not form a clean system due to their electrostatic repulsion and as such, their scattering length varies from system to system, sometimes exhibiting a bound state and having an opposite sign. Superfluidity in clean neutron systems has been studied over time [207]. In a realistic atomic nucleus, protons and neutrons are mixed, so their scattering must be taken into account.

Fortunately, the proton-neutron scattering does allow for a bound state: A Deuterium ion. Thus, the scattering length in most setups is positive, meaning ^{2}H is on the BEC side of the BEC-BCS crossover. This is the main reason the initial interest in those systems was larger [208–210]. Systems with mainly protons and neutrons are called hadron fluids [199, 200, 203, 211] and are generally seen for low baryonic chemical potentials[1] and low temperatures, compared to the typical scales of subatomic systems. They are seen in the light blue region of Fig. 1.7. The superfluid states are shown in the pink region for low temperatures. These hadronic superfluids eventually give rise to quantised vortices similar to ultracold Fermi gases [212–214].

If the temperature is increased, the hadrons melt, giving rise to the hypothetical quark-gluon plasma, shown as the dark blue region in Fig. 1.7. The gluons are the force-carrying bosons of the strong force. This is a high-temperature region not of interest in this thesis. However, when the baryonic chemical potential is increased, and the temperature is decreased, we eventually reach a phase, which gained a lot of interest, also in the field of ultracold quantum gases, the colour superconductor (CSC). This is a variant of the quark-gluon plasma, where the three colour charges of the strong force serve as internal states to form Cooper-pair-like structures, giving rise to a superconducting state [199, 215–220]. In the CSC, the $\mathrm{SU}(3)$ symmetry of the strong force is spontaneously broken, which leads to the superconducting properties. This phase is depicted in Fig. 1.7 (a) as the orange region. Using ultracold gases like ^{6}Li, it is possible to also describe states similar to a Quantum Chromodynamic (QCD) CSC by using three hyperfine states of Li instead of the standard two states used in a typical BCS setup [135–138]. When the temperature is further reduced, or the chemical potential is increased, flavour (or spin) pairs can also form. Thus, in addition to the colour pairs, regular spin Cooper pairs might form, strongly coupling the colour and flavour symmetries, leading to the hypothetical phase of a colour-flavour locking (CFL) superfluid [221, 222], illustrated in Fig. 1.7 (a) as the red region.

Hadron superfluids are thought to show up in nature in heavy but finite nuclei, as investigated in Refs. [223, 224]. Additionally, they are also thought to be present in the crusts and outer cores of neutron stars [225–227] as well as white dwarfs. CSC phases are more speculative, but there is a consensus in astrophysics that they should show up in extreme setups like the cores of neutron stars. In the next section, we will have a more detailed look at the topic of astrophysical Fermi superfluids.

1.5.2 Astrophysical superfluids

Fermi superfluids are generally thought to exist in extreme circumstances in astrophysical objects. This may be surprising, as a typical neutron star is relatively hot compared to temperatures normally found in the proximity of the solar system. After its formation neutron stars can have temperatures up to $10^{11}\ \mathrm{K}$ [228–230], with densities from $10^{11}\ \mathrm{g\,cm^{-3}}$ in the outer crust up to $10^{15}\ \mathrm{g\,cm^{-3}}$ in the core [206, 231], being one order of magnitude higher than the average density of a nucleus. Those high densities increase the Fermi temperature to values between $10^6\ \mathrm{K}$ for the neutron star crust and $10^{12}\ \mathrm{K}$ for the neutron star core. This means that neutron stars are, compared to their Fermi temperature, low-temperature objects after cooling down from their extremely hot initial state. Fermi superfluids are now believed to follow the universal phase diagram shown in Fig. 1.6 [86], ignoring the CSC

[1] The baryonic chemical potential is a measure of how many excess baryons are in a system. In subatomic systems, a quark sea might arise, causing baryons and anti-baryons to exist simultaneously. The baryonic chemical potential quantifies how large the imbalance of baryons and anti-baryons is.

for now. This means that, after cooling down, neutron star crusts and cores should undergo a phase transition to a superfluid state. Due to the varying density of those objects, there might be spatially modulated crossovers from a BEC to a BCS regime, depending on the constituent particles. An illustration of the interior of a neutron star is presented in Fig. 1.7 (b), where the outer core is region 2 and the crust spans region 3-5.

In nuclear systems, the effective range of particle scattering is of the order of the average distance between them, a feature commonly neglected in the literature on ultracold atomic systems. Therefore, this thesis will put a great emphasis on the concept of the interaction range in ultracold atomic gas setups. First theoretical ideas were put forward at the end of the 1960s [232], but the theoretical investigation of both the crusts [233–240] and cores [241–244] of neutron stars turned out to accelerate within the last decade.

An observation that supports the idea of superfluidity in these extreme objects was the observation of glitches in the rotation of neutron stars. Rapidly spinning neutron stars with strong magnetic fields spill out jets of high-energy particles and γ-radiation along their poles. If the γ-radiation jet crosses the Earth within a rotation, such objects are known as pulsars. The frequency of pulsars is extremely precise, as there are no outer processes to alter them, making them more accurate than most atomic clocks. A glitch is a sudden increase in the frequency of a pulsar, followed by a slow decrease to the pre-glitch frequency. They were first observed in 1969 [245, 246], and since then, over 700 glitches in around 250 pulsars have been observed until 2023 [247]. Glitches are thought to be directly related to the superfluid property of the neutron star, especially from its outer core to the crust. In the outer core, the superconducting protons can form quantised vortices that store angular momentum. Those vortex lines, in general, are pinned to their position, but there are processes going beyond the scope of this introduction that allow those vortex lines to unpin. This unpinning ultimately transfers their angular momentum from the rapidly spinning core to the slower, but nevertheless fast, spinning surface, increasing its frequency in the process [230, 248–253]. This is a direct effect of the charged superfluid in a stellar remnant having an impact on astronomic objects of the size of a small city. Therefore, studying Fermi superfluids in atomic clouds provides insights way beyond the laboratory where the experiment is performed.

It should be mentioned that Fermi superfluids are also present in the more speculative field of physics beyond the standard model, where some exotic types of Cooper pairs are also a potential candidate to explain dark matter [254–262] and cosmic inflation [258, 263] by extensions of the basic idea of Leggett's BEC-BCS crossover.

We have seen in this section that the study of superfluids in a laboratory on Earth can serve as a playground for studying objects that are beyond the reach of any experiment on Earth. In doing so, we are able to obtain an in-depth understanding of the complicated physics of some of the most extreme environments in our universe.

1.6 Summary of superfluid systems

To summarise, the fermionic superfluids discussed so far appear in a wide range of systems in nature. We illustrate those in Fig. 1.8, ranging more than 30 orders of magnitude in density and 20 orders of magnitude in temperature. At low temperatures and low densities, one generally finds quantum fluids, depicted in the figure as the blue region, including ^{6}Li, as well as ^{40}K and heteronuclear mixtures. Those are commonly known as *ultracold quantum gases*. In this region, we also include liquid ^{3}He, which has a density of classical liquids and hence a much higher Fermi temperature. For densities comparable to liquid

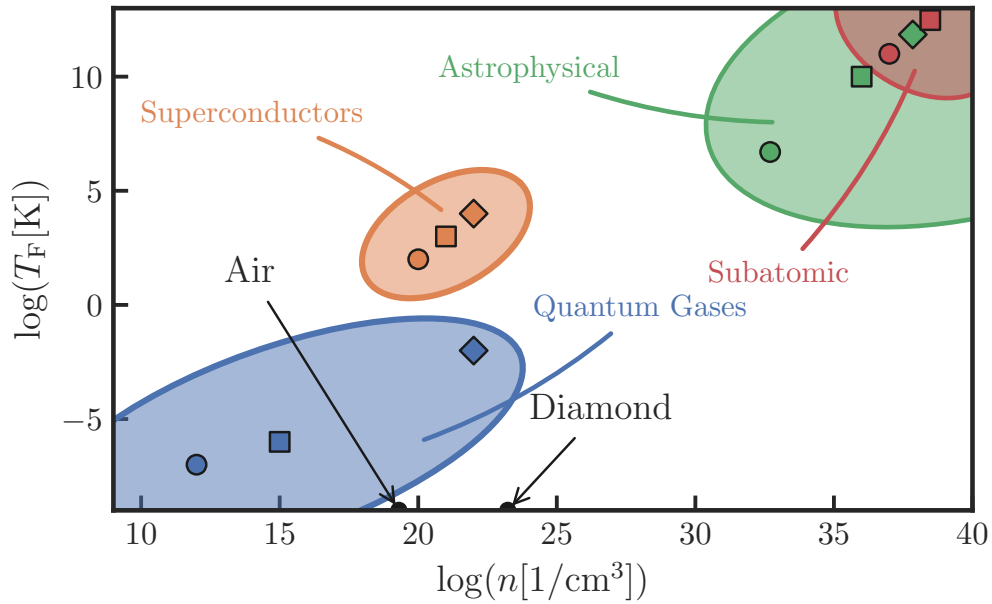


Figure 1.8: Illustration of various system categories of fermionic superfluids. Blue region: Quantum gases with circle as low density ^{6}Li, square as high density ^{6}Li and diamond as liquid ^{3}He [53, 180, 264]. Orange region: Superconductors with circle as heavy-fermion, square as high T_c and diamond as conventional superconductor [265]. Green region: Astrophysical superfluids in various stellar objects, depicted as circles for white dwarfs, squares for neutron star crust and diamonds for neutron star cores [206, 228–231]. Lastly red region shows subatomic superfluids, the circle represents heavy nuclei and the square quark-matter superfluids [266].

Helium we find the superconductors as orange region. Due to the lower electron mass compared to atomic masses, their Fermi temperature is above room temperature and, as such, much higher than that of liquid ^{3}He, despite similar densities. Increasing the temperature further, we find the astrophysical realisations of fermionic superfluids at densities at least 7 orders of magnitude larger than that of diamond. Those are found mostly in the remnants of stellar objects, white dwarfs and neutron stars, and span a large range of densities and temperatures. Those systems are represented as green region. Lastly, the red region incorporated in the green one are the subatomic superfluids, which only appear for extremely large temperatures and densities and are impossible to prepare in any experimental setup.

1.7 Outline of thesis

This thesis is organised as follows. In Chapter 2, we summarise the basic theoretical tools that are necessary to develop and apply the formalism established in the thesis. In Section 2.1, we briefly review the phenomenological development of theories of superconductivity and their generalisation to neutral superfluids. Afterwards, Section 2.2 outlines the main framework in which this thesis works, the Bardeen-Cooper-Schrieffer theory of superconductivity and the BEC-BCS crossover in ultracold Fermi gases. As a consequence, in Section 2.3 we discuss the modern, quantum field-theoretical approach to neutral superfluids by discussing the functional integral approach to the BEC-BCS crossover, the development of the mean-field theory and tools to go beyond mean-field. As a follow-up,

we present an alternative formulation of the BEC-BCS crossover by diagrammatic means in Section 2.4, dealing not only with Cooper pairing, but also with the so-called particle-hole sector. Because of this, Section 2.5 discusses the issues arising from the formulations discussed in the previous sections. We point out a certain degree of arbitrariness in the field-theoretical description, arising from the choice of a Hubbard-Stratonovich channel, as well as in the diagrammatic approaches, rooted in the selection of Feynman diagrams included in the theory.

The following Chapter 3 addresses exactly this arbitrariness of both approaches. We present an extensive discussion of the method we developed in Ref. [P1], going way beyond the content of the original publication. In Section 3.1 we discuss the need for a systematic extension of the standard single-channel description of the BEC-BCS crossover in ultracold Fermi gases. Following this, in Section 3.2, we show how this is practically done. By self-consistently partitioning the interaction, it becomes possible to include more than one of the three different two-body interaction channels, which are called after Hartree, Fock and Bogoliubov. In doing so, we formulate a self-consistent framework by applying separate Hubbard-Stratonovich transformations in all three channels and call it the *weighted Hartree-Fock-Bogoliubov* method. We then proceed in Section 3.3 by using the formalism developed for a spin-mixture of two hyperfine-states of fermionic atoms in thermal equilibrium and with equal populations in the framework of a saddle-point approximation. The resulting self-consistency equations are discussed, and it is shown that the partitioning lowers the ground-state energy compared to a single-channel approach, which is a special case included in the presented approach. Additionally, in Appendix 3.A we discuss the mathematical details of the underlying transformation and a way to generalise the application to arbitrary systems.

Next, in Chapter 4 we discuss the implications made by the previously developed formalism considering a balanced Fermi spin-mixture in three spatial dimensions and thermal equilibrium. The original results are discussed in Ref. [P1], but we present additional findings here that further support the necessity of the developed method. In Section 4.2, we have to establish an improved two-channel scattering renormalisation, introducing the effective range as an essential system parameter. This will show that corrections to a truly universal gas are needed in order to include the particle-hole sector, which is described by the Hartree and Fock channels. In Section 4.3, we use this renormalisation prescription to investigate the new ground state of our multi-channel theory by looking at the emerging Hartree-superfluid region, where, besides the standard superfluid order parameter, also a Hartree self-energy becomes important. We discuss the weak and strong coupling regimes and their asymptotics. Thereafter, in Section. 4.4 we investigate the thermodynamic properties of the ground state by looking at the free energy and its thermodynamic response functions. In particular, we outline possible experimental fingerprints for testing this finding of a newly emerging Hartree-superfluid phase. As a last part in Section 4.5, we briefly outline the finite-temperature implications of the developed multi-channel theory. We see that the Hartree-superfluid will prove to be an intermediate step between a normal fluid and a conventionally known type-I superfluid. At the end of this chapter, we present two appendices that contain mathematical details not directly needed to fully understand the approach presented. In Appendix 4.A we present an explicit calculation that allows for the first analytic solution to the Cooper pair size in three spatial dimensions. After this, in Appendix 4.B we explicitly work out the weak- and strong-coupling approximate solutions to the multi-channel theory, deriving the analytic limits found in the main body of Chapter 4.

After this, we have an in-depth look at correlation phenomena in ultracold Fermi

spin mixtures in Chapter 5, representing an extended discussion of our original publication [P2]. We provide introductory comments in Section 5.1, motivating the need for a precise method to calculate spatial correlation functions due to recent experimental developments in the realm of continuous quantum gas microscopy. Following this, in Section 5.2, we establish a set of basic constraints that any theory dealing with spatial correlations has to agree with, in order to be able to describe an experimental outcome. We do so by considering only fundamental principles of many-body quantum mechanics. In order to comply with these restrictions, in Section 5.3 we perform a linear response theory for Fermi spin mixtures, which explicitly takes the $\mathrm{U}(1)$ gauge freedom into account. To this end, we consider quantum fluctuations of the superfluid pair field, ultimately coupling collective modes to the density-density response. Following this, we present the results of our approach in a simplified model system at $T = 0$ and in two dimensions in Section 5.4. There, we evaluate various density-density correlation functions in real space, yielding good qualitative agreement with recent experimental data and providing an analytical explanation for the observed anticorrelations between opposite-spin fermions. To finalise our approach, we go beyond the measured data in Section 5.5, where we make quantitative predictions for the depth and width of the emerging anti-correlation region. Afterwards, we present in Appendix 5.A explicit analytical expressions for the loop functions used in the main text, before we establish in Appendix 5.B the set of Feynman diagrams relevant in our approach.

We summarise our findings in Chapter 6 concisely by referring explicitly to central equations and figures. After this, in Chapter 7 we discuss further research directions, some of which are already work in progress. In Section 7.1, we briefly outline how to extend the weighted Hartree-Fock-Bogoliubov method from Chapters 3 and 4 to two-dimensional systems. We discuss the challenges and show first numerical results for the ground state. Furthermore, we discuss whether the Fermi liquid theory can emerge naturally from our approach. In Section 7.2, we then discuss the path to a beyond saddle-point description of the weighted Hartree-Fock-Bogoliubov method. We outline how simultaneous fluctuations in the channels arise and how they couple. We strengthen our discussion by showing how particle-hole fluctuations affect the low-energy Goldstone mode of the broken-symmetry superfluid phase and how a naive standard procedure from the literature would fail when trying to include the particle-hole sector. We then take this a step further in Section 7.3by illustrating how the weighted Hartree-Fock-Bogoliubov framework can be merged with the Pauli principle condition established in Chapter 5. This is about combining all the findings in this thesis and extending it to a full theory of superfluid Fermi gases in a mathematically clean, unambiguous framework. Finalising this, in Section 7.4 we briefly discuss non-singular interaction potentials and how to alter our findings in this spirit, before closing with Section 7.5, where we mention a few other questions, which we open by the research presented throughout this thesis.

After this, we finalise the thesis with two appendices. In Appendix A, we set up the mathematical framework in which this thesis is set. In particular, we explain the formal definition of the quantum statistical field theory we work in. In Section A.1, we work out the idea of second quantisation. We follow standard textbook procedures in introducing many-body quantum mechanics from an operator perspective to form a common foundation. We finalise this by introducing the Fermi coherent states. Those states are then used in Section A.2 to work out the concept of functional integration. In particular, we define the functional integral in a discrete form to avoid mathematical difficulties. This becomes important in Appendix B, where we explicitly show how we calculate Matsubara

sums. There, in Section B.1, we introduce formally the concept of Matsubara summations, for which we present the most common solution strategy in Section B.2, which is the contour integration. This method, however, has limited application because it relies on an ill-defined version of the functional integral. Therefore, we use the discrete functional integral defined in Appendix A.2 and, in Section B.3, develop a new way of solving Matsubara sums as finite products rather than infinite sums. This comes from the fact that interchanging operations for formally divergent objects is an ill-defined mathematical operation which obscures the ordering of the coherent states. We avoid this issue with the new calculation method. Ultimately, we present in Section B.4 a numerical strategy how to evaluate zero-temperature Matsubara sums.

Chapter 2

Previous theories of superfluids and superconductors

If I have seen further, it is by standing on the shoulders of giants

Isaac Newton, 1675, in a letter to Robert Hooke

2.1 Phenomenological theories for superfluids 23
2.1.1 Landau's two-fluid model 24
2.1.2 Ginzburg-Landau theory 24
2.2 BCS and Leggett BEC-BCS crossover theories 27
2.2.1 Bardeen-Cooper-Schrieffer theory of superconductivity 27
2.2.2 Leggett's BEC-BCS crossover 28
2.3 Functional integral approach to BEC-BCS crossover 30
2.3.1 Gaussian Pair Fluctuations 32
2.3.2 Collective modes 34
2.3.3 Critical temperature 35
2.4 Diagrammatic approach to BEC-BCS crossover 36
2.4.1 Pair fluctuations from diagrammatic theories 37
2.4.2 Particle-hole screening 37
2.5 Arbitrariness of approaches 39

2.1 Phenomenological theories for superfluids

In the first part of this chapter, we briefly outline two phenomenological descriptions of superfluidity that are still widely used today. We first focus on the two-fluid model established by Landau, describing a superfluid as a two-component system, where one is an ideal fluid, while the other is a standard fluid having internal friction. After this, we discuss the Ginzburg-Landau theory, describing the superfluid phase transition, which was initially developed for superconductors.

2.1.1 Landau's two-fluid model

Landau developed the two-fluid model by assuming that superfluid ^{4}He consists of two separate fluids with different properties. One fluid would be a standard viscous system, which represents the normal-fluid parts described by a standard Navier-Stokes equation. The second, and arguably more important, component is an ideal fluid without internal viscosity, described by an Euler equation. This is the superfluid part. The respective mass densities of the two fluids add up to the total density that is $\rho = \rho_\mathrm{n} + \rho_\mathrm{s}$, and their flow is characterized by their respective velocity vectors $\boldsymbol{v}_\mathrm{n}$ and $\boldsymbol{v}_\mathrm{s}$. The resulting mass current density in the fluid is then given by

$$\boldsymbol{j} = \rho_\mathrm{n}\boldsymbol{v}_\mathrm{n} + \rho_\mathrm{s}\boldsymbol{v}_\mathrm{s}, \tag{2.1}$$

where the superfluid velocity field is usually assumed to be curl-free, i.e. $\nabla \times \boldsymbol{v}_\mathrm{s} = \boldsymbol{0}$. Furthermore, the conservation of particles demands a continuity equation, which is rearranged into a second-order partial differential equation coupling the mass density ρ and the pressure p via the Newton-like equation of motion

$$0 = \frac{\partial^2 \rho(t, \boldsymbol{x})}{\partial t^2} - \nabla^2 p(t, \boldsymbol{x}). \tag{2.2}$$

The following results are obtained by standard procedures and are well known in the literature. Using the GibbsDuhem relation, introducing entropy per unit mass and particle as s and linearising the continuity equation leads to first, second, and third sound in superfluids [267]. Here, we do not perform the derivation directly, but in order to gain a better understanding, it is worth discussing the results for different sound modes. The first sound propagates with

$$c_1^2 = \left.\frac{\partial p}{\partial \rho}\right|_T \tag{2.3}$$

and describes the propagation of pressure modes when the density is altered. The speed of sound is the isothermal sound velocity. The second sound is always slower than the first sound, hence the name, and describes temperature waves for constant densities, propagating with

$$c_2^2 = \frac{\rho_\mathrm{s}}{\rho_n}\frac{s^2}{c}T. \tag{2.4}$$

The quantity c stands for the specific heat per unit mass at constant volume. The third sound velocity is not associated directly with a propagating wave but is a measure of the coupling of first and second sound. It is a vital quantity in calculating the adiabatic sound velocity [267].

The two-fluid model was quickly accepted at the time, leading to various applications, including predictions of first and second sound [268], hydrodynamic and collisionless applications [269], and much more [270]. Furthermore, microscopic theories were also developed showing how the phenomenological model arises from a more fundamental theory [271, 272]. In this context, it is not surprising that Landau solely won the Nobel Prize in 1962 *'for his pioneering theories for condensed matter, especially liquid helium'* [273].

2.1.2 Ginzburg-Landau theory

In this section, we focus on a phenomenological approach to describing neutral superfluids, namely the Ginzburg-Landau (GL) theory. The GL theory for superconductors is rather complicated. To provide a concise formulation, we focus directly on neutral superfluids.

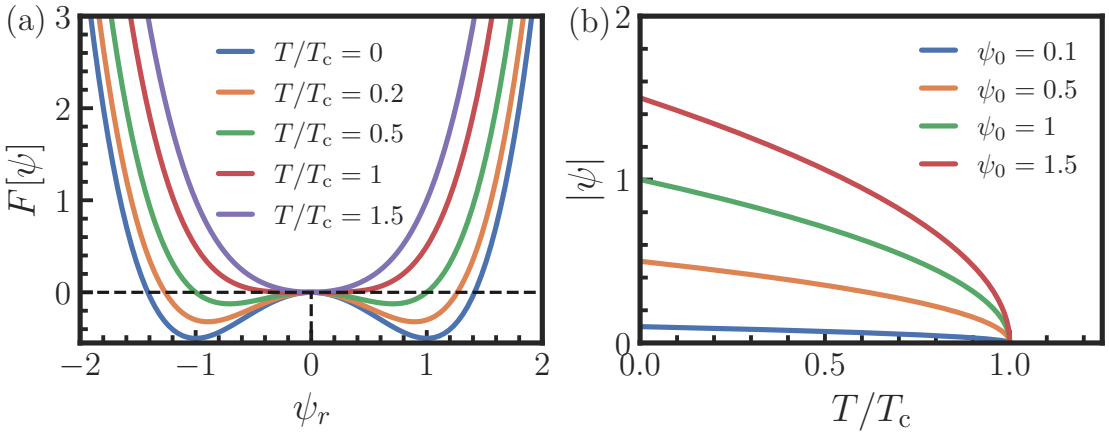


Figure 2.1: Illustration of broken $\mathrm{U}(1)$ symmetry in Landau theory. Panel (a) shows free energy functional (2.5) for various temperatures (see legend inset). Panel (b) shows the value of ψ which minimizes the free energy for various values of ψ_0 versus temperature in terms of critical temperature T_c.

We start with the static Landau theory of phase transitions, as outlined in several textbooks [274–278], which this section concisely summarises. It is based on the concept of a complex *order parameter*, which we subsequently call ψ. The idea is to consider the free energy F as a function of ψ, which for small values reads

$$F[\psi] = \alpha|\psi|^2 + \frac{\beta}{2}|\psi|^4 + \mathcal{O}(\psi^6). \tag{2.5}$$

The simplest assumption is now that $\beta > 0$, i.e. the free energy has a minimum. The properties of the actual order parameter depend on the sign of the parameter α. For $\alpha \geq 0$, only the trivial solution $\psi = 0$ minimises the free energy. It becomes interesting once $\alpha < 0$ since there the previous energy minimum at $\psi = 0$ becomes unstable and a whole, continuous set of solutions emerges, described by $|\psi| = \sqrt{-\alpha/\beta}$. One speaks of spontaneous symmetry breaking, since the field acquires a non-vanishing vacuum expectation value with a different symmetry than the underlying Lagrangian. In this special case, the symmetry which is spontaneously broken is the $\mathrm{U}(1)$-symmetry of multiplication with a complex phase. The breaking of $\mathrm{U}(1)$ announces a phase transition from a disordered phase ($\psi = 0$) to an ordered phase ($\psi \neq 0$). In a superconductor, the parameter β is essentially a constant. However, for α it is assumed that $\alpha = \alpha_0(T - T_c)$, where T_c denotes the critical temperature of the phase transition. A generic illustration of this is seen in Fig. 2.1 (a), where the free energy (2.5) is shown versus the real part of $\psi = \psi_r + i\psi_i$. We see that for temperatures below T_c separate minima develop, while for $T \geq T_c$ only the trivial minimum $\psi = 0$ exists. Under those circumstances, the order parameter becomes

$$|\psi| = \psi_0\sqrt{1 - \frac{T}{T_c}}, \tag{2.6}$$

where the prefactor is given by $\psi_0 = \sqrt{T_c\alpha_0/\beta}$. This is illustrated in Fig. 2.1 (b), which shows various values of ψ_0 over T/T_c, sometimes referred to as reduced temperature.

Considering spatial and temporal variations promotes ψ to a complex field $\psi(t, \boldsymbol{r})$. The dynamics of this field are understood in the framework of the Ginzburg-Landau La-

grangian density

$$\mathcal{L}_{\mathrm{GL}} = i\psi^*\partial_t\psi - \frac{1}{2m}|\nabla\psi|^2 - \alpha|\psi|^2 - \frac{\beta}{2}|\psi|^4. \tag{2.7}$$

The Euler-Lagrange equation associated with this Lagrangian density reads

$$i\partial_t\psi = \left[-\frac{1}{2m}\nabla^2 + \alpha + \beta|\psi|^2\right]\psi. \tag{2.8}$$

In order to solve this equation of motion, it is advantageous to decompose the field ψ into the static and homogeneous result ψ_0 obtained by the Landau free energy functional (2.5) as well as an amplitude and a phase fluctuation part, reading

$$\psi(t,\boldsymbol{r}) = \left[\psi_0 + h(t,\boldsymbol{r})\right] e^{i\chi(t,\boldsymbol{r})}. \tag{2.9}$$

Performing a Taylor expansion for small h and χ and eliminating the phase χ as a dynamical Degree of Freedom (DoF) yields a residual equation for the amplitude h, which is of the form

$$0 = \left[\partial_t^2 + \frac{\nabla^4}{4m^2} - \frac{|\psi_0|^2}{m}\nabla^2\right] h(t,\boldsymbol{r}). \tag{2.10}$$

Going to momentum space then leads to the dispersion of the amplitude fluctuations h, which turns out to be a standard Bogoliubov dispersion

$$\omega(\boldsymbol{k}) = c|\boldsymbol{k}|\sqrt{1+\gamma^2\boldsymbol{k}^2}, \tag{2.11}$$

with the speed of sound being

$$c^2 = \frac{\alpha_0 T_\mathrm{c}}{\beta m}(T_\mathrm{c} - T) \tag{2.12}$$

and $\gamma^2 = \beta/[4m\alpha_0(T_\mathrm{c} - T)]$. For small momenta, this dispersion approaches the regular Bogoliubov sound mode $\omega \sim c|\boldsymbol{k}|$ while for large momenta, the free particle dispersion is approached $\omega \sim \boldsymbol{k}^2/(2m)$. It has to be noted that the phase mode χ obtains the same dispersion (2.11). Only in a relativistic setup, using the relativistic Ginzburg-Landau Lagrangian

$$\mathcal{L} = \left(\partial^\mu\psi^*\right)\left(\partial_\mu\psi\right) - \alpha|\psi|^2 - \frac{\beta}{2}|\psi|^4, \tag{2.13}$$

two separate dispersion branches for amplitude h and phase χ occur. There, the phase fluctuations follow, in a first approximation, a linear sound dispersion due to the Goldstone theorem, while the amplitude fluctuations follow a gapped Higgs dispersion. In a superconductor, electric charge conservation prevents explicit breaking of $\mathrm{U}(1)$ symmetry, and, as such, the Goldstone theorem is circumvented. Regarding the ground state, this is closely related to the impossibility of a spontaneous breaking of local symmetries, commonly known as Elitzur's theorem [279]. Therefore, a superconductor does not exhibit a massless and gapless Goldstone mode. Even though the notion of relativistic superfluids is not further considered in this thesis, the notion of a Goldstone (phase) and a Higgs (amplitude) mode often appears in the literature regarding non-relativistic superfluids and also in this thesis. This is the reason we introduce the concept here in a much simpler setup.

After having discussed the phenomenological GL theory, we continue with the first true microscopic description of superconductivity, the Bardeen-Cooper-Schrieffer theory.

2.2 BCS and Leggett BEC-BCS crossover theories

In this section, we investigate the mathematical properties of the Bardeen-Cooper-Schrieffer theory, describing type I superconductors. Afterwards, we outline Leggett's version of the crossover between a BCS and a BEC state for alkaline atoms.

2.2.1 Bardeen-Cooper-Schrieffer theory of superconductivity

Here, we discuss a toy-model description of the BCS theory, which simplifies the complicated phonon-mediated attractive interactions between electrons [280]. The toy model considers two distinguishable electrons of opposite spin directions $\uparrow$ and $\downarrow$, described by the fermionic creation and annihilation operators $\hat{c}_{\mathrm{s},\boldsymbol{k}}, \hat{c}^\dagger_{\mathrm{s},\boldsymbol{k}}$, fulfilling the anti-commutator relation $\{\hat{c}_{\mathrm{s},\boldsymbol{k}}, \hat{c}^\dagger_{\mathrm{s}',\boldsymbol{k}'}\} = \delta_{\mathrm{ss}'}\delta_{\boldsymbol{k}\boldsymbol{k}'}$. Only opposite spin fermions interact attractively via a simplified model potential $V_{\boldsymbol{k},\boldsymbol{k}'} = -g\theta(k_\mathrm{D} - |\boldsymbol{k} - \boldsymbol{k}'|)$, with k_D as Debye wavenumber and $g > 0$ as interaction strength. This is due to the Debye momentum describing the maximum wavenumber a phonon can have in a lattice, due to the wavelengths being restricted via the lattice constant. This is known as the Fröhlich model. We follow the presentation of Refs. [14, 18, 281, 282], using the Hamiltonian

$$\hat{H}_\mathrm{BCS} = \sum_{\mathrm{s},\boldsymbol{k}} \xi_{\mathrm{s},\boldsymbol{k}} \hat{c}^\dagger_{\mathrm{s},\boldsymbol{k}} \hat{c}_{\mathrm{s},\boldsymbol{k}} + \sum_{\boldsymbol{k},\boldsymbol{k}'} V_{\boldsymbol{k},\boldsymbol{k}'} \hat{c}^\dagger_{\uparrow,\boldsymbol{k}} \hat{c}^\dagger_{\downarrow,-\boldsymbol{k}} \hat{c}_{\downarrow,-\boldsymbol{k}'} \hat{c}_{\uparrow,\boldsymbol{k}'}, \tag{2.14}$$

where $\xi_{\mathrm{s},\boldsymbol{k}} = \boldsymbol{k}^2/(2m_\mathrm{s}) - \mu$ denotes the free particle dispersion with $\hbar = 1$. What Schrieffer realised was that the four fermion operators in the interaction could be wrapped up as two bosonic operators. Those are associated with the creation and annihilation of pairs of fermions, which will be denoted by $\hat{b}^\dagger_{\boldsymbol{k}} = \hat{c}^\dagger_{\uparrow,\boldsymbol{k}} \hat{c}^\dagger_{\downarrow,-\boldsymbol{k}}$ and its hermitian conjugate. This introduces the reduced Hamiltonian

$$\hat{H}_\mathrm{BCS} = \sum_{\mathrm{s},\boldsymbol{k}} \xi_{\mathrm{s},\boldsymbol{k}} \hat{c}^\dagger_{\mathrm{s},\boldsymbol{k}} \hat{c}_{\mathrm{s},\boldsymbol{k}} + \sum_{\boldsymbol{k},\boldsymbol{k}'} V_{\boldsymbol{k},\boldsymbol{k}'} \hat{b}^\dagger_{\boldsymbol{k}} \hat{b}_{\boldsymbol{k}'}. \tag{2.15}$$

Bardeen, Cooper and Schrieffer applied a Hartree-like method to approximate the ground state of this Hamiltonian. Introducing complex modes with the property $|u_{\boldsymbol{k}}|^2 + |v_{\boldsymbol{k}}|^2 = 1$ gives rise to a so-called Bogoliubov transformation, allowing a variational ansatz to the BCS ground state, which is generated from the vacuum state $|0\rangle$ as

$$|\mathrm{BCS}\rangle = \prod_{\boldsymbol{k}} \left(u_{\boldsymbol{k}} + v_{\boldsymbol{k}} \hat{b}^\dagger_{\boldsymbol{k}}\right) |0\rangle. \tag{2.16}$$

Minimizing the ground state energy $E_0 = \langle \mathrm{BCS}|\hat{H}|\mathrm{BCS}\rangle$ leads to a solution for the modes u, v in terms of the free particle dispersion $\xi_{\boldsymbol{k}} = \boldsymbol{k}^2/(2m) - \mu$ and the energy gap of the superconductor, conventionally denoted as Δ. The resulting quasiparticle and quasi-hole amplitudes are

$$|u_{\boldsymbol{k}}|^2 = \frac{1}{2}\left(1 + \frac{\xi_{\boldsymbol{k}}}{E_{\boldsymbol{k}}}\right), \tag{2.17a}$$

$$|v_{\boldsymbol{k}}|^2 = \frac{1}{2}\left(1 - \frac{\xi_{\boldsymbol{k}}}{E_{\boldsymbol{k}}}\right), \tag{2.17b}$$

respectively. The quasiparticle dispersion used here is

$$E_{\boldsymbol{k}} = \sqrt{\xi^2_{\boldsymbol{k}} + |\Delta|^2}. \tag{2.18}$$

Element	Mercury [283]	Thallium [283]	Lead [284–286]	Niobium [287]
Θ_D in K	71.9 ± 0.2	78.5 ± 0.2	105	271 ± 5
T_c in K	4.16	2.38	7.22	9.16 ± 0.02
$T_\mathrm{c}/\Theta_\mathrm{D}$	0.06	0.03	0.07	0.03

Table 2.1: Typical values for Debye temperature Θ_D, critical temperature T_c and relative temperature $T_\mathrm{c}/\Theta_\mathrm{D}$ of some pure metal superconductors.

The energy gap has to be determined self-consistently by the *gap equation*

$$\frac{1}{g} = \frac{1}{V}\sum_{\boldsymbol{k}\leq k_\mathrm{D}} \frac{1}{2E_{\boldsymbol{k}}}. \tag{2.19}$$

Furthermore, BCS and later authors worked at $T = 0$, as in a metal the critical temperature T_c is small compared to the Debye parameter Θ_D, that is $T_\mathrm{c}/\Theta_\mathrm{D} \ll 1$. Some typical values are shown in Table 2.1.

The BCS mechanism describes weak interactions. It was soon realised that the idea of a BEC of charged molecules, introduced by Blatt [17], is capable of describing the strongly attracting limit of an electron system. For neutral superfluids, this is more prominently known as the BEC-BCS crossover, which we discuss next.

2.2.2 Leggett's BEC-BCS crossover

In this section, we review the basic steps in order to obtain Leggett's theory of the BEC-BCS crossover and discuss some fundamental properties. We follow the operator approach outlined in Refs. [66, 154, 288], applying a variational perturbative approach in a mean-field approximation, inspired by Ref. [289]. The starting point is the second quantised Hamiltonian

$$\hat{H} = \int \mathrm{d}^3 r \left\{ \sum_\mathrm{s} \hat{\psi}_\mathrm{s}^\dagger(\boldsymbol{r}) \left[-\frac{\nabla^2}{2m} - \mu \right] \hat{\psi}_\mathrm{s}(\boldsymbol{r}) - g\hat{\psi}_\uparrow^\dagger(\boldsymbol{r})\hat{\psi}_\downarrow^\dagger(\boldsymbol{r})\hat{\psi}_\downarrow(\boldsymbol{r})\hat{\psi}_\uparrow(\boldsymbol{r}) \right\}, \tag{2.20}$$

being a real-space version of the BCS toy-model (2.14) in continuous space. Here, the field operators follow an anti-commutation relation $\left\{\hat{\psi}_\mathrm{s}(\boldsymbol{r}), \hat{\psi}_{\mathrm{s}'}(\boldsymbol{r}')\right\} = \delta_{\mathrm{ss}'}\delta(\boldsymbol{r}-\boldsymbol{r}')$ with all other anti-commutators vanishing. We replace the four-field product in a mean-field approximation by the anomalous terms, as they lead to superfluidity

$$\hat{\psi}_\uparrow^\dagger\hat{\psi}_\downarrow^\dagger\hat{\psi}_\downarrow\hat{\psi}_\uparrow \approx \langle\hat{\psi}_\uparrow^\dagger\hat{\psi}_\downarrow^\dagger\rangle\,\hat{\psi}_\downarrow\hat{\psi}_\uparrow + \langle\hat{\psi}_\downarrow\hat{\psi}_\uparrow\rangle\,\hat{\psi}_\uparrow^\dagger\hat{\psi}_\downarrow^\dagger - \langle\hat{\psi}_\uparrow^\dagger\hat{\psi}_\downarrow^\dagger\rangle\,\langle\hat{\psi}_\downarrow\hat{\psi}_\uparrow\rangle, \tag{2.21}$$

dropping the $\boldsymbol{r}$ arguments. Here $\langle\circ\rangle$ corresponds to a currently unknown ensemble expectation value. This approximation neglects particle-hole contributions since they are thought to be largely irrelevant in mean-field descriptions of superfluids or superconductors [290]. A great part of this thesis will deal with the question of whether this is really the case or too large an oversimplification. Defining the superfluid order parameter as $\Delta = g\langle\hat{\psi}_\downarrow\hat{\psi}_\uparrow\rangle$ and treating it as static and homogeneous we obtain

$$\hat{H}_\mathrm{MF} = \int \mathrm{d}^3 r \left\{ \sum_\mathrm{s} \hat{\psi}_\mathrm{s}^\dagger(\boldsymbol{r}) \left[-\frac{\nabla^2}{2m} - \mu \right] \hat{\psi}_\mathrm{s}(\boldsymbol{r}) + \overline{\Delta}\hat{\psi}_\downarrow(\boldsymbol{r})\hat{\psi}_\uparrow(\boldsymbol{r}) + \Delta\hat{\psi}_\uparrow^\dagger(\boldsymbol{r})\hat{\psi}_\downarrow^\dagger(\boldsymbol{r}) + \frac{|\Delta|^2}{g} \right\}. \tag{2.22}$$

With the above Hamiltonian and the inverse temperature $\beta = 1/T$, using $k_\mathrm{B} = 1$, we calculate the grand-canonical partition function $\mathcal{Z}_\mathrm{MF} = \mathrm{Tr}\exp\left(-\beta\hat{H}_\mathrm{MF}\right)$. This gives rise to

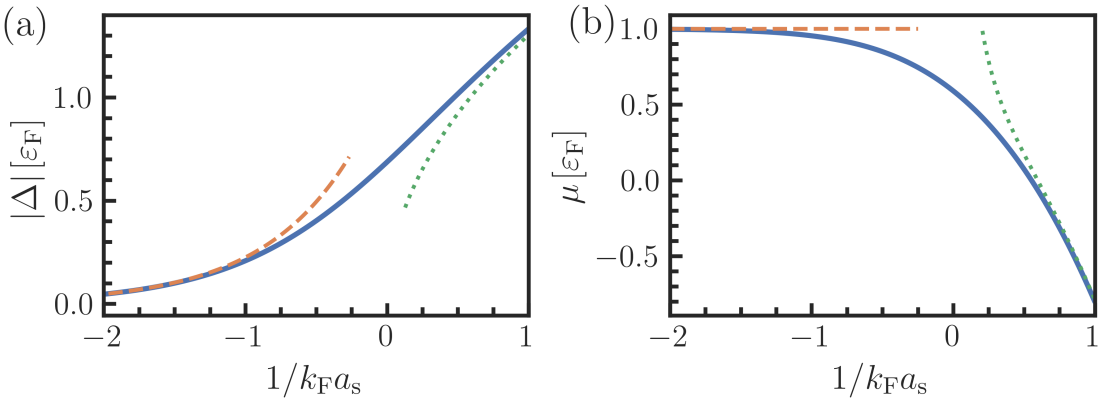


Figure 2.2: Crossover from BCS to BEC regimes at $T = 0$. Panels (a) and (b) depict superfluid order parameter and chemical potential versus $1/k_F a_s$. In both panels dashed orange line represents the BCS solution for weak couplings, while the dotted green line corresponds to BEC approximation.

the free energy $F_{MF} = -T \ln \mathcal{Z}_{MF}$, whose minimisation amounts to a semi-classical solution. In short, we replace $\langle \circ \rangle$ by the mean-field expectation value $\langle \circ \rangle_{MF}$. To evaluate the trace, Eq. (2.22) has to be diagonalised. This is done in momentum space, introducing the fermionic ladder operators

$$\hat{\psi}_s(\boldsymbol{r}) = \frac{1}{\sqrt{V}} \sum_{\boldsymbol{k}} e^{-i\boldsymbol{k}\cdot\boldsymbol{r}} \hat{c}_{s,\boldsymbol{k}}. \tag{2.23}$$

We then diagonalise the system by introducing new Fermi operators in momentum space, which are

$$\hat{\alpha}_{\boldsymbol{k}} = u_{\boldsymbol{k}} \hat{c}_{\uparrow,\boldsymbol{k}} - v_{\boldsymbol{k}} \hat{c}^\dagger_{\downarrow,-\boldsymbol{k}} \tag{2.24a}$$

$$\hat{\gamma}_{\boldsymbol{k}} = u_{\boldsymbol{k}} \hat{a}_{\downarrow,-\boldsymbol{k}} + v_{\boldsymbol{k}} \hat{a}^\dagger_{\uparrow,\boldsymbol{k}}. \tag{2.24b}$$

This is the Bogoliubov transform also found in the standard BCS approach of the previous section, using the quasiparticle and quasi-hole modes established in Eqs. (2.17a) and (2.17b). The diagonalised Hamiltonian reads

$$\hat{H}_{MF} = \sum_{\boldsymbol{k}} E_{\boldsymbol{k}} \begin{pmatrix} \hat{\alpha}^\dagger_{\boldsymbol{k}} & \hat{\gamma}^\dagger_{\boldsymbol{k}} \end{pmatrix} \begin{pmatrix} \hat{\alpha}_{\boldsymbol{k}} \\ \hat{\gamma}_{\boldsymbol{k}} \end{pmatrix}. \tag{2.25}$$

Its minimisation with respect to the superfluid order parameter and evaluating the trace in the α, γ basis leads to the superfluid order parameter equation

$$\Delta = g \frac{1}{V} \sum_{\boldsymbol{k}} u^*_{\boldsymbol{k}} v_{\boldsymbol{k}} \tanh\left(\frac{\beta}{2} E_{\boldsymbol{k}}\right). \tag{2.26}$$

This equation is sometimes referred to as the gap equation. This terminology is not accurate in the BEC-BCS crossover setup as the energy gap in the BEC limit, obtained by the quasiparticle dispersion (2.18), is given by $\sqrt{\mu^2 + |\Delta|^2}$. Hence, the superfluid order parameter is only equal to the gap in the BCS regime, when $\mu > 0$. Furthermore, we obtain the equation of state via $nV = -(\partial F_{MF}/\partial \mu)_{T,V}$, leading to the result

$$n = \frac{1}{V} \sum_{\boldsymbol{k}} \langle \hat{\alpha}^\dagger_{\boldsymbol{k}} \hat{\alpha}_{\boldsymbol{k}} + \hat{\gamma}^\dagger_{\boldsymbol{k}} \hat{\gamma}_{\boldsymbol{k}} \rangle_{MF} = \frac{1}{V} \sum_{\boldsymbol{k}} \frac{v^2_{\boldsymbol{k}} + u_{\boldsymbol{k}} e^{-\beta E_{\boldsymbol{k}}}}{1 + e^{-\beta E_{\boldsymbol{k}}}}. \tag{2.27}$$

The solutions to this at $T = 0$ are shown in Fig. 2.2, where panel (a) and (b) show the solution of the superfluid order parameter and chemical potential, respectively. For weak interactions, the chemical potential approaches the Fermi energy, that is $\mu(T = 0, g \to 0) = \varepsilon_\mathrm{F}$. In both panels, the x-axis represents the renormalized interaction strength, which is $1/k_\mathrm{F}a_\mathrm{s}$, where $k_\mathrm{F} = \sqrt{2m\varepsilon_\mathrm{F}}$ is the Fermi momentum. The s-wave scattering length is the renormalised interaction strength and obtained via the Lippmann-Schwinger Equation (LSE) [87] as

$$\frac{1}{g} = -\frac{m}{4\pi a_\mathrm{s}} + \sum_{\boldsymbol{k}} \frac{m}{\boldsymbol{k}^2}. \tag{2.28}$$

Instead, evaluating the two self-consistency equations at $T = T_\mathrm{c}$ requires setting $\Delta = 0$. With this, we obtain the critical temperature approximately as

$$T_\mathrm{c} \approx \frac{\pi}{8}\frac{\gamma_\mathrm{E}}{e^2} T_\mathrm{F} e^{-\frac{\pi}{2|k_\mathrm{F}a_\mathrm{s}|}}, \tag{2.29}$$

using $\gamma_\mathrm{E} \approx 0.577$ as the Euler-Mascheroni constant [66].

This mean-field approximation is only valid for the weakly interacting BCS side. To achieve the crossover towards the BEC side and to make reliable predictions, we need a beyond-mean-field theory. This is difficult to accomplish in an operator approach, although Refs. [66, 289] outlined an idea on how to perform this. The more established approach in the literature is the functional integral approach, which is discussed in the next section.

2.3 Functional integral approach to BEC-BCS crossover

In this section, we discuss the basis of this thesis, the functional integral approach to the BEC-BCS crossover. It was first developed by Sá de Melo, Randeria, and Engelbrecht in 1993 and 1997 [87, 88] and is based on the mathematical many-body description presented in Appendix A. The modern theoretical description of the BEC-BCS crossover starts with the Lagrangian density of a contact interacting spin-mixture of two distinct states of the same atom with mass m, which reads

$$\mathcal{L} = \sum_\mathrm{s} \left\{ \overline{\psi}_\mathrm{s}(x) \left[-G_0^{-1}(x,x) \right] \psi_\mathrm{s}(x) - g\overline{\psi}_\uparrow(x)\overline{\psi}_\downarrow(x)\psi_\downarrow(x)\psi_\uparrow(x) \right\}, \tag{2.30}$$

with $\overline{\psi}, \psi$ as fermionic coherent states that are eigenstates of the field operators $\hat{\psi}^\dagger, \hat{\psi}$. Here, both pseudo-spin states also have the same chemical potential μ, indicating identical spin populations. Furthermore, $x = (\tau, \boldsymbol{x})$ denotes the joint space-time position and

$$G_0^{-1}(x,x) = -\partial_\tau + \frac{\boldsymbol{\nabla}^2}{2m} + \mu \tag{2.31}$$

represents the inverse single-particle Green's function. The action of this system reads $\mathcal{S} = \int \mathrm{d}x \mathcal{L}$ with $\mathrm{d}x = \mathrm{d}\tau \mathrm{d}^3x$ being the joint space-time measure. The partition function is defined by

$$\mathcal{Z} = \oint_\mathrm{A} \mathcal{D}[\overline{\psi}, \psi] e^{-\mathcal{S}[\overline{\psi}, \psi]}. \tag{2.32}$$

Here, $\oint_\mathrm{A}$ stands for the anti-periodic functional integral and $\mathcal{D}$ represents the functional measure. We go deeper into the details of the underlying field quantisation in Appendix A.2.

To evaluate the partition function, we invoke a Hubbard-Stratonovich (HS) transformation that couples the fermions $\overline{\psi}, \psi$ to the complex pair field $\overline{\Delta}, \Delta$. Thus, we decouple the

fermions, making the functional integral executable. This is a standard procedure seen in many textbooks, see for instance Refs. [274, 275, 291]. To perform the functional integral end, we go to momentum space $(\tau, \boldsymbol{x}) = x \to k = (ik_n, \boldsymbol{k})$ with $\boldsymbol{k}$ being the momentum and $k_n = (2n+1)\pi T$, for $n \in \mathbb{Z}$, defining the anti-periodic Matsubara frequencies. This results in the effective action

$$\mathcal{S}_{\mathrm{HS}}[\Delta; \overline{\boldsymbol{\psi}}, \boldsymbol{\psi}] = \sum_k \sum_q \left\{ \overline{\boldsymbol{\psi}}_{k-q/2} \left[-\boldsymbol{G}^{-1}(k, k+q) \right] \boldsymbol{\psi}_{k+q/2} + \beta V \frac{\overline{\Delta}_q \Delta_q}{g} \right\}, \tag{2.33}$$

using the Nambu-Spinor

$$\overline{\boldsymbol{\psi}}^{\mathrm{T}}_{k-q/2} = \begin{pmatrix} \overline{\psi}_{\uparrow, k-q/2} & \psi_{\downarrow, k-q/2} \end{pmatrix} \tag{2.34}$$

and the inverse Nambu-Gor'Kov Green's function

$$\boldsymbol{G}^{-1}(k, k+q) = \begin{pmatrix} (ik_n - \xi_{\boldsymbol{k}})\, \delta_{q,0} & -\overline{\Delta}_{-q} \\ -\Delta_q & (ik_n + \xi_{\boldsymbol{k}})\, \delta_{q,0} \end{pmatrix}. \tag{2.35}$$

This gives rise to the grand-canonical partition function

$$\mathcal{Z} = \oint_{\mathrm{A}} \mathcal{D}[\overline{\boldsymbol{\psi}}, \boldsymbol{\psi}] \oint_{\mathrm{P}} \mathcal{D}[\overline{\Delta}, \Delta] e^{-\mathcal{S}_{\mathrm{HS}}[\Delta; \overline{\boldsymbol{\psi}}, \boldsymbol{\psi}]}, \tag{2.36}$$

with $\oint_{\mathrm{P}}$ denoting the periodic functional integral over the bosonic degrees of freedom. The action is now quadratic in the fermions, and hence they can be integrated out, leading to an effective action depending solely on the bosonic auxiliary field

$$\mathcal{S}_{\mathrm{Eff}}[\Delta] = -\mathrm{Tr} \ln \left[-\beta \hat{\boldsymbol{G}}^{-1} \right] + \beta V \sum_q \frac{|\Delta_q|^2}{g}. \tag{2.37}$$

We use the basis-less version of the Green's function as an operator, as established in the Appendix in Eq. (A.81), and Tr denotes the full trace.

We perform a Saddle-Point (SP) approximation since for any partition function, the classical path has the largest contribution in the functional integral, as the action appears with a negative sign in the exponent. We obtain the classical path as the solution of the Euler-Lagrange equation by extremising the action. To this end, we perform the decomposition

$$\Delta_q = \Delta_0 \delta_{q,0} + \eta_q, \tag{2.38}$$

where Δ_0 stands for the static and homogeneous classical field and η_q the quantum fluctuation around it. We separate the fluctuations by writing the inverse Green's function in momentum space as

$$\boldsymbol{G}^{-1}(k, k') = \langle k | \hat{\boldsymbol{G}}^{-1} | k' \rangle = \langle k | \hat{\boldsymbol{G}}^{-1}_{\mathrm{SP}} - \hat{\boldsymbol{\Xi}} | k' \rangle, \tag{2.39}$$

with the inverse SP Green's function being

$$\boldsymbol{G}^{-1}_{\mathrm{SP}}(k, k') = \langle k | \hat{\boldsymbol{G}}^{-1}_{\mathrm{SP}} | k' \rangle = \begin{pmatrix} ik_n - \xi_{\boldsymbol{k}} & -\Delta \\ -\overline{\Delta} & ik_n + \xi_{\boldsymbol{k}} \end{pmatrix} \delta_{kk'} \tag{2.40}$$

and the fluctuation matrix

$$\boldsymbol{\Xi}(k, k') = \langle k | \hat{\boldsymbol{\Xi}} | k' \rangle = \begin{pmatrix} 0 & \eta_{k-k'} \\ \overline{\eta}_{k'-k} & 0 \end{pmatrix} = \eta_{k-k'} \boldsymbol{\sigma}_+ + \overline{\eta}_{k'-k} \boldsymbol{\sigma}_-, \tag{2.41}$$

where we use the spin-raising and lowering matrices $\boldsymbol{\sigma}_\pm = (\boldsymbol{\sigma}_x \pm i\boldsymbol{\sigma}_y)/2$ with $\boldsymbol{\sigma}_x$ and $\boldsymbol{\sigma}_y$ as first and second Pauli matrix, respectively. Expanding the action in Eq. (2.37) up to second order in η results in

$$\mathcal{S}_{\text{Eff}} = \mathcal{S}_{\text{SP}} + \mathcal{S}_{\text{Lin}} + \mathcal{S}_{\text{Gauss}} + \mathcal{O}(\eta)^3. \tag{2.42}$$

We call

$$\mathcal{S}_{\text{SP}} = -\text{Tr}\ln\left(-\beta\hat{\boldsymbol{G}}_{\text{SP}}^{-1}\right) + \beta V\frac{|\Delta_0|^2}{g} \tag{2.43}$$

the SP action, giving rise to the SP conditions, which is the superfluid order parameter equation. It arises from minimizing $\partial\mathcal{S}_{\text{SP}}/\partial\Delta_0 = 0$. This is an equivalent derivation of the Leggett theory derived in Eq. (2.26). As a result, it is straightforward to show that the linear terms of the action

$$\mathcal{S}_{\text{Lin}} = -\text{Tr}\left\{-\hat{\boldsymbol{G}}_{\text{SP}}\hat{\boldsymbol{\Xi}}\right\} + \beta V\sum_q \frac{\Delta_0\overline{\eta}_q + \overline{\Delta}_0\eta_q}{g} \tag{2.44}$$

vanishes as it obeys $\mathcal{S}_{\text{Lin}} \propto \partial\mathcal{S}_{\text{SP}}/\partial\Delta_0 = 0$. Therefore, the effects of quantum fluctuations arise on a Gaussian level, of which the action reads

$$\mathcal{S}_{\text{Gauss}} = \frac{1}{2}\text{Tr}\left\{\hat{\boldsymbol{G}}_{\text{SP}}\hat{\boldsymbol{\Xi}}\hat{\boldsymbol{G}}_{\text{SP}}\hat{\boldsymbol{\Xi}}\right\} + \beta V\sum_q \frac{|\eta_q|^2}{g}. \tag{2.45}$$

It is known that the SP description is flawed and qualitatively fails when evaluating the critical temperature of the superfluid to normal fluid phase transition. For comparison, see the pink curve in Fig. 1.6. This is rooted in the resulting grand-canonical potential

$$\frac{\Omega_{\text{SP}}(V,T,\mu)}{V} = \frac{|\Delta_0|^2}{g} - \frac{1}{V}\sum_{\boldsymbol{k}}\left[E_{\boldsymbol{k}} - \xi_{\boldsymbol{k}} + \frac{2}{\beta}\ln\left(1 + e^{-\beta E_{\boldsymbol{k}}}\right)\right] \tag{2.46}$$

and the corresponding Equation of State (EoS). There, the contribution of the composite bosons is neglected, and only the unbound fermions are included. For weak interactions, where most fermions are unbound, this is an appropriate approximation. However, for stronger interactions, this is no longer valid, as most fermions are found in bound states. To correct the SP grand-canonical potential (2.46), either diagrammatic means are needed, as was worked out in the 1980s in Ref. [80], or, like in this section, one has to go up to the Gaussian order as shown by Refs. [87, 88].

2.3.1 Gaussian Pair Fluctuations

To improve the SP partition function, we approximate (2.36) up to second order in η. The result is the so-called Gaussian Pair Fluctuations (GPF) partition function

$$\mathcal{Z} \approx e^{-\mathcal{S}_{\text{SP}}}\oint_{\text{P}}\mathcal{D}[\overline{\eta},\eta]e^{-\mathcal{S}_{\text{Gauss}}[\overline{\eta},\eta]} = \mathcal{Z}_{\text{SP}}\mathcal{Z}_{\text{GPF}}. \tag{2.47}$$

This causes the SP grand-canonical potential from Eq. (2.46) to be extended to

$$\Omega \approx \Omega_{\text{SP}} + \Omega_{\text{GPF}}. \tag{2.48}$$

Let us consider in more detail the trace term in Eq. (2.45). We evaluate the trace in the plane wave basis, yielding

$$\mathrm{Tr}\left\{\hat{\boldsymbol{G}}_{\mathrm{SP}}\hat{\boldsymbol{\Xi}}\hat{\boldsymbol{G}}_{\mathrm{SP}}\hat{\boldsymbol{\Xi}}\right\} = \sum_{k}\mathrm{tr}\langle k|\hat{\boldsymbol{G}}_{\mathrm{SP}}\hat{\boldsymbol{\Xi}}\hat{\boldsymbol{G}}_{\mathrm{SP}}\hat{\boldsymbol{\Xi}}|k\rangle \tag{2.49a}$$

$$= \sum_{k,k',p,p'}\mathrm{tr}\langle k|\hat{\boldsymbol{G}}_{\mathrm{SP}}|p\rangle\langle p|\hat{\boldsymbol{\Xi}}|k'\rangle\langle k'|\hat{\boldsymbol{G}}_{\mathrm{SP}}|p'\rangle\langle p'|\hat{\boldsymbol{\Xi}}|k\rangle \tag{2.49b}$$

$$= \sum_{kk'}\mathrm{tr}\left\{\boldsymbol{G}_{\mathrm{SP}}(k)\boldsymbol{\Xi}(k,k')\boldsymbol{G}_{\mathrm{SP}}(k')\boldsymbol{\Xi}(k',k)\right\}, \tag{2.49c}$$

where tr stands for the trace over Nambu (Spin) space. Further, we used Eq. (2.41) for the fluctuation matrix and the Green's function representation

$$\langle k|\hat{\boldsymbol{G}}_{\mathrm{SP}}|k'\rangle = \frac{1}{(ik_n)^2 - E_{\boldsymbol{k}^2}}\begin{pmatrix} ik_n - \xi_{\boldsymbol{k}} & \Delta_0 \\ \overline{\Delta}_0 & ik_n + \xi_{\boldsymbol{k}}\end{pmatrix}\delta_{kk'} = \boldsymbol{G}_{\mathrm{SP}}(k)\delta_{kk'}, \tag{2.50}$$

with the quasiparticle dispersion from Eq. (2.18). To continue, it is advantageous to introduce some more terminology in expressing the Green's function (2.50) as

$$\boldsymbol{G}_{\mathrm{SP}}(k) = \begin{pmatrix} G_{\mathrm{SP}}^{\uparrow\uparrow}(k) & F_{\mathrm{SP}}^{\uparrow\downarrow}(k) \\ F_{\mathrm{SP}}^{\downarrow\uparrow}(k) & G_{\mathrm{SP}}^{\downarrow\downarrow}(k)\end{pmatrix}, \tag{2.51}$$

where the diagonals (off-diagonals) are called the normal (anomalous) Green's functions. With this, the Gaussian action is of the form

$$\mathcal{S}_{\mathrm{Gauss}} = \frac{1}{2}\beta\sum_{q}\begin{pmatrix}\overline{\eta}_q & \eta_q\end{pmatrix}\begin{pmatrix} 1/g - \chi_{+-}(q) & -\chi_{--}(q) \\ -\chi_{++}(q) & 1/g - \chi_{-+}(q)\end{pmatrix}\begin{pmatrix}\eta_q \\ \overline{\eta}_q\end{pmatrix}, \tag{2.52}$$

with the fermionic loop functions (susceptibilities)

$$\chi_{\pm\pm'}(q) = -\frac{1}{\beta}\sum_{k}\mathrm{tr}\left\{\boldsymbol{G}_{\mathrm{SP}}(k)\boldsymbol{\gamma}_{\pm}\boldsymbol{G}_{\mathrm{SP}}(k+q)\boldsymbol{\gamma}_{\pm'}\right\}. \tag{2.53}$$

Here $\boldsymbol{\gamma}_+ = \boldsymbol{\sigma}_+$ and $\boldsymbol{\gamma}_- = \boldsymbol{\sigma}_-$ denote spin raising and lowering matrices, denoted as vertices. We further introduce the renormalised loop functions

$$\Gamma_{ab}(q) = \frac{V}{g}\delta_{ab} - \chi_{ab}(q) \tag{2.54}$$

which then yield the GPF action to become

$$\mathcal{S}_{\mathrm{Gauss}} = \frac{\beta}{2}\sum_{q}\overline{\boldsymbol{\eta}}_q\boldsymbol{\Gamma}(q)\boldsymbol{\eta}_q. \tag{2.55}$$

We integrate out the fluctuations as they constitute a Gaussian functional integral, resulting in the GPF partition function

$$\mathcal{Z}_{\mathrm{GPF}} = \prod_{q}\frac{1}{\det\boldsymbol{\Gamma}(q)} =: \prod_{q}\Gamma^{-1}(q), \tag{2.56}$$

with $\Gamma(q) = \det\boldsymbol{\Gamma}(q)$ as pair vertex function and $\det$ as determinant in Nambu space. With this, we obtain the GPF part of the grand-canonical potential as

$$\Omega_{\mathrm{GPF}} = T\sum_{q}\ln\Gamma(q). \tag{2.57}$$

To obtain the EoS we make use of Eq. (2.48). Being careful with the partial derivatives, including the depletion of the order parameter, as was first described by J. Keeling *et al.* [93], we find

$$V n_{\mathrm{GPF}} = -\left.\frac{\partial \Omega_{\mathrm{GPF}}}{\partial \mu}\right|_{T,V,\Delta_0} - \left.\frac{\partial \Omega_{\mathrm{GPF}}}{\partial \Delta_0}\right|_{T,V,\mu} \left.\frac{\partial \Delta_0(\mu)}{\partial \mu}\right|_{T,V}. \tag{2.58}$$

We now briefly discuss the consequences in two cases: collective excitations and the GPF critical temperature.

2.3.2 Collective modes

To investigate the collective modes, we restrict the discussion to $T = 0$ [88]. We decompose the pair fluctuations according to $\eta_q = \lambda_q + i\theta_q$. For small fluctuations, λ_q is associated with the amplitude and θ_q with the phase fluctuations. Performing this basis change results in the pair propagator

$$\mathbf{\Gamma}_{\mathrm{coll}}(\omega + i0^+, \boldsymbol{q}) = \begin{pmatrix} \Gamma_{xx}(\omega + i0^+, \boldsymbol{q}) & \Gamma_{xy}(\omega + i0^+, \boldsymbol{q}) \\ \Gamma_{yx}(\omega + i0^+, \boldsymbol{q}) & \Gamma_{yy}(\omega + i0^+, \boldsymbol{q}) \end{pmatrix}, \tag{2.59}$$

this time using $\boldsymbol{\gamma}_{x,y} = \boldsymbol{\sigma}_{x,y}$ in the definition of the renormalized loop functions (2.54). Here we used the analytic continuation $iq_\ell \to \omega + i0^+$, ensuring time order and, as such, causality. The action of the collective modes becomes, up to irrelevant constant terms,

$$\mathcal{S}_{\mathrm{coll}} = \frac{1}{2} \sum_{\boldsymbol{q}} \int_{-\infty}^{\infty} \mathrm{d}\omega \begin{pmatrix} \lambda_{-\boldsymbol{q}}(-\omega) & \theta_{-\boldsymbol{q}}(-\omega) \end{pmatrix} \mathbf{\Gamma}_{\mathrm{coll}}(\omega + i0^+, \boldsymbol{q}) \begin{pmatrix} \lambda_{\boldsymbol{q}}(\omega) \\ \theta_{\boldsymbol{q}}(\omega) \end{pmatrix}. \tag{2.60}$$

A collective mode exists for $(\omega, \boldsymbol{q})$ if and only if $\det \mathbf{\Gamma}_{\mathrm{coll}}(\omega + i0^+, \boldsymbol{q}) = 0$. Evaluating the collective modes in general is a numerically hard task, as for frequencies larger than the pair breaking $E_{\mathrm{PB}} = \min_{\boldsymbol{k}}\{E_{\boldsymbol{k}} + E_{\boldsymbol{k}+\boldsymbol{q}}\}$, $\det\mathbf{\Gamma}(\omega + i0^+, \boldsymbol{q})$ has a branch-cut identified with the continuum of broken pairs. However, for small energies $\omega \ll E_{\mathrm{PB}}$ and small momenta, approximate solutions can be found analytically. For instance, Refs. [88, 122] showed that amplitude and phase decouple at zero frequency, i.e. the matrix $\mathbf{\Gamma}_{\mathrm{coll}}(0 + i0^+, \boldsymbol{q})$ becomes diagonal. Only here can one speak of pure phase (Goldstone) or amplitude (Higgs) modes, while for $|\omega| > 0$ these modes mix. Further, at zero momentum, we find

$$\mathbf{\Gamma}_{\mathrm{coll}}(0 + i0^+, \mathbf{0}) = \begin{pmatrix} \Gamma_{xx}(0 + i0^+, \mathbf{0}) & 0 \\ 0 & 0 \end{pmatrix}, \tag{2.61}$$

where $\Gamma_{xx}(0 + i0^+, \mathbf{0}) \neq 0$ is the gap of the amplitude mode. This means the phase fluctuation propagator has a pole at zero energy and momentum, indicating a gapless mode. This is the broken $\mathrm{U}(1)$ sound mode found in neutral superfluids due to the Goldstone theorem [90, 91]. For small momenta, the Goldstone dispersion becomes

$$\omega_{\mathrm{GS}}(\boldsymbol{q}) = c|\boldsymbol{q}| \left[1 + \frac{\gamma}{8} \left(\frac{|\boldsymbol{q}|}{mc} \right)^2 + \frac{\eta}{16} \left(\frac{|\boldsymbol{q}|}{mc} \right)^4 + \mathcal{O}\left(\frac{|\boldsymbol{q}|}{mc} \right)^6 \right], \tag{2.62}$$

for some expansion parameters γ, η which are functions of the interaction parameters. The Goldstone speed of sound c was calculated in 3D [88] and 2D [107] using the above outlined formulation. The amplitude fluctuations also exhibit a collective mode, which is gapped by E_{PB}, thus being located in the pair-breaking continuum, damping it.

After discussing the collective excitations in the ground state, we focus on the critical temperature for the superfluid to normal-fluid transition.

2.3.3 Critical temperature

When approaching $T \to T_c$, we have $|\Delta_0| \to 0$ so the off-diagonal elements of $\mathbf{\Gamma}(q)$ vanish [87]. This leaves only the diagonal entries $\Gamma_{+-} = \Gamma_{-+} = \Gamma_0$. Thus, we find the pair susceptibility in the normal state, which reads

$$\chi_{\text{pair}}(q) = \sum_{\boldsymbol{k}} \frac{1 - n_{\text{F}}(\xi_{\boldsymbol{k}}) - n_{\text{F}}(\xi_{\boldsymbol{k}+\boldsymbol{q}})}{(\xi_{\boldsymbol{k}} + \xi_{\boldsymbol{k}+\boldsymbol{q}}) - iq_\ell}, \tag{2.63}$$

with q_ℓ as bosonic Matsubara frequency and n_{F} denoting the Fermi-Dirac distribution. With this, the vertex function in the normal state becomes

$$\Gamma_0(q) = \frac{V}{g} - \chi_{\text{pair}}(q). \tag{2.64}$$

Eliminating the bare coupling g by using the Lippmann-Schwinger equation (2.28) we obtain the regularized vertex function

$$\Gamma_0(q) = -\frac{m}{4\pi a_{\text{s}}} - \frac{1}{V}\sum_{\boldsymbol{k}} \left[\frac{1 - n_{\text{F}}(\xi_{\boldsymbol{k}}) - n_{\text{F}}(\xi_{\boldsymbol{k}+\boldsymbol{q}})}{(\xi_{\boldsymbol{k}} + \xi_{\boldsymbol{k}+\boldsymbol{q}}) - iq_\ell} - \frac{m}{\boldsymbol{k}^2} \right]. \tag{2.65}$$

To evaluate the critical temperature, we first convert the summation over the bosonic Matsubara frequencies in Eq. (2.57) into a real frequency integral by a Kramers-Kronig like relation known as the trick of Noziére [292]

$$\Gamma_0(iq_\ell, \boldsymbol{q}) = \int_{-\infty}^{\infty} \frac{\mathrm{d}\omega}{\pi} \frac{\mathfrak{Im}\Gamma_0(\omega + i0^+, \boldsymbol{q})}{iq_\ell - \omega}, \tag{2.66}$$

using analytic continuation $iq_m \to \omega + i0^+$. The derivation of the above expression is straightforward, but for the sake of conciseness, we do not demonstrate it here. Evaluating the Matsubara summation in Eq. (2.66) using the residue theorem results in a Bose distribution, yielding the GPF grand-canonical potential in the form of

$$\Omega_{\text{GPF}} = -\frac{1}{\pi}\sum_{\boldsymbol{q}} \int_{-\infty}^{\infty} \mathrm{d}\omega \; n_{\text{B}}(\omega) \mathfrak{Im} \ln \Gamma_0(\omega + i0^+, \boldsymbol{q}). \tag{2.67}$$

Physically $\mathfrak{Im} \ln \Gamma_0(\omega + i0^+, \boldsymbol{q})$ represents the phase of the retarded inverse pairing T-matrix, connected to the scattering resonances in the system. This phase consists of two separate contributions. The first contribution is related to the pair-breaking continuum, where the energy ω is larger than twice the gap of the quasiparticle dispersion and hence breaks the pairs. The second one only arises when the scattering length becomes positive. This announces the emergence of a true two-body bound state, in contrast to the Cooper pairs already found in the SP description, which are many-body bound states. For strong interactions, the two-body bound states contribute significantly to the pair vertex function and, as such, greatly affect the GPF grand-canonical potential in Eq (2.67). One can evaluate the critical temperature using two equations. The first is the Thouless criterion corresponding to the Cooper instability. It is defined as the vanishing of the pair vertex Eq. (2.65) for zero momentum and energy

$$\Gamma_0(0, \mathbf{0}) = -\frac{m}{4\pi a_{\text{s}}} + \sum_{\boldsymbol{k}} \left[\frac{\tanh\left(\frac{\xi_{\boldsymbol{k}}}{2T_c}\right)}{2\xi_{\boldsymbol{k}}} - \frac{m}{\boldsymbol{k}^2} \right] = 0. \tag{2.68}$$

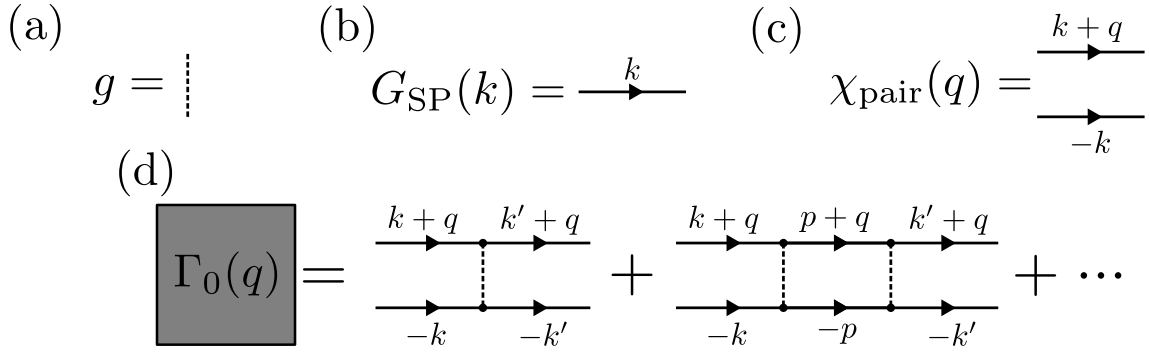


Figure 2.3: Feynman diagrams of pair fluctuations in normal state. Panel (a) represents bare two-particle interaction as a dashed line. Panel (b) depicts SP Green's function of momentum $k = (ik_n, \boldsymbol{k})$ as a solid line. Panel (c) visualises pair susceptibility via propagation of two pairs with centre of mass momentum $q = (iq_\ell, \boldsymbol{q})$. Those are used in ladder summation of panel (d), where a geometric series generates pairing T-matrix Γ. All internal fermionic momenta are denoted by p rather than k.

This corresponds to a pole in the many-body T-matrix $\Gamma_0^{-1}(q)$, showing the emergence of Cooper pairs at zero momentum. The second equation determines the chemical potential at the critical temperature and formally reads

$$n = -\frac{1}{V}\frac{\partial \Omega_{\mathrm{SP}}}{\partial \mu}\bigg|_{T,V} - \frac{1}{V}\frac{\partial \Omega_{\mathrm{GPF}}}{\partial \mu}\bigg|_{T,V} = n_0 + n_{\mathrm{GFP}}, \tag{2.69}$$

where the second term arises from Eq. (2.58). There, the order parameter derivatives vanish in the normal state due to $\Delta_0 = 0$. Solving Eqs. (2.68) and (2.69) self-consistently leads to the critical temperature depicted as the solid blue line in Fig. 1.6, improving the SP result, shown as pink curve. This evaluation is restricted to the 3D case since only the collective modes arising from small quantum fluctuations are relevant. In contrast, when fluctuations are not assumed to be small, quantised vortices also arise. Those are of great importance in 2D due to the BKT mechanism.

Having discussed the effects of quantum fluctuations in the functional integral approach, we switch gears and discuss the diagrammatic technique.

2.4 Diagrammatic approach to BEC-BCS crossover

A different formalism for incorporating beyond mean-field effects and describing the BEC-BCS crossover is based on Feynman diagrams. They also serve as a powerful tool, since they offer a straightforward physical interpretation. However, their application relies heavily on physical intuition about the relevance of certain diagram types, while functional integration provides a more structured way of calculating, but lacks a direct physical interpretation. In this section, we first discuss the idea of describing pair fluctuations using diagrammatic methods. We mostly follow the idea of NSR [80] and some follow-up works [81, 100]. After this, we review particle-hole screening, known as the GMB extension, which relies on a different choice of diagrams.

2.4.1 Pair fluctuations from diagrammatic theories

As the name suggests, pair fluctuations include the description of pairs of two opposite-spin fermions. These pairs are described by the propagation of the two fermions with a fixed momentum relation. Diagrammatically, we describe the propagation of a single fermion by a solid line with an arrow depending on the propagation direction, a spin index and a momentum. This is seen in Fig. 2.3 (b), coming from the normal state. We use certain Feynman rules here. First, the interaction g is denoted by a dashed line without an arrow, see panel (a). Connecting fermionic lines is only possible either at an interaction vertex g, connecting four fermion lines, or a direct fermionic vertex, connecting only two lines. At any vertex, momentum and spin have to be conserved. Therefore, the propagation of a singlet pair, consisting of an $\uparrow$ and a $\downarrow$ line, can not be a closed loop because of the spins. Thus, the pair susceptibility has to be constructed of two parallel lines, see Fig. 2.3 (c). Since k is a free parameter in this diagram, not constrained from the outside, we sum over k. Furthermore, we suppress the spin index here, as for balanced populations in the normal state, we have a perfect $\mathrm{SU}(2)$ symmetry. This indicates that the pair susceptibility in Eq. (2.63) is constructed as a ladder of Green's functions

$$\chi_{\mathrm{pair}}(q) = -\beta \sum_k G_{\mathrm{SP}}(-k) G_{\mathrm{SP}}(k+q). \tag{2.70}$$

The pairs can also interact, so we have to combine two pairs susceptibilities via an interaction vertex g. The full vertex function is then the geometric series of all interaction events, as illustrated by the box in Fig. 2.3 (d). This is known as the Ladder summation [78, 80, 81, 84] and reads

$$V\Gamma_0^{-1}(q) = g + g\frac{\chi_{\mathrm{pair}}(q)}{V}g + g\frac{\chi_{\mathrm{pair}}(q)}{V}g\frac{\chi_{\mathrm{pair}}(q)}{V}g + \dots . \tag{2.71}$$

This geometric series is solved analytically to reveal

$$V\Gamma_0^{-1}(q) = \frac{g}{1 - g\chi_{\mathrm{pair}}(q)/V}, \tag{2.72}$$

which, when inverted, leads to Eq. (2.64) already found in the functional integral approach. Further rearranging the pair vertex function reveals

$$V\Gamma^{-1}(q) = g\left[1 + \chi_{\mathrm{pair}}(q)\Gamma(q)\right], \tag{2.73}$$

showing that the geometric series obtained in Fig. 2.3 (d) and Eq. (2.71) is the ladder approximation of the Bethe-Salpeter equation [81]. We note that in most diagrammatic approaches, the volume factor V is defined in the pair susceptibility (2.70). To stick to the convention used throughout this thesis, we do not do this, at the cost of the volume factor appearing in Eqs. (2.71) and (2.72).

After discussing the diagrammatic approach to the pair fluctuations, we continue by considering a different set of diagrams, leading to the particle-hole screening known as the GMB mechanism.

2.4.2 Particle-hole screening

Particle-hole screening was first introduced by GMB [94] for superconductors. The basic idea is that the presence of particle-hole processes screens the interaction and, as such, reduces the superfluid order parameter. This leads to a reduction of the critical temperature

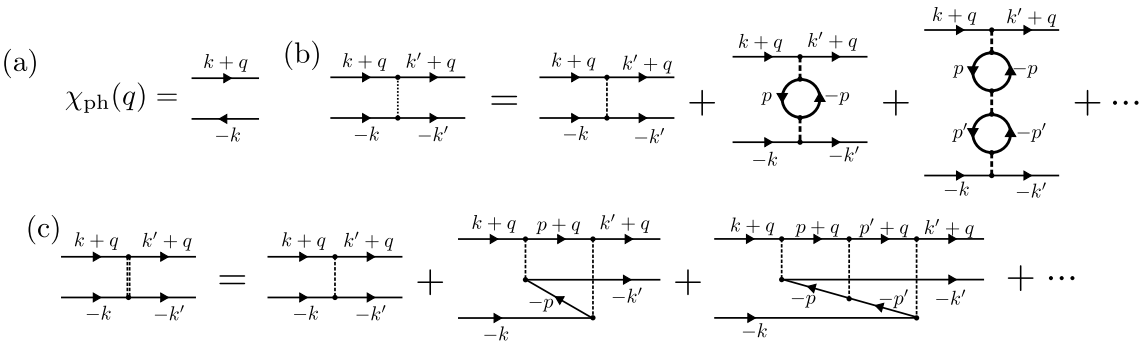


Figure 2.4: Feynman diagrams of particle-hole induced interaction screening. Panel (a) depicts particle-hole susceptibility of opposite spin. Panel (b) represents screening of interaction in ladder diagram by particle-hole pairs being created and annihilated. Panel (c) shows a different type of screening used in the generalised GMB theory, where a particle converts into a hole and back. Panels (b) and (c) show the infinite summation of diagrams of the same type, both known as bubble summations.

by a numerical factor of 2.2 in the weakly interacting limit. Here we discuss the modern implementation of the GMB mechanism for neutral superfluids, which goes beyond the original idea, see Refs. [78, 97, 99]. The emergence of particle-hole interactions, in its most fundamental form shown as the particle-hole susceptibility in Fig. 2.4 (a), screens the bare interaction appearing in the ladder summation, shown in Fig. 2.3 (d), by replacing g with g_{eff}. The respective summation is shown in Fig. 2.4 (c) and represented as the thick dashed line. GMB [94] initially only considered processes up to $\mathcal{O}(g^2)$ as corrections to the ladder summation found in the pair fluctuation theory, compare the first two diagrams used in Fig. 2.4 (c). The modern approach discussed here takes into account the full resummation of all diagrams up to infinite order. As such, the total effective interaction reads

$$U_{\mathrm{eff}}(q) = \frac{g}{1 + g\chi_{\mathrm{ph}}(q)/V}, \tag{2.74}$$

with q denoting the centre of mass momentum. The particle-hole susceptibility in the normal state is given by

$$\chi_{\mathrm{ph}}(q) = \beta \sum_{p} G_{\mathrm{SP}}(p+q) G_{\mathrm{SP}}(p), \tag{2.75}$$

where G_{SP} stands for the saddle-point Green's function. Again, since the two spins obey a $\mathrm{SU}(2)$ symmetry, we neglect the spin indices when dealing with the Green's function. At low temperatures and weak interaction, only s-wave interactions take place, which happen exactly at the Fermi surface, meaning that the effective interaction can be approximated by a constant

$$g_{\mathrm{eff}} \approx \frac{g}{1 - g\langle\chi_{\mathrm{ph}}\rangle/V}. \tag{2.76}$$

Here, the angular average of the particle-hole susceptibility is approximated by [97, 98]

$$\frac{\langle\chi_{\mathrm{ph}}\rangle}{V} \approx -\frac{\ln(4e)}{3}\frac{mk_{\mathrm{F}}}{2\pi^2}. \tag{2.77}$$

Using this, we replace the inverse bare interaction in the Thouless criterion (2.68) by

$$\frac{1}{g_{\mathrm{eff}}} \approx \frac{1}{g} + \frac{\ln(4e)}{3}\frac{mk_{\mathrm{F}}}{2\pi^2} + \mathcal{O}(g). \tag{2.78}$$

In combination with the SP EoS (2.27) this leads to a reduced critical temperature, reading

$$T_{\mathrm{c}}^{\mathrm{GMB}} \approx \left(\frac{2}{e}\right)^{7/3} \frac{\gamma}{\pi} T_{\mathrm{F}} e^{-\frac{\pi}{2|k_{\mathrm{F}} a_{\mathrm{s}}|}}. \tag{2.79}$$

Comparing this with the mean-field critical temperature seen in Eq. (2.29), we find that it is reduced by a numerical factor of $(4e)^{1/3} \approx 2.2$. It is also possible to extend this beyond weak coupling, which has been done, for instance, in Refs. [97, 99]. However, this is beyond the scope of this introduction.

This finishes the discussion of the three distinct formulations of the BEC-BCS crossover used in modern condensed matter theory. Those three approaches, while able to successfully describe the crossover, all share one major flaw: a certain degree of arbitrariness. We elaborate on this issue in the next section.

2.5 Arbitrariness of approaches

In this chapter, we have discussed so far how to develop a theory of the BEC-BCS crossover from first principles. Furthermore, we presented its mean-field approximation, as well as extensions based on pair fluctuations and the GMB mechanism. However, the choices made here intrinsically possess some degree of arbitrariness. In an operator-based approach, when using an Hartree-Fock-Bogoliubov (HFB) approximation, all three interaction channels can be accounted for. However, this has the possibility of overestimating the energy as a variational approach is done on the level of the Hamiltonian, potentially assigning the same state to several scattering events. Conversely, in a functional integral approach using a HS transformation, only one channel can be chosen. Although the transformation is exact, when performing explicit calculations, the ambiguity of the transformation causes issues, as on any level of approximation, the choice of the interaction decomposition has a massive impact on the outcome. This is best seen if, instead of the pair field, the density fields, i.e. for charged systems, the plasmons, are considered. In such a case, no superfluid or superconducting properties can be described. Lastly, in diagrammatic approaches, the choice of diagrams has the same effect. For instance, when, instead of choosing the GMB type diagrams, we would apply a different type of particle-hole screening, for instance, by the diagrams seen in Fig. 2.4 (b), we would find an entirely different critical temperature. Although this process is thought to be strongly suppressed in ultracold s-wave systems [97], the choice of neglecting those diagrams has to be made arbitrarily, or out of physical intuition, both of which lack systematics. The choice of diagrams has the potential of strongly altering the theoretical outcome, analogously to the choice of the HS decomposition. In an experiment, however, all diagrams contribute, even though with different relevance. Hence, a systematic approach of sorting the numerous families of processes is needed. This arbitrariness will be addressed in the next chapter, where we develop the *weighted Hartree-Fock-Bogoliubov* method as a self-consistent field theoretical approach of sorting competing processes in a quantum many-body system. We will base the method on the functional integral formulation of quantum field theory to avoid the ambiguous choice of diagrams.

Chapter 3

Weighted Hartree-Fock-Bogoliubov theory

Divide et impera - Divide and conquer

Ancient roman maxim, attributed later to Niccolò Machiavelli

3.1 Introduction . . . 42
3.2 Decomposing interactions . . . 42
3.2.1 Action of interacting fermions . . . 43
3.2.2 Contact interaction . . . 44
3.2.3 Ambiguous interaction decomposition and its cure . . . 45
3.2.4 Momentum space . . . 50
3.2.5 Effective action . . . 52
3.3 Saddle-point analysis of WHFB action . . . 53
3.3.1 Saddle-point approximation . . . 53
3.3.2 Establishing self-consistency . . . 54
3.3.3 Equation of state . . . 56
3.3.4 Hartree self-energy as order parameter . . . 57
3.A More general Hubbard-Stratonovich transformations . . . 58
3.A.1 Hartree channel . . . 59
3.A.2 Fock channel . . . 59
3.A.3 Bogoliubov channel . . . 60
3.A.4 Hartree-Fock-Bogoliubov self-energy . . . 61

3.1 Introduction

The functional integral theory of superfluidity was established by the work of Sá de Melo, Randeria, and Engelbrecht, published in 1993 and 1997 [87, 88]. Those approaches mostly focus on short-range s-wave interactions, even though generalisations to p- and d-waves were subsequently worked out [293, 294]. All functional integral approaches have in common that they include only the Bogoliubov channel, responsible for the emergence of Cooper pairs. Other approaches work in a diagrammatic framework [80, 81, 84, 100, 295], where the choice of included diagrams poses a bias. Typically, only the diagrams responsible for pairing are included, and no Hartree shift emerges on a mean-field level.

It is known that for weak interactions, particle-hole processes play an important role in renormalising the critical temperature of superfluidity and superconductivity, known as the GMB mechanism [94]. On a mean-field level, those particle-hole processes are associated with the Hartree shift of the chemical potential. As such, they are treated in most approaches as a constant shift of the chemical potential and hence they are formally absorbed into it or even neglected [28]. The value of the chemical potential with respect to the band minimum, however, determines the number of particles in a system. Therefore, an exact quantitative prediction of the chemical potential is crucial for any experiment.

Some recent publications included the Hartree channel into the framework [154, 296, 297]. Those approaches lack a controlling mechanism to prevent overcounting the quantum states involved. They impose an arbitrary decomposition of the interaction, which introduces another bias into the theory. As such, a more fundamental treatment is needed to remove this arbitrariness.

A second source of problems arises when performing the standard regularisation of the interaction. The energies associated with particle-hole processes generally scale with the bare interaction strength, which any regularisation scheme must account for. A widespread strategy in the literature is to extend the weak coupling approximation of the bare interaction strength to stronger interactions, which causes unphysical divergences of, for instance, the chemical potential and ground-state energy [28, 296]. This led to the wrong conclusion that the Hartree shift has to be neglected in cold atomic Fermi gases to avoid these divergences.

In this chapter, which is a more detailed version of Ref. [P1], we show that the common approach of including the particle-hole sector in the mean-field theory of the BEC-BCS crossover is problematic. We show how to partition the interaction consistently and how minimising the action, as a fundamental principle, solves all the problems listed above. Further, we demonstrate that the Hartree shift is an essential ingredient when describing weakly interacting Fermi gases and investigate how its relevance decreases as interactions grow stronger, until a gas of composite bosons is reached.

3.2 Decomposing interactions

In this section, we review the action of s-wave interacting fermions in a continuum. Subsequently, we decompose the interactions into all possible channels, i.e. the Hartree, Fock and Bogoliubov channels. We perform separate Hubbard-Stratonovich (HS) transformations in each channel to eliminate the quartic interaction term in the Lagrangian in favour of bosonic auxiliary fields.

3.2.1 Action of interacting fermions

We start the discussion by analysing the Euclidean action[1] of a Fermi spin mixture. The action functional is the integral of a Lagrangian density $\mathcal{L}$ over the D-dimensional spatial coordinate $\boldsymbol{x}$ and imaginary time τ, which we express as

$$\mathcal{S}[\overline{\psi},\psi] = \int \mathrm{d}x\, \mathcal{L} = \int \mathrm{d}^D\boldsymbol{x} \int_0^\beta \mathrm{d}\tau\, \mathcal{L}. \tag{3.1}$$

Here $\beta = 1/T$ denotes the inverse temperature. Instead of deriving and solving the Euler-Lagrange equations of the fields associated with $\mathcal{L}$, we take the thermodynamic approach. Thus, we introduce the partition function

$$\mathcal{Z} = \mathrm{Tr}\left\{e^{-\beta\hat{H}}\right\}, \tag{3.2}$$

where $\hat{H}$ is the original Hamiltonian operator and Tr represents the operator trace. In the following, we calculate $\mathcal{Z}$, using the second quantised version of the Feynman path integral [298, 299]. The path integral approach is a formulation of quantum mechanics equivalent to the operator-based formalism developed by Schrödinger, Heisenberg, and Bohr, which we review in Appendix A.

The Lagrangian density in Eq. (3.1) consists of a kinetic energy term and an interaction term. The kinetic Lagrangian density of a set f of $|f| = M$ different species of fermions in a grand-canonical ensemble reads

$$\mathcal{L}_0 = \sum_{\mathrm{s}\in f} \overline{\psi}_\mathrm{s}(x)\left[\partial_\tau - \frac{\nabla^2}{2m_\mathrm{s}} - \mu_\mathrm{s}\right]\psi_\mathrm{s}(x). \tag{3.3}$$

Here $\overline{\psi},\psi$ are the fermionic Grassmann fields, ∂_τ stands for the derivative in imaginary time, ∇ the gradient in real space, m_s the mass of the species s, and μ_s the chemical potential, controlling the number of particles N_s of each species. Henceforth, we consider the different species $\mathrm{s} \in f$ as internal degrees of freedom of the fermions, which are throughout this thesis mostly given by their pseudo-spin. The object in the brackets is the negative, inverse free particle Green's function of the species s

$$G^{-1}_{\mathrm{s},0}(x,x) = -\partial_\tau + \frac{\nabla^2}{2m_\mathrm{s}} + \mu_\mathrm{s}. \tag{3.4}$$

Remark: Unit system

We use a unit system with $\hbar = 1$ and $k_\mathrm{B} = 1$. This means that frequency is equivalent to energy ($\hbar = 1$) and temperature ($k_\mathrm{B} = 1$).

Remark: Two-particle scattering

Two-particle scattering is an approximation, valid when the timescale t_int of an interaction is much smaller than the time between two interactions t_0. When $t_\mathrm{int}/t_0 \ll 1$, we assume that most interactions involve exactly two particles. In experimental setups, higher scattering processes create loss channels which become important on longer timescales [300–307].

[1] For convenience, we will, from now on, refer to the Euclidean action simply as action.

In order to describe any interesting physical system, we also have to include interactions between the particles. In the remainder of this thesis, we will restrict ourselves to two-particle interactions as a powerful theoretical idealisation. This interaction is described by a bi-local potential $U(\boldsymbol{x}, \boldsymbol{x}')$, where $\boldsymbol{x}, \boldsymbol{x}'$ are the positions of the two particles. Because the timescale of the interaction is small compared to the other timescales in the system, we assume instantaneous interactions, so the potential U does not explicitly depend on time. Furthermore, we care for translational invariant systems, yielding $U(\boldsymbol{x}, \boldsymbol{x}') = U(\boldsymbol{x} - \boldsymbol{x}')$. The interaction Lagrangian density then reads

$$\mathcal{L}_{\mathrm{int}} = \int \mathrm{d}x' \sum_{\mathrm{ss}'\epsilon f} \overline{\psi}_{\mathrm{s}}(x)\overline{\psi}_{\mathrm{s}'}(x')U(\boldsymbol{x} - \boldsymbol{x}')\delta(\tau - \tau')\psi_{\mathrm{s}'}(x')\psi_{\mathrm{s}}(x). \tag{3.5}$$

The full Lagrangian density is just the sum of those two terms

$$\mathcal{L} = \mathcal{L}_0 + \mathcal{L}_{\mathrm{int}}. \tag{3.6}$$

In the functional integral approach, the partition function results from an integration over all possible anti-periodic field configurations of the Grassmann fields, reading

$$\mathcal{Z} = \oint_{\psi(0,\boldsymbol{x})=-\psi(\beta,\boldsymbol{x})} \mathcal{D}[\overline{\psi}, \psi] e^{-\mathcal{S}[\overline{\psi},\psi]} = \oint_{\mathrm{A}} \mathcal{D}[\overline{\psi}, \psi] e^{-\mathcal{S}[\overline{\psi},\psi]}, \tag{3.7}$$

where, after the second equality, the A subscript of the integral sign is an abbreviation for anti-periodic. Conversely, for bosonic integrals, where the coherent states are complex-valued functions periodic in imaginary time, we use a P subscript. The partition function encodes all the thermodynamic information of a system.

3.2.2 Contact interaction

For the remainder of this thesis, we deal with low-energy s-wave interactions. This means that, when decomposing any interaction potential into partial waves, only the leading-order contribution will be of interest. The scattering channel of lowest energy, the s-wave channel, has no angular momentum $\ell = 0$ For higher angular momenta, the potential obtains the so-called *centrifugal barrier*, scaling as $E_{\mathrm{CB}} \sim \ell^2$.

The typical energy scale of the scattering events is of the order of the temperature T. For temperatures typical in quantum gas experiments, we have $T \ll E_{\mathrm{CB}}$. Furthermore, quantum gas setups in general deal with dilute systems. This means that the typical distance between particles $d \sim n^{-1/D}$ is at least an order of magnitude smaller than the interaction range. Henceforth, we approximate the interaction as contact-like. This strong restriction makes calculations much easier, as microscopic details can be disregarded, giving rise to the concept we will call *strong universality*. In this thesis, however, we will find out that strong universality is theoretically impractical, as its very founding idea that the thermodynamic properties of a quantum gas

Definition: Strong universality

Strong universality means that all the properties of a system are expressed by a single internal length scale, the s-wave scattering length a_{s}. Furthermore, we have two external length scales, associated here with the density n and the thermal wavelength $\lambda_{\mathrm{T}} \sim \sqrt{T^{-1}}$.

depend only on two length scales and not on the microscopic details of the potential, prevents us from incorporating important physical effects. In any case, contact interaction is a useful tool to describe the general behaviour of a dilute ultracold system and consequently is used excessively, though with some caution. For contact interactions, we use

$$U_{ss'}(\boldsymbol{x}-\boldsymbol{x}') = \pm g\delta^D(\boldsymbol{x}-\boldsymbol{x}')\,(1-\delta_{ss'})\,, \tag{3.8}$$

where the sign determines the nature of the interaction. We use the convention $g \geq 0$, meaning a positive sign represents repulsive while a negative sign stands for attractive interactions. The final bracket ensures that equal spins do not interact in a contact-like manner due to the Pauli exclusion principle. In the literature [28, 154, 296] one often finds a replacement rule of the bare interaction in favour of the s-wave scattering length, $g \propto a_s$. This is an approximation valid for weak interactions only, where the range of the interaction is larger than the scattering length and should not be used for arbitrary interaction strengths. Using Eq. (3.8) we find the action to simplify to

$$\mathcal{S}[\overline{\psi},\psi] = \int \mathrm{d}x \sum_s \left\{ \overline{\psi}_s(x)\left[-G^{-1}_{s,0}(x,x)\right]\psi_s(x) - g\frac{1}{2}\sum_{s'\neq s}\overline{\psi}_s(x)\overline{\psi}_{s'}(x)\psi_{s'}(x)\psi_s(x)\right\}. \tag{3.9}$$

This is the standard action used in many functional integral approaches to the BEC-BCS crossover [87, 88, 113, 115, 122, 291] with great success. However, the model quickly reaches its boundaries due to the aforementioned singularity of the interaction. However, as long as those validity regions are respected, it can predict many physical observables with great accuracy. In the following, we introduce the standard procedure of the Hubbard-Stratonovich transformation and its ambiguity. Following this, we present the Weighted Hartree-Fock-Bogoliubov (WHFB) method as a resolution of this ambiguity, which gives name to this chapter.

3.2.3 Ambiguous interaction decomposition and its cure

In this section, we apply the Hubbard-Stratonovich (HS) transformations in various interaction channels. It is an exact method to deal with interacting systems, first published by R. Stratonovich [308] and shortly after by J. Hubbard [309]. The transformation involves introducing a bosonic auxiliary field that couples to quadratic fermion terms. However, the transformation is ambiguous, which was already pointed out in Ref. [289]. Since two Fermi fields are eliminated in favour of a bosonic field, the choice of which two fields to eliminate has a physical meaning. Those choices are referred to as *channels*, which are better understood in the operator-based HFB approximation.

Context: Hartree-Fock-Bogoliubov approximation

In a HFB operator approximation [310, 311], the quartic interaction decomposes like

$$\begin{aligned}\hat{\psi}^\dagger_s\hat{\psi}^\dagger_{s'}\hat{\psi}_{s'}\hat{\psi}_s \approx &+\langle\hat{\psi}^\dagger_s\hat{\psi}_s\rangle\hat{\psi}^\dagger_{s'}\hat{\psi}_{s'} + \langle\hat{\psi}^\dagger_{s'}\hat{\psi}_{s'}\rangle\hat{\psi}^\dagger_s\hat{\psi}_s - \langle\hat{\psi}^\dagger_s\hat{\psi}_s\rangle\langle\hat{\psi}_{s'}\hat{\psi}^\dagger_{s'}\rangle\\ &-\langle\hat{\psi}^\dagger_s\hat{\psi}_{s'}\rangle\hat{\psi}^\dagger_{s'}\hat{\psi}_s - \langle\hat{\psi}^\dagger_{s'}\hat{\psi}_s\rangle\hat{\psi}^\dagger_s\hat{\psi}_{s'} + \langle\hat{\psi}^\dagger_s\hat{\psi}_{s'}\rangle\langle\hat{\psi}^\dagger_{s'}\hat{\psi}_s\rangle\\ &+\langle\hat{\psi}^\dagger_s\hat{\psi}^\dagger_{s'}\rangle\hat{\psi}_{s'}\hat{\psi}_s + \langle\hat{\psi}_{s'}\hat{\psi}_s\rangle\hat{\psi}^\dagger_s\hat{\psi}^\dagger_{s'} - \langle\hat{\psi}^\dagger_s\hat{\psi}^\dagger_{s'}\rangle\langle\hat{\psi}_{s'}\hat{\psi}_s\rangle.\end{aligned} \tag{3.10}$$

Here we used $\hat{\psi}_s(x)$ as the respective field operator associated to $\psi_s(x)$. Furthermore,$\langle\circ\rangle$ denotes the operator expectation value.

In Eq. (3.10), the first line stands for the Hartree, or direct, channel. It is associated with a shift in the chemical potential proportional to the density. The second term is the Fock, or exchange, channel. It involves spin flips and acquires an overall negative sign because the fields describe fermions. Those two terms are commonly known as the Hartree-Fock approximation, which is widely used in solid-state physics. One seminal application is the Jellium model of conductivity, where both Hartree and Fock energies are necessary for an adequate description [274]. Those two channels are *particle-hole* processes. The last term is vital for superconductivity, the Bogoliubov or pairing channel. It is, in contrast to the former two, a particle-particle process in which the associated quasiparticles are Cooper pairs. Note that Bardeen, Cooper and Schrieffer did not explicitly use this decomposition in their original work [18], although it became common later.

Interaction channel decomposition

After this short foray, we focus on the analogous formulation within a functional integral approach. Here, the ordering of the fields in the Lagrangian is associated with one channel. The Lagrangian density present in the action in Eq. (3.9) is in normal order, such that the vacuum has no energy. Incidentally, this is already the order fitting the pairing channel. When doing the HS transformation, the bosonic field is associated with the first or last two fields in the interaction Lagrangian. Since performing a HS transformation eliminates the interaction term, most authors choose one channel by physical reasoning. Describing plasmons or any density-like excitations in a normal fluid typically relies on the direct channel [312–314], leading either to charge waves or longitudinal spin waves. The exchange channel is relevant in order to describe transverse spin waves and magnetisation. In theories dealing with superfluidity or superconductivity, the pairing channel is used, see for instance Refs. [80, 87, 88, 115, 291, 293–295]. There are some approaches dealing with multiple interaction channels [154, 319, 320], where direct and pairing channels are used in a HFB approximation. Applications are atomic [321] or nuclear superfluids [322], or the aforementioned Jellium model [274, 275, 311]. In those cases, an arbitrary partitioning, if any, is used. An interesting approach is worked out in Ref. [296], where a multi-channel HS transformation is applied. However, the partition-

Definition: Particles and holes

We follow the conventions of solid-state theory here and refer to $\overline{\psi}_\mathrm{s}$ as particles and ψ_s as holes. Therefore, $\langle\overline{\psi}\psi\rangle$ is associated to a particle-hole process, while $\langle\overline{\psi\psi}\rangle$ denotes a particle-particle process.

Context: Hyperfine-states

The elements of f correspond to different hyperfine-states written in the basis $|F, m_F\rangle$, with $F = I+J$ as total angular momentum of the atom and m_F as the magnetic quantum number. Prime examples for those spin-mixtures are the two hyperfine-states of ^{6}Li, prepared in the two states $|\uparrow\rangle = |1/2, 1/2\rangle$ and $|\downarrow\rangle = |1/2, -1/2\rangle$ [144, 151, 152, 164, 165, 315, 316]. They have a Feshbach resonance at 832 G, see Table 1.1. The second most prominent example is ^{40}K, where the hyperfine states are usually $|\uparrow\rangle = |9/2, 9/2\rangle$ and $|\downarrow\rangle = |9/2, 7/2\rangle$ [317, 318].

ing of the interaction is arbitrary and, due to an invalid approximation of the scattering strength $g \sim a_\mathrm{s}$, the conclusion there is that the direct channel can not contribute.

In the following, we show that, in fact, the direct channel is a vital ingredient in describing Fermi gases on a more fundamental and consistent level. To do so, we restrict ourselves to a Fermi spin mixture with two hyperfine-states in pseudo-spin notation $f = \{\uparrow, \downarrow\}$. Furthermore, we assume that the system is in thermal equilibrium and has perfectly balanced populations $n_\uparrow = n_\downarrow = n/2$. This has important consequences which will arise when the exchange channel is discussed.

To describe Hartree, Fock and Bogoliubov channels, our ansatz is to write the interaction strength g as a sum of three channel-specific interactions

$$g = g_\mathrm{H} + g_\mathrm{F} + g_\mathrm{B} \quad \Leftrightarrow \quad \mathcal{L}_\mathrm{int} = \mathcal{L}_\mathrm{int,H} + \mathcal{L}_\mathrm{int,F} + \mathcal{L}_\mathrm{int,B}, \tag{3.11}$$

in each channel, rearranging the anti-commuting fields to become

$$\mathcal{L}_\mathrm{int,H} = -g_\mathrm{H}\overline{\psi}_\uparrow(x)\psi_\uparrow(x)\overline{\psi}_\downarrow(x)\psi_\downarrow(x), \tag{3.12a}$$
$$\mathcal{L}_\mathrm{int,F} = +g_\mathrm{F}\overline{\psi}_\uparrow(x)\psi_\downarrow(x)\overline{\psi}_\downarrow(x)\psi_\uparrow(x), \tag{3.12b}$$
$$\mathcal{L}_\mathrm{int,B} = -g_\mathrm{B}\overline{\psi}_\uparrow(x)\overline{\psi}_\downarrow(x)\psi_\downarrow(x)\psi_\uparrow(x). \tag{3.12c}$$

This means associating a global weight to each interaction channel, which is a natural consequence of a time and translational invariant system, i.e. $g_\mathrm{H} = hg$, $g_\mathrm{F} = fg$, and $g_\mathrm{B} = bg$ such that $h + f + b = 1$. We do not assume the specific domain for h, f, b and their value can be whatever minimises the energy. Using the interaction decomposition from Eq. (3.11) and the definition of the interaction actions

$$\mathcal{S}_\mathrm{J}[\overline{\psi}, \psi] = \int \mathrm{d}x\, \mathcal{L}_\mathrm{int,J} \tag{3.13}$$

the action from Eq. (3.9) becomes

$$\mathcal{S}[\overline{\psi}, \psi] = \mathcal{S}_\mathrm{kin}[\overline{\psi}, \psi] + \mathcal{S}_\mathrm{int,H}[\overline{\psi}, \psi] + \mathcal{S}_\mathrm{int,F}[\overline{\psi}, \psi] + \mathcal{S}_\mathrm{int,B}[\overline{\psi}, \psi]. \tag{3.14}$$

Here, we set the kinetic part of the action to be

$$\mathcal{S}_\mathrm{kin}[\overline{\psi}, \psi] = \int \mathrm{d}x \sum_\mathrm{s} \overline{\psi}_\mathrm{s}(x)\left[-G^{-1}_{\mathrm{s},0}(x,x)\right]\psi_\mathrm{s}(x). \tag{3.15}$$

In the following, we discuss the three different HS transformations using the contact interaction. A discussion for general interactions is found in Appendix 3.A. Our restriction to contact interaction yields one large simplification: The Lagrangian is $\mathrm{SU}(2)$-symmetric. This means that the Lagrangian density is invariant under a rotation of the spin basis, which leads, due to Noether's theorem [323], to a conserved quantity, namely the spin polarization [324, 325]. Because the system is initially unpolarized, it remains without spin polarisation. Since the Fock term causes spin flips, this would inevitably lead to a spontaneous breaking of $\mathrm{SU}(2)$, which is something we do not consider here. It follows that the Fock term has to be zero, leading to $g_\mathrm{F} = 0$. It should be noted that the imbalanced Fermi gas was intensively discussed in the literature, see for example Refs. [109, 110, 112–119, 322, 326, 327]. Those results will also be affected by the partitioning method outlined in this thesis.

Therefore, in the following, we take $g = g_\mathrm{H} + g_\mathrm{B}$ and subsequently perform the HS transform in detail.

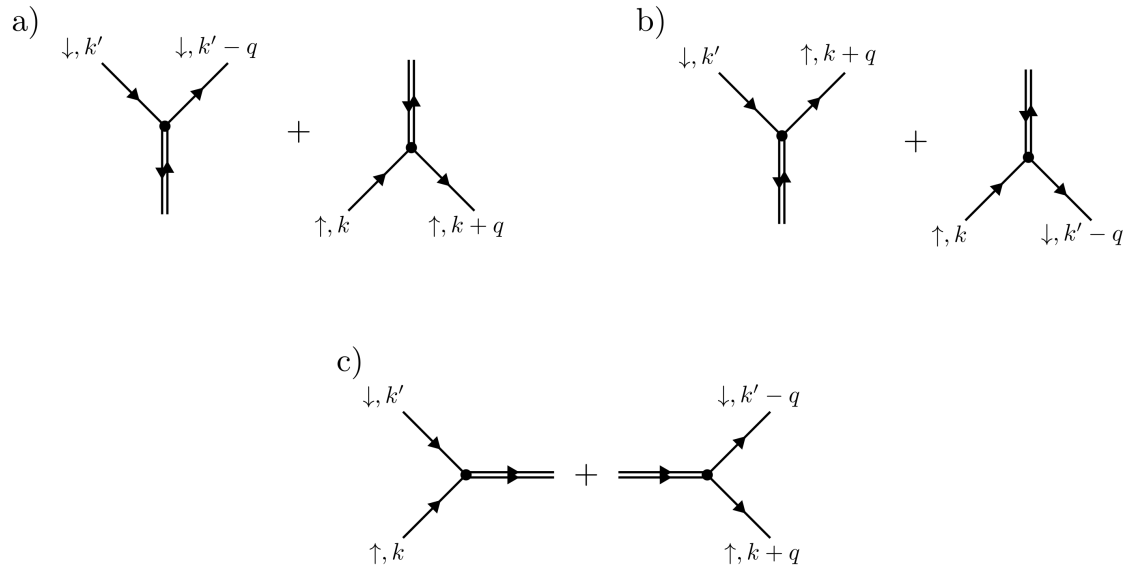


Figure 3.1: Feynman diagrammatic representation of the three interaction channels. The single thin lines represent the many-body Green's functions, the double lines the HS fields. In a), one sees the normal Green's function coupled to the Hartree field, while in b), it couples to a complex spin-flip Fock field. Figure c) shows the anomalous Green's functions coupling to the Cooper pair, that is, the Bogoliubov HS field.

Hubbard-Stratonovich transformations

In this section, we perform the direct and pairing HS transformations and derive the full effective action of the system. We present diagrammatic representations of the three channels in Fig.3.1. Panel (a) represents the Hartree, panel (b) for completeness the Fock, and panel (c) the Bogoliubov channel. We start with the pairing channel before adding the direct channel, and hence removing the arbitrariness in the standard procedure.

As the pair field is associated with anomalous expectation values, it must be a complex field. We introduce the auxiliary fields $\overline{\Delta}_{\mathrm{B}}(x), \Delta_{\mathrm{B}}(x) \in \mathbb{C}$ and couple them via sources to the anomalous terms. In a functional form, this means introducing the pairing Lagrangian density

$$\mathcal{L}_{\mathrm{B}} = \frac{1}{2} M_{\mathrm{B}}^2 \overline{\Delta}_{\mathrm{B}}(x)\Delta_{\mathrm{B}}(x) + \overline{j}_{\mathrm{B}}(x)\Delta_{\mathrm{B}}(x) + \overline{\Delta}_{\mathrm{B}}(x) j_{\mathrm{B}}(x), \tag{3.16}$$

where M_{B} is the field theoretical "mass" of the field. The complex source terms are

$$j_{\mathrm{B}}(x) = \psi_{\downarrow}(x)\psi_{\uparrow}(x) \qquad , \qquad \overline{j}_{\mathrm{B}}(x) = \overline{\psi}_{\uparrow}(x)\overline{\psi}_{\downarrow}(x). \tag{3.17}$$

This Lagrangian is quadratic in the bosonic fields $\overline{\Delta}_{\mathrm{B}}, \Delta_{\mathrm{B}}$ and, hence, the functional integration for its generating functional can be performed, leading to

$$\mathcal{Z}_{\mathrm{B}}[\overline{j}_{\mathrm{B}}, j_{\mathrm{B}}] = \mathcal{N}_{\mathrm{B}} \oint_{\mathrm{P}} \mathcal{D}[\overline{\Delta}_{\mathrm{B}}, \Delta_{\mathrm{B}}] e^{-\int \mathrm{d}x\, \mathcal{L}_{\mathrm{B}}} = e^{-\int \mathrm{d}x\, \frac{2}{M_{\mathrm{B}}^2} \overline{j}_{\mathrm{B}}(x) j_{\mathrm{B}}(x)} = e^{-\mathcal{S}_{\mathrm{B}}[\overline{\psi},\psi]}. \tag{3.18}$$

The last equality comes from identifying $M_{\mathrm{B}}^2 = 2/g_{\mathrm{B}}$. This means the exponential of the pairing interaction can be replaced by the functional integral over the auxiliary fields $\overline{\Delta}_{\mathrm{B}}, \Delta_{\mathrm{B}}$, up to an irrelevant normalisation constant $\mathcal{N}_{\mathrm{B}}$. For more details about this constant, see Eq. (B.61) in Appendix B. To summarise this, we can eliminate a normal ordered ψ^4 term in the action via

$$e^{-\mathcal{S}_{\mathrm{B}}[\overline{\psi},\psi]} = \mathcal{N}_{\mathrm{B}} \oint_{\mathrm{P}} \mathcal{D}[\overline{\Delta}_{\mathrm{B}}, \Delta_{\mathrm{B}}] e^{-\mathcal{S}_{\mathrm{aux,B}}[\overline{\Delta}_{\mathrm{B}}, \Delta_{\mathrm{B}}; \overline{\psi}, \psi]}, \tag{3.19}$$

using the auxiliary action

$$\mathcal{S}_{\mathrm{aux,B}} = \int \mathrm{d}x \left[\frac{\overline{\Delta}_{\mathrm{B}}(x)\Delta_{\mathrm{B}}(x)}{g_{\mathrm{B}}} + \overline{\psi}_{\uparrow}(x)\overline{\psi}_{\downarrow}(x)\Delta_{\mathrm{B}}(x) + \overline{\Delta}_{\mathrm{B}}(x)\psi_{\downarrow}(x)\psi_{\uparrow}(x) \right]. \tag{3.20}$$

This is the standard procedure when considering a functional integral BCS theory including only the pairing channel, as outlined in Refs. [87, 88, 93, 122, 128].

In addition to the pair interactions, the goal of this chapter is to obtain a fully self-consistent treatment including the direct channel. As such, an additional field is introduced, which is the real-valued Hartree field $\boldsymbol{\Delta}_{\mathrm{H}}(x)$. This field is vector-valued since the two spin densities are, in principle, separate from each other. Therefore, the Lagrangian density associated with the Hartree auxiliary field is

$$\mathcal{L}_{\mathrm{H}} = \frac{1}{4} M_{\mathrm{H}}^2 \boldsymbol{\Delta}_{\mathrm{H}}^{\mathrm{T}}(x)\boldsymbol{\sigma}_{\mathrm{x}}\boldsymbol{\Delta}_{\mathrm{H}}(x) + \boldsymbol{\rho}^{\mathrm{T}}(x)\boldsymbol{\Delta}_{\mathrm{H}}(x), \tag{3.21}$$

where we use the spinor describing the densities

$$\boldsymbol{\rho}^{\mathrm{T}}(x) = \begin{pmatrix} \overline{\psi}_{\uparrow}(x)\psi_{\uparrow}(x) & \overline{\psi}_{\downarrow}(x)\psi_{\downarrow}(x) \end{pmatrix}, \tag{3.22}$$

as a source term. Furthermore, $\boldsymbol{\sigma}_x$ stands for the first Pauli matrix, which seems off at first, since the mass term is not diagonal. This is because the spins are not an appropriate basis for the Hartree channel. Instead, the proper basis consists of the total density $n = n_\uparrow + n_\downarrow$ and the longitudinal magnetisation $m = n_\uparrow - n_\downarrow$. However, this notation can lead to spurious terms containing equal-spin interactions of the fermions, being explicitly forbidden by the Pauli principle. To avoid them, we either have to be cautious with the transformation or stay in this off-diagonal basis. Now identifying that the Hartree interaction term is expressible in terms of the density spinor, the Hartree channel HS transformation reads

$$\mathcal{Z}_{\mathrm{H}}[\boldsymbol{\rho}] = e^{-\mathcal{S}_{\mathrm{H}}[\overline{\psi},\psi]} = \mathcal{N}_{\mathrm{H}} \oint_{\mathrm{P}} \mathcal{D}[\boldsymbol{\Delta}_{\mathrm{H}}]\, e^{-\mathcal{S}_{\mathrm{aux,H}}[\boldsymbol{\Delta}_{\mathrm{H}};\overline{\psi},\psi]}, \tag{3.23}$$

using the auxiliary action

$$\mathcal{S}_{\mathrm{aux,H}}[\boldsymbol{\Delta}_{\mathrm{H}};\overline{\psi},\psi] = \int \mathrm{d}x\, \mathcal{L}_{\mathrm{H}} \tag{3.24}$$

as well as the identification $M_{\mathrm{H}}^2 = 1/g_{\mathrm{H}}$. The Hartree auxiliary field has two components, associated with density expectation values. Since only opposite-spin atoms interact with each other, the naming is given as

$$\boldsymbol{\Delta}_{\mathrm{H}}^{\mathrm{T}}(x) = \begin{pmatrix} \Delta_{\mathrm{H},\downarrow}(x) & \Delta_{\mathrm{H},\uparrow}(x) \end{pmatrix}. \tag{3.25}$$

With those two transformations and the absence of exchange terms, we briefly summarise the resulting HS action in the following.

Effective action and Nambu spinor

To discuss the HS action, we dissect the partition function $\mathcal{Z}$ defined in Eq. (3.7). Inserting the pairing and direct channel HS transformations from Eqs. (3.19) and (3.23), respectively, the partition function becomes

$$\mathcal{Z} = \oint_{\mathrm{A}} \mathcal{D}[\overline{\psi},\psi] e^{-\mathcal{S}_{\mathrm{kin}}[\overline{\psi},\psi]} \mathcal{Z}_{\mathrm{B}}[\overline{j}_{\mathrm{B}}, j_{\mathrm{B}}] \mathcal{Z}_{\mathrm{H}}[\boldsymbol{\rho}]. \tag{3.26a}$$

$$= \mathcal{N}_{\mathrm{B}}\mathcal{N}_{\mathrm{H}} \oint_{\mathrm{A}} \mathcal{D}[\overline{\psi},\psi] \oint_{\mathrm{P}} \mathcal{D}[\overline{\Delta}_{\mathrm{B}},\Delta_{\mathrm{B}}] \oint_{\mathrm{P}} \mathcal{D}[\boldsymbol{\Delta}_{\mathrm{H}}] e^{-\mathcal{S}_{\mathrm{HS}}[\overline{\Delta}_{\mathrm{B}},\Delta_{\mathrm{B}},\boldsymbol{\Delta}_{\mathrm{H}},\overline{\psi},\psi]}. \tag{3.26b}$$

After introducing the additional functional integrals, the system is governed by the HS action, given as

$$\begin{aligned}\mathcal{S}_{\mathrm{HS}}[\overline{\Delta}_{\mathrm{B}},\Delta_{\mathrm{B}},\boldsymbol{\Delta}_{\mathrm{H,s}},\overline{\psi},\psi] = \int \mathrm{d}x \Bigg\{ &\sum_{\mathrm{s}=\uparrow,\downarrow} \overline{\psi}_{\mathrm{s}}(x)\left[-G_{\mathrm{s},0}^{-1}(x,x)\right]\psi_{\mathrm{s}}(x) \\ &+ \Delta_{\mathrm{H},\downarrow}(x)\overline{\psi}_{\uparrow}(x)\psi_{\uparrow}(x) + \Delta_{\mathrm{H},\uparrow}(x)\overline{\psi}_{\downarrow}(x)\psi_{\downarrow}(x) + \overline{\Delta}_{\mathrm{B}}(x)\psi_{\downarrow}(x)\psi_{\uparrow}(x) \\ &+ \overline{\psi}_{\uparrow}(x)\overline{\psi}_{\downarrow}(x)\Delta_{\mathrm{B}}(x) + \frac{\overline{\Delta}_{\mathrm{B}}(x)\Delta_{\mathrm{B}}(x)}{g_{\mathrm{B}}} + \frac{\Delta_{\mathrm{H},\uparrow}(x)\Delta_{\mathrm{H},\downarrow}(x)}{g_{\mathrm{H}}}\Bigg\}.\end{aligned} \tag{3.27}$$

This is the HS action of pair and direct interactions and therefore a straightforward generalisation of actions which only include the pair channel. Equal spin populations demand $\Delta_{\mathrm{H},\uparrow} = \Delta_{\mathrm{H},\downarrow} = \Delta_{\mathrm{H}}$ and $\mu_{\uparrow} = \mu_{\downarrow} = \mu$, leading to equal free Green's functions. Thus, the spin index is disregarded. The action then simplifies to

$$\begin{aligned}\mathcal{S}_{\mathrm{HS}}[\overline{\Delta}_{\mathrm{B}},\Delta_{\mathrm{B}},\boldsymbol{\Delta}_{\mathrm{H}},\overline{\psi},\psi] = \int \mathrm{d}x \Bigg\{ &\sum_{\mathrm{s}=\uparrow,\downarrow} \overline{\psi}_{\mathrm{s}}(x)\left[-G_{0}^{-1}(x,x) + \Delta_{\mathrm{H}}(x)\right]\psi_{\mathrm{s}}(x) \\ &+ \overline{\Delta}_{\mathrm{B}}(x)\psi_{\downarrow}(x)\psi_{\uparrow}(x) + \overline{\psi}_{\uparrow}(x)\overline{\psi}_{\downarrow}(x)\Delta_{\mathrm{B}}(x) + \frac{\overline{\Delta}_{\mathrm{B}}(x)\Delta_{\mathrm{B}}(x)}{g_{\mathrm{B}}} + \frac{\Delta_{\mathrm{H}}(x)^2}{g_{\mathrm{H}}}\Bigg\}.\end{aligned} \tag{3.28}$$

In order to compress the action into a compact form, we introduce **Nambu-spinors** [89, 328] which combine a particle and a hole field as

$$\overline{\boldsymbol{\Psi}}^{\mathrm{T}}(x) = \begin{pmatrix}\overline{\psi}_{\uparrow}(x) & \psi_{\downarrow}(x)\end{pmatrix} \qquad \text{and} \qquad \boldsymbol{\Psi}(x) = \begin{pmatrix}\psi_{\uparrow}(x) \\ \overline{\psi}_{\downarrow}(x)\end{pmatrix}. \tag{3.29}$$

This is equivalent to performing a particle-hole transformation in the $\downarrow$-fermions. Using this notation, the HS action ends up being in a spinor notation with a 2×2 inverse Green's function, which is the **Nambu-Gor'Kov Green's function**

$$\boldsymbol{G}^{-1}(x,x) = \begin{pmatrix}G_{0}^{-1}(x,x) & 0 \\ 0 & -G_{0}^{-1}(-x,-x)\end{pmatrix} + \begin{pmatrix}-\Delta_{\mathrm{H}}(x) & -\Delta_{\mathrm{B}}(x) \\ -\overline{\Delta}_{\mathrm{B}}(x) & \Delta_{\mathrm{H}}(x)\end{pmatrix} \tag{3.30a}$$

$$=: \boldsymbol{G}_{0}^{-1}(x,x) - \boldsymbol{\Sigma}_{\mathrm{HB}}(x,x). \tag{3.30b}$$

Thus, the Green's function follows a Dyson equation $\boldsymbol{G} = \boldsymbol{G}_0 + \boldsymbol{G}_0\boldsymbol{\Sigma}_{\mathrm{HB}}\boldsymbol{G}$ with $\boldsymbol{\Sigma}_{\mathrm{HB}}(x,x)$ as matrix-valued self-energy originating from direct and pair interactions. With all this notation, the HS action reads

$$\mathcal{S}_{\mathrm{HS}}[\{\Delta\},\overline{\Psi},\Psi] = \int \mathrm{d}x \left\{\overline{\boldsymbol{\Psi}}(x)\left[-\boldsymbol{G}^{-1}(x,x)\right]\boldsymbol{\Psi}(x) + \frac{|\Delta_{\mathrm{B}}(x)|^2}{g_{\mathrm{B}}} + \frac{\Delta_{\mathrm{H}}(x)^2}{g_{\mathrm{H}}}\right\}, \tag{3.31}$$

using $\{\Delta\} = \{\overline{\Delta}_{\mathrm{B}},\Delta_{\mathrm{B}},\Delta_{\mathrm{H}}\}$ as shorthand notation for the set of HS fields. So far, the calculations have been implemented in real space. To perform any explicit calculation, it is convenient to transform to momentum space, which is done next.

3.2.4 Momentum space

This section contains a lot of necessary notation. To go to momentum space we treat all present functions as elements of a dual space of mappings from $\mathcal{V} = [0,\beta]\times\mathbb{R}^D \to \mathbb{K}$, which we denote as $\mathfrak{F}(\mathcal{V};\mathbb{K})$, where $\mathbb{K} = \mathbb{C}$ for complex valued functions and $\mathbb{K} = \mathbb{G}$ stands

for a set of Grassmann numbers representing the Fermi fields. This allows to express any function $f \in \mathfrak{F}(\mathcal{V};\mathbb{K})$ in a dual-space representation similar to the bra-ket notation

$$f(x) = \langle x|f\rangle \qquad \text{and} \qquad \overline{f}(x) = \langle f|x\rangle. \tag{3.32}$$

For instance, the Nambu spinors after the particle-hole transformation are expressed via $\boldsymbol{\Psi}(x) = \langle x|\boldsymbol{\Psi}\rangle$. Further, we express bi-local mappings like the inverse Green's function as $\boldsymbol{G}^{-1}(x,x') = \langle x|\hat{\boldsymbol{G}}^{-1}|x'\rangle$. We denote all basis-less objects with a hat, and remove the hat once a basis, here real or reciprocal space, is chosen. This, in turn, has the consequence that differential operators like $\boldsymbol{G}^{-1}(x,x')$ are represented without a hat. To avoid confusion between basis-less operators and their basis-dependent differential operator form, we keep the notation like this, which differs from most textbooks. Since we deal with contact interaction, the inverse Green's function is local in real space $\langle x|\hat{\boldsymbol{G}}^{-1}|x'\rangle = \boldsymbol{G}^{-1}(x,x')\delta(x-x')$, with $\delta(x-x') = \delta(\tau-\tau')\delta^D(\boldsymbol{x}-\boldsymbol{x}')$ as space-time Dirac-δ distribution. The Green's function is obtained as *functional inverse*

$$\int \mathrm{d}x''\boldsymbol{G}^{-1}(x,x'')\boldsymbol{G}(x'',x') = \delta(x-x'). \tag{3.33}$$

Those properties of the inverse Green's function require that the bi-local self-energy reduces to a local form as well. Therefore, we set

$$\langle x|\hat{\boldsymbol{\Sigma}}|x'\rangle = \boldsymbol{\Sigma}(x,x') = \boldsymbol{\Sigma}(x,x)\delta(x-x') \;\Leftrightarrow\; \langle x|\Delta_{\mathrm{J}}|x'\rangle = \Delta_{\mathrm{J}}(x)\delta(x-x'), \tag{3.34}$$

using $J \in \{\mathrm{H},\mathrm{B}\}$ as an interaction channel index. To complete this set of notational conventions, we introduce a trace by summing over all diagonal elements

$$\mathrm{Tr}\hat{O} = \int \frac{\mathrm{d}x}{\beta L^D}\,\mathrm{tr}\langle x|\hat{O}|x\rangle. \tag{3.35}$$

Here Tr is the trace over all degrees of freedom, while tr denotes the trace only in spin space. Equivalently, the determinant is defined via the trace of the logarithm

$$\mathrm{Det}\hat{O} = e^{\mathrm{Tr}\ln\hat{O}} = \exp\left(\int \frac{\mathrm{d}x}{\beta L^D}\,\mathrm{tr}\ln\langle x|\hat{O}|x\rangle\right) = \prod_x \det\langle x|\hat{O}|x\rangle, \tag{3.36}$$

where an infinite measure is absorbed into the continuous product sign. Again, the capitalised determinant is over all degrees of freedom, while the lowercase $\det$ only incorporates the spin space.

To go to reciprocal space, we introduce Matsubara frequencies, using $k_n = (2n+1)\pi T$ for $n \in \mathbb{Z}$ as anti-periodic fermionic, and $q_\ell = 2\ell\pi T$ for $\ell \in \mathbb{Z}$ as periodic bosonic frequencies. We further go into detail in Appendix B. To define the Matsubara-Fourier transformation, we use a plane wave basis on $[0,\beta]\times\mathbb{R}^D$ conventionally defined as

$$\langle x|k\rangle = e^{i\langle x,k\rangle} = e^{i\boldsymbol{k}\cdot\boldsymbol{x}-ik_n\tau}. \tag{3.37}$$

Analogously to the space-time coordinates x, also a four-momentum $k = (ik_n,\boldsymbol{k})$ is used. Plane waves fulfil a completeness

$$\mathbb{I} = \int \frac{\mathrm{d}x}{\beta L^D}|x\rangle\langle x| = \sum_k |k\rangle\langle k| \tag{3.38}$$

and an orthogonality relation

$$\langle x|x'\rangle = \delta(x-x') \qquad , \qquad \langle k|k'\rangle = \delta_{kk'}. \tag{3.39}$$

As such, a basis change from real to momentum space is realised as

$$f(x) = \sum_k \langle x|k\rangle\langle k|f\rangle = \sum_k e^{i\boldsymbol{k}\cdot\boldsymbol{x}-ik_n\tau} f_k, \tag{3.40}$$

while for differential operators one obtains correspondingly $\partial_\tau \to -ik_n$ and $\nabla \to i\boldsymbol{k}$. The local self-energy components transformed to momentum space depend solely on the momentum transfer

$$\boldsymbol{\Sigma}(k;k') = \begin{pmatrix} \Delta_{\mathrm{H},k-k'} & \overline{\Delta}_{\mathrm{B},k-k'} \\ \Delta_{\mathrm{B},k'-k} & -\Delta_{\mathrm{H},k-k'} \end{pmatrix}. \tag{3.41}$$

A generalisation of this self-energy including the Fock channel is found in Eq. (3.A.31) in Appendix 3.A.4.

With the conventions outlined above the HS action from Eq. (3.31) becomes

$$\begin{aligned} \mathcal{S}_{\mathrm{HS}}[\{\Delta\};\overline{\boldsymbol{\Psi}},\boldsymbol{\Psi}] = \beta L^D \sum_q \Bigg\{ \sum_k \overline{\boldsymbol{\Psi}}^{\mathrm{T}}_{k-q/2} \left[-\boldsymbol{G}^{-1}(k,k+q)\right] \boldsymbol{\Psi}_{k+q/2} \\ + \frac{\overline{\Delta}_{\mathrm{B},q}\Delta_{\mathrm{B},q}}{g_{\mathrm{B}}} + \frac{\Delta_{\mathrm{H},q}\Delta_{\mathrm{H},-q}}{g_{\mathrm{H}}} \Bigg\}. \end{aligned} \tag{3.42}$$

This action describes the interaction of two Nambu spinors in momentum space, exchanging a bosonic momentum $q = (iq_\ell, \boldsymbol{q})$ via the matrix-valued inverse Green's function $\boldsymbol{G}^{-1}(k,k+q)$. Additionally, the action contains some offset value associated with the field theoretical mass of the auxiliary bosons $\Delta_{\mathrm{H,B}}$. As the action in Eq. (3.42) contains fermionic degrees of freedom in a Gaussian form, we can integrate them out, see Appendix A.2.4. We do so in the next section.

3.2.5 Effective action

Because the HS action, in Eq. (3.42), is quadratic, the functional integral in the partition function (3.27) can be evaluated analytically. This leads to the partition function

$$\mathcal{Z} = \oint_{\mathrm{P}} \mathcal{D}[\{\Delta\}] e^{-\mathcal{S}_{\mathrm{Eff}}[\{\Delta\}]}, \tag{3.43}$$

with the functional measure of the bosons being $\mathcal{D}[\{\Delta\}] = \mathcal{N}_{\mathrm{H}}\mathcal{N}_{\mathrm{B}}\mathcal{D}[\Delta_{\mathrm{H}}]\mathcal{D}[\overline{\Delta}_{\mathrm{B}},\Delta_{\mathrm{B}}]$. In this expression, the argument of the exponential function is the so-called effective action.

Result: Effective Action

$$\mathcal{S}_{\mathrm{Eff}}[\{\Delta\}] = -\ln\left[\beta^2 \mathrm{Det}\hat{\boldsymbol{G}}^{-1}\right] + \beta L^D \sum_q \left(\frac{|\Delta_{\mathrm{B},q}|^2}{g_{\mathrm{B}}} + \frac{\Delta_{\mathrm{H},q}\Delta_{\mathrm{H},-q}}{g_{\mathrm{H}}} \right). \tag{3.44}$$

This effective action is an exact result, no approximations were made so far. However, taking just one channel is also exact when the full interaction g is used. So why shall we implement the formalism of partitioning the interaction into several channels? The functional integral presented in Eq. (3.43) is not analytically solvable by any standard or advanced techniques. As in any many-body system, approximations must be made, and

their quality depends strongly on the choice of included channels. As mentioned earlier, choosing the wrong interaction channel can easily lead to relevant physics being missed. For example, if any channel, except the pairing channel, is chosen, the phenomenon of superconductivity can not be described. This might be avoidable when only one channel is dominant, but in many systems, two or even all three channels are relevant and compete for energy. This can never be captured by one specific choice of HFB channel, unless all orders of a perturbative series are summed up, which still would lack non-perturbative effects. In order to ensure fast convergence to the true physics within an approximative scheme, to capture competitions between channels and to avoid an arbitrarily chosen partitioning, the method developed in this thesis is not only necessary, but it solves the problem by resorting to more fundamental concepts. The detailed procedure is outlined in the following sections of this thesis, where we begin with the saddle-point (SP) evaluation of the derived effective action.

3.3 Saddle-point analysis of WHFB action

A SP approximation is the first step to any application to real systems. It resides on the fact that the partition function is dominated by the field which minimises the action because of the negative sign in the exponential of Eq. (3.43). By assuming a static and homogeneous saddle, this is equivalent to an operator theory where a mean-field approximation is applied, but be aware that a SP approximation can also go beyond a simple mean-field theory. The SP approximation serves as a good starting point for incorporating beyond mean-field effects, which become more important for lower dimensional systems.

3.3.1 Saddle-point approximation

We follow the standard procedure of imposing the SP approximation. Since we deal with an infinite, homogeneous, and isotropic system in thermal equilibrium, the saddle point acquires a static and homogeneous value in real space, and as such is fully localised in momentum space at $q = 0$. Therefore, we have

$$\Delta_{\mathrm{H},q} = \Delta_{\mathrm{H},0}\delta_{q,0} + \eta_{\mathrm{H},q}, \tag{3.45a}$$

$$\Delta_{\mathrm{B},q} = \Delta_{\mathrm{B},0}\delta_{q,0} + \eta_{\mathrm{B},q} \tag{3.45b}$$

where $\eta_{\mathrm{H,B},q}$ denotes quantum fluctuations around the SP in momentum space. This expands the partition function around the extreme point of the action, which contributes the most to the functional integral of $\mathcal{Z}$, approximating it as

$$\mathcal{Z} \approx e^{-\mathcal{S}_0(\{\Delta_0\})} \oint_{\mathrm{P}} \mathcal{D}[\{\eta\}] e^{-\mathcal{S}_{\mathrm{Fluct}}[\{\Delta_0\};\{\eta\}]} = \mathcal{Z}_0 \mathcal{Z}_{\mathrm{Fluct}}. \tag{3.46}$$

Here we separate the so-called SP action $\mathcal{S}_0(\{\Delta_0\}) = \mathcal{S}_{\mathrm{Eff}}[\{\Delta\}]\,|_{\Delta_{\mathrm{J},q}=\Delta_{\mathrm{J},0}}$, giving rise to the SP partition function

$$\mathcal{Z}_0 = e^{-\mathcal{S}_0(\{\Delta_0\})} \tag{3.47}$$

from the remaining fluctuation contribution, containing quantum fluctuation effects. For the remainder of this chapter, we neglect the fluctuation action, which is the semi-classical approximation. On this SP level, the self energy becomes

$$\boldsymbol{\Sigma}(k;k') = \begin{pmatrix} \Delta_{\mathrm{H},k-k'} & \overline{\Delta}_{\mathrm{B},k-k'} \\ \Delta_{\mathrm{B},k'-k} & -\Delta_{\mathrm{H},k-k'} \end{pmatrix} \delta_{kk'} = \left[\Delta_{\mathrm{H},0}\boldsymbol{\sigma}_z + \Delta_{\mathrm{B},0}\boldsymbol{\sigma}_+ + \overline{\Delta}_{\mathrm{B},0}\boldsymbol{\sigma}_-\right]\delta_{kk'}, \tag{3.48}$$

using the spin raising and lowering matrices $\boldsymbol{\sigma}_\pm = (\boldsymbol{\sigma}_x \pm i\boldsymbol{\sigma}_y)/2$, respectively. As such, the dressed inverse SP Green's function is also diagonal in momentum space due to the locality of the interaction in real space. It reads

$$\boldsymbol{G}_{\mathrm{SP}}^{-1}(k) = ik_n\boldsymbol{\sigma}_0 - (\xi_{\boldsymbol{k}} + \Delta_{\mathrm{H},0})\,\boldsymbol{\sigma}_z - \Delta_{\mathrm{B},0}\boldsymbol{\sigma}_+ - \overline{\Delta}_{\mathrm{B},0}\boldsymbol{\sigma}_-, \tag{3.49}$$

using $\boldsymbol{\sigma}_0$ as identity matrix in spin-$1/2$ space and the grand-canonical free particle dispersion $\xi_{\boldsymbol{k}} = \boldsymbol{k}^2/(2m) - \mu$. The SP action is obtained by evaluating the determinant via the definition, Eq. (3.36), after which we use the completeness of the plane wave basis (3.38) to go to momentum space. This results in

$$\mathcal{S}_0(\{\Delta_0\}) = -\sum_k \ln\left[\beta^2 \det\hat{\boldsymbol{G}}_{\mathrm{SP}}^{-1}(k)\right] + \beta L^D\left(\frac{|\Delta_{\mathrm{B},0}|^2}{g_{\mathrm{B}}} + \frac{\Delta_{\mathrm{H},0}^2}{g_{\mathrm{H}}}\right), \tag{3.50}$$

where we calculate the spin determinant as

$$\det\left[\beta\boldsymbol{G}_{\mathrm{SP}}^{-1}(k)\right] = \beta^2(ik_n + E_{\boldsymbol{k}})(ik_n - E_{\boldsymbol{k}}), \tag{3.51}$$

which involves the quasi-particle dispersion

$$E_{\boldsymbol{k}} = \sqrt{(\xi_{\boldsymbol{k}} + \Delta_{\mathrm{H},0})^2 + |\Delta_{\mathrm{B},0}|^2}. \tag{3.52}$$

3.3.2 Establishing self-consistency

The optimal value of the SP auxiliary fields is determined by extremising the SP action, obtaining the so-called *classical field* [329]. The conditions read

$$\frac{\partial\mathcal{S}_0(\{\Delta_0\})}{\partial\Delta_{\mathrm{H},0}} = 0, \tag{3.53a}$$

$$\frac{\partial\mathcal{S}_0(\{\Delta_0\})}{\partial\overline{\Delta}_{\mathrm{B},0}} = 0. \tag{3.53b}$$

We obtain the following two SP conditions

$$\Delta_{\mathrm{H},0} = \frac{g_{\mathrm{H}}}{2}\frac{1}{\beta L^D}\sum_k \mathrm{tr}\left\{\boldsymbol{G}_{\mathrm{SP}}(k)\frac{\partial\boldsymbol{G}_{\mathrm{SP}}^{-1}(k)}{\partial\Delta_{\mathrm{H},0}}\right\}, \tag{3.54a}$$

$$\Delta_{\mathrm{B},0} = g_{\mathrm{B}}\frac{1}{\beta L^D}\sum_k \mathrm{tr}\left\{\boldsymbol{G}_{\mathrm{SP}}(k)\frac{\partial\boldsymbol{G}_{\mathrm{SP}}^{-1}(k)}{\partial\overline{\Delta}_{\mathrm{B},0}}\right\}. \tag{3.54b}$$

Evaluating the derivatives leads to a more concise expression for the SP equations

$$\Delta_{\mathrm{H},0} = -\frac{g_{\mathrm{H}}}{2}\frac{1}{\beta L^D}\sum_k \mathrm{tr}\left\{\boldsymbol{G}_{\mathrm{SP}}(k)\boldsymbol{\sigma}_z\right\} = -\frac{g_{\mathrm{H}}}{2}\frac{1}{\beta L^D}\sum_k\left[G_{\mathrm{SP}}^{\uparrow\uparrow}(k) - G_{\mathrm{SP}}^{\downarrow\downarrow}(k)\right], \tag{3.55a}$$

$$\Delta_{\mathrm{B},0} = -g_{\mathrm{B}}\frac{1}{\beta L^D}\sum_k \mathrm{tr}\left\{\boldsymbol{G}_{\mathrm{SP}}(k)\boldsymbol{\sigma}_-\right\} = -g_{\mathrm{B}}\frac{1}{\beta L^D}\sum_k F_{\mathrm{SP}}^{\uparrow\downarrow}(k). \tag{3.55b}$$

Here, we introduce a notation which we use throughout the thesis, as we write the Green's function matrix as

$$\boldsymbol{G}_{\mathrm{SP}}(k) = \begin{pmatrix} G_{\mathrm{SP}}^{\uparrow\uparrow}(k) & F_{\mathrm{SP}}^{\uparrow\downarrow}(k) \\ F_{\mathrm{SP}}^{\downarrow\uparrow}(k) & G_{\mathrm{SP}}^{\downarrow\downarrow}(k) \end{pmatrix} \tag{3.56a}$$

$$= \frac{1}{(ik_n)^2 - E_{\boldsymbol{k}}^2}\begin{pmatrix} ik_n + \xi_{\boldsymbol{k}} + \Delta_{\mathrm{H},0} & \Delta_{\mathrm{B},0} \\ \overline{\Delta}_{\mathrm{B},0} & ik_n - \xi_{\boldsymbol{k}} - \Delta_{\mathrm{H},0} \end{pmatrix}. \tag{3.56b}$$

In the following $G_{\mathrm{SP}}^{\uparrow\uparrow}$ will be the normal Green's function of the spin-↑ particles, $G_{\mathrm{SP}}^{\downarrow\downarrow}$ will be the normal Green's function of the spin-↓ holes while $F_{\mathrm{SP}}^{\uparrow\downarrow}$ and $F_{\mathrm{SP}}^{\downarrow\uparrow}$ are the anomalous Green's functions.

Both Matsubara sums in Eqs. (3.55a, 3.55b) are explicitly solved in Appendix B, leading to a momentum sum left for the SP conditions

$$\Delta_{\mathrm{H},0} = -\frac{g_{\mathrm{H}}}{2}\frac{1}{L^D}\sum_{\boldsymbol{k}}\left[1 - \frac{\xi_{\boldsymbol{k}} + \Delta_{\mathrm{H},0}}{E_{\boldsymbol{k}}}\tanh\left(\frac{\beta}{2}E_{\boldsymbol{k}}\right)\right], \tag{3.57a}$$

$$\Delta_{\mathrm{B},0} = g_{\mathrm{B}}\Delta_{\mathrm{B},0}\frac{1}{L^D}\sum_{\boldsymbol{k}}\frac{\tanh\left(\frac{\beta}{2}E_{\boldsymbol{k}}\right)}{2E_{\boldsymbol{k}}}. \tag{3.57b}$$

These two equations are implicit, coupled equations for the Hartree and Bogoliubov SP fields and generally can not be solved analytically. Therefore, numerical self-consistent methods have to be applied. The presented set of equations is incomplete in the sense that there is still an arbitrary parameter, which is the partitioned interaction strengths. To ensure a consistent theory and to prevent over- or undercounting of states in the two channels, the idea is to extremize the action with respect to the partitioning, subject to the constraint $g_{\mathrm{H}} + g_{\mathrm{B}} = 1$. This can be done by directly inserting this constraint into the action or by using Lagrange multipliers. In both cases, taking the partial derivatives and setting them to zero yields

$$\frac{\partial \mathcal{S}_0}{\partial g_{\mathrm{B}}} = 0 \Rightarrow g_{\mathrm{B}} = \frac{|\Delta_{\mathrm{B},0}|}{|\Delta_{\mathrm{H},0}| + |\Delta_{\mathrm{B},0}|}g \leq g. \tag{3.58}$$

We separate out the partitioning and the bare interaction strength, yielding $g_{\mathrm{H}} = h_0 g$ and $g_{\mathrm{B}} = b_0 g$, with

$$h_0 = \frac{|\Delta_{\mathrm{H},0}|}{|\Delta_{\mathrm{H},0}| + |\Delta_{\mathrm{B},0}|}, \tag{3.59a}$$

$$b_0 = \frac{|\Delta_{\mathrm{B},0}|}{|\Delta_{\mathrm{H},0}| + |\Delta_{\mathrm{B},0}|}, \tag{3.59b}$$

ensuring $h_0 + b_0 = 1$. This means we always find $0 \leq h_0, b_0 \leq 1$, which is why we interpret these partitioning factors as probability values on how much of the amplitude of the scattering of two atoms is in the respective channel. This is a SP approximation again, and one could certainly think of situations where h, b would be some sort of fields. However, in the idealised system of contact potentials with balanced populations, this seems overcomplicated.

We have derived a set of self-consistent equations, determining the superfluid order parameter $\Delta_{\mathrm{B},0}$, the Hartree self-energy shift $\Delta_{\mathrm{H},0}$ and the partitioning h_0, b_0 as functions of the chemical potential μ, the temperature T, and the bare interaction strength g. The dependence on the bare interaction strength will be eliminated later on by a renormalisation scheme, as it is standard in condensed matter systems. For an experimental test of the theory, the chemical potential μ does prove not to be of great use. In general, the chemical potential is not freely tunable in a system, as it is determined by the particle density. Experiments in general act in an (almost) canonical ensemble, where the density is fixed as an experimental parameter, not the chemical potential as in a grand-canonical system. Therefore, for experimental applications, one has to determine the equation of state that relates the chemical potential to the number density. We accomplish this in the next part.

3.3.3 Equation of state

To obtain the equation of state the thermodynamic potential is needed first. We obtain the grand-canonical potential $\Omega = -T \ln \mathcal{Z}$. In a SP approximation, this becomes

$$\Omega_0(L^D, T, \mu) = -T \ln \mathcal{Z}_0 = T\mathcal{S}_0(\{\Delta_0\}). \tag{3.60}$$

Because the logarithm appears in the action, the action itself is multivalued when retaining the Matsubara summation. The grand-canonical potential per unit volume is evaluated from Eq. (3.50) using Eqs. (3.51) and (3.52), leading to

$$\frac{\Omega_0(L^D, T, \mu)}{L^D} = \left[\frac{\Delta_{\mathrm{H},0}^2}{g_{\mathrm{H}}} + \frac{|\Delta_{\mathrm{B},0}|^2}{g_{\mathrm{B}}}\right] - \frac{1}{L^D}\sum_{\boldsymbol{k}} T \sum_{ik_n} \ln\left[\beta^2(ik_n + E_{\boldsymbol{k}})(ik_n - E_{\boldsymbol{k}})\right]. \tag{3.61}$$

The multivalued property rooted in the branch cut of the logarithm is a consequence of switching integration and limiting process in the definition of the functional integral, see Appendix A. To solve this one, one either has to restrict the logarithm to the principal Riemann sheet, introduce convergence factors, and take care of the branch cut, or derive the corresponding counter term in an operator-based approach to account for the branch cut. We determine this Matsubara sum in Appendix B differently, by keeping a discrete imaginary-time partition function, in which the action is not a multivalued function. The final result for the grand-canonical potential is

$$\frac{\Omega_0(L^D, T, \mu)}{L^D} = \frac{\Delta_{\mathrm{H},0}^2}{g_{\mathrm{H}}} + \frac{|\Delta_{\mathrm{B},0}|^2}{g_{\mathrm{B}}} - \frac{1}{L^D}\sum_{\boldsymbol{k}}\left[E_{\boldsymbol{k}} - \xi_{\boldsymbol{k}} - \Delta_{\mathrm{H},0} + \frac{2}{\beta}\ln\left(1 + e^{-\beta E_{\boldsymbol{k}}}\right)\right]. \tag{3.62}$$

This also gives rise to the SP conditions, Eqs. (3.57a), (3.57b), (3.59a) and (3.59b).

The particle density $n = N/L^D$, where N denotes the total number of particles, is determined by the thermodynamic relation

$$n_0 = -\frac{1}{L^D}\frac{\partial \Omega_0}{\partial \mu}\bigg|_{T, L^D} \tag{3.63}$$

at the SP level. Performing this derivative results in the SP EoS

$$n_0 = \frac{1}{L^D}\sum_{\boldsymbol{k}}\left[1 - \frac{\xi_{\boldsymbol{k}} + \Delta_{\mathrm{H},0}}{E_{\boldsymbol{k}}}\tanh\left(\frac{\beta}{2}E_{\boldsymbol{k}}\right)\right]. \tag{3.64}$$

When comparing this equation of state with the Hartree self-energy from Eq. (3.57a), we realise that the momentum sums are identical. Hence, we replace the momentum sum in Eq. (3.57a) with the particle density from Eq. (3.64), yielding a familiar form for the self-energy

Result: Hartree self-energy

$$\Delta_{\mathrm{H},0} = -\frac{g_{\mathrm{H}} n_0}{2} = -\frac{g h_0 n_0}{2}. \tag{3.65}$$

Consequently, we obtain a set of coupled self-consistency equations to determine the system's thermodynamic properties. We have four equations for four variables, the Hartree-self energy $\Delta_{\mathrm{H},0}$, the superfluid order parameter $\Delta_{\mathrm{B},0}$, the partitioning b_0 and the chemical potential μ. In the following, we discuss the implications of those self-consistency equations in detail and show how the Hartree self-energy becomes an order parameter.

3.3.4 Hartree self-energy as order parameter

We notice that the total density, Eq. (3.64), is always positive. Furthermore, we also have $g_{\mathrm{H}} \geq 0$ for an attractive interaction. This means that the only physical solutions for the Hartree self-energy from Eq. (3.65) can be either $\Delta_{\mathrm{H},0} = 0$, if $g_{\mathrm{H}} = 0$, or $\Delta_{\mathrm{H},0} < 0$ for $g_{\mathrm{H}} \neq 0$. We use Eq. (3.59a) to eliminate the weight h_0 from Eq. (3.65), which leads to

$$\Delta_{\mathrm{H},0} = -\frac{|\Delta_{\mathrm{H},0}|}{|\Delta_{\mathrm{H},0}| + |\Delta_{\mathrm{B},0}|}\frac{gn_0}{2}. \tag{3.66}$$

We notice that Eq. (3.66) has indeed $\Delta_{\mathrm{H},0} = 0$ as a trivial solution. Under the assumption of a non-vanishing solution, we rearrange this expression to obtain an explicit value for the Hartree self-energy

$$\Delta_{\mathrm{H},0} = -\frac{gn_0}{2} + |\Delta_{\mathrm{B},0}|. \tag{3.67}$$

Since this has to be negative or zero, this can only be solved if $|\Delta_{\mathrm{B},0}| \leq gn_0/2$. Thus, for sufficiently large interaction strengths g, the Hartree self-energy has to vanish. The transition will happen exactly when $|\Delta_{\mathrm{B},0}| = gn_0/2$. We summarize the functional dependence of $\Delta_{\mathrm{H},0}$ as

$$\Delta_{\mathrm{H},0} = \min\left\{0; -\frac{gn_0}{2} + |\Delta_{\mathrm{B},0}|\right\} = \begin{cases} -\frac{gn_0}{2} + |\Delta_{\mathrm{B},0}| & \text{if } |\Delta_{\mathrm{B},0}| \leq gn_0/2 \\ 0 & \text{if } |\Delta_{\mathrm{B},0}| > gn_0/2 \end{cases}. \tag{3.68}$$

To further evaluate the self-consistency equations, we go to the thermodynamic limit, meaning we send the hyper-volume L^D and the total number of particles N to infinity, keeping the density constant, i.e. $L \to \infty, N \to \infty$ while $N/L^D = n = \mathrm{const}$. This is a good approximation for systems with a large number of particles. Implementing this procedure leads to the replacement rule for the sum

$$0 = \frac{1}{L^D}\sum_{\boldsymbol{k}} \to \int_{\mathbb{R}^D} \frac{\mathrm{d}^D k}{(2\pi)^D}. \tag{3.69}$$

In the thermodynamic limit the superfluid order parameter, equation (3.57b), reads

$$0 = \Delta_{\mathrm{B},0}\left[\frac{1}{g_{\mathrm{B}}} - \int_{\mathbb{R}^D} \frac{\mathrm{d}^D k}{(2\pi)^D}\frac{\tanh\left(\frac{\beta}{2}E_{\boldsymbol{k}}\right)}{2E_{\boldsymbol{k}}}\right], \tag{3.70}$$

while particle number equation (3.64) becomes

$$n_0 = \int_{\mathbb{R}^D} \frac{d^D k}{(2\pi)^D}\left[1 - \frac{\xi_{\boldsymbol{k}} + \Delta_{\mathrm{H},0}}{E_{\boldsymbol{k}}}\tanh\left(\frac{\beta}{2}E_{\boldsymbol{k}}\right)\right]. \tag{3.71}$$

The above equations are formally equivalent to the standard theory where the Hartree equation is ignored, when we would hypothetically send $b_0 \to 1$, meaning $h_0 \to 0$, hence including the standard approach as a special case of our formalism. In the presence of a Hartree term we have $b_0 \leq 1$, giving rise to an altered superfluid order parameter.

To explicitly determine the solution and discuss the physical implications, we have to eliminate the bare interaction g. This has to be done in order to regularise the superfluid order parameter equation (3.70). In order to remain consistent, since in general $g_{\mathrm{B}} \neq g$ in general, the renormalisation scheme has to be changed. Although the considerations in this chapter have been general and do not depend on the dimensionality of the system, any further specification must address the proper scattering regularisation, which strongly depends on the system's dimensionality. In the next chapter, we focus on the three-dimensional Fermi spin-mixture.

Appendix

3.A Hubbard-Stratonovich transformation: A more general view

In this Appendix, we discuss in detail the Hubbard-Stratonovich transformation for the Hartree, Fock, and Bogoliubov channels. We investigate the transformations for an arbitrary interaction potential $U_{\mathrm{ss}'}(|\boldsymbol{r}-\boldsymbol{r}'|)$, which only depends on the distance and is instantaneous in imaginary time. Furthermore, we take into account that the interaction might be different for distinct flavours s and s'. We use the word *flavour* here as a more general concept than the pseudo-spin used in the main text. We consider the action from the main text, Eq. (3.1), using the generalisation of the interaction term defined in Eq. (3.5). The key idea to generalise the WHFB method is that for any interaction with a non-local component, the separation of the interaction becomes a field as well

$$1 = h_{\mathrm{ss}'}(|\boldsymbol{x}-\boldsymbol{x}'|) + f_{\mathrm{ss}'}(|\boldsymbol{x}-\boldsymbol{x}'|) + b_{\mathrm{ss}'}(|\boldsymbol{x}-\boldsymbol{x}'|), \tag{3.A.1}$$

for real functions h, f, b of the distance and being matrices in flavour-space. This separates the Lagrangian and, as such, the action into a kinetic term seen in Eq. (3.15) in the main text and three distinct interaction terms

$$\mathcal{S}_{\mathrm{int,H}}[\overline{\psi},\psi] = -\sum_{\mathrm{ss}'}\int \mathrm{d}x\mathrm{d}x' h_{\mathrm{ss}'}(|\boldsymbol{x}-\boldsymbol{x}'|)U_{\mathrm{ss}'}(|\boldsymbol{x}-\boldsymbol{x}'|)\delta(\tau-\tau')\overline{\psi}_{\mathrm{s}}(x)\psi_{\mathrm{s}}(x)\overline{\psi}_{\mathrm{s}'}(x')\psi_{\mathrm{s}'}(x'),$$

$$\mathcal{S}_{\mathrm{int,F}}[\overline{\psi},\psi] = +\sum_{\mathrm{ss}'}\int \mathrm{d}x\mathrm{d}x' f_{\mathrm{ss}'}(|\boldsymbol{x}-\boldsymbol{x}'|)U_{\mathrm{ss}'}(|\boldsymbol{x}-\boldsymbol{x}'|)\delta(\tau-\tau')\overline{\psi}_{\mathrm{s}}(x)\psi_{\mathrm{s}'}(x')\overline{\psi}_{\mathrm{s}'}(x')\psi_{\mathrm{s}}(x),$$

$$\mathcal{S}_{\mathrm{int,B}}[\overline{\psi},\psi] = -\sum_{\mathrm{ss}'}\int \mathrm{d}x\mathrm{d}x' b_{\mathrm{ss}'}(|\boldsymbol{x}-\boldsymbol{x}'|)U_{\mathrm{ss}'}(|\boldsymbol{x}-\boldsymbol{x}'|)\delta(\tau-\tau')\overline{\psi}_{\mathrm{s}}(x)\overline{\psi}_{\mathrm{s}'}(x')\psi_{\mathrm{s}'}(x')\psi_{\mathrm{s}}(x).$$

The subsequent discussions are easier in momentum space. Two of the three HS fields have to be bi-local in space and momentum, which was already applied to composite fields in quark theories [330, 331]. The bi-locality is better understood in momentum space and provides us with a straightforward physical picture as discussed in the derivation of Eq. (3.41). We go from real space x to momentum space k as described in Section 3.2.4. For a given interaction channel $\mathrm{J} \in \{\mathrm{H},\mathrm{F},\mathrm{B}\}$ the channel specific interaction becomes a convolution of partitioning $j_{\mathrm{ss}'} \in \{h_{\mathrm{ss}'}, f_{\mathrm{ss}'}, b_{\mathrm{ss}'}\}$ and the original interaction

$$U^{\mathrm{J}}_{\mathrm{ss}',q} = \sum_{q'} j_{\mathrm{ss}',q-q'}U_{\mathrm{ss}',q'}. \tag{3.A.2}$$

We obtain the interaction terms of the action in momentum space as

$$\mathcal{S}_{\mathrm{int,H}}[\overline{\psi},\psi] = -\sum_{\mathrm{ss}'}\sum_{kk'}\sum_{q}\overline{\psi}_{\mathrm{s},k}\psi_{\mathrm{s},k-q}U^{\mathrm{H}}_{\mathrm{ss}',q}\overline{\psi}_{\mathrm{s}',k'}\psi_{\mathrm{s}',k'+q}, \tag{3.A.3a}$$

$$\mathcal{S}_{\mathrm{int,F}}[\overline{\psi},\psi] = +\sum_{\mathrm{ss}'}\sum_{kk'}\sum_{q}\overline{\psi}_{\mathrm{s},k}\psi_{\mathrm{s}',k'+q}U^{\mathrm{F}}_{\mathrm{ss}',q}\overline{\psi}_{\mathrm{s}',k'}\psi_{\mathrm{s},k-q}, \tag{3.A.3b}$$

$$\mathcal{S}_{\mathrm{int,B}}[\overline{\psi},\psi] = -\sum_{\mathrm{ss}'}\sum_{kk'}\sum_{q}\overline{\psi}_{\mathrm{s},k}\overline{\psi}_{\mathrm{s}',k'}U^{\mathrm{B}}_{\mathrm{ss}',q}\psi_{\mathrm{s}',k'+q}\psi_{\mathrm{s},k-q}. \tag{3.A.3c}$$

Subsequently, we perform the three separate HS transformations in the Hartree, Fock, and Bogoliubov channels by introducing the respective auxiliary fields and coupling them to the corresponding source terms. To do so, we introduce a last convention by setting the interaction potential to be

$$U^{\mathrm{J}}_{\mathrm{ss}',q} = g^{\mathrm{J}}_{\mathrm{ss}'}\left[\Gamma^{\mathrm{J}}_{\mathrm{ss}',q}\right]^2, \tag{3.A.4}$$

where $g^{\mathrm{J}}_{\mathrm{ss}'}$ is the channel-specific and spin-resolved interaction strength, while $\Gamma^{\mathrm{J}}_{\mathrm{ss}',q}$ is a real function containing information about the shape of the potential. Note that, as we absorb the sign of the interaction into g, the functions Γ are always positive semi-defined. By specializing $\Gamma^{\mathrm{J}}_{\mathrm{ss}',q} = 1 - \delta_{\mathrm{ss}'}$ and $g^{\mathrm{J}}_{\mathrm{ss}'} = g_{\mathrm{J}}$, we reproduce the contact interaction for opposite spins used in the main text in Eq. (3.8).

3.A.1 Hartree channel

The Hartree channel is the interaction that couples the local densities in real space. To make use of this, we define the Fourier transform of the local density field

$$n_{\mathrm{s},q} = \sum_k \overline{\psi}_{\mathrm{s},k+q}\psi_{\mathrm{s},k}, \tag{3.A.5}$$

so that the interaction action from Eq. (3.A.3a) reads

$$\mathcal{S}_{\mathrm{int,H}}[\overline{\psi},\psi] = -\sum_q n_{\mathrm{s},q}U^{\mathrm{H}}_{\mathrm{ss}',q}n_{\mathrm{s}',-q}. \tag{3.A.6}$$

We introduce a real-valued set of fields $\Delta^{\mathrm{s}}_{\mathrm{H},q}$ which couples to the local densities via the action

$$\mathcal{S}_{\mathrm{H}}[\Delta^{\mathrm{s}}_{\mathrm{H}};n_{\mathrm{s}}] = \sum_{\mathrm{ss}'}\sum_q \Delta^{\mathrm{s}}_{\mathrm{H},q}\left[\frac{1}{g^{\mathrm{H}}_{\mathrm{ss}'}}\Delta^{\mathrm{s}'}_{\mathrm{H},-q} + \Gamma^{\mathrm{H}}_{\mathrm{ss}',q}n_{\mathrm{s}',-q}\right], \tag{3.A.7}$$

We note that this could be summarised in a spinor notation using a $M \in \mathbb{N}$ sized spinor and a $M \times M$ matrix encoding the interaction and M as the number of species considered. For the sake of clarity, this is not done, but notice that evaluating the functional integral is easier with a spinor notation. In a formal replacement, we use the partition function of the above action and identify it with the exponential of the Hartree interaction term. This means we apply the equality

$$e^{-\mathcal{S}_{\mathrm{int,H}}[\overline{\psi},\psi]} = \mathcal{N}_{\mathrm{H}}\oint_{\mathrm{P}}\mathcal{D}[\Delta^{\mathrm{s}}_{\mathrm{H}}]e^{-\mathcal{S}_{\mathrm{H}}[\Delta^{\mathrm{s}}_{\mathrm{H}};n_{\mathrm{s}}]}. \tag{3.A.8}$$

This is the Hartree HS transformation, which describes the particle-hole interaction associated with the equal-spin normal Green's functions. Next, we continue with the Fock channel, also called the exchange channel, consisting of opposite-spin particle-hole processes.

3.A.2 Fock channel

In any fermionic system with attractive interactions, the Fock channel is challenging because the interaction acquires a statistical sign, making it repulsive. This is complicated because the functional integral necessary for the HS transformation is thus not convergent for a complex field with a finite real part. There are two possibilities for how we might approach this issue. The first idea is to assign a formally different sign to the interaction,

allowing the Fock term to be attractive as well. This in turn would cause $f_{\mathrm{ss}',q} < 0$, meaning that the sum of Hartree and Bogoliubov weights would have to be larger than 1. Therefore, we will not choose the first idea of an ad-hoc sign change and instead utilise the second possibility to resolve the convergence issue. We couple the bi-local exchange fields

$$\zeta_{\mathrm{ss}',k,k'} = \overline{\psi}_{\mathrm{s},k}\psi_{\mathrm{s}',k'} \tag{3.A.9}$$

to imaginary source terms. This has been done in a different context, for instance, repulsively interacting superconductors, in Refs. [276, 332]. The corresponding auxiliary action reads

$$\begin{aligned}\mathcal{S}_{\mathrm{F}}[\overline{\Delta}_{\mathrm{F}}^{\mathrm{ss}'}, \Delta_{\mathrm{F}}^{\mathrm{ss}'}; \overline{\zeta}_{\mathrm{ss}'}, \zeta_{\mathrm{ss}'}] = \sum_{\mathrm{ss}'}\sum_{kk'q}\Bigg[&\frac{\overline{\Delta}^{\mathrm{ss}'}_{\mathrm{F},k+q/2,k'+q/2}\Delta^{\mathrm{ss}'}_{\mathrm{F},k-q/2,k'-q/2}}{g^{\mathrm{F}}_{\mathrm{ss}'}}\\ &+i\Gamma^{\mathrm{F}}_{\mathrm{ss}',q}\left(\overline{\Delta}^{\mathrm{ss}'}_{\mathrm{F},k+q/2,k'+q/2}\zeta_{\mathrm{ss}',k-q/2,k'-q/2} + \overline{\zeta}_{\mathrm{ss}',k+q/2,k'+q/2}\Delta^{\mathrm{ss}'}_{\mathrm{F},k-q/2,k'-q/2}\right)\Bigg].\end{aligned} \tag{3.A.10}$$

Note that the introduced Fock auxiliary field $\Delta^{\mathrm{ss}'}_{\mathrm{F},p,p'}$ has to be bi-local as well. The imaginary unit in front of the source term is squared when integrating over the Fock auxiliary fields $\Delta^{\mathrm{ss}'}_{\mathrm{F}}$ and, as such, causes the statistical sign of the Fock term. Formally the HS transformation reads

$$e^{-\mathcal{S}_{\mathrm{int,F}}[\overline{\psi},\psi]} = \mathcal{N}_{\mathrm{F}}\oint_{\mathrm{P}}\mathcal{D}[\overline{\Delta}_{\mathrm{F}}^{\mathrm{ss}'}, \Delta_{\mathrm{F}}^{\mathrm{ss}'}]e^{-\mathcal{S}_{\mathrm{F}}[\overline{\Delta}_{\mathrm{F}}^{\mathrm{ss}'}, \Delta_{\mathrm{F}}^{\mathrm{ss}'}; \overline{\zeta}_{\mathrm{ss}'}, \zeta_{\mathrm{ss}'}]}. \tag{3.A.11}$$

This completes the two particle-hole processes. The last thing to tackle is the particle-particle processes treated in the next section.

3.A.3 Bogoliubov channel

In this section, we investigate the pair channel HS transformation dealing with anomalous processes, that is, the formation of pairs. As we allow for equal and unequal flavour pairs, this section contains both singlet and to an extent triplet Cooper pairs when disregarding their magnetic properties. To this end, we introduce the anomalous field products as

$$\phi_{\mathrm{ss}',k-q/2,k'+q/2} = \psi_{\mathrm{s},k-q/2}\psi_{\mathrm{s}',k'-q/2}. \tag{3.A.12}$$

For $\mathrm{s} \neq \mathrm{s}'$ we speak of a singlet, whereas for $\mathrm{s} = \mathrm{s}'$ of a triplet pair. We couple the anomalous field products to a complex bosonic field in the action

$$\begin{aligned}\mathcal{S}_{\mathrm{B}}[\overline{\Delta}_{\mathrm{B}}^{\mathrm{ss}'}, \Delta_{\mathrm{B}}^{\mathrm{ss}'}; \overline{\phi}_{\mathrm{ss}'}, \phi_{\mathrm{ss}'}] = \sum_{\mathrm{ss}'}\sum_{kk'q}\Bigg[&\frac{\overline{\Delta}^{\mathrm{ss}'}_{\mathrm{B},k+q/2,k'-q/2}\Delta^{\mathrm{ss}'}_{\mathrm{B},k-q/2,k'+q/2}}{g^{\mathrm{B}}_{\mathrm{ss}'}}\\ &+\Gamma^{\mathrm{B}}_{\mathrm{ss}',q}\left(\overline{\Delta}^{\mathrm{ss}'}_{\mathrm{B},k+q/2,k'-q/2}\phi_{\mathrm{ss}',k-q/2,k'+q/2} + \overline{\phi}_{\mathrm{ss}',k+q/2,k'-q/2}\Delta^{\mathrm{ss}'}_{\mathrm{B},k-q/2,k'+q/2}\right)\Bigg].\end{aligned} \tag{3.A.13}$$

Up to the imaginary source term coupling in the exchange channel seen in Eq. (3.A.10) the above action is formally similar to the Fock channel. Both describe a complex bi-local auxiliary field coupling non-locally to two fermion fields. For singlet pairs, the Bogoliubov auxiliary field Δ_{B} is a spinless composite boson field. In the case of triplet pairing, like for instance in ^{3}He, the Bogoliubov field is a spin-carrying field similar to the Fock

contribution found in Eq. (3.A.10). This was already pointed out for a similar system in Ref. [332]. Formally the HS transform reads

$$e^{-\mathcal{S}_{\mathrm{int,B}}[\overline{\psi},\psi]} = \mathcal{N}_{\mathrm{B}} \oint_{\mathrm{P}} \mathcal{D}\big[\overline{\Delta}_{\mathrm{B}}^{\mathrm{ss}'}, \Delta_{\mathrm{B}}^{\mathrm{ss}'}\big] e^{-\mathcal{S}_{\mathrm{B}}[\overline{\Delta}_{\mathrm{B}}^{\mathrm{ss}'}, \Delta_{\mathrm{B}}^{\mathrm{ss}'}; \overline{\phi}_{\mathrm{ss}'}, \phi_{\mathrm{ss}'}]}. \tag{3.A.14}$$

With this, we wrap up the three interaction channels, which are used to decompose the interaction term into three auxiliary fields coupling to the fermions. In the next section, we discuss the full WHFB transformation as well as the resulting Green's function and self-energy.

3.A.4 Hartree-Fock-Bogoliubov self-energy

We apply the WHFB transformation using the previous sections across all three channels. As such, we replace the interaction term as

$$e^{-\mathcal{S}_{\mathrm{int}}[\overline{\psi},\psi]} = \mathcal{N}_{\mathrm{HFB}} \oint_{\mathrm{P}} \mathcal{D}\big[\{\Delta\}\big] e^{-\mathcal{S}_{\mathrm{H}}[\Delta_{\mathrm{H}}^{\mathrm{s}}; n_{\mathrm{s}}] - \mathcal{S}_{\mathrm{F}}[\overline{\Delta}_{\mathrm{F}}^{\mathrm{ss}'}, \Delta_{\mathrm{F}}^{\mathrm{ss}'}; \overline{\zeta}_{\mathrm{ss}'}, \zeta_{\mathrm{ss}'}] - \mathcal{S}_{\mathrm{B}}[\overline{\Delta}_{\mathrm{B}}^{\mathrm{ss}'}, \Delta_{\mathrm{B}}^{\mathrm{ss}'}; \overline{\phi}_{\mathrm{ss}'}, \phi_{\mathrm{ss}'}]}, \tag{3.A.15}$$

where $\mathcal{N}_{\mathrm{HFB}} = \mathcal{N}_{\mathrm{H}}\mathcal{N}_{\mathrm{F}}\mathcal{N}_{\mathrm{B}}$ denotes the full normalisation constant and $\mathcal{D}\big[\{\Delta\}\big]$ stands for the functional measure over the set of auxiliary fields. Combining the three auxiliary field actions with the kinetic action from Eq. (3.15), we obtain the HS action

$$\begin{aligned}
\mathcal{S}_{\mathrm{HS}}\big[\overline{\psi},\psi;\{\Delta\}\big] = \sum_{\mathrm{ss}'}\sum_{kk'}\sum_{q} \Bigg\{ & \overline{\psi}_{\mathrm{s},k+q/2}\Big[-G_{\mathrm{s},0}^{-1}(k)\delta_{q,0} + \Gamma^{\mathrm{H}}_{\mathrm{ss}',q}\Delta^{\mathrm{s}'}_{\mathrm{H},q}\Big]\delta_{k,k'}\psi_{\mathrm{s},k'-q/2} \\
& + \overline{\psi}_{\mathrm{s},k+q/2} i\Gamma^{\mathrm{F}}_{\mathrm{ss}',q}\overline{\Delta}^{\mathrm{ss}'}_{\mathrm{F},k-q/2,k'-q/2}\psi_{\mathrm{s}',k'+q/2} + \overline{\psi}_{\mathrm{s}',k'-q/2} i\Gamma^{\mathrm{F}}_{\mathrm{ss}',q}\Delta^{\mathrm{ss}'}_{\mathrm{F},k+q/2,k'+q/2}\psi_{\mathrm{s},k-q/2} \\
& + \overline{\psi}_{\mathrm{s},k+q/2}\Gamma^{\mathrm{B}}_{\mathrm{ss}',q}\Delta^{\mathrm{ss}'}_{\mathrm{B},k-q/2,k'+q/2}\overline{\psi}_{\mathrm{s}',k'-q/2} + \psi_{\mathrm{s}',k'+q/2}\Gamma^{\mathrm{B}}_{\mathrm{ss}',q}\overline{\Delta}^{\mathrm{ss}'}_{\mathrm{B},k+q/2,k'-q/2}\psi_{\mathrm{s},k-q/2} \Bigg\} \\
& + \sum_{\mathrm{ss}'}\sum_{kk'}\sum_{q}\Bigg[\frac{\Delta^{\mathrm{s}}_{\mathrm{H},q}\Delta^{\mathrm{s}'}_{\mathrm{H},-q}}{g^{\mathrm{H}}_{\mathrm{ss}'}}\delta_{k,k'}\delta_{k,0} \\
& \qquad + \frac{\overline{\Delta}^{\mathrm{ss}'}_{\mathrm{F},k+q/2,k'+q/2}\Delta^{\mathrm{ss}'}_{\mathrm{F},k-q/2,k'-q/2}}{g^{\mathrm{F}}_{\mathrm{ss}'}} + \frac{\overline{\Delta}^{\mathrm{ss}'}_{\mathrm{B},k+q/2,k'-q/2}\Delta^{\mathrm{ss}'}_{\mathrm{B},k-q/2,k'+q/2}}{g^{\mathrm{B}}_{\mathrm{ss}'}}\Bigg].
\end{aligned} \tag{3.A.16}$$

We relabel momenta in selected terms in order to produce the same structure in any term, where the field to the left has momentum k and the field to the right k', leading to

$$\begin{aligned}
\mathcal{S}_{\mathrm{HS}}\big[\overline{\psi},\psi;\{\Delta\}\big] = \sum_{\mathrm{ss}'}\sum_{kk'}\sum_{q} \Bigg\{ & \overline{\psi}_{\mathrm{s},k}\Big[-G_{\mathrm{s},0}^{-1}(k)\delta_{q,0} + \Gamma^{\mathrm{H}}_{\mathrm{ss}',q}\Delta^{\mathrm{s}'}_{\mathrm{H},q}\Big]\delta_{k-k',q}\psi_{\mathrm{s},k'} \\
& + \overline{\psi}_{\mathrm{s},k} i\Gamma^{\mathrm{F}}_{\mathrm{ss}',q}\overline{\Delta}^{\mathrm{ss}'}_{\mathrm{F},k-q,k'-q}\psi_{\mathrm{s}',k'} + \overline{\psi}_{\mathrm{s}',k} i\Gamma^{\mathrm{F}}_{\mathrm{ss}',q}\Delta^{\mathrm{ss}'}_{\mathrm{F},k'+q,k+q}\psi_{\mathrm{s},k'} \\
& + \overline{\psi}_{\mathrm{s},k}\Gamma^{\mathrm{B}}_{\mathrm{ss}',q}\Delta^{\mathrm{ss}'}_{\mathrm{B},k-q,k'+q}\overline{\psi}_{\mathrm{s}',k'} + \psi_{\mathrm{s}',k}\Gamma^{\mathrm{B}}_{\mathrm{ss}',q}\overline{\Delta}^{\mathrm{ss}'}_{\mathrm{B},k+q,k'-q}\psi_{\mathrm{s},k'} \Bigg\} + \mathcal{S}_{\mathrm{HS},0}
\end{aligned} \tag{3.A.17}$$

with

$$\begin{aligned}
\mathcal{S}_{\mathrm{HS},0} = \sum_{\mathrm{ss}'}\sum_{kk'}\sum_{q}\Bigg[& \frac{\Delta^{\mathrm{s}}_{\mathrm{H},q}\Delta^{\mathrm{s}'}_{\mathrm{H},-q}}{g^{\mathrm{H}}_{\mathrm{ss}'}}\delta_{k,k'}\delta_{k,0} \\
& + \frac{\overline{\Delta}^{\mathrm{ss}'}_{\mathrm{F},k+q/2,k'+q/2}\Delta^{\mathrm{ss}'}_{\mathrm{F},k-q/2,k'-q/2}}{g^{\mathrm{F}}_{\mathrm{ss}'}} + \frac{\overline{\Delta}^{\mathrm{ss}'}_{\mathrm{B},k+q/2,k'-q/2}\Delta^{\mathrm{ss}'}_{\mathrm{B},k-q/2,k'+q/2}}{g^{\mathrm{B}}_{\mathrm{ss}'}}\Bigg],
\end{aligned} \tag{3.A.18}$$

summarising the offset energy of the auxiliary fields. In this most general case, the whole system is too complicated to solve analytically. Therefore, we focus on calculating the matrix-valued inverse Green's function and the corresponding self-energy. To this end, we symmetrise the action. This results in

$$\begin{aligned}
\mathcal{S}_{\mathrm{HS}}[\overline{\psi},\psi;\{\Delta\}] - \mathcal{S}_{\mathrm{HS},0} = \frac{1}{2}\sum_{\mathrm{ss}'}\sum_{kk'}\sum_{q}\Bigg\{ & \overline{\psi}_{\mathrm{s},k}\left[-G^{-1}_{\mathrm{s},0}(k)\delta_{q,0} + \Gamma^{\mathrm{H}}_{\mathrm{ss}',q}\Delta^{\mathrm{s}'}_{\mathrm{H},q}\right]\delta_{k-k',q}\psi_{\mathrm{s},k'} \\
& + \psi_{\mathrm{s},k}\left[G^{-1}_{\mathrm{s},0}(-k)\delta_{q,0} - \Gamma^{\mathrm{H}}_{\mathrm{ss}',q}\Delta^{\mathrm{s}'}_{\mathrm{H},q}\right]\delta_{k'-k,q}\overline{\psi}_{\mathrm{s},k'} \\
& + \overline{\psi}_{\mathrm{s},k} i\Gamma^{\mathrm{F}}_{\mathrm{ss}',q}\overline{\Delta}^{\mathrm{ss}'}_{\mathrm{F},k-q,k'-q}\psi_{\mathrm{s}',k'} + \overline{\psi}_{\mathrm{s}',k} i\Gamma^{\mathrm{F}}_{\mathrm{ss}',q}\Delta^{\mathrm{ss}'}_{\mathrm{F},k'+q,k+q}\psi_{\mathrm{s},k'} \\
& - \psi_{\mathrm{s}',k} i\Gamma^{\mathrm{F}}_{\mathrm{ss}',q}\overline{\Delta}^{\mathrm{ss}'}_{\mathrm{F},k'-q,k-q}\overline{\psi}_{\mathrm{s},k'} - \psi_{\mathrm{s},k} i\Gamma^{\mathrm{F}}_{\mathrm{ss}',q}\Delta^{\mathrm{ss}'}_{\mathrm{F},k+q,k'+q}\overline{\psi}_{\mathrm{s}',k'} \\
& + \overline{\psi}_{\mathrm{s},k}\Gamma^{\mathrm{B}}_{\mathrm{ss}',q}\Delta^{\mathrm{ss}'}_{\mathrm{B},k-q,k'+q}\overline{\psi}_{\mathrm{s}',k'} + \psi_{\mathrm{s}',k}\Gamma^{\mathrm{B}}_{\mathrm{ss}',q}\overline{\Delta}^{\mathrm{ss}'}_{\mathrm{B},k+q,k'-q}\psi_{\mathrm{s},k'} \\
& - \overline{\psi}_{\mathrm{s}',k}\Gamma^{\mathrm{B}}_{\mathrm{ss}',q}\Delta^{\mathrm{ss}'}_{\mathrm{B},k'-q,k+q}\overline{\psi}_{\mathrm{s},k'} - \psi_{\mathrm{s},k}\Gamma^{\mathrm{B}}_{\mathrm{ss}',q}\overline{\Delta}^{\mathrm{ss}'}_{\mathrm{B},k'+q,k-q}\psi_{\mathrm{s}',k'}\Bigg\}.
\end{aligned} \tag{3.A.19}$$

At this point, we realise a few symmetry properties concerning the spins, being for the Fock field that

$$\Gamma^{\mathrm{F}}_{\mathrm{ss}',q}\overline{\Delta}^{\mathrm{ss}'}_{\mathrm{F},k-q,k'-q} = \Gamma^{\mathrm{F}}_{\mathrm{s}'\mathrm{s},q}\Delta^{\mathrm{s}'\mathrm{s}}_{\mathrm{F},k'+q,k+q} \tag{3.A.20}$$

and for the Bogoliubov field that

$$\Gamma^{\mathrm{B}}_{\mathrm{ss}',q}\Delta^{\mathrm{ss}'}_{\mathrm{B},k-q,k'+q} = -\Gamma^{\mathrm{B}}_{\mathrm{s}'\mathrm{s},q}\Delta^{\mathrm{s}'\mathrm{s}}_{\mathrm{B},k'-q,k+q}. \tag{3.A.21}$$

Applying that the interactions are reciprocal, that is $\Gamma^{\mathrm{J}}_{\mathrm{ss}',q} = \Gamma^{\mathrm{J}}_{\mathrm{s}'\mathrm{s},q}$ and $\Gamma^{\mathrm{J}}_{\mathrm{ss}',q} = \Gamma^{\mathrm{J}}_{\mathrm{ss}',-q}$, provides us with clear symmetry rules for exchanging flavour indices:

$$\overline{\Delta}^{\mathrm{ss}'}_{\mathrm{F},k-q,k'-q} = \Delta^{\mathrm{s}'\mathrm{s}}_{\mathrm{F},k'+q,k+q} \tag{3.A.22}$$

$$\Delta^{\mathrm{ss}'}_{\mathrm{B},k-q,k'+q} = -\Delta^{\mathrm{s}'\mathrm{s}}_{\mathrm{B},k'-q,k+q}. \tag{3.A.23}$$

Using this, we label all the auxiliary fields in the action (3.A.19) such that the species indices match the Fermi fields, i.e.

$$\begin{aligned}
\mathcal{S}_{\mathrm{HS}}[\overline{\psi},\psi;\{\Delta\}] - \mathcal{S}_{\mathrm{HS},0} = \frac{1}{2}\sum_{\mathrm{ss}'}\sum_{kk'}\sum_{q}\Bigg\{ & \overline{\psi}_{\mathrm{s},k}\left[-G^{-1}_{\mathrm{s},0}(k)\delta_{q,0} + \Gamma^{\mathrm{H}}_{\mathrm{ss}',q}\Delta^{\mathrm{s}'}_{\mathrm{H},q}\right]\delta_{k-k',q}\psi_{\mathrm{s},k'} \\
& + \psi_{\mathrm{s},k}\left[G^{-1}_{\mathrm{s},0}(-k)\delta_{q,0} - \Gamma^{\mathrm{H}}_{\mathrm{ss}',q}\Delta^{\mathrm{s}'}_{\mathrm{H},q}\right]\delta_{k'-k,q}\overline{\psi}_{\mathrm{s},k'} \\
& + \overline{\psi}_{\mathrm{s},k} i\Gamma^{\mathrm{F}}_{\mathrm{ss}',q}\overline{\Delta}^{\mathrm{ss}'}_{\mathrm{F},k-q,k'-q}\psi_{\mathrm{s}',k'} + \overline{\psi}_{\mathrm{s}',k} i\Gamma^{\mathrm{F}}_{\mathrm{s}'\mathrm{s},q}\overline{\Delta}^{\mathrm{s}'\mathrm{s}}_{\mathrm{F},k'-q,k-q}\psi_{\mathrm{s},k'} \\
& - \psi_{\mathrm{s}',k} i\Gamma^{\mathrm{F}}_{\mathrm{s}'\mathrm{s},q}\Delta^{\mathrm{s}'\mathrm{s}}_{\mathrm{F},k'+q,k+q}\overline{\psi}_{\mathrm{s},k'} - \psi_{\mathrm{s},k} i\Gamma^{\mathrm{F}}_{\mathrm{ss}',q}\Delta^{\mathrm{ss}'}_{\mathrm{F},k+q,k'+q}\overline{\psi}_{\mathrm{s}',k'} \\
& + \overline{\psi}_{\mathrm{s},k}\Gamma^{\mathrm{B}}_{\mathrm{ss}',q}\Delta^{\mathrm{ss}'}_{\mathrm{B},k-q,k'+q}\overline{\psi}_{\mathrm{s}',k'} - \psi_{\mathrm{s}',k}\Gamma^{\mathrm{B}}_{\mathrm{s}'\mathrm{s},q}\overline{\Delta}^{\mathrm{s}'\mathrm{s}}_{\mathrm{B},k'+q,k-q}\psi_{\mathrm{s},k'} \\
& + \overline{\psi}_{\mathrm{s}',k}\Gamma^{\mathrm{B}}_{\mathrm{s}'\mathrm{s},q}\Delta^{\mathrm{s}'\mathrm{s}}_{\mathrm{B},k-q,k'+q}\overline{\psi}_{\mathrm{s},k'} - \psi_{\mathrm{s},k}\Gamma^{\mathrm{B}}_{\mathrm{ss}',q}\overline{\Delta}^{\mathrm{ss}'}_{\mathrm{B},k'+q,k-q}\psi_{\mathrm{s}',k'}\Bigg\}.
\end{aligned} \tag{3.A.24}$$

We now introduce particle and hole spinors in order to achieve a concise notation. This means we have set

$$\boldsymbol{\psi}_k = \begin{pmatrix} \psi_{\mathrm{s}_1,k} \\ \psi_{\mathrm{s}_2,k} \\ \vdots \\ \psi_{\mathrm{s}_M,k} \end{pmatrix} \qquad \text{and} \qquad \overline{\boldsymbol{\psi}}_k = \begin{pmatrix} \overline{\psi}_{\mathrm{s}_1,k} & \overline{\psi}_{\mathrm{s}_2,k} & \cdots & \overline{\psi}_{\mathrm{s}_M,k} \end{pmatrix}, \tag{3.A.25}$$

which allows us to write the action as

$$\mathcal{S}_{\mathrm{HS}}[\overline{\psi},\psi;\{\Delta\}]-\mathcal{S}_{\mathrm{HS},0}=\frac{1}{2}\sum_{\mathrm{ss}'}\sum_{kk'}\Bigg\{\overline{\boldsymbol{\psi}}_k\left[-\boldsymbol{G}^{-1}_{0,k}\delta_{k,k'}+\boldsymbol{\Sigma}^{\mathrm{HF}}_{k,k'}\right]\boldsymbol{\psi}_{k'} + \boldsymbol{\psi}^{\mathrm{T}}_{k'}\left[\boldsymbol{G}^{-1}_{0,-k}\delta_{k,k'}-\left(\boldsymbol{\Sigma}^{\mathrm{HF}}_{k',k}\right)^{\mathrm{T}}\right]\overline{\boldsymbol{\psi}}^{\mathrm{T}}_{k'}+\overline{\boldsymbol{\psi}}_k\boldsymbol{\Sigma}^{\mathrm{B}}_{k,k'}\overline{\boldsymbol{\psi}}^{\mathrm{T}}_{k'}+\boldsymbol{\psi}^{\mathrm{T}}_k\overline{\boldsymbol{\Sigma}}^{\mathrm{B}}_{k',k}\boldsymbol{\psi}_{k'}\Bigg\}. \tag{3.A.26}$$

Here, we defined the species diagonal non-interacting inverse Green's function

$$-\boldsymbol{G}^{-1}_{0,k}=\begin{pmatrix}G^{-1}_{\mathrm{s}_1,0}(k) & 0 & \cdots & 0\\ 0 & G^{-1}_{\mathrm{s}_2,0}(k) & \cdots & 0\\ \vdots & \vdots & \ddots & \vdots\\ 0 & 0 & \cdots & G^{-1}_{\mathrm{s}_M,0}(k)\end{pmatrix}. \tag{3.A.27}$$

Together with the Hartree-Fock self-energy $\boldsymbol{\Sigma}^{\mathrm{HF}}_{k,k'}$ with matrix elements

$$\boldsymbol{\Sigma}^{\mathrm{HF}}_{\mathrm{s}_1\mathrm{s}_2,k,k'}=\sum_q\left[\sum_{\mathrm{s}'}\Gamma_{\mathrm{s}_1\mathrm{s}',q}\Delta^{\mathrm{s}_1}_{\mathrm{H},q}\delta_{\mathrm{s}_1\mathrm{s}_2}\delta_{k-k',q}-i\Gamma^{\mathrm{F}}_{\mathrm{s}_1\mathrm{s}_2,q}\left(\overline{\Delta}^{\mathrm{s}_1\mathrm{s}_2}_{\mathrm{F},k-q,k'-q}+\overline{\Delta}^{\mathrm{s}_1\mathrm{s}_2}_{\mathrm{F},k'-q,k-q}\right)\right] \tag{3.A.28}$$

follows a matrix-valued Dyson equation $\boldsymbol{G}^{-1}_{\mathrm{HF},k,k'}=\boldsymbol{G}^{-1}_{0,k}\delta_{k,k'}-\boldsymbol{\Sigma}^{\mathrm{HF}}_{k,k'}$. The Hartree-Fock self-energy has Hartree shifts on the diagonal entries, and the Fock energies appear on the off diagonals. Furthermore, the pairing or Bogoliubov self-energy matrix $\boldsymbol{\Sigma}^{\mathrm{B}}_{k,k'}$ has elements

$$\boldsymbol{\Sigma}^{\mathrm{B}}_{s_1,s_2,k,k'}=2\sum_q\Gamma^{\mathrm{B}}_{\mathrm{s}_1\mathrm{s}_2,q}\Delta^{\mathrm{s}_1\mathrm{s}_2}_{\mathrm{B},k-q,k'+q}, \tag{3.A.29}$$

where the diagonal entries represent triplet-pairing, while the other elements describe singlet Cooper pairs. Thus, we summarise the action further to find

$$\mathcal{S}_{\mathrm{HS}}[\overline{\psi},\psi;\{\Delta\}]-\mathcal{S}_{\mathrm{HS},0} =\frac{1}{2}\sum_{\mathrm{ss}'}\sum_{kk'}\begin{pmatrix}\overline{\boldsymbol{\psi}}_k & \boldsymbol{\psi}^{\mathrm{T}}_k\end{pmatrix}\begin{pmatrix}-\boldsymbol{G}^{-1}_{0,k}\delta_{k,k'}+\boldsymbol{\Sigma}^{\mathrm{HF}}_{k,k'} & \boldsymbol{\Sigma}^{\mathrm{B}}_{k,k'}\\ \overline{\boldsymbol{\Sigma}}^{\mathrm{B}}_{k',k} & \boldsymbol{G}^{-1}_{0,-k}\delta_{k,k'}-\left(\boldsymbol{\Sigma}^{\mathrm{HF}}_{k',k}\right)^{\mathrm{T}}\end{pmatrix}\begin{pmatrix}\boldsymbol{\psi}_{k'}\\ \overline{\boldsymbol{\psi}}^{\mathrm{T}}_{k'}\end{pmatrix}. \tag{3.A.30}$$

This results in the Hartree-Fock-Bogoliubov self-energy matrix expressed in the extended Nambu basis

$$\boldsymbol{\Sigma}^{\mathrm{HFB}}_{k,k'}=\begin{pmatrix}\boldsymbol{\Sigma}^{\mathrm{HF}}_{k,k'} & \boldsymbol{\Sigma}^{\mathrm{B}}_{k,k'}\\ \overline{\boldsymbol{\Sigma}}^{\mathrm{B}}_{k',k} & -\left(\boldsymbol{\Sigma}^{\mathrm{HF}}_{k',k}\right)^{\mathrm{T}}\end{pmatrix}, \tag{3.A.31}$$

being a $2M\times 2M$ matrix. It is a generalisation of the Hartree-Bogoliubov 2×2 self-energy matrix found in Eq. (3.41) of the main text.

Considering now contact interaction and two different flavour fermions with $\Gamma^{\mathrm{J}}_{\mathrm{ss}',q}=1-\delta_{\mathrm{ss}'}$ we obtain the Hartree-Fock self-energy matrix elements (3.A.28) as

$$\boldsymbol{\Sigma}^{\mathrm{HF}}_{k,k'}=\begin{pmatrix}\Delta^{\uparrow}_{\mathrm{H},k-k'} & -i\left(\overline{\Delta}^{\uparrow\downarrow}_{\mathrm{F},k-k'}+\overline{\Delta}^{\uparrow\downarrow}_{\mathrm{F},k'-k}\right)\\ -i\left(\overline{\Delta}^{\downarrow\uparrow}_{\mathrm{F},k-k'}+\overline{\Delta}^{\downarrow\uparrow}_{\mathrm{F},k'-k}\right) & \Delta^{\downarrow}_{\mathrm{H},k-k'}\end{pmatrix}, \tag{3.A.32}$$

while the anomalous self-energy matrix reads

$$\boldsymbol{\Sigma}^{\mathrm{B}}_{k,k'}=\begin{pmatrix}0 & 2\Delta^{\uparrow\downarrow}_{\mathrm{B},k+k'}\\ 2\Delta^{\downarrow\uparrow}_{\mathrm{B},k+k'} & 0\end{pmatrix}. \tag{3.A.33}$$

Since equal flavours are not interacting, the diagonal entries in the pair self-energy (3.A.33) vanish. This announces the absence of triplet pairing. We now use Eq. (3.A.20) to see that the off-diagonal entries of the Hartree-Fock self-energy matrix (3.A.32) are proportional to the real part of the Fock energy. Subsequent application of the SP approximation reveals that the Fock contribution for contact interactions is purely imaginary. Hence, it can be gauged away via a suitable rotation of the flavour basis, which technically absorbs the Fock contribution into a Hartree term. This means in a SP approximation we find

$$\boldsymbol{\Sigma}^{\mathrm{HF}}_{\mathrm{SP}} = \begin{pmatrix} \Delta^{\uparrow}_{\mathrm{H},0} & 0 \\ 0 & \Delta^{\downarrow}_{\mathrm{H},0} \end{pmatrix} \delta_{k,k'}. \tag{3.A.34}$$

Analogously, performing a SP approximation in the Bogoliubov channel leads to the anomalous self-energy

$$\boldsymbol{\Sigma}^{\mathrm{B}}_{\mathrm{SP}} = \begin{pmatrix} 0 & \Delta_{\mathrm{B},0} \\ \Delta_{\mathrm{B},0} & 0 \end{pmatrix} \delta_{k,-k'}, \tag{3.A.35}$$

with the mean-field $2\Delta^{s\bar{s}}_{\mathrm{B},k+k'} = \Delta_{\mathrm{B},0}\delta_{k,-k'}$. Now inverting the momenta of all $\downarrow$ results in the SP Hartree-Bogoliubov self-energy, seen in Eq. (3.48) in the main text.

Chapter 4

Three-dimensional Fermi spin-mixtures

All nature is but art, unknown to thee;
All chance, direction, which thou canst not see;

Alexander Pope

4.1 Introduction . . . 66
4.2 Scattering Renormalization in three dimensions . . . 66
4.2.1 Effective range scattering theory . . . 66
4.2.2 Effective pairing channel scattering regularisation . . . 68
4.2.3 Screened interactions and non-analytic couplings . . . 70
4.3 Ground state properties . . . 71
4.3.1 Scattering properties and phase diagram . . . 72
4.3.2 Order parameters and chemical potential . . . 74
4.3.3 Weakly interacting limit . . . 78
4.3.4 Unitary gas . . . 81
4.3.5 Strong interactions . . . 82
4.4 Thermodynamics of WHFB ground state . . . 86
4.4.1 Free energy . . . 86
4.4.2 Isothermal compressibility . . . 89
4.4.3 Tan's contact . . . 92
4.4.4 Cooper pair size . . . 93
4.5 Impact of Thermal fluctuations . . . 95
4.5.1 Effective range at finite temperatures . . . 95
4.5.2 Fixed temperature . . . 96
4.5.3 Fixed effective range . . . 99
4.5.4 Normal fluid gas . . . 101
4.A Calculating the Cooper pair size . . . 102
4.A.1 Normalization factor . . . 102
4.A.2 Expectation value of relative position . . . 104
4.B Asymptotic expansions for weak and strong interactions . . . 105
4.B.1 Weakly interacting expansions . . . 105
4.B.2 Strong coupling expansion . . . 107

4.1 Introduction

Three-dimensional (3D) systems play a central role in many-body physics, as most systems encountered in nature are inherently three-dimensional. Consequently, they constitute the most direct experimental realisation, whereas reducing dimensionality typically requires additional challenges. Experimental realisations of degenerate quantum gases of fermionic atoms started in the 2000s [147, 148], initially focused on the easier to prepare strong interaction limit of composite bosons in harmonic traps. More recently, the development of DMDs allowed to investigate homogeneous bulk systems, reducing the influence of trap geometries and allowing experimental studies of the properties of BCS superfluids [155–159]. Both in homogeneous and inhomogeneous setups, this led to a tremendous amount of experimental insight into the BEC-BCS crossover in three spatial dimensions [144, 166, 333, 334].

In contrast to lower-dimensional systems, attractive interactions in 3D do not necessarily support a two-body bound state at arbitrarily small interactions. Below a critical interaction threshold, only scattering states are accessed by particles, causing a negative scattering length. Contrarily, for interaction strengths stronger than the respective onset, a two-body bound state emerges with lower energy than free particles, resulting in a positive scattering length. These two regimes are separated by the unitary point, where the scattering length diverges.

For Fermi spin mixtures, theoretical investigations of the BEC-BCS crossover go back to Leggett [76], with a significant advance in theoretical modelling by NSR [80] and following the functional integral treatment in the context of 3D superconductors [87, 88]. However, as outlined in Chapter 2, Section 2.5, all those theories either rely on an arbitrary choice of diagrams, interaction channels or miscount states. As such, the aim of the upcoming chapter is to apply the WHFB approach, which we developed for D dimensions in Chapter 3, to a 3D Fermi spin-mixture with equal populations of both spin states. This requires revisiting 3D scattering theory and taking into account finite-energy scattering via the effective range parameter. Ultimately, a new length scale emerges in the system, characterising how dilute the system is.

4.2 Scattering Renormalization in three dimensions

In this section, we adapt the standard regularisation procedure required to obtain finite physical results from the derived self-consistency equations. To this end, we separate the discussion into two parts. First, we derive the standard regularisation for low-energy scattering events following the approach of H. Bethe [335–337]. After this, we establish a partitioned version of the scattering regularisation, taking into account the effects of the coupling between HS channels. From now on, we will explicitly deal with 3D scattering, and hence all integrals are evaluated in three spatial dimensions.

4.2.1 Effective range scattering theory

In this short detour, we investigate the scattering in the case of $g_{\mathrm{B}} \to g$. Two-body scattering in cold environments is well described by the Lippmann-Schwinger equation (LSE) [62, 63, 274] that leads to the scattering phase shift for the s-wave contact potential

$$q \cot \delta_0(\boldsymbol{q}) = \frac{4\pi}{mg} - \frac{2k_{\mathrm{c}}}{\pi} + \frac{2}{\pi k_{\mathrm{c}}} q^2 + \mathcal{O}(q)^4 \tag{4.1}$$

with $\boldsymbol{q}$ being the scattering momentum of the two particles and k_c a momentum scale serving as an Ultra-violet (UV) cutoff. For any spherical symmetric scattering potential, the phase shift for small scattering momenta generically reads

$$q \cot \delta_0(\boldsymbol{q}) = -\frac{1}{a_\mathrm{s}} + \frac{r_\mathrm{e}}{2} q^2 + \mathcal{O}(q)^4. \tag{4.2}$$

Here a_s denotes the s-wave scattering length as a measure for the zero-energy interaction strength and r_e is the effective range, associated with the leading order energy dependence of the scattering phase shift. The effective range in general is related to the overlap of incoming and scattering state wavefunctions [337]. Comparing coefficients of Eq. (4.1) and Eq. (4.2) leads to the standard regularization prescription

$$\frac{1}{g(k_\mathrm{c})} = -\frac{m}{4\pi a_\mathrm{s}} + \frac{m}{2\pi^2} k_\mathrm{c} = -\frac{m}{4\pi a_\mathrm{s}} + \frac{1}{L^3} \sum_{|\boldsymbol{k}| \leq k_\mathrm{c}} \frac{m}{\boldsymbol{k}^2}, \tag{4.3}$$

depending on the UV cutoff. Normally, this is sufficient in order to regularise the order parameter equation (3.70) by sending $k_\mathrm{c} \to \infty$ while sending $g \to 0$, such that a_s remains constant. The scattering length then serves as the renormalised interaction strength. This prescription, however, leads via Eq. (3.65) to a vanishing Hartree term, as it depends explicitly on the bare g. An infinite-cutoff theory fails to describe the self-energy arising from particle-hole processes. Keeping k_c finite allows for a non-zero solution for the Hartree self-energy, but introduces an explicit cutoff dependence into the theory. So solve this issue, we look at the second-order momentum dependence of Eq. (4.1) and Eq. (4.2). This relates the UV cutoff to the effective range via

$$k_\mathrm{c}(r_\mathrm{e}) = \frac{4}{\pi r_\mathrm{e}}. \tag{4.4}$$

Therefore, replacing the UV cutoff by the effective range leads to a physical interpretation of k_c and allows us to include leading order contributions of finite range potentials in the easiest approximation. It also tells us that the Hartree self-energy is connected deeply to the shape of the interaction, making it a non-universal quantity. To obtain the scattering length, we introduce in Eq. (4.3) the resonance interaction strength $g_\mathrm{Res} = \pi^3 r_\mathrm{e}/(2m)$ using Eq. (4.4). This gives rise to

$$a_\mathrm{s} = \frac{\pi^2}{8} r_\mathrm{e} \frac{g/g_\mathrm{Res}}{g/g_\mathrm{Res} - 1}, \tag{4.5}$$

resulting in negative scattering lengths for weak interactions, below the resonance value and positive scattering lengths with $a_\mathrm{s} \geq r_\mathrm{e}\pi^2/8$ for stronger interactions.

For concrete calculations, we have to obtain the effective range of the most common atomic species used in Fermi gas experiments. For nucleon scattering, where the effective range expansion was developed [335], measuring scattering lengths and effective ranges of $n-n$, p^+-p^+, and $n-p^+$ scatterings is routinely done. For cold atomic gases, measuring the effective range is not so easy due to its small value. Thus, we rely upon standard scattering theory. We are interested in broad Feshbach resonances, where the effective range is approximately independent of the scattering length. Therefore, we approximate the effective range via [70]

$$r_\mathrm{e} \approx \frac{\Gamma(1/4)^2}{3\pi} \left(2 m_\mathrm{r} C_6\right), \tag{4.6}$$

Element	Lithium (^{6}Li)	Potassium (^{40}K)
$\overline{n_0}$ in cm^{-3}	3×10^{12} [180] to 1×10^{15} [264]	$\approx 2 \times 10^{13}$ [140, 339]
C_6 in ${a_0}^4/\mathrm{u}$	1393	3400
r_e in a_0	87.19	174.95
$k_\mathrm{F} r_\mathrm{e}$	0.02 to 0.14	≈ 0.08

Table 4.1: Typical values for ^{6}Li and ^{40}K in ultracold setups. We mentioned the experimental peak densities $\overline{n_0}$ in $3D$ harmonic traps in the first line. In the last line we calculated the effective range parameter $k_\mathrm{F} r_\mathrm{e}$.

where m_r represents the reduced mass of the atoms and C_6 stands for the van der Waals coefficient of the atom. In the unit system used throughout this thesis (remember, $\hbar = 1 = k_\mathrm{B}$) the C_6-coefficient is expressed in terms of Bohr radii a_0 and the atomic mass unit u. We obtained the results for the C_6-coefficient of ^{6}Li and ^{40}K from Ref. [338]. In Table 4.1, we mention the experimentally achieved peak densities in harmonic traps in the first, the C_6-coefficient in the second, and the resulting effective range in units of a_0 in the third line. The last line shows an independent tuning parameter of the system, which is the effective range parameter $k_\mathrm{F} r_\mathrm{e}$, where $k_\mathrm{F} = (3\pi^2 n)^{1/3}$ denotes the Fermi momentum, tuneable by adjusting the density. We visualise the scattering properties of ^{6}Li and ^{40}K in Fig. 4.1, where we illustrate the scattering length a_s versus the scaled bare coupling strength g/g_Res. In panel (a) we show a_s in units of a_0 for ^{6}Li with $r_\mathrm{e}^{^6\mathrm{Li}} \approx 87\ a_0$ (solid blue line) and ^{40}K with $r_\mathrm{e}^{^{40}\mathrm{K}} \approx 175\ a_0$ (solid orange line). Both curves show an essential singularity at the resonance coupling strength $g/g_\mathrm{Res} = 1$, where the scattering length diverges. For smaller interactions, the scattering length is negative and approaches zero from below as the interactions become infinitely weak. For interaction parameters $g/g_\mathrm{Res} > 1$, the scattering length is positive and decreases towards a constant value, depending on the effective range parameter. The asymptotic scattering length for infinitely strong interactions is shown as the dashed line in the respective colour. At weak interactions, the scattering length is approximately independent of the effective range. When approaching or crossing the resonance, the scattering length changes drastically with the effective range, making it not a strongly universal property. In panel (b), we see that the scattering length for various elements collapses onto a single curve when scaled according to the effective range

$$\frac{k_\mathrm{F} a_\mathrm{s}}{k_\mathrm{F} r_\mathrm{e}} = \frac{\pi^2}{8} \frac{g/g_\mathrm{Res}}{g/g_\mathrm{Res} - 1}, \tag{4.7}$$

where besides the effective range parameter $k_\mathrm{F} r_\mathrm{e}$ also the inverse scattering parameter $k_\mathrm{F} a_\mathrm{s}$ is used. This scaled property will henceforth be referred to as **weak universality**.

With the scattering regularisation established until now, it is possible to regularise the standard BEC-BCS crossover theory. This, however does not apply to our partitioned approach, since the divergence appearing in the superfluid order parameter equation (3.70) does not diverge with the UV cutoff k_c but with $b_0 k_\mathrm{c} \leq k_\mathrm{c}$, which makes a formal regularization not possible. In order to do so, we need to modify the standard approach to capture the divergences appearing in the respective HS channels, which then presents a suitable regularisation scheme. This is done in the next part.

4.2.2 Effective pairing channel scattering regularisation

Since the partitioned interaction is smaller than or equal to the bare interaction strength, we have to take this into account in the scattering problem to regularise the superfluid

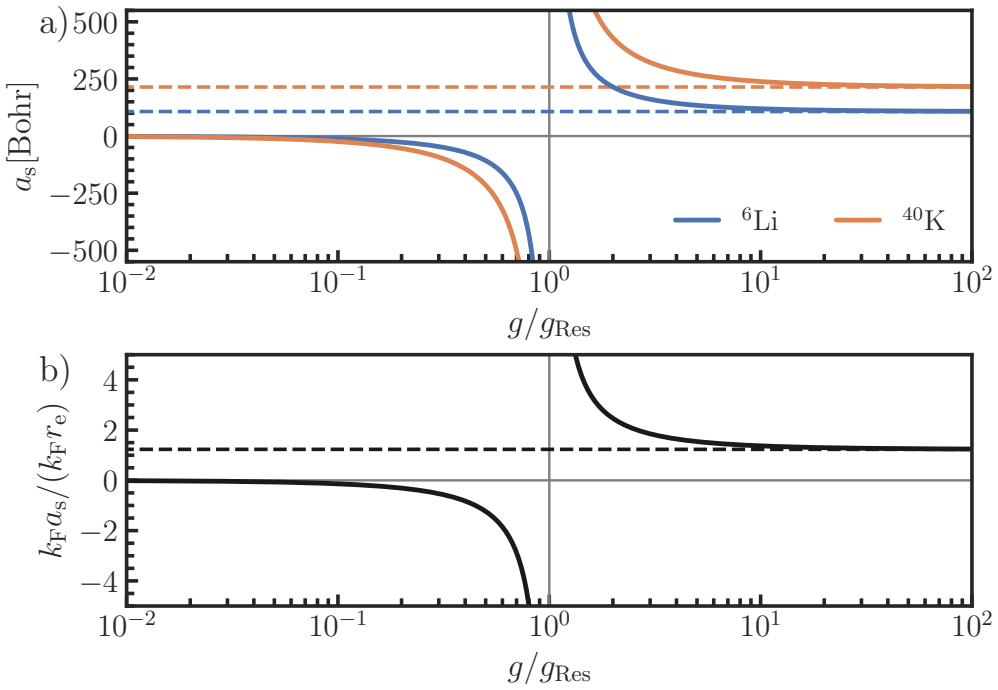


Figure 4.1: Relation between scattering length a_s and coupling strength g in terms of the resonance coupling g_{Res}. In panel (a), we show the scattering length in Bohr radii versus g/g_{Res} for ^{6}Li (solid blue line) and ^{40}K (solid orange line). The dashed line stands for the infinite interaction scattering length. In panel (b), we portray the scaled scattering lengths and their collapse onto a single universal curve.
Adapted from [P1] under the terms of the Creative Commons Attribution 4.0 International (CC BY 4.0) license.

order parameter equation (3.70). Restricting the LSE to the Bogoliubov channel yields

$$\frac{1}{b_0 g} = \frac{1}{g_{\mathrm{B}}} = -\frac{m}{4\pi b_0 a_s} + \frac{m}{2\pi^2 b_0} k_c. \tag{4.8}$$

We factor out the standard scattering length term appearing in the original LSE (4.3), since the scattering length is an observable, and obtain

$$\frac{1}{g_{\mathrm{B}}} = -\frac{m}{4\pi a_s} + \frac{m}{2\pi^2}\left[\frac{k_c}{b_0} + \frac{\pi}{2a_s}\frac{h_0}{b_0}\right]. \tag{4.9}$$

This gives rise to the effective UV cutoff of the Bogoliubov channel

$$k_{c,\mathrm{B}} = \frac{k_c}{b_0} + \frac{\pi}{2a_s}\frac{h_0}{b_0} = \frac{4}{\pi r_{e,\mathrm{B}}}, \tag{4.10}$$

where, for consistency, we introduced the same behaviour derived earlier for a pairing effective range. Using Eq. (4.4) to express the pair effective range in terms of r_e yields

$$r_{e,\mathrm{B}} = r_e \frac{b_0}{1 - h_0 \frac{\pi^2}{8}\frac{k_F r_e}{k_F a_s}} \leq r_e. \tag{4.11}$$

Now, we know from Fig. 4.1 that $1/a_s \leq 8/(\pi^2 r_e)$. Thus, the pairing effective range is always less than or equal to the bare two-body effective range. This is interpreted as a

screening effect of the particle-hole sector onto the pair channel, reducing the effective range of the interaction that forms Cooper pairs. Normally, such effects are derived in a random phase approximation in the framework of the GMB correction [94] and are a pure fluctuation effect on top of a clean Bogoliubov saddle. In our approach, it naturally arises in a mean-field description.

It is useful to directly show this idea of screening in the grand-canonical potential as well, which we do in the next part.

4.2.3 Screened interactions and non-analytic couplings

To illustrate the concept of channel screening, we consider the grand-canonical potential (3.62). More specifically, we investigate the energy offset term, which explicitly includes the partitioned coupling strength. We eliminate the partitioning factors by making use of Eqs. (3.59a) and (3.59b), resulting in

$$\frac{\Delta_{\mathrm{H},0}^2}{g_{\mathrm{H}}} + \frac{|\Delta_{\mathrm{B},0}|^2}{g_{\mathrm{B}}} = \frac{\Delta_{\mathrm{H},0}^2}{g} + \frac{|\Delta_{\mathrm{B},0}|^2}{g} + \frac{2}{g}|\Delta_{\mathrm{H},0}||\Delta_{\mathrm{B},0}|. \tag{4.12}$$

Inserting this into the grand-canonical potential, we obtain the thermodynamic potential with eliminated weighting factors, where an explicit coupling of the channels appears:

$$\begin{aligned}\frac{\Omega_0}{L^3} =& \frac{\Delta_{\mathrm{H},0}^2}{g} + \frac{|\Delta_{\mathrm{B},0}|^2}{g} + \frac{2}{g}|\Delta_{\mathrm{H},0}||\Delta_{\mathrm{B},0}| \\ &- \int_{\mathbb{R}^3} \frac{\mathrm{d}^3k}{(2\pi)^3}\left[E_{\boldsymbol{k}} - \xi_{\boldsymbol{k}} - \Delta_{\mathrm{H},0} + \frac{2}{\beta}\ln\left(1+e^{-\beta E_{\boldsymbol{k}}}\right)\right].\end{aligned} \tag{4.13}$$

We interpret this as follows: The partitioned interaction strength is an effective field-theoretical device to describe the underlying physical mechanism, which is the coupling of Hartree self-energy and pair field. This interaction appears explicitly in the resulting self-consistency equations, which show the non-analytic coupling between the channels. We have the self-consistency equation governing the Hartree term, Eq. (3.68), which reads after eliminating the interaction

$$\Delta_{\mathrm{H},0} = \min\left\{0; \frac{n_0}{2}\left[\frac{m}{4\pi a_{\mathrm{s}}} - \frac{2m}{\pi^3 r_{\mathrm{e}}}\right]^{-1} + |\Delta_{\mathrm{B},0}|\right\}. \tag{4.14}$$

This equation deviates from the naive Hartree channel equation, as seen in Refs. [154, 296], in two ways. First, the effective range is a vital part of the self-energy because it is explicitly dependent on the shape of the interaction potential. Second, the explicit and non-analytic coupling to the superfluid order parameter $|\Delta_{\mathrm{B},0}|$, which manifests in the second term and the minimum function. The density is governed by the SP equation of state (3.64), coupling explicitly to $\Delta_{\mathrm{H},0}$ and $|\Delta_{\mathrm{B},0}|$. In three spatial dimensions it explicitly reads

$$n_0 = \int_{\mathbb{R}^3} \frac{\mathrm{d}^3k}{(2\pi)^3}\left[1 - \frac{\xi_{\boldsymbol{k}} + \Delta_{\mathrm{H},0}}{E_{\boldsymbol{k}}}\tanh\left(\frac{\beta}{2}E_{\boldsymbol{k}}\right)\right]. \tag{4.15}$$

The superfluid order parameter itself also couples directly to the Hartree self-energy as well as the chemical potential through the quasiparticle dispersion (3.52). Eliminating the bare interaction in Eq. (3.70) results in

$$0 = \Delta_{\mathrm{B},0}\left\{\frac{m}{4\pi a_{\mathrm{s}}} - \int_{|\boldsymbol{k}|\leq k_{\mathrm{c,B}}} \frac{\mathrm{d}^3k}{(2\pi)^3}\left[\frac{m}{\boldsymbol{k}^2} - \frac{\tanh\left(\frac{\beta}{2}E_{\boldsymbol{k}}\right)}{2E_{\boldsymbol{k}}}\right]\right\}. \tag{4.16}$$

Additionally, this also includes the fourth self-consistency equation, which is the pair channel UV cutoff, which, when the weights are eliminated, reads

$$k_{\mathrm{c,B}} = \frac{4}{\pi}\frac{1}{r_\mathrm{e}} + \frac{|\Delta_{\mathrm{H},0}|}{|\Delta_{\mathrm{B},0}|}\left(\frac{4}{\pi}\frac{1}{r_\mathrm{e}} - \frac{\pi}{2}\frac{1}{a_\mathrm{s}}\right). \tag{4.17}$$

To solve the presented self-consistency equations, we express all quantities in Fermi units to achieve system-independent results. Therefore, we scale all the momenta in terms of the Fermi momentum k_F and all energies in terms of the Fermi energy $\varepsilon_\mathrm{F} = k_\mathrm{F}^2/(2m)$. For any energy, we use $\Delta = \varepsilon_\mathrm{F}\widetilde{\Delta}$. We further convert the momentum integral to an energy integral with $x = \boldsymbol{k}^2/(2m\varepsilon_\mathrm{F}^2)$ and use $\mathcal{D}(x) = \sqrt{x}$ as density of states in 3D. Lastly, we exploit the spherical symmetry of an infinite system to evaluate the angular integrals. With this the Hartree self-energy (4.14) reduces to

$$\widetilde{\Delta}_{\mathrm{H},0} = \min\left\{0; \frac{4}{3\pi}k_\mathrm{F}a_\mathrm{s}\left[1 - \frac{8}{\pi^2}\frac{k_\mathrm{F}a_\mathrm{s}}{k_\mathrm{F}r_\mathrm{e}}\right] + \widetilde{\Delta}_{\mathrm{B},0}\right\}. \tag{4.18}$$

For the superfluid order parameter we set $|\Delta_{\mathrm{B},0}| = \varepsilon_\mathrm{F}\widetilde{\Delta}_{\mathrm{B},0}$, leading for Eq. (4.16) to become

$$0 = \widetilde{\Delta}_{\mathrm{B},0}\left\{\frac{\pi}{k_\mathrm{F}a_\mathrm{s}} - \int_0^{x_{\mathrm{c,B}}} \mathrm{d}x\, \mathcal{D}(x)\left[\frac{1}{x} - \frac{\tanh\left(\frac{\widetilde{\beta}}{2}\widetilde{E}\right)}{\widetilde{E}}\right]\right\}, \tag{4.19}$$

where we use the dimensionless dispersion $\widetilde{E} = \sqrt{(x - \widetilde{\mu} + \widetilde{\Delta}_{\mathrm{H},0})^2 + \widetilde{\Delta}_{\mathrm{B},0}^2}$. Additionally, this equation uses the rescaled pairing UV cutoff, which due to Eq. (4.17) appears as

$$x_{\mathrm{c,B}} = \left[\frac{4}{\pi}\frac{1}{k_\mathrm{F}r_\mathrm{e}} + \frac{|\widetilde{\Delta}_{\mathrm{H},0}|}{\widetilde{\Delta}_{\mathrm{B},0}}\left(\frac{4}{\pi}\frac{1}{k_\mathrm{F}r_\mathrm{e}} - \frac{\pi}{2}\frac{1}{k_\mathrm{F}a_\mathrm{s}}\right)\right]^2. \tag{4.20}$$

The last self-consistency equation now determines the chemical potential, since, in Fermi units, we fix the density n_0. The EoS (4.15) reads

$$\frac{4}{3} = \int_0^\infty \mathcal{D}(x)\left[1 - \frac{x - \widetilde{\mu} + \widetilde{\Delta}_{\mathrm{H},0}}{\widetilde{E}}\tanh\left(\frac{\widetilde{\beta}}{2}\widetilde{E}\right)\right]. \tag{4.21}$$

Having established self-consistency, we evaluate the four equations and compare the result to the standard mean-field theory outlined, for example, in Refs. [66, 154]. We divide this into two parts. First, we evaluate the ground state at $T = 0$ before discussing the effects of thermal fluctuations at $T > 0$.

4.3 Ground state properties

We evaluate the system in the ground state, that is, at $T = 0$. In this limit, the hyperbolic tangent function appearing in the thermal factors of Eqs. (4.19) and (4.21) converges to 1. Thus, all results depend on two external parameters, which are experimentally accessible. The first is the dimensionless scattering parameter $1/k_\mathrm{F}a_\mathrm{s}$, which is controlled by a magnetic Feshbach field and tunes the interaction. The second one is the dimensionless effective range parameter $k_\mathrm{F}r_\mathrm{e}$, tuneable by changing the density, since the two-body effective range is approximately a constant over a broad Feshbach resonance [70] and hence

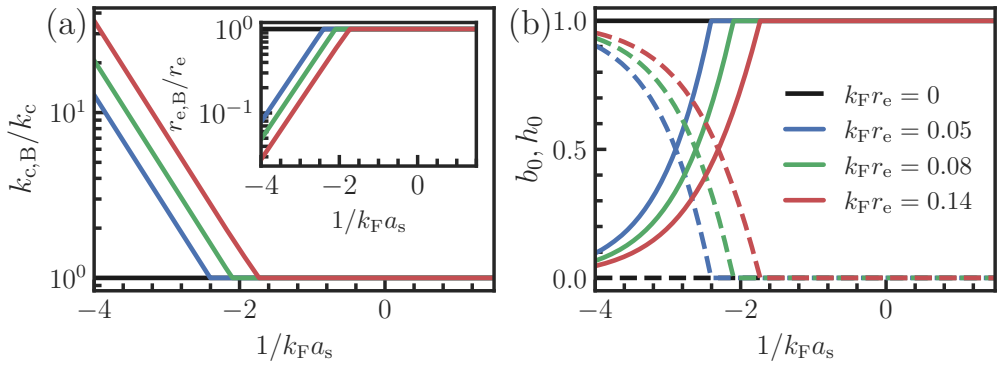


Figure 4.2: (a) Pairing UV cutoff $k_{c,B}$ in units of two-body cutoff k_c (main figure) and the many-body effective range $r_{e,B}$ in units of the two-body effective range r_e (inset). (b) Hartree and Bogoliubov partitioning factors h_0 and b_0 as dashed and solid lines, respectively, versus $1/k_F a_s$. The effective range parameters used are indicated in the figure and explained at the beginning of this section.
Adapted from [P1] under the terms of the Creative Commons Attribution 4.0 International (CC BY 4.0) license.

an atom-specific, unchangeable quantity. The effective range parameter serves as a measure on how dilute the gas is. It becomes evident that larger values of $k_F r_e$ cause stronger deviations of the system from a strongly universal gas, while the zero-range limit corresponds to the standard strongly universal theory. In what follows, we start by discussing the effective scattering properties before diving into the emerging T=0-phase diagram and its characterisations. After this, a detailed discussion of the phases and regimes follows.

We choose to illustrate four cases in all the figures from now on for the rest of this section. We always include a solid black reference line corresponding to the standard theory with zero effective range [66]. In addition, we illustrate three different values of the effective range parameter, inspired by experimentally realistic values, see Table 4.1. The first value is $k_F r_e = 0.05$, which corresponds for ^{6}Li to a homogeneous density of $n \approx 4.3{\times}10^{13}$ cm^{-3}, represented by blue lines. The second value for Lithium is $k_F r_e = 0.14$, which is realised for ^{6}Li by a homogeneous density of $n \approx 1 \times 10^{15}$ cm^{-3}, represented by red lines. The last value is $k_F r_e = 0.08$, which for ^{40}K corresponds to a homogeneous density of $n \approx 2 \times 10^{13}$ cm^{-3}, depicted by green lines. In some figures, we add a dash-dotted magenta line, representing the standard approach with zero effective range, using a naive Hartree shift reading $\widetilde{\Delta}_{H,0} = 4/(3\pi)k_F a_s$. We do so because this approach to the Hartree shift is widely used in low-density Fermi gases, see for example Refs. [28, 168, 296]. However, this approach is only valid below a certain interaction strength, which we derive later on, and it causes massive problems when extrapolated beyond its validity, which unfortunately is often done.

4.3.1 Scattering properties and phase diagram

We start the discussion by investigating the screened scattering properties. We illustrate the pair UV cutoff and the weight factors h_0, b_0 in Fig. 4.2 versus $1/k_F a_s$. In panel (a), the main figure shows the pairing UV momentum cutoff normalised in terms of the two-body cutoff, while the inset illustrates the ratio of pairing and two-body effective ranges, $r_{e,B}/r_e$. Note the logarithmic scaling of the y-axis. Starting from large values $k_{c,B}/k_c \gg 1$ for weak

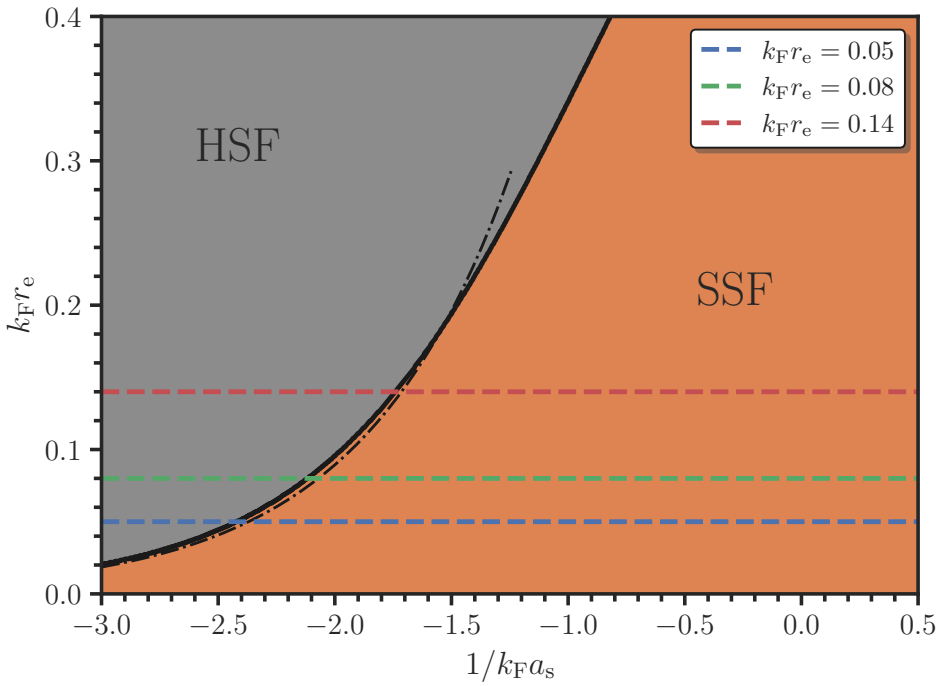


Figure 4.3: Ground-state phase diagram in $k_\mathrm{F}r_\mathrm{e}$ - $1/k_\mathrm{F}a_\mathrm{s}$ plane. Hartree superfluid (HSF) is shown as grey and standard superfluid (SSF) as orange area, separated by a solid black phase transition line. Dash-dotted line is an analytic approximation to the phase boundary, and dashed coloured lines show the illustrative values of the effective range parameter used in the other figures.

Adapted from [P1] under the terms of the Creative Commons Attribution 4.0 International (CC BY 4.0) license.

interactions, the UV cutoff decreases exponentially when going to stronger interactions, until it reaches k_c, where it remains stable. For weak coupling, the appearance of a Hartree channel screens the pair interactions, and thereby increases the UV cutoff in the Bogoliubov channel. Hence, via Eq. (4.10), the pair effective range decreases exponentially, as seen in the inset of panel (a). Conversely, for strong interactions we find $k_{\mathrm{c,B}} = k_\mathrm{c}$ and hence $r_{\mathrm{e,B}} = r_\mathrm{e}$. Panel (b) shows explicitly the partitioning factors h_0 (dashed lines) and b_0 (solid lines) versus $1/k_\mathrm{F}a_\mathrm{s}$. For weak interactions, we observe a mix of the two channels as both weights acquire a finite value. For extremely weak interactions, b_0 approaches zero, while the Hartree weight $h_0 = 1 - b_0$ tends asymptotically to one. For strong interactions, b_0 eventually reaches one, causing $h_0 = 0$. For even stronger interactions, only the pair channel is present, rendering it the standard approach with finite effective range. The boundary where the transition to a single-channel model occurs shifts towards stronger interactions as the effective range parameter increases. We use the partitioning factors to characterise the phases in the ground state, illustrated in Fig. 4.3. The x-axis resembles the interaction strength, and the y-axis the effective range parameter. We added three coloured dashed lines indicating the effective range parameters of $k_\mathrm{F}r_\mathrm{e} = 0.05$ (blue line), $k_\mathrm{F}r_\mathrm{e} = 0.08$ (green line) and $k_\mathrm{F}r_\mathrm{e} = 0.14$ (red line) elaborated previously. The grey region corresponds to a new phase which emerges due to the non-analytic coupling of the two order parameters, associated with non-vanishing values for both h_0 and b_0. Thus, we call this phase the Hartree Superfluid (HSF). In contrast, the Standard Superfluid (SSF) phase is known from previous approaches, where only pair processes are present. This phase is

defined by $h_0 = 0$ and $b_0 = 1$. In general, the HSF phase appears at large effective ranges and small interactions, when the pairing is too weak to dominate all interaction processes and particle-hole scattering occupies most of the states. The phase boundary between HSF and SSF phase is characterised by setting the non-trivial solution of the order parameter equation (4.18) to zero. We find an implicit equation, characterising the phase transition and the critical effective range parameter

$$(k_\mathrm{F} r_\mathrm{e})_\mathrm{c} = \frac{8}{\pi^2}\left[\frac{1}{k_\mathrm{F} a_\mathrm{s}} + \frac{4}{3\pi}\frac{1}{\widetilde{\Delta}_{\mathrm{B},0}}\right]^{-1}, \tag{4.22}$$

where $\widetilde{\Delta}_{\mathrm{B},0}$ is a function of both $1/k_\mathrm{F} a_\mathrm{s}$ and $k_\mathrm{F} r_\mathrm{e}$. This is illustrated as solid black line, whereas the dash-dotted black line corresponds to an analytical approximation derived later.

Having discussed the phase diagram, we investigate the two emerging phases separately by analysing the order parameters and the chemical potential in two consecutive steps. We first discuss the overall behaviour of the quantities evaluated numerically, and then investigate the limiting cases by deriving analytic approximations.

4.3.2 Order parameters and chemical potential

We want to compare our WHFB framework to the unweighted theory in the literature. The standard procedure for including multiple interaction channels is the HFB approximation, see Eq. (3.10), in the framework of variational perturbation theory [28, 154, 289] for operator-based approaches. This approach amounts to setting $b_0 = h_0 = 1$, doubling the interaction. We distinguish two cases of this standard approach. The first one uses the correct two-body effective range regularisation derived in Section 4.2.1, which results in

$$\widetilde{\Delta}_{\mathrm{H},0}^{(\mathrm{Standard})} = \frac{4}{3\pi} k_\mathrm{F} a_\mathrm{s}\left[1 - \frac{8}{\pi^2}\frac{k_\mathrm{F} a_\mathrm{s}}{k_\mathrm{F} r_\mathrm{e}}\right]. \tag{4.23}$$

In contrast to this, a lot of work has been done using a naive replacement of the bare coupling strength by $g = 4\pi a_\mathrm{s}/m$, which is valid for extremely weak interactions only. Often, this relation is justified by the argument that the divergent momentum sum appearing in g is a higher-order term. However, this argument is invalid, as it relies on the same order of approximation for the scattering phase shift, namely the zero-energy limit. Nevertheless, we choose to highlight this approach in order to demonstrate its failure. This naive replacement leads to the well-known self-energy term

$$\widetilde{\Delta}_{\mathrm{H},0}^{(\mathrm{Naive})} = \frac{4}{3\pi} k_\mathrm{F} a_\mathrm{s}, \tag{4.24}$$

which diverges at the unitary point $a_\mathrm{s} \to \pm\infty$. Despite that, the above relation has been extended way beyond the validity region of $a_\mathrm{s} \ll r_\mathrm{e}$, for instance in Refs. [154, 296]. We compare our WHFB results with both versions of the standard approach, only showing the naive regularisation where it fails. The Hartree self-energy is depicted in Fig. 4.4. In panel (a), we illustrate the modulus of the Hartree self-energy $\Delta_{\mathrm{H},0}$ in units of ε_F in the plane of the effective range and the dimensionless scattering parameter as a heat map. The black region indicates a vanishing self-energy $\Delta_{\mathrm{H},0} = 0$. The dashed white curve shows the previously detected phase boundary. We find $\Delta_{\mathrm{H},0} = 0$ in the SSF phase, as expected since there we have $h_0 = 0$. We further observe that higher effective range parameters correspond

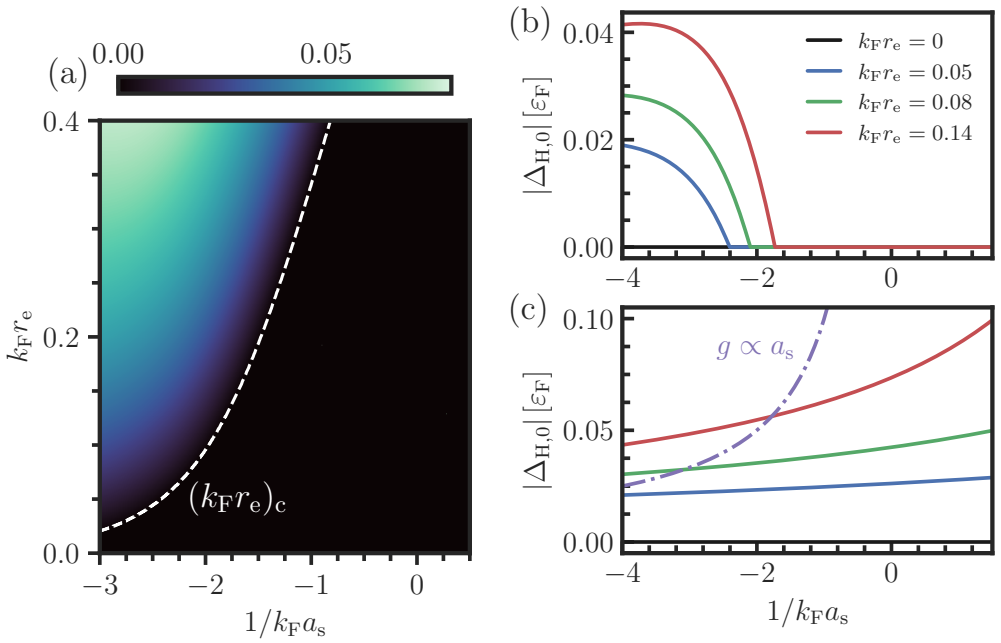


Figure 4.4: WHFB solution of Hartree self-energy. Panel (a) shows $\Delta_{\mathrm{H},0}$ in units of ε_{F} in the $k_{\mathrm{F}}r_{\mathrm{e}}$ - $1/k_{\mathrm{F}}a_{\mathrm{s}}$ plane in a colour code. Dashed white line illustrates the phase transition line. Panel (b) shows the WHFB Hartree self-energy versus $1/k_{\mathrm{F}}a_{\mathrm{s}}$ for effective ranges announced in the figure. Panel (c) shows the Hartree self-energy in the standard approach for the same effective range parameters. Additionally, we added the dash-dotted purple line as an illustration of a naive renormalisation scheme applied, for instance, in Refs. [28, 154, 296].

to larger self-energy shifts. This strengthens the notion of the Hartree channel being associated with finite range scattering processes in the particle-hole sector. As expected, for $k_{\mathrm{F}}r_{\mathrm{e}} = 0$ no Hartree shift exists. Thus, our approach incorporates the BCS mean-field theory as a special case. In panel (b), we show slices of constant effective range, plotting $\Delta_{\mathrm{H},0}$ versus $1/k_{\mathrm{F}}a_{\mathrm{s}}$ for the previously discussed $k_{\mathrm{F}}r_{\mathrm{e}}$ values, see panel legend. For any $k_{\mathrm{F}}r_{\mathrm{e}} > 0$ some scattering parameter exists, below which there is a non-zero self-energy, and above which there is none. At this scattering parameter, the Hartree self-energy continuously tends to 0 at the HSF-SSF transition line from weak interactions.

Comparing our results with the unweighted approach shown in Fig. 4.4 (c), we conclude that there is no phase transition when the fields are not coupled, irrespective of the effective range. The Hartree self-energy is present for any interaction strength and monotonically increases $1/k_{\mathrm{F}}a_{\mathrm{s}}$, diverging at $1/k_{\mathrm{F}}a_{\mathrm{s}} = (8/\pi^2)1/k_{\mathrm{F}}r_{\mathrm{e}}$. The dash-dotted magenta line follows from the unweighted approach when ignoring the effective range, see Eq. (4.24), yielding a divergence at unitarity. The numerical values have been rescaled by a factor of $1/10$ for better visibility.

In Fig. 4.5 we show the behaviour of the superfluid order parameter $|\Delta_{\mathrm{B},0}|$ in terms of the Fermi energy ε_{F}. Panel (a) represents a density plot of $|\Delta_{\mathrm{B},0}|/\varepsilon_{\mathrm{F}}$ in the $k_{\mathrm{F}}r_{\mathrm{e}}$-$1/k_{\mathrm{F}}a_{\mathrm{s}}$ plane. The dashed line shows the HSF-SSF transition. We recognise that the superfluid order parameter does not depend strongly on the interaction range. In contrast, the crossover from weak (left side) to strong (right side) interactions significantly alters the order parameter. Panel (b) depicts slices of constant effective range, where $|\Delta_{\mathrm{B},0}|$ is shown versus $1/k_{\mathrm{F}}a_{\mathrm{s}}$. We conclude that the effective range has little influence, as already expected from

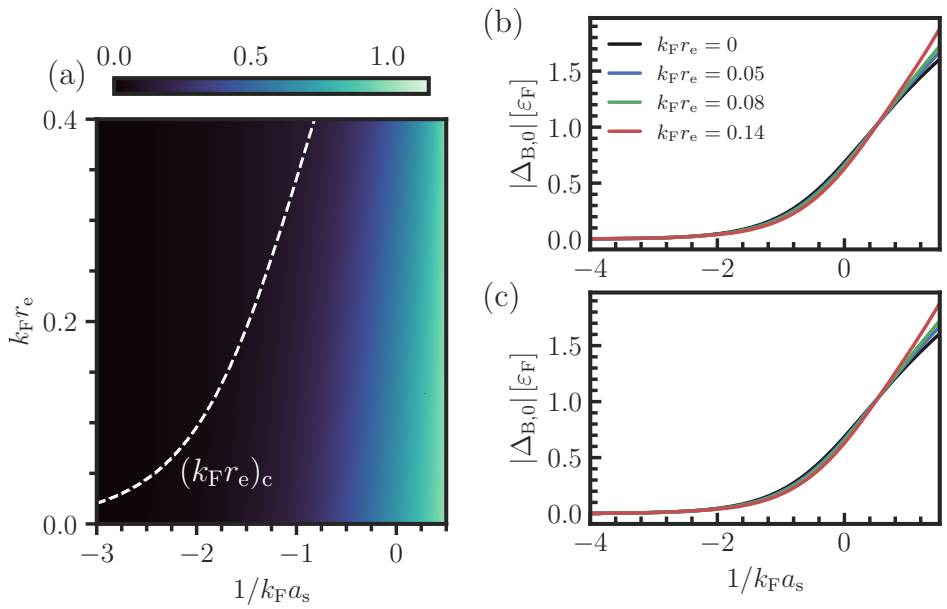


Figure 4.5: WHFB solution of superfluid order parameter. Panel (a) shows $|\Delta_{\mathrm{B},0}|$ in units of ε_{F} in $k_{\mathrm{F}}r_{\mathrm{e}}$ - $1/k_{\mathrm{F}}a_{\mathrm{s}}$ plane and dashed white line illustrates the HSF-SSF transition. Panel (b) depicts the WHFB superfluid order parameter versus $1/k_{\mathrm{F}}a_{\mathrm{s}}$ for effective ranges indicated in the figure. Panel (c) represents the superfluid order parameter in the standard approach for the same effective range parameters.

panel (a), as the curves are closely spaced. There are no strong modulations caused by the effective range parameter. In general, the superfluid order parameter is a monotonically increasing function of the interaction strength. For weak interactions, i.e., $1/k_{\mathrm{F}}a_{\mathrm{s}} \to -\infty$, it decreases exponentially, whereas for larger interaction strengths, its behaviour becomes polynomial in $1/k_{\mathrm{F}}a_{\mathrm{s}}$. However, an effective range $k_{\mathrm{F}}r_{\mathrm{e}} > 0$ slightly reduces the order parameter for interaction strengths smaller than $1/k_{\mathrm{F}}a_{\mathrm{s}} \leq 0.55$, while increasing $|\Delta_{\mathrm{B},0}|$ for stronger interactions. As we will see later, this change is caused by the chemical potential switching sign from positive for $1/k_{\mathrm{F}}a_{\mathrm{s}} < 0.55$ to negative for $1/k_{\mathrm{F}}a_{\mathrm{s}} > 0.55$. Comparing this observation with panel (c) reveals that there is no visible change in the superfluid due to the coupling to the Hartree self-energy using the effective range regularisation.

The last quantity we discuss is the chemical potential μ. In Fig. 4.6 (a) we show a heat map of $\mu/\varepsilon_{\mathrm{F}}$ in the plane of scattering (x-axis) and effective range parameter (y-axis). The dashed black line indicates the HSF-SSF transition. For weak interactions, the chemical potential approaches the Fermi energy, whereas it decreases for stronger interactions. The most striking property of the WHFB approach is that the chemical potential reaches a maximum for fixed effective range at the HSF-SSF phase transition. For weaker interactions, i.e. at the left of the dashed line, we are in the HSF, where the presence of non-vanishing Hartree self-energy reduces the chemical potential by taking the particle-hole sector into account. On the right-hand side of the dashed line, there is no self-energy shift, and particle-hole processes play no role in the SP theory. Panel (b) shows slices of fixed effective range, making the maximum more visible. We notice that for weak interactions, the chemical potential shifts towards lower values relative to the zero-effective-range reference represented by the solid black line. Larger effective range parameters, see, for instance the red curve, produce stronger Hartree shifts for weak interactions, compare Fig. 4.4 (b). As interactions increase, the Hartree shift becomes small and vanishes at the

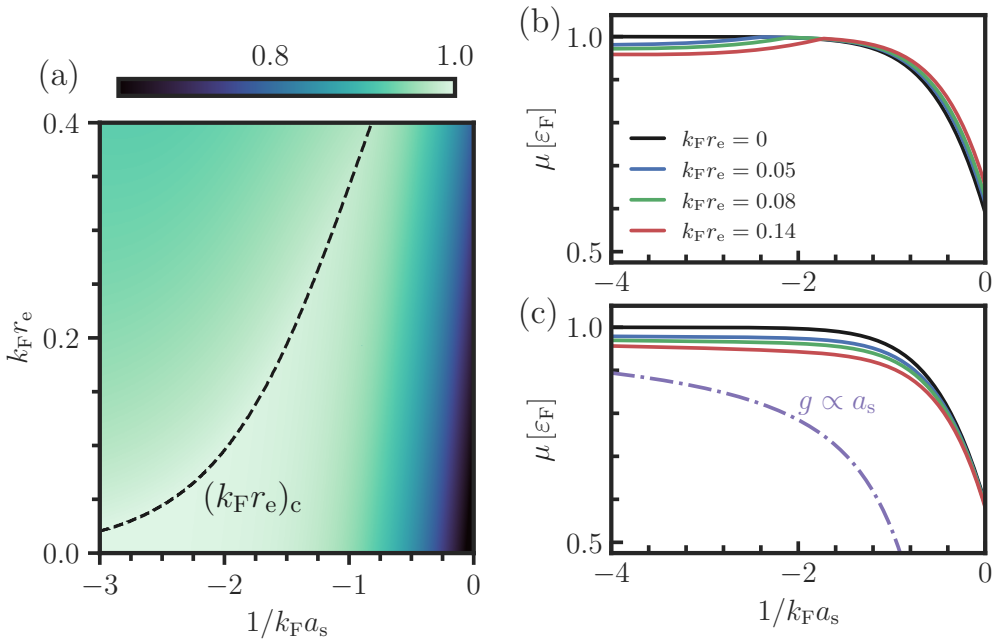


Figure 4.6: Illustration of chemical potential obtained in the WHFB calculation. Panel (a) shows μ in terms of Fermi energy in the $k_F r_e$ - $1/k_F a_s$ plane. Dashed black line illustrates HSF-SSF transition. Panel (b) depicts WHFB chemical potential over $1/k_F a_s$, effective ranges indicated in the figure. Panel (c) pictures μ/ε_F in standard approach using identical effective range parameters as well as naive regularisation chemical potential in dash-dotted purple line.

phase transition, at which point the corresponding shifted chemical potential matches the zero-range reference line. Further increasing the interaction leads to a small increase in μ due to the finite effective range, which is not counteracted by a Hartree shift. In other words, the Hartree self-energy, arising from particle-hole processes, plays a role only at weak interactions, where it reduces the chemical potential with respect to the band minimum. A similar behaviour was already imposed by G. Strinati et al. in Refs. [100, 340] by diagrammatic methods. There, a mean-field self-energy shift was found to be vital for the consistency of pair fluctuations and GMB physics. In their analysis, they found that inconsistencies arise when keeping the self-energy shift for larger interactions. Hence, they used a heuristically chosen scattering parameter to turn off the self-energy shift of the chemical potential. Our analysis provides a physical explanation of this observation by noticing that at strong interactions, pairing processes are favoured over the particle-hole sector, and hence they dominate all interaction processes, causing $\Delta_{H,0} = 0$. For weak interactions, pairing is exponentially small and therefore, particle-hole processes can reduce the ground-state energy. In panel (c), we see the unregulated standard approach, which does not show this behaviour. Since Hartree self-energy is always finite, the chemical potential always acquires a Hartree shift. Furthermore, the naive procedure of ignoring the effective range leads to a singularity in the chemical potential at unitarity, rendering the theory unphysical for $1/|k_F a_s| < 1$. Since the true value of the chemical potential with respect to the bottom of the bands dictates the particle number, this flaw is a catastrophic error in the standard naive approach, revealing its unphysical predictions. This point was plainly "swept under the carpet" by simply ignoring the Hartree term in theoretical investigations [28].

In conclusion, the problems arising in a naive version of a multichannel model are solved by invoking a higher principle of action minimization and partitioning of interactions. This provides a natural solution for the problem of divergences and miscounting of states in the standard HFB approximation. This finding is consistent with diagrammatic investigations [100, 340] of the particle-hole sector in a superfluid, where the self-energy is heuristically introduced for weak interactions, but would cause problems when considering stronger interactions. We now continue with an in-depth discussion of the different phases and asymptotic limits.

4.3.3 Weakly interacting limit

In this section, we discuss the weakly interacting BCS side. This regime is most affected by the presence of the particle-hole sector, as shown already by GMB over half a century ago [94]. As BCS side, we denote strictly negative values of the scattering parameter $1/k_\mathrm{F}a_\mathrm{s} < 0$ for $g < g_\mathrm{Res} = \pi^3 r_\mathrm{e}/(2m)$. In this regime, the system does not support two-body bound states, but allows the formation of large-scale, delocalized pairs in momentum space, facilitated by the Fermi surface and represented by the superfluid order parameter $|\Delta_{\mathrm{B},0}|$. Presence of a Fermi surface means $\mu > 0$, leading to the energy gap

$$E_\mathrm{Gap} = |\Delta_{\mathrm{B},0}|. \tag{4.25}$$

The minimum of the quasi-particle dispersion appears at the Fermi surface $k = \sqrt{2m\mu}$.

We read off the phase diagram in Fig. 4.3 that the HSF-SSF phase boundary always happens at small $k_\mathrm{F}r_\mathrm{e}$ in the BCS regime. Therefore, we consider the HSF and the SSF states separately with the aim of deriving an analytic approximation to the transition line. To this end, we need to know how the superfluid order parameter behaves in the asymptotic BCS regime. We show in Appendix 4.B.1 that approximating Eq. (4.19) leads to

$$|\Delta_{\mathrm{B},0}| \approx \frac{8\varepsilon_\mathrm{F}}{e^2} e^{-1/\sqrt{x_{\mathrm{c,B}}}} \exp\left(-\frac{\pi}{2|k_\mathrm{F}a_\mathrm{s}|}\right), \tag{4.26}$$

when $1/|k_\mathrm{F}a_\mathrm{s}| \ll 1$, which still depends on the many-body UV cutoff from Eq. (4.20). The presence of an effective range parameter leads to a reduction of the order parameter in the BCS regime. When the effective range approaches zero, we have $x_{\mathrm{c,B}} \to \infty$. There, $|\Delta_{\mathrm{B},0}|$ converges to the well-known weakly interacting asymptote [28, 78, 87, 274] with corrections of the order $\mathcal{O}(r_{\mathrm{e,B}})$. We will see in the next two paragraphs that the corrections implied by a finite effective range parameter are fundamentally different in the HSF and SSF regions.

The Hartree superfluid

The HSF region is visualised as the grey coloured area in Fig. 4.3. When investigating the cutoff in Eq. (4.20) and using the non-trivial solution of Eq. (4.18), we eliminate the Hartree self-energy in the pair cutoff, resulting in

$$x_{\mathrm{c,B}} = \left(\frac{2}{3}\frac{\varepsilon_\mathrm{F}}{|\Delta_{\mathrm{B},0}|} - \frac{\pi}{2|k_\mathrm{F}a_\mathrm{s}|}\right)^2. \tag{4.27}$$

Surprisingly, this expression is independent of the two-body effective range parameter. This means that the Hartree self-energy screens the true interaction range by capturing all

the long-range effects, leaving only a remnant of the effective range in the form of the pair cutoff presented above. For weak interactions, the order parameter term dominates in the pair cutoff as it is exponentially small compared to the polynomial factor of $1/k_\mathrm{F}a_\mathrm{s}$. Using this in Eq. (4.26) we obtain the asymptotic limit

$$|\Delta_{\mathrm{B},0}| \approx \frac{8\varepsilon_\mathrm{F}}{e^2}\left[1-\frac{12}{e^2}\left(-\frac{\pi}{2|k_\mathrm{F}a_\mathrm{s}|}\right)\right]\exp\left(-\frac{\pi}{2|k_\mathrm{F}a_\mathrm{s}|}\right). \tag{4.28}$$

This agrees well with the numerical evaluation shown in Fig. 4.5 (b).

To obtain a corresponding asymptotic expansion of the Hartree self-energy, we have to make one further distinction. As the self-energy depends explicitly on the scattering parameter and the effective range, their dimensionless ratio leads to two distinct asymptotic regimes. Therefore, we investigate the following two cases: (1) $k_\mathrm{F}r_\mathrm{e} \ll |k_\mathrm{F}a_\mathrm{s}| \ll 1$ and (2) $|k_\mathrm{F}a_\mathrm{s}| \ll k_\mathrm{F}r_\mathrm{e} \ll 1$. Close to the HSF-SSF transition we are in the regime of small effective range compared to the scattering length, that is $k_\mathrm{F}r_\mathrm{e} \ll |k_\mathrm{F}a_\mathrm{s}|$, leading to an asymptotic expansion of Eq. (4.18) reading

$$\begin{aligned}\frac{\Delta_{\mathrm{H},0}}{\varepsilon_\mathrm{F}} =& -\frac{\pi}{6}k_\mathrm{F}r_\mathrm{e}\left[1-\frac{\pi^2}{8}\frac{k_\mathrm{F}r_\mathrm{e}}{|k_\mathrm{F}a_\mathrm{s}|}+\mathcal{O}\left(\frac{k_\mathrm{F}r_\mathrm{e}}{|k_\mathrm{F}a_\mathrm{s}|}\right)^2\right]\\ &+\frac{8\varepsilon_\mathrm{F}}{e^2}\left[1-\frac{12}{e^2}\left(-\frac{\pi}{2|k_\mathrm{F}a_\mathrm{s}|}\right)\right]\exp\left(-\frac{\pi}{2|k_\mathrm{F}a_\mathrm{s}|}\right).\end{aligned} \tag{4.29}$$

When decreasing the interaction strength further, the sensitivity of $\Delta_{\mathrm{H},0}$ to $k_\mathrm{F}a_\mathrm{s}$ increases and vice versa the sensitivity to $k_\mathrm{F}r_\mathrm{e}$ decreases. This leads to

$$\begin{aligned}\frac{\Delta_{\mathrm{H},0}}{\varepsilon_\mathrm{F}} =& -\frac{4}{3\pi}|k_\mathrm{F}a_\mathrm{s}|\left[1-\frac{8}{\pi^2}\frac{|k_\mathrm{F}a_\mathrm{s}|}{k_\mathrm{F}r_\mathrm{e}}+\mathcal{O}\left(\frac{|k_\mathrm{F}a_\mathrm{s}|}{k_\mathrm{F}r_\mathrm{e}}\right)^2\right]\\ &+\frac{8\varepsilon_\mathrm{F}}{e^2}\left[1-\frac{12}{e^2}\left(-\frac{\pi}{2|k_\mathrm{F}a_\mathrm{s}|}\right)\right]\exp\left(-\frac{\pi}{2|k_\mathrm{F}a_\mathrm{s}|}\right).\end{aligned} \tag{4.30}$$

The leading-order term is simply the result obtained using a naive approach, neglecting the effective range. This demonstrates that the naive approach in Eq. (4.24) is only valid when $k_\mathrm{F}a_\mathrm{s} \ll k_\mathrm{F}r_\mathrm{e}$. Naturally, this is never the case when approaching unitarity, where the scattering length diverges, thereby demonstrating the failure of the naive approach. Ultimately, we conclude that always the smaller length scale determines the leading behaviour of $\Delta_{\mathrm{H},0}$.

For weak interactions, the Hartree self-energy is the main reason the chemical potential differs from the Fermi energy. We see this when considering Eq. (4.21), which depends exponentially small on $\Delta_{\mathrm{B},0}$ at weak interactions. Since $\Delta_{\mathrm{H},0}$ has the two hierarchies of length scales, the chemical potential behaves differently in the two asymptotic regimes, leading to

$$\frac{\mu}{\varepsilon_\mathrm{F}} = 1-\frac{\pi}{6}k_\mathrm{F}r_\mathrm{e}\left[1-\frac{\pi^2}{8}\frac{k_\mathrm{F}r_\mathrm{e}}{|k_\mathrm{F}a_\mathrm{s}|}+\mathcal{O}\left(\frac{k_\mathrm{F}r_\mathrm{e}}{|k_\mathrm{F}a_\mathrm{s}|}\right)^2\right], \tag{4.31}$$

for $k_\mathrm{F}r_\mathrm{e} \ll |k_\mathrm{F}a_\mathrm{s}|$ and

$$\frac{\mu}{\varepsilon_\mathrm{F}} = 1-\frac{4}{3\pi}|k_\mathrm{F}a_\mathrm{s}|\left[1-\frac{8}{\pi^2}\frac{|k_\mathrm{F}a_\mathrm{s}|}{k_\mathrm{F}r_\mathrm{e}}+\mathcal{O}\left(\frac{|k_\mathrm{F}a_\mathrm{s}|}{k_\mathrm{F}r_\mathrm{e}}\right)^2\right], \tag{4.32}$$

for $|k_{\mathrm{F}}a_{\mathrm{s}}| \ll k_{\mathrm{F}}r_{\mathrm{e}}$. Here, we neglected exponentially small corrections due to the superfluid order parameter, as they are small compared to the Hartree shift.

After having discussed the three physical quantities present in the WHFB evaluation in the HSF regime, we continue by considering the SSF phase at the BCS side.

Standard Superfluid

The standard superfluid is characterized by $h_0 = 0$, leading to $\Delta_{\mathrm{H},0} = 0$, highlighted as the orange region in Fig. 4.3. Here, all the interaction energy is used to form Cooper pairs since the interaction strength is sufficiently large to suppress the particle-hole sector. In this phase, we investigate the finite-range implications, as this is vital to understanding finite effective-range interactions. Since the Hartree self-energy vanishes, the pairing UV cutoff from Eq. (4.20) reduces to the standard two-body cutoff dictated by the two-body effective range parameter

$$x_{\mathrm{c,B}} = \frac{16}{\pi^2}\frac{1}{(k_{\mathrm{F}}r_{\mathrm{e}})^2}. \tag{4.33}$$

Because of that, the superfluid order parameter $\Delta_{\mathrm{B},0}$ in the SSF phase is directly affected by $k_{\mathrm{F}}r_{\mathrm{e}}$, unlike in the HSF phase.

Since the HSF-SSF transition occurs for $k_{\mathrm{F}}r_{\mathrm{e}} \ll |k_{\mathrm{F}}a_{\mathrm{s}}|$, and the SSF is only present for effective ranges smaller than the critical effective range, the SSF phase only contains the hierarchy $k_{\mathrm{F}}r_{\mathrm{e}} \ll |k_{\mathrm{F}}a_{\mathrm{s}}| \ll 1$. In this limit, we obtain the superfluid order parameter approximated to be

$$\frac{|\Delta_{\mathrm{B},0}|}{\varepsilon_{\mathrm{F}}} \approx \frac{8}{e^2}\exp\left(-\frac{\pi}{4}k_{\mathrm{F}}r_{\mathrm{e}}\right)\exp\left(-\frac{\pi}{2|k_{\mathrm{F}}a_{\mathrm{s}}|}\right). \tag{4.34}$$

This tells us that the presence of a finite effective range reduces $\Delta_{\mathrm{B},0}$ weakly when considering the weak-coupling side of the SSF region, proportional to the effective range. Furthermore, because the Hartree self-energy is not present, also any change in the chemical potential is of the order of$\Delta_{\mathrm{B},0}$, which ultimately results in

$$\frac{\mu}{\varepsilon_{\mathrm{F}}} = 1 - \mathcal{O}\left(\frac{|\Delta_{\mathrm{B},0}|}{\varepsilon_{\mathrm{F}}}\right)^2. \tag{4.35}$$

After having solved asymptotically for the self-consistent variables, we use Eq. (4.34) and insert it into the HSF-SSF transition condition (4.22), yielding

$$(k_{\mathrm{F}}r_{\mathrm{e}})_{\mathrm{c}} \approx \frac{48}{e^2\pi}\exp\left(-\frac{\pi}{2|k_{\mathrm{F}}a_{\mathrm{s}}|}\right). \tag{4.36}$$

This formula is a good approximation to the transition region as long as $1/k_{\mathrm{F}}a_{\mathrm{s}} \ll 1$, which is shown as the dash-dotted black line in Fig. 4.3.

To summarise, in the BCS regime, there are two types of superfluids. The standard superfluid (SSF) and the Hartree superfluid (HSF). The HSF supports particle-hole processes and with this a range-dependent self-energy contribution affecting the chemical potential, known as the Hartree shift. The non-analytic coupling between $\Delta_{\mathrm{H},0}$ and $\Delta_{\mathrm{B},0}$ provides a mechanism that allows the particle-hole sector to screen the range of the pair interaction, making the formation of Cooper pairs insensitive to the two-body effective range. The same non-analytic coupling allows $\Delta_{\mathrm{H},0} = 0$, leading to the SSF phase. Here, the attractive interaction is so large that pairing is energetically favourable so that no states

are used up in the Hartree channel. This means no screening effects are present. Thus, in the SSF region $\Delta_{\mathrm{B},0}$ acquires an explicit dependence on the effective range.

Having discussed the weakly interacting limit, we investigate the unitary gas.

4.3.4 Unitary gas

The unitary Fermi gas is characterised by a diverging scattering length when approaching the Feshbach resonance magnetic induction B_{res}, namely $a_{\mathrm{s}} \to \pm\infty$ $(1/k_{\mathrm{F}}a_{\mathrm{s}} \to 0)$. A large number of experimental and theoretical investigations have focused on this case. It is believed to exhibit universal behaviour in the form of scale invariance [341], as is well known for cold quantum gases like ^{6}Li or ^{40}K [77]. In the aforementioned systems, r_{e} generally was not considered in the theoretical description so far. For nuclear systems, which typically have much higher densities, the effective range is of the order of the mean distance between the particles, and hence, has crucial effects, preventing universal behaviour in such setups [206, 231]. Furthermore, tuning physical systems to the unitary point is, generally speaking, only asymptotically possible by adjusting the density in nuclear systems. The naive standard approach (4.24) causes the Hartree self-energy to diverge at unitarity. Such divergences can not occur in real experimental setups, and hence, this is a hint of the incompleteness of the underlying theory. Additionally, because of the functional shape of the naive Hartree self-energy (4.24), it would have a singularity at unitarity followed by a switch sign. As such, in the proximity to unitarity, the chemical potential would acquire any real value ranging from $-\infty$ to ∞.

The WHFB approach solves this issue in two ways. The first, and more relevant point, is the proper regularisation of the bare interaction strength g, which does not rely on any assumption about weak interactions. This renders our approach more reliable, as we directly include the effects of the interaction potential's shape, which is vital for a proper description of the particle-hole sector [342]. Our procedure shifts the divergence of the self-energy towards $k_{\mathrm{F}}a_{\mathrm{s}} = (\pi^2/8)k_{\mathrm{F}}r_{\mathrm{e}} > 0$, which corresponds to an infinitely strong interaction. Due to the coupling of the two channels, the Bogoliubov channel occupies all states at strong interactions, as there the formation of Cooper pairs is energetically favoured, preventing the divergence. This is an important physical consequence of the partitioning.

At unitarity the Hartree self-energy in Eq. (4.18) simplifies to

$$\frac{\Delta_{\mathrm{H},0}}{\varepsilon_{\mathrm{F}}} = \min\left\{0; -\frac{\pi}{6}k_{\mathrm{F}}r_{\mathrm{e}} + \widetilde{\Delta}_{\mathrm{B},0}\right\}. \tag{4.37}$$

A non-trivial solution for this minimum function at unitarity can only occur for large values of $k_{\mathrm{F}}r_{\mathrm{e}}$, which are not experimentally achievable in cold gas setups. Therefore, in any such setup we find $\Delta_{\mathrm{H},0}\,|_{a_{\mathrm{s}}\to\pm\infty} = 0$. Hence, the unitary regime is always in the SSF phase. This agrees well with the finding of Zhang and Leggett [290]. They argued that the dimensionless effective range parameter should play a role when the length scale of the scattering length itself vanishes, as it remains the only ratio of length scales in the system. However, in practice, they acknowledged that in cold quantum gases, this ratio, even in the densest experimental setups, is too small to be observed experimentally. At unitarity, our findings are important from a conceptual and theoretical standpoint on the consistency of describing Fermi systems. The method itself leads to non-trivial effects in more dense frameworks, such as nuclei and neutron stars. This is again a notion of the weak universality established previously, which plays its biggest role at unitarity. When the effective

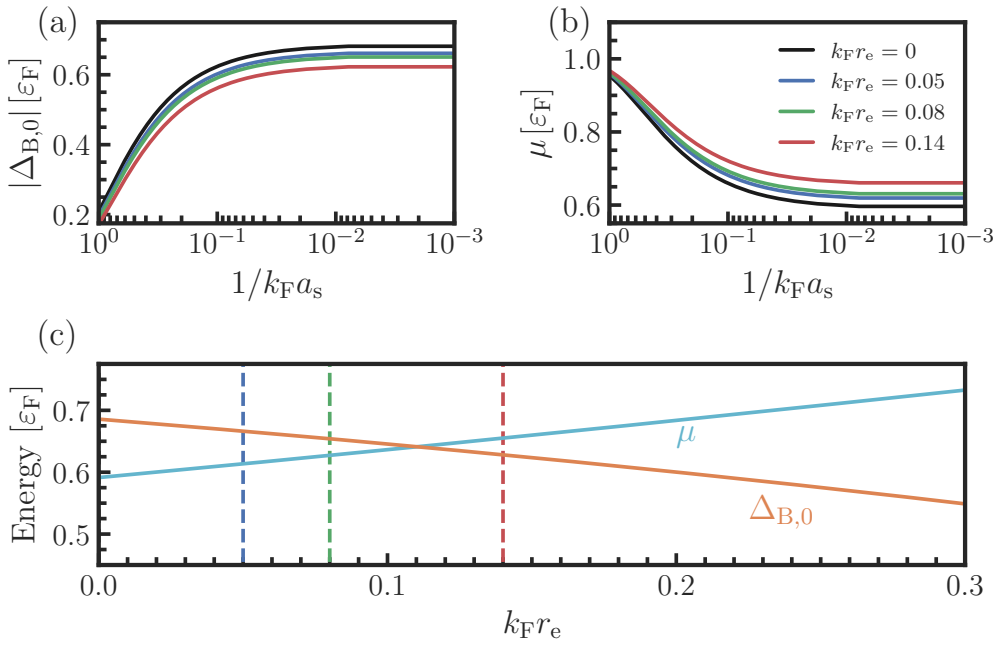


Figure 4.7: Panel (a) and (b) represent SP values of $|\Delta_{B,0}|$ and μ for various values of $k_F r_e$ versus $1/k_F a_s$ on a logarithmic axis. This illustrates how the self-consistent parameters approach their value at unitarity, which is on the infinite right of the panels. Panel (c) shows the unitarity value of $|\Delta_{B,0}|$ (solid orange line) and μ (solid turquoise line) versus the effective range parameter. The dashed lines illustrate the $k_F r_e$ parameters used in panels (a) and (b).

range becomes larger, the system behaves less universal.

In Fig. 4.7 we depict the values of $\Delta_{B,0}$ and μ in units of ε_F at unitarity. Panel (a) resembles the order parameter and panel (b) the chemical potential versus $1/k_F a_s$ when approaching unitarity from the BCS side. This illustration is motivated by Ref. [343] and uses a logarithmic scaling to illustrate the approach to unitarity. We find good qualitative agreement with their work, as for increasing effective range parameter, the unitarity value of the order parameter decreases, while the chemical potential increases. Thus, we find that the presence of a non-vanishing length scale at unitarity weakens pairing and enhances the degeneracy. In panel (c) we show how the superfluid order parameter (solid orange line) and the chemical potential (solid turquoise line) change with $k_F r_e$ at unitarity. The dashed lines in the respective colour correspond to the values chosen in panels (a) and (b). We observe that, for increasing effective range, the order parameter decreases linearly, while the chemical potential increases linearly with $k_F r_e$. This puts the qualitative statement just made in the previous panels into quantitative terms.

Having discussed the unitary regime, the next section deals with strong interactions.

4.3.5 Strong interactions

In this section, we elaborate on the strongly interacting regime of the WHFB theory. To this end, we define the strong interaction regime as the region via $1/k_F a_s > 0$, such that a true two-body bound state exists. Even though the SP description is not a reliable theory to describe strong interactions, our approach provides an improved starting point for a beyond SP theory. For strong coupling, we are always in the SSF region with $\Delta_{H,0} = 0$, as can be

identified in Fig. 4.3. The chemical potential decreases for increasing interaction strength, eventually crossing zero and becoming negative. As a result, the Fermi surface dissolves entirely, and the gas is now closer to a system of composite bosons. This is related to the idea of Blatt [17], where charged electron dimers undergo a BEC transition. In our case, the dimers are neutral molecules. When the chemical potential switches sign, the energy gap of the quasiparticle dispersion increases. For positive chemical potential, we had an energy gap of $|\Delta_{\mathrm{B},0}|$, as already stated in Eq. (4.25). For a negative chemical potential, the energy gap becomes

$$E_{\mathrm{Gap}} = \sqrt{\mu^2 + |\Delta_{\mathrm{B},0}|^2} > |\Delta_{\mathrm{B},0}| \,, \tag{4.38}$$

making it harder to dissolve the pairs. Note that this energy gap is reached at $k = 0$, and not at the Fermi surface.

Before we go into detail in the discussion of the asymptotic limits of $\Delta_{\mathrm{B},0}$ and μ, we derive an analytic expression for the location of the sign switch of μ and how the presence of an effective range alters this location. To this end, we set $\mu = 0$ and use the fact that in the SSF we have $\Delta_{\mathrm{H},0} = 0$. Further, we perform an integration by parts in the superfluid order parameter equation (4.19) and extend the integral to infinity by adding and subtracting the $[x_{\mathrm{c,B}}, \infty)$ tail. This results in

Definition: Euler-β function

For $\alpha, \gamma \in \mathbb{C}$ the β-function is defined as

$$\mathrm{B}(\alpha, \gamma) = \int_0^\infty \mathrm{d}u \, \frac{u^{\alpha-1}}{(1+u)^{\alpha+\gamma}} \tag{4.39}$$

$$\frac{\pi}{k_{\mathrm{F}} a_{\mathrm{s}}} = I_0 + I_{\mathrm{R}} \tag{4.40}$$

with the zero-range part of the superfluid order parameter equation being

$$I_0 = 2\widetilde{\Delta}_{\mathrm{B},0}^2 \int_0^\infty \mathrm{d}x \, \frac{\sqrt{x}}{(x^2 + \widetilde{\Delta}_{\mathrm{B},0}^2)^{3/2}}, \tag{4.41}$$

and the correction due to the effective range parameter

$$I_{\mathrm{R}} = -2\widetilde{\Delta}_{\mathrm{B},0}^2 \int_{x_{\mathrm{c,B}}}^\infty \mathrm{d}x \, \frac{\sqrt{x}}{(x^2 + \widetilde{\Delta}_{\mathrm{B},0}^2)^{3/2}} + 2\sqrt{x_{\mathrm{c,B}}} \left[1 - \frac{x_{\mathrm{c,B}}}{\sqrt{x_{\mathrm{c,B}}^2 + \widetilde{\Delta}_{\mathrm{B},0}^2}} \right]. \tag{4.42}$$

The integral in I_{R} arises from extending the domain of integration, whereas the second term stems from the boundary of the integration domain. Using the substitution $u = x^2/\widetilde{\Delta}_{\mathrm{B},0}^2$ and the definition of the Euler-β function, the zero-range term becomes

$$I_0 = \sqrt{\widetilde{\Delta}_{\mathrm{B},0}} \mathrm{B}\left(\frac{3}{4}, \frac{3}{4}\right). \tag{4.43}$$

For small effective range parameters we have $\widetilde{\Delta}_{\mathrm{B},0} \ll x_{\mathrm{c,B}}$ and hence we expand I_{R} for small $\widetilde{\Delta}_{\mathrm{B},0}/x_{\mathrm{c,B}}$, ultimately leading to

$$I_{\mathrm{R}} = -\frac{1}{3}\sqrt{x_{\mathrm{c,B}}} \left(\frac{\widetilde{\Delta}_{\mathrm{B},0}}{x_{\mathrm{c,B}}} \right)^2 + \frac{3}{28}\sqrt{x_{\mathrm{c,B}}} \left(\frac{\widetilde{\Delta}_{\mathrm{B},0}}{x_{\mathrm{c,B}}} \right)^4 + \mathcal{O}\left(\frac{\widetilde{\Delta}_{\mathrm{B},0}}{x_{\mathrm{c,B}}} \right)^6. \tag{4.44}$$

Next, we solve the number equation (4.21) at $T = 0$ in order to obtain $\widetilde{\Delta}_{\mathrm{B},0}(\mu = 0)$ explicitly. An integration by parts results in

$$2 = \int_0^\infty \mathrm{d}x\, \widetilde{\Delta}_{\mathrm{B},0}^2 \left(\frac{x}{x^2 + \widetilde{\Delta}_{\mathrm{B},0}^2} \right)^{3/2} . \tag{4.45}$$

Performing the same substitution as before allows us to solve the integral employing the β-function, yielding

$$\frac{|\Delta_{\mathrm{B},0}|}{\varepsilon_{\mathrm{F}}} = \widetilde{\Delta}_{\mathrm{B},0} = \left(\frac{4}{\mathrm{B}\left(\frac{5}{4}, \frac{1}{4}\right)} \right)^{2/3} \approx 1.053. \tag{4.46}$$

We reinsert this result into the integrals (4.43) and (4.44) from Eq. (4.40) to obtain the transition scattering parameter as a perturbation series in $k_{\mathrm{F}} r_{\mathrm{e}}$ of the form

$$\frac{1}{k_{\mathrm{F}} a_{\mathrm{s}}} = \eta - \gamma (k_{\mathrm{F}} r_{\mathrm{e}})^3 + \zeta (k_{\mathrm{F}} r_{\mathrm{e}})^7 + \mathcal{O}(k_{\mathrm{F}} r_{\mathrm{e}})^{11}. \tag{4.47}$$

The corresponding numerical expansion coefficients are

$$\eta = \frac{\mathrm{B}\left(\frac{3}{4}, \frac{3}{4}\right)}{\pi} \left(\frac{4}{\mathrm{B}\left(\frac{5}{4}, \frac{1}{4}\right)} \right)^{1/3} \approx 0.553, \tag{4.48a}$$

$$\gamma = \frac{\pi^2}{192} \left(\frac{4}{\mathrm{B}\left(\frac{5}{4}, \frac{1}{4}\right)} \right)^{4/3} \approx 0.057, \tag{4.48b}$$

$$\zeta = \frac{3\pi^6}{458752} \left(\frac{4}{\mathrm{B}\left(\frac{5}{4}, \frac{1}{4}\right)} \right)^{8/3} \approx 0.008\,. \tag{4.48c}$$

The explicit values of γ and ζ are much less than one. Thus, we conclude that the sign switch of the chemical potential is only weakly influenced by $k_{\mathrm{F}} r_{\mathrm{e}}$.

Having located the transition point, we now focus on scattering lengths $1/k_{\mathrm{F}} a_{\mathrm{s}} \gg 0.55$. The superfluid order parameter was already discussed in the context of Fig. 4.5 (b), where it was found that $|\Delta_{\mathrm{B},0}|$ increases for increasing $k_{\mathrm{F}} r_{\mathrm{e}}$. Compared to the weakly interacting limit, where the effects of $k_{\mathrm{F}} r_{\mathrm{e}}$ are small, for strong interactions, its effect becomes substantial. To solidify this, we derive an asymptotic expansion in Appendix 4.B.2, reading

$$\frac{|\Delta_{\mathrm{B},0}|}{\varepsilon_{\mathrm{F}}} = \frac{4}{\sqrt{3\pi}} \frac{1}{\sqrt{k_{\mathrm{F}} a_{\mathrm{s}}}} \left[1 + \frac{1}{4} \frac{k_{\mathrm{F}} r_{\mathrm{e}}}{k_{\mathrm{F}} a_{\mathrm{s}}} + \mathcal{O}\left(\frac{k_{\mathrm{F}} r_{\mathrm{e}}}{k_{\mathrm{F}} a_{\mathrm{s}}} \right)^2 \right]. \tag{4.49}$$

This quantifies the effect of a finite $k_{\mathrm{F}} r_{\mathrm{e}}$ for increasing the superfluid order parameter perturbatively. Because μ varies strongly from weak to strong coupling, we illustrate the intermediate to strong interacting values separately in Fig. 4.8. There, in panel (a), the result for the chemical potential in terms of ε_{F} around unitarity is illustrated as a heatmap in the $k_{\mathrm{F}} r_{\mathrm{e}}$ - $1/k_{\mathrm{F}} a_{\mathrm{s}}$ plane. The dashed white line indicates the numerically determined line of vanishing chemical potential. It agrees well with the analytic expression derived in Eq. (4.47). Panels (b) and (c) represent the chemical potential in terms of the Fermi energy versus $1/k_{\mathrm{F}} a_{\mathrm{s}}$ for various values of the effective range parameter, indicated in the figure legend. Panel (b) shows the WHFB approach and panel (c) the unweighted approach. The

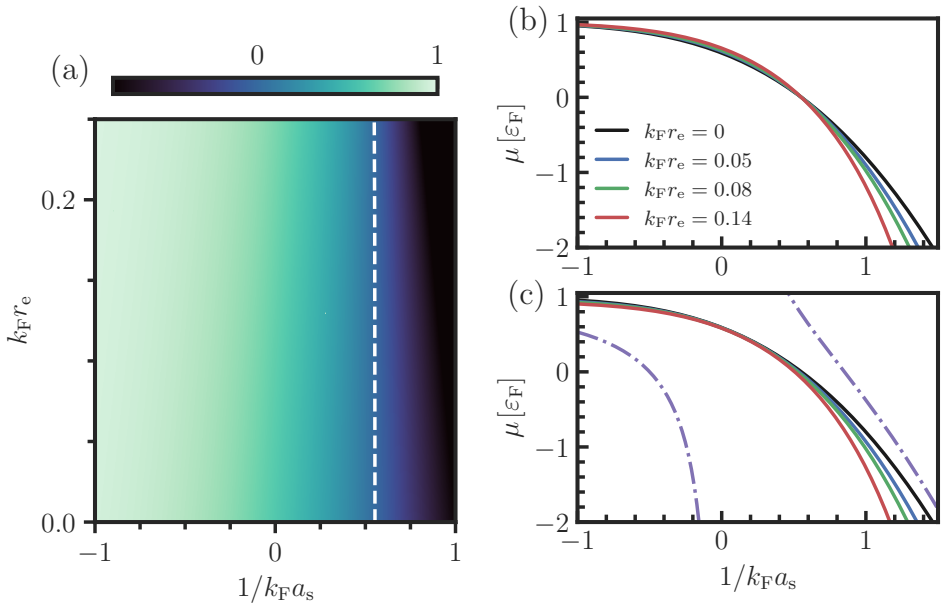


Figure 4.8: Chemical potential μ obtained in WHFB calculation for intermediate to strong interactions. Panel (a) shows μ in terms of Fermi energy in the $k_F r_e$ - $1/k_F a_s$ plane. Dashed white line indicates where μ switches sign. Panel (b) shows WHFB chemical potential over $1/k_F a_s$ for effective ranges indicated in the figure. Panel (c) depicts μ/ε_F in the standard approach for the same effective range parameters as well as the naive approach via the dash-dotted purple line.

unweighted and WHFB approaches lead nearly to the same result, with deviations arising only from the presence of a small Hartree shift in the unweighted approach, while the WHFB approach does not have a Hartree shift in this region. We conclude that the effective range substantially decreases the chemical potential in the strong-coupling regime due to the degeneracy of the Fermi gas. This comes from the circumstance that the effective range increases the binding energy of the two-body bound states. For strong interactions, a perturbative calculation is performed in Appendix 4.B.2, resulting in a decrease in the chemical potential according to

$$\frac{\mu}{\varepsilon_F} = -\frac{1}{2}\frac{E_B}{\varepsilon_F} + \frac{2}{3\pi}k_F a_s\left[1 + \frac{k_F r_e}{k_F a_s} + \mathcal{O}\left(\frac{k_F r_e}{k_F a_s}\right)^2\right] + \mathcal{O}\left(k_F a_s\right)^2, \tag{4.50}$$

agreeing well with the numerical evaluation depicted in Fig. 4.8 panel (b). Here, we use the binding energy

$$E_B = \frac{\varepsilon_F}{(k_F a_s)^2}\left[1 + \frac{k_F r_e}{k_F a_s} + \mathcal{O}\left(\frac{k_F r_e}{k_F a_s}\right)^2\right]. \tag{4.51}$$

In contrast, we find in panel (c) that the naive approach, as is also discussed in Refs. [154, 289, 296], fails around unitarity and for strong interactions. This is because there is a singularity of the chemical potential at $1/k_F a_s = 0$, discussed already in Section 4.3.4. Beyond that, the Hartree shift becomes positive and pushes the chemical potential up, as if the original Fermi interactions were repulsive, although they are forming two-body bound states. Thus, the necessity of the WHFB approach in combination with the correct effective range regularisation to go beyond a simple weak coupling description becomes evident.

So far, we discussed the immediate consequences of the WHFB treatment for a Fermi spin mixture in the ground state. In the following, we consider secondary consequences of our approach by investigating some thermodynamic properties $T = 0$ in the next section.

4.4 Thermodynamics of WHFB ground state

In this section, we work out some thermodynamic properties of the WHFB ground-state evaluated for a two-component Fermi spin mixture in 3D with equal spin populations based on the evaluation in the previous section. We start by discussing the free energy of the ground state, which represents the basis of the following discussion. Afterwards, we evaluate the compressibility as a second derivative of the free energy, which allows us to characterise the HSF-SSF transition from the viewpoint of critical phenomena. Furthermore, we consider the behaviour of Tan's universal contact relation. We find that the WHFB approach can predict the correct contact relation for weak interactions at the mean-field level, where the standard approach fails. Finally, we derive an analytic expression for the size of the Cooper pairs and evaluate the influence of the effective range on this physically important length scale.

4.4.1 Free energy

By choosing Fermi units, we fix the particle number, and hence we effectively perform a Legendre transformation from the grand-canonical to the canonical ensemble. Thus, the appropriate thermodynamic potential is the Helmholtz free energy $\mathcal{F} = \Omega + \mu N$ using the total particle number $N = n_0 V$, with n_0 as the SP particle number and V as the sample volume. At $T = 0$ this gives rise to the ground-state energy $\mathcal{E} = \mathcal{F}|_{T=0}$. With the Legendre transformation, the non-analytic term in the grand-canonical potential is eliminated by using the equation of state $\mu = \mu(n)$. This cancels all terms in Ω, which are not particle conserving, resulting in the ground-state energy per particle in units of ε_F

$$\begin{aligned}\frac{\mathcal{E}}{N\varepsilon_\mathrm{F}} = &-\frac{3\pi}{8}\left[\frac{|\Delta_{\mathrm{B},0}|^2}{\varepsilon_\mathrm{F}^2 k_\mathrm{F} a_\mathrm{s}} - \frac{\Delta_{\mathrm{H},0}^2}{\varepsilon_\mathrm{F}^2}\left(\frac{1}{k_\mathrm{F} a_\mathrm{s}} - \frac{8}{\pi^2}\frac{1}{k_\mathrm{F} r_\mathrm{e}}\right)\right] \\ &+ \frac{\mu(n) - \Delta_{\mathrm{H},0}}{\varepsilon_\mathrm{F}} - \frac{3}{4\varepsilon_\mathrm{F}^{5/2}}\int_0^\infty \mathrm{d}\epsilon\sqrt{\epsilon}\left[E(\epsilon) - \xi(\epsilon)\right],\end{aligned} \tag{4.52}$$

with $\xi(\epsilon) = \epsilon - \mu(n) + \Delta_{\mathrm{H},0}$ and $E(\epsilon) = \sqrt{\xi(\epsilon)^2 + |\Delta_{\mathrm{B},0}|^2}$.

We evaluate the above integrals numerically and present the results in Fig. 4.9. To resolve all the fine details, we split the figure into two parts. Panels (a)-(c) focus on the weakly interacting regime, whereas panels (d)-(f) deal with stronger interactions. Hence, we correspondingly split up the discussion in a similar way. In Fig. 4.9 (a) the ground-state energy per particle in units of ε_F is illustrated as a density map in the $k_\mathrm{F} r_\mathrm{e}$ - $1/k_\mathrm{F} a_\mathrm{s}$ plane. The dashed black line shows the HSF-SSF transition. For fixed $1/k_\mathrm{F} a_\mathrm{s}$ when increasing the effective range, the energy decreases due to a larger Hartree self-energy in the HSF phase. In the SSF phase, this shift is not present and, thus, we can not identify such a clear connection. This is a subleading effect, as its size, as indicated by the colour bar, is small compared to the total free energy. In panel (b), we show slices of constant effective range illustrated versus $1/k_\mathrm{F} a_\mathrm{s}$ from -4 to 0. As already visible from panel (a) in the HSF region, the ground-state energy per particle is reduced due to the emergence of a Hartree

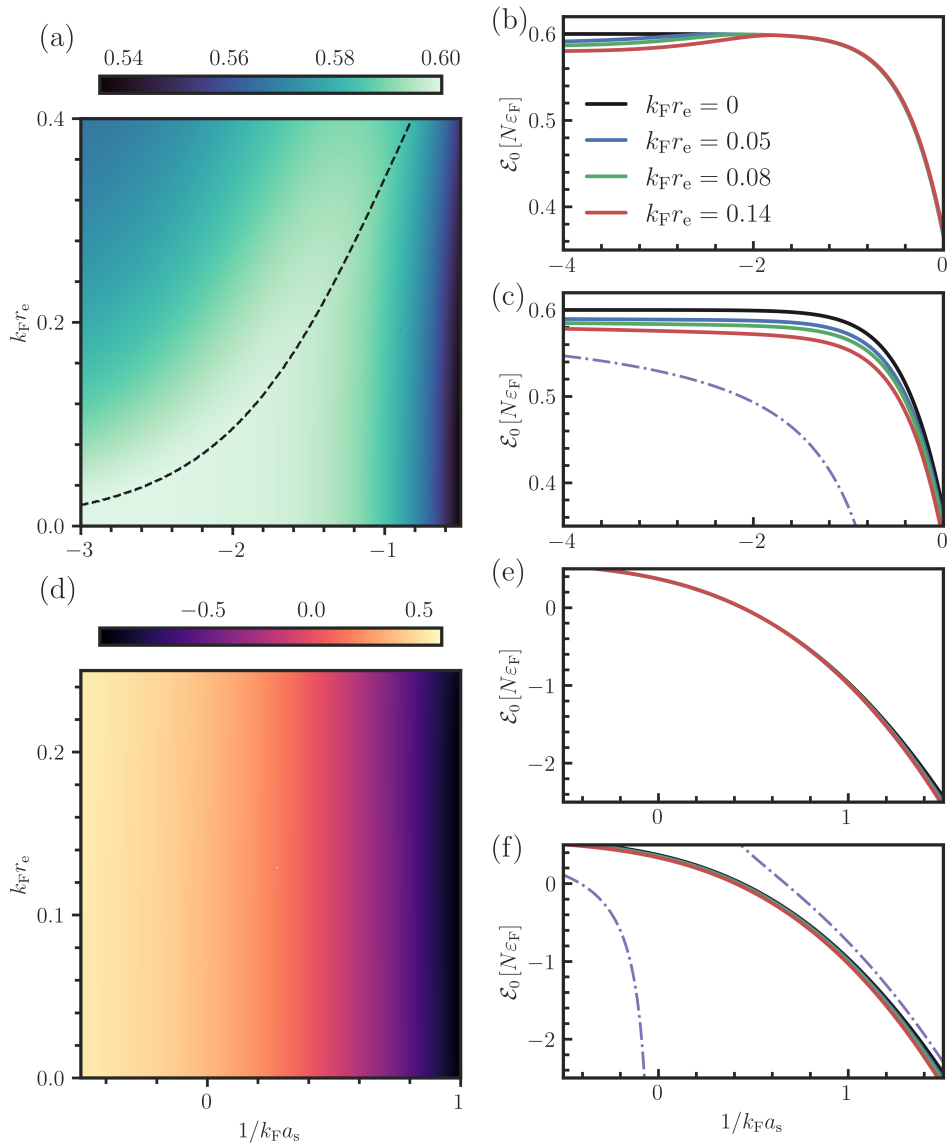


Figure 4.9: Free energy of the WHFB system. Panel (a) and (d) represent a density plot of free energy per particle in units of the Fermi energy in the $k_F r_e$ - $1/k_F a_s$ plane. In panel (a) we show weak, in panel (d) strong interactions. In panel (a) dashed black line shows HSF-SSF transition line. Panels (b) and (e) show free energy in WHFB approach for various effective ranges versus $1/k_F a_s$, with weak and strong interactions depicted in panels (b) and (e), respectively. For the same convention of interaction strengths, panels (c) and (f) depict equally weighted free energy per particle versus $1/k_F a_s$ for the same effective range parameters. Dash-dotted magenta line corresponds to the naive regularisation scheme without effective range, leading to a singularity of free energy at $1/k_F a_s = 0$.

self-energy. This reduction is stronger for larger $k_F r_e$ and vanishes when $k_F r_e = 0$, see solid black line. We also recognise that, as soon as we approach the HSF-SSF boundary with $\Delta_{H,0} = 0$, the ground state energy per particle has a local maximum with a kink. For larger interactions, namely in the SSF phase, the Hartree self-energy vanishes, and no corresponding effect on the free energy is visible. A tiny increase of the ground-state energy due to the direct influence of the effective range on $\Delta_{B,0}$ and μ happens in the SSF phase. However, it is not resolvable in the scales illustrated in Fig. 4.9 (b). Panel (c)

illustrates the ground-state energy per particle against $1/k_\mathrm{F}a_\mathrm{s}$ for the same effective range parameters and the unweighted standard approach. There, the ever-present Hartree self-energy reduces the ground-state energy over the whole range of the illustrated scattering parameters. This reduction of the energy overestimates the effects of both channels. A smaller overall energy does not necessarily mean a closer match to the true ground state, as our approach is variational in the Lagrangian, not in the states. We further show the naive result, used in Refs. [28, 154, 296], which neglects the effective range, as dash-dotted magenta line. It shows the unphysical divergence at $1/k_\mathrm{F}a_\mathrm{s} = 0$.

For $1/k_\mathrm{F}a_\mathrm{s} \ll -1$ we take into account $\mu = \varepsilon_\mathrm{F} + \Delta_{\mathrm{H},0}$ and evaluate the integral in Eq. (4.52) in analogy to the integrals solved in Appendix 4.B.1 to obtain

$$\frac{\mathcal{E}}{N\varepsilon_\mathrm{F}} = \frac{3}{5} - \frac{3\pi}{8}\left(\frac{1}{|k_\mathrm{F}a_\mathrm{s}|} + \frac{8}{\pi^2}\frac{1}{k_\mathrm{F}r_\mathrm{e}}\right)\frac{\Delta_{\mathrm{H},0}^2}{\varepsilon_\mathrm{F}^2} - \frac{3}{8}\left(1 - \frac{\pi}{2}k_\mathrm{F}r_\mathrm{e,B}\right)\frac{|\Delta_{\mathrm{B},0}|^2}{\varepsilon_\mathrm{F}^2}. \tag{4.53}$$

The first term is the ground-state energy of the free Fermi gas, whereas the second term shows the energy gain due to the appearance of a Hartree self-energy for weak interactions. The last term originates from the energy gain due to the formation of Cooper pairs. In the following, we again distinguish between HSF and SSF region, starting with the HSF asymptotes. The two length scale hierarchies of a_s and r_e must be considered. For extremely weak interactions, i.e. $k_\mathrm{F}r_\mathrm{e} \ll |k_\mathrm{F}a_\mathrm{s}| \ll 1$ we obtain

$$\begin{aligned}\frac{\mathcal{E}}{N\varepsilon_\mathrm{F}} = \frac{3}{5} - \frac{\pi}{12}k_\mathrm{F}r_\mathrm{e}\left[1 - \frac{\pi^2}{8}\frac{k_\mathrm{F}r_\mathrm{e}}{|k_\mathrm{F}a_\mathrm{s}|} + \mathcal{O}\left(\frac{k_\mathrm{F}r_\mathrm{e}}{|k_\mathrm{F}a_\mathrm{s}|}\right)^2\right] + \mathcal{O}\left(k_\mathrm{F}r_\mathrm{e}\right)^2 \\ - \frac{24}{e^4}\left[1 - \frac{12}{e^2}e^{-\frac{\pi}{2|k_\mathrm{F}a_\mathrm{s}|}}\right]^3 e^{-\frac{\pi}{|k_\mathrm{F}a_\mathrm{s}|}}.\end{aligned} \tag{4.54}$$

For stronger interactions, i.e. $|k_\mathrm{F}a_\mathrm{s}| \ll k_\mathrm{F}r_\mathrm{e} \ll 1$, but still in the HSF region we get

$$\begin{aligned}\frac{\mathcal{E}}{N\varepsilon_\mathrm{F}} = \frac{3}{5} - \frac{2}{3\pi}|k_\mathrm{F}a_\mathrm{s}|\left[1 - \frac{6}{\pi}\frac{|k_\mathrm{F}a_\mathrm{s}|}{k_\mathrm{F}r_\mathrm{e}} + \mathcal{O}\left(\frac{|k_\mathrm{F}a_\mathrm{s}|}{k_\mathrm{F}r_\mathrm{e}}\right)^2\right] + \mathcal{O}\left(|k_\mathrm{F}a_\mathrm{s}|\right)^2 \\ - \frac{24}{e^4}\left[1 - \frac{12}{e^2}e^{-\frac{\pi}{2|k_\mathrm{F}a_\mathrm{s}|}}\right]^3 e^{-\frac{\pi}{|k_\mathrm{F}a_\mathrm{s}|}}.\end{aligned} \tag{4.55}$$

In both cases, the energy gain due to the formation of Cooper pairs does not depend on $k_\mathrm{F}r_\mathrm{e}$, while the Hartree shift of the energy is strongly affected by the hierarchy of the length scales. In the SSF region only one asymptotic limit exists, that is $k_\mathrm{F}r_\mathrm{e} \ll |k_\mathrm{F}a_\mathrm{s}| \ll 1$, where the ground-state energy reads

$$\frac{\mathcal{E}}{N\varepsilon_\mathrm{F}} = \frac{3}{5} - \frac{24}{e^4}\left(1 - \frac{\pi}{2}k_\mathrm{F}r_\mathrm{e}\right)e^{-\frac{\pi}{2}k_\mathrm{F}r_\mathrm{e}}e^{-\frac{\pi}{|k_\mathrm{F}a_\mathrm{s}|}}. \tag{4.56}$$

Here, only an energy gain through the formation of pairs occurs.

At unitarity $1/k_\mathrm{F}a_\mathrm{s} = 0$ and for stronger interactions, the ground-state energy per particle is illustrated in units of the Fermi energy as a density map in Fig. 4.9 panel (d) in the $k_\mathrm{F}r_\mathrm{e}$ - $1/k_\mathrm{F}a_\mathrm{s}$ plane. We use a different colour scheme compared to panel (a) to avoid confusion. For strong interactions, the effective range plays a minimal role. This is visible by the colour gradient in panel (d), which reveals changes in x-direction but little changes in y-direction. We further illustrate this by discussing specific curves of the ground-state energy per particle versus $1/k_\mathrm{F}a_\mathrm{s}$ for various effective range parameters in panel (e). The colours chosen are the same as those indicated in panel (b). Here, the ground-state energy

decreases with increasing interaction strength. Finite effective-range parameters further decrease the ground-state energy for strong interactions when the chemical potential becomes negative. The same overall effect is seen in panel (f), in a comparison with the unweighted approach ground-state energy per particle. There, we recognise the full singularity of the naive approach, rendering this method completely unphysical beyond weak interactions. When comparing the same effective range curves from panels (e) and (f), we conclude that the Hartree shift would play only a minor role in the ground-state energy, even if it existed, due to its small value in the unweighted approach. The main influence on the ground-state energy for strong interactions stems from the formation of Cooper pairs.

Having discussed the free energy in the ground state as a starting point, we now turn to the isothermal compressibility, which is a thermal response function of particular interest.

4.4.2 Isothermal compressibility

One benchmark property to investigate is the isothermal compressibility κ_T, defined by

$$\kappa_\mathrm{T} = -\frac{1}{V}\left(\frac{\partial V}{\partial p}\right)_{T,N}. \tag{4.57}$$

It constitutes a measure of how a system reacts when pressure is applied, keeping temperature and particle number constant. We use some thermodynamic properties [344] in order to obtain the isothermal compressibility as

$$\kappa_\mathrm{T} = \frac{V}{N^2}\left(\frac{\partial N}{\partial \mu}\right)_{T,V}, \tag{4.58}$$

with the equation of state being $N = -(\partial\Omega/\partial\mu)_{T,V}$. From now on, we will suppress temperature T and volume V indices in thermodynamic derivatives. To calculate the compressibility, we have to take all the partial derivatives into account. As such, we have to consider $\Delta_{\mathrm{H},0} = \Delta_{\mathrm{H},0}(\mu)$ and $\Delta_{\mathrm{B},0} = \Delta_{\mathrm{B},0}(\mu)$. To this end, we formally write $\Omega_0 = \Omega_0(\mu, \Delta_{\mathrm{B},0}, \Delta_{\mathrm{H},0})$ exploiting the $\mathrm{U}(1)$-symmetry of the superfluid order parameter. Dealing with all the partial derivatives, we obtain

$$\begin{aligned}\kappa_\mathrm{T} =& \frac{V}{N^2}\left(\frac{\partial N(\mu,\Delta_{\mathrm{H},0},\Delta_{\mathrm{B},0})}{\partial\mu}\right)_{\Delta_{\mathrm{H},0},\Delta_{\mathrm{B},0}} \\ &+ \frac{V}{N^2}\left(\frac{\partial N(\mu,\Delta_{\mathrm{H},0},\Delta_{\mathrm{B},0})}{\partial\Delta_{\mathrm{H},0}}\right)_{\mu,\Delta_{\mathrm{B},0}}\left(\frac{\Delta_{\mathrm{H},0}(\mu)}{\partial\mu}\right)_{\Delta_{\mathrm{B},0}} \\ &+ \frac{V}{N^2}\left(\frac{\partial N(\mu,\Delta_{\mathrm{H},0},\Delta_{\mathrm{B},0})}{\partial\Delta_{\mathrm{B},0}}\right)_{\mu,\Delta_{\mathrm{H},0}}\left(\frac{\Delta_{\mathrm{B},0}(\mu)}{\partial\mu}\right)_{\Delta_{\mathrm{H},0}}.\end{aligned} \tag{4.59}$$

The first line is the simple partial derivative keeping the self-consistent auxiliary fields constant. However, their response to a change in the chemical potential is vital in order to obtain the compressibility, as their behaviour dictates how the Cooper pairs and the density fields react to an applied pressure. We formally write the equation of state as

$$N = -\frac{1}{\beta}\sum_k \mathrm{tr}\left\{\boldsymbol{G}_\mathrm{SP}(k)\boldsymbol{\gamma}_z\right\}, \tag{4.60}$$

with $\boldsymbol{G}_\mathrm{SP}(k)$ being the SP Green's function from Eq. (3.56a) and $\boldsymbol{\gamma}_{x,z} = \boldsymbol{\sigma}_{x,z}$ as Pauli matrix. To calculate the derivative of the equation of state, we use $\mathbf{1} = \boldsymbol{G}_\mathrm{SP}^{-1}\boldsymbol{G}_\mathrm{SP}$ to find

$$\frac{\partial \boldsymbol{G}_\mathrm{SP}(k)}{\partial\zeta} = -\boldsymbol{G}_\mathrm{SP}(k)\frac{\partial \boldsymbol{G}_\mathrm{SP}^{-1}(k)}{\partial\zeta}\boldsymbol{G}_\mathrm{SP}(k), \tag{4.61}$$

for an arbitrary energy variable $\zeta = \mu, \Delta_{\mathrm{H},0}, \Delta_{\mathrm{B},0}$. Using the inverse SP Green's function from Eq. (3.49), we obtain the following three derivatives of the equation of state

$$\left(\frac{\partial N(\mu,\Delta_{\mathrm{H},0},\Delta_{\mathrm{B},0})}{\partial\mu}\right)_{\Delta_{\mathrm{H},0},\Delta_{\mathrm{B},0}} = -\frac{1}{\beta}\sum_k \mathrm{tr}\left\{\boldsymbol{G}_{\mathrm{SP}}(k)\boldsymbol{\gamma}_z\boldsymbol{G}_{\mathrm{SP}}(k)\boldsymbol{\gamma}_z\right\}, \tag{4.62a}$$

$$\left(\frac{\partial N(\mu,\Delta_{\mathrm{H},0},\Delta_{\mathrm{B},0})}{\partial\Delta_{\mathrm{H},0}}\right)_{\mu,\Delta_{\mathrm{B},0}} = \frac{1}{\beta}\sum_k \mathrm{tr}\left\{\boldsymbol{G}_{\mathrm{SP}}(k)\boldsymbol{\gamma}_z\boldsymbol{G}_{\mathrm{SP}}(k)\boldsymbol{\gamma}_z\right\}, \tag{4.62b}$$

$$\left(\frac{\partial N(\mu,\Delta_{\mathrm{H},0},\Delta_{\mathrm{B},0})}{\partial\Delta_{\mathrm{B},0}}\right)_{\mu,\Delta_{\mathrm{H},0}} = \frac{1}{\beta}\sum_k \mathrm{tr}\left\{\boldsymbol{G}_{\mathrm{SP}}(k)\boldsymbol{\gamma}_z\boldsymbol{G}_{\mathrm{SP}}(k)\boldsymbol{\gamma}_x\right\}. \tag{4.62c}$$

Here we recognize the loop functions, defined in Eq. (2.53), and restated here

$$V\Lambda_{ab}(q) = \frac{1}{\beta}\sum_k \mathrm{tr}\left\{\boldsymbol{G}_{\mathrm{SP}}(k)\boldsymbol{\gamma}_a\boldsymbol{G}_{\mathrm{SP}}(k+q)\boldsymbol{\gamma}_b\right\}, \tag{4.63}$$

resulting in

$$\left(\frac{\partial N(\mu,\Delta_{\mathrm{H},0},\Delta_{\mathrm{B},0})}{\partial\mu}\right)_{\Delta_{\mathrm{H},0},\Delta_{\mathrm{B},0}} = -V\Lambda_{zz}(q=0), \tag{4.64a}$$

$$\left(\frac{\partial N(\mu,\Delta_{\mathrm{H},0},\Delta_{\mathrm{B},0})}{\partial\Delta_{\mathrm{H},0}}\right)_{\mu,\Delta_{\mathrm{B},0}} = V\Lambda_{zz}(q=0), \tag{4.64b}$$

$$\left(\frac{\partial N(\mu,\Delta_{\mathrm{H},0},\Delta_{\mathrm{B},0})}{\partial\Delta_{\mathrm{B},0}}\right)_{\mu,\Delta_{\mathrm{H},0}} = V\Lambda_{zx}(q=0). \tag{4.64c}$$

Thus, the derivatives of the equation of state are directly related to the zero momentum ($\boldsymbol{q} = \boldsymbol{0}$) and zero frequency ($iq_\ell = 0$) Fermi loop functions. It remains to evaluate the partial derivative of the SP conditions with respect to μ. Since the grand-canonical potential is at a SP with respect to the fields $\Delta_{\mathrm{H/B},0}$ we find that

$$0 = \frac{\mathrm{d}}{\mathrm{d}\mu}\left(\frac{\partial\Omega_0(\mu,\Delta_{\mathrm{H},0}(\mu),\Delta_{\mathrm{B},0}(\mu))}{\partial\Delta_{\mathrm{J},0}(\mu)}\right). \tag{4.65}$$

This is straightforwardly rearranged to

$$\left(\frac{\partial\Delta_{\mathrm{J},0}(\mu)}{\partial\mu}\right)_{\Delta_{\overline{\mathrm{J}},0}} = \left(\frac{\partial N(\mu,\Delta_{\mathrm{H},0},\Delta_{\mathrm{B},0})}{\partial\Delta_{\mathrm{J},0}}\right)_{\Delta_{\overline{\mathrm{J}},0}}\left[\left(\frac{\partial^2\Omega_0(\mu,\Delta_{\mathrm{H},0},\Delta_{\mathrm{B},0})}{\partial\Delta_{\mathrm{J},0}^2}\right)_{\Delta_{\overline{\mathrm{J}},0}}\right]^{-1} \tag{4.66}$$

with the convention of $\overline{\mathrm{J}}$ being the other field for a chosen $\mathrm{J} \in \{\mathrm{H},\mathrm{B}\}$. Expressed in Fermi loop functions, the two partial derivatives read

$$\left(\frac{\partial\Delta_{\mathrm{H},0}(\mu)}{\partial\mu}\right)_{T,\Delta_{\mathrm{B},0}} = \frac{\Lambda_{zz}(q=0)}{\Pi_{zz}(q=0)} \tag{4.67a}$$

$$\left(\frac{\partial\Delta_{\mathrm{B},0}(\mu)}{\partial\mu}\right)_{T,\Delta_{\mathrm{H},0}} = \frac{\Lambda_{zx}(q=0)}{\Pi_{xx}(q=0)}, \tag{4.67b}$$

with the regularised loop functions

$$\Pi_{ab}(q) = \frac{1}{g_{\mathrm{a}}}\delta_{ab}\left(\delta_{ax}+\delta_{az}\right) + \Lambda_{ab}(q). \tag{4.68}$$

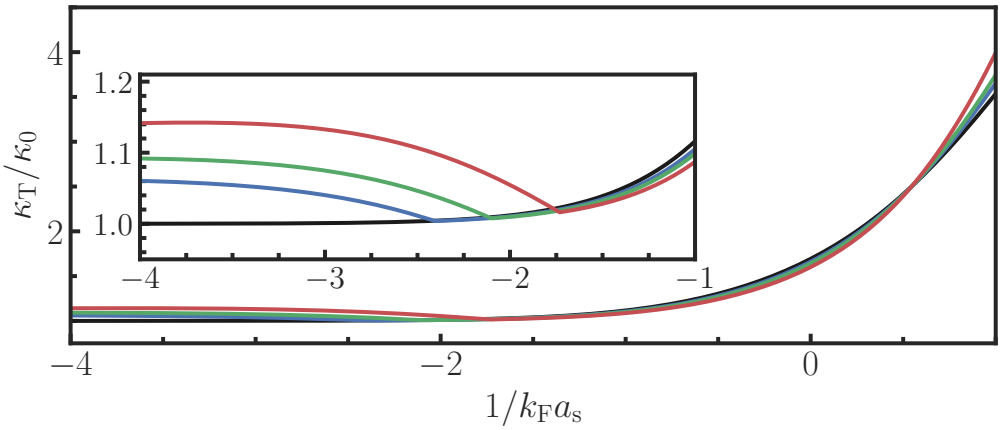


Figure 4.10: Isothermal compressibility in units of κ_0 of WHFB ground state. We show κ_T for a selected set of effective range parameters versus $1/k_F a_s$.

Here, g_a represents the partitioned interaction g_H for $a = z$ or g_B for $a = x$. Due to the offset term in the grand-canonical potential, the second derivatives with respect to the order parameters always lead to the regularised loop functions, while as soon as a derivative with respect to μ is involved, only the standard loop functions Λ show up. Using this, the compressibility (4.59) reads

$$n^2\kappa_T = -\Lambda_{zz}(q=0) + \frac{\Lambda_{zz}^2(q=0)}{\Pi_{zz}(q=0)} + \frac{\Lambda_{xz}^2(q=0)}{\Pi_{xx}(q=0)}. \tag{4.69}$$

The second term is the additional contribution arising from the Hartree self-energy in the HSF phase. Evaluating the loop functions using the SP Green's function (3.56a) leads to

$$\Lambda_{zz}(q=0) = -\frac{1}{V}\sum_{\boldsymbol{k}} \frac{|\Delta_{B,0}|^2}{E_{\boldsymbol{k}}^3}, \tag{4.70a}$$

$$\Lambda_{xz}(q=0) = -\frac{1}{V}\sum_{\boldsymbol{k}} \frac{|\Delta_{B,0}|(\xi_{\boldsymbol{k}} + \Delta_{H,0})}{E_{\boldsymbol{k}}^3}, \tag{4.70b}$$

$$\Pi_{xx}(q=0) = \frac{1}{V}\sum_{\boldsymbol{k}\leq k_{c,B}} \frac{|\Delta_{B,0}|^2}{E_{\boldsymbol{k}}^3}, \tag{4.70c}$$

$$\Pi_{zz}(q=0) = \frac{1}{g_H} - \frac{1}{V}\sum_{\boldsymbol{k}} \frac{|\Delta_{B,0}|^2}{E_{\boldsymbol{k}}^3}. \tag{4.70d}$$

In Fig. 4.10 we depict the isothermal compressibility in units of $\kappa_0 = 9\pi^2 m/k_F^5$, which is the isothermal compressibility of an ideal Fermi. We use the established colour scheme for various values of the effective range parameter with the solid black reference line for $k_F r_e = 0$. In the inset, we visualise an enlarged version of weak interactions. We observe that in the HSF region the Hartree shift causes the compressibility to be enlarged, scaling with $k_F r_e$, as the attractive interactions give a positive contribution to the compressibility via the Hartree self-energy. This decreases as the interaction strength increases until the HSF-SSF boundary is eventually reached. There, we find a non-differentiable point in the compressibility as the Hartree term vanishes. In the SSF region for positive chemical potentials, the effective range causes the system to be more degenerate as superfluid order is slightly reduced. This manifests as reduced compressibility, since the pairing is weaker than in the standard zero-range theory. Once the chemical potential switches sign, i.e. the

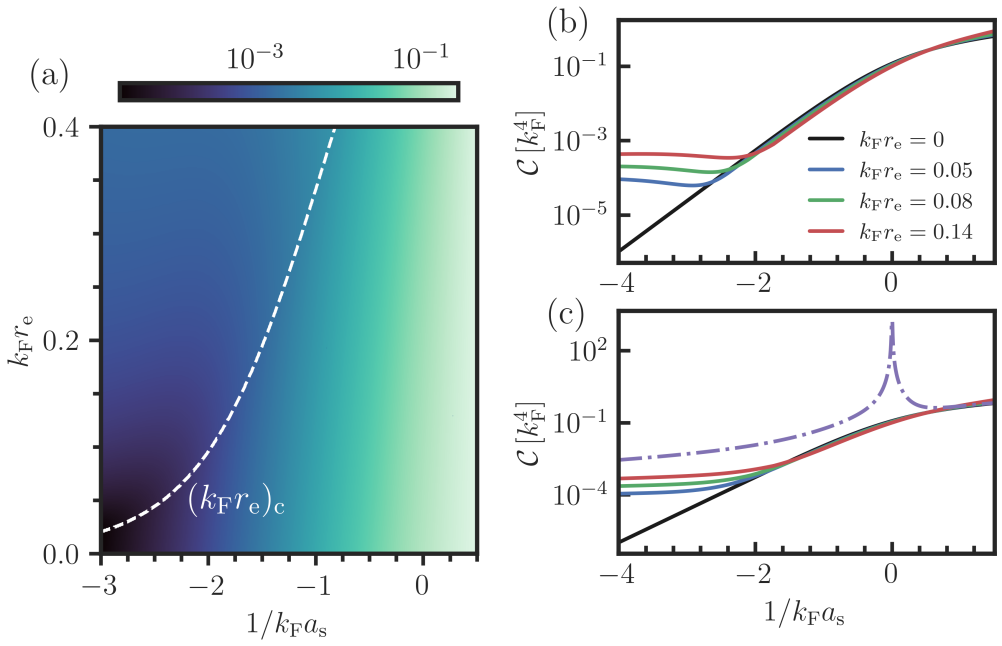


Figure 4.11: Tan contact of WHFB ground state. Panel (a) shows the contact as a density plot with a logarithmically scaled colour bar in the $k_\mathrm{F} r_\mathrm{e}$ - $1/k_\mathrm{F} a_\mathrm{s}$ plane. Dashed white line indicates the HSF-SSF transition. Panel (b) depicts WHFB contact for a selected set of effective range parameters versus $1/k_\mathrm{F} a_\mathrm{s}$ with a logarithmic y-axis. Panel (c) shows the contact obtained from an unweighted theory versus $1/k_\mathrm{F} a_\mathrm{s}$. The dash-dotted magenta line illustrates here the naive regularisation-free approach.

Fermi surface dissolves, the gas behaves more bosonic and the effective range, as discussed in Fig. 4.5 (b), enhances pairing. Therefore, in the BEC region, the presence of a finite effective range has to enlarge the compressibility quite substantially.

After discussing the compressibility, we will focus on another important quality that quantifies any cold atomic gas system, given by Tan's contact.

4.4.3 Tan's contact

One important aspect of quantum gases in any dimension is the universal contact relation, established by S. Tan [345–347]. It yields a fundamental connection of most thermodynamic properties, provided the gas is sufficiently dilute, meaning $k_\mathrm{F} r_\mathrm{e} \ll 1$. Tan's contact is originally defined as

$$\mathcal{C} = \frac{4\pi m a_\mathrm{s}^2}{V} \left(\frac{\partial F}{\partial a_\mathrm{s}} \right)_{T,V,\mu}, \tag{4.71}$$

with F being the Helmholtz free energy. In a sense, this formally means that the contact $\mathcal{C}$ is the thermodynamic conjugate variable to the inverse scattering length $1/a_\mathrm{s}$. As the partial derivatives $\partial F/\partial \Delta_{\mathrm{J},0}$ vanish due to the SP condition, we obtain the contact via the ground-state energy (4.52), yielding

$$\mathcal{C} = \frac{1}{4\varepsilon_\mathrm{F}^2} k_\mathrm{F}^4 \left(\Delta_{\mathrm{H},0}^2 + |\Delta_{\mathrm{B},0}|^2 \right). \tag{4.72}$$

This extends to the standard BCS mean-field result $\mathcal{C}_\mathrm{BCS} = k_\mathrm{F}^4 |\Delta_{\mathrm{B},0}|^2/(4\varepsilon_\mathrm{F}^2)$. Because for weak interactions we have $\Delta_{\mathrm{H},0} \gg |\Delta_{\mathrm{B},0}|$, our improvements are of qualitative measure,

rather than a small quantitative change of the BCS contact. In the HSF region and for extremely weak interactions, i.e. $|k_\mathrm{F}a_\mathrm{s}| \ll k_\mathrm{F}r_\mathrm{e} \ll 1$, we obtain

$$\begin{aligned}\mathcal{C} = \frac{k_\mathrm{F}^4}{4}\Bigg[&\frac{16}{9\pi^2}|k_\mathrm{F}a_\mathrm{s}|^2\left(1-\frac{16}{\pi^2}\frac{|k_\mathrm{F}a_\mathrm{s}|}{k_\mathrm{F}r_\mathrm{e}}+\mathcal{O}\left(\frac{|k_\mathrm{F}a_\mathrm{s}|}{k_\mathrm{F}r_\mathrm{e}}\right)^2\right)+\frac{128}{e^4}e^{-\frac{\pi}{|k_\mathrm{F}a_\mathrm{s}|}}\\ &-\frac{64}{3e^2\pi}|k_\mathrm{F}a_\mathrm{s}|e^{-\frac{\pi}{2|k_\mathrm{F}a_\mathrm{s}|}}\left(1-\frac{8}{\pi^2}\frac{|k_\mathrm{F}a_\mathrm{s}|}{k_\mathrm{F}r_\mathrm{e}}+\mathcal{O}\left(\frac{|k_\mathrm{F}a_\mathrm{s}|}{k_\mathrm{F}r_\mathrm{e}}\right)^2\right)\left(1-\frac{12}{e^2}e^{-\frac{\pi}{2|k_\mathrm{F}a_\mathrm{s}|}}\right)\Bigg].\end{aligned} \tag{4.73}$$

When increasing the interaction strength for constant effective range, we reach $k_\mathrm{F}r_\mathrm{e} \ll |k_\mathrm{F}a_\mathrm{s}| \ll 1$, with

$$\begin{aligned}\mathcal{C} = \frac{k_\mathrm{F}^4}{4}\Bigg[&\frac{\pi^2}{36}(k_\mathrm{F}r_\mathrm{e})^2\left(1-\frac{\pi^2}{4}\frac{k_\mathrm{F}r_\mathrm{e}}{|k_\mathrm{F}a_\mathrm{s}|}+\mathcal{O}\left(\frac{k_\mathrm{F}r_\mathrm{e}}{|k_\mathrm{F}a_\mathrm{s}|}\right)^2\right)+\frac{128}{e^4}e^{-\frac{\pi}{|k_\mathrm{F}a_\mathrm{s}|}}\\ &-\frac{4\pi}{3e^2}k_\mathrm{F}r_\mathrm{e}e^{-\frac{\pi}{2|k_\mathrm{F}a_\mathrm{s}|}}\left(1-\frac{\pi^2}{8}\frac{k_\mathrm{F}r_\mathrm{e}}{|k_\mathrm{F}a_\mathrm{s}|}+\mathcal{O}\left(\frac{k_\mathrm{F}r_\mathrm{e}}{|k_\mathrm{F}a_\mathrm{s}|}\right)^2\right)\left(1-\frac{12}{e^2}e^{-\frac{\pi}{2|k_\mathrm{F}a_\mathrm{s}|}}\right)\Bigg].\end{aligned} \tag{4.74}$$

In both cases, we neglected all exponentials decaying faster than $\exp(-\pi/|k_\mathrm{F}a_\mathrm{s}|)$. We see a polynomial decay of the contact, proportional to $(k_\mathrm{F}a_\mathrm{s})^2$ at weak interactions (4.73), differing from the BCS asymptote, as mentioned above, as it decays exponentially for weak interactions. This reproduced weak coupling expansions of the GPF beyond SP calculation, which can be derived by looking at the free energy of Ref. [122].

We illustrate the contact in units of k_F^4 in Fig. 4.11. Panel (a) depicts the contact as a density plot in the $k_\mathrm{F}r_\mathrm{e}$ - $1/k_\mathrm{F}a_\mathrm{s}$ plane with a logarithmic colour gradient. In the SSF region, the contact increases for increasing interaction strength, where it is insensitive to the effective range parameter. As soon as the HSF-SSF boundary is crossed, in the HSF phase the contact stagnates at an almost constant value depending on $k_\mathrm{F}r_\mathrm{e}$. We further deepen this understanding in panel (b), where the contact is plotted versus the $1/k_\mathrm{F}a_\mathrm{s}$ for constant values of $k_\mathrm{F}r_\mathrm{e}$. The black line is the reference to the zero-range theory, which shows the exponential decay of the standard BCS theory only. The unweighted approach shown in panel (c) also exhibits this stagnation of the contact due to the different asymptotic regions. For weak interactions, all the values shown are in the regime where we have $k_\mathrm{F}r_\mathrm{e} \leq |k_\mathrm{F}a_\mathrm{s}|$. Only the asymptote shown in Eq. (4.74) is reached. In contrast, when considering the regularisation-free approach (magenta dash-dotted line) from Refs. [28, 154, 296], the contact has a qualitatively different behaviour and diverges at unitarity. This again shows that the standard regularisation can not be used away from weak interactions.

We now continue with the size of the Cooper pairs as a last characterisation of the pairing.

4.4.4 Cooper pair size

The Cooper pair size is the spatial extent of the Cooper pair wavefunction [88, 348]

$$\chi(\boldsymbol{x}) = \frac{1}{V}\sum_{\boldsymbol{k}}\chi_{\boldsymbol{k}}e^{i\boldsymbol{k}\cdot\boldsymbol{x}}, \tag{4.75}$$

where

$$\chi_{\boldsymbol{k}} = \frac{\Delta_{\mathrm{B},0}}{2E_{\boldsymbol{k}}} \tag{4.76}$$

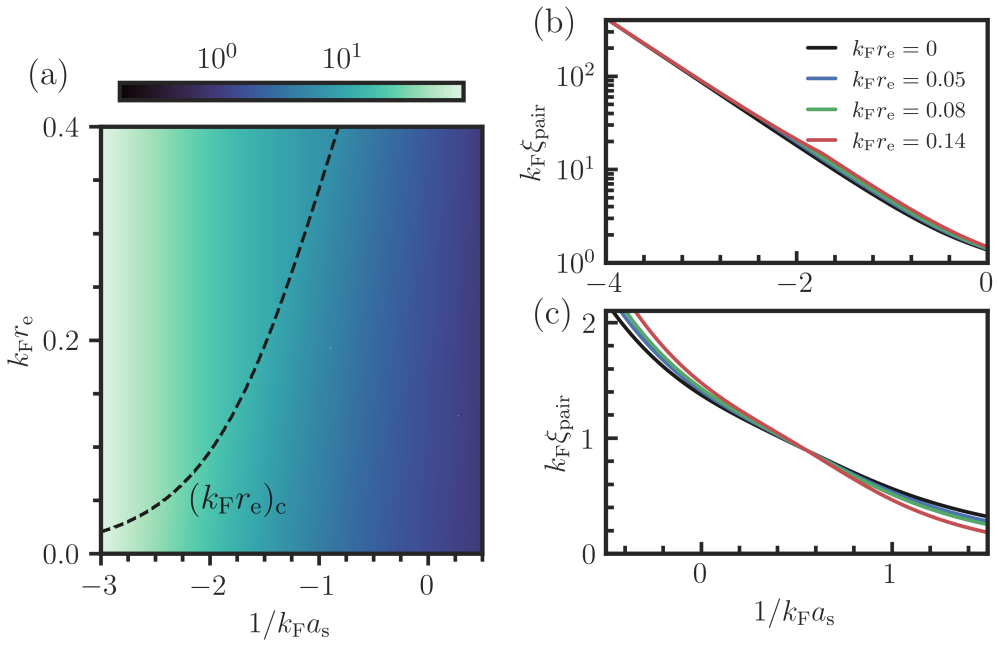


Figure 4.12: Dimensionless pair size $k_\mathrm{F}\xi_\mathrm{pair}$. Panel (a) illustrates $k_\mathrm{F}\xi_\mathrm{pair}$ in the $k_\mathrm{F}r_\mathrm{e}$ - $1/k_\mathrm{F}a_\mathrm{s}$ plane as colour gradient. The dashed black line shows critical effective range parameter of HSF-SSF transition. Panels (b) and (c) show WHFB pair size versus $1/k_\mathrm{F}a_\mathrm{s}$ for various effective range parameters. Panel (b) highlights the BCS side for weak coupling with a logarithmically scaled y-axis, whereas panel (c) focuses upon the region around unitarity towards the BEC region with a linearly scaled y-axis.

is the Cooper pair wave function in momentum space. The size of a Cooper pair is defined as the variation of this wavefunction

$$\xi_\mathrm{pair}^2 = \frac{\int_{\mathbb{R}^3} \mathrm{d}^3x\, \overline{\chi}(\boldsymbol{x})\boldsymbol{x}^2\chi(\boldsymbol{x})}{\int_{\mathbb{R}^3} \mathrm{d}^3x\, |\chi(\boldsymbol{x})|^2} = -\frac{\sum_{\boldsymbol{k}} \overline{\chi}_{\boldsymbol{k}}\nabla_{\boldsymbol{k}}^2\chi_{\boldsymbol{k}}}{\sum_{\boldsymbol{k}} |\chi_{\boldsymbol{k}}|^2}. \tag{4.77}$$

Using residue integration shown in Appendix 4.A, we obtain the first-ever analytic solution for the Cooper pair size in 3D, which is

$$(k_\mathrm{F}\xi_\mathrm{pair})^2 = \frac{\varepsilon_\mathrm{F}}{4\sqrt{2}} \frac{5|\Delta_{\mathrm{B},0}|^2 + 2(\mu - \Delta_{\mathrm{H},0})[\mu - \Delta_{\mathrm{H},0} + E_{\boldsymbol{0}}]}{|\Delta_{\mathrm{B},0}|^2 E_{\boldsymbol{0}}}, \tag{4.78}$$

with $E_{\boldsymbol{0}} = \sqrt{(\mu - \Delta_{\mathrm{H},0})^2 + |\Delta_{\mathrm{B},0}|^2}$ as the quasi-particle dispersion evaluated at zero momentum. We portray this finding in Fig. 4.12, agreeing with a direct numerical calculation. In panel (a), we show $k_\mathrm{F}\xi_\mathrm{pair}$ as a colour gradient in the plane of effective range parameter on the y- and scattering parameter on the x-axis. Note the logarithmically scaled colour bar. For weak interactions, the size of the Cooper pairs is much larger than the typical interparticle spacing d, decreasing for stronger interactions, where ξ_pair is of the order of d. Furthermore, the effective range plays a minor role for the pair size when the Cooper pairs are large at weak interactions. In panel (b), we have the WHFB pair size for selected $k_\mathrm{F}r_\mathrm{e}$ values illustrated as a function of $1/k_\mathrm{F}a_\mathrm{s}$. This shows that the pair size decreases exponentially when the interaction increases, with a small kink at the HSF-SSF transition. The effective range, as expected from panel (a), plays only a minor role. In panel (c), we show the pair size around the unitary regime and beyond for stronger interactions. Here, the

pair size starts to depend polynomially on $1/k_{\mathrm{F}}a_{\mathrm{s}}$ instead of exponentially. In this regime, we ultimately see an influence of the effective range parameter. As long as the chemical potential is positive, for $1/k_{\mathrm{F}}a_{\mathrm{s}} \leq 0.55$, an increase in the effective range increases the pair size. When the chemical potential switches sign and the Fermi surface dissolves the presence of a non-zero effective range facilitates the formation of bound states as the binding energy becomes larger, see Eq. (4.51). Thus, the pair size is reduced by an increasing $k_{\mathrm{F}}r_{\mathrm{e}}$. We do not show the standard approach here, as the pair size only depends on the effective chemical potential $\mu_{\mathrm{H}} = \mu - \Delta_{\mathrm{H},0}$, which is divergence-free.

To further investigate the influence of the WHFB approach, we determine the asymptotic behaviours of the pair size. In the weakly interacting limit, it does not depend on the hierarchy of the scales r_{e} and a_{s} as the Hartree self-energy is fully absorbed into an effective chemical potential. Hence, the HSF asymptotic expansion reads

$$k_{\mathrm{F}}\xi_{\mathrm{pair}} = \frac{e^2}{8\sqrt{2}}\left[1 + \frac{12}{e^2}e^{-\frac{\pi}{2|k_{\mathrm{F}}a_{\mathrm{s}}|}}\right]e^{\frac{\pi}{2|k_{\mathrm{F}}a_{\mathrm{s}}|}}. \tag{4.79}$$

The pair size is therefore independent of the effective range. Furthermore, Eq. (4.79) tells us that the standard BCS result is altered by an exponentially weak correction. Moreover, in the SSF region we obtain

$$k_{\mathrm{F}}\xi_{\mathrm{pair}} = \frac{e^2}{8\sqrt{2}}e^{\frac{\pi}{4}k_{\mathrm{F}}r_{\mathrm{e}}}e^{\frac{\pi}{2|k_{\mathrm{F}}a_{\mathrm{s}}|}} = \frac{e^2}{8\sqrt{2}}\left[1 + \frac{\pi}{4}k_{\mathrm{F}}r_{\mathrm{e}} + \mathcal{O}\left(k_{\mathrm{F}}r_{\mathrm{e}}\right)^2\right]e^{\frac{\pi}{2|k_{\mathrm{F}}a_{\mathrm{s}}|}}. \tag{4.80}$$

Here, the pair size is weakly altered by the effective range due to a linear perturbative correction to the standard result. When the chemical potential vanishes we use Eq. (4.46) to obtain

$$k_{\mathrm{F}}\xi_{\mathrm{pair}} = \frac{1}{2}\sqrt{\frac{5}{\sqrt{2}}}\left[\frac{\mathrm{B}\left(\frac{5}{4},\frac{1}{4}\right)}{4}\right]^{1/3} \approx 0.917 \in \mathcal{O}(1). \tag{4.81}$$

This is the crossover superfluid, where the pairs are of the order of the average distance between the particles. This region of great theoretical interest is depicted in the middle panel of Fig. 1.5. Increasing the interaction parameter for strong coupling, $1/k_{\mathrm{F}}a_{\mathrm{s}} \gg 1$ we find

$$k_{\mathrm{F}}\xi_{\mathrm{pair}} = \frac{1}{\sqrt{2}}\left[k_{\mathrm{F}}a_{\mathrm{s}} - \frac{1}{2}k_{\mathrm{F}}r_{\mathrm{e}}\right], \tag{4.82}$$

i.e. the pair size is dictated by the difference between the scattering length and half of the effective range. Note that since $k_{\mathrm{F}}a_{\mathrm{s}} \geq r_{\mathrm{e}}\pi^2/8$, see Section 4.2, the pair size is always positive.

4.5 Impact of Thermal fluctuations

After we discussed the ground state at $T = 0$, we investigate the influence of thermal fluctuations. We consider the self-consistency equations from section 4.2.3 at $T \geq 0$. To this end, we will briefly discuss the scattering theory at finite T and how the screening arises, before focussing on the $T \geq 0$ properties of the order parameters.

4.5.1 Effective range at finite temperatures

The scattering of two particles is an isolated process, only depending on their mass, spin, and relative momentum. Although the average relative momentum depends on the temperature, the scattering event of two particles is not affected by the temperature of the

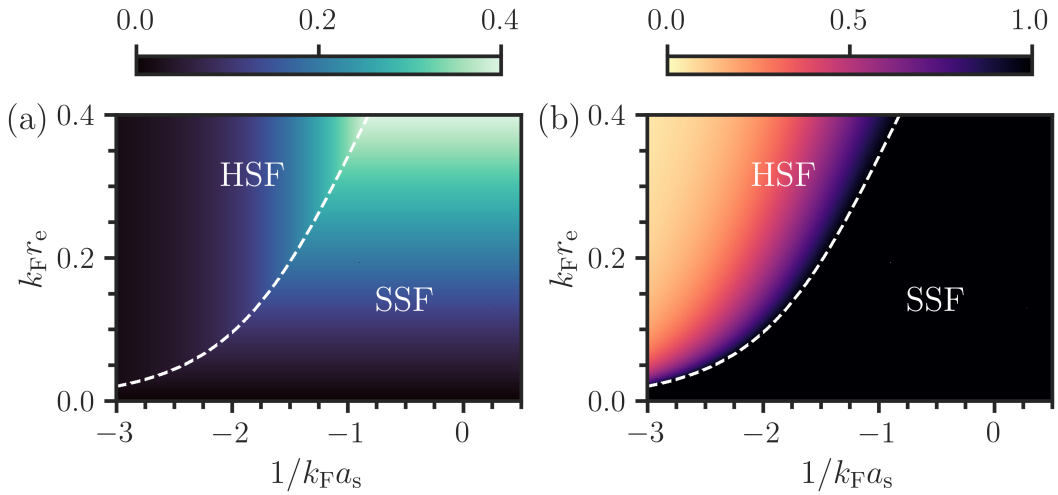


Figure 4.13: Value of pairing effective range $r_{\mathrm{e,B}}$ as density plot in plane of effective range and scattering parameter. Panel (a) depicts $k_\mathrm{F} r_{\mathrm{e,B}}$, while panel (b) shows $r_{\mathrm{e,B}}/r_\mathrm{e}$. In both panels dashed white line illustrates HSF-SSF boundary.

ensemble. Two particles by themselves do not follow the concept of temperature, meaning in dilute systems the scattering should be treated as $T = 0$ event. Thus, even though the partitioning functions h_0, b_0 depend on T, the screened pairing effective range $r_{\mathrm{e,B}}$ does not. As a consequence, also the UV cut-off is independent of T. This reduces the number of free parameters to determine, since the pair effective range is obtained at $T = 0$. We illustrate the effective range used in the calculation and determined at $T = 0$ in Fig. 4.13. In both panels, we show $r_{\mathrm{e,B}}$ as a colour plot in the $k_\mathrm{F} r_\mathrm{e}$ - $1/k_\mathrm{F} a_\mathrm{s}$ plane. We use different colour bars to avoid confusion. Panel (a) shows $r_{\mathrm{e,B}}$ range scaled with the Fermi momentum k_F. We see that $r_{\mathrm{e,B}}$ becomes small either for a small two-body effective range, or in the HSF region where we have $1/k_\mathrm{F} a_\mathrm{s} \to -\infty$. In the HSF region $r_{\mathrm{e,B}}$ is determined by the scattering parameter and is independent of r_e. In the SSF region we see that $r_{\mathrm{e,B}}$ loses its sensitivity to the scattering parameter and only depends on r_e. This is evident when looking at the colour gradient, which in the HSF region is along the $1/k_\mathrm{F} a_\mathrm{s}$-axis, while in the SSF region it is along the $k_\mathrm{F} r_\mathrm{e}$-axis. Panel (b) visualises the pair effective range $r_{\mathrm{e,B}}$ scaled by the two-body effective range r_e. We notice that this ratio is always 1 in the SSF region, supporting the statement made in the discussion of panel (a). Furthermore, in the HSF region, the effective range of the Bogoliubov channel is strictly smaller than the two-body effective range. This ratio depends on the proximity to the phase boundary.

We use the data obtained for $r_{\mathrm{e,B}}$ to determine the weights and order parameters at finite temperatures. The results are discussed in the next sections.

4.5.2 Fixed temperature

The phase diagram of the WHFB theory has three free parameters, and thus, the full phase diagram is three-dimensional. Illustrating this in its full extent is hard without losing information due to the third parameter dimension. Therefore, we restrict ourselves to two-dimensional slices of the three-dimensional parameter space, keeping one variable fixed. A prime example was already discussed in the last section, where we kept the temperature constant at $T = 0$, while varying the $k_\mathrm{F} r_\mathrm{e}$ and $1/k_\mathrm{F} a_\mathrm{s}$. In this section, we follow the same strategy in keeping the temperature fixed and focus our attention to the $k_\mathrm{F} r_\mathrm{e}$ - $1/k_\mathrm{F} a_\mathrm{s}$

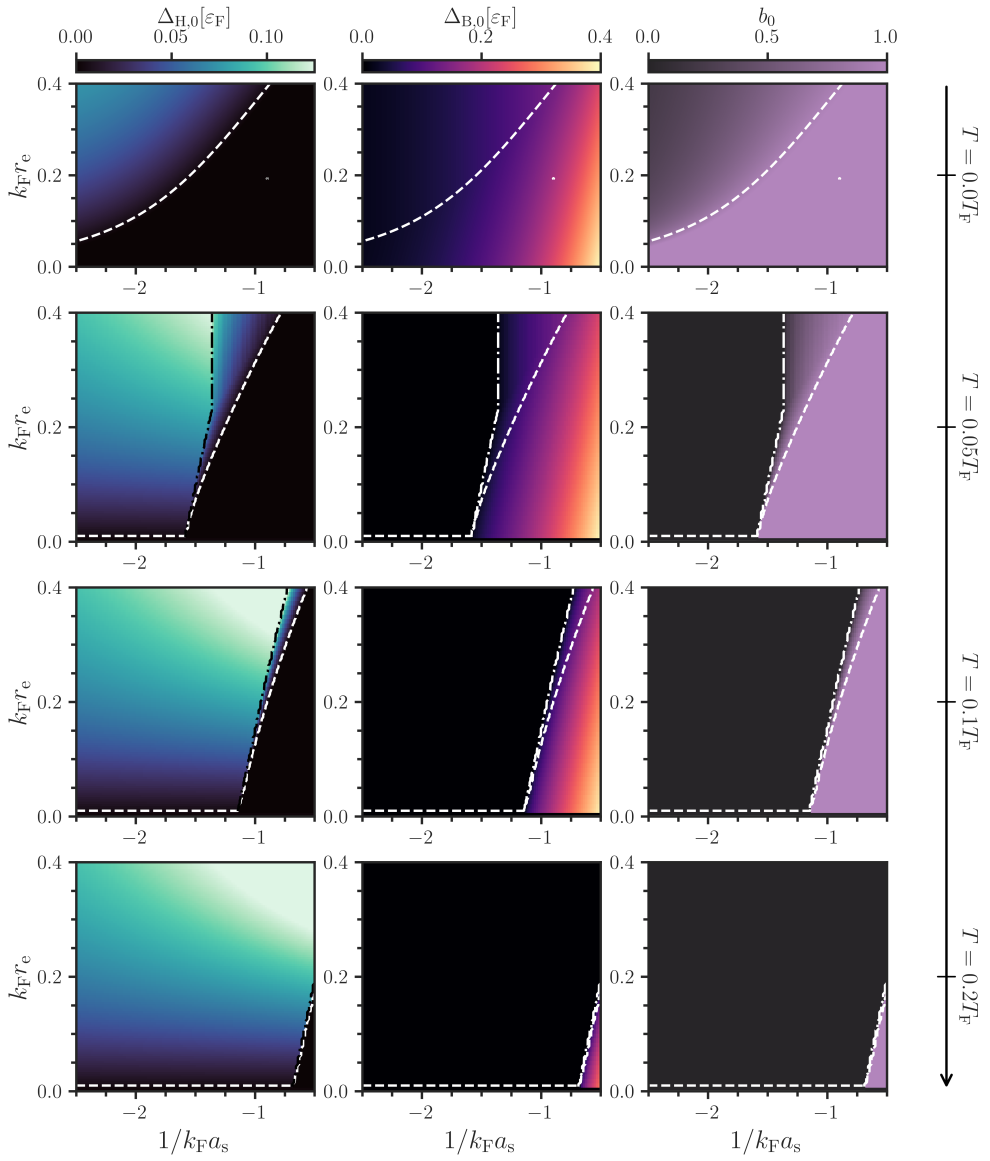


Figure 4.14: Finite-temperature evaluation of order parameters $\Delta_{\mathrm{H},0}$,$\Delta_{\mathrm{B},0}$ (first/second column) in units of Fermi energy and partitioning factor b_0 (third column) in the $k_\mathrm{F} r_\mathrm{e}$ - $1/k_\mathrm{F} a_\mathrm{s}$ plane for various temperatures T in units of Fermi temperature T_F: $T = 0T_\mathrm{F}$ (1^{st} line), $T = 0.05T_\mathrm{F}$ (2^{nd} line), $T = 0.1T_\mathrm{F}$ (3^{rd} line), $T = 0.2T_\mathrm{F}$ (4^{th} line). Dashed line shows HSF-SSF transition, dash-dotted line transition between HSF and normal fluid.

slice for various temperatures. We only consider the weakly interacting regime, as we are interested in the influence of the Hartree shift, which only appears for weak interactions in the superfluid phase. We show the results of the numerical evaluation in Fig. 4.14 as colour maps in the $k_\mathrm{F} r_\mathrm{e}$ - $1/k_\mathrm{F} a_\mathrm{s}$ plane. The columns illustrate different quantities, where the left column depicts $\Delta_{\mathrm{H},0}$, the middle column $|\Delta_{\mathrm{B},0}|$ and the right column b_0. The rows all stand for a different temperature, increasing from the top row with $T = 0$ over the second and third rows, with $T = 0.05\ T_\mathrm{F}$ and $T = 0.1\ T_\mathrm{F}$, respectively, to the lowest row with $T = 0.2\ T_\mathrm{F}$. We use different colour schemes that illustrate different quantities. The dashed line shows the HSF-SSF boundary, whereas the dash-dotted line follows the boundary between a superfluid and a normal fluid state. Considering the Hartree self-energy, we recognise that the region of $\Delta_{\mathrm{H},0} = 0$ moves towards larger scattering parameters for higher

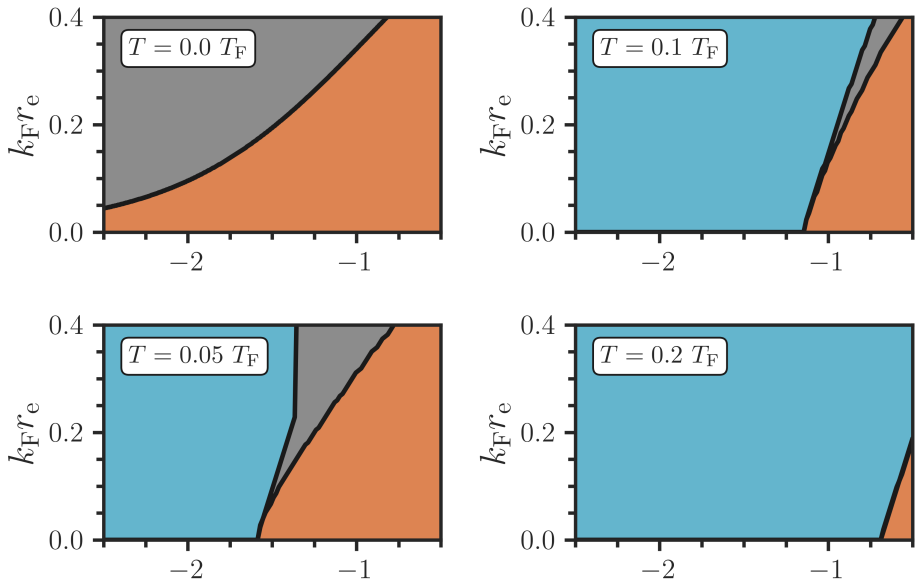


Figure 4.15: Fixed temperature phase diagram of WHFB theory in $k_\mathrm{F} r_\mathrm{e}$ - $1/k_\mathrm{F} a_\mathrm{s}$ plane for four different temperature values in units of T_F. Black lines show boundaries between the phases SSF (orange region), HSF (grey region), and normal fluid (light blue region).

temperatures. For a given temperature, the critical scattering length curves bend toward stronger interactions as the effective range parameter increases. This happens up to a point beyond which further increasing the effective range no longer influences the critical scattering parameter. This is mainly seen in the second row as the dash-dotted line. At higher temperatures, this point shifts towards larger effective ranges, beyond the validity region of our approach. In the normal fluid phase, the Hartree self-energy shift increases with higher effective ranges and scattering parameters. Looking at $\Delta_{\mathrm{B},0}$ in the second column, we see a similar behaviour. Since the superfluid order parameter only depends weakly on the effective range, the influence on the phase transition is also small. Again, the critical scattering length saturates and remains constant at a certain effective range parameter, even when increasing $k_\mathrm{F} r_\mathrm{e}$. This arises because, at this particular scattering parameter, the interaction is so strong that the Hartree channel cannot absorb all the interaction energy, leaving some energy for the pair field. For smaller effective ranges, the Hartree self-energy could host all interactions, but is too weak to completely win the competition against the Bogoliubov channel. Again, for larger temperatures, this critical scattering length is only reached for effective range parameters $k_\mathrm{F} r_\mathrm{e} \leq 0.4$, which is outside of the validity region of our theory. Lastly, we discuss the partitioning factor in the third column. There, we see exactly the same qualitative behaviour as in the previous two columns. The partitioning factor is unity in the SSF phase and zero in the normal fluid, where all the interaction energy is used up in the particle-hole sector. In the HSF region, the partitioning is $0 < b_0 < 1$.

We use this partitioning factor to obtain the phase-diagram slices for fixed temperature in Fig. 4.15. There, we show the phase diagram for the values of T/T_F used also in Fig. 4.14. Similar to the ground state for $T = 0$ we define the SSF phase by $b_0 = 1$. The HSF phase is defined by $0 < b_0 < 1$, meaning the presence of a superfluid order parameter as well as a non-vanishing Hartree self-energy. Further, we define the normal-fluid phase by a vanishing of the superfluid order parameter, and as such by $b_0 = 0$. The SSF and normal-fluid phases are therefore characterised by the presence of exactly one interaction

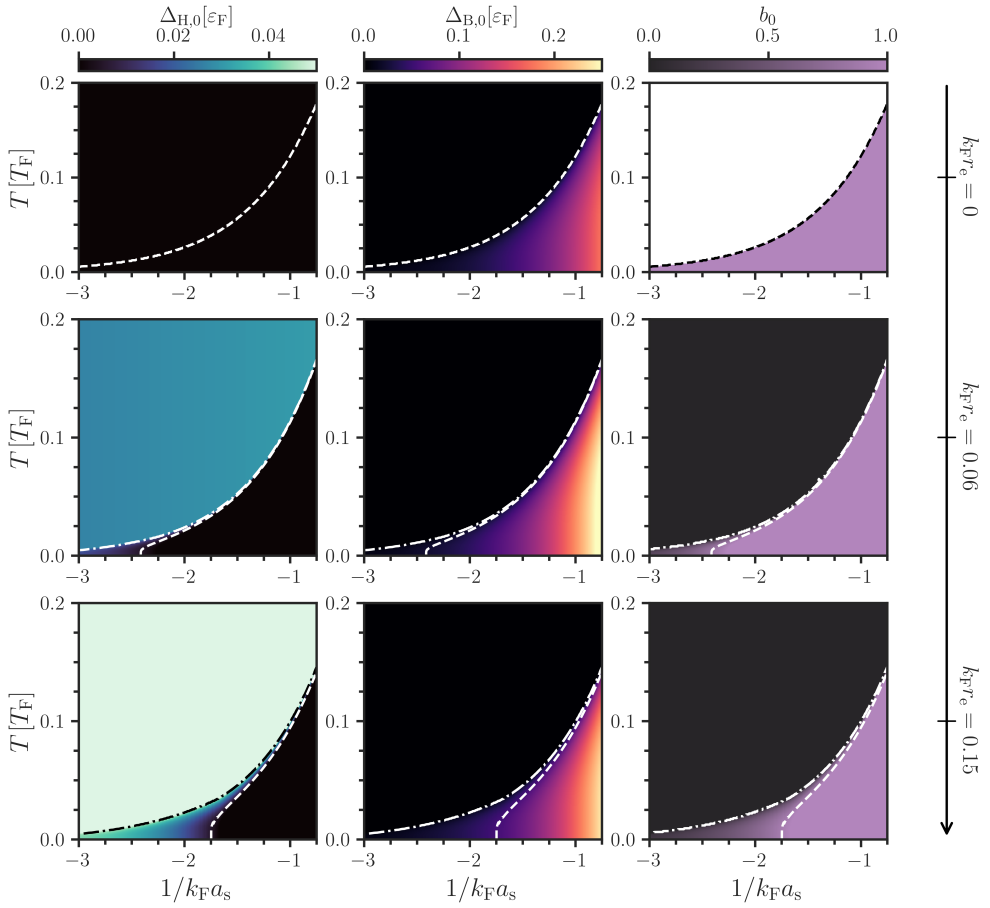


Figure 4.16: Finite-temperature results of order parameters $\Delta_{H,0}$,$\Delta_{B,0}$ (first/second column) and partitioning factor b_0 (third column) in T/T_F - $1/k_Fa_s$ plane for various k_Fr_e: $k_Fr_e = 0$ (1st line), $k_Fr_e = 0.06$ (2nd line), $k_Fr_e = 0.15$ (3rd line). Dashed line shows HSF-SSF transition, dash-dotted line transition between HSF and normal fluid.

channel, while in contrast, the HSF is a phase in which both channels are finite and no channel wins the competition.

After having discussed 2D slices of the 3D phase diagram with fixed temperature, we investigate the slices of a constant k_Fr_e.

4.5.3 Fixed effective range

The standard mean-field phase diagram, depicted for instance as the solid purple line in the iconic Fig. 1.6, is the $k_Fr_e = 0$ slice of ourWHFB theory. Thus, it is included as a special case in our theory. We generalise this in the following by looking at slices with non-zero effective ranges. We discuss two example parameters of $k_Fr_e = 0.06$ and $k_Fr_e = 0.15$. The first is the mean value of the low-density ^{6}Li and ^{40}K effective range parameters. Further, the larger value corresponds to the peak Lithium densities reached in experiments, see Table 4.1, illustrating the findings for high densities.

We depict the numerical results in Fig. 4.16. The first row corresponds to the standard $k_Fr_e = 0$ theory evaluated at many instances in the past. The middle row represents the low effective range parameter $k_Fr_e = 0.06$ and lastly the lower row visualizes $k_Fr_e = 0.14$. The left column shows the Hartree and the middle column the Bogoliubov order parame-

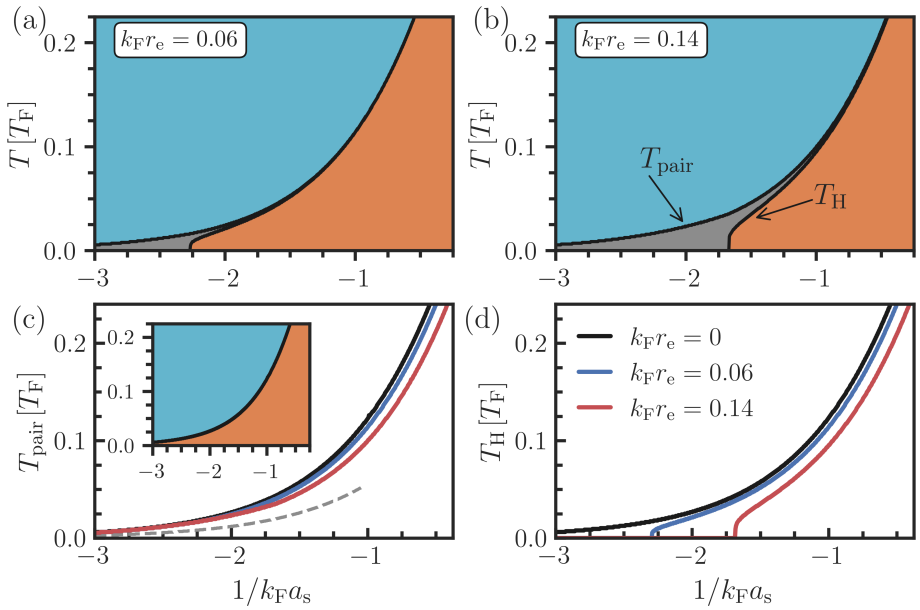


Figure 4.17: Phase diagram slice for fixed effective range in the temperature - scattering parameter plane. Panel (a) shows the $k_F r_e = 0.06$ and panel (b) the $k_F r_e = 0.14$ case. The orange region shows the SSF, the grey the HSF and the light blue the normal fluid phases. Panel (c) depicts the critical temperature between normal fluid and superfluid, with the $k_F r_e = 0$ phase diagram as an inset. Lastly panel (d) shows the critical temperature of the HSF-SSF transition.

ter, while the right column reveals the partitioning factor. The dash-dotted line stands for the normal fluid to HSF, the dashed line for the HSF-SSF transition. For illustrative purposes, we depict both lines in either white or black colour, depending on the background. The $k_F r_e = 0$ diagram shows no Hartree self-energy at all. When increasing the effective range, the self-energy grows proportional to $k_F r_e$. In the normal fluid phase, the variations of $\Delta_{H,0}$ due to a change of the scattering parameter are small. Thus, the normal fluid phase has an almost uniform Hartree self-energy. In the middle row, we identify that close to the phase boundary between normal fluid and superfluid, the superfluid order parameter depends weakly on the effective range, as this transition is always in the HSF region, as long as $k_F r_e > 0$. The biggest influence of the effective range occurs at low temperature and large scattering parameters, where the order parameter shows deviations from the zero effective range case. Lastly, the right column shows that the partitioning follows the same pattern, where b_0 vanishes above the superfluid phase-transition temperature. It becomes unity below the HSF-SSF transition line and follows a shallow gradient before. For large temperatures, the two boundary lines asymptotically approach each other, meaning a HSF phase is a complex task to prepare experimentally, as the region in parameter space exhibiting a HSF is small. As such, at experimentally achievable temperatures, the normal fluid to HSF and the SSF-HSF phase transition will occur at almost the same time. This might explain why the HSF phase has not yet been observed.

The phase diagram extracted from Fig. 4.16 is shown in Fig.4.17. In panels (a) and (b), we illustrate the phase diagram slice for $k_F r_e = 0.06$ and $k_F r_e = 0.15$, respectively. The inset of panel (c) shows, as a reference, the $k_F r_e = 0$ phase diagram. As expected from the analysis of $\Delta_{H,0}$ we see that the HSF region becomes more prominent the higher $k_F r_e$ is, extending to larger $1/k_F a_s$ and temperatures. Furthermore, for large temperatures,

the extent of the HSF phase in this parameter space shrinks until it is not visible any more. This already happens at relatively low temperatures around $T \approx 0.1\ T_\mathrm{F}$, which shows that the HSF is a weakly interacting extreme low-temperature phase of superfluid Fermi gases. In panel (b), we annotated the two transition lines. The normal fluid to HSF transition is the standard T_pair temperature where the Cooper pairs form in a mean-field theory and become superfluid. The temperature $T_\mathrm{H} < T_\mathrm{pair}$ denotes the transition temperature between SSF and HSF. At this transition, thermal fluctuations can not dissolve the pairs. Hence, this leads to an energetic preference for the Bogoliubov channel over the Hartree channel. This temperature eventually vanishes when decreasing the interaction strength for constant $k_\mathrm{F} r_\mathrm{e}$. This is equivalent to the transition line seen in the $T = 0$ phase diagram of Fig. 4.3. Panels (c) and (d) show T_pair and T_H in units of T_F, respectively. A general trend we observe is that both critical temperatures decrease as the effective range parameter increases. In panel (c), we additionally show the critical temperature obtained by GMB [94] via including particle-hole fluctuations on top of the zero effective range saddle, only including the Bogoliubov channel as the dashed grey line. Our results reduce the critical temperature towards the GMB result, but not as strongly as particle-hole fluctuations by a factor of 2.2. This shows that the WHFB theory developed here serves as a better starting point for obtaining results beyond SP and should therefore be preferred over the standard approach. In panel (d), we lastly observe that the critical temperature for the HSF-SSF transition at low temperatures approaches zero for weak interactions. However, for stronger interactions and larger temperatures, it approaches the pairing temperature.

After we discussed slices of the phase diagram, we close this chapter with some remarks on the normal fluid gas, highlighting a key difference to the standard SP theory for quantum gases.

4.5.4 Normal fluid gas

Discussing the normal fluid requires to first establish what the standard mean-field theory [66] predicts. Because only the pair channel is included, the standard approach predicts an ideal Fermi gas above T_pair. For obvious reasons, this is directly wrong. However, since the theory is not designed to describe the normal fluid gas, this is expected. Our approach can change this. In a homogeneous system, since the gas is translational invariant, the interactions only cause a shift in the chemical potential due to attractive interactions. This is the Hartree-Fock approach, known, for instance, in a more complicated setup from the Jellium model. Our approach not only describes the superfluid state by the Bogoliubov channel, but it also captures the main contribution of the self-energy in the normal fluid by the Hartree channel. The missing of a Fock contribution is not a problem, as in $\mathrm{SU}(2)$ invariant systems, like the one discussed here, the Fock contribution can be absorbed into the Hartree shift by an appropriate rotation of the spin basis. As such, the partitioning $h_0 = 1$ yields a self-energy shift of

$$\Delta_{\mathrm{H},0} = \frac{4\varepsilon_\mathrm{F}}{3\pi} k_\mathrm{F} a_\mathrm{s} \left[1 - \frac{8}{\pi^2} \frac{k_\mathrm{F} a_\mathrm{s}}{k_\mathrm{F} r_\mathrm{e}}\right] \tag{4.83}$$

for weak interactions, which is to be expected in the normal fluid, provided the correct regularisation procedure is used, including the effective range.

Appendix

4.A Calculating the Cooper pair size

In this Appendix, we calculate the analytic expression for the Cooper pair size from the main text, Eq. (4.78), using the Cooper pair wave function [88, 348] in momentum space

$$\chi_{\boldsymbol{k}} = \frac{\Delta_{\mathrm{B},0}}{2E_{\boldsymbol{k}}}, \tag{4.A.1}$$

where $E_{\boldsymbol{k}}$ is the Bogoliubov dispersion from Eq. (3.52). This gives rise to the pair size as

$$\xi_{\mathrm{pair}}^2 = -\frac{\sum_{\boldsymbol{k}} \overline{\chi}_{\boldsymbol{k}} \nabla_{\boldsymbol{k}}^2 \chi_{\boldsymbol{k}}}{\sum_{\boldsymbol{k}} |\chi_{\boldsymbol{k}}|^2}. \tag{4.A.2}$$

Furthermore, to simplify the notation we define $\mu_{\mathrm{H}} = \mu - \Delta_{\mathrm{H},0}$. We treat the numerator and denominator separately, as will be done in the next two subsections.

4.A.1 Normalization factor

The more illustrative calculation is to find the norm of the Cooper pair wave function. In the thermodynamic limit in $D = 3$ spatial dimensions, we obtain

$$N = \sum_{\boldsymbol{k}} |\chi_{\boldsymbol{k}}|^2 = \frac{V}{(2\pi)^3} \frac{|\Delta_{\mathrm{B},0}|^2}{4} \int_{\mathbb{R}^3} \frac{\mathrm{d}^3 k}{E_{\boldsymbol{k}}^2}. \tag{4.A.3}$$

We substitute $u = k/\sqrt{2m}$, use the quasiparticle dispersion (3.52), and the evenness of the integrand with spherical symmetry to obtain

$$N = \frac{V}{(2\pi)^3} \int_{-\infty}^{\infty} \mathrm{d}u \frac{|\Delta_{\mathrm{B},0}|^2 \sqrt{2\pi} m^{3/2} u^2}{(u^2 - \mu_{\mathrm{H}})^2 + |\Delta_{\mathrm{B},0}|^2}. \tag{4.A.4}$$

The denominator factorises into complex roots with equal modulus and different phases. Those are the De Moivre roots of the denominator and are given by $\gamma, -\gamma, \overline{\gamma}, -\overline{\gamma}$, where

$$\gamma = |\gamma| e^{i\theta/2}, \tag{4.A.5}$$

with the modulus

$$|\gamma| = \left(\mu_{\mathrm{H}}^2 + |\Delta_{\mathrm{B},0}|^2\right)^{1/4}. \tag{4.A.6}$$

The angle depends on the sign of μ_{H}. For illustrative purposes, we assume $\mu_{\mathrm{H}} > 0$ but keep in mind that for negative μ_{H} the calculation works analogously. Under our assumptions, the De Moivre phase is

$$\theta = \arctan\left(\frac{|\Delta_{\mathrm{B},0}|}{\mu_{\mathrm{H}}}\right). \tag{4.A.7}$$

Using these roots, we rearrange the integrand and find

$$N = \frac{V}{(2\pi)^3} \int_{-\infty}^{\infty} \mathrm{d}u \frac{|\Delta_{\mathrm{B},0}|^2 \sqrt{2\pi} m^{3/2} u^2}{(u^2 - \gamma^2)(u^2 - \overline{\gamma^2})}. \tag{4.A.8}$$

We perform an analytic continuation of the real variable $u \to z \in \mathbb{C}$ and define a closed contour in the complex plane. We set $\Gamma_R = [-R, R] \cup C_R$, where C_R represents a half-circle in the upper half plane with radius $R > |\gamma|$, always enclosing the roots. The contour, as well as the De Moivre roots, are depicted in Fig. 4.A.1. For a given function $f : \mathbb{C} \to \mathbb{C}$, being analytic on the real axis, the integral along the complex contour separates into two terms

$$\oint_{\Gamma_R} \mathrm{d}z\, f(z) = \int_{-R}^{R} \mathrm{d}z\, f(z) + \int_{C_R} \mathrm{d}z\, f(z).$$

Analysing the integrand in Eq. (4.A.8) we see that $f(z) \sim z^{-2}$ as $|z| \to \infty$. Therefore, when sending $R \to \infty$, Jordan's Lemma dictates the contour integral along the infinite half-circle C_∞ to vanish, and we are left with

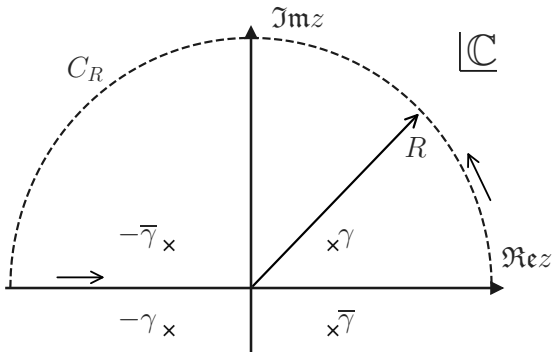


Figure 4.A.1: Illustration of the De Moivre roots and the integration contour in the complex plane.
Reprint from [P1] under the terms of the Creative Commons Attribution 4.0 International (CC BY 4.0) license.

$$\int_{-\infty}^{\infty} \mathrm{d}z\, f(z) \oint_{\Gamma_\infty} \mathrm{d}z\, f(z) = 2i\pi \sum_{z_0 \in \mathcal{P}_+[f]} \operatorname*{Res}_{z=z_0}[f(z)], \tag{4.A.9}$$

where for the last equality sign we used the Residue theorem [349]. Here $\mathcal{P}_+[f] = \{\gamma, -\overline{\gamma}\}$ is the set of all poles of f with positive imaginary part. Moving all the constants in front of the integral, we set our function to be

$$f(z) = \frac{z^2}{(z^2 - \gamma^2)(z^2 - \overline{\gamma}^2)}, \tag{4.A.10}$$

with residues

$$\operatorname*{Res}_{z=\gamma}[f(z)] = \frac{1}{2}\frac{\gamma}{\gamma^2 - \overline{\gamma}^2} \tag{4.A.11a}$$

$$\operatorname*{Res}_{z=-\overline{\gamma}}[f(z)] = \frac{1}{2}\frac{\overline{\gamma}}{\gamma^2 - \overline{\gamma}^2}, \tag{4.A.11b}$$

since f only has simple poles. We express γ and $\overline{\gamma}$ using Eq. (4.A.5) to obtain

$$N = \frac{V}{(2\pi)^3}|\Delta_{\mathrm{H},0}|^2\sqrt{2}\pi m^{3/2}\frac{2i\pi}{4i|\gamma|\sin(\theta/2)}. \tag{4.A.12}$$

With $\mu_\mathrm{H} > 0$ we use Eq. (4.A.7) and the identity $\sin\arctan x = x/\sqrt{1+x^2}$ to find

$$N = \frac{V}{(2\pi)^3}2\pi^2\left(\frac{m}{2}\right)^{3/2}|\Delta_{\mathrm{B},0}|\sqrt{\mu_\mathrm{H} + |\gamma|^2}. \tag{4.A.13}$$

We use Eq. (4.A.6) to identify $|\gamma|^2 = E_\mathbf{0}$, meaning $|\gamma|^2$ is the quasiparticle dispersion at zero momentum. For $\mu_\mathrm{H} < 0$, we have to be careful with a factor of π in Eq. (4.A.7), rotating the roots. In the end there are two additional negative signs showing up that cancel each other. Thus, the final result in Eq. (4.A.13) is valid for all values of μ_H and always positive, since $E_\mathbf{0} \geq |\mu_\mathrm{H}|$.

Having calculated the normalisation factor, we continue by calculating the expectation value of the relative position operator.

4.A.2 Expectation value of relative position

In this part, we determine the expectation value of $\boldsymbol{x}^2$, which in momentum space is a Laplace operator. Integration by parts for the numerator of Eq. (4.A.2) leads to

$$R = -\frac{V}{(2\pi)^3}\int_{\mathbb{R}^3} |\nabla_{\boldsymbol{k}}\chi_{\boldsymbol{k}}|^2. \tag{4.A.14}$$

We again apply the substitution introduced earlier, $u = k/\sqrt{2m}$, set

$$g(u) = \frac{u^4(u^2-\mu_{\mathrm{H}})^2}{\left[(u^2-\mu_{\mathrm{H}})^2 + |\Delta_{\mathrm{B},0}|^2\right]^3}, \tag{4.A.15}$$

and use spherical symmetry together with evenness of g to rearrange

$$R = -\frac{V}{(2\pi)^3} 2\sqrt{2m}\pi|\Delta_{\mathrm{B},0}|^2 \int_{-\infty}^{\infty} \mathrm{d}u\; g(u). \tag{4.A.16}$$

Similarly to N, we consider the analytic continuation of the function $g(u) \to g(z)$, using the identical contour integration technique, as the poles of g are identical to the poles of f. A subtle difference is that the poles of g are, in contrast to the poles of f, not simple, but third-order poles. We again apply Jordan's Lemma, as for $|z| \to \infty$ the function behaves as $g(z) \sim z^{-6}$, leading to

$$R = -\frac{V}{(2\pi)^3} 4i\pi^2\sqrt{2m}|\Delta_{\mathrm{B},0}|^2 \sum_{z_0\in\mathcal{P}_+[g]} \operatorname*{Res}_{z=z_0}[g(z)], \tag{4.A.17}$$

with $\mathcal{P}_+[g] = \mathcal{P}_+[f]$. To evaluate the residue, we need to take the aforementioned order of the pole into account. For any pole of order $n > 1$ the residue is calculated by [349]

$$\operatorname*{Res}_{z=z_0}[g(z)] = \frac{1}{(n-1)!}\lim_{z\to z_0}\frac{\mathrm{d}^{n-1}}{\mathrm{d}z^{n-1}}\left[(z-z_0)^n g(z)\right]. \tag{4.A.18}$$

Thus, we evaluate the residues in Eq. (4.A.17). Unlike in Eqs. (4.A.11a,4.A.11b), the isolated residues are rather long expressions, but their sum greatly simplifies. We hence obtain

$$\sum_{z_0\in\mathcal{P}_+[g]} \operatorname*{Res}_{z=z_0}[g(z)] = -\frac{|\gamma|^2(\gamma^2+\overline{\gamma}^2-5|\gamma|^2)+6|\gamma|^2\mu_{\mathrm{H}}-3\mu_{\mathrm{H}}^2}{16|\gamma|^2(\gamma-\overline{\gamma})^5}. \tag{4.A.19}$$

At this point we apply Eq. (4.A.5) to identify $\gamma^2+\overline{\gamma}^2 = 2|\gamma|^2\cos\theta$ and $\gamma-\overline{\gamma} = 2i|\gamma|\sin(\theta/2)$. We eliminate the phase using Eq. (4.A.7) with $\cos\arctan x = 1/\sqrt{1+x^2}$ to end up with

$$\sum_{z_0\in\mathcal{P}_+[g]} = \frac{\sqrt{2}(\mu_{\mathrm{H}}+|\gamma|^2)^{5/2}}{128i|\gamma|^2|\Delta_{\mathrm{B},0}|^5}(|\gamma|^2-\mu_{\mathrm{H}})(5|\gamma|^2-3\mu_{\mathrm{H}}). \tag{4.A.20}$$

The final result for the relative position expectation value follows from inserting the above expression into Eq. (4.A.17), resulting in

$$R = -\frac{V}{(2\pi)^3}\frac{\pi^2}{16}\frac{(\mu_{\mathrm{H}}+E_{\boldsymbol{0}})^{3/2}(E_{\boldsymbol{0}}^2-\mu_{\mathrm{H}}^2)(5E_{\boldsymbol{0}}-3\mu_{\mathrm{H}})}{E_{\boldsymbol{0}}|\Delta_{\mathrm{B},0}|^3}. \tag{4.A.21}$$

This result is strictly negative. The pair size squared is obtained from Eq. (4.A.2) and reads $\xi_{\mathrm{pair}} = -R/N$, where the volume and measure factors cancel out. Finally, scaling with the Fermi momentum and doing some basic algebra yields Eq. (4.78) from the main text.

4.B Asymptotic expansions for weak and strong interactions

In this Appendix, we explicitly perform analytic expansions of the integrals appearing in the WHFB self-consistency equations. We look into the superfluid order parameter equation (4.19) and the particle number equation (4.21). We first evaluate the weakly interacting BCS limit, after which we focus our attention on the strong coupling BEC side.

4.B.1 Weakly interacting expansions

The weakly interacting limit is special, since the positive chemical potentials cause the integrand of Eqs. (4.19) to peak at the Fermi surface. As such, there is no globally small parameter and a standard Taylor expansion in the integral proofs impossible. Instead, we resort to a different scheme of evaluating the integrals by cutting out the Fermi surface. We divide the integration domain into three intervals, one of which is centred around the Fermi energy. Then we approximate the integral in each interval separately. After this, we send the width of the interval around the Fermi surface to zero, making the result independent of the arbitrarily chosen cutting points.

To capture the influence of the many-body UV cutoff in the superfluid order parameter equation (4.19), we extend the integral towards infinity and subtract the tail, yielding

$$\frac{\pi}{k_{\mathrm{F}} a_{\mathrm{s}}} = \int_0^\infty \mathrm{d}x\, \mathcal{D}(x) f(x, \widetilde{\Delta}_{\mathrm{B},0}) - \int_{x_{\mathrm{c,B}}}^\infty \mathrm{d}x\, \mathcal{D}(x) f(x, \widetilde{\Delta}_{\mathrm{B},0}), \tag{4.B.22}$$

where the integrand is

$$f(x, \widetilde{\Delta}_{\mathrm{B},0}) = \frac{1}{x} - \frac{1}{\sqrt{(x-1)^2 + \widetilde{\Delta}_{\mathrm{B},0}^2}}. \tag{4.B.23}$$

Here we use that the effective chemical potential in the weakly interacting limit is close to the Fermi energy $\mu_{\mathrm{H}} \approx \varepsilon_{\mathrm{F}}$. We start by evaluating the first integral in Eq. (4.B.22) as the zero-range limit, after which we evaluate the second integral as a perturbative correction. To this end, we divide the half-infinite interval as $[0, \infty) = [0, 1-\omega] \cup (1-\omega, 1+\omega) \cup [1+\omega, \infty)$, using $\widetilde{\Delta}_{\mathrm{B},0} \ll \omega \ll 1$. This divides up the first integral in Eq. (4.B.22) as

$$\begin{aligned}\int_0^\infty \mathrm{d}x\, \mathcal{D}(x) f(x, \widetilde{\Delta}_{\mathrm{B},0}) = &\int_0^{1-\omega} \mathrm{d}x\, \mathcal{D}(x) f(x, \widetilde{\Delta}_{\mathrm{B},0}) + \int_{1-\omega}^{1+\omega} \mathrm{d}x\, \mathcal{D}(x) f(x, \widetilde{\Delta}_{\mathrm{B},0}) \\ &+ \int_{1+\omega}^\infty \mathrm{d}x\, \mathcal{D}(x) f(x, \widetilde{\Delta}_{\mathrm{B},0}).\end{aligned} \tag{4.B.24}$$

The infinite tail is well-behaved in the sense that a local Taylor expansion there is mathematically possible because $\widetilde{\Delta}_{\mathrm{B},0}$ is an absolutely small parameter when $x \gg 1$ or $x \ll 1$. Therefore, in the regions outside the interval $[1-\omega, 1+\omega]$ we perform a series expansion of the function f and truncate it after leading order. Furthermore, inside the central interval, since $\omega \ll 1$, the density of states is approximately constant, as $\sqrt{1 \pm \omega} = 1 \pm \mathcal{O}(\omega)^{3/2}$, hence in this region we approximate the density of states by $\mathcal{D}(x) \approx 1$. This means the over-all integral in Eq. (4.B.24) is approximated as

$$\begin{aligned}\int_0^\infty \mathrm{d}x\, \mathcal{D}(x) f(x, \widetilde{\Delta}_{\mathrm{B},0}) = &\int_0^{1-\omega} \mathrm{d}x\, \mathcal{D}(x) f(x, \widetilde{\Delta}_{\mathrm{B},0}) + \int_{1-\omega}^{1+\omega} \mathrm{d}x\, \mathcal{D}(1) f(x, \widetilde{\Delta}_{\mathrm{B},0}) \\ &+ \int_{1+\omega}^\infty \mathrm{d}x\, \mathcal{D}(x) f(x, \widetilde{\Delta}_{\mathrm{B},0}) + \mathcal{O}\left(\widetilde{\Delta}_{\mathrm{B},0}^2\right) + \mathcal{O}(\omega^{3/2}).\end{aligned} \tag{4.B.25}$$

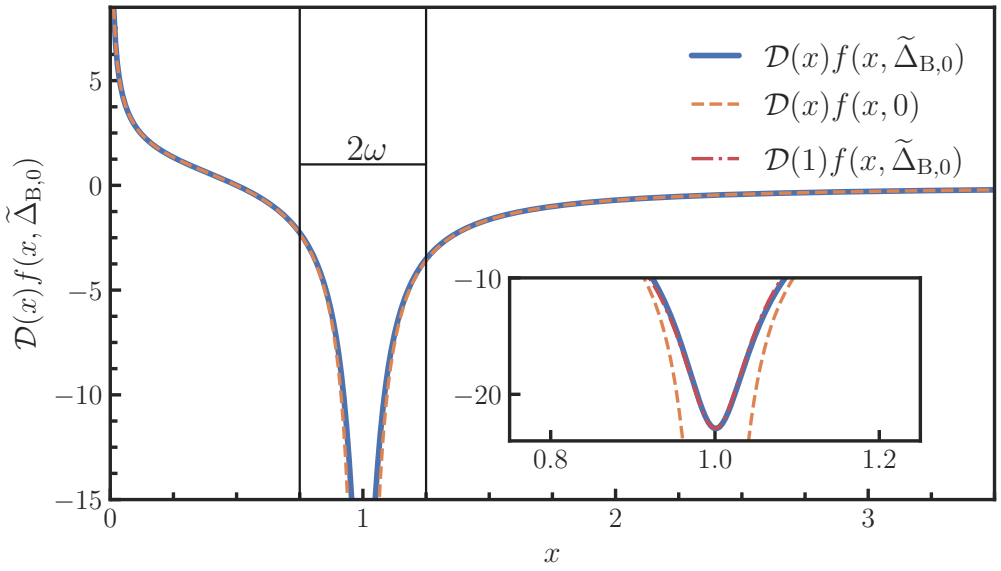


Figure 4.B.2: Integrand of superfluid order parameter equation for $1/k_{\mathrm{F}}a_{\mathrm{s}} = -2$ and $k_{\mathrm{F}}r_{\mathrm{e}} = 0.06$. Solid blue line represents the exact integrand, dashed orange line depicts approximation made to the tails, while dash-dotted red line stands for constant density of states around the Fermi surface.

The Taylor series of the two tail integrals are solved analytically, with the low-energy integral

$$\int_0^{1-\omega} \mathrm{d}x\, \mathcal{D}(x) f(x,\widetilde{\Delta}_{\mathrm{B},0}) = 4\sqrt{1-\omega} + \ln\left(1-\sqrt{1-\omega}\right) - \ln\left(1+\sqrt{1-\omega}\right) \tag{4.B.26}$$

exhibiting a logarithmic divergence for $\omega \to 0$. The large energy integral contains the same type of divergence when $\omega \to 0$, and reads

$$\int_{1+\omega}^{\infty} \mathrm{d}x\, \mathcal{D}(x) f(x,\widetilde{\Delta}_{\mathrm{B},0}) = \ln\left(1+\sqrt{1+\omega}\right) - \ln\left(\sqrt{1+\omega}-1\right). \tag{4.B.27}$$

In order to send $\omega \to 0$, we have to consider also the Fermi surface term from Eq. (4.B.24). To this end, we rescale all variables to ensure that $\delta = \widetilde{\Delta}_{\mathrm{B},0}/\omega \ll 1$. Thus, we substitute $y = (x-1)/\widetilde{\Delta}_{\mathrm{B},0}$, leading to

$$\int_{1-\omega}^{1+\omega} \mathrm{d}x\, \mathcal{D}(1) f(x,\widetilde{\Delta}_{\mathrm{B},0}) = \ln(1+\omega) - \ln(1-\omega) - \int_{-1/\delta}^{1/\delta} \frac{\mathrm{d}y}{\sqrt{1+y^2}}. \tag{4.B.28}$$

We solve this integral explicitly by standard means, yielding

$$\int_{1-\omega}^{1+\omega} \mathrm{d}x\, \mathcal{D}(1) f(x,\widetilde{\Delta}_{\mathrm{B},0}) = \ln(1+\omega) - \ln(1-\omega) + \ln\left(\sqrt{1+\delta^2}-1\right) - \ln\left(\sqrt{1+\delta^2}+1\right). \tag{4.B.29}$$

Since we have to choose the cut ω accordingly, as already mentioned, we perform a Taylor expansion for $\delta \to 0$. The relevant terms then become

$$\ln\left(\sqrt{1+\delta^2}-1\right) - \ln\left(\sqrt{1+\delta^2}+1\right) = \ln\delta^2 - 2\ln 2 + \mathcal{O}(\delta)^2. \tag{4.B.30}$$

Adding the three intervals back together and sending $\omega \to 0$, the divergences cancel, leading to

$$\int_0^{\infty} \mathrm{d}x\, \mathcal{D}(x) f(x,\widetilde{\Delta}_{\mathrm{B},0}) = 4 - 6\ln 2 + \ln\left(\widetilde{\Delta}_{\mathrm{B},0}^2\right) + \mathcal{O}\left(\widetilde{\Delta}_{\mathrm{B},0}\right)^2, \tag{4.B.31}$$

This is the zero range result. Using then the superfluid order parameter equation (4.B.22) results in the standard weak coupling expression

$$\widetilde{\Delta}_{\mathrm{B},0} = \frac{8}{e^2} e^{-\frac{\pi}{2|k_\mathrm{F} a_\mathrm{s}|}}, \tag{4.B.32}$$

which is non-perturbative in $1/k_\mathrm{F}a_\mathrm{s}$. To obtain the leading order correction of a non-vanishing effective range parameter, we have to solve the subtracted tail seen in Eq. (4.B.22). Since $x_{\mathrm{c,B}} \gg \widetilde{\Delta}_{\mathrm{B},0}$ we approximate the integral as

$$\begin{aligned}\int_{x_{\mathrm{c,B}}}^{\infty} \mathrm{d}x\, \mathcal{D}(x) f(x, \widetilde{\Delta}_{\mathrm{B},0}) &= \ln\Big(1 - \sqrt{1/x_{\mathrm{c,B}}}\Big) - \ln\Big(1 + \sqrt{1/x_{\mathrm{c,B}}}\Big) \\ &= -\frac{2}{\sqrt{x_{\mathrm{c,B}}}} + \mathcal{O}(x_{\mathrm{c,B}})^{-3/2}.\end{aligned} \tag{4.B.33}$$

This extra term yields an additional, exponential correction when solving Eq. (4.B.22) for the superfluid order parameter, ultimately causing it to be

$$|\Delta_{\mathrm{B},0}| \approx \frac{8\varepsilon_\mathrm{F}}{e^2} e^{-1/\sqrt{x_{\mathrm{c,B}}}} e^{-\frac{\pi}{2|k_\mathrm{F} a_\mathrm{s}|}}, \tag{4.B.34}$$

which is the result seen in the main text, see Eq. (4.26). This is the easiest approximation that can be made, exploiting the numerically obtained information that $\mu_\mathrm{H} \approx \varepsilon_\mathrm{F}$ for weak coupling. Note that we could avoid that assumption by cutting out the energies around μ_H instead and perform a similar calculation also of the particle number equation (4.21). However, in a leading order approximation, this yields the same result. The only difference is that we would also be able to obtain the corrections to μ_H as well. This would be of the order $\mathcal{O}(\widetilde{\Delta}_{\mathrm{B},0})^2$ [66, 122].

4.B.2 Strong coupling expansion

We now continue obtaining the strong coupling expansion. This is more straightforward, as the dissolution of the Fermi surface makes the superfluid order parameter a globally small quantity, as $\xi_{\boldsymbol{k}} > |\mu| \gg |\Delta_{\mathrm{B},0}|$ in the strong coupling regime. Therefore, we define $\zeta = \widetilde{\Delta}_{\mathrm{B},0}/|\widetilde{\mu}| \ll 1$ and substitute $y = x/|\widetilde{\mu}|$, with which the superfluid order parameter (4.19) and particle number equation (4.21) read

$$\frac{1}{k_\mathrm{F} a_\mathrm{s}} = \frac{2}{\pi}\sqrt{|\widetilde{\mu}|} \int_0^{y_{\mathrm{c,B}}} \mathrm{d}y\, \mathcal{D}(y) \left[\frac{1}{y} - \frac{1}{\sqrt{(y+1)^2 + \zeta^2}}\right], \tag{4.B.35a}$$

$$\frac{4}{3} = |\widetilde{\mu}|^{3/2} \int_0^{y_{\mathrm{c,B}}} \mathrm{d}y\, \mathcal{D}(y) \left[1 - \frac{y+1}{\sqrt{(y+1)^2 + \zeta^2}}\right]. \tag{4.B.35b}$$

In this regime, the two equations switch roles. The second equation determines the order parameter ζ, and the first is then used to find $|\widetilde{\mu}|$. We expand both equations as a series in ζ, truncating after the second order

$$\frac{1}{k_\mathrm{F} a_\mathrm{s}} = \frac{4}{\pi}\sqrt{|\widetilde{\mu}|} \arctan(y_{\mathrm{c,B}}) \left[1 + \frac{1}{16}\left(1 + \frac{\sqrt{y_{\mathrm{c,B}}}(y_{\mathrm{c,B}} - 1)}{(1 + y_{\mathrm{c,B}})^2 \arctan(y_{\mathrm{c,B}})}\right)\zeta^2 + \mathcal{O}(\zeta)^4\right], \tag{4.B.36a}$$

$$\frac{16}{3\pi} = |\widetilde{\mu}|^{3/2}\zeta^2 + \mathcal{O}(\zeta)^4. \tag{4.B.36b}$$

We assume that $|\widetilde{\mu}| = \widetilde{\mu}^{(0)} + \widetilde{\mu}^{(2)}\zeta^2 + \mathcal{O}(\zeta)^4$ is a power series as well. We also know that the chemical potential should, in leading order, be half the negative of the binding energy. This means we characterize $\widetilde{\mu}^{(0)} = -E_{\mathrm{B}}/2$. When inserting the series expansion of $\widetilde{\mu}$ in Eq. (4.B.36a) we obtain the binding energy

$$E_{\mathrm{B}} = \frac{\varepsilon_{\mathrm{F}}}{(k_{\mathrm{F}}a_{\mathrm{s}})^2}\left[1 + \frac{k_{\mathrm{F}}r_{\mathrm{e}}}{k_{\mathrm{F}}a_{\mathrm{s}}} + \mathcal{O}\left(\frac{k_{\mathrm{F}}r_{\mathrm{e}}}{k_{\mathrm{F}}a_{\mathrm{s}}}\right)^2\right], \tag{4.B.37}$$

which we already saw in the main text, see Eq. (4.51). We use this result in Eq. (4.B.36b) to find

$$\widetilde{\Delta}_{\mathrm{B},0} = \frac{4}{\sqrt{3\pi}}\frac{1}{\sqrt{k_{\mathrm{F}}a_{\mathrm{s}}}}\left[1 + \frac{1}{4}\frac{k_{\mathrm{F}}r_{\mathrm{e}}}{k_{\mathrm{F}}a_{\mathrm{s}}} + \mathcal{O}\left(\frac{k_{\mathrm{F}}r_{\mathrm{e}}}{k_{\mathrm{F}}a_{\mathrm{s}}}\right)^2\right], \tag{4.B.38}$$

which is then used in the second order expansion of Eq. (4.B.36a) to obtain the chemical potential up to second order in ζ, reading

$$\widetilde{\mu} = -\frac{E_{\mathrm{B}}}{2\varepsilon_{\mathrm{F}}} + \frac{2}{3\pi}k_{\mathrm{F}}a_{\mathrm{s}}\left(1 + \frac{k_{\mathrm{F}}r_{\mathrm{e}}}{k_{\mathrm{F}}a_{\mathrm{s}}}\right) + \mathcal{O}\left(\frac{k_{\mathrm{F}}r_{\mathrm{e}}}{k_{\mathrm{F}}a_{\mathrm{s}}}\right)^2. \tag{4.B.39}$$

The two expressions above are the final results in the main text, see Eqs. (4.49) and (4.50).

Chapter 5

Two-point correlation functions in BEC-BCS crossover

> The best thing most of us can hope to achieve in physics is simply to misunderstand at a deeper level.
>
> Wolfgang Pauli

5.1 Introduction . . . 110
5.2 Field theory of correlation functions . . . 112
5.2.1 Basic constraints for two-point correlation functions . . . 112
5.2.2 Generating functional and expectation values . . . 117
5.3 Linear response theory with gauge fixing . . . 118
5.3.1 Response theory up to Gaussian approximation . . . 119
5.3.2 Incorporating collective modes . . . 123
5.3.3 Diagrammatic interpretation . . . 126
5.3.4 Equation of state and gauge symmetry . . . 129
5.3.5 2D BEC-BCS crossover with improved equation of state . . . 130
5.4 Real-space correlation functions . . . 132
5.4.1 Equal-spin density-density correlations . . . 133
5.4.2 Opposite-spin density-density correlations . . . 134
5.4.3 Charge density-density correlations . . . 136
5.4.4 Influence of irreducible terms . . . 137
5.5 Anti-bunching of fermions in the continuum . . . 138
5.5.1 Comparison with experiment . . . 139
5.5.2 Correlation hole . . . 141
5.A Explicit expressions for D-dimensional loop functions . . . 144
5.A.1 General expressions in D dimensions . . . 144
5.A.2 Simplifications for 2D, infinite rotationally symmetric systems . . . 145
5.B Gauge invariance and ladder summation . . . 146
5.B.1 Diagrammatic representation of Gaussian equation of state . . . 146
5.B.2 Diagrams of irreducible contribution . . . 150

5.1 Introduction

In the previous chapters, we discussed thermodynamic properties of Fermi spin-mixtures in the ground state and at finite temperatures. We worked within the framework of a self-consistent weighted theory, which allowed us to account for multiple interaction channels. In this chapter, we focus on correlation functions in the standard, single-channel, beyond saddle-point framework of the BEC-BCS crossover, inspired by recent experiments in ^{6}Li [187]. Using only the Bogoliubov channel is sufficient here because the pairing is the reason for the observed anti-correlations, and the Hartree channel will only lead to quantitative improvements. We present a more detailed version of Ref. [P2].

Correlation functions have been investigated throughout all scales, ranging from atomic nuclei [350–355], cold quantum gases [106, 121, 126, 150, 177, 179, 356–358], superconductors [359–367], even to astronomical objects, for instance neutron stars [368–375]. Such research poses profound insights in the properties of matter in degenerate states, here with a focus on fermionic systems. The BEC-BCS crossover represents an ideal platform for theoretical and experimental investigations [376–379] due to the high controllability of the interactions via Fano-Feshbach resonances [60, 61, 65]. The insights gathered in the Laboratory are widely useful due to the concept of quantum simulation in order to emulate all sorts of systems [189–192], encompassing the examples mentioned above.

In momentum space, the correlations of Fermi spin-mixtures were thoroughly investigated theoretically [88, 92, 107, 128, 173, 380, 381] by evaluating the low-energy and long-wavelength collective modes. For instance, Bragg-spectroscopy gives direct access to the dynamical structure factor and as such to collective excitations, both in 3D and in 2D [334, 382, 383]. Conversely, real-space correlation functions have been less explored due to limited experimental accessibility. To resolve the fine details of spatial correlation functions, lattice quantum gas microscopes [190, 192, 384–390] are not sufficient as their resolution in real space is limited by the lattice constant. This is of the order of the typical particle distance and, thus, restricted to larger distances at standard densities. Furthermore, due to the hopping energy term J in Hubbard models, there is an additional energy scale which alters the correlations compared to continuum systems.

However, the recent development of continuous quantum gas microscopes (CQGMs) made it possible to investigate real-space correlation functions for very dilute Bose and Fermi systems [183–188]. Furthermore, in continuous space, no minimal energy J for an interaction is required, and hence, low-energy scattering properties might be probed. CQGMs operate differently from their lattice counterparts, allowing for thermalisation in continuous space. After thermalisation, an optical lattice with a fine spacing is rapidly turned on, pinning the particles to their instantaneous position, after which they are cooled, and an in-situ image is taken. By counting the number of particles at a given distance from a reference particle, real-space correlation functions are experimentally accessible. These measurements lead to results as those depicted in Fig. 5.1, where equal-spin, charge and opposite-spin density-density correlation functions are shown versus the dimensionless distance. Furthermore, these results are compared with auxiliary-field quantum Monte-Carlo calculations as solid lines, and mean-field theories as dashed lines. As illustrated, mean-field fails to explain the experimental results, in particular, the drop of the opposite-spin correlation function below one at intermediate distances and away from weak interactions. The findings obtained via CQGMs necessitate new theoretical investigation of real-space correlations in the continuous space, beyond a simple mean-field approach.

It was pointed out early on that in momentum space, conservation laws and gauge

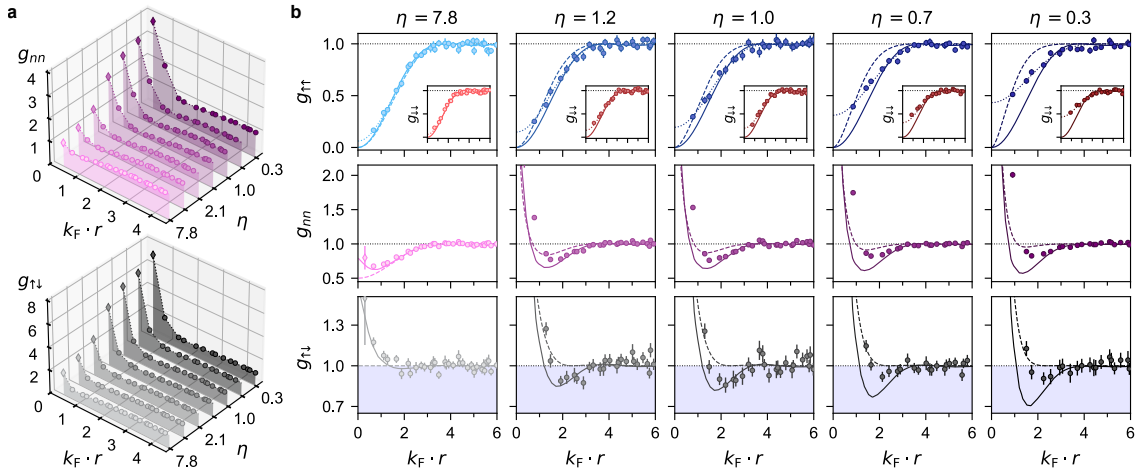


Figure 5.1: Experimental measurement of density-density correlation functions. Panel (a) shows charge and opposite-spin density-density correlation functions in the plane of dimensionless distance and interaction parameter $\eta = \ln k_F a$ in upper and lower panels, respectively. Panel (b) depicts the data for various interaction parameters. The upper row shows equal-spin, middle row charge density-density correlation measurement. The lower panel represents the opposite-spin density-density correlation function obtained via the former two. The data is visualised as balls, the solid lines stand for auxiliary-field quantum Monte Carlo calculations and the dashed lines portray the mean-field theoretical calculation. The dotted line represents a two-parameter fit, see Ref. [187] for more details. Reprinted figure with permission from [187], © Copyright (2026) by the American Physical Society.

symmetries lead to important benchmarks such as sum rules [328, 391]. In the context of superconductors, this has been recently studied [392–399], results of which also found application in the realm of the BEC-BCS crossover in ultracold atomic gases [126]. Generally, low-energy response theories are successful in their range of validity. Here, theories that are in agreement with conservation laws and gauge symmetries, like Baym-Kadanoff [400–402] or parquet approaches [403, 404], are exceptionally useful. However, in most systems, those frameworks are difficult to apply exactly. Many practical calculations require truncations within the framework, suited to the momentum scale of interest. Low-energy truncated Baym-Kadanoff approaches allow for precise calculations of collective excitations at the cost of losing information about high-energy contributions, preventing the fulfilment of sum rules [405–407] and Ward-Takahashi identities [408, 409]. Extending those low-energy Baym-Kadanoff calculations by enforcing sum rules violates Pauli's exclusion principle [410]. As a consequence, using Baym-Kadanoff approaches is very complicated when aiming to calculate real-space correlation functions, as there all energy scales are involved, unless a conserving theory of all energy scales is obtained.

In this chapter, we present a formulation of quantum statistical field theory which allows us to calculate real-space correlation functions in agreement with basic conservation laws and the Pauli exclusion principle. To this end, in Section 5.2 we establish basic constraints essential to fermionic correlation functions rooted in fundamental rules of quantum many-body physics. Subsequently, in Section 5.3, we focus on the specific example of the BEC-BCS crossover to calculate the correlation functions up to Gaussian order. We find that so-called two-particle irreducible terms are vital not only for the correlation functions, but also for the equation of state, which has to be derived in a consistent way from a linear

response theory. Beyond this, we compare our resulting theory to two existing proposals in the standard literature and show that both of the existing approaches are in conflict with Pauli's exclusion principle. In Section 5.4 we then consider the specific case of a two-dimensional (2D) Fermi gas at $T = 0$. Here, we prove that our approach is able to describe the correct behaviour of the spin-resolved density-density correlation functions found in Ref. [187]. In Section 5.5 we further characterise the emerging anti-correlations of opposite-spin fermions that were observed experimentally. This chapter provides an analytical explanation and physical interpretation of a so far not fully understood behaviour of opposite-spin fermions in a Fermi spin-mixture.

5.2 Field theory of correlation functions

In this section, we establish the general framework of correlation functions we work in. Enforcing basic symmetry principles allows us to introduce a set of constraints that any observable correlation function must fulfil to make reliable predictions. Subsequently, we provide a brief derivation of the correlation functions in the general framework of functional integration.

5.2.1 Basic constraints for two-point correlation functions

In this part, we discuss the general properties of density-density correlation functions in D-dimensional Fermi systems. Our main interest lies in the spin-resolved density-density correlation function of a Fermi-spin mixture. To this end, we define the spin-resolved density operator $\hat{n}_\mathrm{s}(x) = \hat{\psi}^\dagger_\mathrm{s}(x)\hat{\psi}_\mathrm{s}(x)$. Throughout this section, we use the word *spin* as a short version of pseudo-spin.

Definitions

We consider the correlation tensor as a time-ordered expectation value of two density operators

$$\varrho_{\mathrm{ss}'}(t,\boldsymbol{x};t',\boldsymbol{x}') = \langle \hat{T}\,[\hat{n}_\mathrm{s}(t,\boldsymbol{x})\hat{n}_{\mathrm{s}'}(t',\boldsymbol{x}')]\rangle \tag{5.1a}$$

$$= \Theta(t-t')\langle \hat{n}_\mathrm{s}(t,\boldsymbol{x})\hat{n}_{\mathrm{s}'}(t',\boldsymbol{x}')\rangle - \Theta(t'-t)\langle \hat{n}_{\mathrm{s}'}(t',\boldsymbol{x}')\hat{n}_\mathrm{s}(t,\boldsymbol{x})\rangle. \tag{5.1b}$$

Here $\langle \hat{O}\rangle$ stands for the ensemble average of a given operator $\hat{O}$ at any temperature, and $\hat{T}$ is the time ordering operator using the Heaviside function Θ. Since we are interested in causal correlation functions, we restrict ourselves to $t' \leq t$, hence assuming that all density-density products are already time ordered. We strictly distinguish this from the pair correlation tensor, which is the expectation value of the respective normal-ordered product, defined as

$$P_{\mathrm{ss}'}(t,\boldsymbol{x};t',\boldsymbol{x}') = \langle :\hat{n}_\mathrm{s}(x)\hat{n}_{\mathrm{s}'}(x):\rangle = \langle \hat{\psi}^\dagger_\mathrm{s}(x)\hat{\psi}^\dagger_{\mathrm{s}'}(x')\hat{\psi}_{\mathrm{s}'}(x')\hat{\psi}_\mathrm{s}(x)\rangle. \tag{5.2}$$

By using the anti-commuting nature of the fermionic field operators, i.e.

$$\hat{\psi}^\dagger_\mathrm{s}(t,\boldsymbol{x})\hat{\psi}_{\mathrm{s}'}(t',\boldsymbol{x}') + \hat{\psi}_{\mathrm{s}'}(t',\boldsymbol{x}')\hat{\psi}^\dagger_\mathrm{s}(t,\boldsymbol{x}) = \delta_{\mathrm{ss}'}\delta(t-t')\delta^D(\boldsymbol{x}-\boldsymbol{x}'), \tag{5.3}$$

we see that density-density and pair correlators differ by a singular contribution, namely

$$\varrho_{\mathrm{ss}'}(x;x') - P_{\mathrm{ss}'}(x;x') = \delta_{\mathrm{ss}'}\delta(x-x')\langle \hat{n}_\mathrm{s}(x)\rangle, \tag{5.4}$$

with $\delta(x - x') = \delta(t - t')\delta^D(\boldsymbol{x} - \boldsymbol{x}')$. From now on, we use a $D + 1$ vector notation for space-time arguments, with $x = (t, \boldsymbol{x})$ and $x' = (t', \boldsymbol{x}')$. We separate space and time only when it is illustrative for physical understanding. An important aspect is that the density-density correlation function has to have a singular point for equal spins and space-time positions $x = x'$, whereas the pair correlation has to obey

$$P_{\mathrm{ss}}(x; x) = 0. \tag{5.5}$$

This is due to the fermions obeying the Pauli principle, expressed as $[\hat{\psi}_{\mathrm{s}}(x)]^2 = 0$. With those things clarified, we define the normalised spin-resolved two-point correlation functions [173, 187]

$$g^{(2)}_{\mathrm{ss}'}(x; x') = \frac{\varrho_{\mathrm{ss}'}(x; x')}{\langle \hat{n}_{\mathrm{s}}(x)\rangle\langle \hat{n}_{\mathrm{s}'}(x')\rangle}. \tag{5.6}$$

For $\mathrm{s} = \mathrm{s}'$ we speak of equal-spin, for $\mathrm{s} \neq \mathrm{s}'$ of opposite-spin density-density correlation functions. Furthermore, $t = t'$ implies equal-time correlations. While the latter are the main focus of this chapter, all the general statements made so far and in the upcoming sections also apply to unequal time correlations. Hence, we specify $t = t'$ at a later point.

Furthermore, we introduce the total density operator $\hat{n}(x) = \sum_{\mathrm{s}} \hat{n}_{\mathrm{s}}(x)$, which allows us to define the charge density-density correlation function

$$g^{(2)}_{nn}(x; x') = \frac{\langle \hat{n}(x)\hat{n}(x')\rangle}{\langle \hat{n}(x)\rangle\langle \hat{n}(x')\rangle}. \tag{5.7}$$

By using the linearity of the expectation value, it is straightforward to obtain

$$g^{(2)}_{nn}(x; x') = \sum_{\mathrm{ss}'} \frac{\langle \hat{n}_{\mathrm{s}}(x)\rangle\langle \hat{n}_{\mathrm{s}'}(x')\rangle}{\langle \hat{n}(x)\rangle\langle \hat{n}(x')\rangle} g^{(2)}_{\mathrm{ss}'}(x; x'). \tag{5.8}$$

Gauge symmetry of expectation values

For a Fermi spin-mixture in a homogeneous D-dimensional system of hypervolume L^D, the fermionic nature dictates some basic symmetry properties that the introduced correlation functions have to fulfil. These are independent of the underlying realisation. The density-density/pair correlation functions (5.6) have to be invariant under a local $\mathrm{U}(1)$ gauge transformation

$$\hat{\psi}_{\mathrm{s}}(t, \boldsymbol{x}) \xrightarrow{\mathrm{U}(1)} \hat{\psi}_{\mathrm{s}}(t, \boldsymbol{x}) e^{i\phi_{\mathrm{s}}(t,\boldsymbol{x})}. \tag{5.9}$$

This is because the local density operator acquires phases of creation- and annihilation-operators, which are of opposite sign, thus transforming $\hat{n}_{\mathrm{s}}(t, \boldsymbol{x}) \to \hat{n}_{\mathrm{s}}(t, \boldsymbol{x})$. This remains true even if the system locally breaks $\mathrm{U}(1)$ symmetry due to the presence of a complex superfluid order parameter connected to the anomalous terms

$$\hat{\psi}_{\uparrow}(t, \boldsymbol{x})\hat{\psi}_{\downarrow}(t, \boldsymbol{x}) \xrightarrow{\mathrm{U}(1)} \hat{\psi}_{\uparrow}(t, \boldsymbol{x})\hat{\psi}_{\downarrow}(t, \boldsymbol{x}) e^{i[\phi_{\uparrow}(t,\boldsymbol{x})+\phi_{\downarrow}(t,\boldsymbol{x})]}. \tag{5.10}$$

To investigate the correlation functions, we need to separate the correlations induced by interactions and statistical properties from the background value. One way to do this is to assume $\hat{n}_{\mathrm{s}}(x) = n_{\mathrm{s}}(x) + \delta\hat{n}_{\mathrm{s}}(x)$, where $n_{\mathrm{s}}(x) = \langle \hat{n}_{\mathrm{s}}(x)\rangle$ denotes the background density and $\delta\hat{n}_{\mathrm{s}}(x)$ represents local density fluctuations. With this decomposition, the density-density correlation tensor from Eq. (5.1a) reads

$$\varrho_{\mathrm{ss}'}(x; x') = n_{\mathrm{s}}(x)n_{\mathrm{s}'}(x') + \langle \delta\hat{n}_{\mathrm{s}}(x)\delta\hat{n}_{\mathrm{s}'}(x')\rangle. \tag{5.11}$$

Another approach, which ultimately yields the same result, is to formally separate disconnected from connected Feynman diagrams [14, 344, 411] so that

$$\varrho_{\mathrm{ss}'}(x;x') = \langle\hat{n}_{\mathrm{s}}(x)\rangle\langle\hat{n}_{\mathrm{s}'}(x)\rangle + \langle\hat{n}_{\mathrm{s}}(x)\hat{n}_{\mathrm{s}'}(x')\rangle_{\mathrm{c}}. \tag{5.12}$$

We hence define the connected correlation tensor via the local density fluctuations

$$\chi_{\mathrm{ss}'}(x;x') = \langle\hat{n}_{\mathrm{s}}(x)\hat{n}_{\mathrm{s}'}(x')\rangle_{\mathrm{c}} = \langle\delta\hat{n}_{\mathrm{s}}(x)\delta\hat{n}_{\mathrm{s}'}(x')\rangle, \tag{5.13}$$

allowing us to express the correlation functions (5.6) as

$$g^{(2)}_{\mathrm{ss}'}(x;x') = 1 + \frac{\chi_{\mathrm{ss}'}(x;x')}{n_{\mathrm{s}}(x)n_{\mathrm{s}'}(x')}. \tag{5.14}$$

We directly identify that the connected correlator tensor (5.13) contains regular and irregular terms, where the latter arise from the anti-commutator (5.3), separating as

$$\chi_{\mathrm{ss}'}(x;x') = \chi^{\mathrm{reg}}_{\mathrm{ss}'}(x;x') + \delta_{\mathrm{ss}'}\delta(x-x')n_{\mathrm{s}}(x). \tag{5.15}$$

Consequently, we see that the pair correlation tensor (5.2) is expressed via the regular connected correlation tensor by the relation

$$P_{\mathrm{ss}'}(x;x') = n_{\mathrm{s}}(x)n_{\mathrm{s}'}(x') + \chi^{\mathrm{reg}}_{\mathrm{ss}'}(x;x'). \tag{5.16}$$

Using the expression above, we express the Pauli-principle (5.5) in the more useful way

Result: Pauli-Principle

$$\chi^{\mathrm{reg}}_{\mathrm{ss}}(x;x) = -\left[n_{\mathrm{s}}(x)\right]^2 \Leftrightarrow \langle\hat{n}_{\mathrm{s}}(x)\rangle = \sqrt{-\chi^{\mathrm{reg}}_{\mathrm{ss}}(x;x)}. \tag{5.17}$$

The condition above represents a local equation of state (EoS), fixing the particle number in a way that is consistent with the Pauli principle. This is one of the most important constraints of quantum many-body physics. As such, fulfilling the Pauli principle is absolutely essential in any theory dealing with real-space correlations. This EoS is independent of any properties of the system, including temperature, dimensionality, population or mass imbalances, interactions and spatial inhomogeneities in the trapping potential.

Wick decomposition

After having established the connected and disconnected pieces in Eq. (5.12), we now take a different perspective by imposing Wick's theorem [412]. To this end, we analyse the content of the connected expectation value by applying the Wick decomposition to the pair correlation tensor in Eq. (5.2), which in full detail reads

$$\begin{aligned}\langle{:}\hat{n}_{\mathrm{s}}(x)\hat{n}_{\mathrm{s}'}(x'){:}\rangle =& \langle\hat{n}_{\mathrm{s}}(x)\rangle\langle\hat{n}_{\mathrm{s}'}(x')\rangle - \langle\hat{\psi}^{\dagger}_{\mathrm{s}}(x)\hat{\psi}_{\mathrm{s}'}(x')\rangle\langle\hat{\psi}^{\dagger}_{\mathrm{s}'}(x')\hat{\psi}_{\mathrm{s}}(x)\rangle \\ &+ \langle\hat{\psi}^{\dagger}_{\mathrm{s}}(x)\hat{\psi}^{\dagger}_{\mathrm{s}'}(x')\rangle\langle\hat{\psi}_{\mathrm{s}'}(x')\hat{\psi}_{\mathrm{s}}(x)\rangle + \langle\hat{n}_{\mathrm{s}}(x)\hat{n}_{\mathrm{s}'}(x')\rangle_{\mathrm{irr}}.\end{aligned} \tag{5.18}$$

The first three terms of the above equality capture all the contractions of the fields in the expectation value. The first term represents the product of the local densities and hence the disconnected expectation value. In particular, we obtain the so-called tadpole diagrams. In the sense of the HFB approximation, see Chapter 3 for a more detailed interpretation,

this is identified with the Hartree term. The second term stands for the normal Green's function of spins s and s', which we express as

$$G_{\mathrm{ss}'}(t,\boldsymbol{x};t',\boldsymbol{x}') = \langle\hat{\psi}^\dagger_{\mathrm{s}}(t,\boldsymbol{x})\hat{\psi}_{\mathrm{s}'}(t',\boldsymbol{x}')\rangle. \tag{5.19}$$

This can be identified with a Fock-like term in a HFB approximation. The local density of the first term is then

$$n_{\mathrm{s}}(t,\boldsymbol{x}) = G_{\mathrm{ss}}(t,\boldsymbol{x};t,\boldsymbol{x}). \tag{5.20}$$

The third term in Eq. (5.18) consists of anomalous Green's functions, which we define as

$$F_{\mathrm{ss}'}(t,\boldsymbol{x};t',\boldsymbol{x}) = \langle\hat{\psi}_{\mathrm{s}}(t,\boldsymbol{x})\hat{\psi}_{\mathrm{s}'}(t',\boldsymbol{x}')\rangle. \tag{5.21}$$

This is a term related to local pairing in the system and associated with the Bogoliubov channel, crucial in theories of superfluids and superconductors. Note that the anomalous Green's functions are not invariant under a local $\mathrm{U}(1)$ gauge transformation, and neither are the spin off-diagonal elements of the normal Green's function. The last term in Eq. (5.18) consists of all the two-particle irreducible diagrams, which are not expressible as contractions, i.e. the product of two-particle Green's functions. This irreducible contribution contains two-body bound states, entanglement information, collective excitations and scattering states. We represent it by

$$\varrho^{\mathrm{irr}}_{\mathrm{ss}'}(x;x') = \langle\hat{n}_{\mathrm{s}}(x)\hat{n}_{\mathrm{s}'}(x')\rangle_{\mathrm{irr}}. \tag{5.22}$$

Comparing the Wick decomposition (5.18) with Eq. (5.12) we find that the connected correlation tensor (5.13) is identified by

$$\begin{aligned}\chi_{\mathrm{ss}'}(x;x') = &-|G_{\mathrm{ss}'}(x;x')|^2 + |F_{\mathrm{ss}'}(x;x')|^2 \\ &+ \varrho^{\mathrm{irr}}_{\mathrm{ss}'}(x;x') + \delta_{ss'}\delta(x-x')\langle\hat{n}_s(x)\rangle,\end{aligned} \tag{5.23}$$

and as such gauge invariant. Comparing this equation with Eq. (5.15) reveals that the regular correlator, which is imperative for the Pauli principle (5.17), contains not only the reducible normal and anomalous Green's functions, but also the two-particle irreducible diagrams

$$\chi^{\mathrm{reg}}_{\mathrm{ss}'}(x;x') = -|G_{\mathrm{ss}'}(x;x')|^2 + |F_{\mathrm{ss}'}(x;x')|^2 + \varrho^{\mathrm{irr}}_{\mathrm{ss}'}(x;x'). \tag{5.24}$$

Now that we have the regular correlator matrix in its most detailed form, we continue by specifying to homogeneous systems and $\mathrm{SU}(2)$ invariant interactions.

Homogeneity and spin symmetry

Before focusing on an explicit system, we perform some simplifications that are valid for a large variety of systems. We start by considering the spins to represent two hyperfine states of an atomic species. In cold, dilute systems, only s-wave scattering happens, which restricts the possibility of pairing processes. In such systems, there is no triplet pairing and the equal spin anomalous Green's function vanishes

$$F_{\mathrm{ss}}(x;x') = 0 \tag{5.25}$$

regardless of the space-time positions x, x' of the two particles. This excludes, for instance, superfluid ^{3}He. Hence, the equal-spin density-density correlation function becomes

$$g^{(2)}_{\mathrm{ss}}(x;x') = 1 - \frac{|G_{\mathrm{ss}}(x;x')|^2}{n_{\mathrm{s}}(x)n_{\mathrm{s}'}(x')} + \frac{\varrho^{\mathrm{irr}}_{\mathrm{ss}}(x;x')}{n_{\mathrm{s}}(x)n_{\mathrm{s}'}(x)} + \frac{\delta(x-x')}{n_{\mathrm{s}}(x)}, \tag{5.26}$$

where the first term corresponds to the uncorrelated gas. The second term arises from the normal Green's function and conveys the two-particle properties. It always poses a negative contribution, showing that equal-spin fermions anti-correlate due to the exclusion principle. This is true even in a non-interacting system, for instance, in a spin-polarised Fermi gas due to quantum statistics. The third term represents the contributions from two-particle irreducible diagrams, while the last term is the irregular part. As a consequence of Eq. (5.25), the anomalous term does not contribute to the Pauli principle (5.17)

$$[n_{\mathrm{s}}(x)]^2 = |G_{\mathrm{ss}}(x;x)|^2 - \rho^{\mathrm{irr}}_{\mathrm{ss}}(x;x) \Leftrightarrow \langle \hat{n}_{\mathrm{s}}(x)\rangle = \sqrt{|G_{\mathrm{ss}}(x;x)|^2 - \rho^{\mathrm{irr}}_{\mathrm{ss}}(x;x)}. \tag{5.27}$$

Furthermore, spin-flip processes are prohibited in our system, as we assume a model in which the z-direction of the magnetization commutes with the Lagrangian. Thus, the total longitudinal magnetisation is conserved, and the opposite-spin normal Green's function vanishes

$$G_{\mathrm{s}\bar{\mathrm{s}}}(x;x') = 0, \tag{5.28}$$

where $\bar{\mathrm{s}}$ indicates the opposite spin of s. Therefore, the opposite-spin density-density correlation function reads

$$g^{(2)}_{\mathrm{s}\bar{\mathrm{s}}}(x;x') = 1 + \frac{|F_{\mathrm{s}\bar{\mathrm{s}}}(x;x')|^2}{n_{\mathrm{s}}(x)n_{\bar{\mathrm{s}}}(x')} + \frac{\varrho^{\mathrm{irr}}_{\mathrm{s}\bar{\mathrm{s}}}(x;x')}{n_{\mathrm{s}}(x)n_{\bar{\mathrm{s}}}(x')} \tag{5.29}$$

which is regular even at equal positions. As for the equal-spin case, the first term denotes the uncorrelated system and the second term stands for the correlation arising from anomalous (pairing) effects. This effect is always positive, meaning that opposite-spin fermions tend to correlate due to anomalous terms. The irreducible contribution can still cause anti-correlations, as its sign is not set and depends on the irreducible diagrams involved.

Another great simplification is posed by the assumption of a homogeneous, infinite system in thermal equilibrium. In such a system, the background density is a constant, and we have $n_{\mathrm{s}}(t,\boldsymbol{x}) = n_{\mathrm{s}}$. Therefore, we set $x' = x + \delta x$, which allows us to integrate out the absolute coordinate x such that only the relative distance δx remains. The relative distance in space and time is defined by $\delta x = (\delta t, \delta \boldsymbol{r})$. For the remainder of this chapter, we will focus on relative distance correlation functions, which we define as

$$g^{(2)}_{\mathrm{ss}'}(\delta x) = \int_0^\beta \frac{\mathrm{d}\tau}{\beta} \int_{L^D} \frac{\mathrm{d}^D x}{L^D} g^{(2)}_{\mathrm{ss}'}(x; x+\delta x). \tag{5.30}$$

In a homogeneous system, this can be further simplified to

$$g^{(2)}_{\mathrm{ss}'}(\delta x) = g^{(2)}_{\mathrm{ss}'}(0;\delta x), \tag{5.31}$$

as well as for the correlation tensor in real space $\chi_{\mathrm{ss}'}(\delta x) = \chi_{\mathrm{ss}'}(0;\delta x)$. As such, the second statistical moments read

$$g^{(2)}_{\mathrm{ss}'}(\delta x) = 1 + \frac{\chi_{\mathrm{ss}'}(\delta x)}{n_{\mathrm{s}} n_{\mathrm{s}'}}. \tag{5.32}$$

We perform a Fourier transform in space and time to obtain

$$g^{(2)}_{\mathrm{ss}'}(\delta t, \delta \boldsymbol{r}) = 1 + \frac{1}{n_{\mathrm{s}} n_{\mathrm{s}'}} \sum_{\boldsymbol{q}} \int_{-\infty}^{\infty} \mathrm{d}\omega\, \chi_{\mathrm{ss}'}(\omega, \boldsymbol{q}) e^{-i\boldsymbol{q}\cdot\delta\boldsymbol{r} + i\omega\delta t}, \tag{5.33}$$

where $\boldsymbol{q}$ is the D-dimensional momentum and ω the frequency. The momentum space representation $\chi_{\mathrm{ss}'}(\omega,\boldsymbol{q})$ is the spin-resolved density-density response function.

Equal-time correlation functions

In the rest of this chapter, we focus on equal-time correlation functions, that is, $t' \to t^-$, where the limit is taken from below to account for the time order. This means we have $\delta t = t' - t = 0^-$. To this end, we now specialise our approach to equal times. The equal-time density-density correlation function hence becomes

$$g^{(2)}_{\mathrm{ss}'}(\delta\boldsymbol{r}) = g^{(2)}_{\mathrm{ss}'}(0^-, \delta\boldsymbol{r}) = 1 + \frac{1}{n_\mathrm{s} n_{\mathrm{s}'}} \sum_{\boldsymbol{q}} \int_{-\infty}^{\infty} \mathrm{d}\omega\, \chi_{\mathrm{ss}'}(\omega, \boldsymbol{q}) e^{-i\boldsymbol{q}\cdot\delta\boldsymbol{r} + i\omega 0^-}. \tag{5.34}$$

After this rounding up of symmetry rules and general properties, the next step will be a brief introduction on how we calculate the response function $\chi_{\mathrm{ss}'}(\omega, \boldsymbol{q})$ or the correlator $\chi_{\mathrm{ss}'}(t, \boldsymbol{x})$ in a functional integral approach.

5.2.2 Generating functional and expectation values

In quantum statistical field theory, the expectation value of a field $\mathcal{A}$ associated with an operator $\hat{A}$ is defined via a functional integral

$$\langle \hat{A} \rangle = \frac{\oint_\mathrm{A} \mathcal{D}[\overline{\psi}, \psi]\, \mathcal{A}\, e^{-\mathcal{S}[\overline{\psi}, \psi]}}{\oint_\mathrm{A} \mathcal{D}[\overline{\psi}, \psi] e^{-\mathcal{S}[\overline{\psi}, \psi]}}, \tag{5.35}$$

where $\mathcal{S}[\overline{\psi}, \psi]$ is the Euclidean action of the system. Note that we now deal with operators and fields in imaginary time τ as we want to obtain thermodynamic response functions for equal times. Because of the Wick rotation, for causal correlation functions we have to replace $\delta t = 0^- \to \delta\tau = i0^+$. In our case, we focus on operators $\hat{A}$ that are products of density operators and are either time- or normal-ordered. Therefore, we add a linear coupling of the density to some fictitious source terms $j_\mathrm{s}(\tau, \boldsymbol{x})$. The coupling reads

$$\mathcal{S} \to \mathcal{S}_\mathrm{J}[\overline{\psi}, \psi; j] = \mathcal{S}[\overline{\psi}, \psi] - \int_0^\beta \mathrm{d}\tau \int_{L^D} \mathrm{d}^D\boldsymbol{x} \sum_\mathrm{s} n_\mathrm{s}(\tau, \boldsymbol{x}) j_\mathrm{s}(\tau, \boldsymbol{x}). \tag{5.36}$$

Taking the functional derivative of $\exp(-\mathcal{S}_\mathrm{J})$ with respect to the source term, the density appears in front of the exponential. As such, it is straightforward to see that the causal equal-time spin-resolved density-density correlations read

$$\langle \hat{n}_\mathrm{s}(\tau, \boldsymbol{x}) \hat{n}_{\mathrm{s}'}(\tau, \boldsymbol{x}') \rangle = \frac{1}{\mathcal{Z}} \oint_\mathrm{A} \mathcal{D}[\overline{\psi}, \psi] \frac{\delta^2}{\delta j_{\mathrm{s}'}(\tau, \boldsymbol{x}') \delta j_\mathrm{s}(\tau, \boldsymbol{x})} e^{-\mathcal{S}_\mathrm{J}[\overline{\psi}, \psi; j]} \bigg|_{j=0}. \tag{5.37}$$

Since we can exchange functional integration and derivative, we define the Z-generating functional as

$$\mathcal{Z}[j] = \oint_\mathrm{A} \mathcal{D}[\overline{\psi}, \psi] e^{-\mathcal{S}_\mathrm{J}[\overline{\psi}, \psi; j]}, \tag{5.38}$$

with which the expectation value (5.36) reads

$$\langle \hat{n}_\mathrm{s}(\tau, \boldsymbol{x}) \hat{n}_{\mathrm{s}'}(\tau, \boldsymbol{x}') \rangle = \frac{1}{\mathcal{Z}[j=0]} \frac{\delta^2 \mathcal{Z}[j]}{\delta j_{\mathrm{s}'}(\tau, \boldsymbol{x}') \delta j_\mathrm{s}(\tau, \boldsymbol{x})} \bigg|_{j=0}. \tag{5.39}$$

Thus the Z-generating functional gives rise to the expectation value via (5.39). However, as we are interested in the response function $\chi_{\mathrm{ss}'}(\tau, \boldsymbol{x}; \tau, \boldsymbol{x}')$, which is the connected expectation value, we introduce a second type of generating functional given by

$$W[j] = \ln \mathcal{Z}[j]. \tag{5.40}$$

We call this W-generating functional, and it yields the connected diagrams [126, 411] via

$$\langle \hat{n}_{\mathrm{s}}(\tau,\boldsymbol{x})\hat{n}_{\mathrm{s}'}(\tau,\boldsymbol{x}')\rangle_{\mathrm{c}} = \left.\frac{\delta^2 W[j]}{\delta j_{\mathrm{s}'}(\tau,\boldsymbol{x}')\delta j_{\mathrm{s}}(\tau,\boldsymbol{x})}\right|_{j=0}. \tag{5.41}$$

Compared to Ref. [126], we have an inverted sign here, since we define χ as the negative of the physical response. Thus, in momentum space, we obtain the response function as

$$\chi_{\mathrm{ss}'}(iq_\ell,\boldsymbol{q}) = \left.\frac{\delta^2 W[j]}{\delta j_{\mathrm{s},-q}\delta j_{\mathrm{s},q}}\right|_{j=0}, \tag{5.42}$$

where $j_{\mathrm{s},q}$ denotes the Fourier-Matsubara transform of the local source term $j_{\mathrm{s}}(\tau,\boldsymbol{x})$ using $q = (iq_\ell,\boldsymbol{q})$ with $q_\ell = 2\ell\pi T$ as bosonic Matsubara frequency.

In the following, we aim to calculate this linear response function for the BEC-BCS crossover in D spatial dimensions, while fulfilling the constraints summarised in Section 5.2.1. We establish the theoretical framework on how to do this in the next section.

5.3 Linear response theory with gauge fixing

We investigate the action already seen in Eq. (3.9), describing a Fermi spin mixture with possibly unequal populations or masses. In our case, we write the action as

$$\mathcal{S}[\overline{\psi},\psi] = \int \mathrm{d}x\, \left\{\sum_{\mathrm{s}}\overline{\psi}_{\mathrm{s}}(x)\left[\partial_\tau - \frac{\nabla^2}{2m_{\mathrm{s}}} - \mu_{\mathrm{s}}\right]\psi_{\mathrm{s}}(x) - g\overline{\psi}_\uparrow(x)\overline{\psi}_\downarrow(x)\psi_\downarrow(x)\psi_\uparrow(x)\right\}. \tag{5.43}$$

Coupling it to a local source term and going to momentum space yields

$$\begin{aligned}\mathcal{S}_{\mathrm{J}}[\overline{\psi},\psi;j] = \beta L^D \sum_{kk'}\Bigg\{&\overline{\psi}_{\mathrm{s},k}\left[(ik_n - \xi^{\mathrm{s}}_{\boldsymbol{k}})\,\delta_{kk'} - j_{\mathrm{s},k-k'}\right]\psi_{\mathrm{s},k'} \\ &- g\sum_q \overline{\psi}_{\uparrow,k}\overline{\psi}_{\downarrow,k'}\psi_{\downarrow,k'+q}\psi_{\uparrow,k-q}\Bigg\},\end{aligned} \tag{5.44}$$

where $\xi^{\mathrm{s}}_{\boldsymbol{k}} = \boldsymbol{k}^2/2m_{\mathrm{s}} - \mu_{\mathrm{s}}$ denotes the free particle dispersion with respect to the spin-dependent chemical potential μ_{s}. We identify the non-interacting Green's function as

$$\mathcal{G}_{\mathrm{s}}(ik_n,\boldsymbol{k}) = \frac{1}{ik_n - \xi^{\mathrm{s}}_{\boldsymbol{k}}}. \tag{5.45}$$

Due to the translational symmetry, $\boldsymbol{k}$ is associated with the relative position $\delta\boldsymbol{r}$ via Fourier transformation. Calculating the Green's functions for an interacting system is harder. To this end, we rely on the Hubbard-Stratonovich (HS) transformation to make analytical progress. In this chapter, we only consider the pairing channel, as deep in the superfluid state, the largest contribution to interaction mediated correlation arises from Cooper pairs. We justify this choice at the end of this chapter, where we will see that including the pair interactions is necessary and sufficient to qualitatively describe experimental observations. A full WHFB evaluation, as in Chapters 3 and 4, will only lead to quantitative improvements and is, therefore, omitted in this stage. When imposing the HS transformation in momentum space, we obtain the HS action as

$$\mathcal{S}_{\mathrm{HS}}[\overline{\boldsymbol{\Psi}},\boldsymbol{\Psi};\overline{\Delta},\Delta;j] = \beta L^D \sum_{kk'}\left\{\overline{\boldsymbol{\Psi}}_k\left[-\boldsymbol{G}^{-1}(k,k')\right]\boldsymbol{\Psi}_{k'} + \frac{|\Delta_{k-k'}|^2}{g}\right\}, \tag{5.46}$$

with the Nambu Gor'Kov spinors

$$\overline{\mathbf{\Psi}}_k = \begin{pmatrix} \overline{\psi}_{\uparrow,k} & \psi_{\downarrow,k} \end{pmatrix}, \qquad \mathbf{\Psi}_{k'} = \begin{pmatrix} \psi_{\uparrow,k'} \\ \overline{\psi}_{\downarrow,k'} \end{pmatrix} \tag{5.47}$$

and the full inverse Green's function

$$\boldsymbol{G}^{-1}(k,k') = \begin{pmatrix} (ik_n - \xi^{\uparrow}_{\boldsymbol{k}})\delta_{k,k'} - j_{\uparrow,k-k'} & -\Delta_{k-k'} \\ -\overline{\Delta}_{k'-k} & (ik_n + \xi^{\downarrow}_{\boldsymbol{k}})\delta_{k,k'} + j_{\downarrow,k-k'} \end{pmatrix}. \tag{5.48}$$

For more details, the reader is referred to Chapter 3. After the HS transformation, the Z-generating functional reads

$$\mathcal{Z}[j] = \oint_{\mathrm{A}} \mathcal{D}[\overline{\psi},\psi] \oint_{\mathrm{P}} \mathcal{D}[\overline{\Delta},\Delta] e^{-\mathcal{S}_{\mathrm{HS}}[\overline{\mathbf{\Psi}},\mathbf{\Psi};\overline{\Delta},\Delta;j]}. \tag{5.49}$$

To obtain the W-generating functional, both functional integrals must be performed. The fermionic integral is done via a Gaussian integral, see Appendix A.2.4, yielding

$$\mathcal{Z}[j] = \oint_{\mathrm{P}} \mathcal{D}[\overline{\Delta},\Delta] e^{-\mathcal{S}_{\mathrm{Eff}}[\overline{\Delta},\Delta;j]}. \tag{5.50}$$

The resulting effective action here is a special case of the one seen in Eq. (3.44), namely for $g_{\mathrm{B}} = g$, $g_{\mathrm{H}} = 0$ and reads

$$S_{\mathrm{Eff}}[j] = \beta L^D \sum_q \frac{|\Delta_q|^2}{g} - \sum_{kk'} \ln \mathrm{Det}\left[-\beta \hat{\boldsymbol{G}}^{-1}\right]. \tag{5.51}$$

The remaining integral over the pair auxiliary field in (5.50) is not so simple and therefore, as in Chapter 3, a saddle-point approximation is performed. Unlike there, in the following we will go beyond the SP theory and evaluate the partition function up to the Gaussian order in the quantum fluctuations of the pair field.

5.3.1 Response theory up to Gaussian approximation

In this section, we decompose the pair field into a static and uniform background and quantum fluctuations. This approach is necessary as any SP approximation fixes the gauge (complex phase) of the superfluid order parameter. Due to the requirement of gauge symmetry, it is necessary to take all possible gauge choices into account. Hence, we expand up to Gaussian pair fluctuations (GPF) and integrate them out, as this corresponds to an integral over all possible gauge choices.

Fluctuation decomposition

We choose to separate the pair field into a SP value and amplitude/phase fluctuations λ,θ, yielding

$$\Delta_q = \Delta_0 \delta_{q,0} + \lambda_q + i\theta_q. \tag{5.52}$$

Both source terms j_{s} and pair fluctuations λ, θ are assumed to be small compared to the other energy scales in the system. As such, we treat those fields on the same footing and summarise them into a source-fluctuation matrix, which is

$$\mathbf{\Xi}_{\mathrm{J}}(k;k') = \begin{pmatrix} -j_{\uparrow,k-k'} & \lambda_{k-k'} + i\theta_{k-k'} \\ \lambda_{k'} - i\theta_{k'-k} & +j_{\downarrow,k-k'} \end{pmatrix}. \tag{5.53}$$

With this, it becomes possible to separate the SP inverse Green's function from the fluctuations via a Dyson equation

$$\boldsymbol{G}^{-1}(k;k') = \boldsymbol{G}^{-1}_{\mathrm{SP}}(k;k') + \boldsymbol{\Xi}_{\mathrm{J}}(k;k'). \tag{5.54}$$

The SP inverse Green's function is analogous to the one seen in Eq. (3.49) up to a vanishing Hartree self-energy term and reads

$$\boldsymbol{G}^{-1}_{\mathrm{SP}}(k;k') = \begin{pmatrix} ik_n - \xi^{\uparrow}_{\boldsymbol{k}} & -\Delta_0 \\ -\overline{\Delta}_0 & ik_n + \xi^{\downarrow}_{\boldsymbol{k}} \end{pmatrix} \delta_{k,k'} = \boldsymbol{G}^{-1}_{\mathrm{SP}}(k)\delta_{k,k'}. \tag{5.55}$$

Using the basis-less notation introduced in Appendix A.2, we expand the effective action (5.51) analogously to the standard GPF procedure outlined in Eq. (2.42). This results in

$$\mathcal{S}_{\mathrm{Eff}}[j] = \mathcal{S}_0 + \mathcal{S}_{\mathrm{Lin}} + \mathcal{S}_{\mathrm{Gauss}} + \mathcal{O}(j,\lambda,\theta)^3. \tag{5.56}$$

The leading order term is independent of the sources and quantum fluctuations, resulting in the SP

$$\mathcal{S}_0 = -\mathrm{Tr}\ln\left(-\beta\hat{\boldsymbol{G}}^{-1}_{\mathrm{SP}}\right) + \beta L^D \frac{|\Delta_0|^2}{g}. \tag{5.57}$$

This action is used to determine the mean-field value of the superfluid order parameter Δ_0 by extremising the action with respect to Δ_0. This reproduces the Leggett-BCS mean-field theory discussed Chapter 2.2.2, or more specifically in Eq. (2.26).

The SP condition of the order parameter is then used to eliminate the fluctuation terms in the linear action, since it turns out to be proportional to $\partial\mathcal{S}_{\mathrm{eff}}/\partial\Delta_0 = 0$. As a consequence, the linear action only consists of source terms, which then reads

$$\mathcal{S}_{\mathrm{Lin}}[j] = \sum_{kq}\sum_{\mathrm{s}} G^{\mathrm{ss}}_{\mathrm{SP}}(k+q) j_{\mathrm{s},q}\delta_{q,0}. \tag{5.58}$$

We keep the general form of the q sum as it is illustrative of the fact that only the zero-momentum component couples to the SP Green's function that is obtained as the matrix inverse of Eq. (5.55). We denote the formal result of the matrix inversion as

$$\boldsymbol{G}_{\mathrm{SP}}(k) = \begin{pmatrix} G^{\uparrow\uparrow}_{\mathrm{SP}}(k) & F^{\uparrow\downarrow}_{\mathrm{SP}}(k) \\ F^{\downarrow\uparrow}_{\mathrm{SP}}(k) & G^{\downarrow\downarrow}_{\mathrm{SP}}(k) \end{pmatrix}, \tag{5.59}$$

with the matrix elements being the same as in Eq. (3.56b) when the Hartree self-energy is set to zero. The matrix elements of the above matrix are related to the Fourier transforms of the real-space Green's functions defined in the context of Wick's theorem (5.18) in a SP approximation. This holds true up to a volume factor, which, for conventional reasons, is added to the Fourier transformation. Thus, we obtain the SP approximation

$$G^{\mathrm{ss}}_{\mathrm{SP}}(k) \approx \int \frac{\mathrm{d}x}{\beta} \int \mathrm{d}(\delta x)\, G_{\mathrm{ss}}(x; x+\delta x) e^{-i\boldsymbol{k}\cdot\delta\boldsymbol{r} + ik_n\delta\tau}, \tag{5.60}$$

with an analogous relation holding for the anomalous Green's functions $F^{\mathrm{ss}'}$ at a SP level. Note that the additional factor β appears because we choose the Green's function to have dimensions of inverse energy.

After the linear term comes the GPF term, which in our case is of second order in λ, θ and the sources j_{s}. The Gaussian action reads

$$\mathcal{S}_{\mathrm{Gauss}} = \frac{1}{2}\mathrm{Tr}\left\{\hat{\boldsymbol{G}}_{\mathrm{SP}}\hat{\boldsymbol{\Xi}}_{\mathrm{J}}\hat{\boldsymbol{G}}_{\mathrm{SP}}\hat{\boldsymbol{\Xi}}_{\mathrm{J}}\right\} + \beta V \sum_q \frac{\lambda_q^2 + \theta_q^2}{g}. \tag{5.61}$$

Evaluating the matrix trace, we summarise all terms in a spinor-matrix notation, i.e.

$$S_{\mathrm{Gauss}}[\lambda,\theta;j] = \frac{\beta}{2}\sum_q \boldsymbol{\phi}_{-q}^{\mathrm{T}}\boldsymbol{\Pi}(q)\boldsymbol{\phi}_q, \tag{5.62}$$

using the spinor

$$\boldsymbol{\phi}_q = \begin{pmatrix}\boldsymbol{j}_q\\ \boldsymbol{\eta}_q\end{pmatrix} \qquad \text{with} \qquad \boldsymbol{j}_q = \begin{pmatrix}j_{\uparrow,q}\\ j_{\downarrow,q}\end{pmatrix} \quad \text{and} \quad \boldsymbol{\eta}_q = \begin{pmatrix}\lambda_q\\ \theta_q\end{pmatrix}. \tag{5.63}$$

We use the regularized Fermi loop functions defined in Eq. (2.54) and restated here

$$\Pi_{ab}(q) = \frac{2L^D\delta_{ab}\zeta_{ab}}{g} - \frac{i^{\delta_{ay}+\delta_{by}}}{\beta}\sum_k \mathrm{tr}\left\{\boldsymbol{G}_{\mathrm{SP}}(k)\boldsymbol{\gamma}_a\boldsymbol{G}_{\mathrm{SP}}(k+q)\boldsymbol{\gamma}_b\right\}, \tag{5.64}$$

with the symmetry factor $\zeta_{ab} = \delta_{ax} + \delta_{ay}$, to simplify the action. Here we have to use the full set of two-particle vertices, which are in our case the first and third Pauli matrices $\boldsymbol{\gamma}_{x,z} = \boldsymbol{\sigma}_{x,z}$, a modified second Pauli matrix $\boldsymbol{\gamma}_y = i\boldsymbol{\sigma}_y$ and the projections onto the spin axis $\boldsymbol{\gamma}_\uparrow = (\boldsymbol{\sigma}_z + \boldsymbol{\sigma}_0)/2$ and $\boldsymbol{\gamma}_\downarrow = (\boldsymbol{\sigma}_z - \boldsymbol{\sigma}_0)/2$ with a statistical sign of the $\downarrow$ projection due to the Nambu notation. We denote as $\boldsymbol{\sigma}_0$ the identity matrix. In general, we call

$$\chi_{ab}(q) = -\frac{1}{\beta}\sum_k \mathrm{tr}\left\{\boldsymbol{G}_{\mathrm{SP}}(k)\boldsymbol{\gamma}_a\boldsymbol{G}_{\mathrm{SP}}(k+q)\boldsymbol{\gamma}_b\right\} = \chi_{ba}(-q) \tag{5.65}$$

the elements of a susceptibility matrix. With this notation, the Gaussian action (5.62) is expressed using the matrix $\boldsymbol{\Pi}(q) = [\Pi_{ab}(q)]_{ab\in\{\uparrow,\downarrow,x,y\}}$ and explicitly reads

$$\boldsymbol{\Pi}(q) = \left(\begin{array}{cc|cc} \Pi_{\uparrow\uparrow}(q) & \Pi_{\uparrow\downarrow}(q) & \Pi_{\uparrow\mathrm{x}}(q) & \Pi_{\uparrow\mathrm{y}}(q)\\ \Pi_{\downarrow\uparrow}(q) & \Pi_{\downarrow\downarrow}(q) & \Pi_{\downarrow\mathrm{x}}(q) & \Pi_{\downarrow\mathrm{y}}(q)\\ \hline \Pi_{\mathrm{x}\uparrow}(q) & \Pi_{\mathrm{x}\downarrow}(q) & \Pi_{\mathrm{xx}}(q) & \Pi_{\mathrm{xy}}(q)\\ \Pi_{\mathrm{y}\uparrow}(q) & \Pi_{\mathrm{y}\downarrow}(q) & \Pi_{\mathrm{yx}}(q) & \Pi_{\mathrm{yy}}(q) \end{array}\right) \tag{5.66}$$

$$= \left(\begin{array}{c|c} -\widetilde{\boldsymbol{\chi}}^{(0)}(q) & -\boldsymbol{\Lambda}^{\mathrm{T}}(q)\\ \hline -\boldsymbol{\Lambda}(q) & \boldsymbol{\Gamma}(q) \end{array}\right). \tag{5.67}$$

This matrix contains all the information about the linear response theory established here. Before integrating out the Gaussian fluctuations λ, θ, we briefly discuss the properties of this matrix and its physical meaning.

Fermi loop matrix

From the definition of the loop functions (5.64), it is straightforward to read off their symmetry $\Pi_{ab}(q) = \Pi_{ba}(-q)$ due to the cyclic property of the trace. The matrix elements of the upper left matrix

$$\widetilde{\boldsymbol{\chi}}^{(0)}(q) = \begin{pmatrix}\widetilde{\chi}^{(0)}_{\uparrow\uparrow}(q) & \widetilde{\chi}^{(0)}_{\uparrow\downarrow}(q)\\ \widetilde{\chi}^{(0)}_{\downarrow\uparrow}(q) & \widetilde{\chi}^{(0)}_{\downarrow\downarrow}(q)\end{pmatrix} \tag{5.68}$$

are the source-source correlation functions, which are obtained using a standard mean-field response theory [106, 174, 187]. They are commonly known as particle-hole bubble diagrams and turn out to pose two-particle reducible responses of the fermionic density to an infinitesimal perturbation. By explicitly evaluating the diagonal responses, we find bubble diagrams of normal Green's functions

$$\widetilde{\chi}^{(0)}_{\mathrm{ss}}(q) = -\frac{1}{\beta}\sum_k G^{\mathrm{ss}}_{\mathrm{SP}}(k)G^{\mathrm{ss}}_{\mathrm{SP}}(k+q), \tag{5.69}$$

while the off-diagonal matrix elements are bubbles of the anomalous Green's functions

$$\widetilde{\chi}^{(0)}_{\mathrm{s\bar{s}}}(q) = \frac{1}{\beta}\sum_k F^{\mathrm{\bar{s}s}}_{\mathrm{SP}}(k) F^{\mathrm{s\bar{s}}}_{\mathrm{SP}}(k+q). \tag{5.70}$$

We evaluate the fermionic Matsubara sum in the Appendix in Eqs. (5.A.2) and (5.A.3). Comparing with the Wick decomposition in real space (5.18) and performing the transformation back to the real space relative distance δr confirms the relation established in the beginning and results in

$$\chi^{(0)}_{\mathrm{ss}}(\delta r) = G^{\mathrm{ss}}_{\mathrm{SP}}(\delta r) G^{\mathrm{ss}}_{\mathrm{SP}}(-\delta r) \tag{5.71a}$$

$$\chi^{(0)}_{\mathrm{s\bar{s}}}(\delta r) = -F^{\mathrm{s\bar{s}}}_{\mathrm{SP}}(\delta r) F^{\mathrm{\bar{s}s}}_{\mathrm{SP}}(-\delta r). \tag{5.71b}$$

Due to the anti commuting nature of the Fermions the Green's functions behave like $G^{\mathrm{ss}}_{\mathrm{SP}}(-\delta r) = [G^{\mathrm{ss}}_{\mathrm{SP}}(\delta r)]^* + \delta(\delta r)$ and $F^{\mathrm{\bar{s}s}}_{\mathrm{SP}}(-\delta r) = [F^{\mathrm{s\bar{s}}}_{\mathrm{SP}}(\delta r)]^*$, where * denotes the complex conjugate. Therefore, we find

$$\chi^{(0)}_{\mathrm{ss}}(\delta r) = -|G^{\mathrm{ss}}_{\mathrm{SP}}(\delta r)|^2 + \delta(\delta r) G^{\mathrm{ss}}_{\mathrm{SP}}(0) \tag{5.72a}$$

$$\chi^{(0)}_{\mathrm{s\bar{s}}}(\delta r) = |F^{\mathrm{s\bar{s}}}_{\mathrm{SP}}(\delta r)|^2. \tag{5.72b}$$

Here also the irregular term is included due to the anti-commutator and imaginary-time ordering, proportional to the thermodynamic particle number $n_{\mathrm{s}} = G^{\mathrm{ss}}_{\mathrm{SP}}(0)$ at the SP.

Next, we investigate the pair fluctuation matrix $\mathbf{\Gamma}(q)$, which in general is the inverse of the pair vertex $\mathbf{\Gamma}^{-1}(q)$. We define it as

$$\mathbf{\Gamma}(q) = \begin{pmatrix} \Gamma_{xx}(q) & \Gamma_{xy}(q) \\ \Gamma_{yx}(q) & \Gamma_{yy}(q) \end{pmatrix}. \tag{5.73}$$

Its entries are the propagators of the collective modes, more specifically $\Gamma_{xx}(q)$ and $\Gamma_{yy}(q)$ stand for the amplitude λ and phase θ propagators, with the respective coupling elements on the off-diagonals $\Gamma_{xy}(q)$ and $\Gamma_{yx}(q)$. By evaluating the trace in the definition of the loop functions (5.64), we obtain the amplitude propagator

$$\begin{aligned}\Gamma_{xx}(q) = \frac{2L^D}{g} + \frac{1}{\beta}\sum_k \big[&G^{\uparrow\uparrow}_{\mathrm{SP}}(k) G^{\downarrow\downarrow}_{\mathrm{SP}}(k+q) + G^{\downarrow\downarrow}_{\mathrm{SP}}(k) G^{\uparrow\uparrow}_{\mathrm{SP}}(k+q) \\ &+ F^{\uparrow\downarrow}_{\mathrm{SP}}(k) F^{\uparrow\downarrow}_{\mathrm{SP}}(k+q) + F^{\downarrow\uparrow}_{\mathrm{SP}}(k) F^{\downarrow\uparrow}_{\mathrm{SP}}(k+q)\big]\end{aligned} \tag{5.74}$$

and the phase propagator

$$\begin{aligned}\Gamma_{yy}(q) = \frac{2L^D}{g} + \frac{1}{\beta}\sum_k \big[&G^{\uparrow\uparrow}_{\mathrm{SP}}(k) G^{\downarrow\downarrow}_{\mathrm{SP}}(k+q) + G^{\downarrow\downarrow}_{\mathrm{SP}}(k) G^{\uparrow\uparrow}_{\mathrm{SP}}(k+q) \\ &- F^{\uparrow\downarrow}_{\mathrm{SP}}(k) F^{\uparrow\downarrow}_{\mathrm{SP}}(k+q) - F^{\downarrow\uparrow}_{\mathrm{SP}}(k) F^{\downarrow\uparrow}_{\mathrm{SP}}(k+q)\big].\end{aligned} \tag{5.75}$$

These two propagators are more complicated objects than the source-source response bubbles appearing in Eq. (5.68), as they now involve not only ladder diagrams of the anomalous Green's functions directly associated with the pairing but also the particle-hole ladders of the normal Green's functions. Due to the appearance of those anomalous Green's functions, the amplitude-amplitude and phase-phase propagators are not invariant under a $\mathrm{U}(1)$-gauge transformation when considered isolated. The coupling element is

$$\begin{aligned}\Gamma_{xy}(q) = \Gamma_{yx}(-q) = i\frac{1}{\beta}\sum_k \big[&G^{\downarrow\downarrow}_{\mathrm{SP}}(k) G^{\uparrow\uparrow}_{\mathrm{SP}}(k+q) - G^{\uparrow\uparrow}_{\mathrm{SP}}(k) G^{\downarrow\downarrow}_{\mathrm{SP}}(k+q) \\ &+ F^{\uparrow\downarrow}_{\mathrm{SP}}(k) F^{\uparrow\downarrow}_{\mathrm{SP}}(k+q) - F^{\downarrow\uparrow}_{\mathrm{SP}}(k) F^{\downarrow\uparrow}_{\mathrm{SP}}(k+q)\big].\end{aligned} \tag{5.76}$$

Note that due to the gauge freedom, most authors choose the saddle-point Δ_0 to be real, which causes the anomalous terms to vanish in the above expression, since $F^{\uparrow\downarrow}(k) = \overline{F^{\downarrow\uparrow}(k)}$. Here we do not make this choice to avoid fixing the gauge as long as possible. By $\Gamma_{xy}(q) = \Gamma_{xy}(-q)$ we find $\Gamma_{xy}(0) = 0$, meaning amplitude and phase decouple for zero momentum and energy. We present the explicit expressions of the pair propagator matrix elements in the Appendix in Eqs. (5.A.4a) and (5.A.4b) for the diagonal entries and in Eq. (5.A.5) for the coupling elements.

Having discussed the collective excitations, we further investigate the coupling matrix $\mathbf{\Lambda}$ between the quantum fluctuations, λ,θ and the density source terms j_s. Due to the cyclic property of the trace, we only need to discuss $\mathbf{\Lambda}$ and can omit $\mathbf{\Lambda}^{\mathrm{T}}$. The matrix reads

$$\mathbf{\Lambda}(q) = \begin{pmatrix} \Lambda_{x\uparrow}(q) & \Lambda_{x\downarrow}(q) \\ \Lambda_{y\uparrow}(q) & \Lambda_{y\downarrow}(q) \end{pmatrix}. \tag{5.77}$$

The couplings of the amplitude fluctuation with the two densities are given by

$$\Lambda_{x\uparrow}(q) = \frac{1}{\beta}\sum_k G^{\uparrow\uparrow}_{\mathrm{SP}}(k)\left[F^{\downarrow\uparrow}_{\mathrm{SP}}(k+q) + F^{\uparrow\downarrow}_{\mathrm{SP}}(k-q)\right], \tag{5.78a}$$

$$\Lambda_{x\downarrow}(q) = -\frac{1}{\beta}\sum_k G^{\downarrow\downarrow}_{\mathrm{SP}}(k)\left[F^{\uparrow\downarrow}_{\mathrm{SP}}(k+q) + F^{\downarrow\uparrow}_{\mathrm{SP}}(k-q)\right], \tag{5.78b}$$

while the couplings of the phase fluctuations to the densities read

$$\Lambda_{y\uparrow}(q) = i\frac{1}{\beta}\sum_k G^{\uparrow\uparrow}_{\mathrm{SP}}(k)\left[F^{\downarrow\uparrow}_{\mathrm{SP}}(k+q) - F^{\uparrow\downarrow}_{\mathrm{SP}}(k-q)\right], \tag{5.79a}$$

$$\Lambda_{y\downarrow}(q) = i\frac{1}{\beta}\sum_k G^{\downarrow\downarrow}_{\mathrm{SP}}(k)\left[F^{\uparrow\downarrow}_{\mathrm{SP}}(k+q) - F^{\downarrow\uparrow}_{\mathrm{SP}}(k-q)\right]. \tag{5.79b}$$

All those coupling matrix elements are not invariant under a global $\mathrm{U}(1)$ gauge transformation. At $q = 0$, they are either proportional to the real or the imaginary part of Δ_0. We will see shortly that this is necessary for a response function with gauge fixing. We present explicit expressions for all the loop functions discussed here in Appendix 5.A.

Having discussed the matrix elements of the 4×4 Fermi loop function matrix (5.66), we continue the calculation by integrating out the Gaussian fluctuations, in order to incorporate the collective excitations into the linear response functions.

5.3.2 Incorporating collective modes

To integrate out the collective modes, we use the fluctuation decomposition of Section 5.3.1 to simplify the Z-generating functional (5.50), which then reads

$$\mathcal{Z}[j] \approx \mathcal{Z}_{\mathrm{SP}} e^{-\mathcal{S}_{\mathrm{Lin}}[j]} \oint_{\mathrm{P}} \mathcal{D}[\lambda,\theta] e^{-\mathcal{S}_{\mathrm{Gauss}}[\lambda,\theta;j]}. \tag{5.80}$$

Here $\mathcal{Z}_{\mathrm{SP}} = \exp(-\mathcal{S}_0)$ uses the zeroth-order action from Eq. (5.57), serving as the source-free SP partition function. We perform the Gaussian functional integral in Eq. (5.80) to obtain the generating functional

$$\mathcal{Z}[j] = e^{W[j]}. \tag{5.81}$$

Up to Gaussian order in the quantum fluctuations and second order in the source terms, the W-generating functional is approximated to be

$$W[j] \approx W_0 + W_1[j] + W_2[j] + \mathcal{O}(j)^3. \tag{5.82}$$

The leading order term is independent of the sources and is given by

$$W_0 = \sum_k \ln\det\left[-\beta \boldsymbol{G}_{\mathrm{SP}}^{-1}(k)\right] - \beta V \frac{|\Delta_0|^2}{g} - \frac{1}{2}\sum_q \ln\det\left[\beta \boldsymbol{\Gamma}(q)\right], \tag{5.83}$$

which is directly related to the GPF thermodynamic potential via $W_0 = -\beta\Omega(L^D, T, \mu_{\mathrm{s}})$. A diagrammatic interpretation of this thermodynamic potential is found in Appendix 5.B. The linear term in the sources turns out to be not directly affected by the quantum fluctuations when they are integrated out, and we obtain from (5.58) the relation

$$W_1[j] = -\sum_k \sum_{\mathrm{s}} G_{\mathrm{SP}}^{\mathrm{ss}}(k) j_{\mathrm{s},0}. \tag{5.84}$$

Lastly, the second-order term gives rise to the linear response function and reads

$$W_2[j] = \frac{\beta}{2}\sum_q \boldsymbol{j}_{-q}^{\mathrm{T}} \widetilde{\boldsymbol{\chi}}(q) \boldsymbol{j}_q. \tag{5.85}$$

In this expression,

$$\widetilde{\boldsymbol{\chi}}(q) = \widetilde{\boldsymbol{\chi}}^{(0)}(q) + \widetilde{\boldsymbol{\chi}}^{\mathrm{irr}}(q) = \begin{pmatrix} \widetilde{\chi}_{\uparrow\uparrow}(q) & \widetilde{\chi}_{\uparrow\downarrow}(q) \\ \widetilde{\chi}_{\downarrow\uparrow}(q) & \widetilde{\chi}_{\downarrow\downarrow}(q) \end{pmatrix} \tag{5.86}$$

denotes the globally gauge invariant density-density linear response function up to Gaussian order in the superfluid fluctuations. The leading term is simply the SP response function found already in Eq. (5.68), while the second term

$$\widetilde{\boldsymbol{\chi}}^{\mathrm{irr}}(q) = \boldsymbol{\Lambda}^{\mathrm{T}}(-q)\boldsymbol{\Gamma}^{-1}(q)\boldsymbol{\Lambda}(q), \tag{5.87}$$

represents the two-particle irreducible contribution seen in the Wick decomposition (5.23) in a Gaussian approximation. The irreducible term captures the collective excitations in the system, the bound states, as well as the vertex corrections, i.e. the self-energy terms. Here $\boldsymbol{\Gamma}^{-1}(q)$ is the matrix inverse of Eq. (5.73) and represents pair vertex, proportional to the T-matrix, of the collective excitations. It is well known that the integer zeros of $\det \boldsymbol{\Gamma}(q)$ give rise to the collective modes in a superfluid [88].

We obtain the matrix-valued response kernel (5.86) via straightforward matrix multiplication, resulting in the matrix elements to be

$$\widetilde{\chi}_{\mathrm{ss}'}(q) = \widetilde{\chi}_{\mathrm{ss}'}^{(0)}(q) + \widetilde{\chi}_{\mathrm{ss}'}^{\mathrm{irr}}(q), \tag{5.88}$$

where the two-particle irreducible part is given by

$$\widetilde{\chi}_{\mathrm{ss}'}^{\mathrm{irr}}(q) = D_{\mathrm{ss}'}(q) - K_{\mathrm{ss}}(q). \tag{5.89}$$

Although this expression has already been encountered in several contexts [121, 126, 395, 398], mostly as an electromagnetic response tensor, the interpretation as irreducible diagrams was not presented so far. Here, the two terms represent different physical quantities. The first expression

$$D_{\mathrm{ss}'}(q) = \frac{\Lambda_{\mathrm{s}y}(q)\Gamma_{xx}(q)\Lambda_{y\mathrm{s}'}(q) + \Lambda_{\mathrm{s}x}(q)\Gamma_{yy}(q)\Lambda_{x\mathrm{s}'}(q)}{\Gamma_{xx}(q)\Gamma_{yy}(q) - \Gamma_{xy}(q)\Gamma_{yx}(q)} \tag{5.90}$$

represents the direct coupling of the densities to the bare amplitude and phase collective modes. This happens via the propagators of the modes and the coupling elements of the other mode to the density The second term

$$K_{\mathrm{ss}'}(q) = \frac{\Lambda_{\mathrm{s}x}(q)\Gamma_{xy}(q)\Lambda_{y\mathrm{s}'}(q) + \Lambda_{\mathrm{s}y}(q)\Gamma_{yx}(q)\Lambda_{x\mathrm{s}'}(q)}{\Gamma_{xx}(q)\Gamma_{yy}(q) - \Gamma_{xy}(q)\Gamma_{yx}(q)} \tag{5.91}$$

describes the influence of the mode mixing on the spin-resolved density-density response. It comes from the fact that at finite momenta and finite energy, the two modes λ and θ mix up to form the collective excitations. No pure amplitude or phase mode exists away from $q = 0$. Speaking of the zero-momentum and zero-energy limit, it is well known that the compressibility matrix [413] is related to the response function at $\boldsymbol{q} = \mathbf{0}$ and $\omega = 0 + i0^+$, with ω being the causal analytic continuation of the Matsubara frequencies on the real line [126]. Hence, the isothermal compressibility reads

$$\kappa_{\mathrm{T}}^{\mathrm{ss}'} = \lim_{\boldsymbol{q}\to\mathbf{0}} \widetilde{\chi}_{\mathrm{ss}'}(0 + i0^+, \boldsymbol{q}) = \widetilde{\chi}^{(0)}_{\mathrm{ss}}(0, \mathbf{0}) + \lim_{\boldsymbol{q}\to\mathbf{0}} \widetilde{\chi}^{\mathrm{irr}}_{\mathrm{ss}'}(0 + i0^+, \boldsymbol{q}), \tag{5.92}$$

where first the frequency has to be taken to $i0^+$ before the momentum limit is taken, since the response function caused by the gapless collective mode shows a discontinuity at $q = (0, \mathbf{0})$. This is a fundamental requirement of response theories taking gauge freedom fully into account, and it is known as the most straightforward Ward-Takahashi identity [394–398, 408, 409]. Furthermore, Ref. [126] shows that a response function derived analogously to our results also agrees with the f-sum rule. However, one has to be careful with the sign there, as in most references, the response is defined with an additional negative sign in order to represent the true system response. Looking at the irreducible contribution to the response function at $q = 0$, straightforward algebra yields $K_{\mathrm{ss}\prime}(0) = 0$. This identity originates in the decoupling of amplitude and phase fluctuations at zero momentum and zero energy, that is $\Gamma_{xy}(0) = 0$. Furthermore, since the phase (Goldstone) mode is gapless at $q = 0$, the phase propagator vanishes, i.e. $\Gamma_{yy}(0) = 0$. Thus, the only contribution to the compressibility coming from the two-particle irreducible term reads

$$\chi^{\mathrm{irr}}_{\mathrm{ss}'}(0 + i0^+, \mathbf{0}) = \Lambda_{\mathrm{s}x}(0)\Gamma^{-1}_{xx}(0)\Lambda_{x\mathrm{s}'}(0). \tag{5.93}$$

Hence, the compressibility is dictated by the off-resonance behaviour of the amplitude mode λ, as the Goldstone mode reacts resonantly at $q = 0$, having no effect on the compression.

Finally, we note that the charge density-density $\langle \hat{n}_{-q}\hat{n}_q \rangle_{\mathrm{c}}$ and the spin density-density $\langle \hat{m}_{-q}\hat{m}_q \rangle_{\mathrm{c}}$ response functions, for $\hat{n} = \hat{n}_\uparrow + \hat{n}_\downarrow$ and $\hat{m} = \hat{n}_\uparrow - \hat{n}_\downarrow$, are separated analogously via

$$\{D\backslash K\}_{nn}(q) = \sum_{\mathrm{ss}'} D\backslash K_{ss'}(q) \tag{5.94}$$

and

$$\{D\backslash K\}_{mm}(q) = \sum_{\mathrm{ss}'} (-1)^{1-\delta_{\mathrm{ss}'}} D\backslash K_{ss'}(q), \tag{5.95}$$

where we use $\backslash$ to denote that those expressions hold for D and K. We mention that when dealing with a spin mixture of two species with equal masses and equal populations, we have that for all spins $\chi^{\mathrm{irr}}_{\mathrm{s}_1\mathrm{s}'_1}(q) = \chi^{\mathrm{irr}}_{\mathrm{s}_2\mathrm{s}'_2}(q)$, meaning that $\chi^{\mathrm{irr}}_{mm}(q) = 0$ and the spin density-density response function is decoupled from the collective modes. This is a direct consequence of the underlying $\mathrm{SU}(2)$ symmetry [394–398].

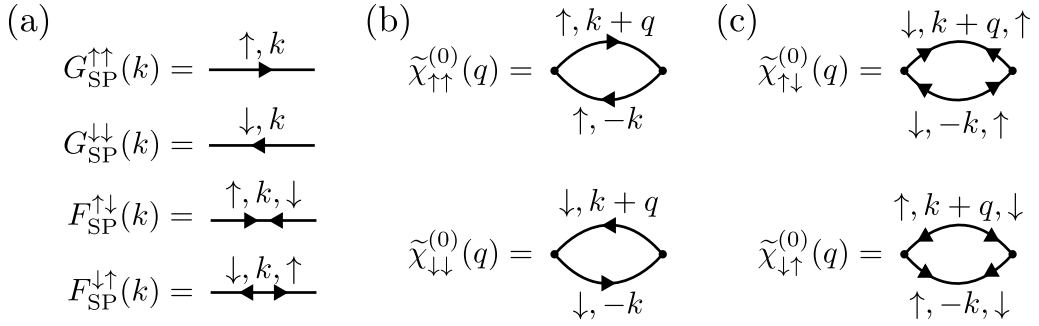


Figure 5.2: Panel (a): Graphical representation of the four distinct single-particle lines associated to either normal or anomalous Green's functions. Panel (b): Normal particle-hole bubbles of equal spin lines. Panel (c): Anomalous bubble diagrams.

5.3.3 Diagrammatic interpretation

To gain further physical insight into the response functions, we use this section to construct all Feynman diagrams that contribute to the two-point correlation functions. To this end, we distinguish between SP diagrams and the irreducible diagrams. Note that we will not discuss the trivial disconnected tadpole diagrams.

Simple Diagrams

In this part, we establish the convention used. This is a generalisation of the notation already introduced in Chapter 2, where we mainly focused on the diagrammatic approach in the normal state. Here we deal with the corresponding diagrams appearing in the superfluid state, causing four fundamental lines, which are depicted in Fig. 5.2 (a). These are the entries of the SP Green's function (5.59). The two normal Green's functions are solid lines with one arrow pointing to the right (particles) or to the left (holes). Additionally, we have the two anomalous Green's functions associated to pairs of particles and holes. These have two arrows, either to the inside of the line (Cooper pair particle) or to the outside (Cooper pair hole). Whenever two or more lines meet, we speak of a local vertex. We introduce the following Feynman rules: Any vertices have to fulfil the conservation of (i) baryonic number, (ii) the total spin, and (iii) obey momentum and energy conservation. All annotated momenta show the momentum flow from left to right. If not otherwise stated, the start- and end-points of the diagrams all have momentum q, which denotes the coupling to the source terms $j_{\mathrm{s},\pm q}$. Any degrees of freedom not fixed from the outside, be it momentum or spin, are implicitly assumed to be summed over, with a multiplicative factor of $1/\beta$ for dimensionality reasons. We use those lines to draw the diagrams associated with the mean-field response in Fig. 5.2 in panel (b) for the normal and in panel (c) for the anomalous bubble diagrams. In all these diagrams, the left and right vertices have momentum q, following the above outlined convention.

We remark that the diagonals of the response kernel (5.68) are normal particle-hole bubbles as they represent correlations of equal-spin fermions, with their functional form given in Eq. (5.69). More interesting are the off-diagonal entries, depicted in panel (c) and indicated by the anomalous bubbles. These show that the correlations of opposite fermions are directly connected to the Cooper pairs found in Eq. (5.70).

After the SP diagrams, we now focus on the individual pieces to construct the two-particle irreducible response up to Gaussian order. First, we have a closer look at the entries of the fluctuation matrix (5.73). When evaluating the matrix traces in the en-

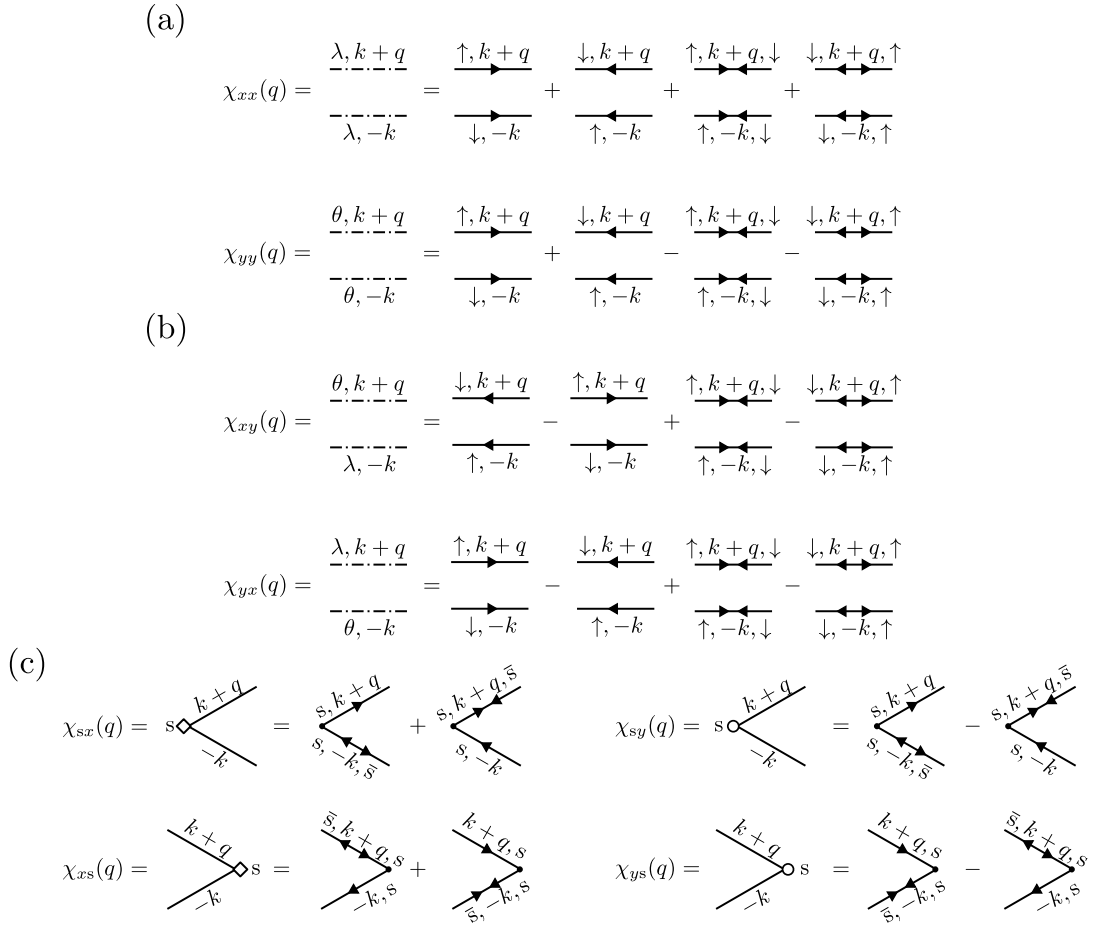


Figure 5.3: Building blocks of two-particle irreducible diagrams. Panel (a) stands for $\lambda-\lambda$ (xx) and $\theta-\theta$ (yy) susceptibilities. Panel (b) shows coupling susceptibility represented as arrow-less dash-dotted parallel lines. In both panels, we find so-called ladder diagrams, as no vertex preserves spin and momentum simultaneously. Panel (c) depicts binding blocks of collective modes and density source terms as external vertices. We denote the amplitude-spin vertices with an empty diamond, whereas the phase-spin ones with empty circles with spin indices.

tries (5.74), (5.75) and (5.76) we find

$$\Gamma_{xx}(q) = \frac{2L^D}{g} - \chi_{xx}(q), \tag{5.96a}$$

$$\Gamma_{yy}(q) = \frac{2L^D}{g} - \chi_{yy}(q), \tag{5.96b}$$

$$\Gamma_{xy}(q) = -i\chi_{xy}(q), \tag{5.96c}$$

$$\Gamma_{yx}(q) = -i\chi_{yx}(q), \tag{5.96d}$$

where the χ functions are the respective loop diagrams, associated to either the amplitude-amplitude (xx), the phase-phase (yy) or their coupling (xy and yx) susceptibilities. Here, we also need the bare interactions yielding an additional Feynman rule. The bare coupling $\overline{g} = g/2L^D$ is represented as a dashed line without a label. All lines connected via a coupling have to fulfil momentum, spin and baryonic number conservation, as the interaction is local in real space. Furthermore, we also consider the couplings for a given spin s to amplitude (x) and phase (y) fluctuations, seen in the matrix (5.77). Again, evaluating the

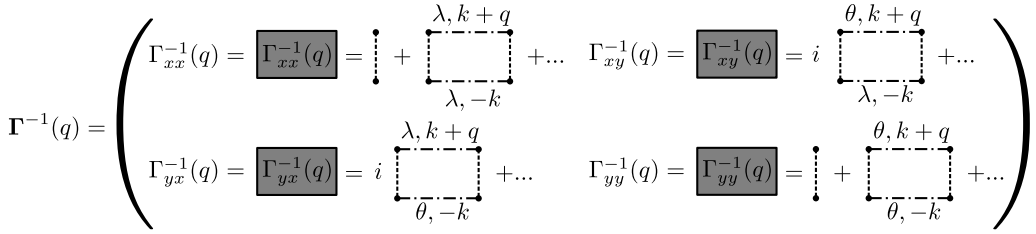


Figure 5.4: Diagrammatic representation of pair vertex (5.98) according to Eq. (5.99) up to $\mathcal{O}(g^2)$ as ladder-like summation.

Nambu-trace yields

$$\Lambda_{xs}(q) = (-1)^{\delta_{s\downarrow}}\chi_{xs}(q) \tag{5.97a}$$

$$\Lambda_{ys}(q) = i\chi_{ys}(q). \tag{5.97b}$$

We illustrate them diagrammatically in Fig. 5.3 with the same Feynman rules as above. Physically, these diagrams represent the vertex coupling of the density sources j_s to the collective modes via a normal and an anomalous propagator. It resembles a process involving the induced interactions via Cooper pairs. More important is the pair vertex function $\mathbf{\Gamma}^{-1}$, which reads

$$\mathbf{\Gamma}^{-1} = \frac{\overline{g}}{(1-\overline{g}\chi_{xx})(1-\overline{g}\chi_{yy}) + \overline{g}^2\chi_{xy}\chi_{yx}} \begin{pmatrix} 1-\overline{g}\chi_{yy} & \overline{g}i\chi_{xy} \\ \overline{g}i\chi_{yx} & 1-\overline{g}\chi_{xx} \end{pmatrix}, \tag{5.98}$$

where we neglected the q arguments for conciseness. To draw actual Feynman diagrams for the irreducible contribution, we expand the above expression in orders of the bare coupling $\overline{g}$ up to second order. As a result, we find a Random-Phase-Approximation (RPA)-like result as a resummation of ladder type, see Chapter 2, which reads

$$\mathbf{\Gamma}^{-1} = \begin{pmatrix} \overline{g} + \overline{g}^2\chi_{xx} & i\overline{g}^2\chi_{xy} \\ i\overline{g}^2\chi_{yx} & \overline{g} + \overline{g}^2\chi_{yy} \end{pmatrix} + \mathcal{O}(\overline{g}^3). \tag{5.99}$$

Hence, we directly observe that the $\lambda - \lambda$ and $\theta - \theta$ matrix elements are of the order $\mathcal{O}(g)$, while the coupling of amplitude and phase is of the order $\mathcal{O}(g^2)$. We illustrate the ladder summations in Fig. 5.4. However, we note that the ladder becomes more complicated from the third order on, as it involves products of susceptibilities in all the matrix elements.

Having established all the building blocks of the diagrammatic representation, we now proceed with constructing the diagrams of the irreducible contribution.

Irreducible diagrams

In this section, we provide a brief discussion of the physical meaning of the irreducible part of the response function (5.89), which we separated into the direct coupling to the amplitude and phase fluctuations $D_{ss'}(q)$ and the contribution coming from the mode-mixing $K_{ss'}(q)$ in Eqs. (5.90) and (5.91), respectively. We see that both functions D and K have the same type of topology. Both couple the source terms to a part of the pair vertex function via the direct exchange of a Cooper pair. We illustrate this in Fig. 5.5. A direct comparison with Fig. 5.4 reveals that D is a RPA summed diagram, as it directly couples to amplitude-amplitude (xx) and phase-phase (yy) fluctuations. For weak interactions, D scales as $\mathcal{O}(g)$, while K is of the order $\mathcal{O}(g)^2$, leading to $K \ll D$, and we can treat

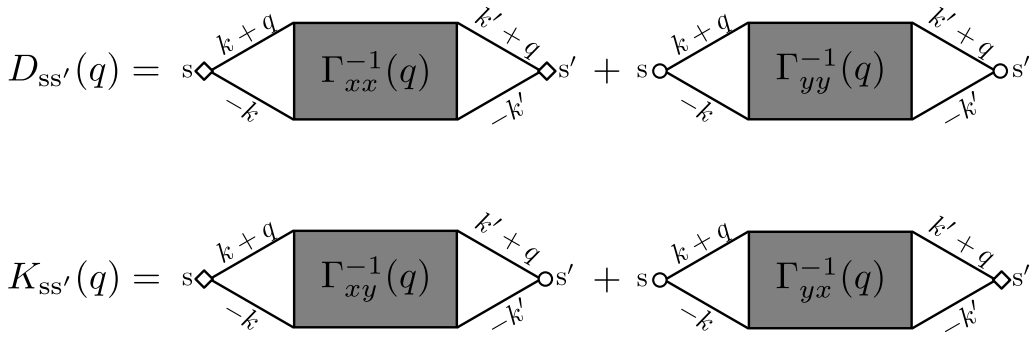


Figure 5.5: Gauge invariant irreducible diagrams in Gaussian fluctuation response tensor, separated into clean $\lambda - \lambda$ or $\theta - \theta$ diagrams in the upper row, $D_{ss'}$ and mode-mixing contributions in the lower row, $K_{ss'}$.

the irreducible diagrams in a perturbative way by only looking at isolated amplitude and phase modes. Only when the interactions grow stronger, the influence of the mode mixing becomes relevant, namely in the BEC limit. The resulting response function $\widetilde{\chi}^{\mathrm{irr}}_{ss'}(q)$ is invariant under $\mathrm{U}(1)$ gauge transformation in any order of g, as we illustrate diagrammatically in Appendix 5.B. This is an important observation and validation of our explicit calculation, as the result agrees with the general statements in Section 5.2.1, where we derived constraints on the correlation and response functions. In Appendix 5.B.2 we go into deeper detail on the structure of the irreducible contribution when expanding it as a ladder-like summation in g, and the consequences for the EoS.

Having thoroughly investigated the response functions systematically and their diagrammatic interpretation, in the following, we combine the information gathered in the last three sections to improve the GPF EoS of the BEC-BCS crossover.

5.3.4 Equation of state and gauge symmetry

To obtain the EoS, various approaches are found in the literature. We focus here on the equations of state, which can be derived in a functional-integral formalism. The standard procedure is to start with the SP EoS, which we already derived previously in Eq. (3.63), in our formulation expressed as

$$n_{\mathrm{SP,s}} = \frac{1}{\beta L^D} \sum_k G^{\mathrm{ss}}_{\mathrm{SP}}(k). \tag{5.100}$$

It is hence governed by only the normal Green's function for equal spins. The second equation of state we consider is the one obtained by including GPF. We derive it via the thermodynamic relation of $N = -\partial\Omega/\partial\mu$, with $\Omega = -TW_0$, which leads to

$$n_{\mathrm{GP,s}} = \frac{1}{\beta L^D} \sum_k G^{\mathrm{ss}}_{\mathrm{SP}}(k) - \frac{1}{2\beta L^D} \sum_q \frac{\partial}{\partial \mu_{\mathrm{s}}} \ln\det\left[\beta \mathbf{\Gamma}(q)\right]. \tag{5.101}$$

Both equations of state (5.100) and (5.101) follow from thermodynamic considerations in the grand-canonical ensemble, which is not locally particle conserving, even though choosing Fermi units later on fixed the total (global) number of particles. This is equivalent to being globally, but not locally $\mathrm{U}(1)$ gauge invariant, which is straightforward to see as both equations of state depend solely on $|\Delta_0|^2$ and hence are not affected by the gauge choice. Since the GPF EoS does not include the local coupling of the density to

the collective excitations via $\mathbf{\Lambda}$, using Eq. (5.101) as an EoS is not a viable option when thinking about experimental setups, where a local particle density is relevant. To take this into account, we consider the fluctuation-dissipation theorem, relating the compressibility matrix and the response functions to a local equation of state. The fluctuation-dissipation theorem [413] reads

$$\chi_{\mathrm{ss}'}(t,\boldsymbol{x};t,\boldsymbol{x}') = \frac{T}{L^{2D}} \frac{\delta^2 W[j]}{\delta j_{\mathrm{s}}(t,\boldsymbol{x})\delta j_{\mathrm{s}'}(t,\boldsymbol{x}')}\bigg|_{j_{\mathrm{s}}=0}, \tag{5.102}$$

which leads to the equal real-time response function in real space and is the Wick rotation of Eq. (5.41). The response in the fluctuation-dissipation theorem has to be equal to the product of the expectation value of two density operators, which for equal positions $\boldsymbol{x} = \boldsymbol{x}'$ and equal spins $\mathrm{s} = \mathrm{s}'$ ultimately leads to the fluctuation-dissipation equation of state reading

$$n^2_{\mathrm{PR,s}} = -\frac{1}{\beta L^{2D}} \sum_q \widetilde{\chi}^{(0)}_{\mathrm{ss}}(q) - \frac{1}{\beta L^{2D}} \sum_q \widetilde{\chi}^{\mathrm{irr}}_{\mathrm{ss}}(q). \tag{5.103}$$

This equation of state is in agreement with gauge symmetry and the Pauli exclusion principle by design, which is why from now on, we refer to it as the Pauli-respecting (PR) EoS. We review the various diagrams that contribute to all equations of state in Appendix 5.B.

The above discussion is valid for any dimensionality D and any mass and population imbalances of the fermions. In the next section, we particularise the discussion to a two-dimensional system, $D = 2$, of a Fermi spin mixture with equal masses and equal populations, since recent experimental developments allow for a direct measurement of the correlation functions in such systems [183–187].

5.3.5 2D BEC-BCS crossover with improved equation of state

In this section, we focus on the three equations of state elaborated in the previous section, namely the SP (5.100), the GPF (5.101) and PR (5.103) equations of state. We evaluate the Matsubara sums at $T = 0$ using the technique described in Appendix B.4, which is imaginary frequency integration. This leads to

$$n_{\mathrm{SP,s}} = \frac{1}{2\pi}\int_0^\infty \mathrm{d}p\, p\left[1 - \frac{\xi_q}{E_q}\right] = \frac{m}{2\pi}\left[\mu + \sqrt{\mu^2 + |\Delta_0|^2}\right] \tag{5.104}$$

for the SP equation of state, using $\xi_p = p^2/(2m) - \mu$ for the free and $E_p = \sqrt{\xi_p^2 + |\Delta_0|^2}$ for the quasiparticle dispersion. Furthermore, we obtain

$$n_{\mathrm{GF,s}} = \frac{1}{2\pi}\int_0^\infty \mathrm{d}p\, p\left[1 - \frac{\xi_q}{E_q}\right] - \frac{1}{4\pi}\int_{-\infty}^\infty \frac{\mathrm{d}q_\ell}{2\pi}\int_0^\infty \mathrm{d}Q\, Q \frac{\partial}{\partial\mu} \ln\det\left[\beta\mathbf{\Gamma}(iq_\ell, Q)\right] \tag{5.105}$$

as the GPF equation of state, already investigated in 2D for instance from Refs. [102, 107], where $Q = |\boldsymbol{q}|$ since the system is isotropic. Lastly, we obtain

$$n^2_{\mathrm{PR,s}} = n^2_{\mathrm{SP,s}} + \frac{1}{4\pi}\int_{-\infty}^\infty \frac{\mathrm{d}q_\ell}{2\pi}\int_0^\infty \mathrm{d}Q\, Q \frac{\widetilde{\chi}^{\mathrm{irr}}_{\mathrm{ss}}(iq_\ell, Q)}{L^2} \tag{5.106}$$

from the PR formulation. The L^2 term is absorbed to solve the $\boldsymbol{k}$-sum in $\widetilde{\chi}^{\mathrm{irr}}_{\mathrm{ss}}(Q, iq_\ell)$ in the thermodynamic limit. In addition, the 2D version of the superfluid order parameter

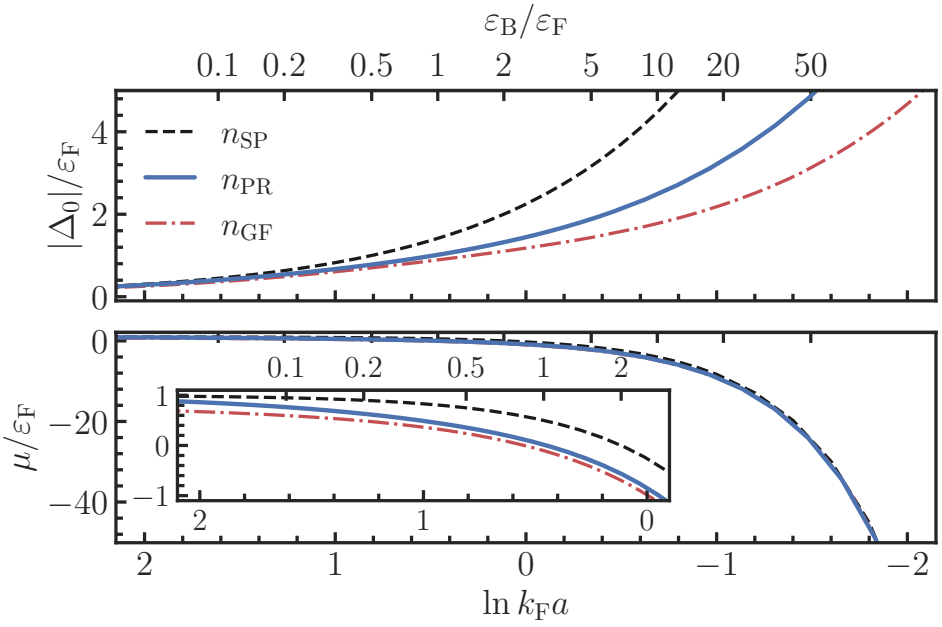


Figure 5.6: Order parameter and chemical potential in units of Fermi energy ε_F versus scattering parameter (lower x-axis) and binding energy (upper x-axis) in upper and lower panel respectively. The left side, i.e. $\varepsilon_B \to 0$ represents BCS side, while $\varepsilon_B \to \infty$ corresponds to BEC limit. Lower panel shows an inset with a zoom to BCS side to better resolve differences between the approaches. Dashed black line stands for the SP, dash-dotted red line for GPF and solid blue line for PR equation of state.
Reprint from [P2] under the terms of the Creative Commons Attribution 4.0 International (CC BY 4.0) license.

equation, $0 = \partial \mathcal{S}_{SP}/\partial \Delta_0$, is used. At $T = 0$ the summation is explicitly solvable [107], leading to

$$|\Delta_0| = \sqrt{\varepsilon_B \left(\varepsilon_B + 2\mu\right)}. \tag{5.107}$$

Since in 2D a contact potential always exhibits a bound state, we use the binding energy $\varepsilon_B > 0$ as interaction parameter, where $\varepsilon_B \to 0^+$ corresponds to the BCS and $\varepsilon_B \to +\infty$ to the BEC side. Fixing the particle number leads now to Fermi units, with the Fermi energy $\varepsilon_F = k_F^2/(2m)$ and the Fermi momentum k_F. This allows us to relate the binding energy and the 2D scattering parameter [414, 415],

$$\ln k_F a = \ln(8\varepsilon_F/\varepsilon_B)/2 - \gamma_E, \tag{5.108}$$

where $\gamma_E \approx 0.577$ is the Euler-Mascheroni constant.

We depict the findings of the three different equations of state in Fig. 5.6, where the upper panel illustrates the order parameter $|\Delta_0|$, while the lower panel depicts the chemical potential μ in units of ε_F against the scattering parameter $\ln k_F a$ (lower x-axis) and the binding energy $\varepsilon_B/\varepsilon_F$ (upper x-axis). The inset illustrates a close-up of the chemical potential in the BCS side. The GPF equation of state overestimates the influence of the bound states as well as vertex corrections by neglecting the coupling of the collective modes to the density itself. This leads to an underestimation of both $|\Delta_0|$ and μ compared to the PR approach, where these effects are consistently accounted for by invoking gauge symmetry and the Pauli principle. Hence, our novel PR results always lie between SP and GPF theory because it allows for a self-consistent feedback loop between density and collective excitations.

Case	Equation of state	Response function	Gauge	Pauli	Line style
I	SP (5.104)	only $\widetilde{\chi}^{(0)}_{ss'}$ (5.68)	✓	✓	dashed black
II	SP (5.104)	full $\widetilde{\chi}_{ss'}$ (5.88)	✓	×	dotted green
III	GPF (5.105)	full $\widetilde{\chi}_{ss'}$ (5.88)	✓	×	dash-dotted red
IV	PR (5.106)	full $\widetilde{\chi}_{ss'}$ (5.88)	✓	✓	solid blue

Table 5.1: Table for different cases covering distinct levels of approximation, depending on the preservation (✓) or violation (×) of gauge invariance (Gauge) and the Pauli exclusion principle (Pauli). The corresponding line styles for figures 5.7, 5.8, 5.9, 5.11 and 5.12 are indicated as well.

These are important findings that may impact various applications in the context of 2D superfluids and are straightforward to extend to three dimensions or to population imbalance. In the remainder of this chapter, we will focus on one particular consequence, which is the prediction of anti-bunching of opposite-spin fermions.

5.4 Real-space correlation functions

In this section, we focus on the findings our improved equation of state provides when considering the density-density correlation function in a spin-resolved way, namely $g^{(2)}_{\uparrow\uparrow}$ and $g^{(2)}_{\uparrow\downarrow}$, as well as the charge density-density correlation function $g^{(2)}_{nn}$. The remainder of the chapter will follow a general convention for the figures and discussions based on the involved equation of state and the approach we use for the correlation functions, shown in Table 5.1. We discuss four different combinations of results for the correlation functions and equations of state in figures 5.7, 5.8, 5.9, 5.11 and 5.12:

I: Using the SP equation of state and the standard SP correlation functions, as done for instance in Refs. [106, 174, 187]. This provides reference curves, as they stem from a globally gauge invariant equation of state with a Pauli principle respecting response function. The results are presented as dashed black lines.

II: Using the SP equation of state and the correlation functions including the irreducible terms, a procedure which is close to what was proposed in Refs. [397, 398]. These curves are depicted as dotted green lines.

III: Using the GPF equation of state together with the full correlation function including the irreducible terms. This is the standard fluctuation approach to the correlation functions, similar to the treatment in supplemental material of Ref. [107]. We illustrate those as dash-dotted red curves.

IV: Using the fully gauge invariant equation of state derived in this section. In addition, the correlation functions, including the irreducible contributions, are considered. We represent the findings extending our original publication [P2] as solid blue lines.

We exploit the rotational symmetry of the system, allowing us to evaluate the azimuthal angle integral, resulting in a Bessel function of the first kind in 2D. Furthermore, in the ground state, the Matsubara sum becomes an integral along the imaginary line, see Appendix B.4, ultimately resulting in

$$g^{(2)}_{\uparrow\downarrow}(\delta r) = 1 + \int_{-\infty}^{\infty} \frac{\mathrm{d}q_\ell}{2\pi} \int_0^{\infty} \frac{\mathrm{d}Q}{2\pi}\, Q\, \widetilde{\chi}_{\uparrow\downarrow}(Q, iq_\ell) J_0(Q\delta r), \tag{5.109}$$

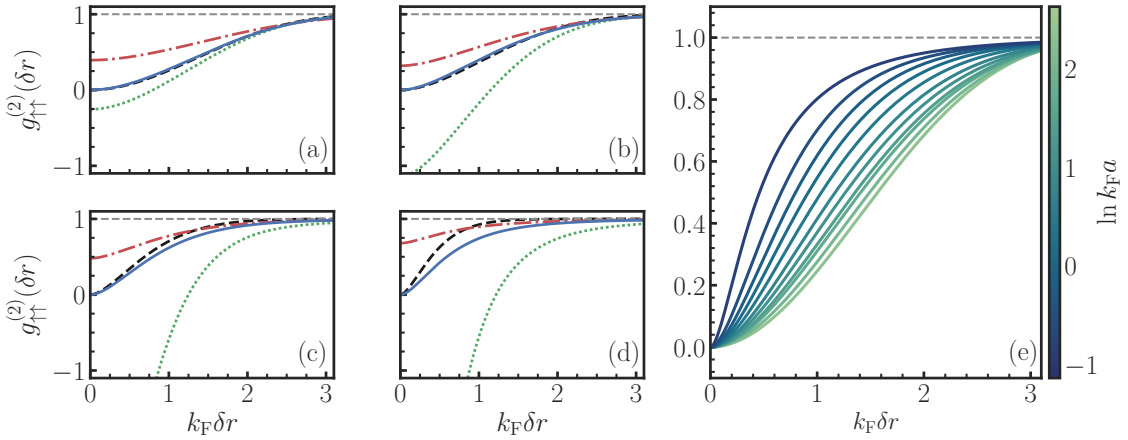


Figure 5.7: Equal-spin density-density correlation function in case I (dashed black line), case II (dotted green line), case III (dash-dotted red line) and case IV (solid blue line) for different scattering parameters. Those are $\ln k_F a = 2.1$ in (a), $\ln k_F a = 1.1$ in (b), $\ln k_F a = 0$ in (c) and $\ln k_F a = -0.6$ in panel (d). Finally, panel (e) shows case IV for large range of scattering parameters illustrated by colour code.

with $Q = |\boldsymbol{q}|$ and $\delta r = |\delta \boldsymbol{r}|$. For case I we replace $\widetilde{\chi}_{ss'}(Q, iq_\ell)$ with the SP response function $\widetilde{\chi}^{(0)}_{ss'}(Q, iq_\ell)$. To obtain the charge density-density correlation function we use $g^{(2)}_{nn}(\delta r) = \sum_{ss'} g^{(2)}_{ss'}(\delta r)/4$ since $n_\uparrow = n_\downarrow$. In the following, we analyse the three different correlation functions separately, starting with the equal-spin case.

5.4.1 Equal-spin density-density correlations

In this section, we investigate $g^{(2)}_{ss}(\delta r)$. Because of $\mathrm{SU}(2)$ symmetry, we only investigate the case for $s = \uparrow$. This correlation function includes the irregular term at $\delta r = 0$, as $\widetilde{\chi}_{\uparrow\uparrow}$ probes the density-density correlation function. Due to our numerical routine, we show only $\delta r > 0$, which is why our result is indistinguishable from the pair correlation function.

We evaluate both integrals in Eq. (5.109) numerically, whose results are shown in Fig. 5.7. Here panels (a) to (d) each depict all four cases discussed in Table 5.1 for different interaction strengths ranging from the BCS to the BEC limit, with panel (a) representing $\ln k_F a = 2.1$, panel (b) showing $\ln k_F a = 1.1$, panel (c) $\ln k_F a = 0$ and finally panel (d) depicts $\ln k_F a = -0.6$. We observe that only the two cases I and IV fulfil the Pauli principle, i.e. follow $g^{(2)}_{\uparrow\uparrow}(\delta r) \to 0$ as $\delta r \to 0$. On the other hand, case II, using the SP EoS together with the gauge invariant response function, undershoots the correlation function, leading to a negative correlation function at small distances. This is unphysical as $g^{(2)}_{ss'}$ measures a scaled number of particles. Case III, in contrast, using the GPF EoS and the gauge invariant response function, overshoots the correlations, which cause the Pauli hole to be filled up to a certain degree. In case II, the violation of the exclusion principle becomes larger for stronger interactions. In case III, the violation of the Pauli principle is quantitatively smaller, but nevertheless this disqualifies the approach. This shows that the vertex corrections presented by the Λ functions are indispensable, not only for the correlation functions, but also to obtain the correct equation of state. The failure of both cases II and III illustrates the increasing importance of the vertex corrections, present only in the EoS discussed in case IV. Comparing the two theoretically consistent cases I and IV for weak interactions, we see that the SP (case I) and the self-consistent fluctuation results

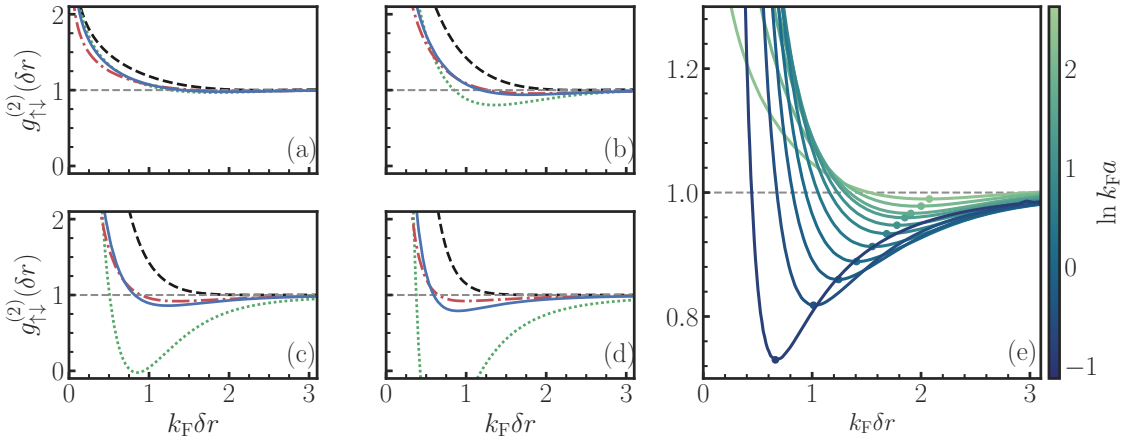


Figure 5.8: Opposite-spin density-density correlation function evaluated for cases I (dashed black line), II (dotted green line), III (dash-dotted red line) and IV (solid blue line) for various scattering parameters: $\ln k_F a = 2.1$ in (a), $\ln k_F a = 1.1$ in (b), $\ln k_F a = 0$ in (c) and $\ln k_F a = -0.6$ in panel (d). Panel (e) depicts case IV for large range of $\ln k_F a$ denoted by a colour code.

(case IV) produce indistinguishable equal-spin density-density correlation functions. This is because most fermions are essentially free particles. Thus, the influence of interactions encapsulated in the irreducible terms has to be small. For stronger interactions, see in particular panels (c) and (d), where we are in the crossover, and BEC regime, the SP and PR correlation functions deviate, with the SP approaching a fully uncorrelated system much faster. This manifests in a closing of the Pauli hole, which corresponds to the drop of $g^{(2)}_{\uparrow\uparrow}$ to 0 at small distances. This closing does not happen as fast in the PR approach, where fluctuations reduce the order in the system. This shows that the mean-field theory overestimates the influence of pairs in the strong coupling regime. A quantitative illustration of the PR approach is seen in Fig. 5.7 (e), where we depict the results of case IV for interaction parameters ranging from $\ln k_F a = 2.5$ (BCS) to $\ln k_F a = -1$ (BEC), corresponding to binding energies of $\varepsilon_B = 0.02\ \varepsilon_F$ to $\varepsilon_B = 18.6\ \varepsilon_F$, encoded by the colour bar. From weak to strong interactions, the Pauli hole is continuously shrinking. For weak interactions, $\ln k_F a > 0$ the size of the Pauli hole barely changes, and for $\ln k_F a \to \infty$, $\varepsilon_B \to 0$ it approaches a universal shape, which we identify with the Pauli hole of the ideal Fermi gas. In contrast, at strong interactions, that is for negative $\ln k_F a$ or for $\varepsilon_B \gg \varepsilon_F$, the width of the Pauli hole changes a lot with the interaction strength. This is due to the pairs being more tightly bound, which causes the gas to behave similarly to a system of composite bosons, which are only affected by their composing fermions at small distances. For distances larger than the pair size, equal-spin particles are essentially uncorrelated due to a lack of equal-spin interactions. This was also seen in recent experiments and supported by QMC calculations [187]. A deeper analysis of the experimental findings needs more details about opposite-spin and charge correlation functions and is found in Section 5.5. Therefore, next we analyse the opposite-spin density-density correlation function.

5.4.2 Opposite-spin density-density correlations

In this section, we evaluate the opposite-spin density-density correlation function $g^{(2)}_{s\bar{s}}(\delta r)$. Like in the previous section, the explicit choice of spins is irrelevant due to $\mathrm{SU}(2)$ symme-

try, which is why we restrict the discussion to $g^{(2)}_{\uparrow\downarrow}(\delta r)$. Since we deal with opposite spins, no irregular terms are present, meaning density-density and pair correlation functions are identical.

We again evaluate the correlation functions numerically, showing our results in Fig. 5.8. As in the previous section, we choose to depict the four approaches discussed in Table 5.1 for interaction parameters of $\ln k_\mathrm{F} a = 2.1$ in panel (a), $\ln k_\mathrm{F} a = 1.1$ in panel (b), $\ln k_\mathrm{F} a = 0$ in panel (c) and finally $\ln k_\mathrm{F} a = -0.6$ in panel (d). A first remark is that, even though the opposite-spin correlations also rule out case II, as in panel (d), the opposite spin correlation function becomes negative. An argument like this is not possible for case III, represented by the dash-dotted red line. However, we know from the equal-spin correlation functions that this approach is disqualified because it violates the Pauli principle. Therefore, we will not discuss further the dotted green or dash-dotted red line in this section. However, before dismissing cases II and III, it is worth mentioning that the opposite-spin correlation functions in all approaches diverge like $\ln^2(k_\mathrm{F}\delta r)$ at small distances. The prefactor of this divergence, up to numerical constants, is known as Tan's contact [357]. We already discussed it in the context of the 3D WHFB approach in Section 4.4. Analysing the SP evaluation of case I, illustrated as the dashed black line, we notice that the correlation function is strictly larger than 1. This was already expected due to the functional form in real space observed in Eq. (5.29). Since in case I the irreducible terms are not present, the correlation function reads

$$g^{(2)}_{\uparrow\downarrow,\mathrm{SP}}(\delta r) = 1 + \frac{|F_{\uparrow\downarrow}(\delta r)|^2}{n_\uparrow n_\downarrow}, \tag{5.110}$$

with the homogeneous anomalous Green's function $F_{\uparrow\downarrow}(\delta r) = F_{\uparrow\downarrow}(0,0;0,|\delta \boldsymbol{r}|)$. Comparing this case to case IV we see that the irreducible parts, which are negative in this case, lead to an anti-bunching at intermediate distances. We define anti-bunching as a region of the correlation function below the uncorrelated value of 1. Interestingly, this has recently been experimentally observed for the first time in Ref. [187] in a 2D spin-mixture of ^{6}Li. This is a non-trivial effect of the coupling of the collective excitations in the system to the density via the vertex $\boldsymbol{\Lambda}$. The physical origin of this effect lies in the irreducible term, which reduces correlations in the system due to pair fluctuations. What is happening microscopically is that opposite-spin particles attract and hence approach each other. This causes an excess of opposite-spin fermions at small separations, but leaves a lack of particles at distances of the order of the non-interacting average distance between atoms, due to the local particle number conservation in our theory. For large distances, we see that $g^{(2)}_{\uparrow\downarrow}(\delta r)$ approaches 1 from below, which agrees with the expectation of a free Bose gas.

We go further into detail in Fig. 5.8 (e), showing the results of case IV for opposite-spin density-density correlation function versus the dimensionless distance $k_\mathrm{F}\delta r$ for a set of interaction parameters $\ln k_\mathrm{F} a$ ranging from 2.5, to $\ln k_\mathrm{F} a = -1$. We represent the minimum for each scattering parameter as a dot in the respective colour. In general, weaker interactions cause a smaller dip of the correlation below 1, which occurs at larger separations compared to stronger interactions. For strong interactions, the minimum is deeper, showing the stronger binding between opposite-spin particles. An in-depth discussion of the correlation minimum will follow in Section 5.5. Before doing so, we use the upcoming section to combine the equal- and opposite-spin correlation functions to discuss the charge correlation function, which is the easiest to access experimentally.

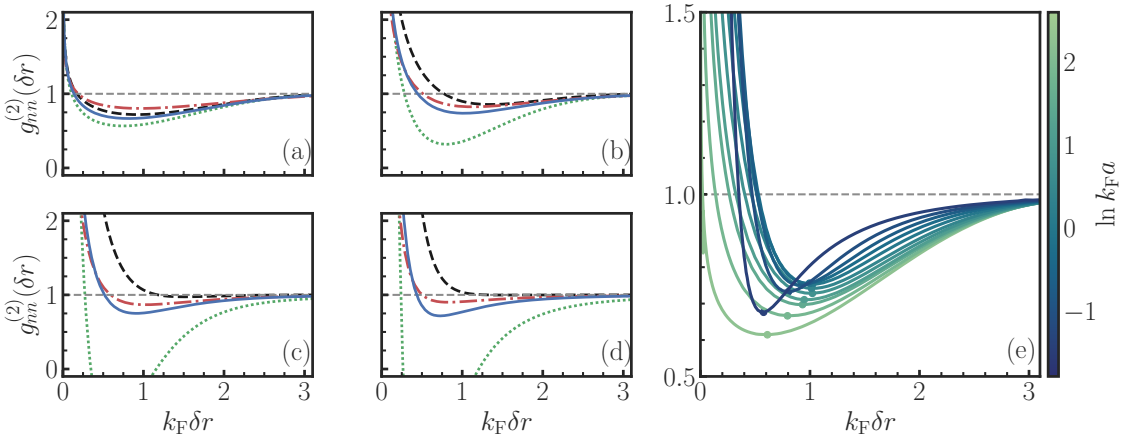


Figure 5.9: Charge density-density correlation function $g^{(2)}_{nn}$ for cases I (dashed black line), II (dotted green line), III (dash-dotted red line) and IV (solid blue line) using a set of scattering parameters being $\ln k_F a = 2.1$ in panel (a), $\ln k_F a = 1.1$ in (b), $\ln k_F a = 0$ in (c) and $\ln k_F a = -0.6$ in (d). Panel (e) represents charge correlation function in case IV for a range of $\ln k_F a$ denoted by a colour code.

5.4.3 Charge density-density correlations

We investigate the charge density-density correlation function by adding the equal- and opposite-spin correlation functions, see Eq. (5.8). We present the results in Fig. 5.9, where in panels (a) to (d) we again compare the four approaches, cases I to IV, for $\ln k_F a = 2.1$ in panel (a), $\ln k_F a = 1.1$ in panel (b), $\ln k_F a = 0$ in panel (c) and finally $\ln k_F a = -0.6$ in panel (d). In this evaluation, we discard the discussion of cases II and III because of the already mentioned violations of the Pauli principle. However, for the sake of completeness, these cases are nevertheless shown in the figure. As in the previous two cases, we see that in the weakly interacting limit, panel (a), the two cases I an IV are close to one another, as the irreducible terms are small compared to the reducible contributions and the bound states have a small binding energy, that is $\varepsilon_B \ll \varepsilon_F$. On the other hand, when going to larger interactions as in panels (c) and (d), we see that in case I, representing the SP theory as dashed black line, the correlation hole below 1 closes. This comes from the Pauli hole shrinking, compare for instance the dashed black line in Fig. 5.7 (c) and (d). Conversely, in case IV the behaviour of the correlation hole changes dramatically for strong interactions, since the irreducible term grows, enlarging the anti-bunching in $g^{(2)}_{\uparrow\downarrow}$, while the shrinking Pauli hole in $g^{(2)}_{\uparrow\uparrow}$ makes equal-spin particles essentially uncorrelated. This causes the charge correlation function to retain an anti-correlated region at distances around $k_F\delta r \in \mathcal{O}(1)$. Again, as for the opposite-spin correlations, this is related to the local conservation of particles.

We investigate case IV in more detail in Fig. 5.9 panel (e), where we illustrate a large set of scattering parameters from the BCS side $\ln k_F a = 2.5$, to the BEC side $\ln k_F a = -1$. For weak interactions, i.e. $\ln k_F a \gg 1$, the anti-correlation is large in magnitude and spans a large range of separations $k_F\delta r$. This comes from $g^{(2)}_{\uparrow\uparrow}$ exhibiting a large Pauli hole, while at the same time the divergence in $g^{(2)}_{\uparrow\downarrow}$ is happening at small distances. The minimum in $g^{(2)}_{nn}$ is therefore mostly determined by the equal-spin properties. When slightly increasing the interaction, the Pauli hole does not change much, while the divergence of the opposite-spin correlation function becomes more pronounced, ultimately taking over

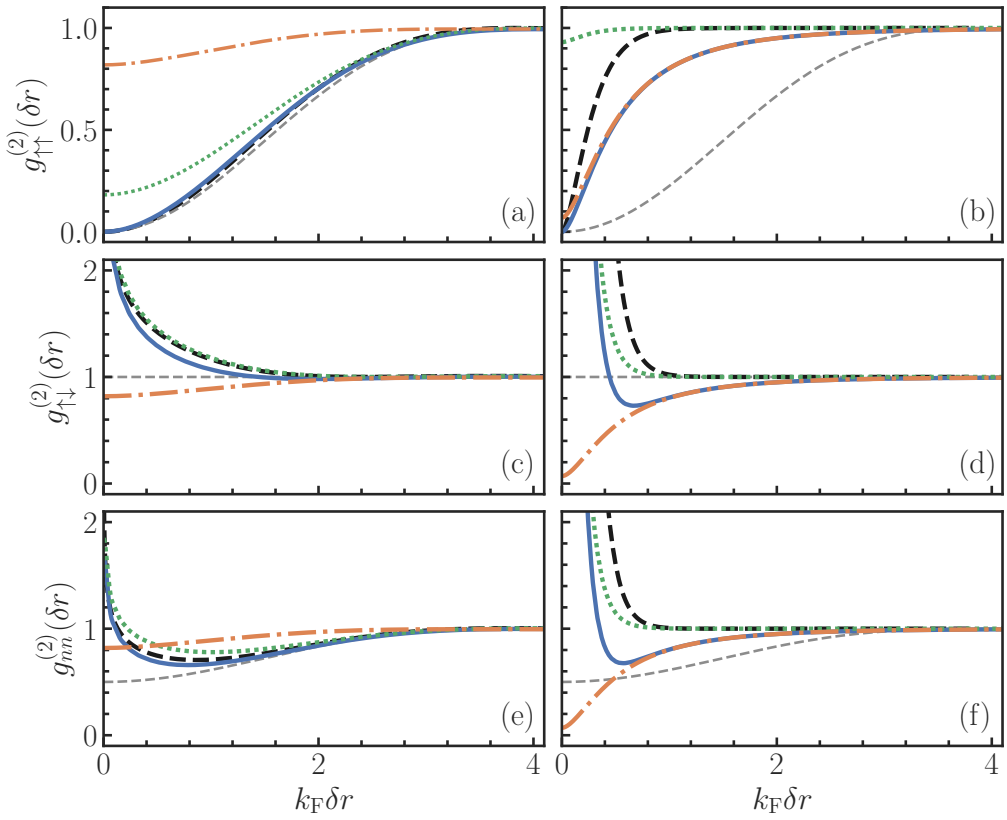


Figure 5.10: Correlation contributions to the full equal-spin, panels (a) and (b), opposite-spin, panels (c) and (d), as well as charge, panels (e) and (f), density-density correlation functions. Interaction parameters in panels (a), (c), (e): $\ln k_F a = 2.1$ (BCS limit), and $\ln k_F a = -1.1$ (BEC limit) in panels (b), (d) and (f). Dashed black line shows the SP reference curve, dashed grey depicts ideal Fermi gas. Solid blue line depicts case IV result, dotted green curve represents $g^{(2)}_{\mathrm{red},ss'}(\delta r)$, while dash-dotted orange line stands for $g^{(2)}_{\mathrm{irr},ss'}(\delta r)$.

and closing the correlation hole in $g^{(2)}_{nn}$. However, when the interactions become strong, towards the crossover regime and beyond, as we discussed in the previous section, the Pauli hole shrinks, making the equal-spin components of the gas uncorrelated outside a narrow range of separations near the origin. At the same time, the correlation hole in $g^{(2)}_{\uparrow\downarrow}$ grows, making it the dominant over the equal-spin correlation function. As a result, the charge density-density correlation function starts to be solely determined by $g^{(2)}_{\uparrow\downarrow}$, meaning that the trend of a closing anti-correlation reverts and the correlation hole grows again. This effect is best seen by analysing the marked dots in panel (e), showing the position of the minimum as well as its depth.

Before analysing the minima, we want to first understand what the direct influence of the terms in case IV actually is. Hence, in the next section, we focus solely on case IV and discuss the contributions coming from the reducible and irreducible terms separately.

5.4.4 Influence of irreducible terms

In this section, we examine the various contributions to the full correlation functions (5.109) using the locally gauge invariant linear response function (5.88) and the EoS (5.106). We

make this comparison in Fig. 5.10 for two distinct scattering parameters, $\ln k_{\mathrm{F}} a = 2.1$ in the left and $\ln k_{\mathrm{F}} a = 0$ in the right column. We added two reference lines, already discussed in the previous sections, that are the dashed black line, i.e. case I, and the dashed grey line, representing the ideal Fermi gas. The solid blue line stands for case IV result, which is obtained via Eq. (5.88). We make use of the decomposition in this equation to define the correlation obtained via the reducible terms as

$$g^{(2)}_{\mathrm{red},\mathrm{ss}'}(\delta r) = 1 + \int_{-\infty}^{\infty} \frac{\mathrm{d}q_\ell}{2\pi} \int_0^{\infty} \frac{\mathrm{d}^2 Q}{(2\pi)^2}\, Q\, \widetilde{\chi}^{(0)}_{\mathrm{ss}'}(Q, iq_\ell) J_0(Q\delta r), \tag{5.111}$$

as well as the correlations coming from the irreducible terms

$$g^{(2)}_{\mathrm{irr},\mathrm{ss}'}(\delta r) = 1 + \int_{-\infty}^{\infty} \frac{\mathrm{d}q_\ell}{2\pi} \int_0^{\infty} \frac{\mathrm{d}^2 Q}{(2\pi)^2}\, Q\, \widetilde{\chi}^{\mathrm{irr}}_{\mathrm{ss}'}(Q, iq_\ell) J_0(Q\delta r), \tag{5.112}$$

illustrated in the dotted green and dash-dotted orange lines, respectively. We observe that for weak interactions (left column), the reducible terms dominate the full correlation function. This is true for all three versions of the density-density correlation function. Physically, this is straightforward to understand as, when dealing with weak interactions, the energy of the bound state is small, being $\varepsilon_{\mathrm{B}} = 0.04\ \varepsilon_{\mathrm{F}}$. This means that the bound states are too weak and too delocalized to alter the system's overall behaviour away from a purely fermionic nature. In other words, the gas consists primarily of free fermions with weak attractive interactions, whose behaviour is well captured by a SP description.

In contrast, when considering strong interactions with a binding energy of $\varepsilon_{\mathrm{B}} = 23\ \varepsilon_{\mathrm{F}}$ (right column), almost all fermions are found in two-body bound states, and only a small fraction of fermions act as unbound particles. The gas behaves more like a gas of composite bosons with a small spatial extent compared to the mean distance between two particles. This becomes evident when considering the equal-spin correlation function in panel (b), where the reducible correlation function only deviates slightly from 1, while the full correlation function follows the irreducible term. For the opposite-spin and charge density-density correlation function, we observe a dominance of the irreducible contributions only for larger separations. Only for those ranges of separations, the full correlation function follows $g^{(2)}_{\mathrm{irr},\mathrm{ss}'}(\delta r)$. For small distances, the composite bosons follow their fermionic nature and the pairing divergence. Therefore, at small distances, two-body physics is observed, while at large separations, low-energy collective excitations dominate. This makes sense also considering that at $T = 0$ the Goldstone mode is excited due to small quantum fluctuations. As no thermal fluctuations are present, the pair breaking and the amplitude mode are only relevant via virtual processes. These modes are all captured in the irreducible term and are the main source of correlations at distances comparable with the possible wavelengths of the Goldstone mode.

After understanding the physical reasons behind the anti-correlation effects and the role that the irreducible diagrams play, we continue in the upcoming section by performing a qualitative comparison with recent experimental data and making predictions.

5.5 Anti-bunching of fermions in the continuum

This section is divided into two separate parts. In the first part, we compare our results, discussed in the previous section, directly with recent experimental data and QMC calculations found in Ref. [187]. The data is obtained via continuous quantum gas microscopy,

Column	$\ln k_\mathrm{F} a^\mathrm{theo}$	$\ln k_\mathrm{F} a^\mathrm{exp}$	$\varepsilon_\mathrm{B}^\mathrm{theo}\ [\varepsilon_\mathrm{F}]$	$\varepsilon_\mathrm{B}^\mathrm{exp}\ [\varepsilon_\mathrm{F}]$	$T^\mathrm{exp}\ [T_\mathrm{F}]$
1	2.15	$2.08^{+0.13}_{-0.13}$	0.03	$0.04^{+0.01}_{-0.01}$	0.11 ± 0.02
2	1.17	$1.21^{+0.10}_{-0.09}$	0.24	$0.22^{+0.04}_{-0.04}$	0.09 ± 0.01
3	1.01	$0.98^{+0.09}_{-0.09}$	0.33	$0.36^{+0.06}_{-0.06}$	0.09 ± 0.01
4	0.68	$0.66^{+0.06}_{-0.06}$	0.65	$0.67^{+0.11}_{-0.11}$	0.08 ± 0.01
5	0.36	$0.28^{+0.06}_{-0.08}$	1.23	$1.44^{+0.23}_{-0.17}$	0.08 ± 0.01

Table 5.2: Comparison of parameters used in numerical evaluation of correlation functions in Fig. 5.11 and experimental parameters found when evaluating the data and used for the auxiliary field QMC calculation [187]. We present the values sorted by the columns of Fig. 5.11 and give theoretical and experimental values of scattering parameter $\ln k_\mathrm{F} a$, binding energy ε_B in units of ε_F and temperature. The temperature used in our theoretical evaluation is always $T^\mathrm{theo} = 0$.

developed recently by several groups [183–187] for Fermi and Bose quantum gases. The QMC data is obtained via auxiliary field QMC methods, which is a numerical procedure close to the HS transformation formulation we use in our analytic approach. In the second part, we use the numerically obtained data to make predictions on the location and depth of the correlation hole for equal- and opposite-spin correlation functions, which are possibly experimentally measurable within the near future.

5.5.1 Comparison with experiment

In the recent experimental work of Ref. [187], a 2D spin-mixture of equal populations, $n_\uparrow = n_\downarrow$ of ^{6}Li has been prepared in a homogeneous 2D trap, with a tight harmonic confinement in the third dimension. As such, for weak interactions, their data can be seen as a strict 2D gas. For strong interactions, there is, however, the possibility of exciting higher modes in the third dimension, making the gas a quasi-2D gas. Therefore, comparing the experimental data with a pure 2D theory is only viable for weak interactions, as no good 2D confinement is possible for strong interactions.

We present our findings in comparison with experimental results in Fig. 5.11, where the solid blue line represents case IV, i.e. the Gaussian fluctuation response function with PR EoS. The dashed line stands for the mean-field correlation function, denoted by case I from Table 5.1, the orange points show measurements obtained with CQGMs and the dotted cyan line auxiliary field QMC calculations, both from Ref. [187]. First, we consider the equal-spin correlation function in the upper row of Fig. 5.11. For weak interactions, the measurement of $g^{(2)}_{\uparrow\uparrow}$ shows the Pauli hole, tending to 0 as small separations are approached. For stronger interactions, this is no longer true as higher z-dimension modes are occupied. Due to the measurement method, different particles appear at the same position in the 2D projection, while their positions in the third dimension are not directly resolvable. Hence, there is an offset for the equal-spin correlation function at zero separation, constituting a measure of the quality of 2D confinement. Besides this effect, the general trend in the experimental data and the QMC results is that the Pauli hole is bigger than expected from the mean-field evaluation, especially for stronger interactions. This qualitatively agrees with our observation, but not to the extent predicted by QMC calculations. A possible explanation is that non-Gaussian fluctuations become important at larger interaction strengths in 2D and a different EoS is used in the QMC calculation. Furthermore, we restricted the calculation to $T = 0$, while QMC calculations were performed at

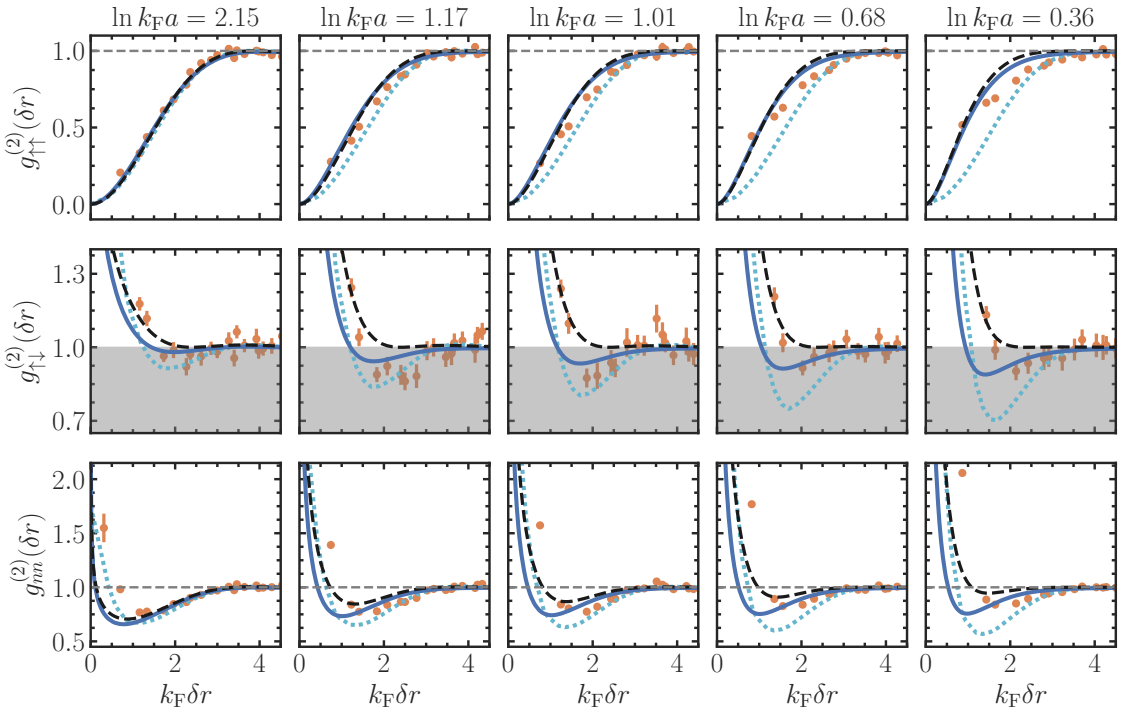


Figure 5.11: Numerical results for $g^{(2)}_{\uparrow\uparrow}(\delta r)$ in top panels, $g^{(2)}_{\uparrow\downarrow}(\delta r)$ in middle panels and $g^{(2)}_{nn}(\delta r)$ in bottom panels versus distance $k_F \delta r$. Dashed black line illustrate case I, solid blue line stands for case IV, see table 5.1. Grey area in middle panel shows anti-correlation region. Theoretical interaction parameter $\ln k_F a$ ranges from 2.15 in BCS regime (left side) to 0.36 in crossover regime (right side) and are related to experimental values used in Ref. [187]. In middle and bottom panels y axis start at 0.7 and 0.5 respectively, to highlight anti-correlation effects. We compare with experimental data from Ref. [187] as orange dots and auxiliary field QMC data at finite temperatures as dotted cyan line. Measured interaction parameters and temperatures of both measurements and QMC curves are found in Table. 5.2.

experimental temperatures, and we used slightly different scattering parameters due to our numerical routine, see Table 5.2 for more details.

We now move on to consider the opposite-spin density-density correlation functions in the middle row in Fig. 5.11. While equal-spin and charge correlation functions are directly measured in the experiment, the opposite-spin correlation functions are extracted using the experimental data for $g^{(2)}_{\uparrow\uparrow}$ and $g^{(2)}_{nn}$ in combination with equation (5.8). Experimentally, an anti-correlation $g^{(2)}_{\uparrow\downarrow} < 1$, was observed, conflicting the standard mean-field theory of case I, see the dashed black line. The QMC data presented in Ref. [187] also shows the correlation hole, whose location and depth are comparable to the results we obtain within the gauge-invariant and Pauli-respecting calculation, case IV in Table 5.1. For stronger interactions, the QMC data, as well as our theoretical results, deviate quite a lot from the experimentally obtained correlations. This is attributed to the quasi-2D confinement as well as the finite temperature in the experiment, being of the order of $T \sim 0.1 T_F$ (see Table 5.2), making the appearance of vortices important. These are effects not captured in our approach. On the other hand, it remains unclear whether these effects are intrinsically included in the QMC calculation.

Lastly, we compare the charge density-density correlation function measured in the

experiment as well as QMC calculations with our results in the lower row of Fig. 5.11. Unsurprisingly, the charge correlation function shows a minimum below one for intermediate distances away from the pairing divergence. For weak interactions, the data follow closely the SP curve obtained via case I, which in this regime is close to the curve predicted by case IV. At strong interactions, deviations from the SP curve occur, as the minimum of the correlation function does not close as strongly as the SP evaluation would suggest. Instead, the minimum remains open but closes stronger than predicted by QMC calculations or our case IV, both of which are similar, again because of the finite temperature and the quasi-2D confinement. As such, we can safely state that our approach can qualitatively explain the experimental data and the QMC calculations. With this, we provide the first physical explanation for the anti-correlations of opposite-spin fermions, which was first seen in a numerical calculation in 3D [173] without a physical picture explaining why this effect occurs. To quantitatively explain the experimental data, we would need to extend the calculation to finite temperatures and potentially include particle-hole fluctuations, see Chapter 3. We prepared the formalism to describe finite temperatures as well. The final evaluation of the bosonic Matsubara summation over q_ℓ is more involved for $T > 0$ and hence not done in this thesis. Furthermore, for stronger interactions, also the third dimension becomes relevant, together with vortex creation.

After having thoroughly compared our results with recent experimental data, we conclude by presenting predictions concerning the minimum of the correlation functions, in order to present a possibility of quantitatively testing our approach in the near future.

5.5.2 Correlation hole

In this section, we quantitatively evaluate specific properties of the density-density correlation functions, which are in principle experimentally accessible, even though the current data sets are too noisy to make a quantitative statement. These quantities are shown in Fig. 5.12, being the half-width $k_\mathrm{F} r_\mathrm{p}$ of the Pauli-hole, defined via $g^{(2)}_{\uparrow\uparrow}(k_\mathrm{F} r_\mathrm{p}) = 1/2$ in the top panel, the width of the correlation hole $k_\mathrm{F}\delta r_\mathrm{min}$ in the middle panels, and the depth h_min of opposite-spin and charge density-density correlation functions in the lower panel. The latter is defined via $h_\mathrm{min} = |g^{(2)}(k_\mathrm{F}\delta r_\mathrm{min}) - 1|$, where for $g^{(2)}$ we either insert $g^{(2)}_{\uparrow\downarrow}$ or $g^{(2)}_{nn}$. The solid red line shows all quantities obtained for $g^{(2)}_{\uparrow\uparrow}$, the solid blue line denotes results for $g^{(2)}_{\uparrow\downarrow}$, while the solid green line represents $g^{(2)}_{nn}$. Furthermore, we add the specific values of the interaction parameters used in Fig. 5.11 as red squares, blue circles and green diamonds. The size of the Pauli hole for weak interactions approaches a constant at $k_\mathrm{F} r_\mathrm{p} \approx 1.6$, associated with the Pauli hole seen in an ideal Fermi gas at $T = 0$ and in 2D. Starting from there, $k_\mathrm{F} r_\mathrm{p}$ reduces when the interactions become stronger, which we quantify in the upper panel. This happens when ε_B becomes comparable or larger than ε_F, and means that indistinguishable fermions become uncorrelated at smaller distances, as they are found only in two-body bound states once the interaction is large enough. Only when the composite bosons have a small separation are they affected by their underlying fermionic nature, which is best seen by the fact that, despite the Pauli-hole shrinking, it never disappears at any finite interaction strength. As such, the width of the Pauli hole for increasing interaction strength approaches zero asymptotically.

Analysing the middle panel, we observe that for weak interactions the location of the minima of $g^{(2)}_{\uparrow\downarrow}$ and $g^{(2)}_{nn}$ are at different scales and behave qualitatively differently. The minimum of $g^{(2)}_{\uparrow\downarrow}$ at weak interactions is at larger separations and fully controlled by the

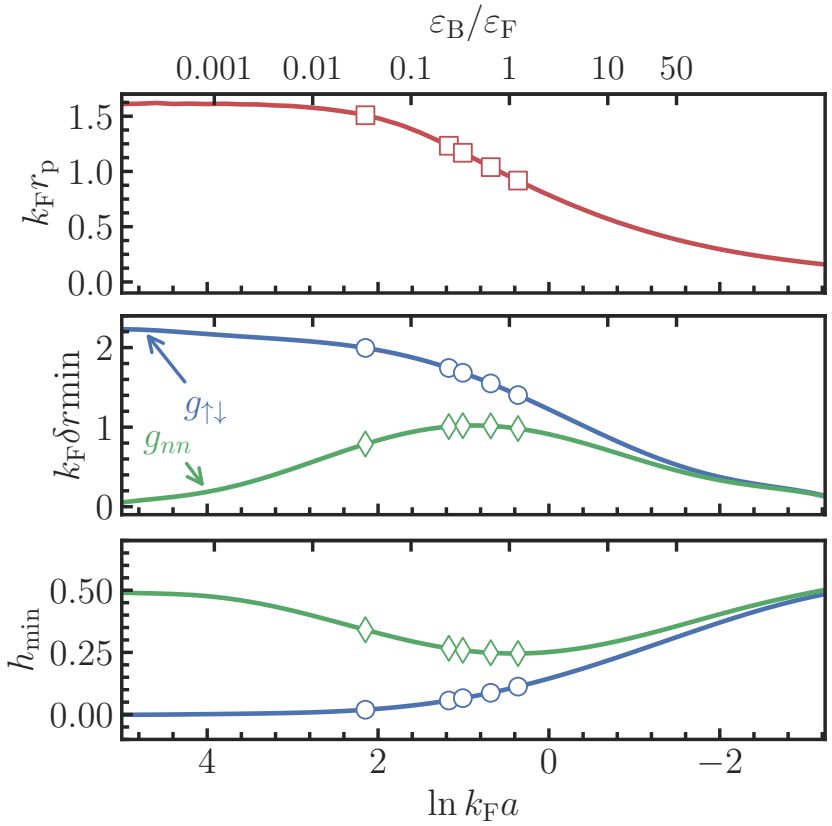


Figure 5.12: Half-width of Pauli hole, $k_F r_p$ in panel (a), location of correlation minima in panel (b) and depth of correlation hole in panel (c) versus dimensionless scattering parameter $\ln k_F a$ (binding energy $\varepsilon_B/\varepsilon_F$) on lower (upper) x-axis. Solid red line shows equal-, solid blue line opposite-spin and solid green line charge density-density correlation function. The red squares/blue circles/green diamonds show values of scattering parameter used in Fig 5.11, strongly oriented on values measured in Ref. [187].
Adapted from [P2] under the terms of the Creative Commons Attribution 4.0 International (CC BY 4.0) license.

irreducible contributions. In contrast, the minimum of $g_{nn}^{(2)}$ is dominated by the Pauli principle, since equal-spin fermions are anti-bunching. This identification becomes evident as the minimum of $g_{nn}^{(2)}$ is at almost zero separation, exactly where the Pauli hole is located. When increasing the interaction, we already established in the discussion of the top panel that the Pauli hole shrinks. Thus, no correlation contribution in the charge density-density correlation function comes from equal-spin fermions. All the correlations of the full density must originate from the correlations of opposite-spin atoms. Thus, we observe in the figure that the two lines representing $g_{\uparrow\downarrow}^{(2)}$ and $g_{nn}^{(2)}$ approach each other and merge when considering strong interactions with binding energies $\varepsilon_B \gg \varepsilon_F$. The anti-correlation in the opposite-spin density-density correlation function shifts to smaller separations and deepens as collective modes become more important for stronger interactions.

Ultimately, in the bottom panel, we see the same qualitative behaviour of h_{min}. For weak interactions, opposite-spin and charge density-density correlation functions behave differently. The depth of the minimum of $g_{nn}^{(2)}$ is solely determined by $g_{\uparrow\uparrow}^{(2)}$ and hence close to $1/2$, while the depth of the minimum of $g_{\uparrow\downarrow}^{(2)}$ is close to 0. At larger interactions, the curves merge again, as the equal-spin fermions become uncorrelated at $\delta r \gg 0$.

Having derived general statements for fermionic correlation functions, applied the theory in $2D$, and discussed experimental data, we present further details in the Appendix.

Appendix

5.A Explicit expressions for D-dimensional loop functions

In this Appendix, we present explicit expressions for all the loop functions beyond the formal version found in the main chapter. To this end, we evaluate the ik_n Matsubara summations and present the resulting loop functions as momentum sums in D dimensions. In general, these were evaluated using Cauchy's residue theorem, formally explained in Appendix B. We do not present the explicit calculations there, as they are straightforward following the examples given in Appendix B. After this, we particularise to 2D in the thermodynamic limit, and present the angular and radial integrals, together with more details on the numerical strategy for evaluating them. To have a concise notation we set $\xi = \xi_{\boldsymbol{k}} = \boldsymbol{k}^2/(2m) - \mu$ and $\xi' = \xi_{\boldsymbol{k}+\boldsymbol{q}}$, as well as $E = E_{\boldsymbol{k}} = \sqrt{\xi^2 + |\Delta_0|^2}$ and $E' = E_{\boldsymbol{k}+\boldsymbol{q}}$. We focus on the equal-spin population case to obtain simpler expressions. Generalizing to the $n_\uparrow \neq n_\downarrow$ or $m_\uparrow \neq m_\downarrow$ case is straight-forward.

5.A.1 General expressions in D dimensions

Saddle-point response functions

At first, we evaluate the SP response functions, found in the matrix (5.68). We start with the two equal-spin density-density susceptibilities seen in Eq. (5.69) for two ↑-spins

$$\widetilde{\chi}^{(0)}_{\uparrow\uparrow}(q) = \sum_{\boldsymbol{k}} \left[\frac{E+E'}{2EE'} \frac{EE' - \xi\xi'}{(iq_\ell)^2 - (E+E')^2} - \frac{iq_\ell}{2EE'} \frac{\xi E' - \xi' E}{(iq_\ell)^2 - (E+E')^2} \right]. \tag{5.A.1}$$

Although the second term vanishes as it is antisymmetric under the transformation $\boldsymbol{k} \to -\boldsymbol{k}$, we mention it for completeness because it is relevant in the case where $\mathrm{SU}(2)$ symmetry is explicitly broken. Using the above symmetry, we simplify and find

$$\widetilde{\chi}^{(0)}_{\uparrow\uparrow}(q) = \sum_{\boldsymbol{k}} \frac{E+E'}{2EE'} \frac{EE' - \xi\xi'}{(iq_\ell)^2 - (E+E')^2}. \tag{5.A.2}$$

In the case of balanced populations we find $\widetilde{\chi}^{(0)}_{\uparrow\uparrow}(q) = \widetilde{\chi}^{(0)}_{\downarrow\downarrow}(q)$. We also consider the off-diagonal matrix elements of the SP response tensor found in Eq. (5.70), which evaluates to

$$\widetilde{\chi}^{(0)}_{\uparrow\downarrow}(q) = \sum_{\boldsymbol{k}} \frac{E+E'}{2EE'} \frac{|\Delta_0|^2}{(iq_\ell)^2 - (E+E')^2}. \tag{5.A.3}$$

Having the SP expressions, we continue with the pair fluctuations.

Pair vertex function

We now evaluate the Fermi Matsubara sums of the elements of the fluctuation matrix (5.73). To obtain amplitude-amplitude (xx) and phase-phase (yy) propagators from Eqs. (5.74)

and (5.75), respectively, we use the superfluid order parameter equation (2.26) in order to eliminate the bare coupling, independent of the dimensionality. This leads to

$$\Gamma_{xx}(q) = \sum_{\boldsymbol{k}} \left[\frac{1}{E} + \frac{E+E'}{EE'} \frac{EE' + \xi\xi' - \mathfrak{Re}\Delta_0^2}{(iq_\ell)^2 - (E+E')^2} \right], \tag{5.A.4a}$$

$$\Gamma_{yy}(q) = \sum_{\boldsymbol{k}} \left[\frac{1}{E} + \frac{E+E'}{EE'} \frac{EE' + \xi\xi' + \mathfrak{Re}\Delta_0^2}{(iq_\ell)^2 - (E+E')^2} \right]. \tag{5.A.4b}$$

Furthermore, we obtain the amplitude-phase coupling element (5.76) via

$$\Gamma_{xy}(q) = -i \sum_{\boldsymbol{k}} \frac{iq_\ell}{EE'} \frac{E\xi' + E'\xi - i\mathfrak{Im}\Delta_0^2}{(iq_\ell)^2 - (E+E')^2}, \tag{5.A.5}$$

which also includes the second off-diagonal element via $\Gamma_{yx}(q) = \Gamma_{xy}(-q) = -\Gamma_{xy}(q)$ as the function is odd.

Fluctuation-density couplings

To determine the elements of the density-fluctuation coupling matrix (5.77), we exploit the $\mathrm{SU}(2)$ symmetry when the spin populations and masses are identical. Hence, for an arbitrary spin s we obtain

$$\Lambda_{\mathrm{s}x}(q) = \sum_{\boldsymbol{k}} \frac{E+E'}{2EE'} \frac{\Delta_0(\xi+\xi')}{(iq_\ell)^2 - (E+E')^2}, \tag{5.A.6a}$$

$$\Lambda_{\mathrm{s}y}(q) = -i \sum_{\boldsymbol{k}} \frac{E+E'}{2EE'} \frac{iq_\ell\Delta_0}{(iq_\ell)^2 - (E+E')^2}, \tag{5.A.6b}$$

for the density-amplitude (5.78a,5.78b) and the density-phase coupling (5.79a,5.79b) respectively. Those expressions are valid for all dimensions D and all temperatures T. We now particularise to a spherically symmetric homogeneous system in 2D in the thermodynamic limit.

5.A.2 Simplifications for 2D, infinite rotationally symmetric systems

Spherical symmetry allows for an alignment of the $\boldsymbol{k}_1$ vector along $\boldsymbol{q}$, so that without loss of generality we have $\boldsymbol{k}\cdot\boldsymbol{q} = |\boldsymbol{k}||\boldsymbol{q}|\cos\vartheta$. With this, the free dispersion becomes $\xi' = |\boldsymbol{k}|^2/(2m) - \mu + |\boldsymbol{q}|^2/(2m) + |\boldsymbol{k}||\boldsymbol{q}|\cos\vartheta/m$. We now substitute $\epsilon = |\boldsymbol{k}|^2/(2m)$ and set $Q = |\boldsymbol{q}|$ to write $\xi = \epsilon - \mu$ as well as $\xi' = \xi + Q^2/(2m) + \sqrt{2\epsilon/m}Q\cos\vartheta$. Doing so yields a constant dimensionless density of states in 2D, i.e. $D(\epsilon) = 1$. Thus, we obtain the particle-hole bubbles from Eqs. (5.A.2) and 5.A.3) as

$$\widetilde{\chi}^{(0)}_{\uparrow\uparrow}(q) = \frac{m}{8\pi^2} \int_0^{2\pi} \mathrm{d}\vartheta \int_0^\infty \mathrm{d}\epsilon \, \frac{E+E'}{EE'} \frac{EE' - \xi\xi'}{(1q_\ell)^2 - (E+E')^2} \tag{5.A.7a}$$

$$\widetilde{\chi}^{(0)}_{\uparrow\downarrow}(q) = \frac{m}{8\pi^2} \int_0^{2\pi} \mathrm{d}\vartheta \int_0^\infty \mathrm{d}\epsilon \, \frac{E+E'}{EE'} \frac{|\Delta_0|^2}{(iq_\ell)^2 - (E+E')^2}. \tag{5.A.7b}$$

Furthermore, the pair propagators, Eqs. (5.A.4a,5.A.4a) and (5.A.5) become

$$\Gamma_{xx}(q) = \frac{m}{4\pi^2}\int_0^{2\pi}\mathrm{d}\vartheta\int_0^{\infty}\mathrm{d}\epsilon\left[\frac{1}{E}+\frac{E+E'}{EE'}\frac{EE'+\xi\xi'-\mathfrak{Re}\Delta_0^2}{(iq_\ell)^2-(E+E')^2}\right], \tag{5.A.8a}$$

$$\Gamma_{yy}(q) = \frac{m}{4\pi^2}\int_0^{2\pi}\mathrm{d}\vartheta\int_0^{\infty}\mathrm{d}\epsilon\left[\frac{1}{E}+\frac{E+E'}{EE'}\frac{EE'+\xi\xi'+\mathfrak{Re}\Delta_0^2}{(iq_\ell)^2-(E+E')^2}\right], \tag{5.A.8b}$$

$$\Gamma_{xy}(q) = -\frac{im}{4\pi^2}\int_0^{2\pi}\mathrm{d}\vartheta\int_0^{\infty}\mathrm{d}\epsilon\,\frac{iq_\ell}{EE'}\frac{E\xi'+E'\xi-i\mathfrak{Im}\Delta_0^2}{(iq_\ell)^2-(E+E')^2}. \tag{5.A.8c}$$

Lastly, the coupling vertices, Eqs. (5.A.6a) and (5.A.6b) read in the thermodynamic

$$\Lambda_{sx}(q) = \frac{m}{8\pi^2}\int_0^{2\pi}\mathrm{d}\vartheta\int_0^{\infty}\mathrm{d}\epsilon\,\frac{E+E'}{EE'}\frac{\Delta_0(\xi+\xi')}{(iq_\ell)^2-(E+E')^2}, \tag{5.A.9a}$$

$$\Lambda_{sy}(q) = -\frac{im}{8\pi^2}\int_0^{2\pi}\mathrm{d}\vartheta\int_0^{\infty}\mathrm{d}\epsilon\,\frac{E+E'}{EE'}\frac{iq_\ell\Delta_0}{(iq_\ell)^2-(E+E')^2}. \tag{5.A.9b}$$

In order to numerically evaluate the response tensor (5.86) at $T = 0$, it is favourable to scale all the energies in the system not by the Fermi energy ε_F, but by the superfluid order parameter $|\Delta_0| > 0$. We do so, since the entries $\widetilde{\chi}_{ss'}(q)$ are not functions of both μ and $|\Delta_0|$, but can be expressed as a function of $\mu/|\Delta_0|$ only, when multiplied by $|\Delta_0|$. This multiplication comes about when scaling the Q integral with $\sqrt{2m|\Delta_0|}$. Therefore, a whole degree of freedom is eliminated, and we can determine the numerical response tensor much faster.

5.B Gauge invariance and ladder summation

Here, we establish a diagrammatic interpretation of the irreducible contributions derived in Section 5.3 of the main text. We present the full RPA sum of the respective Feynman diagrams to find the correct physical interpretation in the superfluid state. First, we have a more detailed look at the standard GPF equation of state used in most approaches to find the beyond saddle-point description of the BCS-BEC crossover. After this, we evaluate the EoS used in this chapter, respecting the Pauli principle, and express it diagrammatically as an expansion in terms of small g.

5.B.1 Diagrammatic representation of Gaussian equation of state

In this section, we provide a deeper insight into the diagrammatic expansion of the GPF formalism, already started in Fig. 5.4. Most diagrammatic investigations, see for instance Ref. [84, 100], build the diagrams in the normal state and approach the critical temperature from above. In Chapter 5, we are interested in the correlations within the superfluid phase, requiring a closer look at all diagrams, including also anomalous lines, which are only non-zero in the superfluid state. We obtain the corresponding grand-canonical potential via the generating functional (5.83), resulting in

$$\Omega(L^D,T,\mu_\mathrm{s}) = -T\sum_k \ln\det\left[-\beta\boldsymbol{G}_\mathrm{SP}^{-1}(k)\right] + V\frac{|\Delta_0|^2}{g} - \frac{T}{2}\sum_q \ln\det\left[\beta\boldsymbol{\Gamma}^{-1}(q)\right]. \tag{5.B.10}$$

Here we especially care for the GPF contribution $\Omega_\mathrm{GPF}(L^D,T,\mu_\mathrm{s}) = -T/2\sum_q \ln\det\left[\beta\boldsymbol{\Gamma}^{-1}(q)\right]$. Using the expansion for small g in Eq. (5.99) we express the GPF grand-canonical potential

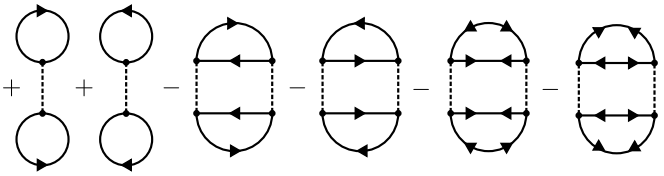
$\beta\Omega_{\mathrm{GPF}}(L^D,T,\mu) = -\ln(\beta\overline{g})$  $+\mathcal{O}(g)^3$

Figure 5.B.1: Vacuum diagrams of the GPF grand-canonical potential up to second order in $\overline{g}$. We suppressed the spin and momentum indices for the sake of simplicity, since they are straightforward to assign considering Eq. (5.B.11).

as

$$\begin{aligned}\Omega_{\mathrm{GPF}}(L^D,T,\mu_{\mathrm{s}}) &= -T\ln(\beta\overline{g}) + 2T\sum_{kq}\left[G^{\uparrow\uparrow}_{\mathrm{SP}}(k+q)G^{\downarrow\downarrow}_{\mathrm{SP}}(k) + G^{\downarrow\downarrow}_{\mathrm{SP}}(k+q)G^{\uparrow\uparrow}_{\mathrm{SP}}(k)\right]\overline{g}\\ &- T\sum_{kk'q}\Big[G^{\uparrow\uparrow}_{\mathrm{SP}}(k+q)G^{\downarrow\downarrow}_{\mathrm{SP}}(k)G^{\uparrow\uparrow}_{\mathrm{SP}}(k')G^{\downarrow\downarrow}_{\mathrm{SP}}(k'+q) + G^{\downarrow\downarrow}_{\mathrm{SP}}(k+q)G^{\uparrow\uparrow}_{\mathrm{SP}}(k)G^{\downarrow\downarrow}_{\mathrm{SP}}(k')G^{\uparrow\uparrow}_{\mathrm{SP}}(k'+q)\\ &+ F^{\uparrow\downarrow}_{\mathrm{SP}}(k+q)F^{\uparrow\downarrow}_{\mathrm{SP}}(k)F^{\downarrow\uparrow}_{\mathrm{SP}}(k')F^{\downarrow\uparrow}_{\mathrm{SP}}(k'+q) + F^{\downarrow\uparrow}_{\mathrm{SP}}(k+q)F^{\downarrow\uparrow}_{\mathrm{SP}}(k)F^{\uparrow\downarrow}_{\mathrm{SP}}(k')F^{\uparrow\downarrow}_{\mathrm{SP}}(k'+q)\Big]\overline{g}^2\\ &+ \mathcal{O}(\overline{g})^3. \end{aligned} \tag{5.B.11}$$

The fermionic sums over k,k' lead to a ladder-type summation, while the bosonic q-sum "*bends*" the lines together. This means that the diagrammatic representation of the GPF grand-canonical potential is as shown in Fig. 5.B.1. We call them vacuum diagrams, as they are completely closed on themselves without any externally fixed degree of freedom. We see a bubble-type summation of particles and holes, akin to the diagrams that would be associated with a Hartree self-energy shift in leading order, i.e. $\mathcal{O}(\overline{g})$. Furthermore, we see higher terms involving ladders with particle-hole bubbles and anomalous bubbles of quasi-particles and quasi-holes as a broken symmetry extension of the diagrams found in Ref. [122]. We have not assumed balanced populations here, so we distinguish between particle and hole diagrams. If we assumed $\mu_\uparrow = \mu_\downarrow$, all diagrams that convert into each other by inverting every arrow direction would be identical and might be summarised, halving the number of diagrams per order in $\overline{g}$. We have an offset of the grand-canonical potential $-\ln(\beta\overline{g})$, which has no thermodynamic relevance.

We obtained the grand-canonical potential expressed as an infinite summation of bend ladder diagrams, which we now want to convert to the particle number equation, including a derivative with respect to the chemical potential. We have to keep in mind that this includes two terms, as already discussed in the introduction of this thesis in Eq. (2.58). The GPF equation of state consists of two terms, which roughly are associated to NSR and superfluid depletion terms, leading to $-\partial\Omega_{\mathrm{GPF}}/\partial\mu_{\mathrm{s}} = n_{\mathrm{s,GPF}} = n_{\mathrm{s,NSR}} + n_{\mathrm{s,depl}}$, which are

$$n_{\mathrm{s,NSR}} = -\left.\frac{\partial\Omega_{\mathrm{GPF}}}{\partial\mu_{\mathrm{s}}}\right|_{T,L,\Delta_0}, \tag{5.B.12a}$$

$$n_{\mathrm{s,depl}} = -\left.\frac{\partial\Omega_{\mathrm{GPF}}}{\partial\Delta_0}\right|_{T,L,\overline{\Delta}_0}\left.\frac{\partial\Delta_0(\mu_{\mathrm{s}})}{\partial\mu_{\mathrm{s}}}\right|_{T,L,\mu_{\overline{s}},\overline{\Delta}_0} - \left.\frac{\partial\Omega_{\mathrm{GPF}}}{\partial\overline{\Delta}_0}\right|_{T,L,\Delta_0}\left.\frac{\partial\overline{\Delta}_0(\mu_{\mathrm{s}})}{\partial\mu_{\mathrm{s}}}\right|_{T,L,\mu_{\overline{s}},\Delta_0}. \tag{5.B.12b}$$

Since we do not invoke any gauge fixing to obtain the full set of diagrams, the depletion term contains both Δ_0 and $\overline{\Delta}_0$ as separate variables. We now aim to determine the Feynman diagrams of the GPF EoS up to $\mathcal{O}(\overline{g})^2$ explicitly.

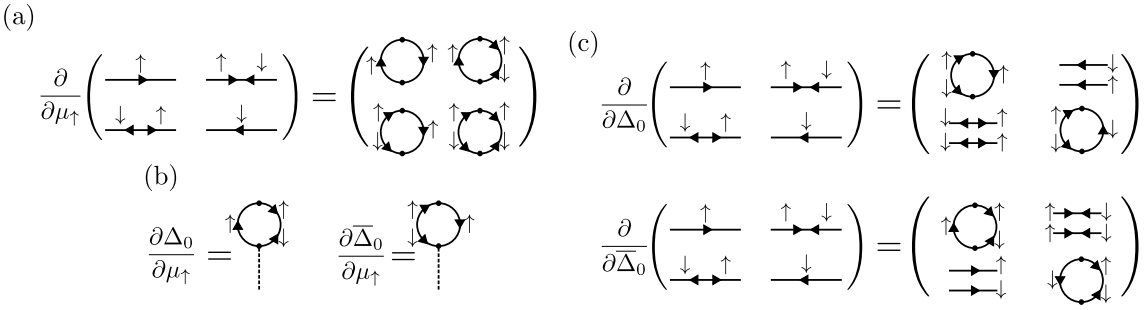


Figure 5.B.2: Illustration of derivatives of Green's function lines. Panel (a) shows derivative of $\boldsymbol{G}_{\mathrm{SP}}$ with respect to $\mu_\uparrow$, panel (b) the order parameter derivatives and panel (c) derivative of $\boldsymbol{G}_{\mathrm{SP}}$ with respect to the superfluid order parameter Δ_0 and its complex conjugate.

In the following, we obtain an explicit representation of $n_\uparrow$, but keep in mind that for $n_\downarrow$ the process is analogous, using inverted spin indices. To see what a derivative does we consider the matrix derivative $\partial\boldsymbol{G}_{\mathrm{SP}}(k)/\partial\mu_\uparrow = \boldsymbol{G}_{\mathrm{SP}}(k)[\partial\boldsymbol{G}^{-1}_{\mathrm{SP}}(k)/\partial\mu_\uparrow]\boldsymbol{G}_{\mathrm{SP}}(k)$. Performing this matrix multiplication reveals

$$\frac{\partial}{\partial\mu_\uparrow}\boldsymbol{G}_{\mathrm{SP}}(k) = \begin{pmatrix} G^{\uparrow\uparrow}_{\mathrm{SP}}(k)G^{\uparrow\uparrow}_{\mathrm{SP}}(k) & G^{\uparrow\uparrow}_{\mathrm{SP}}(k)F^{\uparrow\downarrow}_{\mathrm{SP}}(k) \\ G^{\uparrow\uparrow}_{\mathrm{SP}}(k)F^{\downarrow\uparrow}_{\mathrm{SP}}(k) & F^{\uparrow\downarrow}_{\mathrm{SP}}(k)F^{\downarrow\uparrow}_{\mathrm{SP}}(k) \end{pmatrix}. \tag{5.B.13}$$

Furthermore, the depletion term also requires derivatives with respect to the superfluid order parameter, which, by a similar scheme, leads to

$$\frac{\partial\boldsymbol{G}_{\mathrm{SP}}(k)}{\partial\Delta_0} = \begin{pmatrix} G^{\uparrow\uparrow}_{\mathrm{SP}}(k)F^{\downarrow\uparrow}_{\mathrm{SP}}(k) & G^{\uparrow\uparrow}_{\mathrm{SP}}(k)G^{\downarrow\downarrow}_{\mathrm{SP}}(k) \\ F^{\downarrow\uparrow}_{\mathrm{SP}}(k)F^{\downarrow\uparrow}_{\mathrm{SP}}(k) & G^{\downarrow\downarrow}_{\mathrm{SP}}(k)F^{\downarrow\uparrow}_{\mathrm{SP}}(k) \end{pmatrix}, \tag{5.B.14a}$$

$$\frac{\partial\boldsymbol{G}_{\mathrm{SP}}(k)}{\partial\overline{\Delta}_0} = \begin{pmatrix} G^{\uparrow\uparrow}_{\mathrm{SP}}(k)F^{\uparrow\downarrow}_{\mathrm{SP}}(k) & F^{\uparrow\downarrow}_{\mathrm{SP}}(k)F^{\uparrow\downarrow}_{\mathrm{SP}}(k) \\ G^{\downarrow\downarrow}_{\mathrm{SP}}(k)G^{\uparrow\uparrow}_{\mathrm{SP}}(k) & G^{\downarrow\downarrow}_{\mathrm{SP}}(k)F^{\uparrow\downarrow}_{\mathrm{SP}}(k) \end{pmatrix}. \tag{5.B.14b}$$

Furthermore also the superfluid order parameter itself, as a closed anomalous loop, is needed. Performing those derivatives results in

$$\left.\frac{\partial\Delta_0(\mu_{\mathrm{s}})}{\partial\mu_\uparrow}\right|_{T,L,\mu_\downarrow,\overline{\Delta}_0} = \frac{g}{\beta L^D}\sum_k G^{\uparrow\uparrow}(k)F^{\uparrow\downarrow}_{\mathrm{SP}}(k), \tag{5.B.15a}$$

$$\left.\frac{\partial\overline{\Delta}_0(\mu_{\mathrm{s}})}{\partial\mu_\uparrow}\right|_{T,L,\mu_\downarrow,\Delta_0} = \frac{g}{\beta L^D}\sum_k G^{\uparrow\uparrow}(k)F^{\downarrow\uparrow}_{\mathrm{SP}}(k). \tag{5.B.15b}$$

We diagrammatically represent all these derivatives in Fig. 5.B.2. Panel (a) shows that a derivative of a closed Green's function with respect to $\mu_\uparrow$ also yields a closed loop of two Green's functions, where the derivatives of anomalous terms yield a mix. In the normal state, the $\downarrow$-spins decouple from $\mu_\uparrow$ since the anomalous Green's function vanishes. Panel (b) illustrates that the derivatives of the order parameter variations add a tadpole-like term to a given Feynman diagram, which is used when performing derivatives with respect to the order parameter variations as depicted in panel (c). Furthermore, derivatives of normal Green's functions produce a loop, while derivatives of anomalous Green's functions, associated with Cooper pairs, produce either a normal or an anomalous ladder diagram. Combining panels (b) and (c), we see that, while the NSR contributions are of the same order as the corresponding vacuum diagram from Fig. 5.B.1, the depletion term adds one

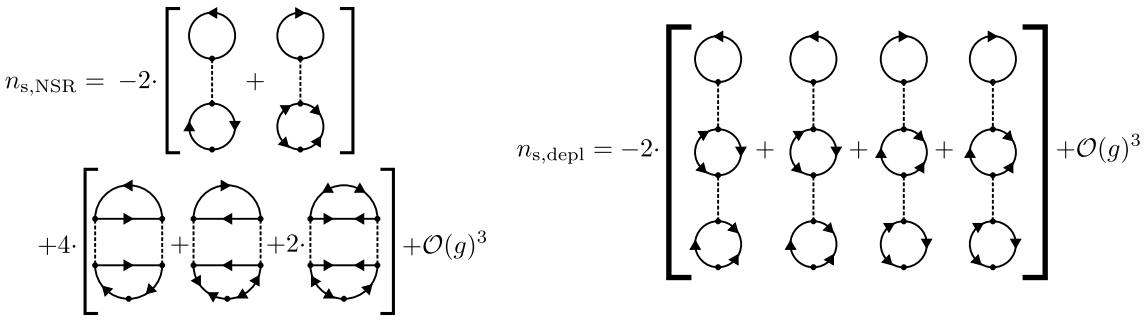


Figure 5.B.3: Diagrammatic representation of GPF particle number as series expansion in interaction strength g, represented as dashed line. Left side illustrates NSR contribution coming directly from thermodynamic derivative with respect to chemical potential, while right side stands for superfluid depletion term arising from change in superfluid order parameter over the crossover.

interaction via $\partial\Delta_0/\partial\mu_\uparrow$, making it sub-leading for weak interactions. Hence, the depletion of the order parameter is relevant only for strong interactions, possibly beyond the two-body bound-state threshold, where resummation of all diagrams becomes necessary. We further note that the only appearing combinations have the same number of $F_{\mathrm{SP}}^{\uparrow\downarrow}$ lines as $F_{\mathrm{SP}}^{\downarrow\uparrow}$, and hence are $\mathrm{U}(1)$-gauge invariant.

Applying the cutting rules established in Fig. 5.B.2 to the vacuum diagrams of the grand-canonical potential in Fig. 5.B.1 yields the particle number equation up to second order in g. We present the resulting diagrams of both the NSR and the depletion contribution in Fig. 5.B.3. We notice that the leading order contribution coming from the NSR scheme, seen in panel (a), is of order $\mathcal{O}(g)$, as already described in Refs. [80, 88]. Hence, the leading-order corrections at weak interactions are Hartree-like bubble contributions altering the particle number obtained in a mean-field description. At the second order, we find diagrams involving particle as well as anomalous ladders, showing that the Cooper pairs in the pair fluctuation pose a second-order effect for weak interactions, explaining why mean-field and pair fluctuation approaches are exponentially close to one another in the deep BCS limit, where $g \to 0$. In addition to the second-order ladder diagrams, we find second-order bubble (beyond mean-field Hartree) diagrams contributing to the GPF number equation, via the superfluid depletion term first described by Ref. [93] and shown on the right side of Fig. 5.B.3. These are bubble-shaped diagrams, involving also partially normal and partially anomalous bubbles, which show the direct interaction of Cooper pairs and unpaired particles. Since these diagrams are of second order, the superfluid depletion is subleading for weak interactions, whereas as interactions grow stronger, the perturbative series must be resummed, yielding an important contribution that adequately describes the crossover. The RPA resummation of the NSR terms leads to a ladder summation, involving normal and anomalous ladders, while the depletion term amounts to a bubble summation involving anomalous bubbles. The bubbles involved in the depletion term are not to be confused with the bubbles of the GMB approach, shown in Fig. 2.4, which only involve normal Green's functions and describe interaction screening. Going to the normal state, all anomalous lines vanish, and only the standard ladder summation remains, additionally to a single Hartree-like diagram in $n_{\mathrm{s,NSR}}$, while the depletion term vanishes, as it always involves anomalous lines.

After establishing the perturbative expansion of the GPF equation of state, we have a look at the results of our PR equation of state in the next section.

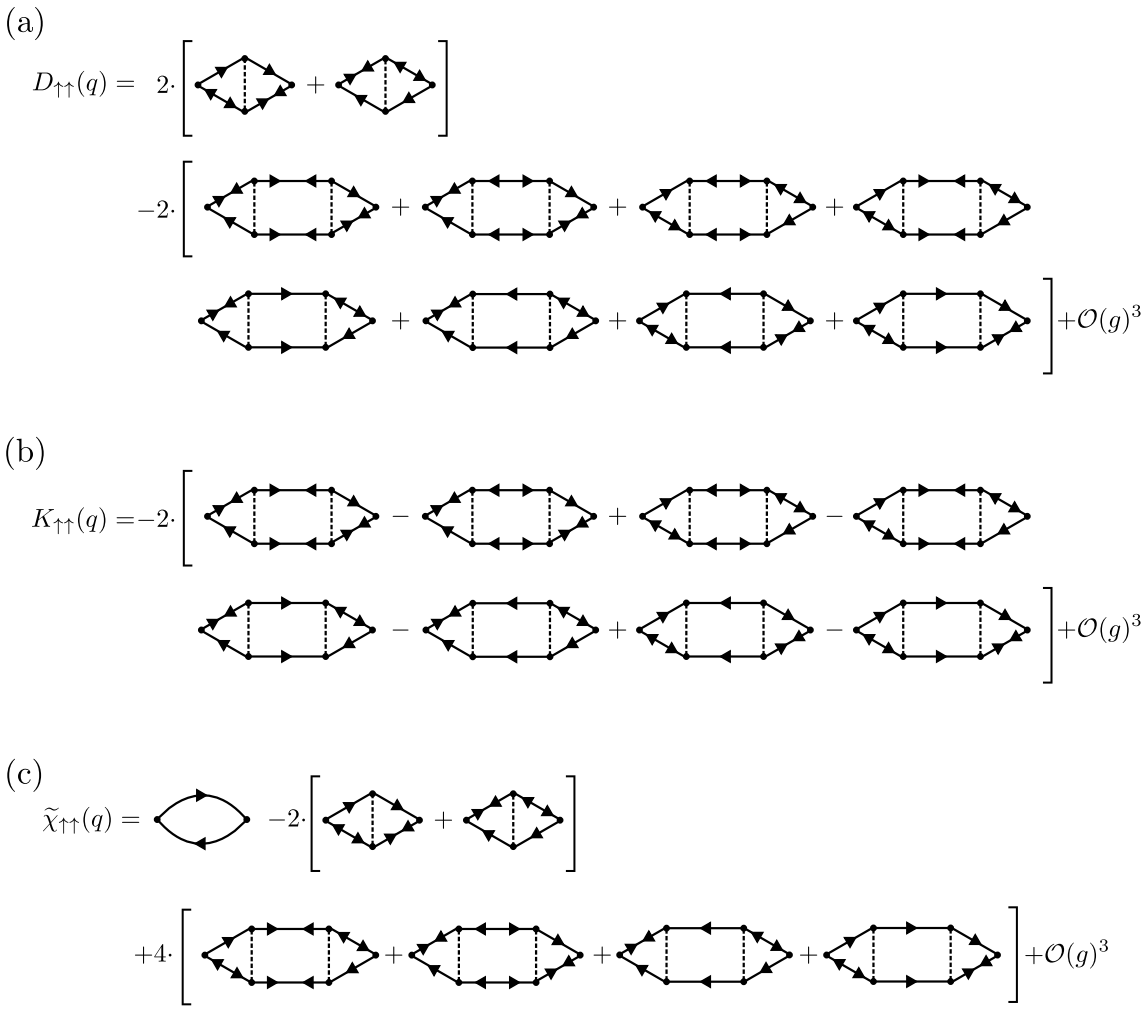


Figure 5.B.4: Feynman diagrams of D function for equal spins in panel (a) and of K function in panel (b). Panel (c) shows full Gaussian approximation to equal-spin response function $\widetilde{\chi}_{\uparrow\uparrow}(q)$ up to next-to-next leading order in g, including two-particle reducible particle-hole bubble as leading order diagram.

5.B.2 Diagrams of irreducible contribution

To obtain the EoS of the PR theory, rooted in a linear-response framework, we first find all the diagrams contributing to the response function. As established in Eq. (5.89) $\chi_{\uparrow\uparrow}(q)$ is separated into pure amplitude and phase terms $D_{\uparrow\uparrow}$ and mixing terms $K_{\uparrow\uparrow}$, all depending explicitly on the gauge of the pair field Δ_0. Only $\chi_{\uparrow\uparrow}(q)$ itself is invariant under $\mathrm{U}(1)$ gauge transformation of the superfluid order parameter Δ_0. We expand the functions $D_{\uparrow\uparrow}$ and $K_{\uparrow\uparrow}$ for small interaction strengths g and present the resulting diagrams in Fig. 5.B.4 (a) and (b). In panel (a), we see that the amplitude-amplitude and phase-phase terms have leading order contributions of the order $\mathcal{O}(g)$. This represents an interaction of the $\uparrow$-density with the propagation of a Cooper pair, represented by the anomalous lines. Although the two diagrams are rotationally symmetric, we represent them separately as they show the symmetry of the momentum q. As rotating the diagram amounts to inverting $q \to -q$, the leading-order contribution of $D_{\uparrow\uparrow}(q)$ is invariant under space-time inversion. Furthermore, we see that in the second order in g there are eight distinct diagrams contributing to $D_{\uparrow\uparrow}(q)$, involving the propagation of particle or hole ladders as well as anomalous ladders, coupling to the density via vertices involving a Cooper pair. Four of these diagrams do not

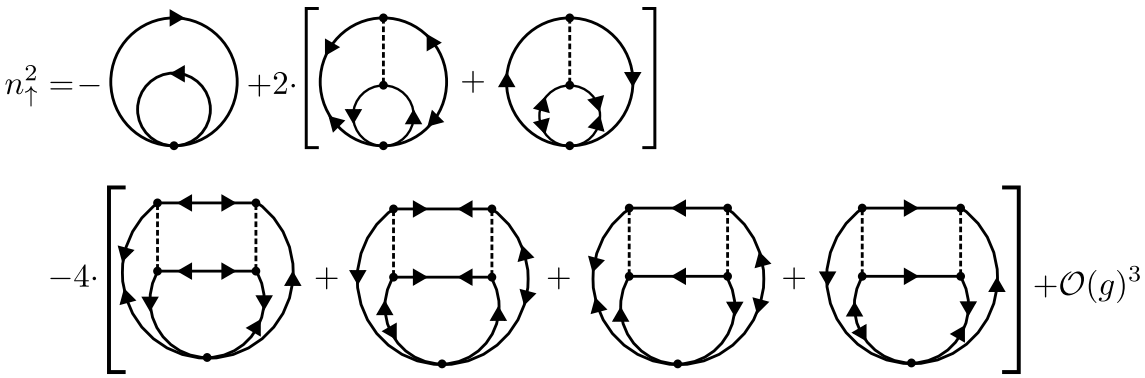


Figure 5.B.5: Feynman diagrams of square of spin-resolved particle number up to next-to-next leading order in g. First line stands for saddle-point result (first diagram) and next-to-leading order corrections of order $\mathcal{O}(g)$. Second line represents next-to-next leading order $\mathcal{O}(g)^2$ involving first ladder terms.

conserve spin at the single-particle vertices, which are represented as black dots. Among these kinds of diagrams, the two involving the anomalous ladders are not $\mathrm{U}(1)$ gauge invariant, as they only include quasi-particles or quasi-holes. The same eight diagrams also appear in the function $K_{\uparrow\uparrow}(q)$, depicted in panel (b) and describing the influence of mode mixing between amplitude and phase. Due to the mixing, four of these elements have opposite signs, while four have the same signs as in $D_{\uparrow\uparrow}(q)$. We notice that the diagrams in conflict with spin conservation retain the sign of $D_{\uparrow\uparrow}(q)$, meaning that in the response function $\widetilde{\chi}_{\uparrow\uparrow}^{(\mathrm{irr})}(q) = K_{\uparrow\uparrow}(q) - D_{\uparrow\uparrow}(q)$ they cancel out. In addition we show the power series of the Gaussian approximation to the response function $\widetilde{\chi}_{\uparrow\uparrow}(q)$ in panel (c), including the standard $\uparrow\uparrow$ particle-hole bubble as the two-particle reducible contribution, as well as the next and next-to-next leading order coming from the two-particle irreducible term up to Gaussian order in the quantum fluctuations.

To obtain the local particle number, we sum over all momenta q, hence closing the diagrams by joining the two external vertices where the source terms couple. This leads again to vacuum diagrams governing the mean particle number square $\langle \hat{n}_\uparrow^2 \rangle$. We depict the diagrams up to next-to-next leading order, i.e. $\mathcal{O}(g)^2$, in Fig. 5.B.5. The mean-square number of $\uparrow$-particles is governed by two intertwined loops of normal $\uparrow$ Green's functions on the SP level, and corrections in the form of ladder summations in the superfluid phase. The irreducible diagrams represent the corrections to the particle number, accounting for the fact that the interaction g is capable of forming Cooper pairs and many-body bound states. They cannot be separated into two diagrams, as in the mean-field diagram. This contains both the ladders of particles and holes, representing the propagation of a Cooper pair, and anomalous ladder diagrams containing processes involving more than one Cooper pair. When crossing towards strong interactions, especially for interactions larger than the threshold g_* announcing the formation of two-body bound states, a resummation of all diagrams is essential to account for the full physics, leading to a RPA result for the mean-square particle number. Finally, it is worth noticing that all the diagrams involving an interaction g contain at least two anomalous propagators, that is, lines with two arrows, proportional to the superfluid order parameter. Thus, all these diagrams contribute to the superfluid broken-symmetry phase but vanish in the normal state. In other words, our corrected equation of state has no reminiscent terms coming from pair fluctuations in the normal state and therefore will not reproduce the NSR approach of T_c [80].

Chapter 6

Summary

> To myself I seem to have been only
> like a boy playing on the seashore [...]
> whilst the great ocean of truth lay all
> undiscovered before me.
>
> Isaac Newton

Degenerate Fermi gases pose an interesting experimental and theoretical playground to investigate the behaviour of many-body quantum systems, consisting of a few thousand atoms. Since they represent an ideal quantum simulator, the insights gained via those small laboratory systems provide us with a deep insight into the structure of matter in constellations, which are hard or even impossible to investigate directly as, for instance, subatomic structures or astrophysical objects. This thesis provided a theoretical framework that helps understanding, analysing, and predicting the behaviour of not only ultracold fermionic quantum gases, but also to extrapolate this knowledge to other physical systems on smaller or larger scales. To establish this theoretical building, we first reviewed the framework to describe the BEC to BCS crossover known in the literature in Chapter 2. In particular, we discussed three different approaches, the operator-based Leggett crossover in Section 2.2, the functional integral approach in Section 2.3 as well as diagrammatic methods in Section 2.4. And we pointed out in Section 2.5 that all those descriptions inherently carry a bias from approximations, an ambiguity in transformations, or even human intuition due to the choice of diagrams.

To circumvent this arbitrariness, an overarching principle is needed, by which the system itself decides which processes are important, i.e. which diagrams contribute to which extent. We developed such a framework formally in Chapter 3 and named it the *Weighted Hartree-Fock-Bogoliubov* (*WHFB*) method. We allowed the interaction to describe Hartree, Fock, and Bogoliubov processes simultaneously by partitioning it according to Eq. (3.11). This enabled us, in turn, to eliminate the ambiguity in the Hubbard-Stratonovich transformations in a functional integral approach by performing all possible transformations simultaneously. As such, we obtained a generalisation of the BCS effective action in the form of Eq. (3.44). We derived the corresponding saddle-point equations in Section 3.3 to investigate the immediate consequences of our partitioning, which lead, in the case of population balance, not only to the self-consistency equations of Hartree (3.57a) and Bogoliubov (3.57b) energies, but also to the partitioning itself (3.59a,3.59b). The par-

titioning we introduced is therefore a mathematical tool to describe the interplay between different interaction processes which represents a new phenomenon of general interest. We found that the partitioning factors, effectively describing the interaction of Hartree and Bogoliubov channels, can be interpreted as a screening effect, which one channel has on another, by assigning different interaction strengths to them via the corresponding weights. This promotes the Hartree self-energy to some order parameter, allowing in mean-field for a splitting of the superfluid phase at weak interactions and large interaction ranges.

We then moved on to explicitly work out the consequences of our approach for a three-dimensional Fermi spin mixture in thermal equilibrium and for equal populations. We aimed to select realistic parameters for our theoretical study, matching the properties of ^{6}Li and ^{40}K in Chapter 4. At the beginning, in Section 4.2, we delved deeper into the theory of ultracold scattering events in order to adequately describe the particle-hole sector, which requires more than the simple zero-energy scattering considered so far in the literature. This necessitates including the effective range as a competing length scale to the s-wave scattering length, characterising the interaction strength of a 3D system. This speaks against the ubiquitous notion of a universal theory and is something not yet considered in the study of quantum gases, but is a consensus, for instance, when describing superfluid properties of nuclei. Due to screening effects, our partitioning method introduced a many-body version of the effective range, with different values in the different channels. We applied this approach in Section 4.3 to investigate the ground state of the spin mixture in a saddle-point approximation and found a new, so far overlooked phase of superfluid fermions, which we named *Hartree superfluid* (HSF), in contrast to the already known *standard superfluid* (SSF). We calculated the ground-state phase diagram of this system and presented our findings in Fig. 4.3. This phase diagram showed that the HSF phase can only exist for weak interactions and relatively large interaction ranges, as otherwise the formation of Cooper pairs is energetically favourable, and, as such, no residual energy can be attributed to particle-hole scattering. After this, we further characterised the two superfluid phases and found that the HSF phase is a superfluid phase supporting interactions in the particle-hole sector, while the SSF phase does not. This finding is striking and shows similarities of ad-hoc assumptions in diagrammatic methods, assuming that a mean-field self-energy shift of the chemical potential is needed to achieve a consistent treatment of the so-called GMB mechanism at weak interactions [100, 340]. We found that our approach solves the issue of including the Hartree channel in a BCS theory as it prevents divergences in the self-energy and, as such, in the chemical potential by proper regularisation. This was a long-standing problem in the literature [28], which until now had no solution and led many groups to disregard the Hartree channel as being irrelevant [290, 296]. This, however, can not be true as the value of the chemical potential is important in an experimental setup because it determines the number of particles. As such, our theory proves to be not only of theoretical importance from the standpoint of a clean, unbiased theory, but also has potentially vast implications on measurable quantities. We investigated a few of those in Section 4.4 in the ground state. At first, we showed that our approach also prevents divergences in the free energy, which in the standard treatment would appear. In particular, it turned out that Tan's contact can be described much better in our approach, improving the qualitatively wrong prediction of a simple BCS treatment, as is illustrated in Fig. 4.11. Furthermore, we also found the first analytical solution for the size of a Cooper pair in three dimensions, which we derived in Eq. (4.78). To wrap this up we investigated the influence of thermal fluctuations in Section 4.5, showing that the HSF is an intermediate phase separating the "clean" Hartree-channel normal fluid at

higher temperatures and the SSF for lower temperatures, including only the Bogoliubov channel. In the end, we analysed slices of the three-dimensional parameter space for fixed temperatures in Fig. 4.15 and fixed range parameters in Fig. 4.17, respectively. And by investigating the critical temperature, we illustrated that our approach partially leads to the same behaviour for the critical temperature as the GMB mechanism, which is a beyond mean-field, i.e. a fluctuation effect. In this way, we confirmed that our newly developed method proves as a better starting point for fluctuation theories than the standard single-channel BCS theory.

After having studied the partitioning of interactions in ultracold Fermi systems, we investigated a different problem motivated by recent experimental findings of continuous quantum gas microscopes [184–187]. Those microscopes are able to analyse short-distance properties of Fermi and Bose gases with a never before seen accuracy in continuous space. As such, they require a precise, realistic, and consistent theoretical background in order to describe and explain their measurements, and to make predictions for further investigations. In Chapter 5 we developed and presented exactly this theoretical framework. To this end, we first considered fundamental rules for fermionic correlation functions in quantum many-body theory, which are indisputable and must be satisfied by any theory that aims to describe experimental findings. Those are the necessity of $\mathrm{U}(1)$ gauge invariance, associated with conservation laws, and the Pauli principle as a fundamental property of fermionic systems. In Section 5.2 we used those seemingly simple constraints and Wick's theorem to formulate several important measures, quantifying the quality of calculated correlation functions independent of the underlying fermionic system. Especially the Pauli principle proved to be of great importance, as it led to an equation of state which goes beyond the standard thermodynamic procedure. By considering not the particle number, but by taking into account the fluctuation-dissipation theorem and the fluctuations of the particle number, we were able to present a local equation of state (5.17), which also includes irreducible Feynman diagrams. The latter describes the influence of quantum entanglement, many-body effects, scattering states, and vertex corrections on the number of particles. We emphasised that this is a fundamental result following from model-independent symmetry considerations and, as such, is applicable irrespective of the exact realisation in a laboratory or natural setup. We then continued in Section 5.3 by specifying the developed theory to the D-dimensional BEC-BCS crossover for an ultracold Fermi spin mixture. To obtain a realistic description, we incorporated Gaussian pair fluctuations only in the Bogoliubov channel into a linear response theory with the aim of fulfilling all established constraints. We found that the effective action (5.62) is expressed as combinations of one-loop integrals (5.64) of Fermi propagators. This action gave rise to the generating functional by integrating out the quantum fluctuations, which essentially means taking all possible $\mathrm{U}(1)$ gauge choices into account. As such, we mended the flaw in the saddle-point theory where the gauge of the pair field is globally fixed, making the response function (5.86) independent of the $\mathrm{U}(1)$ gauge. Comparing with the general results of the previous section, we identified that the correlations arising from pair fluctuations are a Gaussian approximation to the irreducible contributions dictated by Wick's theorem in the form of a ladder summation. Furthermore, those terms have a clear interpretation in terms of amplitude and phase fluctuations of the pair field. With this, we were able to specify the general equation of state (5.17) to the D-dimensional BEC-BCS crossover in Eq. (5.103). Ultimately, we evaluated the three equations of state for mean-field, Gaussian quantum fluctuations, and Pauli-principle ensuring in $D = 2$ dimensions and at $T = 0$ in Fig. 5.6. There, we found that the effects of bare fluctuations are weakened due to

the coupling of the collective excitations to the density response. We used this insight in the subsequent Section 5.4 to evaluate real-space density-density correlation functions and to compare our results with recent measurements [187] in Fig. 5.11, finding good qualitative agreement with both the experimental data and quantum Monte Carlo calculations. We obtained those agreements despite working with an idealised, homogeneous two-dimensional system at zero temperature, which are requirements partially violated in the experiment. This demonstrated the strength of our symmetry approach compared to the approximations found in the standard literature. We showed that quantum fluctuations cause an anti-correlated region for opposite-spin particles due to the local conservation of particles. This is an effect that was so far not described theoretically and was only measured in the recent experimental setup. We do not only find this phenomenon, but also explain it theoretically and, in the following Section 5.5, we even made further predictions on the behaviour of this correlation minimum in Fig. 5.12 in the experimentally accessible weak and intermediate interaction regime. We further extended the theory to strong interactions, where experiments have yet to be performed. All in all, this chapter presents a new, consistent theoretical description of correlation functions in a fermionic system and applies this framework to recent experimental measurements. This refines the fundamental theory of superfluidity and superconductivity, as is recognised and highlighted in Ref. [416].

Lastly, we used the Appendices A and B to build a formal foundation of our work, presented in a clean way in order to allow for further improvements on the basis of this thesis. Appendix A presents the field quantisation and notational conventions to unify the languages of operator, functional integral, and diagrammatic methods for the BEC-BCS crossover. We reviewed the standard means of quantum statistical field theory beyond the common textbook content in keeping causal infinitesimal time factors in the description to agree with basic mathematical rules. This became important in Appendix B, where we discussed the necessity of the infinitesimal time displacements when dealing with formally divergent objects like functional integrals. We first discussed in Section B.2 a heuristic way of curing issues arising from switching limiting procedure and integration. Afterwards, we used Section B.3 to work out how to calculate partition functions in general without the necessity of switching limits and integration, an ill-defined operation applied in most works. With this, we were able to calculate all energy contributions of the BCS free energy without having to deal with complicated complex analysis methods like branch-cut integrations, artificial convergence factors or switching between operator-based and functional integral methods. This is important from a mathematical viewpoint as it shows that the framework used throughout this thesis is mathematically fully consistent.

To summarise, in this thesis, we presented two original improvements of the theoretical description of ultracold Fermi gases. We refined the standard description of Fermi gases by partitioning the interaction and by improving the equation of state based on fundamental symmetries. The latter method was verified by explaining recent measurements. Those findings are significant not only in the area of interest in this thesis, but way beyond, as the description of Fermi superfluids ranges from the smallest imaginable scales of the subatomic world, to the ultra-dense remnants of stars, such as neutron stars and white dwarfs, all of which exhibit a similar behaviour. Our findings are also of importance considering that superconductivity is just the superfluidity of charged fermions, i.e. of electrons. Thus, this thesis potentially presents an important first step towards a unified theoretical description of those vastly different, but nevertheless similar systems.

Chapter 7

Outlook

> The road goes ever on and on, down
> from the door where it began.
>
> J. R. R. Tolkien

In this chapter, we outline future directions opened up by this thesis. To this end, we concisely discuss the respective theoretical foundations and their connections to previous sections as well as preliminary results already obtained.

7.1 WHFB approach in 2D

Since we already established a D dimensional formulation of the WHFB approach in Chapter 3, applied in 3D in Chapter 4 and Ref. [P1], a direct extension is to look also at lower dimensional systems, especially at 2D. Despite the necessity of considering the BKT mechanism at finite temperatures, already at $T = 0$ the mean-field description provides a reliable approximation, which can be extended by including Gaussian pair fluctuations. In question is, however, how to treat the scattering problem in two spatial dimensions. The notion of the effective range parameter is not as straightforward as in 3D. Even if we assign a physical meaning to the UV cutoff in 2D, determining its value is challenging. Possible solutions to this might be to consider the quasi-2D limit, which could allow us to physically relate the two-body effective range to the confinement in the z-direction, expressed in terms of a harmonic oscillator frequency ω_z, to a quasi 2D effective range. In the following, we disregard this problem and only consider the WHFB approach for a Fermi spin-mixture in true 2D, using the UV cutoff k_c as a free parameter. The scattering parameter here is obtained by standard scattering theory, via

$$\frac{1}{g} = \frac{1}{2L^2} \sum_{|\boldsymbol{k}|\leq k_\mathrm{c}} \frac{1}{\boldsymbol{k}^2/(2m) + \varepsilon_\mathrm{B}/2}, \tag{7.1}$$

relating the binding energy ε_B and the scattering parameter $\ln k_\mathrm{F} a$ via the relation $\ln k_\mathrm{F} a = \ln(8\varepsilon_\mathrm{F}/\varepsilon_\mathrm{B})/2 - \gamma_\mathrm{E}$ where $\gamma_\mathrm{E} \approx 0.577$ stands for the Euler-Mascheroni constant [102, 414, 415]. Note that in 2D, there exists a two-body bound state irrespective of the attractive interaction strength, making the scattering length always positive and yielding a non-zero binding energy. In 2D, due to a constant density of states the integrals in the self-consistency equations can be explicitly solved at $T = 0$, leading to the following set of

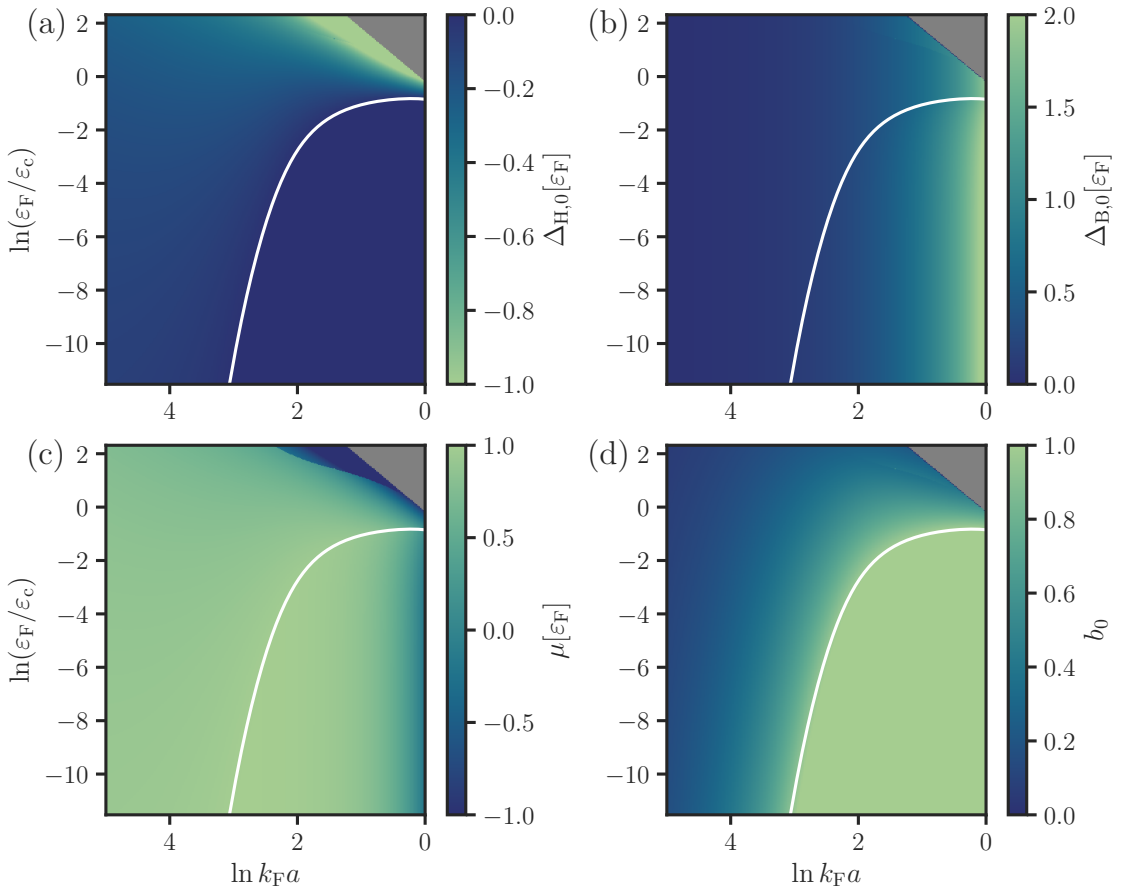


Figure 7.1: Self-consistent solutions to WHFB equations. Panel (a) shows Hartree self-energy, panel (b) superfluid order parameter, panel (c) chemical potential and panel (d) partitioning factor b_0 in the $\ln(\varepsilon_F/\varepsilon_c)$ - $\ln k_F a$ plane. All energies are depicted in units of the Fermi energy ε_F. Solid white line stands for the HSF-SSF transition line and the grey region represents a parameter region, where the notion of a contact potential fails.

equations for $\Delta_{H,0}$,$\Delta_{B,0}$,μ, and $\varepsilon_{c,B}$

$$\Delta_{H,0} = \min\left\{0; -\frac{2\varepsilon_F}{\log(1+2\varepsilon_c/\varepsilon_B)} + |\Delta_{B,0}|\right\}, \tag{7.2a}$$

$$\frac{\varepsilon_{c,B}}{2\varepsilon_{c,B}+\varepsilon_B} = \left[\frac{1}{\varepsilon_B} - \frac{1}{2\varepsilon_{c,B}+\varepsilon_B}\right]\left[\sqrt{(\mu+\Delta_{H,0})^2+|\Delta_{B,0}|^2} - (\mu+\Delta_{H,0})\right], \tag{7.2b}$$

$$2\varepsilon_F = (\mu+\Delta_{H,0}) + \sqrt{(\mu+\Delta_{H,0})^2+|\Delta_{B,0}|^2}, \tag{7.2c}$$

$$\varepsilon_{c,B} = \frac{\varepsilon_B}{2}\left[\left(1+2\frac{\varepsilon_c}{\varepsilon_B}\right)^{1+|\Delta_{H,0}|/|\Delta_{B,0}|} - 1\right]. \tag{7.2d}$$

Afterwards we perform a Taylor-expansion for large UV cutoff $\varepsilon_c = k_c^2/2m \gg \varepsilon_B$ in Eqs. (7.2b) and (7.2c), yielding

$$|\Delta_{B,0}| = \sqrt{2\varepsilon_B}\left[1 - \frac{1}{2}\frac{\varepsilon_B}{\varepsilon_{c,B}} + \mathcal{O}\left(\frac{\varepsilon_B}{\varepsilon_{c,B}}\right)^2\right], \tag{7.3a}$$

$$\mu = \left(\varepsilon_F - \frac{1}{2}\varepsilon_B + \Delta_{H,0}\right) + \frac{1}{2}\frac{\varepsilon_B}{\varepsilon_{c,B}} + \mathcal{O}\left(\frac{\varepsilon_B}{\varepsilon_{c,B}}\right)^2. \tag{7.3b}$$

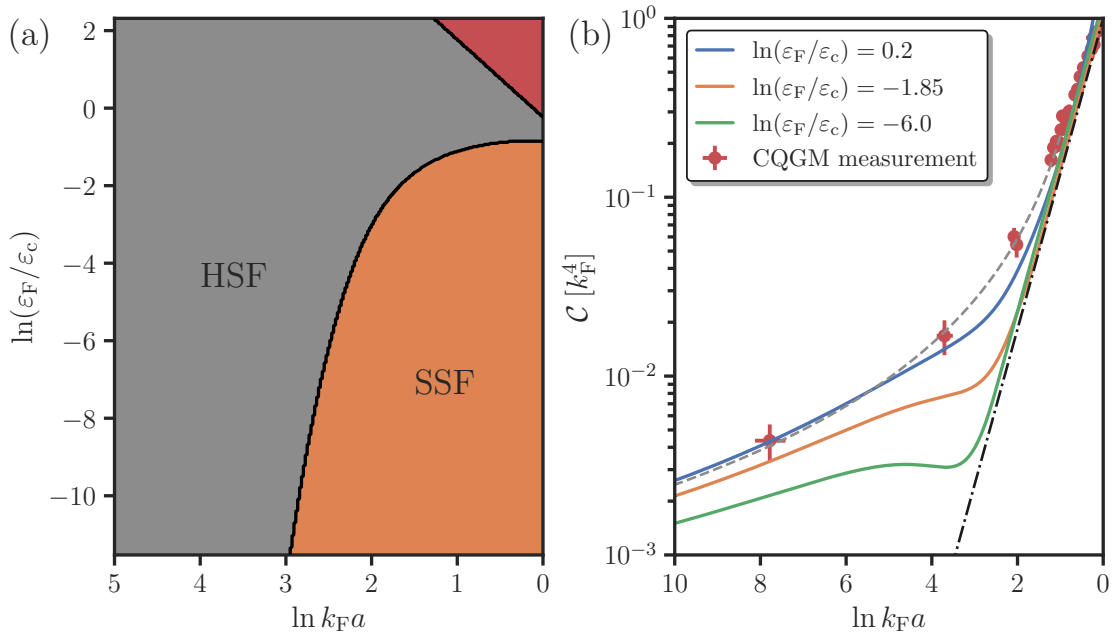


Figure 7.2: Panel (a): Phase diagram of WHFB ground state in the $\ln(\varepsilon_F/\varepsilon_c)$ - $\ln k_F a$ plane. Grey region depicts HSF phase, orange region SSF phase and red region stands for forbidden parameter combinations. Panel (b): Universal contact in units of k_F^4 versus $\ln k_F a$ for various effective range parameters. Red dots indicate experimental measurement from Ref. [187], dashed grey line stands for Fermi liquid prediction and dash-dotted black line depicts zero-range BCS result.

All those energies are functions of the screened many-body UV cutoff (7.2d), which tends to $\varepsilon_{c,B} \to \varepsilon_c$ when $\Delta_{H,0} \to 0$. We illustrate preliminary numerical results in Fig. 7.1, showing the order parameters $\Delta_{H,0}$, $\Delta_{B,0}$, the chemical potential μ, and weighting factor b_0, Eq. (3.59b) in four panels as colour maps in the $\ln(\varepsilon_F/\varepsilon_c)$ - $\ln k_F a$ plane. The boundary between HSF and SSF regions is shown as the solid white line. The figures also have a grey region, where the approximation of a 2D contact potential breaks down due to too large a value of the UV cutoff ε_c compared to Fermi ε_F and binding ε_B energies. We further present the corresponding phase diagram of the WHFB ground state in Fig. 7.2 (a), where, like in the 3D case in Fig. 4.3, the grey region represents the Hartree superfluid (HSF) and the orange region the standard superfluid (SSF). In addition, we represent the forbidden parameter region in red.

We can also obtain the contact $\mathcal{C}$ as a central quantity for quantum gases in general and for crossover physics in particular, which has recently been measured within a continuous quantum gas microscope setup [187]. The contact obtained in our case reads

$$\mathcal{C} = \frac{k_F^4}{4\varepsilon_F^2}\left(|\Delta_{H,0}|^2 + |\Delta_{B,0}|^2\right), \tag{7.4}$$

compare Eq. (4.72). In the SSF phase this reproduces the standard contact obtained in a BCS mean-field theory of $\mathcal{C}_{BCS} = k_F^4 \exp(-2\ln k_F a)$, while in the HSF region and for extreme weak interactions we obtain

$$\mathcal{C} = k_F^4 \frac{1}{4}\left[\frac{1}{(\ln k_F a)^2} - \frac{2\widetilde{\gamma}}{(\ln k_F a)^3} + \mathcal{O}\left(\frac{1}{\ln k_F a}\right)^3\right] + \mathcal{O}\left(e^{-\ln k_F a}\right), \tag{7.5}$$

where the constant in second order depends on the effective range parameter via $\widetilde{\gamma} = \gamma_{\mathrm{E}} - \ln(4)/2 + \ln(\varepsilon_{\mathrm{c}}/\varepsilon_{\mathrm{F}})/2$. This is formally equivalent to the Fermi-liquid prediction, where the second-order prefactor is $\widetilde{\gamma}_{\mathrm{FL}} = 3/4 - \ln(2)$ [187, 357, 417]. We present our results for the contact in Fig. 7.2 (b) for various values of $\ln(\varepsilon_{\mathrm{F}}/\varepsilon_{\mathrm{c}})$, together with the BCS asymptote as dash-dotted black line and the Fermi liquid prediction as dashed grey line. In addition, the experimental data obtained in Ref. [187] are shown as red dots. In the HSF region, the contact obtained in a WHFB approach qualitatively follows a similar behaviour as the Fermi liquid theory, while in the SSF region, we obtain the BCS curve. This is a strong indication that our mean-field analysis is qualitatively capturing effects beyond the standard BCS approach, even if 2D quantum fluctuations are included. However, to understand the discrepancies between $\widetilde{\gamma}$ and $\widetilde{\gamma}_{\mathrm{FL}}$ needs further investigations and might be resolved by including particle-hole fluctuations in addition to pair fluctuations.

7.2 Collective modes of WHFB approach

A straightforward extension of Chapters 3 and 4 is to look beyond the SP analysis by taking into account quantum fluctuations. This has been done over the last decades by various groups considering only the Bogoliubov channel, pioneered in Refs. [87, 88]. In our case, we aim to consider simultaneous quantum fluctuations both in the Bogoliubov and the Hartree channel, for now in general D dimensions. To this end, we again consider a SP decomposition (3.45a) and (3.45b) which reads

$$\Delta_{\mathrm{B},q} = \Delta_{\mathrm{B},0} + \lambda_q + i\theta_q, \tag{7.6a}$$
$$\Delta_{\mathrm{H},q} = \Delta_{\mathrm{H},0} + \eta_{\mathrm{H},q}, \tag{7.6b}$$

with λ_q, θ_q as real fields, representing real part (amplitude) and imaginary part (phase) fluctuations of the pair field, while $\eta_{\mathrm{H},q}$ is a real field describing the fluctuations in the Hartree field. For the sake of conciseness, we consider here only fluctuations of the total Hartree channel, even though imbalance fluctuations might also occur. We expand the action (3.44) from the main text in orders of the quantum fluctuations, leading to a vanishing first order due to the SP condition. The Gaussian term, however, is determined by a 3×3 matrix coupling the quantum fluctuations, formally reading

$$\mathcal{S}_{\mathrm{Gauss}}[\lambda, \theta, \eta_{\mathrm{H}}] = \frac{\beta}{2} \sum_q \boldsymbol{\eta}_{-q}^{\mathrm{T}} \boldsymbol{\Gamma}_{\mathrm{HB}}(q) \boldsymbol{\eta}_q \,. \tag{7.7}$$

This is the effective action describing the quantum fluctuations, summarised in the vector

$$\boldsymbol{\eta}_q = \begin{pmatrix} \lambda_q \\ \theta_q \\ \eta_{\mathrm{H},q} \end{pmatrix} . \tag{7.8}$$

Furthermore, the matrix

$$\boldsymbol{\Gamma}_{\mathrm{HB}}(q) = \begin{pmatrix} \Gamma_{xx}(q) & \Gamma_{xy}(q) & \Gamma_{xz}(q) \\ \Gamma_{yx}(q) & \Gamma_{yy}(q) & \Gamma_{yz}(q) \\ \Gamma_{zx}(q) & \Gamma_{zy}(q) & \Gamma_{zz}(q) \end{pmatrix} \tag{7.9}$$

is the pair propagator, i.e. the inverse t-matrix of the quantum fluctuations, whose zeroes denote collective excitations in the system. As previously discussed, they are carried by

the amplitude or the phase of the superfluid. But in our weighted theory, the fluctuations in the Hartree channel are also capable of supporting a collective excitation. The matrix elements of $\mathbf{\Gamma}_{\mathrm{HB}}(q)$ are fermionic loop functions (2.54), already seen in the introduction, formally written as

$$\Gamma_{ab}(q) = \frac{2L^D\delta_{ab}}{\delta_{az}g_{\mathrm{H}} + (\delta_{ax} - \delta_{ay})g_{\mathrm{B}}} - i^{\zeta_{ab}}\chi_{ab}(q), \tag{7.10}$$

where we define the traces as the respective susceptibilities

$$\chi_{ab}(q) = -\frac{1}{\beta}\sum_k \mathrm{tr}\left\{\boldsymbol{G}_{\mathrm{SP}}(k)\boldsymbol{\gamma}_a\boldsymbol{G}_{\mathrm{SP}}(k+q)\boldsymbol{\gamma}_b\right\}. \tag{7.11}$$

In this definition $\boldsymbol{G}_{\mathrm{SP}}(k)$ is the SP Green's function, see Eq. (3.56b), $\boldsymbol{\gamma}_{x,z} = \boldsymbol{\sigma}_{x,z}$ are the first and third Pauli matrix, respectively and, to take the imaginary unit of the phase into account, we set $\boldsymbol{\gamma}_y = i\boldsymbol{\sigma}_y$, hence the i in the definition (7.10). We now focus only on the matrix elements of Eq. (7.10), which we explicitly obtain at $T = 0$, leading to the functions

$$\Gamma_{xx}(q) = \sum_{|\boldsymbol{k}|\leq k_{\mathrm{c,B}}}\left(\frac{1}{E} + \frac{E+E'}{EE'}\frac{EE' + \xi\xi' - |\Delta_{\mathrm{B},0}|^2}{(iq_\ell)^2 - (E+E')^2}\right), \tag{7.12a}$$

$$\Gamma_{yy}(q) = \frac{1}{L^D}\sum_{|\boldsymbol{k}|\leq k_{\mathrm{c,B}}}\left(\frac{1}{E} + \frac{E+E'}{EE'}\frac{EE' + \xi\xi' + |\Delta_{\mathrm{B},0}|^2}{(iq_\ell)^2 - (E+E')^2}\right), \tag{7.12b}$$

$$\Gamma_{zz}(q) = \frac{2L^D}{g_{\mathrm{H}}} - \sum_{\boldsymbol{k}}\frac{E+E'}{EE'}\frac{EE' - \xi\xi' + |\Delta_{\mathrm{B},0}|^2}{(iq_\ell)^2 - (E+E')^2}, \tag{7.12c}$$

$$\Gamma_{xy}(q) = -i(iq_\ell)\sum_{\boldsymbol{k}}\frac{E\xi' + E'\xi}{EE'}\frac{1}{(iq_\ell)^2 - (E+E')^2}, \tag{7.12d}$$

$$\Gamma_{xz}(q) = \sum_{\boldsymbol{k}}\frac{E+E'}{EE'}\frac{|\Delta_{\mathrm{B},0}|(\xi+\xi')}{(iq_\ell)^2 - (E+E')^2}, \tag{7.12e}$$

$$\Gamma_{yz}(q) = i(iq_\ell)\sum_{\boldsymbol{k}}\frac{E+E'}{EE'}\frac{|\Delta_{\mathrm{B},0}|}{(iq_\ell)^2 - (E+E')^2}. \tag{7.12f}$$

Here we used the shorthand notations for the free dispersions $\xi = \xi_{\boldsymbol{k}}, \xi' = \xi_{\boldsymbol{k}+\boldsymbol{q}}$ and the analogous notation for the quasi-particle dispersions E, E'. Note that we know, for instance, from Refs. [88, 418] that for zero energy and zero momentum, there exists a gapless Goldstone mode. Furthermore, for energies larger than the pair breaking continuum energy $\varepsilon_{\mathrm{PB}}(\boldsymbol{q}) = \min_{\boldsymbol{k}}(E+E') \leq 2|\Delta_{\mathrm{B},0}|$ the collective modes couple to the continuum of free fermions, potentially dissolving the Cooper pairs. In order to investigate the collective modes, we perform an analytic continuation $iq_\ell \to \omega + i0^+$ and expand all the matrix elements for small $\boldsymbol{q}$ and ω. With this, the inverse pair t-matrix reads

$$\Gamma_{\mathrm{HB}}(q) = \begin{pmatrix} A + C|\boldsymbol{q}|^2 - M\omega^2 & iB\omega & F + G|\boldsymbol{q}|^2 - P\omega^2 \\ -iB\omega & Q|\boldsymbol{q}|^2 - R\omega^2 & iS\omega \\ F + G|\boldsymbol{q}|^2 - P\omega^2 & -iS\omega & H + J|\boldsymbol{q}|^2 - K\omega^2 \end{pmatrix}. \tag{7.13}$$

Here, $A, B, C, M, F, G, P, Q, R, S, H, J, K$ are real-valued functions of $\mu, \Delta_{\mathrm{B},0}, \Delta_{\mathrm{H},0}$, and$k_{\mathrm{c,B}}$, the dimensionality D and the length of the confinement L. Here, we note several things. The first notion is that for zero energy, i.e. $\omega \to 0$, the phase mode decouples from the amplitude mode, seen in the xy and yx matrix elements $\pm iB\omega$. This is already known,

but beyond this, we find that the phase mode also decouples from the Hartree mode, as seen in the yz and zy matrix elements, which behave as $\pm iS\omega$. However, amplitude and Hartree mode remain coupled, even at zero energy and zero momentum, with strength F. Furthermore, we recognise that for low momenta and energies the mode associated with the Hartree channel is gapped by $H > 0$ as well, similarly to the amplitude mode, which is gapped by A. The quantity H acts as a mass-square of the Hartree fluctuations and is proportional to $1/g_{\mathrm{H}}$, meaning that in the SSF phase, when $g_{\mathrm{H}} \to 0$, the Hartree fluctuations become infinitely heavy and can not propagate any more.

Using the fluctuation propagator matrix (7.13) we obtain the t-matrix as a scalar function via taking the determinant. For energies below the pair breaking, we find

$$\det \Gamma_{\mathrm{HB}}(\omega, \boldsymbol{q}) \approx \widetilde{C}\left(c_{\mathrm{s}}^2 |\boldsymbol{q}|^2 - \omega^2\right) + \mathcal{O}(|\boldsymbol{q}|, \omega)^4, \tag{7.14}$$

with $\widetilde{C}$ denoting the spectral weight of the phase mode and

$$c_{\mathrm{s}} = \sqrt{\frac{Q\left(1 - \frac{F}{AH}\right)}{R + B^2/A + \alpha}} \tag{7.15}$$

representing the Goldstone speed of sound. The abbreviation

$$\alpha = \frac{F\left(FR + BS\right) + S\left(AS + BF\right)}{AH} \tag{7.16}$$

defines the correction relative to the single-channel BCS Goldstone speed of sound denominator. Furthermore, the numerator also has a correction factor in the brackets. Both corrections are proportional to the inverse of the product of amplitude and Hartree energy gaps and linearly depend on the coupling between amplitude or phase to the Hartree channel, i.e. on F or S, respectively. Because of this, we see that, as soon as the mass of the Hartree fluctuations diverges, for instance when approaching the SSF phase, the corrections vanish, and we find the standard BCS speed of sound $c_{\mathrm{s}} \to \sqrt{Q/(R + B^2/A)}$.

As an example, we illustrate in Fig. 7.3 the speed of sound (7.15) in units of the Fermi velocity $v_{\mathrm{F}} = k_{\mathrm{F}}/m$, using the SP solutions in 3D obtained in Chapter 4. We illustrate the speed of sound versus the dimensionless scattering parameter $1/k_{\mathrm{F}}a_{\mathrm{s}}$ for various effective range parameters, namely $k_{\mathrm{F}}r_{\mathrm{e}} = 0$ (solid black line), $k_{\mathrm{F}}r_{\mathrm{e}} = 0.5$ (solid blue line), $k_{\mathrm{F}}r_{\mathrm{e}} = 0.08$ (solid green line), $k_{\mathrm{F}}r_{\mathrm{e}} = 0.14$ (solid red line), which is the same colour scheme used throughout Chapter 4. We depict the asymptote for weak interactions, i.e. $c_{\mathrm{s}} = v_{\mathrm{F}}/\sqrt{3}$, as dashed grey line. We furthermore represent the ill-regularised theory [28, 296] with a naive Hartree shift as magenta dash-dotted line. Its divergence indicates the necessity of using both the proper effective range regularisation and the partitioning when aiming to include the particle-hole sector into the description of collective excitations. The divergence of the speed of sound in the unweighted and unregularized approach occurs for negative scattering parameters prior to unitarity, after which it becomes imaginary, making the theory completely unphysical. In contrast, our WHFB approach always leads to a real and finite sound velocity. Furthermore, we see that fluctuations in the HSF phase are slowed down, relative to the zero-range theory, due to the finite corrections seen in Eq. (7.15), compared to the standard BCS result, which is valid in the SSF region. As a reminder, the HSF region appears for extremely weak interactions only, $1/k_{\mathrm{F}}a_{\mathrm{s}} \to -\infty$, while for stronger interactions the system is in the SSF region. In the SSF region, the Hartree shift vanishes, and the speed of sound is altered due to the presence of an effective

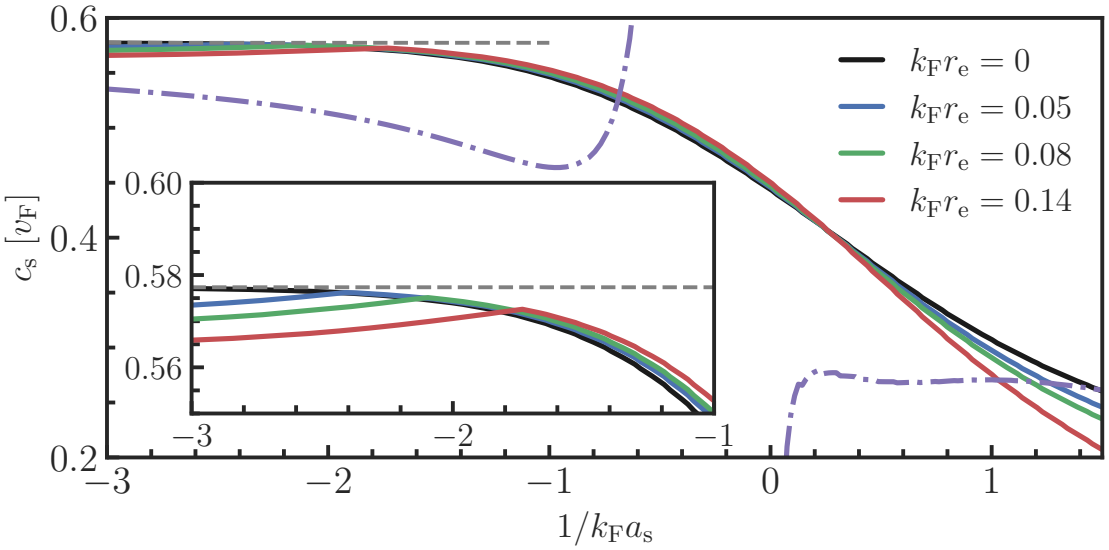


Figure 7.3: Speed of sound c_s in units of v_F at $T = 0$ for 3D WHFB approach, versus interaction parameter $1/k_F a_s$. We use various effective range parameters with colour code indicated in the figure, identical to encoding established in Fig. 4.3, with solid black line as zero-range reference. Dashed grey line is BCS prediction of sound velocity and magenta dash-dotted line represents unweighted poorly regularised standard approach [28]. Inset shows same curves enlarged for weak interactions.

range. This comes about from the fact that a positive chemical potential yields a persisting Fermi surface, and as such, the particles behave fermionic, which means that their Pauli repulsion speeds up the propagation of sound as a pressure wave. When the chemical switches sign for even stronger interactions, we are dealing with a gas of composite bosons, and a finite interaction range actually slows down the broken symmetry sound. The strength of all those effects scales with the effective range parameter. However, one has to be cautious with those preliminary results, as for reliable predictions, it has been shown in 2D [107] that using the SP self-consistent solutions of the order parameters and the chemical potential is not sufficient. Hence, the effect of quantum fluctuations on the equation of state is required to be taken into account for a consistent theory. This is the subject of further studies in progress.

From here on, there are several directions to follow. Obviously evaluating the speed of sound numerically exact and finding the full spectral function beyond small energies is an important benchmark, as this can be accessed via Bragg spectroscopy in two and three dimensions. Besides this, it is worthwhile to obtain an effective field theory for the collective excitations, for instance, the Goldstone mode, by integrating out amplitude and Hartree fluctuations. This would lead to equations of motion going beyond the simple resonant excitation condition $\omega(\boldsymbol{q}) = c_s|\boldsymbol{q}|$. In this context, also calculating the higher-order terms of the Goldstone dispersion beyond the linear regime is a reasonable task in view of a thorough comparison with measurements.

Having achieved this, one could aim to consider the Gaussian equation of state including all quantum fluctuations, and compare it diagrammatically with GPF [84, 88, 418] and GMB [94, 99, 100] formulations.

7.3 Correlation functions from WHFB theory

Based on the previous two sections, the next topic relies on fusing the WHFB approach developed in Chapter 3 and the gauge invariant Pauli principle respecting response theory established in Chapter 5. This envisioned research direction serves two purposes. First, this approach directly allows working out quantum fluctuations simultaneously in different interaction channels, as in the previous section 7.2 in a consistent way, which agrees with the Pauli principle. Secondly, by including the Hartree self-energy and its fluctuations, we would be able to make more reliable predictions regarding two-point correlation functions. This will allow a direct experimental test of the WHFB approach in 2D quantum gas microscope experiments and, if verified, would also enable experimental access to beyond-zero-range physics. To see how this formally works, we again couple the action of the system to bosonic source terms via minimal density-coupling. We then perform the WHFB approach in parallel to the standard BCS approach found in Chapter 5. After this, we include simultaneous quantum fluctuations in both Hartree and Bogoliubov channels, see Eqs. (7.6a) and (7.6b). As a result, we find a Gaussian term of the effective action, similar to the one presented in Eq. (5.62), which reads

$$\mathcal{S}_{\mathrm{Gauss}}[\lambda,\theta,\eta_{\mathrm{H}};j] = \frac{\beta}{2}\sum_{q}\begin{pmatrix}\boldsymbol{j}_{-q}^{\mathrm{T}} & \boldsymbol{\eta}_{-q}^{\mathrm{T}}\end{pmatrix}\left(\begin{array}{c|c}-\widetilde{\boldsymbol{\chi}}^{(0)}(q) & -\boldsymbol{\Lambda}^{\mathrm{T}}(q)\\ \hline -\boldsymbol{\Lambda}(q) & \boldsymbol{\Gamma}_{\mathrm{HB}}(q)\end{array}\right)\begin{pmatrix}\boldsymbol{j}_{q}\\ \boldsymbol{\eta}_{q}\end{pmatrix}. \tag{7.17}$$

In contrast to Eq. (5.62), here we have a 5×5 matrix, since the fluctuation vector $\boldsymbol{\eta}_q$ has three entries according to Eq. (7.8). The upper left matrix is the 2×2 matrix $\widetilde{\boldsymbol{\chi}}^{(0)}(q)$, describing the mean-field response, and coincides with the result obtained without a WHFB approach (5.68), provided we replace $\mu \to \mu + \Delta_{\mathrm{H},0}$. The 3×3 fluctuation propagator $\boldsymbol{\Gamma}_{\mathrm{HB}}(q)$ is the one seen in Eq. (7.9). Here, the notation from Chapter 5 is unhandy, which is why we change it slightly here. From now on, we denote the regularised loop functions by Γ_{ab} instead of Π_{ab}, see the definition in Eq. (7.10). We do so, since the full matrix in Eq. (7.17) contains zz-loop functions in two different ways, regularised ones, in the pair propagator (7.9) and unregularised ones in the coupling matrix

$$\boldsymbol{\Lambda}(q) = \begin{pmatrix}\Lambda_{x\uparrow}(q) & \Lambda_{x\downarrow}(q)\\ \Lambda_{y\uparrow}(q) & \Lambda_{y\downarrow}(q)\\ \Lambda_{z\uparrow}(q) & \Lambda_{z\downarrow}(q)\end{pmatrix}. \tag{7.18}$$

The latter coupling matrix elements hence read

$$\Lambda_{a\mathrm{s}}(q) = \frac{i^{\delta_{ay}}}{\beta}\sum_{k}\mathrm{tr}\left\{\boldsymbol{G}_{\mathrm{SP}}(k)\boldsymbol{\gamma}_a\boldsymbol{G}_{\mathrm{SP}}(k+q)\boldsymbol{\gamma}_{\mathrm{s}}\right\} = i^{\delta_{ay}}\chi_{a\mathrm{s}}(q), \tag{7.19}$$

where a is the index of the quantum fluctuations $a\in\{x,y,z\}$, while $\mathrm{s}\in\{\uparrow,\downarrow\}$ stands for the spin index. Here $\chi_{a\mathrm{s}}(q)$ represents a susceptibility characterising the interplay of quantum fluctuations and spin densities. We obtain the corresponding generating functional by functional integration of all quantum fluctuations, which results in

$$\mathcal{Z}[j] = \mathcal{Z}_{\mathrm{SP}}e^{-\mathcal{S}_{\mathrm{Lin}}[j]}\oint_{\mathrm{P}}\mathcal{D}[\lambda,\theta,\eta_{\mathrm{H}}]e^{-\mathcal{S}_{\mathrm{Gauss}}[\lambda,\theta,\eta_{\mathrm{H}},j]} = e^{W[j]}, \tag{7.20}$$

which is analogous to the result in Eq. (5.80). Expanding the W-generating functional in terms of the source term leads to

$$W[j] \approx W_0 + W_1[j] + W_2[j] + \mathcal{O}(j)^3. \tag{7.21}$$

Here the first term

$$W_0 = \sum_k \ln\det\left[-\beta \boldsymbol{G}_{\mathrm{SP}}^{-1}(k)\right] - \beta V \frac{|\Delta_0|^2}{g} - \frac{1}{2}\sum_q \ln\det\left[\beta \boldsymbol{\Gamma}_{\mathrm{HB}}(q)\right] - \beta\Omega(L^D, T, \mu_{\mathrm{s}}) \quad (7.22)$$

is related to the grand-canonical potential when including quantum fluctuations in both Hartree and Bogoliubov channels. It could also be obtained in Section 7.2 when calculating the thermodynamic potential. The linear term is identical to Eq. (5.84), as quantum fluctuations have no influence on the linear terms in general. And the second-order term in j yields the response function

$$W_2[j] = \frac{\beta}{2}\sum_q \boldsymbol{j}_{-q}^{\mathrm{T}} \widetilde{\boldsymbol{\chi}}(q) \boldsymbol{j}_q, \quad (7.23)$$

which now includes the influence of both pair and Hartree fluctuations. We find the response function to be decomposed similar to Eq. (5.86), reading

$$\widetilde{\boldsymbol{\chi}}(q) = \widetilde{\boldsymbol{\chi}}^{(0)}(q) + \widetilde{\boldsymbol{\chi}}_{\mathrm{HB}}^{\mathrm{irr}}(q) = \begin{pmatrix} \widetilde{\chi}_{\uparrow\uparrow}(q) & \widetilde{\chi}_{\uparrow\downarrow}(q) \\ \widetilde{\chi}_{\downarrow\uparrow}(q) & \widetilde{\chi}_{\downarrow\downarrow}(q) \end{pmatrix}. \quad (7.24)$$

However, in this case, the irreducible contribution includes more families of diagrams as the ones introduced in Chapter 5. The irreducible term reads

$$\widetilde{\boldsymbol{\chi}}_{\mathrm{HB}}^{\mathrm{irr}}(q) = \boldsymbol{\Lambda}^{\mathrm{T}}(-q)\boldsymbol{\Gamma}_{\mathrm{HB}}^{-1}(q)\boldsymbol{\Lambda}(q). \quad (7.25)$$

The full set of diagrams involved here goes beyond the scope of this outlook. A set of additional diagrams will remain finite even upon reaching the normal state. This is due to Hartree fluctuations, allowing for diagrams without anomalous propagators. Furthermore, this yields a set of bubble diagrams, analogous to a bubble summation rather than a ladder summation. In addition to this, we also will find diagrams, starting in second order and becoming more important for even higher orders in g, which involve mixtures of ladder and bubble pieces, reflecting the interplay of pair and Hartree fluctuations on a diagrammatic level.

7.4 Systems with non-singular interactions

To gain more insight into the general properties of the WHFB approach, it is worthwhile to think about systems with non-singular interactions. This means considering interaction potentials beyond a simple contact interaction potential. Steps towards this were already presented in the Appendix 3.A, where we considered a general interaction potential. In this outlook, however, we make things more specific and think explicitly about the Fermi system in question. The most straightforward idea to generalise Chapter 3 is to consider a balanced $\mathrm{SU}(2)$ symmetric Fermi spin mixture, where equal spin particles still do not interact, while opposite spin particles interact via a short-ranged potential, which is separable in momentum space. This means that we are able to express $U_{\boldsymbol{k},\boldsymbol{k}'} = g\Gamma(\boldsymbol{k})\Gamma(\boldsymbol{k}')$, where the function Γ is commonly known as the form factor [67]. This is a simplifying assumption often used in theories of the nucleus [310]. In a standard BCS SP evaluation, we find that the superfluid order parameter becomes a function of the momentum in the form $\Delta_{\mathrm{B},\boldsymbol{k}} = \Delta_{\mathrm{B},0}\Gamma(\boldsymbol{k})$, leading to the superfluid order parameter equation

$$|\Delta_{\mathrm{B},0}| = g\frac{1}{L^D}\sum_{\boldsymbol{k}} \frac{\Gamma(\boldsymbol{k})}{2E_{\boldsymbol{k}}} \tanh\left(\frac{\beta}{2}E_{\boldsymbol{k}}\right), \quad (7.26)$$

where the quasi-particle dispersion is altered via

$$E_{\boldsymbol{k}} = \sqrt{\left(\frac{\boldsymbol{k}^2}{2m} - \mu_{\mathrm{H}}\right)^2 + |\Gamma(\boldsymbol{k})\Delta_{\mathrm{B},0}|^2}. \tag{7.27}$$

Here we use again the shifted chemical potential $\mu_{\mathrm{H}} = \mu + \Delta_{\mathrm{H},0}$, where the Hartree self-energy reads

$$\Delta_{\mathrm{H},0} = \frac{gn}{2}\Gamma(\boldsymbol{0}). \tag{7.28}$$

The latter only depends on the zero-momentum component of the interaction potential, as the Hartree self-energy is diagrammatically an attached bubble diagram, like a tadpole. Hence, no momentum transfer can happen there, see for instance Refs. [5, 419]. The form factor closest to our contact interaction potential is a Heaviside form factor $\Gamma(\boldsymbol{k}) = \Theta(k_{\mathrm{c}} - |\boldsymbol{k}|)$, with the cutoff being determined via the effective range (4.4). However, also more complicated form factors might be considered, like Gaussian or Lorentzian curves, or even further constructions suitable for d-wave superfluids [420].

So far, results in the literature have entirely ignored the partitioning and can be obtained via a standard Hartree-Fock-Bogoliubov approximation. When dealing with our WHFB approach, not only do we need to partition the interaction strength g, but also at the same time the form factor $\Gamma(\boldsymbol{k})$ such that the original interaction is preserved. How this is done explicitly is a subject of an ongoing collaboration with the group of Jacques Tempere at the University of Antwerp. Here, however, we will present a brief summary concerning the Heaviside form factors in three dimensions. When partitioning the interaction, we assume, for simplicity, that both the shape and the strength of the potential are partitioned separately, and hence they do not directly affect each other. Under those circumstances, we perform the same partitioning as in Chapter 4, i.e. $g = g_{\mathrm{H}} + g_{\mathrm{B}}$, for which we then separately solve the respective Lippmann-Schwinger equations. This again leads to the same conditions for the many-body UV cutoff, as we still absorb all the partitioning into the effective range, since the s-wave scattering length, as a physical observable, should be independent of our artificial separation of the interaction. We then continue with the form factors and assume that in the respective form factors we replace the UV cut-off k_{c} by Hartree or Bogoliubov cut-offs, respectively. This is extremely close to the formulation we found in Chapter 4, with the only difference lying in the quasi-particle dispersion (7.27), which in the case presented here has a discontinuity at $|\boldsymbol{k}| = k_{\mathrm{c,B}}$. Thus, momenta smaller than the cut-off are affected by the Cooper pairs, while momenta larger behave like an ideal Fermi gas. However, since we deal with large UV cut-offs by the assumption of a small effective range, compared to the mean-particle distance, the overall effects of the altered dispersion should turn out to be negligible.

A fully self-consistent treatment of the form factors is more involved and part of the ongoing project. Hence, the mathematically rigorous derivation of the WHFB method for separable potentials is not yet done. This includes the question of whether and how the case discussed in Chapter 4 can be explicitly derived from an effective field theory with form factors.

7.5 Further directions

At the end of this outlook, we highlight some other important research questions, which are opened by this thesis and are potential subjects of further research.

Firstly, we aim to consider the WHFB SP theory in 3D and 2D for imbalance populations $n_\uparrow \neq n_\downarrow$, or even for mass-imbalance $m_\uparrow \neq m_\downarrow$, for instance when investigating a mixture of ^{6}Li and ^{40}K. In such a system, the question is, how stable the superfluid actually is and how the influence of the partitioned Fock contribution comes into play. To this end, we aim at investigating the FuldeFerrellLarkinOvchinnikov (FFLO) phase, where Cooper pairs form at a finite momentum $\boldsymbol{q}$ due to Fermi surfaces of different sizes [421]. In addition, there exists the Sarma phase, where the Cooper pairs form with zero momentum, even though there is an imbalance in the system [422]. Although the latter phase is usually unstable, it would be interesting to investigate whether the partitioning of the interaction and the influence of Hartree and Fock channels present a mechanism to potentially stabilise this phase.

Furthermore, in the spirit of the Appendix 3.A and the previous consideration on separable potentials, it is of interest to consider how the WHFB approach deals with dipolar systems. A first step might be to consider a weighted Hartree-Fock theory of the spin-polarised, i.e. one-component dipolar gas, which then can be extended to a full WHFB description of dipolar gases of two components. This is of particular interest, as more experimental setups are able to deal with dipolar gases, to prepare and manipulate them, as well as ultimately to measure their properties.

Especially in the context of the response theory developed in Chapter 5, a more theoretical interest lies in the construction of the Luttinger-Ward energy functional via the effective action approach as a Legendre transformation of the generating functional

$$\Gamma[\phi] = W[j[\phi]] - \int \mathrm{d}^{D+1}x\, \phi(x) j[\phi(x)], \tag{7.29}$$

where $\phi(x) = \delta W[j]/\delta j(x)$ is the Legendre transformed field of the source term $j(x)$ [14, 411]. This effective action poses the set of all one-particle irreducible (1PI) diagrams and is normally difficult to evaluate. Different schemes exist to approximate the effective action, i.e. the Luttinger-Ward energy functional. One example is the Baym-Kadanoff approach, which was already mentioned in the introduction to Chapter 5. Our approach allows for a systematic construction of the Luttinger-Ward functional without an arbitrary choice of various 1PI diagrams. In doing so, we will be able to obtain an effective field theory for density or spin modulations in Fermi gases beyond their background and away from resonant excitations. Furthermore, this also leads to a self-consistent diagrammatic theory because the Luttinger-Ward energy functional allows for the inclusion of all self-energy terms arising from a given set of diagrams. Together with the modified Pauli-respecting equation of state (5.103) via the mean square of the particle number, we aim to close the loop between fluctuation-dissipation theorem and dressed Green's function, potentially generating a scheme for many-body correlation functions, which agrees with both the Pauli-principle and the Ward-Takahashi identities by being Φ-differentiable. We can also think about extending the WHFB response theory, as a fusion of Chapters 3 and 5, in order to go beyond the scope discussed in Section 7.3.

Appendix

Appendix A

Field theoretical considerations

Le bon Dieu est dans le détail (the good god is in the details)

Gustave Flaubert, 19^{th} century

A.1 Second quantization 171
A.1.1 Single particle quantum mechanics 171
A.1.2 Fock space 172
A.1.3 Fermionic coherent states 175
A.2 Quantum (statistical) field theory 178
A.2.1 Feynman path integration 178
A.2.2 Euclidean path integral 183
A.2.3 Functional integration 184
A.2.4 Gaussian functional integrals 190

A.1 Second quantization

In this Appendix, we establish the mathematical and conventional foundations of the field theory used throughout this thesis. In this section, in particular, we discuss the operator-based formulation of many-body quantum mechanics starting from a single-particle framework, ultimately culminating in the introduction of fermionic coherent states. Those are vital to introduce the functional integral version of many-body field theory.

A.1.1 Single particle quantum mechanics

To describe quantum systems, usually the time-dependent Schrödinger equation $i\partial_t|\psi\rangle = \hat{H}|\psi\rangle$ is put to use, where $\hat{H}$ denotes the Hamiltonian of the investigated system. Given an initial configuration of the state at initial time t_i, the time evolution of such a system is described by the unitary time evolution operator $\hat{U}$ via

$$|\psi(t_\mathrm{f})\rangle = \hat{U}(t_\mathrm{i}; t_\mathrm{f})|\psi(t_\mathrm{i})\rangle. \tag{A.1}$$

This, for a time-independent Hamiltonian, reads $\hat{U}(t_\mathrm{i}; t_\mathrm{f}) = \exp\left[-i(t_\mathrm{i} - t_\mathrm{f})\hat{H}\right]$. Note that we use natural units with $\hbar = 1 = k_\mathrm{B}$. When considering a real-space representation, we

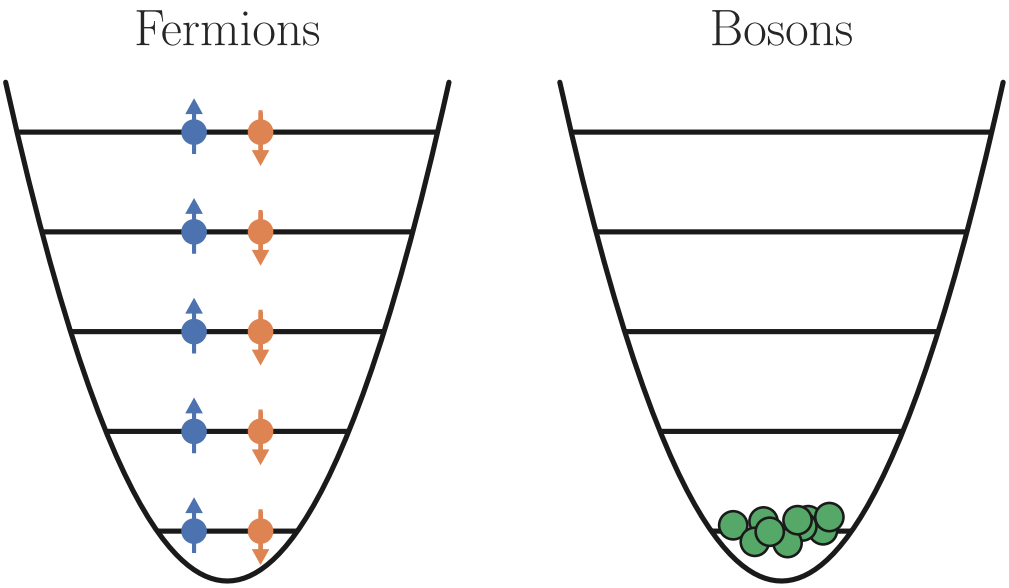


Figure A.1: Illustration of the occupations of 10 particles in a harmonic oscillation in the ground state. The fermions are illustrated for two distinguishable species of fermions with each 5 particles. The bosonic case is illustrated by using 10 indistinguishable bosons with a spread around the ground state for better visibility.

go one step further and obtain the propagator of a particle travelling from $x(t_\mathrm{i}) = x_\mathrm{i}$ to $x(t_\mathrm{f}) = x_\mathrm{f}$ as matrix elements of the time evolution operator, i.e.

$$K(t_\mathrm{f}, x_\mathrm{f}; t_\mathrm{i}, x_\mathrm{i}) = \langle x_\mathrm{f}|\hat{U}(t_\mathrm{f}; t_\mathrm{i})|x_\mathrm{i}\rangle. \tag{A.2}$$

For an initial wave function $\psi(t_\mathrm{i}, x_\mathrm{i})$, we obtain the state of a system at any time via

$$\psi(t_\mathrm{f}, x_\mathrm{f}) = \int \mathrm{d}x_\mathrm{i}\, K(t_\mathrm{f}, x_\mathrm{f}; t_\mathrm{i}, x_\mathrm{i})\psi(t_\mathrm{i}, x_\mathrm{i}). \tag{A.3}$$

Up to a factor of i, these propagators are closely related to the Green's function, which is a *causal* propagator, i.e. $G(t_\mathrm{f}, x_\mathrm{f}; t_\mathrm{i}, x_\mathrm{i}) = -i\Theta(t_\mathrm{f} - t_\mathrm{i})K(t_\mathrm{f}, x_\mathrm{f}; t_\mathrm{i}, x_\mathrm{i})$, of the Schrödinger operator. Throughout this thesis, the phrasing propagator and Green's function appear several times. We mostly use the Green's function in the context of many-body physics but in the literature on superfluidity, the wording propagator is also common.

The next section generalises this methodology by investigating the Fock space.

A.1.2 Fock space

As a prerequisite to developing the technique of functional integration, which is used throughout this thesis, we need to make a brief detour to the concepts of operator many-body physics. To this end, we use this section to discuss the Fock space and coherent states, ultimately leading to functional integration. This section follows the leading textbook description found, for instance, in Refs. [5, 274, 275, 423]. A key difference to single-particle quantum mechanics, which we need to point out early on, is the underlying quantum statistics. Bosons are particles with integer spin, like the fundamental gauge bosons or, more akin to the topic discussed here, the atoms ^{4}He, ^{7}Li and ^{39}K. A collection of those particles

can all occupy the same quantum state. In contrast, fermions, like fundamental quarks and leptons, or in our case the atoms ^{6}Li and ^{40}K, have to be different in at least one property, i.e. one quantum number. This is an expression of the Pauli exclusion principle first developed in 1925 by Wolfgang Pauli in Ref. [54]. This is illustrated for ten particles in Fig. A.1, where the bosons all occupy the same harmonic oscillator ground state, while each state can only host one identical fermion. Since we illustrate two different fermion species, indicated by their pseudospins, each oscillator level hosts exactly two particles.

Fock states

In the following, we consider only fermions, as this thesis investigates the properties of fermionic many-body systems. To obtain the Fock space, we consider a single-particle Hamiltonian $\hat{h}^{\mathrm{s}}$ for particles of spin s. The eigenvalue equation associated with this Hamiltonian is

$$\hat{h}^{\mathrm{s}}|\alpha\rangle_{\mathrm{s}} = \varepsilon^{\mathrm{s}}_{\alpha}|\alpha\rangle_{\mathrm{s}}, \tag{A.4}$$

where α denotes the quantum number of the eigenstate. Those eigenstates should be orthonormal ${}_{\mathrm{s}'}\langle\alpha'|\alpha\rangle_{\mathrm{s}} = \delta_{\alpha\alpha'}\delta_{\mathrm{ss}'}$ and form a complete basis of the underlying Hilbert space. In real space, the eigenstates are represented by $\chi^{\mathrm{s}}_{\alpha}(x) = \langle x|\alpha\rangle_{\mathrm{s}}$, with $x = (t, \boldsymbol{x})$ as position in space-time and are called *orbitals*. Those orbitals form the Hilbert space $\mathcal{H}^{\mathrm{s}}_1$ of one particle. A N-particle state is now a state in the product space $\mathcal{H}^{\mathrm{s}}_N = \bigotimes_{n=1}^{N}\mathcal{H}^{\mathrm{s}}_1$ for $N \geq 1$, with $\mathcal{H}^{\mathrm{s}}_0 = \mathbb{C}$ as vacuum state containing no particles. This space has to be properly antisymmetrised in order to be compatible with the spin-statistics theorem first proposed by Markus Fierz in Ref. [55], who was a student of Pauli. The many-fermion wavefunction has to be antisymmetric under particle exchange. This means the N-particle wave-function describing a system of indistinguishable fermions is expressed as a *Slater determinant*

$$\psi^{\mathrm{s}}(x_1, ..., x_N) = \frac{1}{\sqrt{N}}\begin{vmatrix} \langle x_1 \mid \alpha_1\rangle_{\mathrm{s}} & \langle x_2 \mid \alpha_1\rangle_{\mathrm{s}} & ... & \langle x_N \mid \alpha_1\rangle_{\mathrm{s}} \\ \langle x_1 \mid \alpha_2\rangle_{\mathrm{s}} & \langle x_2 \mid \alpha_2\rangle_{\mathrm{s}} & ... & \langle x_N \mid \alpha_2\rangle_{\mathrm{s}} \\ \vdots & \vdots & \ddots & \vdots \\ \langle x_1 \mid \alpha_N\rangle_{\mathrm{s}} & \langle x_2 \mid \alpha_N\rangle_{\mathrm{s}} & ... & \langle x_N \mid \alpha_N\rangle_{\mathrm{s}} \end{vmatrix}. \tag{A.5}$$

As such the total state is expressed as $|\psi\rangle_{\mathrm{s}} = |\alpha_1\rangle_{\mathrm{s}} \otimes |\alpha_2\rangle_{\mathrm{s}} \otimes ... \otimes |\alpha_N\rangle_{\mathrm{s}}$. Dealing explicitly with these wave functions is quite complicated, so we now switch to field operators. To this end, we first need the vacuum state $|0\rangle_{\mathrm{s}} \in \mathcal{H}^{\mathrm{s}}_0$. A quantum state of N particles is characterized by the occupied orbitals, and thus we describe it by an occupation vector $\boldsymbol{N}_{\mathrm{s}} = \begin{pmatrix} N_{\mathrm{s},\alpha_1} & N_{\mathrm{s},\alpha_2} & ... & N_{\mathrm{s},\alpha_{\mathrm{N}}} & ... \end{pmatrix}$, with α_i as the numbered orbitals. Since we deal with fermions, the only occupation numbers per state allowed are $N_{\mathrm{s},\alpha_i} \in \{0, 1\}$ in the i^{th} orbital, due to the Pauli principle.

Field operators

We now define the annihilation and creation operators $\hat{c}_{\mathrm{s},\alpha}, \hat{c}^{\dagger}_{\mathrm{s},\alpha}$ annihilating or creating a particle of spin s in the orbital α, respectively. Since those operators map between N and $N \pm 1$ particle Hilbert spaces we introduce the **Fock space** $\mathcal{F}^{\mathrm{s}} = \oplus_{N=0}^{\infty}\mathcal{H}^{\mathrm{s}}_N$. The field operators act in the Fock space. Any state with the occupation vector $\boldsymbol{N}_{\mathrm{s}}$ is constructed from the vacuum according to

$$|\boldsymbol{N}_{\mathrm{s}}\rangle_{\mathrm{s}} = \prod_{\alpha}\left(\hat{c}^{\dagger}_{\mathrm{s},\alpha}\right)^{N_{\mathrm{s},\alpha}}|0\rangle_{\mathrm{s}}. \tag{A.6}$$

By the standard second quantisation prescription, non-interacting quantum many-fermion systems are described by a many-body Hamiltonian which reads [424]

$$\hat{H} = \sum_{\mathrm{s}} \sum_{\alpha} \hat{c}^{\dagger}_{\mathrm{s},\alpha} \hat{h}^{\mathrm{s}}_{\mathrm{SP}} \hat{c}_{\mathrm{s},\alpha}. \tag{A.7}$$

We now continue with interactions. To this end, we consider four orbitals $\alpha, \beta, \gamma, \delta$ and an interaction potential V. Assuming we have two isolated particles in orbitals α, β they might interact in the form

$$|\alpha\rangle_{\mathrm{s}} \otimes |\beta\rangle_{\mathrm{s}'} \xrightarrow{V} |\delta\rangle_{\mathrm{s}} \otimes |\gamma\rangle_{\mathrm{s}'}. \tag{A.8}$$

To include this interaction into the Hamiltonian we sum over all possible initial and final orbital configurations, weighted with the respective matrix element of the four-dimensional interaction tensor $V^{\mathrm{ss}'}_{\alpha\beta\to\delta\gamma} = {}_{\mathrm{s}}\langle\alpha|_{\mathrm{s}'}\langle\beta|\hat{V}|\gamma\rangle_{\mathrm{s}'}|\delta\rangle_{\mathrm{s}}$. Using the completeness relation of the orbitals we obtain the Hamiltonian including two-particle interactions

$$\hat{H} = \sum_{\mathrm{s}} \sum_{\alpha} \hat{c}^{\dagger}_{\mathrm{s},\alpha} \hat{h}^{\mathrm{s}}_{\mathrm{SP}} \hat{c}_{\mathrm{s},\alpha} + \frac{1}{2} \sum_{\mathrm{ss}'} \sum_{\alpha\beta\delta\gamma} \hat{c}^{\dagger}_{\mathrm{s},\delta} \hat{c}^{\dagger}_{\mathrm{s}',\gamma} V^{\mathrm{ss}'}_{\alpha\beta\to\delta\gamma} \hat{c}_{\mathrm{s}',\beta} \hat{c}_{\mathrm{s},\alpha}. \tag{A.9}$$

The easiest and, in fact, most used orbital basis would be the basis of plane waves, where the quantum numbers $\alpha, \beta, \gamma, \delta$ are momenta. Under the assumptions of on-shell scattering and translational symmetry, the many-body Hamiltonian reads

$$\hat{H} = \sum_{\mathrm{s}} \sum_{k} \hat{c}^{\dagger}_{\mathrm{s},k} \varepsilon^{\mathrm{s}}_{k} \hat{c}_{\mathrm{s},k} + \frac{1}{2} \sum_{\mathrm{ss}'} \sum_{kk'} \sum_{q} \hat{c}^{\dagger}_{\mathrm{s},k} \hat{c}^{\dagger}_{\mathrm{s}',k'} V^{\mathrm{ss}'}_{k,k',q} \hat{c}_{\mathrm{s}',k'+q} \hat{c}_{\mathrm{s},k-q}, \tag{A.10}$$

which is the standard Hamiltonian used in many approaches. Here k, k' are the incoming momenta of the two particles and q is the exchanged momentum in the scattering. To obtain the original simplified BCS Hamiltonian, we assume that the two particles come in with exactly opposite momenta, meaning $k' = -k$. Rephrasing then $k - q \to k'$ leads to the well-established BCS Hamiltonian Eq. (2.14).

To obtain the picture in real space used in most cases of this thesis, we will proceed to the field operators, which are constructed out of the orbital creation and annihilation operators together with the orbital wave function. They are defined as

$$\hat{\psi}_{\mathrm{s}}(x) = \sum_{\alpha} \hat{c}_{\mathrm{s},\alpha} \chi^{\mathrm{s}}_{\alpha}(x), \tag{A.11a}$$

$$\hat{\psi}^{\dagger}_{\mathrm{s}}(x) = \sum_{\alpha} \hat{c}^{\dagger}_{\mathrm{s},\alpha} \chi^{\mathrm{s}}_{\alpha}(x), \tag{A.11b}$$

with $x = (t, \boldsymbol{x})$ as space-time in $D+1$ dimensions. This means that $\hat{\psi}^{\dagger}_{\mathrm{s}}(x)$ creates a particle of spin s at space-time position x, while $\hat{\psi}_{\mathrm{s}}(x)$ annihilates it. Those operators have to be anti-commuting in order to be compatible with the exclusion principle, leading to

$$\left[\hat{\psi}_{\mathrm{s}}(x), \hat{\psi}^{\dagger}_{\mathrm{s}'}(x')\right]_{+} = \delta_{\mathrm{ss}'} \delta(x - x'), \tag{A.12a}$$

$$\left[\hat{\psi}^{\dagger}_{\mathrm{s}}(x), \hat{\psi}^{\dagger}_{\mathrm{s}'}(x')\right]_{+} = 0 = \left[\hat{\psi}_{\mathrm{s}}(x), \hat{\psi}_{\mathrm{s}'}(x')\right]_{+}, \tag{A.12b}$$

with $[\circ, \circ]_{+}$ being the anti-commutator. This directly causes each field operator to be *nilpotent* $[\hat{\psi}_{\mathrm{s}}(x)]^2 = 0$. With those field operators the many-fermion Hamiltonian from Eq. (A.9) becomes

$$\hat{H} = \int \mathrm{d}x \sum_{\mathrm{s}} \hat{\psi}^{\dagger}_{\mathrm{s}} \hat{h}^{\mathrm{s}} \hat{\psi}_{\mathrm{s}}(x) + \frac{1}{2} \int \mathrm{d}x \mathrm{d}x' \sum_{\mathrm{ss}'} \hat{\psi}^{\dagger}_{\mathrm{s}}(x) \hat{\psi}^{\dagger}_{\mathrm{s}'}(x') V^{\mathrm{ss}'}(x - x') \hat{\psi}_{\mathrm{s}'}(x') \hat{\psi}_{\mathrm{s}}(x). \tag{A.13}$$

Before diving into the realm of path and functional integration, there is one last requirement: We have to introduce the coherent states, which are discussed next.

A.1.3 Fermionic coherent states

In this section, we will discuss the basis in which any functional integral within this thesis is expressed: The fermionic coherent states. We first briefly define the algebra underlying coherent states before discussing their properties. To this end, we need to find an appropriate algebra that resembles the anti-commuting property of the fermionic field operators, which leads to the so-called Grassmann numbers.

Grassmann Algebra

A *Grassmann algebra* $\mathbb{G}(V)$ of order $n \in \mathbb{N}$ is an exterior algebra over a vector space V with n anti-commuting generators $\theta_1, ..., \theta_n$ and dimension $\dim\mathbb{G} = 2^n$, obeying

$$\theta_i\theta_j + \theta_j\theta_i = 0. \tag{A.14}$$

They are nilpotent objects of second order, i.e. $\theta_i^2 = 0$. Additionally, in combination with an object of the parent vector space $x \in V$, we demand commutativity

$$x\theta_i = \theta_i x. \tag{A.15}$$

Any function of those Grassmann generators can be expressed as a summation over all possible permutations of $0, ..., n$ generators weighted by some complex number. In general, the product of two Grassmann numbers is not an element of the Grassmann algebra but rather of the parent vector space V. Considering three Grassmann numbers $\theta_i, \theta_j, \theta_k \in \mathbb{G}(V)$ for which hold the identity

$$\theta_i\theta_j\theta_k = \theta_k\theta_i\theta_j. \tag{A.16}$$

This means that the product of two Grassmann numbers is commutative with a third Grassmann number, yielding $\theta_i\theta_j \in V$. In the following, we define the pseudo-derivatives and the Berezin integration in Grassmann algebras.

Definition: Grassmann pseudo-derivative

One can define a pseudo-derivative operation in a Grassmann algebra by the definition

$$\frac{\mathrm{d}}{\mathrm{d}\theta_i}1 = 0 \qquad \text{and} \qquad \frac{\mathrm{d}}{\mathrm{d}\theta_i}\theta_j = \delta_{ij}.$$

Definition: Berezin integration

The standard integral in a Grassmann algebra is called the *Berezin integral* [425] defined by the properties

$$\int \mathrm{d}\theta_j = 0 \qquad \text{and} \qquad \int \mathrm{d}\theta_j\theta_i = \delta_{ij}.$$

Thus, differentiation and integration are defined by the same rules.

As an example, we consider the special case of a Grassmann algebra with two real generators θ_1, θ_2 and any function f mapping from the Grassmann algebra $\mathbb{G}$ to a sum of

complex and Grassmann numbers. Since we deal here with nilpotent generators, the most general function possible in such an algebra is given by

$$f(\theta_1, \theta_2) = f_{0,0} + f_{1,0}\theta_1 + f_{0,1}\theta_2 + f_{1,1}\theta_1\theta_2. \tag{A.17}$$

Applying the pseudo-derivatives defined earlier leads to the most general derivative in this Grassmann algebra as

$$\frac{\partial}{\partial\theta_1} f(\theta_1, \theta_2) = f_{1,0} + f_{1,1}\theta_2, \tag{A.18a}$$

$$\frac{\partial}{\partial\theta_2} f(\theta_1, \theta_2) = f_{0,1} - f_{1,1}\theta_1, \tag{A.18b}$$

$$\frac{\partial^2}{\partial\theta_1\partial\theta_2} f(\theta_1, \theta_2) = -f_{1,1} = -\frac{\partial^2}{\partial\theta_2\partial\theta_1} f(\theta_1, \theta_2). \tag{A.18c}$$

Since we have these nilpotent generators, all second derivatives of one variable must vanish. Comparing this to the integral Berezin integral, we deduce

$$\int \mathrm{d}\theta_1 f(\theta_1, \theta_2) = f_{1,0} + f_{1,1}\theta_2, \tag{A.19a}$$

$$\int \mathrm{d}\theta_2 f(\theta_1, \theta_2) = f_{0,1} - f_{1,1}\theta_1, \tag{A.19b}$$

$$\int \mathrm{d}\theta_1 \mathrm{d}\theta_2 f(\theta_1, \theta_2) = -f_{1,1} = -\int \mathrm{d}\theta_2 \mathrm{d}\theta_1 f(\theta_1, \theta_2). \tag{A.19c}$$

We directly notice that taking a derivative is equivalent to integrating in a Grassmann algebra.

Complex Grassmann algebra

Correspondingly, complex Grassmann numbers are then constructed as the complexification $V_{\mathbb{C}} = V \otimes \mathbb{C}$. However, since for any real vector space the complexification is isomorphic to the simple complex extension $V_{\mathbb{C}} \cong V \oplus iV$ we will use this instead. Since we know about the isomorphism $\mathbb{R}^2 \cong \mathbb{C}$ we can represent an element of a complex Grassmann algebra, say $\psi \in \mathbb{G}_{\mathrm{c}}$ as a complex version of a two-dimensional Grassmann variable based on $\mathbb{R}^2$, namely $\theta_r, \theta_i \in \mathbb{G}_{\mathrm{r}}$ should be real value based Grassmann numbers. Such a Grassmann number is expressed as

$$\psi = \mathcal{N}(\theta_r + i\theta_i), \tag{A.20}$$

where $\mathcal{N}$ is some normalisation factor that can be used to define a norm in this Grassmann Algebra. Two familiar conventions here are either $\mathcal{N} = 1$ or $\mathcal{N} = 1/\sqrt{2}$, where the first one preserves the regular complex norm while the second one normalises real and imaginary parts to preserve the "vector length" and is more related to the norm of the real-valued Grassmann variables. The conjugate $\overline{\psi} \in \mathbb{G}_{\mathrm{c}}$ is a complex Grassmann number in the same algebra, meaning we demand $\mathbb{G}_{\mathrm{c}}$ to be closed under the Grassmann complex conjugation. This directly requires $\overline{\psi_1\psi_2} = \overline{-\psi_2\psi_1}$ and with that, we define the Grassmann complex conjugation to obey the same rule as the regular complex conjugation:

$$\overline{\psi} = \overline{\mathcal{N}}(\theta_r - i\theta_i). \tag{A.21}$$

By this, the product of a Grassmann variable with its conjugate becomes

$$\overline{\psi}\psi = 2i|\mathcal{N}|^2\theta_i\theta_r \in \mathbb{C}. \tag{A.22}$$

This is not positively semi-defined, nor even a real quantity, since a Grassmann algebra misses relations like that by the anti-commuting property. If we choose $\mathcal{N} = 1/\sqrt{2}$ we obtain the self-product of a Grassmann number as

$$\langle\psi\rangle = \overline{\psi}\psi = i\theta_i\theta_r. \tag{A.23}$$

Grassmann coherent states

Using the elements of a complex Grassmann algebra with $\mathbb{C}$ as the parent vector space, we define the coherent states of an orbital α as the solution to the eigenvalue equation

$$\hat{c}_{\mathrm{s},\alpha}|c_\alpha\rangle_\mathrm{s} = c_{\mathrm{s},\alpha}|c_\alpha\rangle_\mathrm{s}, \tag{A.24}$$

where the eigenvalue $c_{\mathrm{s},\alpha} \in \mathbb{G}$ is a complex Grassmann number. In almost any standard lecture about fermionic field theory, it is shown [274, 411] that this state can be created from the vacuum by applying the displacement operator. Generalised to the many-body picture, this yields

$$|c_\alpha\rangle_\mathrm{s} = \exp\left(-c_{\mathrm{s},\alpha}\hat{c}^\dagger_{\mathrm{s},\alpha}\right)|0\rangle_\mathrm{s}. \tag{A.25}$$

From the coherent state of one orbital in one spin component, the idea of a coherent state can straightforwardly be generalised by implying the same construction to the coherent state wave function, which turns out to be

$$\psi_\mathrm{s}(x) = \sum_\alpha c_{\mathrm{s},\alpha}\chi^\mathrm{s}_\alpha(x). \tag{A.26}$$

It is a Grassmann valued function of space (and time if generalised) and fulfils an eigenvalue equation similar to Eq. (A.24), namely

$$\hat{\psi}_\mathrm{s}(x)|\psi\rangle = \psi_\mathrm{s}(x)|\psi\rangle. \tag{A.27}$$

Note that this coherent state is an eigenstate of all spin field operators at any position and is created by applying the displacement operator

$$|\psi\rangle = \exp\left(-\sum_\mathrm{s}\int dx\ \psi_\mathrm{s}(x)\hat{\psi}^\dagger_\mathrm{s}(x)\right)|0\rangle. \tag{A.28}$$

Remark: Properties of fermionic coherent states

Consider two coherent states $|\psi\rangle, |\phi\rangle$. They have the properties [274, 275, 411]

- Scalar product in Fock space:

$$\langle\phi \mid \psi\rangle = \exp\left(\sum_{\mathrm{s}} \int \mathrm{d}x \overline{\phi}_{\mathrm{s}}(x)\psi_{\mathrm{s}}(x)\right). \tag{A.29}$$

- Coherent states are not orthonormal:

$$\| \psi \|^2 = \langle\psi \mid \psi\rangle = \exp\left(\sum_{\mathrm{s}} \int \mathrm{d}x \overline{\psi}_{\mathrm{s}}(x)\psi_{\mathrm{s}}(x)\right) = \exp\left(\sum_{\mathrm{s},\alpha} \overline{c}_{\mathrm{s},\alpha} c_{\mathrm{s},\alpha}\right) \neq 1. \tag{A.30}$$

- Closure relation:

$$\boldsymbol{id} = \int d\overline{\psi}\, d\psi\, \frac{|\psi\rangle\langle\psi|}{\| \psi \|^2}. \tag{A.31}$$

- Coherent states form a countable discrete degree of freedom besides the spin, hence

$$\mathrm{Tr}\hat{X} = \int d\overline{\psi}\, d\psi\, \frac{\langle\psi|\hat{X}|\psi\rangle}{\| \psi \|^2}.$$

In the above remark, the integration over a coherent state has the combined measure over the spins and the single-particle orbitals $\mathrm{d}\psi = \prod_{\mathrm{s},\alpha} \mathrm{d}c_{\mathrm{s},\alpha}$.

Using the coherent states, we extend the many-body quantum mechanical formulation established in this section to the field integral method, which allows for a formal treatment of quantum field theoretical questions.

A.2 Quantum (statistical) field theory

We discuss here the definitions of the path and functional integral used throughout this thesis. We start with the first quantised version of the one-particle Feynman path integral, which will be an alternative description of Schrödinger systems described in Sec. A.1.1. We will then use the tools developed in Sections A.1.2 and A.1.3 to generalise this path integral concept to many-body systems, giving rise to the functional integral.

A.2.1 Feynman path integration

Time slicing path integral

The idea proposed by Feynman [299] in 1948[1] is to divide a given time interval $[t_{\mathrm{i}}, t_{\mathrm{f}}]$ of the evolution of a state into $N \in \mathbb{N}$ pieces of spacing $\eta = (t_{\mathrm{f}} - t_{\mathrm{i}})/N > 0$. Thus, the time evolution operator decomposes into the steps

$$\hat{U}(t_{\mathrm{f}}; t_{\mathrm{i}}) = \prod_{n=0}^{N-1} \hat{U}(t_{n+1}; t_n), \tag{A.32}$$

[1] Actually the first approaches were developed in Feynman's PhD thesis with John A. Wheeler in 1942 [298] generalizing an idea of Paul Dirac. The approach was unfinished and did only partially work.

where we set the start point to $t_0 = t_\mathrm{i}$ as well as the end point to $t_N = t_\mathrm{f}$. Using the completeness $\boldsymbol{id} = \int dx_n \, |x_n\rangle\langle x_n|$ for $1 \leq n \leq N$, we insert basis projections and use this to express the propagator (A.2) via

$$K(t_\mathrm{f}, x_\mathrm{f}; t_\mathrm{i}, x_\mathrm{i}) = \int \left[\prod_{n=1}^{N-1} dx_n \right] \prod_{n=0}^{N-1} \langle x_{n+1} | \hat{U}(t_{n+1}; t_n) | x_n \rangle. \tag{A.33}$$

The propagator for one particle is hence given by the time-sliced propagator in every step, multiplied over and integrated over all possible intermediate positions at any intermediate time.

To tackle a physical problem, we have to have a closer look at the general structure of some Hamiltonian $\hat{H}$. Any typical Hamiltonian in a first quantized system can be separated into a kinetic term $\hat{T}$ and a potential term $\hat{V}$ by $\hat{H} = \hat{T} + \hat{V}$ that do not commute in general, i.e. $[\hat{T}, \hat{V}]_- \neq 0$. Using the Baker-Campbell-Hausdorff (BCH) formula the exponential of $\hat{H}$ separates according to [411]

$$e^{-i\eta\hat{H}} = e^{-i\eta\hat{T}} e^{-i\eta\hat{V}} e^{-i\eta^2\hat{X}}. \tag{A.34}$$

As we work with the time-sliced Hamiltonian, we only need to consider leading orders in $\eta \ll 1$ since in the end we approach a continuous limit $\eta \to 0$, yielding

$$\hat{X} = \frac{i}{2}[\hat{V}, \hat{T}]_- + \mathcal{O}(\eta). \tag{A.35}$$

As in the continuous limit, the time-slice thickness η goes to zero, we neglect all but the leading terms in η as this is proportional to an error of the order of at least η^2. This renders the kinetic and potential operators approximately commutative and leads only to the two separate exponentials from Eq. (A.34). Using the completeness of the momentum basis, reading $\boldsymbol{id} = \int dk \, |k\rangle\langle k|$, we obtain

$$\langle x_{n+1} | e^{-i\eta\hat{H}} | x_n \rangle \approx \int dk_n \, \langle x_{n+1} | e^{-i\eta\hat{V}} | k_n \rangle \langle k_n | e^{-i\eta\hat{T}} | x_n \rangle + \mathcal{O}(\eta^2). \tag{A.36}$$

To perform the Fourier transform, we use a normalised plane-wave basis $\langle x \mid k \rangle = e^{ikx}/\sqrt{2\pi}$. In the kinetic operator, this replaces derivatives by momentum eigenvalues. Further, we assume a momentum-independent potential, resulting in

$$\langle x_{n+1} | \hat{U}(t_{n+1}; t_n) | x_n \rangle \approx \int dk_n \, e^{-i\eta V(x_{n+1}, t_{n+1})} e^{-i\eta T(k_n, t_n) + ik_n(x_{n+1} - x_n)}. \tag{A.37}$$

The last term in the second exponential is a differential quotient $x_{n+1} - x_n$ coming from the kinetic term, which also leads to the kinetic energy $T(k_n, t_n) = k_n^2/(2m)$. In order to get the standard path-integral definition, we integrate the momenta explicitly. This is possible by using standard Fresnel integration, which can be found in any complex analysis textbook. Using the abbreviations $a = -\eta/(2m)$ and $b = x_{n+1} - x_n$ the integral used is

$$\int dk_n \, e^{i(ak_n^2 + bk_n)} = \sqrt{\frac{-i\pi}{a}} e^{-ib^2/(4a)}, \tag{A.38}$$

using $\sqrt{i} = (1+i)/\sqrt{2} = \exp(i\pi/4)$ as the principle De-Moivre root of the imaginary unit and $-i = 1/i$. Note that this integral is convergent for any complex number $a \in \mathbb{C}$ that has

a non-negative imaginary part, except for the case when $a = 0$. As $\eta > 0$ this condition is always true, and we obtain

$$\langle x_{n+1}|\hat{U}(t_{n+1};t_n)|x_n\rangle \approx e^{-i\eta V(x_{n+1},t_n+1)}\sqrt{\frac{m\pi}{2\pi i\eta}}e^{\frac{im}{2\eta}(x_{n+1}-x_n)^2}. \tag{A.39}$$

As the arguments of the exponential functions are simple C-numbers, we can combine them without the need to worry about the BCH formula. Doing so, we can sort the integrations and the exponentials to rearrange Eq. (A.33) to

$$\begin{aligned} K(t_\mathrm{f},x_\mathrm{f};t_\mathrm{i},x_\mathrm{i}) &= \sqrt{\frac{m}{2i\pi\eta}}\left[\prod_{n=1}^{N-1}\int\frac{dx_n}{\sqrt{2i\pi\eta/m}}\right]\prod_{n=0}^{N-1}\langle x_{n+1}|\hat{U}(t_{n+1};t_n)|x_n\rangle \qquad \text{(A.40)}\\ &= \sqrt{\frac{m}{2i\pi\eta}}\left[\prod_{n=1}^{N-1}\int\frac{dx_n}{\sqrt{2i\pi\eta/m}}\right]\exp\left(i\sum_{n=0}^{N-1}\eta\left[\frac{m}{2}\left(\frac{x_{n+1}-x_n}{\eta}\right)^2 - V(x_{n+1},t_{n+1})\right]\right). \end{aligned}$$

Eq. (A.40) motivates the definition of a discrete path integral measure of spacing $\eta > 0$.

Definition: Discrete path integral

For any path $x_0,\ldots,x_N$ of a countable set of time points $t_0,\ldots,t_N$ with $t_0 = t_\mathrm{i}$, $t_N = t_\mathrm{f}$ and spacing $\eta = t_{n+1} - t_n$ we define a discrete time slicing path integral measure as

$$\mathcal{D}_\eta[x] = \mathcal{N}(\eta)\prod_{n=1}^{N-1}dx(t_n)\,,$$

with $\mathcal{N}(\eta)$ as an appropriate η-dependent normalization constant. A *discrete path integral* over all paths with initial and final positions $x_\mathrm{i} = x(t_0)$ and $x_\mathrm{f} = x(t_N)$ of a functional $\mathcal{F}$ is then defined by

$$\int_{x(t_\mathrm{i})=x_\mathrm{i}}^{x(t_\mathrm{f})=x_\mathrm{f}}\mathcal{D}_\eta[x]\mathcal{F}[x] = \int\prod_{n=1}^{N-1}dx(t_n)\,\mathcal{F}[\{x_0,x_1,\ldots,x_N\}],$$

using the notation $x_n = x(t_n)$.

With this, the discrete path integral for the propagator of a given initial and final positions $x_\mathrm{i} = x(t_\mathrm{i})$ and $x_\mathrm{f} = x(t_\mathrm{f})$ reads

$$K(t_\mathrm{f},x_\mathrm{f};t_\mathrm{i},x_\mathrm{i}) = \int_{x(t_\mathrm{i})=x_\mathrm{i}}^{x(t_\mathrm{f})=x_\mathrm{f}}\mathcal{D}_\eta[x]e^{i\mathcal{A}_\eta[x]}. \tag{A.41}$$

Here we defined the discrete Minkowski action functional $\mathcal{A}_\eta[x]$ as

$$\mathcal{A}_\eta[x] = \eta\sum_{n=1}^{N}\left[\frac{m}{2}(\partial_t^\eta x(t_n))^2 - V(x(t_{n+1}))\right]. \tag{A.42}$$

It uses a differential quotient notation for a discrete derivative

$$\partial_t^\eta x(t_n) = \frac{x(t_n)-x(t_{n-1})}{\eta}. \tag{A.43}$$

Here, we made an index shift in the action for convenience and consistency with later calculations. To deal with continuous quantum mechanics, we generalise this now for continuous time intervals.

Continuous path integral

When sending the number of slicing operations, i.e. the number of included unities, to infinity while keeping the interval finite, we approach the continuous limit. Despite the naming, we have to keep in mind an infinitesimal retardation of the paths as $\eta \to 0^+$, which, in most cases, can be neglected. This is now a major difference to most textbooks, as in

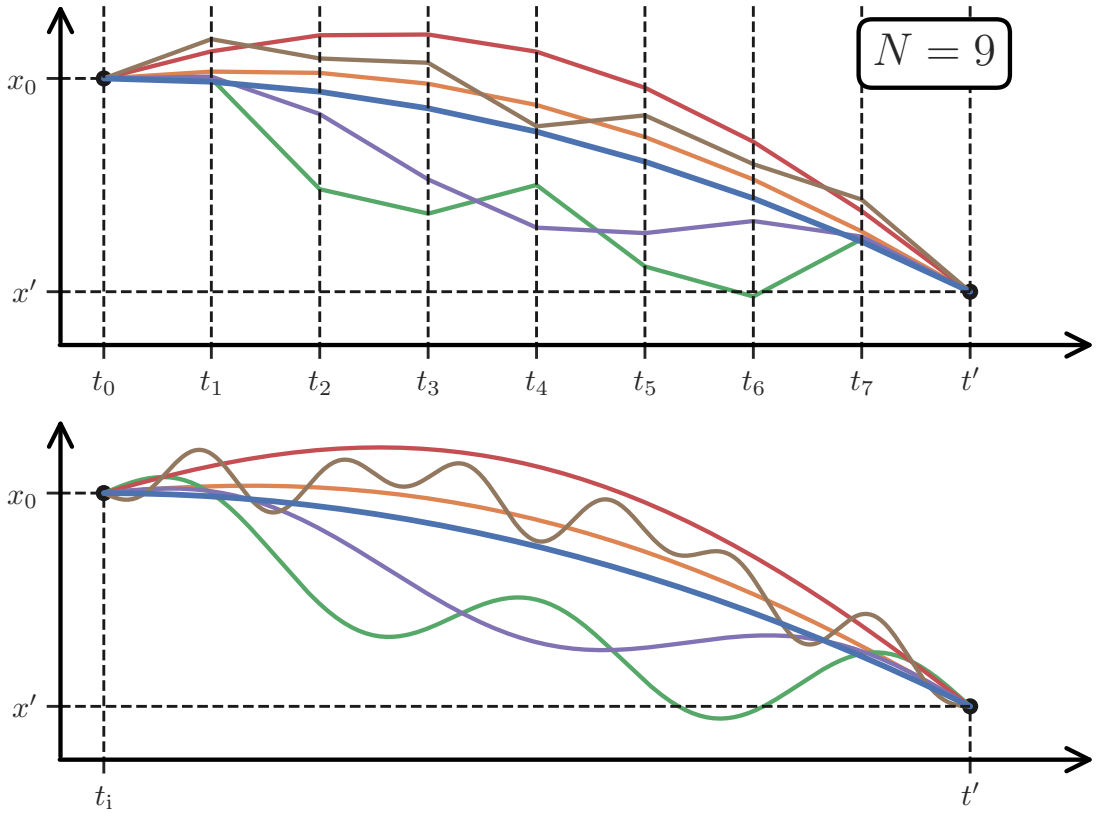


Figure A.2: Illustration of discrete and continuous path integration from $x_0 = x(t_\mathrm{i})$ to $x' = x(t')$ for nine time steps in upper, and infinite time steps in lower panel.

general this fact is just glanced over because in most physical examples, it makes no difference. We point this out in this section of the simple Feynman path integral because it will become important when dealing with second-quantised functional integrals in order to correctly recover the vacuum energy term, which would otherwise be lost due to normal ordering. With this short preliminary comment, we can perform the continuous limit. In this case, the summation over the time indices converges to the Riemann integral $\eta \sum_{n=0}^{N-1} \to \int_{t_0}^{t} ds$. The upper boundary converges to the final time, and as a single point in a continuous interval, it is a set of zero measure. Thus, it is legitimate to evaluate it directly there.

Definition: Continuous Feynman-path integral

Given any discrete set of times, one can transition to the formalism of continuous paths by defining the continuous path-integral measure

$$\mathcal{D}[x] = \lim_{N\to\infty} \mathcal{D}_\eta[x] = \lim_{N\to\infty} \mathcal{N}(\eta(N)) \prod_{n=1}^{N-1} dx(t_n) \, .$$

The continuous path integral reads

$$\int_{x(t_\mathrm{i})=x_\mathrm{i}}^{x(t_\mathrm{f})=x_\mathrm{f}} \mathcal{D}[x]\mathcal{F}[x] = \lim_{N\to\infty} \mathcal{N}(\eta(N)) \prod_{n=1}^{N-1} dx(t_n)\, \mathcal{F}[\{x(t_0), ..., x(t_{N+1})\}].$$

Using the Riemann integral, the sum in the Minkowski action from Eq. (A.42) becomes an integral over a finite domain $[t_\mathrm{i}, t_\mathrm{f}]$ as

$$\mathcal{A}[x] = \lim_{N\to\infty} \mathcal{A}_\eta[x] = \int_{t_\mathrm{i}}^{t_\mathrm{f}} dt \, \left[\frac{m}{2}(\partial_t x(t))^2 - V(x(t))\right], \tag{A.44}$$

Without the index-shift made in Eq. (A.42), the path in the potential term would require an infinitesimal time step added to be $V(x(t+0^+))$. As it shall turn out, when generalising the Feynman path integral to the functional integral, this statement is not so easy to make. Considering the Minkowski action, however, we define the Lagrangian L as

$$L(x(t)) = \frac{m}{2}(\partial_t x(t))^2 - V(x(t)). \tag{A.45}$$

We find an illustration of discrete and continuous path integrals in Fig. A.2 in the upper and lower panels, respectively. With all the introduced terminology, the propagator is the standard form found in the literature

Result: Path integral propagator

$$K(t, x; t_0, x_0) = \int_{x(t_\mathrm{i})=x_\mathrm{i}}^{x(t_\mathrm{f})=x_\mathrm{f}} \mathcal{D}[x] e^{i\mathcal{A}_\eta[x]} = \int_{x(t_\mathrm{i})=x_\mathrm{i}}^{x(t_\mathrm{f})=x_\mathrm{f}} \mathcal{D}[x] e^{i\int_{t_\mathrm{i}}^{t_\mathrm{f}} ds\, L(x(s))}. \tag{A.46}$$

Remark: Convergence issues

The original approach Feynman made contains divergences in most physically realistic cases [411], turning unphysical there. Even the Coulomb problem in first quantisation is not rigorously solvable in the original approach. Despite this, we still chose to present the Feynman path integral here as its construction is instructive and straightforward to understand. It is sufficient to motivate the second quantised functional integral in imaginary time, where the time-slicing issue does not arise, and the integrals are fundamentally convergent. A well-defined version of the path integral was introduced by H. Kleinert in Refs. [426, 427],going beyond the scope of this thesis.

A.2.2 Euclidean path integral

Definition: Trace and determinant

For an operator $\hat{X}$, we define the trace as the sum of all eigenvalues

$$\mathrm{Tr}\,\hat{X} = \int_V dx\ \mathrm{tr}\langle x|\hat{X}|x\rangle,$$

where tr denotes the trace over the discrete degrees of freedom, is

$$\mathrm{tr}\,X(x) = \sum_{\mathrm{s}} \langle \mathrm{s}|X(x)|\mathrm{s}\rangle.$$

The determinant is defined as

$$\mathrm{Det}\hat{X} = \prod_{x\in V} \det\langle x|\hat{X}|x\rangle,$$

where $\det$ stands for the determinant over the discrete degrees of freedom

$$\det\langle x|X(x)|x\rangle = \prod_{\mathrm{s}} \langle \mathrm{s}|X(x)|\mathrm{s}\rangle.$$

To obtain statistical properties of an ensemble at finite temperatures, one generally needs the Boltzmann factor $\exp\left(-\beta\hat{H}\right)$, leading to the partition function

$$\mathcal{Z} = \mathrm{Tr}\exp\left(-\beta\hat{H}\right), \tag{A.47}$$

using the inverse temperature $\beta = T^{-1}$. We use the definition of the trace to obtain the partition function in terms of the Hamiltonian

$$\begin{aligned}\mathcal{Z} &= \int dx\ \langle x|e^{-\beta\hat{H}}|x\rangle \\ &= \int dx\ \langle x|e^{-i\hat{H}(\tau_0-\tau)}|x\rangle,\end{aligned} \tag{A.48}$$

defining the Wick rotation from real to imaginary time $\tau - \tau_0 = -i\beta$, see Ref. [428] for general information about the partition function. W.l.o.g. one sets $\tau_0 = 0$ and again divide the imaginary time interval in N steps to perform the same steps as before, now with imaginary τ. We slice analogously to Eq. (A.33) with equal starting and final positions. Using $\eta = \beta/N$, we perform the same steps as for the real-time propagator and end up with an analogous expression for the imaginary-time propagator, which is equal to the quantum mechanical partition function

$$\mathcal{Z} = \left[\int \prod_{n=1}^{N} \sqrt{\frac{m}{2\pi\eta}} dx_n\right] \exp\left(-\eta \sum_{n=1}^{N} \left[\frac{m}{2}(\partial_\tau^\eta x(\tau_n))^2 + V(x(\tau_n))\right]\right). \tag{A.49}$$

Thus, defining the single-particle Euclidean action on a discrete imaginary time grid as

$$\mathcal{S}_\eta[x] = \eta \sum_{n=1}^{N} \left[\frac{m}{2}(\partial_\tau^\eta x(\tau_n))^2 + V(x(\tau_n))\right], \tag{A.50}$$

allows to write the quantum mechanical partition function as

$$\mathcal{Z} = \oint_{x(0)=x(\beta)} \mathcal{D}_\eta[x] e^{-\mathcal{S}_\eta[x]}. \tag{A.51}$$

The integral sign used in Eq. (A.51) indicates that the starting point $x(0)$ and end point $x(\beta)$ are identical. The partition function is the sum over all periodic paths in $\beta = 1/T$, i.e. $x(\tau_0) = x(\tau_N) = x(\beta)$. We express it using the Euclidean action $\mathcal{S}$ in quasi-continuous time

Result: Continuous partition function

Continuous Euclidean action

$$\mathcal{S}[x] = \int_0^\beta d\tau \left[\frac{m}{2}(\partial_\tau x(\tau))^2 + V(x(\tau + 0^+))\right]. \tag{A.52}$$

Continuous quantum mechanical partition function

$$\mathcal{Z} = \oint_{x(0)=x(\beta)} \mathcal{D}[x] e^{-\mathcal{S}[x]}. \tag{A.53}$$

This procedure generally allows us to investigate single-particle quantum systems by integrating over all possible paths, a powerful tool. We now take this insight one step further. Using the second quantisation developed in Sec. A.1.2, we derive the functional integral as a quantum field theoretical method to investigate many-particle systems.

A.2.3 Functional integration

Many-body Green's function in real time

To generalise the idea of Feynman to the many-body case, we consider now coherent state solutions of the eigenvalue equation in Eq. (A.27). As this equation can have countably many solutions to different coherent states, we shall label them with an index j. We make analogous steps to obtain the real-time Green's function for a transition from one initial coherent state $|\psi_\mathrm{i}\rangle$ at initial time t_i to a final state $|\psi_\mathrm{f}\rangle$ at a later time $t_\mathrm{f} < t_\mathrm{i}$. The propagator from the initial to the final field configuration reads

$$K[\psi_\mathrm{f};\psi_\mathrm{i}](t_\mathrm{f};t_\mathrm{i}) = \langle\psi_\mathrm{f}|e^{-i\hat{H}(t_\mathrm{f}-t_\mathrm{i})}|\psi_\mathrm{i}\rangle. \tag{A.54}$$

We divide the time interval $[t_\mathrm{i}, t_\mathrm{f}]$ into N slices and insert $N-1 \in \mathbb{N}$ identities by the closure relation (A.31). This yields the propagation over a time slice $\eta = (t_\mathrm{f} - t_\mathrm{i})/N$ and by sorting terms we find

$$K[\psi_\mathrm{f};\psi_\mathrm{i}](t_\mathrm{f};t_\mathrm{i}) = \left(\int \prod_{n=1}^{N-1} \frac{d\overline{\psi}_n\, d\psi_n}{\|\psi_n\|^2}\right) \prod_{n=0}^{N-1} \langle\psi_{n+1}|e^{-i\eta\hat{H}}|\psi_n\rangle. \tag{A.55}$$

Definition: Normal order

Consider a product of field operators. The *normal order* is the same product, but with all annihilators to the right and all creators to the left, multiplied by ζ^n (± 1 for bosons/fermions), where n is the number of permutations:

$$:\hat{\psi}_\mathrm{s}(x)\hat{\psi}^\dagger_{\mathrm{s}'}(x'): = \zeta\hat{\psi}^\dagger_{\mathrm{s}'}(x')\hat{\psi}_\mathrm{s}(x).$$

To evaluate this, we want the annihilation operators to all act to the right, while the creation operators should act to the left, so that we can apply the respective eigenvalue

equations (A.27) and the conjugated version of it. Thus, we make the assumption that we deal with a *normal ordered* Hamiltonian. Evaluating the expectation values of the respective time slices is simple for fermions, as the field operators are nilpotent and hence the Taylor series of the exponential only has terms up to linear order. Apply then the eigenvalue equation (A.27) to replace the field operators by the coherent state wave functions that are also nilpotent as Grassmann valued functions. Therefore, the Taylor series we have for the coherent states is rewritten as an exponential of Grassmann variables, hence giving rise to the following identity

$$\langle\psi_{n+1}|{:}\hat{H}{:}|\psi_n\rangle = H[\overline{\psi}_{n+1},\psi_n]\langle\psi_{n+1}\mid\psi_n\rangle. \tag{A.56}$$

Here $H[...]$ denotes the Hamiltonian functional of the Grassmann coherent states, where one has to replace the field operators in Eq. (A.13) by the coherent state wave functions

$$K[\psi_\mathrm{f};\psi_\mathrm{i}](t_\mathrm{f};t_\mathrm{i}) = \left(\int\prod_{n=1}^{N-1} d\overline{\psi}_n\, d\psi_n\, \frac{\langle\psi_{n+1}\mid\psi_n\rangle}{\|\,\psi_n\,\|^2}\right)\langle\psi_1\mid\psi_0\rangle\prod_{n=0}^{N-1} e^{-\eta H[\overline{\psi}_{n+1};\psi_n]}. \tag{A.57}$$

Note that we factored out the end term containing the initial state matrix element $\langle\psi_1\mid\psi_0\rangle$ as it is not fully integrated over, with $\psi_0=\psi_\mathrm{i}$. To obtain the standard representation, we reorder the transition matrix elements $\langle\psi_n\mid\psi_{n-1}\rangle$ factoring out the final state instead of the initial state, leading to

$$K[\psi_\mathrm{f};\psi_\mathrm{i}](t_\mathrm{f};t_\mathrm{i}) = \left(\int\prod_{n=1}^{N-1} d\overline{\psi}_n\, d\psi_n\, \frac{\langle\psi_{n}\mid\psi_{n-1}\rangle}{\|\,\psi_n\,\|^2}\right)\langle\psi_N\mid\psi_{N-1}\rangle\prod_{n=1}^{N} e^{-\eta H[\overline{\psi}_{n+1};\psi_n]} \tag{A.58}$$

To evaluate the propagator, we express the scalar products and the norm by using Eqs. (A.29,A.30)

$$\frac{\langle\psi_n\mid\psi_{n-1}\rangle}{\|\,\psi_n\,\|^2} = \exp\left(-\sum_\mathrm{s}\int d^Dx\,\overline{\psi}_{\mathrm{s},n}(x)[\psi_{\mathrm{s},n}(x)-\psi_{\mathrm{s},n-1}(x)]\right). \tag{A.59}$$

Between time steps, the field evolves from one coherent state to another, meaning $\psi_{\mathrm{s,n}}(x) = \psi_\mathrm{s}(t_n;x)$, with time $t_n = n\eta$, is a time-dependent field.

Definition: Time-sliced functional measure

The generalisation of the discrete path-integral measure

$$\mathcal{D}_\eta[\overline{\psi};\psi] = \prod_{n=1}^{N-1} d\overline{\psi}_n\, d\psi_n \;=\prod_{n=1}^{N-1}\prod_\mathrm{s}\int dx\, d\overline{\psi}_{\mathrm{s},n}(x)\, d\psi_{\mathrm{s},n}(x)\;. \tag{A.60}$$

The functional integral of any functional $\mathcal{F}$ mapping the wavefunctions to a $\mathbb{C}$ number is also defined by

$$\int\mathcal{D}_\eta[\overline{\psi};\psi]\mathcal{F}[\overline{\psi};\psi] = \int\left(\prod_{n=1}^{N-1} d\overline{\psi}_n\, d\psi_n\right)\mathcal{F}[\{\overline{\psi}_1,\overline{\psi}_2,...,\overline{\psi}_N;\psi_1,\psi_2,...,\psi_N\}].$$

We use the definition of the time-sliced functional measure and the discrete derivative to obtain

$$\begin{aligned} K[\psi_\mathrm{f};\psi_\mathrm{i}](t_\mathrm{f};t_\mathrm{i}) = \int_{\psi(t_\mathrm{i})=\psi_\mathrm{i}}^{\psi(t_\mathrm{f})=\psi_\mathrm{f}}\mathcal{D}_\eta[\overline{\psi};\psi]\exp\left(i\eta\sum_{n=1}^{N}\int d^Dx\,\mathcal{L}(t_n;x)\right) \\ \times\exp\left(-\sum_\mathrm{s}\int d^Dx\,\left[\overline{\psi}_\mathrm{s}(t_\mathrm{f};x)\psi_\mathrm{s}(t_N;x)-i\eta\mathcal{H}(\overline{\psi}_\mathrm{s}(t_\mathrm{f};x),\psi_\mathrm{s}(t_N;x))\right]\right), \end{aligned} \tag{A.61}$$

where the discrete Lagrangian density is related to the Hamiltonian density $\mathcal{H}$ that defines the Hamiltonian function $H = \int dx\, \mathcal{H}$ via

$$\mathcal{L}(t_n; x) = \overline{\psi}_{\mathrm{s}}(t_n; x) i\partial_t^{\eta} \psi_{\mathrm{s}}(t_n; x) - \mathcal{H}(\overline{\psi}_{\mathrm{s}}(t_n; x), \psi_{\mathrm{s}}(t_n - \eta; x)). \tag{A.62}$$

Further introducing the Lagrangian $L = \int d^D x\, \mathcal{L}$ we introduce again the Minkowski action as the standard notation

$$\mathcal{A}_\eta[\overline{\psi}; \psi] = \eta \sum_{n=1}^{N} L_\eta[\overline{\psi}(t_n); \psi(t_n)] = \eta \sum_{n=1}^{N} \int d^D x\, \mathcal{L}(t_n; x). \tag{A.63}$$

With this, we write the propagator in the well-known way

$$K[\psi_{\mathrm{f}}; \psi_{\mathrm{i}}](t_{\mathrm{f}}; t_{\mathrm{i}}) = \int_{\psi(t_{\mathrm{i}})=\psi_{\mathrm{i}}}^{\psi(t_{\mathrm{f}})=\psi_{\mathrm{f}}} \mathcal{D}_\eta[\overline{\psi}; \psi] \mathcal{N} e^{i\mathcal{A}_\eta[\overline{\psi};\psi]}, \tag{A.64}$$

where we denoted the exponential of the final state as $\mathcal{N}$. Equivalently, we perform the continuous limit $N \to 0$ yielding

$$G[\psi_{\mathrm{f}}; \psi_{\mathrm{i}}](t_{\mathrm{f}}; t_{\mathrm{i}}) = \mathcal{N} \int_{\psi(t_{\mathrm{i}})=\psi_{\mathrm{i}}}^{\psi(t_{\mathrm{f}})=\psi_{\mathrm{f}}} \mathcal{D}[\overline{\psi}; \psi] e^{i\mathcal{A}[\overline{\psi};\psi]}, \tag{A.65}$$

where the final state weight $\mathcal{N}$ does not contain any integration variables any more and is hence just a weight associated to the final state.

In the following, we will perform a Wick rotation on a formal level to obtain the thermodynamic partition function. The formulation of many-body quantum mechanics is sometimes referred to as thermal field theory or quantum statistical field theory.

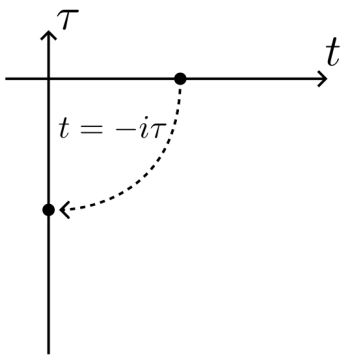


Figure A.3: Illustration of a Wick rotation.

Thermal field theory

To get the quantum mechanical, or grand-canonical, partition function, we first have to generalise the concept of imaginary time introduced before. The general procedure to go from real t to imaginary time τ is called a *Wick rotation* [411, 429, 430]. This allows us to calculate the thermodynamic properties of a system in second quantisation by rotating the time from the real to the imaginary domain. We illustrate this rotation in Fig. A.3 and identify $\tau = it$. Because we want to trace over the Boltzmann factor, we have to consider only coherent state wave functions being either periodic bosons or anti-periodic fermions over one imaginary-time interval $[0, \beta]$. This respects the underlying quantum statistics [411]. The Minkowski action $\mathcal{A}$ is Wick rotated to the Euclidean action $\mathcal{S}$ and the metric signs go from the Minkowski metric, i.e. $(+,-,-,-)$ to the Euclidean metric $(+,+,+,+)$. The partition function is hence nothing else than the Wick rotation of the propagator over a specific time interval, where initial and final coherent state wave functions are identical. Furthermore, we have to integrate over all possible initial states. Following [274] we express the partition function as

$$\mathcal{Z} = \int d\overline{\psi}_0\, d\psi_0\, \frac{\langle \zeta\psi_0 | e^{-\beta\hat{H}} | \psi_0 \rangle}{\| \psi_0 \|}, \tag{A.66}$$

where ζ is the statistical sign of the quantum statistics. With the Wick rotation, we rewrite the above equation to become

$$\mathcal{Z} = \int d\overline{\psi}_0 \, d\psi_0 \, \frac{K[\zeta\psi_0;\psi_0](\beta;0)}{\| \psi_0 \|}. \tag{A.67}$$

We do not repeat the time-slicing steps here, as the idea is the same. Since the starting and ending wave functions are identical due to the anti-periodicity, up to a minus sign, the trace in the definition (A.66) causes an integral also over the initial/final state. In combination with the additional term depending on the final state in the propagator (A.61), when Wick rotated, this leads to

$$\mathcal{Z} = \int \left(d\overline{\psi}_0 \, d\psi_0 \, \mathcal{D}_\eta[\overline{\psi};\psi] \right) e^{-\mathcal{S}_\eta[\overline{\psi};\psi]}. \tag{A.68}$$

Here, the Euclidean action for an imaginary time-sliced system is given as the sum over all discrete time points of the Lagrangian

$$\mathcal{S}_\eta[\overline{\psi};\psi] = \eta \sum_{n=1}^{N} L[\overline{\psi}(\tau_n);\psi(\tau_n)]. \tag{A.69}$$

The imaginary-time Lagrangian is the spatial integral and the spin sum over the Lagrangian density, which is written analogously to the real-time one and is the Legendre transformation of the Hamiltonian density

$$\mathcal{L}(\tau_n;\boldsymbol{x}) = \sum_{\mathrm{s}} \int d^D x \, \left[\overline{\psi}_{\mathrm{s}}(\tau_n;\boldsymbol{x}) \partial_\tau^\eta \psi_{\mathrm{s}}(\tau_n;\boldsymbol{x}) + \mathcal{H}(\overline{\psi}_{\mathrm{s}}(\tau_n;\boldsymbol{x});\psi_{\mathrm{s}}(\tau_n-\eta;\boldsymbol{x})) \right]. \tag{A.70}$$

Definition: Thermal functional integral

We define the thermal field theory discrete functional measure in the continuous limit ($N \to \infty$ and $\eta \to 0^+$) as

$$\mathcal{D}[\overline{\psi};\psi] \; = \lim_{\eta\to 0^+} d\overline{\psi}_0 \, d\psi_0 \, \mathcal{D}_\eta[\overline{\psi};\psi]. \tag{A.71}$$

A continuous functional integral of a functional $\mathcal{F}$ is then defined by the periodic or anti-periodic boundary conditions of the coherent state wave functions ψ and is

$$\oint_{\psi(\beta)=\zeta\psi(0)} \mathcal{D}[\overline{\psi};\psi] \, \mathcal{F}[\overline{\psi};\psi] = \lim_{\eta\to 0^+} \int d\overline{\psi}_0 \, d\psi_0 \, \mathcal{D}_\eta[\overline{\psi};\psi] \mathcal{F}[\{...\}].$$

The shorthand notation $\{...\}$ denotes the set of all coherent states at any point in the discrete imaginary-time domain.

Using the thermal functional integral, the partition function of any fermionic field with inverse temperature $\beta = 1/T$ is given by

$$\mathcal{Z} = \oint_{\psi(\beta)=\zeta\psi(0)} \mathcal{D}[\overline{\psi};\psi] \, e^{-\mathcal{S}[\overline{\psi};\psi]}. \tag{A.72}$$

In the following, we will denote functional integrals with a bosonic sign, i.e. $\zeta = 1$ by $\oint_{\mathrm{P}}$, while fermionic integrals, i.e. having $\zeta = -1$ by $\oint_{\mathrm{A}}$. The Euclidean action for a system

with only two-body interactions can explicitly be expressed by the Lagrangian

$$L[\overline{\psi}(\tau);\psi(\tau)] = \sum_{\mathrm{s}} \int d^D x\, \overline{\psi}_{\mathrm{s}}(\tau;\boldsymbol{x})\partial_\tau \psi_{\mathrm{s}}(\tau;\boldsymbol{x}) + \overline{\psi}_{\mathrm{s}}(\tau;\boldsymbol{x})\hat{h}^{\mathrm{s}}\psi_{\mathrm{s}}(\tau-0^+;\boldsymbol{x}) + \frac{1}{2}\sum_{\mathrm{ss}'} \int d^D(x,x')\, \overline{\psi}_{\mathrm{s}}(\tau;\boldsymbol{x})\overline{\psi}_{\mathrm{s}'}(\tau;\boldsymbol{x}')V^{\mathrm{ss}'}(\boldsymbol{x}-\boldsymbol{x}')\psi_{\mathrm{s}'}(\tau-0^+;\boldsymbol{x})\psi_{\mathrm{s}}(\tau-0^+;\boldsymbol{x}), \tag{A.73}$$

that generates the action by integration over imaginary time. This integration is achieved by taking the sum over all imaginary time steps, which converges to the true Riemann integral in the continuous limit. Most functional integrals, however, have no closed, analytical solution. Therefore, analytic approximations or numerical calculations are often required. To simplify this, in the next section, we introduce a basis-less notation to make calculations formally more concise and general.

Basis-less notation

We now discuss a useful notational technique that will help throughout the main work. Furthermore, it will simplify transformations from real to momentum space. To this end, we note that the coherent state wave function in real space $\psi_{\mathrm{s}}(x)$ with x now being the $D+1$-dimensional time-space vector mentioned before, can be written as dual product $\psi_{\mathrm{s}}(x) = \langle x \mid \psi\rangle_{\mathrm{s}}$. To simplify the notation further, we use the combined Fock space $\mathcal{F} = \bigoplus_{\mathrm{s}} \mathcal{F}^{\mathrm{s}}$ such that we take the full dual product in this space. As such, we have to introduce another way to trace out the species we look at. As the discrete degrees of freedom (the spins, but in general, we can also refer to them as species) for a discrete vector space structure, we can add this as a second type of bra-ket basis and treat it in this space. For example, we could define $\langle\uparrow| = (1,0)$ and $\langle\downarrow| = (0,1)$ in order to form this basis of a two pseudo-spin space. Note that those are not vectors in the coordinate space but elements of the spin space orthogonal to the real space. This notation technique gives rise to a joint position/spin vector to evaluate the dual space coherent state, i.e. for $\psi \in \mathcal{F}$ as an abstract object, in this case

$$\langle x,\mathrm{s}| = \langle x| \otimes \langle \mathrm{s}| \Rightarrow \langle x,\mathrm{s} \mid \psi\rangle = \psi_{\mathrm{s}}(x). \tag{A.74}$$

The kinetic term of the Euclidean action functional is hence the expectation value of the kinetic operator $\hat{T}$ and the temporal derivative of a given coherent state

$$\mathcal{S}[\overline{\psi};\psi] = \langle\psi|[\partial + \hat{T}]|\psi\rangle. \tag{A.75}$$

It is straight-forward to show that this is equivalent to the free Lagrangian, i.e. setting $V = 0$ in Eq. (A.73) by inserting due to the completeness of the real space-time two identities and proposing that $\langle x,\mathrm{s}|[\partial + \hat{\mathcal{T}}]|x',\mathrm{s}'\rangle = [\partial_\tau + \nabla^2/(2m) - \mu_{\mathrm{s}}]\delta_{\mathrm{ss}'}\delta(x-x')$, i.e. the kinetic operator $\hat{T}\delta(x-x') = \langle x|\hat{\mathcal{T}}|x'\rangle$:

$$\mathcal{S}[\overline{\psi};\psi] = \sum_{\mathrm{ss}'} \int d(x;x')\ \langle\psi \mid x,\mathrm{s}\rangle \langle x,\mathrm{s}|[\partial + \hat{\mathcal{T}}]|x',\mathrm{s}'\rangle \langle x',\mathrm{s}' \mid \psi\rangle\,. \tag{A.76}$$

Consistently, the potential operator $V^{\mathrm{ss}'}(\boldsymbol{x}-\boldsymbol{x}')$ is also an abstract object mapping to the complex numbers. However, as we deal with two-body, i.e. four-field interactions, the potential operator $\hat{V}$ is more difficult to break down into that notation, but it is still possible. So far, the interaction had been spin-preserving, meaning $\mathrm{SU}(N)$ symmetric.

However, this was for simplicity, and the notation used here gives rise to a much broader case that is not only capable of breaking the underlying symmetry, but also we could, in principle, allow for non-local terms[2]. The potential, hence, is a mapping that evaluates four fields. The first expectation value gives rise to one particle, if it switches internal or external degrees of freedom, and then the second particle's response to it is evaluated. A general interaction term then reads in this compact form

$$\langle\psi|\langle\psi|\hat{V}|\psi\rangle|\psi\rangle. \tag{A.77}$$

Note that the same state here is used as this is what the action functional describes, mapping one state from the full Fock space to a $\mathbb{C}$-number. Imposing $\mathrm{SU}(N)$-symmetry means that the first expectation value has to preserve the spin. Further, we have to ensure causality, and hence the expectation value reads explicitly

$$\begin{aligned}\langle\psi|\hat{V}|\psi\rangle &= \sum_{\mathrm{ss}'}\int d(x,x')\ \langle\psi\mid x,\mathrm{s}\rangle\langle x,\mathrm{s}|\hat{V}|x',\mathrm{s}'\rangle\langle x',\mathrm{s}'\mid\psi\rangle\\ &= \sum_{\mathrm{ss}'}\int d(x,x')\ \overline{\psi}_{\mathrm{s}}(x)\hat{V}^{\mathrm{s}}(x)\delta_{\mathrm{ss}'}\delta(x-x')\psi_{\mathrm{s}'}(x')\\ &= \sum_{s'}\int dx'\ \overline{\psi}_{\mathrm{s}'}(x')\hat{V}^{\mathrm{s}}(x')\psi_{\mathrm{s}'}(x').\end{aligned} \tag{A.78}$$

In a similar fashion, the second expectation value is also proposed to preserve the underlying symmetry as well as causality, and as such, we can insert two new unities to obtain

$$\langle\psi|\langle\psi|\hat{V}|\psi\rangle|\psi\rangle = \sum_{\mathrm{ss}'}\int d(x,x')\ \overline{\psi}_{\mathrm{s}}(x)\overline{\psi}_{\mathrm{s}'}V^{\mathrm{ss}'}(x-x')\psi_{\mathrm{s}'}(x')\psi_{\mathrm{s}}(x). \tag{A.79}$$

For reasons of translational symmetry, we only consider the distance between the two points in space-time rather than considering them separately. However, this statement is only true in a closed homogeneous system.

Remark: $\mathrm{SU}(N)$ spinors

If instead of evaluating the wave function in the general Fock space $\mathcal{F}$ over all degrees of freedom, we only evaluate the spatial ones, for example, in space and time, we create a $\mathrm{SU}(N)$ spinor object of the internal degrees of freedom, yielding

$$\langle x\mid\psi\rangle = \boldsymbol{\psi}(x) = \begin{pmatrix}\psi_{\mathrm{s}_1}(x)\\ \vdots\\ \psi_{\mathrm{s}_N}(x)\end{pmatrix},$$

where N denotes the number of internal states the joint wave function can have. It behaves like a spinor in the sense that we have the spin degrees of freedom as entries in an abstract object, not being a vector. If the internal degrees of freedom turn out to be, for example, relativistic spins, and we restrict ourselves to $N = 2$, this can in fact describe Dirac spinors.

Using the notation introduced here converts the action functional to a generalised basis-less representation in the form of

$$\mathcal{S}[\overline{\psi};\psi] = \langle\psi|[\partial+\hat{\mathcal{T}}]|\psi\rangle + \langle\psi|\langle\psi|\hat{V}|\psi\rangle|\psi\rangle. \tag{A.80}$$

[2]During this work and also the appendix, we will do neither. Nevertheless, we will consider those general cases here for notational reasons.

The operator in the linear part is nothing but the inverse propagator, giving rise to a representation without the need to specify a certain basis, like real or momentum space. Using the identification $\langle x|\hat{K}^{-1}|x'\rangle = K^{-1}(x;x')$ leads to the representation of the inverse Green's function

$$\hat{G}^{-1} = -\partial - \hat{\mathcal{T}}, \tag{A.81}$$

following, since when Wick rotating the Green's function becomes the causal propagator without prefactors, i.e. $G(x,x') = \Theta(\tau'-\tau)K(x,x')$. This leads to the final formalism we will use whenever we need a quite general picture in which the Euclidean action is given by

$$\boxed{\mathcal{S}[\overline{\psi};\psi] = -\langle\psi|\hat{G}^{-1}|\psi\rangle + \langle\psi|\langle\psi|\hat{V}|\psi\rangle|\psi\rangle.} \tag{A.82}$$

A.2.4 Gaussian functional integrals

Solving functional integrals analytically usually is traced back to Gaussian integrals, an example of which for a scalar case we have already seen in Eq. (A.38). Gaussian integrals commonly describe free theories and, as such, are not only the mathematically simplest case, but they are also physically the basis of any description. It can be shown [430] that such a Gaussian functional integral yields the result

$$\oint_{\psi(\beta)=\zeta\psi(0)} e^{\int dx\ \left[\overline{\psi}(x)G^{-1}\psi(x)+\overline{\psi}(x)j(x)+\overline{j}(x)\psi(x)\right]} = [\mathrm{Det}G]^{\zeta} e^{\int dx\ dx'\ \overline{j}(x)D(x-x')j(x')}. \tag{A.83}$$

The current propagator is denoted by D and solved the equation $G^{-1}D(x-x') = -\delta(\tau-\tau')\delta^D(\boldsymbol{x}-\boldsymbol{x}') =: -\delta(x-x')$. Note that the Greens function has to be negative definite for the integral to exist. Here, we introduced several new notations: First, we define a joint $D+1$-position vector $x = (\tau;x)$ in the Euclidean metric. Consistently also the integral measure is affected by that notation $\int dx = \int_0^\beta d\tau \int d^D x$. The object G^{-1} is a differential operator of the kinetic part and, for all purposes, will be denoted as the inverse Green's function. The determinant here means the product of all eigenvalues of the Green's function operator G. Notably, the bosonic partition function will hence be the determinant of the propagator, while for the fermionic case, the partition function is the determinant of the inverse propagator. Further note that when setting the currents to zero, we replace the inverse Green's function operator by the single-particle Hamiltonian, which then governs the canonical ensemble partition function. As in any experimental setup the particle number is fixed, we perform a transformation to the grand-canonical partition function by shifting from the Helmholtz free energy as the thermodynamic potential, i.e. $\mathcal{F}(V;T;N) = -T\ln\mathcal{Z}$ to the Landau grand-canonical potential $\Omega(V;T;\mu)$ as the correct thermodynamic potential by applying $\hat{H} \to \hat{H} - \mu\hat{N}$ with $\hat{N} = \int d^D x\ \hat{\Psi}(\boldsymbol{x})\hat{\Psi}(\boldsymbol{x})$ being the particle number operator and μ the chemical potential as the corresponding Lagrange multiplier to fix the density. From now on, and in the main work, the sign $\mathcal{Z}$ denotes the grand-canonical partition function associated with the Landau grand-canonical potential $\Omega = -T\ln\mathcal{Z}$. Additionally, we will introduce a new operator in a real space notation, called the kinetic operator $\hat{T} = -\nabla^2/2m - \mu$ describing the kinetic term of a free gas with respect to μ. For said free gas with no external potential and no interactions, the inverse Green's function is $G^{-1}(x;x') = (-\partial_\tau - \hat{T})\delta(x-x')$. The grand-canonical partition function of a free one-species Fermi gas is therefore given as

$$\mathcal{Z}_{\text{free}} = \mathcal{Z}[\overline{j}=0;j=0] = \mathrm{Det}[\hat{G}^{-1}]. \tag{A.84}$$

Appendix B

Matsubara summations

> There is a difference between knowing the path and walking the path.
>
> Morpheus - *The Matrix*

B.1 Matsubara frequencies . . . 191
B.2 Complex integration contours . . . 192
B.2.1 Convergent Matsubara sums . . . 192
B.2.2 Divergent Matsubara sums . . . 194
B.3 Extension: Discrete Matsubara sums . . . 195
B.3.1 Free Fermi spin-mixture . . . 198
B.3.2 Partition function of interacting Fermi gas . . . 201
B.4 Numerical strategy at $T = 0$ . . . 204

In this Appendix, we discuss the method of Matsubara summations, the derivation and two independent ways of solving Matsubara summations analytically, as well as one numerical strategy in the end. We build upon the previous Appendix A, where we already established the Wick rotation as a method to construct a thermal quantum field theory by promoting the time t to an imaginary time $\tau = it$, which then is integrated from 0 to the inverse temperature $\beta = 1/T$. In the whole appendix, we focus on fermions, but keep in mind that all steps here are straightforward to generalise to bosons as well by exchanging fermionic with bosonic Matsubara frequencies, as well as the Fermi-Dirac by the Bose-Einstein distribution. At selected points, we will also state bosonic results. As a reminder, we use notational conventions with $\hbar = 1 = k_{\mathrm{B}}$.

B.1 Matsubara frequencies

In this section, we discuss the concept of Matsubara summation and its role in finite temperature statistical field theory. We consider any function $G(\tau)$, depending on imaginary time $\tau \in [0, \beta]$, which is either periodic, $G(\beta) = G(0)$, or anti-periodic, $G(\beta) = -G(0)$. The discrete Fourier transform, mapping from the imaginary time axis to the imaginary frequency axis, is commonly known as Matsubara transformation [344, 411]. In our con-

ventions, this means

$$G(\tau) = \sum_{n=-\infty}^{\infty} G_{ik_n} e^{-ik_n\tau} = \sum_{ik_n} G_{ik_n} e^{-ik_n\tau}, \tag{B.1}$$

with $k_n = 2n\pi T$ for periodic and $k_n = (2n+1)\pi T$ for anti-periodic functions. We see this when considering $\tau = \beta = 1/T$, the exponential equals either $+1$ or -1. Conversely, the back-transform reads

$$G_{ik_n} = \int_0^\beta \frac{\mathrm{d}\tau}{\beta} G(\tau) e^{ik_n\tau}. \tag{B.2}$$

For the remainder of this appendix, we will deal with Matsubara sums, which we commonly represent as

$$S[G] = \sum_{ik_n} G_{ik_n} = G(\tau = 0). \tag{B.3}$$

In the language of field theory, we are interested in the zero-imaginary time Green's function. Hence, we treat a Matsubara sum as a functional of a given, discrete mapping G. Commonly, bosonic functions are periodic and from now on will be denoted with $q_\ell = 2\ell\pi T$, while fermionic functions are anti-periodic and retain the k_n-notation.

In the next section, we show how analytic continuation provides a powerful tool to evaluate a large set of Matsubara sums, allowing for an analytical solution of those.

B.2 Complex integration contours

In this section, we discuss the method of residue integration in order to solve Matsubara sums of the form of Eq. (B.3). For simplicity, we consider only functions with isolated poles when considering an analytic continuation. This means that functions with branch cuts or essential singularities are excluded. Those are called meromorphic and are mathematically defined by the analytic continuation $G(z)$ for $z \in \mathbb{C}$ only having a point-set of poles in the complex plane, which we call $\mathcal{P}[G]$. We furthermore distinguish two subsets of those functions. The first set we identify as **convergent**, and the second as **divergent** Matsubara sums. They are characterised by their asymptotic behaviour as $|z| \to \infty$ and need to be treated slightly differently.

B.2.1 Convergent Matsubara sums

If $G(z) \propto 1/z^{1+\epsilon}$ for $\epsilon > 0$ and $|z| \to \infty$, we speak of convergent Matsubara sums. This prevents logarithmic divergencies when performing the complex integration. To calculate fermionic Matsubara sums of such functions, we use the fact that the Fermi-Dirac distribution

$$n_\mathrm{F}(z) = \frac{1}{1 + e^{\beta z}} \tag{B.4}$$

has poles at all the fermionic Matsubara frequencies ik_n, with a residue of $-T$. As such we multiply the Matsubara summation of Eq. (B.3) by unities of the form $1 = -\beta \operatorname{Res}_{z=ik_n} n_\mathrm{F}(z)$ [420]. Because the residue is a linear operation, when G does not have a pole at any Matsubara frequency, we obtain

$$S[G] = -\beta \sum_{ik_n} \operatorname*{Res}_{z=ik_n} [G(z) n_\mathrm{F}(z)]. \tag{B.5}$$

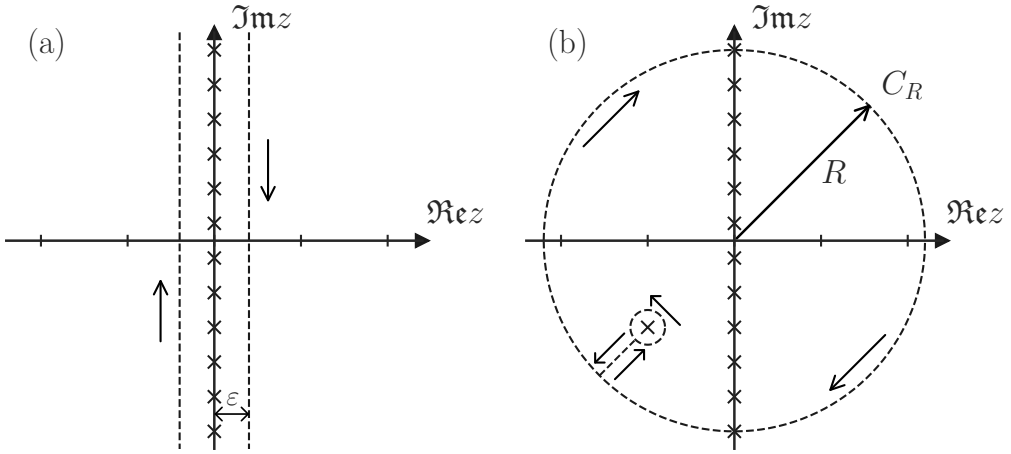


Figure B.1: Illustration of contours used in complex plane for evaluating Matsubara sums of meromorphic functions. Panel (a) shows initial contour along imaginary axis, enclosing only the Matsubara poles of Fermi distribution at distance $\varepsilon > 0$. Panel (b) represents extended contour of circle with radius R, also enclosing poles of the original function G in counterclockwise sense at radius δ_j. For illustration purposes we consider a function with one isolated pole in lower half plane.

We now impose Cauchy's residue theorem [349] to convert the sums over the residues at the Matsubara frequencies to a contour integral in the complex plane along a closed curve C, encircling the imaginary axis clockwise at a positive, infinitesimal distance $\varepsilon > 0$. If there are poles on the imaginary axis, but not on the Matsubara frequencies, we simply wrap the contour around those. As such, all the poles of the function G are excluded of the interior of the contour, while the Matsubara poles of $n_{\mathrm{F}}(z)$ are included. In doing so, the Matsubara sum becomes

$$S[G] = -\beta \oint_C \frac{\mathrm{d}z}{2i\pi} G(z) n_{\mathrm{F}}(z). \tag{B.6}$$

The contour C is shown in Fig. B.1 (a), along the imaginary axis. We deform the contour to a circle of radius $R > 0$, denoted by C_R and depicted in Fig. B.1 (b). However, if the function G has poles on the imaginary axis, we have to exclude those poles to continuously deform the contour. As such any pole $z_j \in \mathcal{P}[G]$ is encircled counter-clockwise with a radius δ by a circle $\Gamma_\delta(z_j)$. This leads to the Matsubara sum becoming

$$S[G] = -\beta \oint_{C_R} \frac{\mathrm{d}z}{2i\pi} G(z) n_{\mathrm{F}}(z) - \beta \sum_{z_j \in \mathcal{P}[G]} \oint_{\Gamma_\delta(z_j)} \frac{\mathrm{d}z}{2i\pi} G(z) n_{\mathrm{F}}(z). \tag{B.7}$$

Since we deal with convergent Matsubara sums, when extending the contour to $R \to \infty$, the outer circle integral vanishes due to Jordan's lemma. Hence, only the isolated poles of G remain, leaving us with

$$S[G] = -\beta \sum_{z_j \in \mathcal{P}[G]} \oint_{\Gamma_\delta(z_j)} \frac{\mathrm{d}z}{2i\pi} G(z) n_{\mathrm{F}}(z). \tag{B.8}$$

We again apply Cauchy's residue theorem and take into account that the contours around the poles are counter-clockwise, eliminating the negative sign and resulting in

Result: Convergent Matsubara sums

$$\frac{1}{\beta}S[G] = \frac{1}{\beta}\sum_{ik_n} G(ik_n) = \sum_{z_j \epsilon \mathcal{P}[G]} \underset{z=z_j}{\mathrm{Res}}[G(z)n_\mathrm{F}(z)]. \tag{B.9}$$

An example for convergent Matsubara sums is the sum over the anomalous propagators found in the BCS order parameter equation in the main text (3.55b). We set $G(ik_n) = F^{\uparrow\downarrow}_{\mathrm{SP}}(ik_n) = \Delta_{\mathrm{B},0}[(ik_n)^2 - E^2_{\boldsymbol{k}}]^{-1}$ and aim to determine the Matsubara sum

$$\frac{1}{\beta}S[G_{\boldsymbol{k}}] = \frac{1}{\beta}\sum_{ik_n} F^{\uparrow\downarrow}_{\mathrm{SP}}(ik_n). \tag{B.10}$$

The set of poles for this anomalous propagator is given by $\mathcal{P}[F^{\uparrow\downarrow}_{\mathrm{SP}}(ik_n)] = \{E_{\boldsymbol{k}}, -E_{\boldsymbol{k}}\}$. Using the rule of L'Hopital, we obtain the two residues as

$$\underset{z=\pm E_{\boldsymbol{k}}}{\mathrm{Res}}\,[F^{\uparrow\downarrow}_{\mathrm{SP}}(z)n_\mathrm{F}(z)] = \mp\Delta_{\mathrm{B},0}\frac{n_\mathrm{F}(\pm E_{\boldsymbol{k}})}{2E_{\boldsymbol{k}}}. \tag{B.11}$$

We reinsert the above residues into Eq. (B.9) to obtain

$$\boxed{\frac{1}{\beta}\sum_{ik_n}\frac{\Delta_{\mathrm{B},0}}{(ik_n)^2 - E^2_{\boldsymbol{k}}} = -\frac{\Delta_{\mathrm{B},0}}{2E_{\boldsymbol{k}}}\tanh\left(\frac{\beta}{2}E_{\boldsymbol{k}}\right),} \tag{B.12}$$

providing the result found in Eq. (3.57b) of the main text. Most Matsubara sums appearing in this thesis are of this form, some more involved ones occur in Chapter 5. Some Matsubara sums we encounter in this thesis are not that simple, which are the divergent Matsubara sums. In the next section, we discuss how to solve those sums systematically.

B.2.2 Divergent Matsubara sums

Matsubara sums of functions G, behaving as $1/z$ as $|z| \to \infty$, we denote as divergent. In those cases, Jordan's lemma is not directly applicable, and hence the contribution of the infinite circle in Fig.B.1 diverges. Matsubara summations of this shape in general are heuristically made convergent by equipping them with an appropriate convergence generating exponential [275, 411, 431]. In the main text, the only divergent Matsubara sum appearing is the momentum distribution, seen in the Hartree equation (3.55a). For spin $\uparrow$, the momentum distribution obtains an exponential factor and reads

$$n^{\uparrow}_{\boldsymbol{k}} = \frac{1}{\beta}\sum_{ik_n} G^{\uparrow\uparrow}_{\mathrm{SP}}(k)e^{ik_n 0^+}, \tag{B.13}$$

This factor is, by most authors, added in an ad-hoc scheme. In Section B.3 we present a formal way which allows us to determine the correct convergence generating factor. The argument appearing is SP normal Green's function (3.56a)

$$G^{\uparrow\uparrow}_{\mathrm{SP}}(k) = \frac{ik_n + \xi^{\uparrow}_{\boldsymbol{k}}}{(ik_n)^2 - E^2_{\boldsymbol{k}}}, \tag{B.14}$$

which for large $ik_n \to z$ behaves as $G^{\uparrow\uparrow}_{\mathrm{SP}}(z, \boldsymbol{k}) \sim z^{-1}$ and hence diverges logarithmically when integrated over. The exponential $e^{ik_n 0^+}$ generates convergence for z with a negative

real part, while for a positive real part, the Fermi-Dirac distribution (B.4) generates convergence. With balanced populations and equal masses, the free dispersion is independent of the spin, and hence we drop the index there. Similar to the anomalous propagator (B.10), this Green's function has poles at $\pm E_{\boldsymbol{k}}$. Due to the convergence generating factor, we are able to apply Eq. (B.9) and hence rewrite the Matsubara sum in Eq. (B.13) as

$$n_{\boldsymbol{k}}^{\uparrow} = \sum_{z_j = \pm E_{\boldsymbol{k}}} \mathrm{Res}\left[\frac{z + \xi_{\boldsymbol{k}}}{z^2 - E_{\boldsymbol{k}}^2} \frac{e^{z0^+}}{1 + e^{\beta z}} \right]_{z=z_j}. \tag{B.15}$$

The residues of those can again be calculated by the rule of L'Hopital and equals

$$\mathrm{Res}\left[\frac{z + \xi_{\boldsymbol{k}}}{z^2 - E_{\boldsymbol{k}}^2} \frac{e^{z0^+}}{1 + e^{\beta z}} \right]_{z=\pm E_{\boldsymbol{k}}} = \frac{E_{\boldsymbol{k}} \mp \xi_{\boldsymbol{k}}}{2E_{\boldsymbol{k}}} \frac{e^{\pm E_{\boldsymbol{k}} 0^+}}{1 + e^{\pm \beta E_{\boldsymbol{k}}}}. \tag{B.16}$$

And hence summing this up gives us the momentum distribution of the particles

$$\boxed{n_{\boldsymbol{k}}^{\mathrm{s}} = \frac{1}{2}\left[1 - \frac{\xi_{\boldsymbol{k}}}{E_{\boldsymbol{k}}} \tanh\left(\frac{\beta}{2} E_{\boldsymbol{k}}\right)\right]}. \tag{B.17}$$

This results in the same momentum distribution found in the main text (3.64). However, one has to be careful, as for instance when considering the $\downarrow$-particles, due to the particle-hole transformation performed in a BCS setup, a different convergence generating factor is required.

Calculating Matsubara sums in the way outlined above is practical, as most Matsubara sums can be evaluated either directly via convergent summation or via convergence generating factors, like for the momentum distribution. However, when dealing with sums that show branch cuts, the residue theorem is difficult to apply. A prominent example here is the free energy, where the Matsubara sum shows a branch cut on the negative real axis due to the logarithm involved, making the action a multivalued function. See here, for instance, the action (3.61) from the main text. In such cases, the Riemann sheet structure has to be taken into account. As it is not always obvious how to accomplish this, we outline in the following section a more systematic way of calculating Matsubara sums in a *discrete* way. This is mandatory as this mathematical difficulty is rooted in the standard definition of the functional integral.

B.3 Extension: Discrete Matsubara sums

To identify the reason for the divergences as well as the multivaluedness of some summations, we have to go back to the previous appendix A. There we made a great effort, when deriving the functional integral, to keep the infinitesimal time spacing in the Lagrangian (A.73). We did so to use this spacing now, as the problem of how to properly evaluate Matsubara summations lies in this spacing. When defining the functional integral we made one implicit assumption, namely that we can exchange integration of coherent states $\mathrm{d}\psi_m$ and limiting procedure of zero time step size $\eta \to 0^+$, in order to go from the discrete (A.60) to the continuous (A.71) functional measure. This is, in a strict mathematical sense, not a valid interchange because functional integrals in general are divergent objects. In most cases, this is not relevant, since we are primarily interested in the finite differences between infinite functional integrals. For Matsubara summations, however, it does not matter, since divergent ground-state energy contributions are potentially lost

when exchanging the limiting procedure and integration. We focus on fermions here because the thesis deals with those particles. In the end, we will also state the corresponding bosonic formulation, as the explicit calculational steps are identical.

To this end, we again have a look at the discretised action of a Fermi system with two-body interactions only, however with a finite imaginary-time step $\eta = \beta/M > 0$, for $M \in \mathbb{N}_+$ time steps, reading

$$\mathcal{S}[\overline{\psi};\psi] = \sum_{\mathrm{s}} \sum_{m=1}^{M} \int d^D x \left[\overline{\psi}_{\mathrm{s}}(\tau_m;\boldsymbol{x}) \partial_\tau^\eta \psi_{\mathrm{s}}(\tau_m;\boldsymbol{x}) + \overline{\psi}_{\mathrm{s}}(\tau_m;\boldsymbol{x}) \hat{h}^{\mathrm{s}} \psi_{\mathrm{s}}(\tau_m - \eta;\boldsymbol{x}) \right. \tag{B.18}$$
$$\left. + \frac{1}{2} \sum_{\mathrm{s}'} \int d^D x' \, \overline{\psi}_{\mathrm{s}}(\tau_m;\boldsymbol{x}) \overline{\psi}_{\mathrm{s}'}(\tau_m;\boldsymbol{x}') V^{\mathrm{ss}'}(\boldsymbol{x}-\boldsymbol{x}') \psi_{\mathrm{s}'}(\tau_m - \eta;\boldsymbol{x}) \psi_{\mathrm{s}}(\tau_m - \eta;\boldsymbol{x}) \right],$$

with $\tau_m = m\eta$ as discrete time steps. For $M \to \infty$, we find the continuous imaginary time limit which, as already mentioned, requires exchanging integration and limiting process. In this continuum limit, the Matsubara transformation reads as at the beginning of this chapter, in Eq. (B.1). However, for finite $M < \infty$ the Matsubara transformation is mathematically a *discrete* Fourier transformation. Formally, we define $T_M = \{m\eta : 1 \leq m \leq M < \infty\}$ as the domain of time steps, such that the discrete Matsubara transformation of a function $f : T_M \to \mathbb{C}$ reads

$$f(\tau_m) = \sum_{n=1}^{M} f_n e^{-i(2n+1)\frac{m}{M}\pi} = \sum_{n=1}^{M} f_n e^{-i(2n+1)\pi T \tau_m}, \tag{B.19}$$

with the inverse transformation reading

$$f_n = f(ik_n) = \frac{1}{M} \sum_{m=1}^{M} f(\tau_m) e^{+i(2n+1)\frac{m}{M}\pi}. \tag{B.20}$$

Note that we have an offset in the frequency of $i\pi/M$ due to the anti-periodicity of the fermionic fields. As such, the frequency domain is also restricted, since on T_M frequencies with $n > M$ are indistinguishable at the time nodes. Due to the definition of discrete Fourier transformations, the frequencies run from 1 to M. The key difference here is the meaning of the discrete derivative ∂_τ^η operator when performing this transformation. Inserting the definition of the Matsubara frequencies and using the differential quotient (A.43) leads, after some basic algebra, to

$$\sum_{m=1}^{M} \overline{\psi}_{\mathrm{s}}(\tau_m) \partial_\tau^\eta \psi_{\mathrm{s}}(\tau_m) = \sum_{n,n'=1}^{M} \overline{\psi}_{\mathrm{s},n} \frac{M}{\beta} \left(1 - e^{i\frac{2n'+1}{M}\pi}\right) \psi_{\mathrm{s},n'} \sum_{m=1}^{M} e^{i2(n-n')\pi\frac{m}{M}}, \tag{B.21}$$

suppressing the spatial arguments. The last sum over the time steps m equals a Kronecker symbol, i.e. a discrete Dirac-δ, according to

$$\sum_{m=1}^{M} e^{i2(n-n')\pi\frac{m}{M}} = M\delta_{n,n'} \tag{B.22}$$

which then yields

$$\sum_{m=1}^{M} \overline{\psi}_{\mathrm{s}}(\tau_m) \partial_\tau^\eta \psi_{\mathrm{s}}(\tau_m) = \sum_{n=1}^{M} \overline{\psi}_{\mathrm{s},n} \zeta_n \psi_{\mathrm{s},n}. \tag{B.23}$$

with the derivative being replaced by the complex energy ζ_n.

Result: Discrete Matsubara sum replacement

In a discrete Matsubara transformation using fermionic frequencies, the differential quotient in a *normal ordered* Grassmann field product is transformed according to

$$\partial_\tau^\eta \to \zeta_n = \frac{M}{\beta}(1-\lambda^{2n+1}), \tag{B.24}$$

with the phase increment $\lambda = e^{i\pi/M}$. Dealing with a bosonic system, the derivative is transformed as

$$\partial_\tau^\eta \to \zeta_n = \frac{M}{\beta}(1-\lambda^{2n}). \tag{B.25}$$

The Matsubara transformation of the discrete derivative ∂_τ^η exhibits real and imaginary parts. However, when the spacing tends to zero, that is $\eta \to 0^+$ for $M \to \infty$, the real part vanishes. This is straightforward to see, considering the Taylor expansion

$$\begin{aligned}\zeta_n &= \frac{M}{\beta}\left[1-1-i\frac{2n+1}{M}\pi-\frac{1}{2}\left(\frac{2n+1}{M}\pi\right)^2+\mathcal{O}(\eta)^3\right]\\ &= -ik_n+\frac{1}{2}(ik_n)^2\eta+\mathcal{O}(\eta)^2,\end{aligned} \tag{B.26}$$

for $n \ll M/2$ when defining the Matsubara frequency $k_n = (2n+1)\pi T$. Furthermore, considering $n = M-m$ and $m \ll M/2$ we analogously find

$$\zeta_{M-m} = -ik_{-m}+\frac{1}{2}(ik_{-m})^2\eta+\mathcal{O}(\eta)^2. \tag{B.27}$$

This means that for $n < M/2$ we converge to the positive, and for $n > M/2$ to the negative Matsubara frequencies in the continuum limit. As such, the continuous imaginary-time limit is included as a limiting case in our approach. For completeness, we furthermore consider an anti-normal ordered product of fields where, by similar reasoning, we obtain

$$\sum_{m=1}^{M}\psi_{\mathrm{s}}(\tau_m)\partial_\tau^\eta\overline{\psi}_{\mathrm{s}}(\tau_m) = M\sum_{n=1}^{M}\psi_{\mathrm{s},n}\overline{\zeta}_n\overline{\psi}_{\mathrm{s},n}, \tag{B.28}$$

where the complex conjugate factor is acquired, that is

$$\overline{\zeta}_n = \frac{M}{\beta}(1-\lambda^{-2n-1}). \tag{B.29}$$

We illustrate those two factors, ζ_n and $\overline{\zeta}_n$, in Fig. B.2 in the complex plane for different numbers of points in units of the temperature T. We notice that the derivative

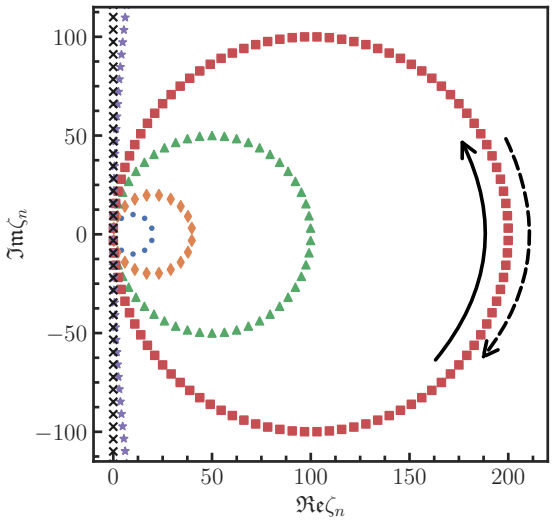


Figure B.2: Illustration of ζ_n and $\overline{\zeta}_n$ with the blue circles representing $M = 10$, orange diamonds $M = 20$, green triangles $M = 50$, red squares $M = 100$ and violet stars $M = 1000$. Black crosses stand for limit of $M \to \infty$, where derivative factor ζ_n approaches Matsubara frequencies $-ik_n$. Solid arrow shows increasing n for ζ_n, while dashed arrow depicts increasing n for $\overline{\zeta}_n$.

factors ζ_n arising from a normal ordered field product circle counter-clockwise. This is associated with the causality imposed by the displacement η. To ensure causality as well, for anti-normal ordered products $\overline{\zeta}_n$ has to run clockwise.

Until now, the discussion has simply shown that the discrete Matsubara transformation changes the meaning of the derivative. We show next that this formulation, which is meant to keep integration and limiting process in the same order, is capable of taking into account infinite ground-state energy contributions. Otherwise, they would possibly be missed when exchanging the two and then naively performing Matsubara summations with branch cuts. To this end, we have to perform Gaussian functional integrals in a discrete setting, after which we evaluate the free energy by solving Matsubara sums.

In the upcoming section B.3.1, we show this for a free Fermi system, whereas section B.3.2 deals with an interacting gas in a BCS setup.

B.3.1 Free Fermi spin-mixture

Here we start with the action of a free Fermi system with two internal states, $\mathrm{s}_1, \mathrm{s}_2$, expressed in the basis of momentum modes $\boldsymbol{k}$ and Matsubara frequencies ik_n. The action is obtained from Eq. (B.18) via discrete Fourier-Matsubara transformation

$$\mathcal{S}_1[\overline{\psi}, \psi] = \eta \sum_{n=1}^{M} \sum_{\mathrm{s},\boldsymbol{k}} \overline{\psi}_{\mathrm{s},\boldsymbol{k},n} \left[-G^{-1}_{\mathrm{s},n}(\boldsymbol{k})\right] \psi_{\mathrm{s},\boldsymbol{k},n}, \tag{B.30}$$

using the complex-valued inverse Green's function

$$-G^{-1}_{\mathrm{s},n}(\boldsymbol{k}) = \zeta_n + \xi_{\mathrm{s},\boldsymbol{k}} e^{ik_n\eta}. \tag{B.31}$$

This action corresponds to the normal ordered Hamiltonian

$$\hat{H}_1 = \int_0^\beta \frac{\mathrm{d}\tau}{\beta} \sum_{\boldsymbol{k}} \left(\xi_{\mathrm{s}_1,\boldsymbol{k}} \hat{\psi}^\dagger_{\mathrm{s}_1,\boldsymbol{k}}(\tau)\hat{\psi}_{\mathrm{s}_1,\boldsymbol{k}}(\tau) + \xi_{\mathrm{s}_2,\boldsymbol{k}} \hat{\psi}^\dagger_{\mathrm{s}_2,\boldsymbol{k}}(\tau)\hat{\psi}_{\mathrm{s}_2,\boldsymbol{k}}(\tau)\right). \tag{B.32}$$

We summarise all the internal degrees of freedom in a spinor notation, reading

$$\boldsymbol{\psi}_{n,\boldsymbol{k}} = \begin{pmatrix} \psi_{\mathrm{s}_1,n,\boldsymbol{k}} \\ \psi_{\mathrm{s}_2,n,\boldsymbol{k}} \end{pmatrix} \tag{B.33}$$

with the matrix-valued inverse Green's function

$$-\boldsymbol{G}^{-1}_n(\boldsymbol{k}) = \begin{pmatrix} -G^{-1}_{\mathrm{s}_1,n}(\boldsymbol{k}) & 0 \\ 0 & -G^{-1}_{\mathrm{s}_2,n}(\boldsymbol{k}) \end{pmatrix}, \tag{B.34}$$

being diagonal in spin space. Using this we write the action of the spinor fields (B.30) as

$$\mathcal{S}_1[\overline{\psi}, \psi] = \eta \sum_{\boldsymbol{k},n} \overline{\boldsymbol{\psi}}_{\boldsymbol{k},n} \left[-\boldsymbol{G}^{-1}_n(\boldsymbol{k})\right] \boldsymbol{\psi}_{\boldsymbol{k},n}, \tag{B.35}$$

which then yields the partition function via

$$\mathcal{Z}_1 = \prod_{\boldsymbol{k}} \prod_{n=1}^{M} \int \mathrm{d}\overline{\boldsymbol{\psi}}_{\boldsymbol{k},n} \mathrm{d}\boldsymbol{\psi}_{\boldsymbol{k},n} e^{-\eta \overline{\boldsymbol{\psi}}_{\boldsymbol{k},n}[-\boldsymbol{G}^{-1}_n(\boldsymbol{k})]\boldsymbol{\psi}_{\boldsymbol{k},n}}, \tag{B.36}$$

where we are allowed to exchange n and $\boldsymbol{k}$ product since one of them is by definition a finite sum. In our case, this is already diagonal in all quantum numbers involved. In a more

general case, the system would need to be diagonalised first. We perform each Gaussian integral of any mode $(\boldsymbol{k}, n)$ separately, leading to

$$\mathcal{Z}_1 = \prod_{\boldsymbol{k}} \prod_{n=1}^{M} \left[-\eta \boldsymbol{G}_n^{-1}(\boldsymbol{k}) \right]. \tag{B.37}$$

Here we used the Berezin integral and the Taylor expansion of the complex Grassmann exponential, seen in Eq. (A.17) and following. We note that this result is just the determinant of a much larger matrix $-\hat{\boldsymbol{G}}^{-1}$, which consists of the inverse Green's function for every wave number separately, that is

$$-\hat{\boldsymbol{G}}^{-1} = \begin{pmatrix} -\hat{\boldsymbol{G}}^{-1}(\boldsymbol{k}_1) & \mathbf{0} & \cdots \\ \mathbf{0} & -\hat{\boldsymbol{G}}^{-1}(\boldsymbol{k}_2) & \cdots \\ \vdots & \vdots & \ddots \end{pmatrix}, \tag{B.38}$$

with the single momentum mode matrices being diagonal $M \times M$ matrices of the form

$$-\hat{\boldsymbol{G}}^{-1}(\boldsymbol{k}_m) = \begin{pmatrix} -\boldsymbol{G}_1^{-1}(\boldsymbol{k}_m) & \mathbf{0} & \cdots & \mathbf{0} \\ \mathbf{0} & -\boldsymbol{G}_2^{-1}(\boldsymbol{k}_m) & \cdots & \mathbf{0} \\ \vdots & \vdots & \ddots & \vdots \\ \mathbf{0} & \mathbf{0} & \cdots & -\boldsymbol{G}_M^{-1}(\boldsymbol{k}_m) \end{pmatrix}. \tag{B.39}$$

Here, we need a countable, possibly infinite, set of modes $\boldsymbol{k}_m$ for $m \in \mathbb{N}$. This means that we separate the partition function now according to

$$\mathcal{Z}_1 = \prod_{\boldsymbol{k}} \mathcal{Z}_{\boldsymbol{k}}, \tag{B.40}$$

where we seek to determine the partition function of a given wave vector

$$\mathcal{Z}_{\boldsymbol{k}} = \prod_{n=1}^{M} \det\left[-\eta \boldsymbol{G}_n^{-1}(\boldsymbol{k}) \right] = \eta^M \prod_{n=1}^{M} (\zeta_n + \xi_{\mathrm{s}_1,\boldsymbol{k}} e^{ik_n\eta}) \; \eta^M \prod_{j=1}^{M} (\zeta_j + \xi_{\mathrm{s}_2,\boldsymbol{k}} e^{ik_j\eta}). \tag{B.41}$$

Since the spins are independent of each other, we evaluate each spin sector separately. Inserting the definition of ζ_n from Eq. (B.24) and factoring out some momentum contributions we find

$$\mathcal{Z}_{\mathrm{s},\boldsymbol{k}} = (1 - \eta\xi_{\mathrm{s},\boldsymbol{k}})^M \prod_{n=1}^{M} \left(\frac{1}{1 - \eta\xi_{\mathrm{s},\boldsymbol{k}}} - \lambda^{2n+1} \right). \tag{B.42}$$

For any complex number $z \in \mathbb{C}$ applying the M^{th} binomial formula reveals

$$\prod_{n=1}^{M} (z - \lambda^{2n+1}) = 1 + z^M. \tag{B.43}$$

Using this general identity to solve the product in Eq. (B.42) leads to the spin- and momentum-dependent pieces of the partition function to become

$$\mathcal{Z}_{\mathrm{s},\boldsymbol{k}} = 1 + \left(1 - \frac{\beta}{M} \xi_{\mathrm{s},\boldsymbol{k}} \right)^M, \tag{B.44}$$

using again the time step $\eta = \beta/M$. Now, taking the product over all spins and all momentum modes leads to the partition function

$$\mathcal{Z}_1 = \prod_{\mathrm{s}} \prod_{\boldsymbol{k}} \mathcal{Z}_{\mathrm{s},\boldsymbol{k}} = \prod_{\boldsymbol{k}} \left[1 + \left(1 - \frac{\beta}{M} \xi_{\mathrm{s}_1,\boldsymbol{k}} \right)^M \right] \left[1 + \left(1 - \frac{\beta}{M} \xi_{\mathrm{s}_2,\boldsymbol{k}} \right)^M \right]. \tag{B.45}$$

In the continuous imaginary-time limit, this converges to

$$\mathcal{Z}_1 \overset{M\to\infty}{=} \prod_{\boldsymbol{k}} \left(1 + e^{-\beta\xi_{\mathrm{s}_1,\boldsymbol{k}}}\right)\left(1 + e^{-\beta\xi_{\mathrm{s}_2,\boldsymbol{k}}}\right). \tag{B.46}$$

We now obtain the thermodynamic potential via $\Omega = -T\ln\mathcal{Z}$, leading to

$$\Omega_1(T,V,\mu) = -T\sum_{\boldsymbol{k}}\left[\ln\left(1 + e^{-\beta\xi_{\mathrm{s}_1,\boldsymbol{k}}}\right) + \ln\left(1 + e^{-\beta\xi_{\mathrm{s}_2,\boldsymbol{k}}}\right)\right]. \tag{B.47}$$

Hence, for $T = 0$ we obtain the ground-state energy in the grand-canonical ensemble to be $\Omega_1(T = 0) = 0$, which is what we would expect, since the Lagrangian associated with the action (B.30) originated from a normal-ordered Hamiltonian, causing $\langle 0|{:}\hat{H}_1{:}|0\rangle = 0$, with $|0\rangle$ being the ground state.

In contrast to this, we now focus on the same system, however, where species s_1 is normal and species s_2 is anti-normal ordered. This system is described by the Hamiltonian

$$\hat{H}_2 = \int_0^\beta \frac{\mathrm{d}\tau}{\beta}\sum_{\boldsymbol{k}}\left[\xi_{\mathrm{s}_1,\boldsymbol{k}}\hat{\psi}^\dagger_{\mathrm{s}_1,\boldsymbol{k}}(\tau)\hat{\psi}_{\mathrm{s}_1,\boldsymbol{k}}(\tau) - \xi_{\mathrm{s}_2,\boldsymbol{k}}\hat{\psi}_{\mathrm{s}_2,\boldsymbol{k}}(\tau)\hat{\psi}^\dagger_{\mathrm{s}_2,\boldsymbol{k}}(\tau)\right]. \tag{B.48}$$

The corresponding action in Fourier-Matsubara space reads

$$\mathcal{S}_2[\overline{\psi},\psi] = \eta\sum_{\boldsymbol{k},n}\left\{\overline{\psi}_{\mathrm{s}_1,\boldsymbol{k},n}\left[-G^{-1}_{\mathrm{s}_1,n}(\boldsymbol{k})\right]\psi_{\mathrm{s}_1,\boldsymbol{k},n} - \psi_{\mathrm{s}_2,\boldsymbol{k},n}\left[\overline{G^{-1}}_{\mathrm{s}_2,n}(\boldsymbol{k})\right]\overline{\psi}_{\mathrm{s}_2,\boldsymbol{k},n}\right\}. \tag{B.49}$$

Here, the second species of fermions propagates with the complex conjugate inverse Green's function, reading

$$\overline{G^{-1}}_{\mathrm{s}_2,n}(\boldsymbol{k}) = \overline{\zeta}_n - \xi_{\mathrm{s}_2,\boldsymbol{k}}e^{-ik_n\eta}. \tag{B.50}$$

We solve the functional integral in the same way as for the fully normal-ordered system, which results in the partition function

$$\mathcal{Z}_2 = \eta^M\prod_{j=1}^{M}\left(\zeta_n + \xi_{\mathrm{s}_1,\boldsymbol{k}}e^{ik_n\eta}\right)\ \eta^M\prod_{n=1}^{M}\left(\overline{\zeta}_n - \xi_{\mathrm{s}_2,\boldsymbol{k}}e^{-ik_n\eta}\right) \tag{B.51}$$

Since the first spin species is normal-ordered, we are able to apply the product formula (B.44) found in the calculation of $\mathcal{Z}_1$, which results in the partition function

$$\mathcal{Z}_2 = \left[1 + \left(1 - \frac{\beta}{M}\xi_{\mathrm{s}_1,\boldsymbol{k}}\right)^M\right]\eta^M\prod_{n=1}^{M}\left(\overline{\zeta}_n - \xi_{\mathrm{s}_2,\boldsymbol{k}}e^{-ik_n\eta}\right). \tag{B.52}$$

We rewrite the second term to become

$$\mathcal{Z}_{\mathrm{s}_2,\boldsymbol{k}} = \left(1 + \eta\xi_{\mathrm{s}_2,\boldsymbol{k}}\right)^M\prod_{n=1}^{M}\left(\frac{1}{1 + \eta\xi_{\mathrm{s}_2,\boldsymbol{k}}} - \lambda^{-2n-1}\right), \tag{B.53}$$

which is solved analogously to the normal-order case using the same product identity (B.43), resulting in

$$\mathcal{Z}_{\mathrm{s}_2,\boldsymbol{k}} = 1 + \left(1 + \frac{\beta}{M}\xi_{\mathrm{s},\boldsymbol{k}}\right)^M. \tag{B.54}$$

With this the partition function of the action (B.49) becomes

$$\mathcal{Z}_2 = \prod_{\mathrm{s}}\prod_{\boldsymbol{k}}\mathcal{Z}_{\mathrm{s},\boldsymbol{k}} = \prod_{\boldsymbol{k}}\left[1 + \left(1 - \frac{\beta}{M}\xi_{\mathrm{s}_1,\boldsymbol{k}}\right)^M\right]\left[1 + \left(1 + \frac{\beta}{M}\xi_{\mathrm{s}_2,\boldsymbol{k}}\right)^M\right], \tag{B.55}$$

which in the continuous imaginary-time limit becomes

$$\mathcal{Z}_2 \overset{M\to\infty}{=} \left(1 + e^{-\beta\xi_{\mathrm{s}_1,\boldsymbol{k}}}\right)\left(1 + e^{\beta\xi_{\mathrm{s}_2,\boldsymbol{k}}}\right). \tag{B.56}$$

We factor out one exponential in the anti-normal ordered species to later on identify the vacuum term, reading

$$\mathcal{Z}_2 \overset{M\to\infty}{=} \left(1 + e^{-\beta\xi_{\mathrm{s}_1,\boldsymbol{k}}}\right)\left(1 + e^{-\beta\xi_{\mathrm{s}_2,\boldsymbol{k}}}\right) e^{\beta\xi_{\mathrm{s}_2,\boldsymbol{k}}}. \tag{B.57}$$

With this, we obtain the grand-canonical potential

$$\Omega_2(T,V,\mu) = -T\sum_{\boldsymbol{k}}\left[\ln\left(1 + e^{-\beta\xi_{\mathrm{s}_1,\boldsymbol{k}}}\right) + \ln\left(1 + e^{-\beta\xi_{\mathrm{s}_2,\boldsymbol{k}}}\right)\right] - \sum_{\boldsymbol{k}}\xi_{\mathrm{s}_2,\boldsymbol{k}}. \tag{B.58}$$

Thus, in the ground state, we now obtain a divergent vacuum expectation value

$$\Omega_2(T=0) = -\sum_{\boldsymbol{k}}\xi_{\mathrm{s}_2,\boldsymbol{k}} = \langle 0|\hat{H}_2|0\rangle \neq 0, \tag{B.59}$$

even though the normal order of both Hamiltonians is identical, i.e. $\langle 0|{:}\hat{H}_2{:}|0\rangle = 0$.

Having discussed the free fermion case, we now include interactions to derive the grand-canonical potential of the BCS Hamiltonian in a discrete sense, including the vacuum terms.

B.3.2 Partition function of interacting Fermi gas

In this section, we present a discrete imaginary-time calculation giving rise to the full vacuum energy contribution of the standard functional integral BCS theory. We will show how the vacuum terms arise from the discretisation of the imaginary-time grid and also derive additional energy contributions arising from the Hubbard-Stratonovich fields. In order to do so we first use the retarded action (B.18) with contact interaction and two species. Then we perform a discrete Fourier-Matsubara transformation. With the BCS approximation, that is $k' = -k$, since Cooper pairs are formed mainly at the Fermi surface, we obtain

$$\begin{aligned}\mathcal{S}_{\mathrm{BCS}}[\overline{\psi},\psi] =& \eta\sum_{n=1}^{M}\sum_{\boldsymbol{k}}\Bigg\{\sum_{\mathrm{s}}\overline{\psi}_{\mathrm{s},n,\boldsymbol{k}}\left[\zeta_n + \xi_{\boldsymbol{k}}\lambda^{2n+1}\right]\psi_{\mathrm{s},n,\boldsymbol{k}} \\ &- \frac{g}{L^D}\sum_{n',\boldsymbol{k}'}\sum_{\ell,\boldsymbol{q}}\overline{\psi}_{\uparrow,n+\ell/2,\boldsymbol{k}+\boldsymbol{q}/2}\overline{\psi}_{\downarrow,-n-\ell/2,-\boldsymbol{k}-\boldsymbol{q}/2}\psi_{\downarrow,-n'-\ell-1,-\boldsymbol{k}'-\boldsymbol{q}}\psi_{\uparrow,n'+\ell-1,\boldsymbol{k}'+\boldsymbol{q}}\Bigg\},\end{aligned} \tag{B.60}$$

with $\xi_{\boldsymbol{k}} = \boldsymbol{k}^2/(2m) - \mu$ as free particle dispersion and L^D as D-dimensional volume. We have to impose here a discrete time version of the Hubbard-Stratonovich transformation, introducing a momentum-dependent complex-valued field $\Delta_{\ell,\boldsymbol{q}}$. We perform the HS transformation, ultimately resulting in the HS action [420]

$$\begin{aligned}\mathcal{S}_{\mathrm{HS}}[\overline{\psi},\psi;\overline{\Delta},\Delta] =& \eta\sum_{n,\boldsymbol{k}}\Bigg\{\sum_{\mathrm{s}}\overline{\psi}_{\mathrm{s},n,\boldsymbol{k}}\left[\zeta_n + \xi_{\boldsymbol{k}}\lambda^{2n+1}\right]\psi_{\mathrm{s},n,\boldsymbol{k}} + L^D\sum_{\ell,\boldsymbol{q}}\frac{|\Delta_{\ell,q}|^2}{g} \\ &+ \sum_{\ell,\boldsymbol{q}}\left[\overline{\psi}_{\uparrow,n+\ell/2,\boldsymbol{k}+\boldsymbol{q}/2}\overline{\psi}_{\downarrow,-n-\ell/2,-\boldsymbol{k}-\boldsymbol{q}/2}\Delta_{\ell-2,\boldsymbol{q}} + \overline{\Delta}_{\ell,\boldsymbol{q}}\psi_{\downarrow,-n-\ell/2-1,-\boldsymbol{k}-\boldsymbol{q}}\psi_{\uparrow,n+\ell/2-1,\boldsymbol{k}+\boldsymbol{q}}\right]\Bigg\}.\end{aligned} \tag{B.61}$$

This allows us to obtain the partition function for a specific imaginary-time spacing as

$$\mathcal{Z}_{\mathrm{BCS}} = \prod_{n=1}^{M}\prod_{\boldsymbol{k}}\prod_{\mathrm{s}}\int \mathrm{d}\overline{\psi}_{\mathrm{s},n,\boldsymbol{k}}\mathrm{d}\psi_{\mathrm{s},n,\boldsymbol{k}}\prod_{\ell=1}^{M}\prod_{\boldsymbol{q}} J_\eta \int \mathrm{d}\overline{\Delta}_{\ell,\boldsymbol{q}}\mathrm{d}\Delta_{\ell,\boldsymbol{q}} e^{-\mathcal{S}_{\mathrm{HS}}[\overline{\psi},\psi;\overline{\Delta},\Delta]}, \tag{B.62}$$

where $J_\eta = \pi g/(L^D\eta)$ is the Jacobian of the HS transformation. Performing the SP approximation resolves the bosonic functional integral by replacing $\Delta_{\ell,\boldsymbol{q}} = \Delta_0\delta_{\ell,0}\delta_{\boldsymbol{q},\boldsymbol{0}}$, ultimately leading to the partition function

$$\mathcal{Z} = \prod_{n=1}^{M}\prod_{\boldsymbol{k}}\prod_{\mathrm{s}}\int \mathrm{d}\overline{\psi}_{\mathrm{s},n,\boldsymbol{k}}\mathrm{d}\psi_{\mathrm{s},n,\boldsymbol{k}} J_\eta^M e^{-\mathcal{S}_{\mathrm{HS}}[\overline{\psi},\psi;\overline{\Delta}_0,\Delta_0]}. \tag{B.63}$$

Note that we do perform the SP approximation before integrating out the fermionic degrees of freedom, since we want to avoid interchanging the order of products. In order to perform the functional integral, we rearrange the HS action at the saddle. To do so, we perform a particle-hole transformation on the $\downarrow$ particles, hence interchanging their order. This leads to the action to become

$$\begin{aligned}\mathcal{S}_{\mathrm{HS}}[\overline{\psi},\psi;\overline{\Delta}_0,\Delta_0] =& \eta\sum_{n=1}^{M}\sum_{\boldsymbol{k}}\begin{pmatrix}\overline{\psi}_{\uparrow,n,\boldsymbol{k}} & \psi_{\downarrow,-n,-\boldsymbol{k}}\end{pmatrix}\begin{pmatrix}\zeta_n+\xi_{\boldsymbol{k}}\lambda^{2n+1} & \Delta_0\lambda^2\\ \overline{\Delta}_0 & -\zeta_{-n}-\xi_{\boldsymbol{k}}\lambda^{-2n+1}\end{pmatrix}\begin{pmatrix}\psi_{\uparrow,n,\boldsymbol{k}}\\ \overline{\psi}_{\downarrow,-n,-\boldsymbol{k}}\end{pmatrix}\\ &+\eta L^D\frac{|\Delta_0|^2}{g}.\end{aligned} \tag{B.64}$$

Note that the $\downarrow$-particles have an inverse order of the Matsubara frequencies due to a change in index according to $n \to -n$, not due to an initial anti-normal order, since the original Lagrangian was normal-ordered. Furthermore, the λ factors still yield $-2n+1$ because they denote odd frequencies. To calculate the functional integral, we also need to anti-commute the measures of the respective particles. As such, considering one momentum mode with $\mathcal{Z}_{\mathrm{BCS}} = \mathcal{Z}_{\mathrm{aux}}\prod_{\boldsymbol{k}}\mathcal{Z}_{\boldsymbol{k}}$ we find

$$\mathcal{Z}_{\boldsymbol{k}} = (-1)^M\prod_{n=1}^{M}\int \mathrm{d}\overline{\psi}_{\uparrow,n,\boldsymbol{k}}\mathrm{d}\psi_{\downarrow,n,\boldsymbol{k}}\mathrm{d}\overline{\psi}_{\downarrow,n,\boldsymbol{k}}\mathrm{d}\psi_{\uparrow,n,\boldsymbol{k}}\; e^{-\mathcal{S}_{\mathrm{HS}}[\overline{\psi},\psi;\overline{\Delta}_0,\Delta_0]}. \tag{B.65}$$

Here, the auxiliary term is

$$\mathcal{Z}_{\mathrm{aux}} = J_\eta^M e^{-\eta L^D|\Delta_0|^2/g} \tag{B.66}$$

associated with the vacuum of the pair field. The integral in Eq. (B.65) is evaluated via diagonalising the Grassmann basis. This is a standard procedure found in many textbooks [274, 275, 411] and the result is simply the determinant of the inverse Green's function, ultimately reading

$$\mathcal{Z}_{\boldsymbol{k}} = (-1)^M\prod_{n=1}^{M}\det\left[-\eta\boldsymbol{G}^{-1}_{\mathrm{SP},n}(\boldsymbol{k})\right], \tag{B.67}$$

using the discrete SP inverse Green's function

$$-\boldsymbol{G}^{-1}_{\mathrm{SP},n}(\boldsymbol{k}) = \begin{pmatrix}\zeta_n+\xi_{\boldsymbol{k}}\lambda^{2n+1} & \Delta_0\lambda^2\\ \overline{\Delta}_0 & -\zeta_{-n}-\xi_{\boldsymbol{k}}\lambda^{-2n+1}\end{pmatrix}. \tag{B.68}$$

We evaluate the matrix determinant, leading to

$$\det\left[-\eta\boldsymbol{G}^{-1}_{\mathrm{SP},n}(\boldsymbol{k})\right] = -1-\lambda^2(1-\eta\xi_{\boldsymbol{k}})-\lambda^2\eta^2|\Delta_0|^2+(1-\eta\xi_{\boldsymbol{k}})\left(\lambda^{2n+1}+\lambda^{-2n-1}\right). \tag{B.69}$$

After this, we factor out $(1-\eta\xi_{\boldsymbol{k}})$ because it yields a vacuum term. Proceeding to this, we expand the determinant in orders of the imaginary-time spacing $\eta = \beta/M$, resulting in

$$\det\left[-\eta \boldsymbol{G}^{-1}_{\mathrm{SP},n}(\boldsymbol{k})\right] = 2(1-\eta\xi_{\boldsymbol{k}})\left[-1-\frac{\lambda^2}{2}\eta^2 E^2_{\boldsymbol{k}} + \frac{1}{2}\left(\lambda^{2n+1}+\lambda^{-2n+1}\right) + \mathcal{O}(\eta)^3\right], \quad \text{(B.70)}$$

using $E_{\boldsymbol{k}} = \sqrt{\xi^2_{\boldsymbol{k}} + |\Delta_0|^2}$ as quasiparticle dispersion. To save space, we set $X = -1 - \lambda^2\eta^2 E^2_{\boldsymbol{k}}/2$ and write $\omega_n = \lambda^{2n+1}$, hence $1/\omega_n = \lambda^{-2n-1}$. We now want to express the determinant of the inverse Green's function as a polynomial in ω_n, which then factorises into roots in the complex plane. To this end we set $z = X + \sqrt{X^2-1}$, with $|X| \geq 1$, allowing us to decompose $X = (z + 1/z)/2$. Doing so makes the determinant factorise into

$$\det\left[-\eta \boldsymbol{G}^{-1}_{\mathrm{SP},n}(\boldsymbol{k})\right] = 2(1-\eta\xi_{\boldsymbol{k}})\frac{\lambda^2}{2z}\left[\omega_n - z\right]\left[z - \frac{\lambda^2}{\omega_n}\right]. \quad \text{(B.71)}$$

We reinsert this into the partition function for a given momentum mode (B.67) to find

$$\mathcal{Z}_{\boldsymbol{k}} = \frac{(-1)^M}{z^M}(1-\eta\xi_{\boldsymbol{k}})^M(-1)^M\prod_{n=1}^{M}\left[z-\lambda^{2n+1}\right]\prod_{j=1}^{M}\left[z-\lambda^{-2j+1}\right]. \quad \text{(B.72)}$$

Both products actually result in the same overall factor, since the terms are identical, only the order of multiplication is inverted due to λ^{2n+1} running counter-clockwise, while λ^{-2n+1} runs clockwise and is slightly displaced, which reads

$$\prod_{n=1}^{M}\left[z-\lambda^{\pm 2n+1}\right] = z^M + 1. \quad \text{(B.73)}$$

With this, the mode partition function becomes

$$\mathcal{Z}_{\boldsymbol{k}} = (-1)^{2M}(1-\eta\xi_{\boldsymbol{k}})^M\left(z^{M/2}+z^{-M/2}\right)^2. \quad \text{(B.74)}$$

This can be expressed in terms of hyperbolic functions, leading to

$$\mathcal{Z}_{\boldsymbol{k}} = (1-\eta\xi_{\boldsymbol{k}})^M 2\left\{\cosh[M\ln(z)]+1\right\}, \quad \text{(B.75)}$$

where we also used, that M is an integer, i.e. $(-1)^{2M} = 1$. In the end, we are interested in the thermodynamic potential for continuous imaginary times. To this end, we use the definition of $z = X + \sqrt{X^2-1}$ as well as $X = -1 - \lambda^2\beta^2 E^2_{\boldsymbol{k}}/(2M^2)$ and perform a series expansion for large M inside the hyperbolic cosine function, resulting in

$$\mathcal{Z}_{\boldsymbol{k}} = (1-\eta\xi_{\boldsymbol{k}})^M 2\left[\cosh\left(-iM\pi - \beta E_{\boldsymbol{k}} + \mathcal{O}\left(\frac{1}{M}\right)\right)+1\right], \quad \text{(B.76)}$$

restricting the logarithm to the principal branch. The direction of the complex limit does not matter, since the hyperbolic cosine is an even function. Since we have $M \in \mathbb{N}$, the complex $\cosh$ function simplifies, and we find

$$\mathcal{Z}_{\boldsymbol{k}} = (1-\eta\xi_{\boldsymbol{k}})^M 2\left[(-1)^M\cosh(\beta E_{\boldsymbol{k}})+1+\mathcal{O}\left(\frac{1}{M}\right)\right]. \quad \text{(B.77)}$$

This reproduces the correct partition function, agreeing with operator approaches, if and only if the number of time steps M is an even number. So, without loss of generality, we assume M to be even. The reason for this is beyond the scope of this appendix, but it

potentially is related to the fermion doubling problem in Fermi lattice theories. Under this assumption, the partition function becomes

$$\mathcal{Z}_{\boldsymbol{k}} = 2(1-\eta\xi_{\boldsymbol{k}})^M \left[\cosh(\beta E_{\boldsymbol{k}}) + 1 + \mathcal{O}\left(\frac{1}{M}\right)\right]. \tag{B.78}$$

We obtain the thermodynamic potential via $\Omega = -T\ln\mathcal{Z} = -T\sum_{\boldsymbol{k}}\ln\mathcal{Z}_{\boldsymbol{k}} - T\ln\mathcal{Z}_{\text{aux}}$,

$$\Omega_{\text{BCS}} = -T\sum_{\boldsymbol{k}}\ln\left(2J_\eta^M(1-\eta\xi_{\boldsymbol{k}})^M\left[\cosh(\beta E_{\boldsymbol{k}})+1\right]\right) + \mathcal{O}\left(\frac{1}{M}\right) + L^D\frac{|\Delta_0|^2}{g}. \tag{B.79}$$

In the large M limit $(1-\eta\xi_{\boldsymbol{k}})^M = \exp(-\beta\xi_{\boldsymbol{k}})$. Using the definition of the hyperbolic cosine with the exponential function, we find the thermodynamic potential to be

$$\Omega_{\text{BCS}} = -T\sum_{\boldsymbol{k}}\ln\left[e^{-\beta(\xi_{\boldsymbol{k}}-E_{\boldsymbol{k}})}\left(1+e^{-\beta E_{\boldsymbol{k}}}\right)^2\right] + M\sum_{\boldsymbol{k}}\ln J_\eta + L^D\frac{|\Delta_0|^2}{g}. \tag{B.80}$$

We separate the logarithm to finally end up with the grand-canonical potential

$$\Omega = \sum_{\boldsymbol{k}}(\xi_{\boldsymbol{k}} - E_{\boldsymbol{k}}) + L^D\frac{|\Delta_0|^2}{g} - 2T\sum_{\boldsymbol{k}}\ln\left(1+e^{-\beta E_{\boldsymbol{k}}}\right) + \lim_{M\to\infty} M\sum_{\boldsymbol{k}}\ln(M\pi T g). \tag{B.81}$$

The first two terms represent the vacuum energy. Here, the first term arises from a proper treatment of the imaginary-time slicing function integral, whereas the second term denotes the vacuum of the auxiliary field, where all the M factors cancel out. Note that due to the original BCS Hamiltonian being normal ordered, the vacuum energy is finite and negative. The third term stands for the thermal contribution to the thermodynamic potential, and the last term represents an infinite energy shift coming from the Jacobian of the HS transformation. In almost all approaches, the latter constant is absorbed into the functional measure of the functional integral itself, since it is a simple offset without any influence on the physics. When extending this calculation to the WHFB approach by $\mu \to \mu + \Delta_{\text{H},0}$, we find a second divergent contribution originating from the Jacobian of the Hartree field. Disregarding all the constant divergent terms, as they do not influence any observable, we end up with the thermodynamic potential found in Eq. (3.62) in the main text.

After this detour in the last section, we focus on a different technique of solving convergent Matsubara sums at $T = 0$, which is mainly used in numerical evaluations.

B.4 Numerical strategy at $T = 0$

In this last section, we briefly present the numerical strategy used in Chapter 5 to solve the $T = 0$ Matsubara sums of the response kernel. We first make some remarks on formal summations at $T = 0$ and illustrate this with a simple analytical example, before explicitly showing how to perform more complicated sums numerically. To this end, we consider a general Matsubara sum of the form seen in Eq. (B.3), which in this specific case we express as

$$2\pi T S[G] = 2\pi T\sum_{n=-\infty}^{\infty} G_{ik_n}. \tag{B.82}$$

We note that, since $k_n = (2n+1)\pi T$, the difference of two consecutive frequencies yields $k_n - k_{n-1} = 2\pi T$. Thus, the sum (B.82) is an upper Riemann sum with step size proportional

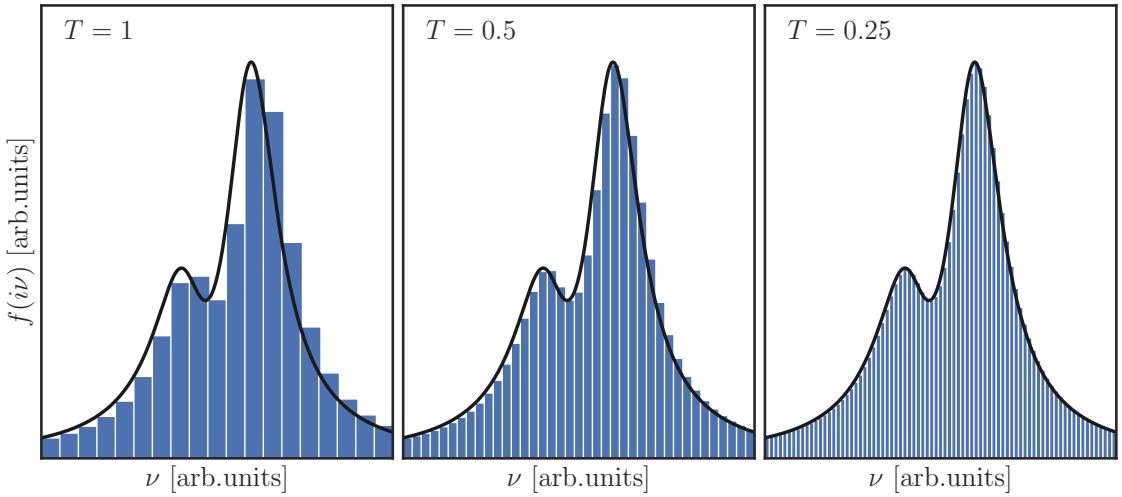


Figure B.3: Representation of finite temperature Matsubara summations for three values of T in arbitrary units, versus imaginary frequency ν. Each term in the respective Riemann sum is represented as the area of a given blue bar. Solid black line depicts the analytic continuation of the function for a continuous set of imaginary frequencies.

to the temperature T. In the limit of zero temperature, this is therefore converging to the Riemann integral, if it exists, yielding

$$2\pi T S[G] \xrightarrow{T=0} \int_{-\infty}^{\infty} \mathrm{d}k_n G(ik_n). \tag{B.83}$$

We schematically represent this limit in Fig. B.3 for different values of temperature in arbitrary units. We represent each term in the Matsubara sum as a bar, which has the area of $2\pi T G(ik_n)$. The solid line stands for the analytic continuation of the sum argument, that is $G(i\nu)$ for $\nu \in \mathbb{R}$ as imaginary frequency. As such, when dealing with any Matsubara sum at $T = 0$ we might evaluate it via

$$T \sum_{n=-\infty}^{\infty} G_{ik_n} = \int_{-\infty}^{\infty} \frac{\mathrm{d}\nu}{2\pi} G(i\nu). \tag{B.84}$$

As an illustrative example, we derive the superfluid order parameter equation (3.57b) in the main text and Eq. (B.12) in this Appendix also via imaginary frequency integration at $T = 0$. The superfluid order parameter equation in the WHFB theory reads

$$\Delta_{\mathrm{B},0} = -\frac{g_{\mathrm{B}}}{L^D} \sum_{\boldsymbol{k}} T \sum_{ik_n} \frac{\Delta_{\mathrm{B},0}}{(ik_n)^2 - E_{\boldsymbol{k}}^2}. \tag{B.85}$$

Applying Eq. (B.84) yields

$$\Delta_{\mathrm{B},0} = \frac{g_{\mathrm{B}}}{L^D} \sum_{\boldsymbol{k}} \int_{-\infty}^{\infty} \frac{\mathrm{d}\nu}{2\pi} \frac{\Delta_{\mathrm{B},0}}{\nu^2 + E_{\boldsymbol{k}}^2}. \tag{B.86}$$

This frequency integral is a standard one, whose antiderivative is the inverse tangent function $\arctan$. Ultimately, this leads to

$$\Delta_{\mathrm{B},0} = \frac{g_{\mathrm{B}}}{L^D} \sum_{\boldsymbol{k}} \frac{\Delta_{\mathrm{B},0}}{2E_{\boldsymbol{k}}}, \tag{B.87}$$

which is the $T = 0$ version of the superfluid order parameter equation.

So far, this was solvable analytically. However, the imaginary frequency integration is more powerful when numerically evaluating Matsubara sums at $T = 0$, which are not solvable analytically by standard means, as for instance when evaluating $T = 0$ Gaussian pair fluctuations [102, 122] or, as in this thesis, beyond SP correlation functions. We do this when evaluating Eq. (5.109) numerically. The density-density correlation function as derived from quantum statistical field theory includes a Matsubara sum at any given temperature T, reading

$$g^{(2)}_{\mathrm{ss}'}(\delta r) = 1 + \frac{1}{L^D}\sum_{\boldsymbol{q}} T \sum_{iq_\ell} \widetilde{\chi}_{\mathrm{ss}'}(\boldsymbol{q}, iq_\ell) e^{-i\boldsymbol{q}\cdot\delta\boldsymbol{r}}, \tag{B.88}$$

where we set the imaginary-time difference to $\delta\tau = 0^+$ and use $iq_\ell = 2i\pi\ell T$ as bosonic Matsubara frequencies. Since the Riemann summation works well both for fermions and bosons, due to the Matsubara frequencies becoming continuous, we again use the replacement (B.84) to obtain

$$g^{(2)}_{\mathrm{ss}'}(\delta r) = 1 + \frac{1}{L^D}\sum_{\boldsymbol{q}} \int_{-\infty}^{\infty} \frac{\mathrm{d}\nu}{2\pi} \widetilde{\chi}_{\mathrm{ss}'}(\boldsymbol{q}, i\nu) e^{-i\boldsymbol{q}\cdot\delta\boldsymbol{r}}. \tag{B.89}$$

For $D = 2$ and spatial homogeneity, we obtain the expression in the main text (5.109). This imaginary frequency integral has no solution in terms of standard functions, but since the response function decays polynomially fast with increasing ν, the integral converges well in $D = 2$ and $D = 3$.

Acknowledgement

Finalizing the PhD is very much like the end of a journey. First and foremost, I want to thank my supervisor Priv.-Doz. Dr Axel Pelster for the opportunity he gave me, for guiding me through new scientific terrain, and for countless hours we spend discussing results, approaches and ideas. Another big thanks I have to direct to Prof. Dr. Carlos A. R. Sá de Melo who, despite being not my supervisor, supported me like a second supervisor during the last three and a half years. Both were a source of inspiration when I was stuck at calculations. To mention are also Prof. Michael Fleischhauer and Prof. James Anglin who enabled me to present my research in their group seminar.

I would also like to thank my family, especially my parents, who supported me from the start. I also want to thank my grandparents for also always supporting me. The same holds for my extended family, which is too large to mention everybody. Immense thanks I also direct to my partner, Sandra, who had to listen to me referring about some mathematical oddity on a Friday evening more than just once.

I also like to thank Sejung for living in the same office with me for four long years now, for the input he gave me and for the open ear when I had some physics to discuss. The same holds for Joshua. Furthermore I have to thank Mathis, Larissa and Daniel for every (extended) Coffee break we had together. Beyond this, a big thank you to Flavia and Marcos, who were both indispensable to me due to their knowledge about computers, without which my computer might have stopped working right at the start. I also want to thank some academia friends who I met outside of Kaiserslautern. A big thanks to Alice and Lucas for the great time and also for the open ear about fermions. I also acknowledge the help of Leon Mixa, who recently entered our group.

Lastly I have to thank friends outside of physics: Celine, Leon, Mirko and Saskia not only for supporting me, but also for enduring my vanishing during the writing process of the PhD.

I hope that most of you will remain part of the journey coming after finalizing the PhD!

Selected Schools, Conferences and Stays

Poster presentations

- "*Steps towards a Beyond Mean-Field Theory of the BEC-BCS crossover for fermionic Lithium*" at Quantum Mixtures School, Les Houches School of Physics (France) , 03. - 06. October 2022
- "*Non-perturbative corrections to the weakly interacting two component Fermi gas*" at Brazilian-German Wilhelm and Else Heraeus Seminar Superconductivity and Superfluidity: From Condensed Matter to Ultracold Quantum Gases, International Institute of Physics (IIP) Natal (Brazil), 14. 18. October 2024 (Awarded with **Best Poster Award**)
- "*Weighted Hartree-Fock-Bogoliubov method for interacting fermions*" at Bad Honnef Physics School on Ultracold Quantum Matter, Physikzentrum Bad Honnef, 10. - 16. August 2025 (Awarded with **Best Poster Award**)
- "*Reduction of pair correlations below the background value in ultracold Fermi gases*" at WEH Seminar on Challenges of Low-Dimensional Quantum Gases, International Center for theoretical physics (ICTP-SAIFR) São Paulo (Brazil), 23. - 27. March 2026

Contributed talks

- "*Hartree-Fock-Bogoliubov Variational Approach for BCS Superfluidity*" at Annual Conference of the DPG and DPG Spring Meeting of SAMOP, Hannover 09. March 2023
- "*A generalized formalism to describe multi-channel Hartree-Fock-Bogoliubov interactions in fermionic systems*" at Annual Conference of the DPG and DPG Spring Meeting of SAMOP, Freiburg 13. March 2024
- "*Weighted Hartree-Fock-Bogoliubov (WHFB) method and its applications to atomic two-component Fermi superfluids in three dimensions*" at APS Division of Atomic, Molecular and Optical Physics Meeting, DAMOP, Portland Oregon, 19. June 2025

Invited seminar talks

- "*A generalized BCS theory for atomic Fermi gases*" at USP São Paulo, Brazil, in Group of Prof. Arnaldo Gammal, 10. October 2024
- "*The Weighted Hartree-Fock-Bogoliubov method for interacting fermions*" at TQC Antwerp, Belgium, in Group of Prof. Jacques Tempere, 19. May 2025

Curriculum Vitae

Personal Data

Name:	Nikolai Kaschewski
Date of Birth:	14. September 1996
Office:	Erwin Schrödinger StraSSe, Building 46, 67663 Kaiserslautern
Phone:	+49 631 205 3167
E-mail:	kaschews@rptu.de



Education

2022-06 Current **Ph.D.: Physics**
Rheinlandpfälzische Technische Universität (RPTU)
Topic: *Multi-channel field theory and two-point correlations for the BEC-BCS crossover*
Supervisor: PD Dr. Axel Pelster

2019-09 2022-03 **Master of Science: Physics**
TU Kaiserslautern
Supervisor: Prof. Dr. James R. Anglin
Final Grade: 1.4

2016-04 2019-09 **Bachelor of Science: Physics**
TU Kaiserslautern
Supervisor: Prof. Dr. James R. Anglin
Final Grade: 2.0

2007-09 2016-04 **Abitur**
Eduard Spranger Gymnasium - Landau
Main Subjects: Mathematics/Physics/History
Final Grade: 2.0

Research Stays

03/2023 06/2023	PhD Exchange Student, Georgia Institute of Technology, USA
09/2024 10/2024	DAAD Exchange program, Universidade de São Paulo, Brazil
05/2025	Visit of TQC at University of Antwerp, Belgium

Academic Service

10/2023 10/2025	Student Representative of SFB/TR 185 (OSCAR)
08/2024	Co-Organizer: SFB/TR 185 OSCAR Intensive Week

Teaching(Selected)

Summer 2021	Tutor "Classical Mechanics" (**Award for outstanding teaching performance**)
Winter 2022/23	Tutor "Classical Electrodynamics" (**Award for outstanding teaching performance**)

Bibliography

[1] J. Dewar and J. A. Fleming, "XXVI. The electrical resistance of metals and alloys at temperatures approaching the absolute zero ", London Edinburgh Philos. Mag. & J. Sci. **36**, 271–299 (1893).

[2] The Nobel Foundation, *The Nobel Prize in Physics 1913. Prize Announcement*, Nobel Prize Outreach AB, (1913) https://www.nobelprize.org/prizes/physics/1913/summary (visited on 12/03/2025).

[3] A. Einstein, "Theoretische Bemerkungen zur Supraleitung der Metalle ", (1922).

[4] W. Meissner and R. Ochsenfeld, "Ein neuer Effekt bei Eintritt der Supraleitfähigkeit", Naturwissenschaften **21**, 787–788 (1933).

[5] A. L. Fetter and J. D. Walecka, *Quantum Theory of Many-Particle Systems* (Dover Publications, June 2003).

[6] F. London and H. London, "The electromagnetic equations of the supraconductor", Proc. A **149**, 71–88 (1935).

[7] F. London and H. London, "Supraleitung und diamagnetismus", Physica **2**, 341–354 (1935).

[8] H. London, "Phase-equilibrium of supraconductors in a magnetic field", Proc. A **152**, 650–663 (1935).

[9] A. B. Pippard and W. L. Bragg, "An experimental and theoretical study of the relation between magnetic field and current in a superconductor", Proc. A **216**, 547–568 (1953).

[10] V. L. Ginzburg and L. D. Landau, "On the Theory of superconductivity", Zh. Eksp. Teor. Fiz. **20**, 1064–1082 (1950).

[11] A. A. Abrikosov, "On the Magnetic Properties of Superconductors of the Second Group", Sov. Phys. JETP **5**, 1174–1182 (1957).

[12] The Nobel Foundation, *The Nobel Prize in Physics 2003. Prize Announcement*, Nobel Prize Outreach AB, (2003) https://www.nobelprize.org/prizes/physics/2003/summary (visited on 12/02/2025).

[13] L. P. Gorkov, "Microscopic derivation of the Ginzburg-Landau equations in the theory of superconductivity", Sov. Phys. JETP **9**, 1364–1367 (1959).

[14] H. Kleinert, *Particles And Quantum Fields* (World Scientific Publishing Company, 2016).

[15] R. A. Ogg, "Bose-Einstein Condensation of Trapped Electron Pairs. Phase Separation and Superconductivity of Metal-Ammonia Solutions", Phys. Rev. **69**, 243–244 (1946).

[16] M. R. Schafroth, "Superconductivity of a Charged Boson Gas", Phys. Rev. **96**, 1149–1149 (1954).

[17] M. R. Schafroth, S. T. Butler, and J. M. Blatt, "Quasichemical equilibrium approach to superconductivity", Helv. Phys. Acta **30**, 93 (1957).

[18] J. Bardeen, L. N. Cooper, and J. R. Schrieffer, "Theory of Superconductivity", Phys. Rev. **108**, 1175–1204 (1957).

[19] J. Bardeen, L. N. Cooper, and J. R. Schrieffer, "Microscopic Theory of Superconductivity", Phys. Rev. **106**, 162–164 (1957).

[20] The Nobel Foundation, *The Nobel Prize in Physics 1972. Prize Announcement*, Nobel Prize Outreach AB, (1972) https://www.nobelprize.org/prizes/physics/1972/summary (visited on 12/03/2025).

[21] J. G. Bednorz and K. A. Müller, "Possible high Tc superconductivity in the Ba-La-Cu-O system", Z. Phys. B: Condens. Matter **64**, 189–193 (1986).

[22] The Nobel Foundation, *The Nobel Prize in Physics 1987. Prize Announcement*, Nobel Prize Outreach AB, (1987) https://www.nobelprize.org/prizes/physics/1987/summary (visited on 12/22/2025).

[23] M. K. Wu, J. R. Ashburn, C. J. Torng, P. H. Hor, R. L. Meng, et al., "Superconductivity at 93 K in a new mixed-phase Y-Ba-Cu-O compound system at ambient pressure", Phys. Rev. Lett. **58**, 908–910 (1987).

[24] A. Schilling, M. Cantoni, J. D. Guo, and H. R. Ott, "Superconductivity above 130 K in the Hg–Ba–Ca–Cu–O system", Nature **363**, 56–58 (1993).

[25] P. Dai, B. Chakoumakos, G. Sun, K. Wong, Y. Xin, and D. Lu, "Synthesis and neutron powder diffraction study of the superconductor HgBa2Ca2Cu3O8 + δ by Tl substitution", Physica C **243**, 201–206 (1995).

[26] Q. Cao, F. Grote, M. Hussmann, and S. Eigler, "Emerging field of few-layered intercalated 2D materials", Nanoscale Adv. **3**, 963–982 (2021).

[27] A. P. Drozdov, P. P. Kong, V. S. Minkov, S. P. Besedin, M. A. Kuzovnikov, et al., "Superconductivity at 250 K in lanthanum hydride under high pressures", Nature **569**, 528–531 (2019).

[28] L. Pitaevskii and S. Stringari, *Bose-Einstein Condensation and Superfluidity*, International Series of Monographs on Physics (OUP Oxford, 2016).

[29] W. Keesom and A. Keesom, "New measurements on the specific heat of liquid helium", Physica **2**, 557–572 (1935).

[30] P. Kapitza, "Viscosity of Liquid Helium below the λ-Point", Nature **141**, 74–74 (1938).

[31] J. F. Allen and A. D. Misener, "Flow of Liquid Helium II", Nature **141**, 75–75 (1938).

[32] E. F. Burton, "Viscosity of Helium I and Helium II", Nature **135**, 265–265 (1935).

[33] The Nobel Foundation, *The Nobel Prize in Physics 1978. Prize Announcement*, Nobel Prize Outreach AB, (1978) https://www.nobelprize.org/prizes/physics/1978/summary (visited on 12/01/2025).

[34] J. F. Allen and A. D. Misener, "Flow Phenomena in Liquid Helium II", Nature **142**, 643–644 (1938).

[35] J. F. Allen and E. Ganz, “The influence of pressure on the thermal conductivity of liquid He ll”, Proc. A **171**, 242–250 (1939).

[36] P. L. Kapitza, “Heat Transfer and Superfluidity of Helium II”, Phys. Rev. **60**, 354–355 (1941).

[37] J. Gao, E. Varga, W. Guo, and W. F. Vinen, “Energy spectrum of thermal counterflow turbulence in superfluid helium-4”, Phys. Rev. B **96**, 094511 (2017).

[38] A. Ulmer, A. Heilrath, B. Senfftleben, S. M. O. O’Connell-Lopez, B. Kruse, et al., “Generation of Large Vortex-Free Superfluid Helium Nanodroplets”, Phys. Rev. Lett. **131**, 076002 (2023).

[39] A. K. Verma, S. Shukla, V. Shukla, A. Basu, and R. Pandit, “Statistical properties of superfluid turbulence in ^{4}He from the Hall-Vinen-Bekharevich-Khalatnikov model”, Phys. Rev. E **108**, 045103 (2023).

[40] F. Brieuc, C. Schran, and D. Marx, “Manifestations of local supersolidity of ^{4}He around a charged molecular impurity”, Phys. Rev. Res. **5**, 043083 (2023).

[41] T. Morresi and G. Garberoglio, “Revisiting the properties of superfluid and normal liquid 4He using ab initio potentials”, J. Low Temp. Phys. **219**, 103–122 (2025).

[42] H. Fröhlich, “Die spezifische Wärme der Elektronen kleiner metallteilchen bei tiefen Temperaturen”, Physica **4**, 639–644 (1937).

[43] A. J. F. and H. Jones, “New Phenomena Connected with Heat Flow in Helium II”, Nature **141**, 243–244 (1938).

[44] F. London, “The λ-Phenomenon of Liquid Helium and the Bose-Einstein Degeneracy”, Nature **141**, 643–644 (1938).

[45] L. Tisza, “Transport Phenomena in Helium II”, Nature **141**, 913–913 (1938).

[46] Bose, S. N., “Plancks Gesetz und Lichtquantenhypothese”, Z. Phys. **26**, 178–181 (1924).

[47] A. Einstein, “Quantentheorie des einatomigen idealen Gases”, Sitzungsber. Preuss. Akad. Wiss., 261 (1924).

[48] A. Einstein, “Quantentheorie des einatomigen idealen Gases. 2. Abhandlung”, Sitzungsber. Preuss. Akad. Wiss., 3 (1925).

[49] L. Landau, “Theory of the Superfluidity of Helium II”, Phys. Rev. **60**, 356–358 (1941).

[50] D. D. Osheroff, R. C. Richardson, and D. M. Lee, “Evidence for a New Phase of Solid He^3”, Phys. Rev. Lett. **28**, 885–888 (1972).

[51] D. D. Osheroff, W. J. Gully, R. C. Richardson, and D. M. Lee, “New Magnetic Phenomena in Liquid He^3 below 3 mK”, Phys. Rev. Lett. **29**, 920–923 (1972).

[52] G. D. Mahan, *Many particle physics*, eng, Physics of solids and liquids (Plenum Press, New York, 1981).

[53] D. Vollhardt and P. Wolfle, *The superfluid phases of helium 3*, third ed. (Philadelphia, PA (USA); Taylor and Francis Inc., Jan. 1990).

[54] W. Pauli, “Über den Zusammenhang des Abschlusses der Elektronengruppen im Atom mit der Komplexstruktur der Spektren”, Z. Phys. **31**, 765–783 (1925).

[55] M. Fierz, "Über die relativistische Theorie kräftefreier Teilchen mit beliebigem Spin", Helv. Phys. Acta **12**, 3 (1939).

[56] P. W. Anderson and P. Morel, "Generalized Bardeen-Cooper-Schrieffer States and the Proposed Low-Temperature Phase of Liquid He^3", Phys. Rev. **123**, 1911–1934 (1961).

[57] R. Balian and N. R. Werthamer, "Superconductivity with Pairs in a Relative p Wave", Phys. Rev. **131**, 1553–1564 (1963).

[58] The Nobel Foundation, *The Nobel Prize in Physics 1996. Prize Announcement*, Nobel Prize Outreach AB, (1996) `https://www.nobelprize.org/prizes/physics/1996/summary` (visited on 12/02/2025).

[59] A. J. Leggett, "Interpretation of Recent Results on He^3 below 3 mK: A New Liquid Phase?", Phys. Rev. Lett. **29**, 1227–1230 (1972).

[60] H. Feshbach, "Unified theory of nuclear reactions", Ann. Phys. (N. Y.) **5**, 357–390 (1958).

[61] U. Fano, "Effects of Configuration Interaction on Intensities and Phase Shifts", Phys. Rev. **124**, 1866–1878 (1961).

[62] H. Friedrich, *Scattering theory*, Vol. 872 (Springer, 2013).

[63] V. Gurarie and L. Radzihovsky, "Resonantly paired fermionic superfluids", Ann. Phys. (N. Y.) **322**, 2–119 (2007).

[64] W. Ketterle and M. W. Zwierlein, "Making, probing and understanding ultracold Fermi gases", La Rivista del Nuovo Cimento **31**, 247–422 (2008).

[65] C. Chin, R. Grimm, P. Julienne, and E. Tiesinga, "Feshbach resonances in ultracold gases", Rev. Mod. Phys. **82**, 1225–1286 (2010).

[66] A. Becker, "BCS Mean-Field Theory for Trapped Fermions", MA thesis (Technische Universität Kaiserslautern, 2021).

[67] D. J. M. Ahmed-Braun, "From few- to many-body physics in strongly interacting quantum gases: A lot about the little and a little about the lot", PhD thesis (Eindhoven University of Technology, May 2023).

[68] J. J. Sakurai and J. Napolitano, *Modern Quantum Mechanics*, 3rd ed. (Cambridge University Press, 2020).

[69] K. M. O'Hara, S. L. Hemmer, M. E. Gehm, S. R. Granade, and J. E. Thomas, "Observation of a Strongly Interacting Degenerate Fermi Gas of Atoms", Science **298**, 2179–2182 (2002).

[70] C. L. Blackley, P. S. Julienne, and J. M. Hutson, "Effective-range approximations for resonant scattering of cold atoms", Phys. Rev. A **89**, 042701 (2014).

[71] M. Bartenstein, A. Altmeyer, S. Riedl, R. Geursen, S. Jochim, et al., "Precise Determination of $^6\mathrm{Li}$ Cold Collision Parameters by Radio-Frequency Spectroscopy on Weakly Bound Molecules", Phys. Rev. Lett. **94**, 103201 (2005).

[72] C. A. Regal, C. Ticknor, J. L. Bohn, and D. S. Jin, "Tuning p-Wave Interactions in an Ultracold Fermi Gas of Atoms", Phys. Rev. Lett. **90**, 053201 (2003).

[73] C. A. Regal, M. Greiner, and D. S. Jin, "Observation of Resonance Condensation of Fermionic Atom Pairs", Phys. Rev. Lett. **92**, 040403 (2004).

[74] C. D'Errico, M. Zaccanti, M. Fattori, G. Roati, M. Inguscio, et al., "Feshbach resonances in ultracold 39K", New J. Phys. **9**, 223 (2007).

[75] D. M. Eagles, "Possible Pairing without Superconductivity at Low Carrier Concentrations in Bulk and Thin-Film Superconducting Semiconductors", Phys. Rev. **186**, 456–463 (1969).

[76] A. J. Leggett, "Diatomic molecules and Cooper pairs", in Modern Trends in the Theory of Condensed Matter (1980), pp. 13–27.

[77] W. Zwerger, *The BCS-BEC crossover and the unitary Fermi gas*, Vol. 836 (Springer Science & Business Media, 2011).

[78] G. C. Strinati, P. Pieri, G. Röpke, P. Schuck, and M. Urban, "The BCSBEC crossover: From ultra-cold Fermi gases to nuclear systems", Phys. Rep. **738**, 1–76 (2018).

[79] Q. Chen, Z. Wang, R. Boyack, S. Yang, and K. Levin, "When superconductivity crosses over: From BCS to BEC", Rev. Mod. Phys. **96**, 025002 (2024).

[80] P. Nozières and S. Schmitt-Rink, "Bose condensation in an attractive fermion gas: From weak to strong coupling superconductivity", J. Low Temp. Phys. **59**, 195–211 (1985).

[81] R. Haussmann, "Crossover from BCS superconductivity to Bose-Einstein condensation: A self-consistent theory", Z. Phys. B: Condens. Matter **91**, 291–308 (1993).

[82] H. Hu, X.-J. Liu, and P. D. Drummond, "Equation of state of a superfluid Fermi gas in the BCS-BEC crossover", Europhys. Lett. **74**, 574 (2006).

[83] R. Haussmann, W. Rantner, S. Cerrito, and W. Zwerger, "Thermodynamics of the BCS-BEC crossover", Phys. Rev. A **75**, 023610 (2007).

[84] M. Pini, P. Pieri, and G. C. Strinati, "Fermi gas throughout the BCS-BEC crossover: Comparative study of t-matrix approaches with various degrees of self-consistency", Phys. Rev. B **99**, 094502 (2019).

[85] H. Tajima, A. Perali, and P. Pieri, "BCS-BEC Crossover and Pairing Fluctuations in a Two Band Superfluid/Superconductor: A T Matrix Approach", Condens. Matter **5**, 10 (2020).

[86] C. A. R. Sá de Melo, "When fermions become bosons: Pairing in ultracold gases", Physics Today **61** (2008).

[87] C. A. R. Sá de Melo, M. Randeria, and J. R. Engelbrecht, "Crossover from BCS to Bose superconductivity: Transition temperature and time-dependent Ginzburg-Landau theory", Phys. Rev. Lett. **71**, 3202–3205 (1993).

[88] J. R. Engelbrecht, M. Randeria, and C. A. R. Sá de Melo, "BCS to Bose crossover: Broken-symmetry state", Phys. Rev. B **55**, 15153–15156 (1997).

[89] P. W. Anderson, "Random-Phase Approximation in the Theory of Superconductivity", Phys. Rev. **112**, 1900–1916 (1958).

[90] J. Goldstone, ""Field theories with ń Superconductor ż solutions"", Il Nuovo Cimento (1955-1965) **19**, 154–164 (1961).

[91] J. Goldstone, A. Salam, and S. Weinberg, "Broken Symmetries", Phys. Rev. **127**, 965–970 (1962).

[92] H. Kurkjian, S. N. Klimin, J. Tempere, and Y. Castin, "Pair-Breaking Collective Branch in BCS Superconductors and Superfluid Fermi Gases", Phys. Rev. Lett. **122**, 093403 (2019).

[93] J. Keeling, P. R. Eastham, M. H. Szymanska, and P. B. Littlewood, "BCS-BEC crossover in a system of microcavity polaritons", Phys. Rev. B **72**, 115320 (2005).

[94] L. Gorkov and T. Melik-Barkhudarov, "Contribution to the theory of superfluidity in an imperfect Fermi gas", Sov. Phys. JETP **13**, 1018 (1961).

[95] L. P. Gor'kov, "Energy spectrum of superconductors", Sov. Phys. - JETP **7:3** (1958).

[96] S. Floerchinger, M. Scherer, S. Diehl, and C. Wetterich, "Particle-hole fluctuations in BCS-BEC crossover", Phys. Rev. B **78**, 174528 (2008).

[97] Z.-Q. Yu, K. Huang, and L. Yin, "Induced interaction in a Fermi gas with a BEC-BCS crossover", Phys. Rev. A **79**, 053636 (2009).

[98] X.-X. Ruan, H. Gong, L. Du, W.-M. Sun, and H.-S. Zong, "Effect of the induced interaction on the superfluid-transition temperature of ultracold Fermi gases within the T-matrix approximation", Phys. Rev. A **87**, 043608 (2013).

[99] Q. Chen, "Effect of the particle-hole channel on BCS–Bose-Einstein condensation crossover in atomic Fermi gases", Sci. Rep. **6**, 25772 (2016).

[100] L. Pisani, A. Perali, P. Pieri, and G. C. Strinati, "Entanglement between pairing and screening in the Gorkov-Melik-Barkhudarov correction to the critical temperature throughout the BCS-BEC crossover", Phys. Rev. B **97**, 014528 (2018).

[101] E. R. Anderson and J. E. Drut, "Pressure, Compressibility, and Contact of the Two-Dimensional Attractive Fermi Gas", Phys. Rev. Lett. **115**, 115301 (2015).

[102] L. He, H. Lü, G. Cao, H. Hu, and X.-J. Liu, "Quantum fluctuations in the BCS-BEC crossover of two-dimensional Fermi gases", Phys. Rev. A **92**, 023620 (2015).

[103] Y. Cao, X.-J. Liu, L. He, G.-L. Long, and H. Hu, "Superfluid density and Berezinskii-Kosterlitz-Thouless transition of a spin-orbit-coupled Fulde-Ferrell superfluid", Phys. Rev. A **91**, 023609 (2015).

[104] B. C. Mulkerin, L. He, P. Dyke, C. J. Vale, X.-J. Liu, and H. Hu, "Superfluid density and critical velocity near the Berezinskii-Kosterlitz-Thouless transition in a two-dimensional strongly interacting Fermi gas", Phys. Rev. A **96**, 053608 (2017).

[105] F. Pascucci and L. Salasnich, "Josephson effect with superfluid fermions in the two-dimensional BCS-BEC crossover", Phys. Rev. A **102**, 013325 (2020).

[106] J. C. Obeso-Jureidini and V. Romero-Rochin, "Density correlation functions and the spatial structure of the two-dimensional BEC-BCS crossover", Phys. Rev. A **105**, 043307 (2022).

[107] S. Van Loon and C. A. R. Sá de Melo, "Effects of Quantum Fluctuations on the Low-Energy Collective Modes of Two-Dimensional Superfluid Fermi Gases from the BCS to the Bose Limit", Phys. Rev. Lett. **131**, 113001 (2023).

[108] S. Ramachandran, S. Jensen, and Y. Alhassid, "Precision thermodynamics of the strongly interacting Fermi gas in two dimensions", Eur. Phys. J. Spec. Top., 10.1140/epjs/s11734-025-02021-z (2025).

[109] T. Mizushima, K. Machida, and M. Ichioka, "Direct Imaging of Spatially Modulated Superfluid Phases in Atomic Fermion Systems", Phys. Rev. Lett. **94**, 060404 (2005).

[110] P. Castorina, M. Grasso, M. Oertel, M. Urban, and D. Zappalà, "Nonstandard pairing in asymmetric trapped Fermi gases", Phys. Rev. A **72**, 025601 (2005).

[111] M. W. Zwierlein, A. Schirotzek, C. H. Schunck, and W. Ketterle, "Fermionic Superfluidity with Imbalanced Spin Populations", Science **311**, 492–496 (2006).

[112] J. Tempere, S. N. Klimin, J. T. Devreese, and V. V. Moshchalkov, "Imbalanced d-wave superfluids in the BCS-BEC crossover regime at finite temperatures", Phys. Rev. B **77**, 134502 (2008).

[113] J. Tempere, S. N. Klimin, and J. T. Devreese, "Phase separation in imbalanced fermion superfluids beyond the mean-field approximation", Phys. Rev. A **78**, 023626 (2008).

[114] A. Bulgac and M. M. Forbes, "Unitary Fermi Supersolid: The Larkin-Ovchinnikov Phase", Phys. Rev. Lett. **101**, 215301 (2008).

[115] S. N. Klimin, J. Tempere, and J. P. A. Devreese, "Pair Excitations and Parameters of State of Imbalanced Fermi Gases at Finite Temperatures", J. Low Temp. Phys. **165**, 261–274 (2011).

[116] S. Klimin, J. Tempere, and J. T. Devreese, "Pseudogap and preformed pairs in the imbalanced Fermi gas in two dimensions", New J. Phys. **14**, 103044 (2012).

[117] T. Kashimura, R. Watanabe, and Y. Ohashi, "Spin susceptibility and fluctuation corrections in the BCS-BEC crossover regime of an ultracold Fermi gas", Phys. Rev. A **86**, 043622 (2012).

[118] S.-G. Peng, X.-J. Liu, and H. Hu, "Large-momentum distribution of a polarized Fermi gas and p-wave contacts", Phys. Rev. A **94**, 063651 (2016).

[119] B. . Tüzemen and T. Sowi ski, "Hierarchy of pairing in an imbalanced three-component one-dimensional Fermi gas", Phys. Rev. A **112**, 023322 (2025).

[120] Y. Ohashi and A. Griffin, "Superfluidity and collective modes in a uniform gas of Fermi atoms with a Feshbach resonance", Phys. Rev. A **67**, 063612 (2003).

[121] R. Combescot, M. Y. Kagan, and S. Stringari, "Collective mode of homogeneous superfluid Fermi gases in the BEC-BCS crossover", Phys. Rev. A **74**, 042717 (2006).

[122] R. B. Diener, R. Sensarma, and M. Randeria, "Quantum fluctuations in the superfluid state of the BCS-BEC crossover", Phys. Rev. A **77**, 023626 (2008).

[123] B. M. Breid and J. R. Anglin, "Postadiabatic Hamiltonian for low-energy excitations in a slowly-time-dependent BCS-BEC crossover", Phys. Rev. A **88**, 033617 (2013).

[124] S. N. Klimin, J. Tempere, G. Lombardi, and J. T. Devreese, "Finite temperature effective field theory and two-band superfluidity in Fermi gases", Eur. Phys. J. B **88**, 122 (2015).

[125] B. Liu, H. Zhai, and S. Zhang, "Evolution of the Higgs mode in a fermion superfluid with tunable interactions", Phys. Rev. A **93**, 033641 (2016).

[126] L. He, "Dynamic density and spin responses of a superfluid Fermi gas in the BCSBEC crossover: Path integral formulation and pair fluctuation theory", Ann. Phys. (N. Y.) **373**, 470–511 (2016).

[127] S. Van Loon, J. Tempere, and H. Kurkjian, "Beyond Mean-Field Corrections to the Quasiparticle Spectrum of Superfluid Fermi Gases", Phys. Rev. Lett. **124**, 073404 (2020).

[128] S. N. Klimin, J. Tempere, and H. Kurkjian, "Collective excitations of superfluid Fermi gases near the transition temperature", Phys. Rev. A **103**, 043336 (2021).

[129] S. N. Klimin, J. Tempere, T. Repplinger, and H. Kurkjian, "Collective excitations of a charged Fermi superfluid in the BCS-BEC crossover", New J. Phys. **25**, 063011 (2023).

[130] M. Iskin, "Structure factors and quantum geometry in multiband BCS superconductors", Phys. Rev. B **112**, 014517 (2025).

[131] E. Taylor, H. Hu, X.-J. Liu, L. P. Pitaevskii, A. Griffin, and S. Stringari, "First and second sound in a strongly interacting Fermi gas", Phys. Rev. A **80**, 053601 (2009).

[132] J. Nespolo, G. E. Astrakharchik, and A. Recati, "AndreevBashkin effect in superfluid cold gases mixtures", New J. Phys. **19**, 125005 (2017).

[133] A. Boulet, G. Wlazowski, and P. Magierski, "Local energy density functional for superfluid Fermi gases from effective field theory", Phys. Rev. A **106**, 013306 (2022).

[134] L. Levrouw, H. Takeuchi, and J. Tempere, "Vortex mass in superfluid Fermi gases along the BEC-BCS crossover", Phys. Rev. A **112**, 043310 (2025).

[135] Á. Rapp, G. Zaránd, C. Honerkamp, and W. Hofstetter, "Color Superfluidity and "Baryon" Formation in Ultracold Fermions", Phys. Rev. Lett. **98**, 160405 (2007).

[136] S.-y. Miyatake, K. Inaba, and S.-i. Suga, "Color superfluidity and trionic state of three-component lattice fermionic atoms", J. Phys. Conf. Ser. **273**, 012008 (2011).

[137] D. M. Kurkcuoglu and C. A. R. Sá de Melo, "Color superfluidity of neutral ultracold fermions in the presence of color-flip and color-orbit fields", Phys. Rev. A **97**, 023632 (2018).

[138] X. Li and Y. Wang, "Coexisting Néel and charge density wave orders in attractive three-color fermions", Phys. Rev. B **110**, 115105 (2024).

[139] C. A. Regal and D. S. Jin, "Measurement of Positive and Negative Scattering Lengths in a Fermi Gas of Atoms", Phys. Rev. Lett. **90**, 230404 (2003).

[140] C. A. Regal, C. Ticknor, J. L. Bohn, and D. S. Jin, "Creation of ultracold molecules from a Fermi gas of atoms", Nature **424**, 47–50 (2003).

[141] M. Greiner, C. A. Regal, and D. S. Jin, "Emergence of a molecular Bose–Einstein condensate from a Fermi gas", Nature **426**, 537–540 (2003).

[142] T. Bourdel, J. Cubizolles, L. Khaykovich, K. M. F. Magalhães, S. J. J. M. F. Kokkelmans, et al., "Measurement of the Interaction Energy near a Feshbach Resonance in a ^{6}Li Fermi Gas", Phys. Rev. Lett. **91**, 020402 (2003).

[143] M. W. Zwierlein, C. A. Stan, C. H. Schunck, S. M. F. Raupach, S. Gupta, et al., "Observation of Bose-Einstein Condensation of Molecules", Phys. Rev. Lett. **91**, 250401 (2003).

[144] T. Bourdel, L. Khaykovich, J. Cubizolles, J. Zhang, F. Chevy, et al., "Experimental Study of the BEC-BCS Crossover Region in Lithium 6", Phys. Rev. Lett. **93**, 050401 (2004).

[145] M. W. Zwierlein, C. A. Stan, C. H. Schunck, S. M. F. Raupach, A. J. Kerman, and W. Ketterle, "Condensation of Pairs of Fermionic Atoms near a Feshbach Resonance", Phys. Rev. Lett. **92**, 120403 (2004).

[146] J. Kinast, S. L. Hemmer, M. E. Gehm, A. Turlapov, and J. E. Thomas, "Evidence for Superfluidity in a Resonantly Interacting Fermi Gas", Phys. Rev. Lett. **92**, 150402 (2004).

[147] J. Kinast, A. Turlapov, J. E. Thomas, Q. Chen, J. Stajic, and K. Levin, "Heat Capacity of a Strongly Interacting Fermi Gas", Science **307**, 1296–1299 (2005).

[148] M. W. Zwierlein, J. R. Abo-Shaeer, A. Schirotzek, C. H. Schunck, and W. Ketterle, "Vortices and superfluidity in a strongly interacting Fermi gas", Nature **435**, 1047–1051 (2005).

[149] G. B. Partridge, K. E. Strecker, R. I. Kamar, M. W. Jack, and R. G. Hulet, "Molecular Probe of Pairing in the BEC-BCS Crossover", Phys. Rev. Lett. **95**, 020404 (2005).

[150] M. Greiner, C. A. Regal, J. T. Stewart, and D. S. Jin, "Probing Pair-Correlated Fermionic Atoms through Correlations in Atom Shot Noise", Phys. Rev. Lett. **94**, 110401 (2005).

[151] B. Gänger, J. Phieler, B. Nagler, and A. Widera, "A versatile apparatus for fermionic lithium quantum gases based on an interference-filter laser system", Rev. Sci. Instrum. **89**, 093105 (2018).

[152] X.-P. Liu, X.-C. Yao, H.-Z. Chen, X.-Q. Wang, Y.-X. Wang, et al., "Observation of the density dependence of the closed-channel fraction of a 6Li superfluid", Natl. Sci. Rev. **9**, nwab226 (2021).

[153] A. Perali, P. Pieri, L. Pisani, and G. C. Strinati, "BCS-BEC Crossover at Finite Temperature for Superfluid Trapped Fermi Atoms", Phys. Rev. Lett. **92**, 220404 (2004).

[154] S. Yong, S. Barbosa, J. Koch, F. Lang, A. Pelster, and A. Widera, *Unravelling Interaction and Temperature Contributions in Unpolarized Trapped Fermionic Atoms in the BCS Regime*, 2023.

[155] A. L. Gaunt, T. F. Schmidutz, I. Gotlibovych, R. P. Smith, and Z. Hadzibabic, "Bose-Einstein Condensation of Atoms in a Uniform Potential", Phys. Rev. Lett. **110**, 200406 (2013).

[156] B. Mukherjee, Z. Yan, P. B. Patel, Z. Hadzibabic, T. Yefsah, et al., "Homogeneous Atomic Fermi Gases", Phys. Rev. Lett. **118**, 123401 (2017).

[157] N. Navon, R. P. Smith, and Z. Hadzibabic, "Quantum gases in optical boxes", Nat. Phys. **17**, 1334–1341 (2021).

[158] K. Hueck, N. Luick, L. Sobirey, J. Siegl, T. Lompe, and H. Moritz, "Two-Dimensional Homogeneous Fermi Gases", Phys. Rev. Lett. **120**, 060402 (2018).

[159] X. Li, S. Wang, X. Luo, Y.-Y. Zhou, K. Xie, et al., "Observation and quantification of the pseudogap in unitary Fermi gases", Nature **626**, 288–293 (2024).

[160] L. Luo and J. E. Thomas, "Thermodynamic Measurements inăaăStrongly Interacting FermiăGas", J. Low Temp. Phys. **154**, 1–29 (2009).

[161] K. Loida, A. Sheikhan, and C. Kollath, "Thermometry of ultracold fermions by (super)lattice modulation spectroscopy", Phys. Rev. A **92**, 043624 (2015).

[162] M. T. Mitchison, T. Fogarty, G. Guarnieri, S. Campbell, T. Busch, and J. Goold, "In Situ Thermometry of a Cold Fermi Gas via Dephasing Impurities", Phys. Rev. Lett. **125**, 080402 (2020).

[163] Z. Yan, P. B. Patel, B. Mukherjee, C. J. Vale, R. J. Fletcher, and M. W. Zwierlein, "Thermography of the superfluid transition in a strongly interacting Fermi gas", Science **383**, 629–633 (2024).

[164] M. Link, K. Gao, A. Kell, M. Breyer, D. Eberz, et al., "Machine Learning the Phase Diagram of a Strongly Interacting Fermi Gas", Phys. Rev. Lett. **130**, 203401 (2023).

[165] D. Eberz, M. Link, A. Kell, M. Breyer, K. Gao, and M. Köhl, "Detecting the phase transition in a strongly interacting Fermi gas by unsupervised machine learning", Phys. Rev. A **108**, 063303 (2023).

[166] C. Chin, M. Bartenstein, A. Altmeyer, S. Riedl, S. Jochim, et al., "Observation of the Pairing Gap in a Strongly Interacting Fermi Gas", Science **305**, 1128–1130 (2004).

[167] Q. Chen, C. A. Regal, M. Greiner, D. S. Jin, and K. Levin, "Understanding the superfluid phase diagram in trapped Fermi gases", Phys. Rev. A **73**, 041601 (2006).

[168] J. Koch, K. Menon, E. Cuestas, S. Barbosa, E. Lutz, et al., "A quantum engine in the BEC–BCS crossover", Nature **621**, 723–727 (2023).

[169] C. Berthod, I. Maggio-Aprile, J. Bruér, A. Erb, and C. Renner, "Observation of Caroli–de Gennes–Matricon Vortex States in $YBa_2Cu_3O_{7-\delta}$", Phys. Rev. Lett. **119**, 237001 (2017).

[170] M. Heyl, K. Adachi, Y. M. Itahashi, Y. Nakagawa, Y. Kasahara, et al., "Vortex dynamics in the two-dimensional BCS-BEC crossover", Nat. Commun. **13**, 6986 (2022).

[171] S. Simonucci, P. Pieri, and G. C. Strinati, "Vortex arrays in neutral trapped Fermi gases through the BCS–BEC crossover", Nat. Phys. **11**, 941–945 (2015).

[172] M. Tylutki and G. Wlazowski, "Universal aspects of vortex reconnections across the BCS-BEC crossover", Phys. Rev. A **103**, L051302 (2021).

[173] C. Lobo, I. Carusotto, S. Giorgini, A. Recati, and S. Stringari, "Pair Correlations of an Expanding Superfluid Fermi Gas", Phys. Rev. Lett. **97**, 100405 (2006).

[174] J. C. Obeso-Jureidini and V. Romero-Rochin, "Spatial structure of the pair wave function and the density correlation functions throughout the BEC-BCS crossover", Phys. Rev. A **101**, 033619 (2020).

[175] M. Pini, P. Pieri, M. Jäger, J. H. Denschlag, and G. C. Strinati, "Pair correlations in the normal phase of an attractive Fermi gas", New J. Phys. **22**, 083008 (2020).

[176] J. Kim, G. Pescia, B. Fore, J. Nys, G. Carleo, et al., "Neural-network quantum states for ultra-cold Fermi gases", Commun. Phys. **7**, 148 (2024).

[177] G. E. Astrakharchik, J. Boronat, J. Casulleras, and S. Giorgini, "Equation of State of a Fermi Gas in the BEC-BCS Crossover: A Quantum Monte Carlo Study", Phys. Rev. Lett. **93**, 200404 (2004).

[178] A. Bulgac, J. E. Drut, and P. Magierski, "Quantum Monte Carlo simulations of the BCS-BEC crossover at finite temperature", Phys. Rev. A **78**, 023625 (2008).

[179] S. Gandolfi, K. E. Schmidt, and J. Carlson, "BEC-BCS crossover and universal relations in unitary Fermi gases", Phys. Rev. A **83**, 041601 (2011).

[180] Z. Hadzibabic, S. Gupta, C. A. Stan, C. H. Schunck, M. W. Zwierlein, et al., "Fifty-fold Improvement in the Number of Quantum Degenerate Fermionic Atoms", Phys. Rev. Lett. **91**, 160401 (2003).

[181] M. Greiner, C. A. Regal, C. Ticknor, J. L. Bohn, and D. S. Jin, "Detection of Spatial Correlations in an Ultracold Gas of Fermions", Phys. Rev. Lett. **92**, 150405 (2004).

[182] T. Schweigler, V. Kasper, S. Erne, I. Mazets, B. Rauer, et al., "Experimental characterization of a quantum many-body system via higher-order correlations", Nature **545**, 323–326 (2017).

[183] J. Verstraten, K. Dai, M. Dixmerias, B. Peaudecerf, T. de Jongh, and T. Yefsah, "In Situ Imaging of a Single-Atom Wave Packet in Continuous Space", Phys. Rev. Lett. **134**, 083403 (2025).

[184] J. Xiang, E. Cruz-Colón, C. C. Chua, W. R. Milner, J. de Hond, et al., "In Situ Imaging of the Thermal de Broglie Wavelength in an Ultracold Bose Gas", Phys. Rev. Lett. **134**, 183401 (2025).

[185] R. Yao, S. Chi, M. Wang, R. J. Fletcher, and M. Zwierlein, "Measuring Pair Correlations in Bose and Fermi Gases via Atom-Resolved Microscopy", Phys. Rev. Lett. **134**, 183402 (2025).

[186] T. de Jongh, J. Verstraten, M. Dixmerias, C. Daix, B. Peaudecerf, and T. Yefsah, "Quantum Gas Microscopy of Fermions in the Continuum", Phys. Rev. Lett. **134**, 183403 (2025).

[187] C. Daix, M. Dixmerias, Y.-Y. He, J. Verstraten, T. de Jongh, et al., "Observing Spatial Charge and Spin Correlations in a Strongly Interacting Fermi Gas", Phys. Rev. Lett. **136**, 153402 (2026).

[188] C. Daix, P. M. Tam, M. Dixmerias, J. Verstraten, T. de Jongh, et al., *Probing the Fermi Sea Topology in a Quantum Gas*, 2025.

[189] I. Bloch, J. Dalibard, and S. Nascimbène, "Quantum simulations with ultracold quantum gases", Nat. Phys. **8**, 267–276 (2012).

[190] C. Gross and I. Bloch, "Quantum simulations with ultracold atoms in optical lattices", Science **357**, 995–1001 (2017).

[191] P. van Wyk, H. Tajima, D. Inotani, A. Ohnishi, and Y. Ohashi, "Superfluid Fermi atomic gas as a quantum simulator for the study of the neutron-star equation of state in the low-density region", Phys. Rev. A **97**, 013601 (2018).

[192] A. J. Daley, I. Bloch, C. Kokail, S. Flannigan, N. Pearson, et al., "Practical quantum advantage in quantum simulation", Nature **607**, 667–676 (2022).

[193] R. P. Feynman, "Simulating physics with computers", Int. J. Theor. Phys. **21**, 467–488 (1982).

[194] D. Bailin and A. Love, "Superfluidity and superconductivity in relativistic fermion systems", Phys. Rep. **107**, 325–385 (1984).

[195] V. Soloviev, "On the superfluid state of the atomic nucleus", Nucl. Phys. **9**, 655–664 (1958).

[196] C. Howell, Q. Chen, T. Carman, A. Hussein, W. Gibbs, et al., "Toward a resolution of the neutron-neutron scattering-length issue", Phys. Lett. B **444**, 252–259 (1998).

[197] D. E. González Trotter, F. Salinas, Q. Chen, A. S. Crowell, W. Glöckle, et al., "New Measurement of the $^1S_0$ Neutron-Neutron Scattering Length Using the Neutron-Proton Scattering Length as a Standard", Phys. Rev. Lett. **83**, 3788–3791 (1999).

[198] S. Gandolfi, A. Gezerlis, and J. Carlson, "Neutron Matter from Low to High Density", Annu. Rev. Nucl. Part. Sci. **65**, 303–328 (2015).

[199] M. G. Alford, A. Schmitt, K. Rajagopal, and T. Schäfer, "Color superconductivity in dense quark matter", Rev. Mod. Phys. **80**, 1455–1515 (2008).

[200] I. Sagert, M. Hempel, G. Pagliara, J. Schaffner-Bielich, T. Fischer, et al., "The strange prospects for astrophysics", J. Phys. G: Nucl. Part. Phys. **36**, 064009 (2009).

[201] D. T. Son, "Finding the critical point in quark-gluon plasma", Physics **2**, 5 (2009).

[202] M. Alford, "Cool Quarks", Physics **3**, 44 (2010).

[203] C. Drischler, J. Holt, and C. Wellenhofer, "Chiral Effective Field Theory and the High-Density Nuclear Equation of State", Annu. Rev. Nucl. Part. Sci. **71**, 403–432 (2021).

[204] N. Chamel, "A stellar superfluid", Physics **4**, 14 (2011).

[205] N. Yunes, M. C. Miller, and K. Yagi, "Gravitational-wave and X-ray probes of the neutron star equation of state", Nat. Rev. Phys. **4**, 237–246 (2022).

[206] A. D. Woodbury, "The Density Profile of a Neutron Star", Entropy **27**, 10.3390/e27020194 (2025).

[207] L. G. Cao, U. Lombardo, and P. Schuck, "Screening effects in superfluid nuclear and neutron matter within Brueckner theory", Phys. Rev. C **74**, 064301 (2006).

[208] A. L. Goodman, "Finite-temperature Hartree-Fock-Bogoliubov calculations in rare earth nuclei", Phys. Rev. C **34**, 1942–1949 (1986).

[209] A. L. Goodman, "Proton-neutron pairing in $Z = N$ nuclei with $A = 76 - -96$", Phys. Rev. C **60**, 014311 (1999).

[210] K. D. Duan, H. B. Zhang, and X. L. Shang, "Phase diagrams of neutron-proton superfluid in asymmetric nuclear matter", Phys. Rev. C **111**, 014320 (2025).

[211] D. Suenaga, "Chiral Effective Model of Cold and Dense Two-Color QCD: The Linear Sigma Model Approach", Symmetry **17**, 10.3390/sym17010124 (2025).

[212] Y. Yu and A. Bulgac, "Spatial Structure of a Vortex in Low Density Neutron Matter", Phys. Rev. Lett. **90**, 161101 (2003).

[213] L. Madeira, S. Gandolfi, K. E. Schmidt, and V. S. Bagnato, "Vortices in low-density neutron matter and cold Fermi gases", Phys. Rev. C **100**, 014001 (2019).

[214] D. P cak, N. Chamel, P. Magierski, and G. Wlazowski, "Properties of a quantum vortex in neutron matter at finite temperatures", Phys. Rev. C **104**, 055801 (2021).

[215] T. Schäfer and F. Wilczek, "Quark description of hadronic phases", Phys. Rev. D **60**, 074014 (1999).

[216] M. Sadzikowski, "Coexistence of pion condensation and color superconductivity in two flavor quark matter", Phys. Lett. B **553**, 45–50 (2003).

[217] H. Abuki, M. Kitazawa, and T. Kunihiro, "How do chiral condensates affect color superconducting quark matter under charge neutrality constraints?", Phys. Lett. B **615**, 102–110 (2005).

[218] H. Abuki and T. Kunihiro, "Extensive study of phase diagram for charge-neutral homogeneous quark matter affected by dynamical chiral condensation: unified picture for thermal unpairing transitions from weak to strong coupling", Nucl. Phys. A **768**, 118–159 (2006).

[219] D. Nickel, R. Alkofer, and J. Wambach, "Unlocking of color and flavor in color-superconducting quark matter", Phys. Rev. D **74**, 114015 (2006).

[220] P.-p. Wu, D.-f. Hou, and H.-c. Ren, "Mass effect in single flavor color superconductivity", Phys. Rev. D **84**, 125031 (2011).

[221] M. Alford, K. Rajagopal, and F. Wilczek, "Color-flavor locking and chiral symmetry breaking in high density QCD", Nucl. Phys. B **537**, 443–458 (1999).

[222] P.-C. Chu, H. Liu, M. Ju, X.-H. Wu, H.-M. Liu, et al., "Quark star matter in color-flavor-locked phase at finite temperature", Phys. Rev. D **110**, 043032 (2024).

[223] A. Migdal, "Superfluidity and the moments of inertia of nuclei", Nucl. Phys. **13**, 655–674 (1959).

[224] E. Litvinova and P. Schuck, "Nuclear superfluidity at finite temperature", Phys. Rev. C **104**, 044330 (2021).

[225] A. Drago, A. Lavagno, and G. Pagliara, "Effects of color superconductivity on the structure and formation of compact stars", Phys. Rev. D **69**, 057505 (2004).

[226] D. Blaschke, E.-O. Hanu, and S. Liebing, "Neutron stars with crossover to color superconducting quark matter", Phys. Rev. C **105**, 035804 (2022).

[227] A. GeiSSel, T. Gorda, and J. Braun, "Color Superconductivity under Neutron-Star Conditions at Next-to-Leading Order", Phys. Rev. Lett. **135**, 211901 (2025).

[228] D. Yakovlev, O. Gnedin, A. Kaminker, K. Levenfish, and A. Potekhin, "Neutron star cooling: theoretical aspects and observational constraints", Adv. Space Res. **33**, 523–530 (2004).

[229] D. Yakovlev, O. Gnedin, M. Gusakov, A. Kaminker, K. Levenfish, and A. Potekhin, "Neutron star cooling", Nucl. Phys. A **752**, 590–599 (2005).

[230] H.-F. Zhu, G.-Z. Liu, J.-R. Wang, and X. Wu, "Superfluid quantum criticality and the thermal evolution of neutron stars", Phys. Rev. D **112**, 043014 (2025).

[231] J. M. Lattimer, "Introduction to neutron stars", AIP Conf. Proc. **1645**, 61–78 (2015).

[232] B. Gordoon, C. Pethick, and D. Pines, "Superfluidity in Neutron Stars", Nature **224**, 673–674 (1969).

[233] D. Pines and M. A. Alpar, "Superfluidity in neutron stars", Nature **316**, 27–32 (1985).

[234] F. De Blasio, G. Lazzari, P. M. Pizzochero, and R. A. Broglia, "Superfluidity and thermal response of neutron star crusts", Phys. Rev. D **53**, 4226–4231 (1996).

[235] M. Borumand, R. Joynt, and W. Klu niak, "Superfluid densities in neutron-star matter", Phys. Rev. C **54**, 2745–2750 (1996).

[236] N. Andersson, G. L. Comer, and D. Langlois, "Oscillations of general relativistic superfluid neutron stars", Phys. Rev. D **66**, 104002 (2002).

[237] N. Andersson, "A Superfluid Perspective on Neutron Star Dynamics", Universe **7**, 10.3390/universe7010017 (2021).

[238] N. Martin and M. Urban, "Superfluid hydrodynamics in the inner crust of neutron stars", Phys. Rev. C **94**, 065801 (2016).

[239] N. Chamel, "Superfluidity and Superconductivity in Neutron Stars", J. Astrophys. Astron. **38**, 43 (2017).

[240] N. Chamel, "Superfluid fraction in the crystalline crust of a neutron star: Role of BCS pairing", Phys. Rev. C **111**, 045803 (2025).

[241] P. M. Pizzochero, L. Viverit, and R. A. Broglia, "Vortex-Nucleus Interaction and Pinning Forces in Neutron Stars", Phys. Rev. Lett. **79**, 3347–3350 (1997).

[242] P. Donati and P. M. Pizzochero, "Is there Nuclear Pinning of Vortices in Superfluid Pulsars?", Phys. Rev. Lett. **90**, 211101 (2003).

[243] B. Link, "Constraining Hadronic Superfluidity with Neutron Star Precession", Phys. Rev. Lett. **91**, 101101 (2003).

[244] J. A. G. Granados, A. M. Mateo, and X. Viñas, "Half-vortex states in the rotating outer core of neutron stars", Phys. Rev. C **111**, 065802 (2025).

[245] P. E. Reichley and G. S. Downs, "Observed Decrease in the Periods of Pulsar PSR 0833–45", Nature **222**, 229–230 (1969).

[246] V. Radhakrishnan and R. N. Manchester, "Detection of a Change of State in the Pulsar PSR 0833-45", Nature **222**, 228–229 (1969).

[247] S. Arumugam and S. Desai, "Classification of pulsar glitch amplitudes using extreme deconvolution", J. High Energy Astrophys. **37**, 46–50 (2023).

[248] P. W. Anderson and N. Itoh, "Pulsar glitches and restlessness as a hard superfluidity phenomenon", Nature **256**, 25–27 (1975).

[249] N. Andersson, G. L. Comer, and R. Prix, "Are Pulsar Glitches Triggered by a Superfluid Two-Stream Instability?", Phys. Rev. Lett. **90**, 091101 (2003).

[250] B. Haskell and A. Melatos, "Models of pulsar glitches", Int. J. Mod. Phys. D **24**, 1530008 (2015).

[251] M. Das, A. Sedrakian, and B. Mukhopadhyay, "Superconductivity in magnetars: Exploring type-I and type-II states in toroidal magnetic fields", Phys. Rev. D **111**, L081307 (2025).

[252] B. Layek, B. K. Saini, and D. Godaba Venkata, "Large-scale unpinning and pulsar glitches due to the forced oscillation of vortices", Phys. Rev. D **112**, L081305 (2025).

[253] G. Almirante and M. Urban, "Superfluid Density in Linear Response Theory: Pulsar Glitches from the Inner Crust of Neutron Stars", Phys. Rev. Lett. **135**, 132701 (2025).

[254] S. Alexander and S. Cormack, "Gravitationally bound BCS state as dark matter", J. Cosmol. Astropart. Phys. **2017**, 005 (2017).

[255] N. Okada and O. Seto, "Superheavy WIMP dark matter from incomplete thermalization", Phys. Lett. B **820**, 136528 (2021).

[256] M. Carena, N. M. Coyle, Y.-Y. Li, S. D. McDermott, and Y. Tsai, "Cosmologically degenerate fermions", Phys. Rev. D **106**, 083016 (2022).

[257] R. Garani, M. H. G. Tytgat, and J. Vandecasteele, "Condensed dark matter with a Yukawa interaction", Phys. Rev. D **106**, 116003 (2022).

[258] M. M. Flores, Y. Lu, and A. Kusenko, "Structure formation after reheating: Supermassive primordial black holes and Fermi ball dark matter", Phys. Rev. D **108**, 123511 (2023).

[259] G. Domènech, D. Inman, A. Kusenko, and M. Sasaki, "Halo formation from Yukawa forces in the very early Universe", Phys. Rev. D **108**, 103543 (2023).

[260] C. E. Yaguna and Ó. Zapata, "Minimal model of fermion FIMP dark matter", Phys. Rev. D **109**, 015002 (2024).

[261] S. Robles, D. Vatsyayan, and G. Busoni, "From capture to collapse: Revisiting black hole formation by fermionic asymmetric dark matter in neutron stars", Phys. Rev. D **112**, 123011 (2025).

[262] G. Liang and R. R. Caldwell, "Cold Dark Matter Based on an Analogy with Superconductivity", Phys. Rev. Lett. **134**, 191004 (2025).

[263] L.-H. Sui, D. Li, J.-Z. Sun, and X.-B. Li, "Signals from Fermionic inflationary cosmology with Yukawa interaction", Phys. Lett. B **870**, 139937 (2025).

[264] Y. Margalit, Y.-K. Lu, F. Ç. Top, and W. Ketterle, "Pauli blocking of light scattering in degenerate fermions", Science **374**, 976–979 (2021).

[265] P. J. Ray, "Structural investigation of La(2-x)Sr(x)CuO(4+y) - Following staging as a function of temperature", MA thesis (University of Copenhagen, Feb. 2016).

[266] W. J. Swiatecki, "The Density Distribution inside Nuclei and Nuclear Shell Structure", Proc. Phys. Soc. Sec. A **63**, 1208 (1950).

[267] C. J. Pethick and H. Smith, *BoseEinstein Condensation in Dilute Gases*, 2nd ed. (Cambridge University Press, 2008).

[268] P. R. Zilsel, "Liquid Helium II: The Hydrodynamics of the Two-Fluid Model", Phys. Rev. **79**, 309–313 (1950).

[269] P. C. Hohenberg and P. C. Martin, "Superfluid Dynamics in the Hydrodynamic ($\omega\tau \ll 1$) and Collisionless ($\omega\tau \gg 1$) Domains", Phys. Rev. Lett. **12**, 69–71 (1964).

[270] A. Miller, D. Pines, and P. Nozières, "Elementary Excitations in Liquid Helium", Phys. Rev. **127**, 1452–1464 (1962).

[271] R. P. Feynman, "Atomic Theory of the Two-Fluid Model of Liquid Helium", Phys. Rev. **94**, 262–277 (1954).

[272] "Microscopic theory of superfluid helium", Ann. Phys. (N. Y.) **34**, 291–359 (1965).

[273] The Nobel Foundation, *The Nobel Prize in Physics 1962. Prize Announcement*, Nobel Prize Outreach AB, (1962) `https://www.nobelprize.org/prizes/physics/1962/summary` (visited on 12/02/2025).

[274] H. Stoof, D. Dickerscheid, and K. Gubbels, *Ultracold Quantum Fields*, Theoretical and Mathematical Physics (Springer Netherlands, 2008).

[275] A. Altland and B. D. Simons, *Condensed Matter Field Theory*, 2nd ed. (Cambridge University Press, 2010).

[276] P. Coleman, *Introduction to Many-Body Physics* (Cambridge University Press, 2015).

[277] N. Goldenfeld, *Lectures on phase transitions and the renormalization group*, eng, 5. print., Frontiers in physics 85 (CRC Press, Boca Raton, 2018).

[278] C. Timm, *Theory of Superconductivity*, 2020.

[279] S. Elitzur, "Impossibility of spontaneously breaking local symmetries", Phys. Rev. D **12**, 3978–3982 (1975).

[280] L. N. Cooper, "Bound Electron Pairs in a Degenerate Fermi Gas", Phys. Rev. **104**, 1189–1190 (1956).

[281] M. Tinkham, *Introduction to superconductivity*, eng, 2. ed., unabridged republ. of the 1996 2. ed. (Dover Publ., Mineola, NY, 2004).

[282] H. Simon, *Lecture Notes for Quantum Matter*, 2022.

[283] B. J. C. van der Hoeven and P. H. Keesom, "Specific Heat of Mercury and Thallium between 0.35 and 4.2řK", Phys. Rev. **135**, A631–A637 (1964).

[284] H. A. Boorse, D. B. Cook, and M. W. Zemansky, "Superconductivity of Lead", Phys. Rev. **78**, 635–636 (1950).

[285] W. B. Pearson and I. M. Templeton, "Superconducting Transition of Lead", Phys. Rev. **109**, 1094–1094 (1958).

[286] B. J. C. van der Hoeven and P. H. Keesom, "Specific Heat of Lead and Lead Alloys Between 0.4 and 4.2řK", Phys. Rev. **137**, A103–A107 (1965).

[287] R. Weber, "Ultrasonic Measurements in Normal and Superconducting Niobium", Phys. Rev. **133**, A1487–A1492 (1964).

[288] S. Yong, "BCS-BEC Crossover of interacting Fermions", MA thesis (University of Kaiserslautern-Landau, 2023).

[289] H. Kleinert, *Hubbard-Stratonovich Transformation: Successes, Failure, and Cure*, 2011.

[290] S. Zhang and A. J. Leggett, "Universal properties of the ultracold Fermi gas", Phys. Rev. A **79**, 023601 (2009).

[291] J. Tempere and J. P. Devreese, "Path-Integral Description of Cooper Pairing", in *Superconductors*, edited by A. Gabovich (IntechOpen, Rijeka, 2012) Chap. 16.

[292] P. Nozières and D. Pines, *The theory of quantum liquids* (Perseus Books, Cambridge, Mass., 1999).

[293] S. S. Botelho and C. A. R. Sá de Melo, "Lifshitz transition in d-wave superconductors", Phys. Rev. B **71**, 134507 (2005).

[294] S. S. Botelho and C. A. R. Sá de Melo, "Quantum Phase Transition in the BCS-to-BEC Evolution of p-wave Fermi Gases", J. Low Temp. Phys. **140**, 409–428 (2005).

[295] M. Marini, F. Pistolesi, and G. C. Strinati, "Evolution from BCS superconductivity to Bose condensation: analytic results for the crossover in three dimensions", Eur. Phys. J. B **1**, 151–159 (1998).

[296] B. Mihaila, J. F. Dawson, F. Cooper, C.-C. Chien, and E. Timmermans, "Auxiliary field formalism for dilute fermionic atom gases with tunable interactions", Phys. Rev. A **83**, 053637 (2011).

[297] J. J. Kinnunen, "Hartree shift in unitary Fermi gases", Phys. Rev. A **85**, 012701 (2012).

[298] R. P. Feynman, "The principle of least action in quantum mechanics", PhD thesis (Princeton U., 1942).

[299] R. P. Feynman, "Space-Time Approach to Non-Relativistic Quantum Mechanics", Rev. Mod. Phys. **20**, 367–387 (1948).

[300] T. Weber, J. Herbig, M. Mark, H.-C. Nägerl, and R. Grimm, "Three-Body Recombination at Large Scattering Lengths in an Ultracold Atomic Gas", Phys. Rev. Lett. **91**, 123201 (2003).

[301] Y. E. Kim and A. L. Zubarev, "Three-body losses in trapped Bose-Einstein-condensed gases", Phys. Rev. A **69**, 023602 (2004).

[302] J. H. Huckans, J. R. Williams, E. L. Hazlett, R. W. Stites, and K. M. O'Hara, "Three-Body Recombination in a Three-State Fermi Gas with Widely Tunable Interactions", Phys. Rev. Lett. **102**, 165302 (2009).

[303] G. J. Conduit and E. Altman, "Effect of three-body loss on itinerant ferromagnetism in an atomic Fermi gas", Phys. Rev. A **83**, 043618 (2011).

[304] S. Zhang and T.-L. Ho, "Atom loss maximum in ultra-cold Fermi gases", New J. Phys. **13**, 055003 (2011).

[305] P. Makotyn, C. E. Klauss, D. L. Goldberger, E. A. Cornell, and D. S. Jin, "Universal dynamics of a degenerate unitary Bose gas", Nat. Phys. **10**, 116–119 (2014).

[306] X.-Y. Chen, M. Duda, A. Schindewolf, R. Bause, I. Bloch, and X.-Y. Luo, "Suppression of Unitary Three-Body Loss in a Degenerate Bose-Fermi Mixture", Phys. Rev. Lett. **128**, 153401 (2022).

[307] S. Haze, J.-L. Li, D. Dorer, J. P. D'Incao, P. S. Julienne, et al., "Controlling few-body reaction pathways using a Feshbach resonance", Nat. Phys. **21**, 228–232 (2025).

[308] R. L. Stratonovich, "On a Method of Calculating Quantum Distribution Functions", Sov. Phys. Dokl. **2** (1957).

[309] J. Hubbard, "Calculation of Partition Functions", Phys. Rev. Lett. **3**, 77–78 (1959).

[310] P. Ring and P. Schuck, *The Nuclear Many-Body Problem*, Physics and astronomy online library (Springer, 2004).

[311] G. Czycholl, *Solid State Theory, Volume 1: Basics: Phonons and Electrons in Crystals* (Springer, 2023).

[312] V. Apinyan and T. K. Kope, "Probing Phase Coherence Via Density of States for Strongly Correlated Excitons", J. Low Temp. Phys. **178**, 295–330 (2015).

[313] E. Vermeyen, C. A. R. Sá de Melo, and J. Tempere, "Exchange interactions and itinerant ferromagnetism in ultracold Fermi gases", Phys. Rev. A **98**, 023635 (2018).

[314] K. Seki and S. Sorella, "Benchmark study of an auxiliary-field quantum Monte Carlo technique for the Hubbard model with shifted-discrete Hubbard-Stratonovich transformations", Phys. Rev. B **99**, 144407 (2019).

[315] I. Boettcher, L. Bayha, D. Kedar, P. A. Murthy, M. Neidig, et al., "Equation of State of Ultracold Fermions in the 2D BEC-BCS Crossover Region", Phys. Rev. Lett. **116**, 045303 (2016).

[316] A. Behrle, T. Harrison, J. Kombe, K. Gao, M. Link, et al., "Higgs mode in a strongly interacting fermionic superfluid", Nat. Phys. **14**, 781–785 (2018).

[317] M. M. Parish, B. Mihaila, B. D. Simons, and P. B. Littlewood, "Fermion-Mediated BCS-BEC Crossover in Ultracold ^{40}K Gases", Phys. Rev. Lett. **94**, 240402 (2005).

[318] M. H. Szyma ska, K. Góral, T. Köhler, and K. Burnett, "Conventional character of the BCS-BEC crossover in ultracold gases of ^{40}K", Phys. Rev. A **72**, 013610 (2005).

[319] M. Grasso and M. Urban, "Hartree-Fock-Bogoliubov theory versus local-density approximation for superfluid trapped fermionic atoms", Phys. Rev. A **68**, 033610 (2003).

[320] M. Urban and S. Ramanan, "Low-momentum interactions for ultracold Fermi gases", Phys. Rev. A **103**, 063306 (2021).

[321] E. Neri, S. F. Caballero-Benítez, V. Romero-Rochín, and R. Paredes, "Pairing and molecule formation along the BCS-BEC crossover for finite range potentials", Phys. Scr. **95**, 034013 (2020).

[322] A. Sedrakian and J. W. Clark, "Superfluidity in nuclear systems and neutron stars", Eur. Phys. J. A **55**, 1–56 (2019).

[323] E. Noether, "Invariante Variationsprobleme", ger, Nachr. Ges. Wiss. Göttingen, Math.-phys. Kl. **1918**, 235–257 (1918).

[324] B. A. Bernevig, J. Orenstein, and S.-C. Zhang, "Exact SU(2) Symmetry and Persistent Spin Helix in a Spin-Orbit Coupled System", Phys. Rev. Lett. **97**, 236601 (2006).

[325] J. D. Koralek, C. P. Weber, J. Orenstein, B. A. Bernevig, S.-C. Zhang, et al., "Emergence of the persistent spin helix in semiconductor quantum wells", Nature **458**, 610–613 (2009).

[326] S. Giorgini, L. P. Pitaevskii, and S. Stringari, "Theory of ultracold atomic Fermi gases", Rev. Mod. Phys. **80**, 1215–1274 (2008).

[327] J. J. Kinnunen, J. E. Baarsma, J.-P. Martikainen, and P. Törmä, "The Fulde Ferrell Larkin Ovchinnikov state for ultracold fermions in lattice and harmonic potentials: a review", Rep. Prog. Phys. **81**, 046401 (2018).

[328] Y. Nambu, "Quasi-Particles and Gauge Invariance in the Theory of Superconductivity", Phys. Rev. **117**, 648–663 (1960).

[329] H. Kleinert, *Collective Classical And Quantum Fields: In Plasmas, Superconductors, Superfluid ^{3}He, And Liquid Crystals*, First (World Scientific Publishing Co. Pte. Ltd., 2017).

[330] H. Kleinert, "Quark pairs inside hadrons", Phys. Lett. B **59**, 163–167 (1975).

[331] H. Kleinert, "Hadronization of quark theories and a bilocal form of QED", Phys. Lett. B **62**, 429–432 (1976).

[332] A. Dalal, J. Ruhman, and V. Kozii, "Field theory of a superconductor with repulsion", Phys. Rev. B **108**, 214521 (2023).

[333] W. Weimer, K. Morgener, V. P. Singh, J. Siegl, K. Hueck, et al., "Critical Velocity in the BEC-BCS Crossover", Phys. Rev. Lett. **114**, 095301 (2015).

[334] H. Biss, L. Sobirey, N. Luick, M. Bohlen, J. J. Kinnunen, et al., "Excitation Spectrum and Superfluid Gap of an Ultracold Fermi Gas", Phys. Rev. Lett. **128**, 100401 (2022).

[335] H. A. Bethe, "Theory of the Effective Range in Nuclear Scattering", Phys. Rev. **76**, 38–50 (1949).

[336] L. B. Madsen, "Effective range theory", Am. J. Phys. **70**, 811–814 (2002).

[337] M. Macêdo-Lima and L. Madeira, "Scattering length and effective range of microscopic two-body potentials", Rev. Bras. Ensino Fís. **45**, e20230079 (2023).

[338] A. Banerjee, J. Autschbach, and A. Chakrabarti, "Time-dependent density-functional-theory calculation of the van der Waals coefficient C_6 of alkali-metal atoms Li, Na, K; alkali-metal dimers Li_2, Na_2, K_2; sodium clusters Na_n; and fullerene C_{60}", Phys. Rev. A **78**, 032704 (2008).

[339] C. A. Regal, M. Greiner, and D. S. Jin, "Lifetime of Molecule-Atom Mixtures near a Feshbach Resonance in ^{40}K", Phys. Rev. Lett. **92**, 083201 (2004).

[340] A. Perali, P. Pieri, G. C. Strinati, and C. Castellani, "Pseudogap and spectral function from superconducting fluctuations to the bosonic limit", Phys. Rev. B **66**, 024510 (2002).

[341] T. Enss, R. Haussmann, and W. Zwerger, "Viscosity and scale invariance in the unitary Fermi gas", Ann. Phys. (N. Y.) **326**, 770–796 (2011).

[342] J. Pera and J. Boronat, "Low-energy scattering parameters: A theoretical derivation of the effective range and scattering length for arbitrary angular momentum", Am. J. Phys. **91**, 90–101 (2023).

[343] S. Mal and B. Deb, "A model study on superfluidity of a unitary Fermi gas of atoms interacting with a finite-ranged potential", J. Phys. B **55**, 035301 (2022).

[344] A. Das, *Finite Temperature Field Theory*, 2nd (WORLD SCIENTIFIC, 2023).

[345] S. Tan, "Energetics of a strongly correlated Fermi gas", Ann. Phys. (N. Y.) **323**, 2952–2970 (2008).

[346] S. Tan, "Large momentum part of a strongly correlated Fermi gas", Ann. Phys. (N. Y.) **323**, 2971–2986 (2008).

[347] S. Tan, "Generalized virial theorem and pressure relation for a strongly correlated Fermi gas", Ann. Phys. (N. Y.) **323**, 2987–2990 (2008).

[348] F. Pistolesi and G. C. Strinati, "Evolution from BCS superconductivity to Bose condensation: Role of the parameter $k_F\xi$", Phys. Rev. B **49**, 6356–6359 (1994).

[349] J. Stalker, *Complex Analysis*, Modern Birkhäuser Classics (Birkhäuser, 1998).

[350] N. Pillet, N. Sandulescu, and P. Schuck, "Generic strong coupling behavior of Cooper pairs on the surface of superfluid nuclei", Phys. Rev. C **76**, 024310 (2007).

[351] A. A. Isayev, "Correlation functions for a di-neutron condensate in asymmetric nuclear matter", Phys. Rev. C **78**, 014306 (2008).

[352] N. Pillet, N. Sandulescu, P. Schuck, and J.-F. Berger, "Two-particle spatial correlations in superfluid nuclei", Phys. Rev. C **81**, 034307 (2010).

[353] E. B. Balbutsev, L. A. Malov, and P. Schuck, "Spatial dependence of pairing in deformed nuclei", Phys. At. Nucl. **74**, 1651–1654 (2011).

[354] R.-D. Lasseri, J.-P. Ebran, E. Khan, and N. Sandulescu, "Localization of pairing correlations in nuclei within relativistic mean field models", Phys. Rev. C **98**, 014310 (2018).

[355] E. Litvinova and P. Schuck, "Many-body correlations in nuclear superfluidity", Phys. Rev. C **102**, 034310 (2020).

[356] E. Altman, E. Demler, and M. D. Lukin, "Probing many-body states of ultracold atoms via noise correlations", Phys. Rev. A **70**, 013603 (2004).

[357] F. Werner and Y. Castin, "General relations for quantum gases in two and three dimensions: Two-component fermions", Phys. Rev. A **86**, 013626 (2012).

[358] J. C. Obeso-Jureidini, G. A. Domínguez-Castro, E. Neri, R. Paredes, and V. Romero-Rochín, "Universal correlations along the BEC-BCS crossover", New J. Phys. **25**, 113019 (2023).

[359] T. Hanaguri, S. Kasahara, J. Böker, I. Eremin, T. Shibauchi, and Y. Matsuda, "Quantum Vortex Core and Missing Pseudogap in the Multiband BCS-BEC Crossover Superconductor FeSe", Phys. Rev. Lett. **122**, 077001 (2019).

[360] C. P. Moca, I. Weymann, M. A. Werner, and G. Zaránd, "Kondo Cloud in a Superconductor", Phys. Rev. Lett. **127**, 186804 (2021).

[361] Y. Nakagawa, Y. Kasahara, T. Nomoto, R. Arita, T. Nojima, and Y. Iwasa, "Gate-controlled BCS-BEC crossover in a two-dimensional superconductor", Science **372**, 190–195 (2021).

[362] Y. Mizukami, M. Haze, O. Tanaka, K. Matsuura, D. Sano, et al., "Unusual crossover from Bardeen-Cooper-Schrieffer to Bose-Einstein-condensate superconductivity in iron chalcogenides", Commun. Phys. **6**, 183 (2023).

[363] T. Kaneko, H. Sakakibara, M. Ochi, and K. Kuroki, "Pair correlations in the two-orbital Hubbard ladder: Implications for superconductivity in the bilayer nickelate $La_3Ni_2O_7$", Phys. Rev. B **109**, 045154 (2024).

[364] J. C. Estrada Saldaña, A. Vekris, L. Pavei, R. itko, K. Grove-Rasmussen, and J. Nygård, "Correlation between two distant quasiparticles in separate superconducting islands mediated by a single spin", Nat. Commun. **15**, 3465 (2024).

[365] C.-H. Huang, A. Skurativska, F. S. Bergeret, and M. A. Cazalilla, "Probing magnetic and triplet correlations in spin-split superconductors with magnetic impurities", Phys. Rev. Res. **6**, 033022 (2024).

[366] M. Thumin and G. Bouzerar, "Correlation functions and characteristic lengthscales in flat band superconductors", SciPost Phys. **18**, 025 (2025).

[367] D. K. Mark, H.-Y. Hu, J. Kwan, C. Kokail, S. Choi, and S. F. Yelin, "Efficiently Measuring d-Wave Pairing and Beyond in Quantum Gas Microscopes", Phys. Rev. Lett. **135**, 123402 (2025).

[368] T. Alm, G. Röpke, A. Schnell, and H. Stein, "Two-nucleon correlations and the nucleon spectral function in nuclear matter at finite temperature: low-density region", Phys. Lett. B **346**, 233–239 (1995).

[369] T. Frick, H. Müther, A. Rios, A. Polls, and A. Ramos, "Correlations in hot asymmetric nuclear matter", Phys. Rev. C **71**, 014313 (2005).

[370] J.-B. Wei, F. Burgio, and H.-J. Schulze, "Nuclear Pairing Gaps and Neutron Star Cooling", Universe **6**, 10.3390/universe6080115 (2020).

[371] D. Durel and M. Urban, "BCS-BEC Crossover Effects and Pseudogap in Neutron Matter", Universe **6**, 10.3390/universe6110208 (2020).

[372] T. S. Wood and V. Graber, "Superconducting Phases in Neutron Star Cores", Universe **8**, 10.3390/universe8040228 (2022).

[373] Y. Minami and G. Watanabe, "Effects of pairing gap and band gap on superfluid density in the inner crust of neutron stars", Phys. Rev. Res. **4**, 033141 (2022).

[374] H.-F. Zhu, X. Wu, and G.-Z. Liu, "Nonperturbative study of quantum many-body correlation effects in neutron stars: Equation of state", Phys. Rev. C **110**, 035810 (2024).

[375] A. Sedrakian, "Short-Range Correlations and Urca Process in Neutron Stars", Phys. Rev. Lett. **133**, 171401 (2024).

[376] J. Hofmann and W. Zwerger, "Deep Inelastic Scattering on Ultracold Gases", Phys. Rev. X **7**, 011022 (2017).

[377] B. Mukherjee, P. B. Patel, Z. Yan, R. J. Fletcher, J. Struck, and M. W. Zwierlein, "Spectral Response and Contact of the Unitary Fermi Gas", Phys. Rev. Lett. **122**, 203402 (2019).

[378] H. Deng, C. Li, Y. Wu, L. Sun, and Q. Chen, "Flat band effects on the ground-state BCS-BEC crossover in atomic Fermi gases in a quasi-two-dimensional Lieb lattice", Ann. Phys. (N. Y.) **463**, 169639 (2024).

[379] E. Dizer, J. Horak, and J. M. Pawlowski, "Spectral properties and observables in ultracold Fermi gases", Phys. Rev. A **109**, 063311 (2024).

[380] S. N. Klimin, J. Tempere, and H. Kurkjian, "Phononic collective excitations in superfluid Fermi gases at nonzero temperatures", Phys. Rev. A **100**, 063634 (2019).

[381] S. Van Loon, J. Tempere, and H. Kurkjian, "Beyond Mean-Field Corrections to the Quasiparticle Spectrum of Superfluid Fermi Gases", Phys. Rev. Lett. **124**, 073404 (2020).

[382] M. Bohlen, L. Sobirey, N. Luick, H. Biss, T. Enss, et al., "Sound Propagation and Quantum-Limited Damping in a Two-Dimensional Fermi Gas", Phys. Rev. Lett. **124**, 240403 (2020).

[383] C. R. Cabrera, R. Henke, L. Broers, J. Skulte, H. P. O. Collado, et al., "Hybridization of the amplitude mode in a confined fermionic superfluid", Phys. Rev. Res. **7**, L032018 (2025).

[384] W. S. Bakr, J. I. Gillen, A. Peng, S. Fölling, and M. Greiner, "A quantum gas microscope for detecting single atoms in a Hubbard-regime optical lattice", Nature **462**, 74–77 (2009).

[385] J. G. Danzl, M. J. Mark, E. Haller, M. Gustavsson, R. Hart, et al., "An ultracold high-density sample of rovibronic ground-state molecules in an optical lattice", Nat. Phys. **6**, 265–270 (2010).

[386] L. W. Cheuk, M. A. Nichols, M. Okan, T. Gersdorf, V. V. Ramasesh, et al., "Quantum-Gas Microscope for Fermionic Atoms", Phys. Rev. Lett. **114**, 193001 (2015).

[387] L. W. Cheuk, M. A. Nichols, K. R. Lawrence, M. Okan, H. Zhang, et al., "Observation of spatial charge and spin correlations in the 2D Fermi-Hubbard model", Science **353**, 1260–1264 (2016).

[388] S. Hollerith, J. Zeiher, J. Rui, A. Rubio-Abadal, V. Walther, et al., "Quantum gas microscopy of Rydberg macrodimers", Science **364**, 664–667 (2019).

[389] C. Gross and W. S. Bakr, "Quantum gas microscopy for single atom and spin detection", Nat. Phys. **17**, 1316–1323 (2021).

[390] A. M. Kaufman and K.-K. Ni, "Quantum science with optical tweezer arrays of ultracold atoms and molecules", Nat. Phys. **17**, 1324–1333 (2021).

[391] I. O. Kulik, O. Entin-Wohlman, and R. Orbach, "Pair susceptibility and mode propagation in superconductors: A microscopic approach", J. Low Temp. Phys. **43**, 591–620 (1981).

[392] H. Guo, C.-C. Chien, Y. He, and K. Levin, "FUNDAMENTAL CONSTRAINTS ON LINEAR RESPONSE THEORIES OF FERMI SUPERFLUIDS ABOVE AND BELOW Tc", Int. J. Mod. Phys. B **27**, 1330010 (2013).

[393] H. Guo, Y. He, C.-C. Chien, and K. Levin, "Compressibility in strongly correlated superconductors and superfluids: From the BCS regime to Bose-Einstein condensates", Phys. Rev. A **88**, 043644 (2013).

[394] H. Guo, C.-C. Chien, and Y. He, "Theories of Linear Response in BCS Superfluids and How They Meet Fundamental Constraints", J. Low Temp. Phys. **172**, 5–46 (2013).

[395] H. Guo, Y. Li, Y. He, and C.-C. Chien, "Density and spin linear response of atomic Fermi superfluids with population imbalance in the BCSBEC crossover", J. Phys. B **47**, 085302 (2014).

[396] H. Guo and Y. He, "Theoretical Approach to the Gauge Invariant Linear Response Theories for Ultracold Fermi Gases with Pseudogap", Adv. Cond. Mat. Phys. **2015**, 582734 (2015).

[397] B. M. Anderson, R. Boyack, C.-T. Wu, and K. Levin, "Going beyond the BCS level in the superfluid path integral: A consistent treatment of electrodynamics and thermodynamics", Phys. Rev. B **93**, 180504 (2016).

[398] R. Boyack, B. M. Anderson, C.-T. Wu, and K. Levin, "Gauge-invariant theories of linear response for strongly correlated superconductors", Phys. Rev. B **94**, 094508 (2016).

[399] H. Guo, Y. He, and L. He, "Dynamic density structure factor of a unitary Fermi gas at finite temperature", J. Phys. Comm. **2**, 045008 (2018).

[400] G. Baym and L. P. Kadanoff, "Conservation Laws and Correlation Functions", Phys. Rev. **124**, 287–299 (1961).

[401] M. Revzen, T. Toyoda, Y. Takahashi, and F. C. Khanna, "Baym-Kadanoff criteria and the Ward-Takahashi relations in many-body theory", Phys. Rev. B **40**, 769–771 (1989).

[402] M. P. von Friesen, C. Verdozzi, and C.-O. Almbladh, "Successes and Failures of Kadanoff-Baym Dynamics in Hubbard Nanoclusters", Phys. Rev. Lett. **103**, 176404 (2009).

[403] F. Krien, A. Kauch, and K. Held, "Tiling with triangles: parquet and $GW\gamma$ methods unified", Phys. Rev. Res. **3**, 013149 (2021).

[404] F. Green and T. L. Ainsworth, "Hamiltonian perspective on parquet theory", Phys. Rev. A **106**, 052208 (2022).

[405] A. A. Katanin, "Fulfillment of Ward identities in the functional renormalization group approach", Phys. Rev. B **70**, 115109 (2004).

[406] J. F. Rentrop, V. Meden, and S. G. Jakobs, "Renormalization group flow of the Luttinger-Ward functional: Conserving approximations and application to the Anderson impurity model", Phys. Rev. B **93**, 195160 (2016).

[407] Y. He, Y.-X. Wang, and H. Guo, "Establishing gauge invariant linear response of fermionic superfluids with pair fluctuations: A diagrammatic approach", Phys. Lett. A **381**, 1603–1610 (2017).

[408] J. C. Ward, "An Identity in Quantum Electrodynamics", Phys. Rev. **78**, 182–182 (1950).

[409] Y. Takahashi, "On the generalized Ward identity", Nuovo Cim. **6**, 371–375 (1957).

[410] S. Allen, A. .-M. S. Tremblay, and Y. M. Vilk, "Conserving Approximations vs. Two-Particle Self-Consistent Approach", in *Theoretical Methods for Strongly Correlated Electrons*, edited by D. Sénéchal, A.-M. Tremblay, and C. Bourbonnais (Springer New York, 2004), pp. 341–355.

[411] H. Kleinert, *Path Integrals in Quantum Mechanics, Statistics, Polymer Physics, and Financial Markets*, Fifth, EBL-Schweitzer (World Scientific, 2009).

[412] G. C. Wick, "The Evaluation of the Collision Matrix", Phys. Rev. **80**, 268–272 (1950).

[413] S. Kangjun and C. A. R. Sá de Melo, *Compressibility and spin susceptibility in the evolution from BCS to BEC superfluids*, 2011.

[414] D. S. Petrov and G. V. Shlyapnikov, "Interatomic collisions in a tightly confined Bose gas", Phys. Rev. A **64**, 012706 (2001).

[415] S. S. Botelho and C. A. R. Sá de Melo, "Vortex-Antivortex Lattice in Ultracold Fermionic Gases", Phys. Rev. Lett. **96**, 040404 (2006).

[416] K. Viebahn, "Superconductor Theory Under Cold-Atom Scrutiny", Physics **19**, 54 (2026).

[417] J. R. Engelbrecht, M. Randeria, and L. Zhang, "Landau f function for the dilute Fermi gas in two dimensions", Phys. Rev. B **45**, 10135–10138 (1992).

[418] L. Salasnich, "Goldstone and Higgs Hydrodynamics in the BCSBEC Crossover", Condens. Matter **2**, 10.3390/condmat2020022 (2017).

[419] C. Zhao, L. Jiang, X. Liu, W. M. Liu, X. Zou, and H. Pu, "Hartree-Fock-Bogoliubov theory of dipolar Fermi gases", Phys. Rev. A **81**, 063642 (2010).

[420] S. S. Botelho, *BCS-to-BEC quantum phase transition in high-Tc superconductors and fermionic atomic gases: A functional integral approach* (Georgia Institute of Technology, 2005).

[421] L. Radzihovsky and D. E. Sheehy, "Imbalanced Feshbach-resonant Fermi gases", Rep. Prog. Phys. **73**, 076501 (2010).

[422] G. Sarma, "On the influence of a uniform exchange field acting on the spins of the conduction electrons in a superconductor", J. Phys. Chem. Sol. **24**, 1029–1032 (1963).

[423] E. Lipparini, *Modern Many-particle Physics: Atomic Gases, Nanostructures and Quantum Liquids* (World Scientific, 2008).

[424] H. Schneider, "Lecture Notes: Theoretical Solid State Physics 1 + 2", Technische Universität Kaiserslautern, SS19 (2019).

[425] D. J. Candlin, "On sums over trajectories for systems with Fermi statistics", Nuovo Cim. **4**, 231–239 (1956).

[426] H. Kleinert, "How to do the time sliced path integral of the H atom", Phys. Lett. A **120**, 361–366 (1987).

[427] H. Kleinert, "Path collapse in Feynman formula. Stable path integral formula from local time reparametrization invariant amplitude", Phys. Lett. B **224**, 313–318 (1989).

[428] M. Laine and A. Vuorinen, *Basics of Thermal Field Theory*, Vol. 925 (Springer, 2016).

[429] M. G. Mustafa, "An introduction to thermal field theory and some of its application", Eur. Phys. J. Spec. Top **232**, 1369–1457 (2023).

[430] A. Zee, *Quantum field theory in a nutshell*, second edition (Princeton University Press, 2010).

[431] A. A. Abrikosov, L. P. Gorkov, and I. Dzyaloshinskii, *Methods of quantum field theory in statistical physics* (Dover, 1975).

Fachbereich Physik

Rheinland-Pfälzische Technische
Universität Kaiserslautern Landau

Postfach 3049
67653 Kaiserslautern, Germany

www.physik.rptu.de/

Rheinland-Pfälzische
Technische Universität
Kaiserslautern
Landau